Université de Strasbourg

UNIVERSITÉ DE STRASBOURG

École doctorale Sciences de la terre et de l'environnement | ED 413 Université de Strasbourg

ÉCOLE DOCTORALE 413 : Sciences de la Terre et de l'Environnement

Institut Terre et Environnement de Strasbourg

THÈSE présentée par / DISSERTATION presented by :

Estelle NEYRINCK

soutenue le /defended on : **25 June 2026**

pour obtenir le grade de / to obtain the grade of :

Docteure de l'Université de Strasbourg / Strasbourg University Doctor

Discipline (Spécialité) / Discipline (Specialty) : Géophysique / Geophysics

Dynamics of transient aseismic slip along the North Anatolian Fault from InSAR observations

THÈSE dirigée par / DISSERTATION supervisor :

DOUBRE Cécile	Physicienne du Globe, ITES/EOST, Université de Strasbourg

RAPPORTEURS / REVIEWERS :

RADIGUET Mathilde	Physicienne-Adjointe du Globe, ISTerre, Université Grenoble Alpes
NOCQUET Jean-Mathieu	Directeur de recherche IRD at Géoazur and IPGP

AUTRES MEMBRES DU JURY / OTHER MEMBERS OF THE JURY :

LASSERRE Cécile	Directrice de recherche CNRS, LGL-TPE, Université de Lyon
MATERNA Kathryn	Associate Professor, University of Colorado Boulder
FRANK William	Associate Professor, Massachusetts Institute of Technology, Boston

---

INVITÉ/ GUEST :

RIVERA Luis	Professeur, ITES/EOST, Université de Strasbourg
ROUSSET Baptiste	Chargé de recherche CNRS, ITES/EOST, Université de Strasbourg Co-encadrant

CC BY

"I had a blank canvas to fill with extraordinary possibilities, a fascinating jigsaw puzzle to piece together."

Marie Tharp (1920-2006)

Remerciements

Avant toute chose, il est nécessaire de souligner que le travail ci-après a été rendu possible grâce à l'aide de nombreuses personnes qui m'ont guidée, épaulée et soutenue, et ont réussi à faire de ces dernières années un moment à la fois riche et inoubliable.

Dans un premier temps, je souhaiterai remercier mes deux rapporteurs Mathilde Radiguet et Jean-Mathieu Nocquet pour leurs rapports de soutenance très détaillés soulevant de nombreux points de discussions pertinents. Je souhaiterai aussi remercier mes examinateurs Cécile Lasserre (présidente du jury), Kathryn Materna et William Frank qui, par leurs remarques et questions, ont permis d'agrémenter la discussion de nouvelles perspectives.

Les différents travaux proposés dans ce manuscrit sont les produits de nombreux échanges: Luis Rivera, Meng Wei, Yoshihiro Kaneko, Émilie Klein, Frédéric Masson, Roger Bilham et Ziyadin Cakir. Je tiens évidemment à remercier l'équipe FLATSIM, et en particulier Cécile Lasserre, Marie-Pierre Doin et Philippe Durand avec qui j'ai pu beaucoup échanger pendant ma thèse afin de prendre en main les données mises à disposition. De plus, les échanges durant ces dernières années avec Olivier Lengliné et Simon Daout en tant que membres de mon Comité de Suivi Individuel (CSI) ont également permis d'avoir un regard extérieur bienveillant sur le bon déroulement de la thèse, que ce soit d'un point de vue scientifique et personnel. Lors de ma thèse, j'ai aussi eu l'occasion de me rendre deux fois en Turquie en compagnie de Baptiste Rousset, Patrice Ulrich, Cyril Lacroix et Ali Özkan, que je remercie énormément pour m'avoir permis de découvrir le domaine de l'acquisition de données, mais aussi de goûter les meilleurs baklavas de la Terre et de fêter mon anniversaire à Adana (avec des pâtisseries incroyables !).

Bien évidemment, et ce non pas sans émotion, je souhaite remercier mes deux directeurs de thèse Cécile Doubre et Baptiste Rousset. Le manuscrit étant assez long, je vais tenter d'être exhaustive malgré le nombre de choses que j'ai à dire ici. Je vous remercie pour votre temps, votre confiance, votre bienveillance et votre partage. Tout le travail qui s'en suit n'a été possible que grâce à des échanges toujours motivants et enthousiastes, pendant lesquels vous avez toujours été à l'écoute, me permettant de travailler ces dernières années dans un cadre parfait. De manière plus personnelle, je suis extrêmement heureuse d'avoir eu l'occasion de vous rencontrer et découvrir, et je dois avouer, presque un peu déçue que la thèse se termine car c'est une grande aventure avec vous qui s'achève. Je vous remercie pour tout ce que vous m'avez appris, et j'ai hâte de re-échanger avec vous dans le futur !

L'environnement de travail étant aussi non négligeable à une thèse agréable, j'aimerai remercier mes collègues, et tout d'abord, mes "collocs" de bureau : Rénier, Zaur et Hamza. Ça a été un réel plaisir de partager avec vous des conversations scientifiques, mais aussi et surtout les pauses café, des blagues, quelques gossip ... bref pleins de beaux moments conviviaux ! *Rénier and Zaur, I aslo have to thank you for the english training haha !* Ensuite, je remercie l'équipe DADR de l'ITES qui m'a accueillie pendant ma thèse, et aussi l'équipe Sismo avec qui j'ai pu aussi beaucoup apprendre et échanger. Enfin, je tiens à remercier de nombreux stagiaires/doctorants/post-doctorants qui ont croisé ma route en espérant n'oublier personne (avec un détail mémorable parmi tant) : Anna (l'escalade haha), Auriane (ton rire si incroyable), Béla (les tiramisus), Camille (ta positivité), Charlotte (ta bienveillance), Cyril (la Chartreuse), Emile (tes pulls de Noël), Emma (the *À l'ombre des* pensées), Farès (tes histoires toujours fascinantes), Joachim (caaafffééé), Lisa (tes récits sportifs toujours aussi fous), Louis (les brocolis),

Lucille (les concerts), Mérédith (les soirées inoubliables), Nico (les traquenards), Pablo (your kindness), Philippe (les ginger beer), Rémi (ton énergie), Roxane (le terrain à Digne), Valentin (le vent). Une petite mention spéciale pour Bastien et Flavien qui resteront mes frères de thèse et que je remercie énormément pour les personnes qu'ils sont et les amis qu'ils sont devenus.

L'environnement tout court étant aussi non négligeable, un immense merci à Margaux et Florian pour votre gentillesse sans limite, à Cam et Morgane pour les soleils que vous êtes, à Samya pour juste être la personne la plus géniale de la Terre, et à Adrien et Lulu pour la dose de fraîcheur (et aussi de bière) ! Et puisqu'au XXIe siècle, on peut aussi communiquer avec des personnes en dehors de notre belle cité strasbourgeoise, je souhaite remercier les personnes qui m'ont supportées et continuent de le faire : Marine, Quentin, Jean, Ugo, Bolito, Cécile, Camille. Un énorme merci à Anna, qui pour le coup me supporte depuis beaucoup d'années, et j'espère encore bien plus dans le futur !

Un immense merci à ma famille, qui a toujours tout mis en place pour que j'en arrive à ce point : maman, papa, Elodie, Jojo, Ewoenam et petit Elio. Vous m'avez soutenu tout au long de mes études, et cela même malgré le fait qu'elles paraissaient interminables. Et le plus exceptionnel pour moi, est que vous avez toujours cru en moi même lorsque moi je n'y arrivais plus, me donnant le courage et la possibilité d'en arriver à ce travail ci-après. Alors, merci pour tout ! Et pour finir, un gigantesque merci à Thomas, sans qui la fin de thèse aurait été très différente. Merci de m'avoir soutenue, aidée, supportée et d'avoir toujours été persuadé que tout allait bien se passer. Merci pour toute ta bienveillance, et merci d'être dans ma vie !

Abstract

The deformation associated with the relative motion of tectonic plates is mainly localized along interplate faults, which may be locked at depth, leading to the accumulation of elastic stress. The initiation and propagation of a seismic rupture release most of the energy almost instantaneously. Some of this energy may also be released aseismically, particularly in the form of slow slips that produce little or no seismic radiation.

Over the past two decades, improvements in and the increasing availability of geodetic observations have led to the detection of slow slip events (SSEs). Initially identified in subduction zones, these events have since been documented in several tectonic settings. However, the mechanisms controlling their occurrence and physical characteristics (location, depth, duration, size, and slip amplitude) remain poorly understood to this day. Some studies have nevertheless shown that SSEs can occur at distinct stages of the seismic cycle, sometimes interacting with earthquakes which they may trigger or by which they may be triggered; and others have suggested that their occurrence could be induced by external forces, seasonal or otherwise, such as hydrology. A better description of SSEs is therefore essential to better understand the mechanisms controlling the seismic and aseismic slip behaviors of fault, and consequently to improve seismic hazard assessment.

Among the available methods, Interferometric Synthetic Aperture Radar (InSAR) which uses SAR satellite imagery, is a particularly well-suited tool for studying surface deformation. Thanks to its spatial coverage and sensitivity to centimeter-scale displacements, it offers great potential for detecting and characterizing SSEs along major continental faults.

The North Anatolian Fault (NAF) in Türkiye provides an ideal setting for study. Since the 1930s, it has been affected by a sequence of seven major earthquakes (magnitude $M_w \geq 7$) propagating from east to west, the most recent being the Izmit (M_w 7.6) and Düzce (M_w 7.2) earthquakes in 1999. The portion of the fault crossing the Sea of Marmara located near Istanbul constitutes a major seismic gap, which motivates research on this area including the adjacent Izmit segment. Recent studies have highlighted the occurrence of SSEs along this segment 16 to 17 *years* after the 1999 earthquake. Its geotectonic context makes it a natural laboratory for studying slip behavior along major continental strike-slip faults, and in particular the mechanisms controlling SSEs.

In this context, the objective of this thesis is to detect, characterize, and model transient slow slips along the NAF by combining InSAR observations which allow for the measurement of the temporal evolution of millimeter-scale ground surface movements, with mechanical modeling. This work aims to better constrain the processes driving seismic and aseismic deformation along this fault.

To do so, I used time series of InSAR displacements covering the period 2016˘2021, derived from *Sentinel-1* radar images and automatically processed as part of the FLATSIM project (a national initiative developed in collaboration between Formater and CNES), based on a "Small Baselines" (NSBAS) processing chain. These products provide dense spatial coverage over continental areas and a temporal resolution of 6 to 12 *days*, corresponding to the revisit cycle of the *Sentinel-1A/B* satellites.

First, I used this exceptional dataset, which covers nearly all of Türkiye, to estimate a large-scale steady-state InSAR tectonic deformation field. A horizontal and vertical decomposition

of the mean velocity field revealed major horizontal deformation associated with the North and East Anatolian faults, as well as more localized phenomena such as the subsidence of sedimentary basins in southwestern Türkiye and anthropogenic deformation linked to the presence of quarries and mines. The details of the deformation field obtained confirm the existence of shallow aseismic slip along the Izmit and Ismetpasa segments. Furthermore, I reprocessed incomplete InSAR tracks to measure the deformation field in the northwestern section and to study the seismic gap in the Sea of Marmara. The joint analysis of these data with GNSS data, carried out by collaborators, aims to estimate the coupling along the fault interface and thus to refine the seismic risk in the Istanbul metropolitan area.

Second, I implemented a method for automatically detecting SSEs in InSAR time series. Originally developed for GNSS time series, this method involves correlating physical slip models (dislocations) representing synthetic SSEs with InSAR time series to identify transient deformation signals that may correspond to SSEs and then to estimate their primary spatiotemporal characteristics (location on the fault interface, initiation time, equivalent magnitude). This method was calibrated using synthetic tests incorporating realistic InSAR noise, then applied to real data focused on the two aseismic creeping segments of the NAF: Izmit and Ismetpasa. The automatic detection of SSEs from InSAR data was first evaluated on datasets with varying levels of noise, depending on the degree of post-processing applied. Synthetic tests incorporating realistic noise made it possible to define probabilistic detection thresholds based on the magnitude and depth of the SSEs. These tests show that the method can detect, with a confidence level greater than or equal to 90 %, shallow SSEs with a magnitude greater than 4.5 from East-West horizontal InSAR time series. It also allows for the detection of events with magnitudes greater than 4.3 with a confidence level of at least 45 %. By applying this method to real data, I was able to detect without prior knowledge three transient events previously reported along the Izmit segment and two along the Ismetpasa segment, with estimated magnitudes ranging from 4.0 to 4.5. I was thus able to validate the methodological approach adapted to spatialized data and confirm the quality of the automatically processed InSAR time series. Despite the high level of noise in the geodetic data, they can indeed be used to extract tectonic signals, particularly slow slip events on the order of a few millimeters, thus representing datasets that are essential for understanding seismic cycles along continental strike-slip faults. Applying this approach on a global scale could enable rapid detection and a first-order characterization of transient slip events.

In the third chapter, I focused on the SSEs detected along the Izmit segment. I developed a post-processing sequence to extract the tectonic signal from the InSAR time series, including GNSS-based referencing, correction for seasonal components, and separation of different sources using independent component analysis (ICA). The time series processed in this way were then used in inverse models to reconstruct the distribution of slip at depth along this fault segment, embedded in a layered elastic half-space. These observations were combined with data from creepmeters to better characterize the temporal dynamics of the SSEs. A detailed analysis of the last two events detected along the Izmit segment in March 2018 and November 2019 reveals magnitudes ranging from 4.3 to 4.4. The associated slip is localized at shallow depth, within the Quaternary sedimentary basin. I also identified a steady-state aseismic slip, mostly located between 2 and 5 km deep just below the sedimentary basin, and likely contributing to the loading of the asperities responsible for the SSEs. Records from two creepmeters during the 2019 event confirm the occurrence of a SSE and allow us for an estimated lateral propagation velocity of 6.4 km/day. Analysis of SSEs along the Izmit segment thus confirms the periodic occurrence of SSEs approximately 20 *years* after the 1999 Izmit earthquake. These observations support a conceptual model in which shallow SSEs develop preferentially in fault segments surrounded by zones of steady-state aseismic slip, and within sedimentary basins where frictional heterogeneity, more deformable materials, and fluid effects combine to produce conditionally stable slip.

Finally, I used mechanical models to reproduce the seismic cycle of the Izmit segment within the framework of the "rate-and-state" friction formalism. Numerical simulations were performed using a quasi-dynamic approach, with a one-dimensional strike-slip fault embedded in a two-dimensional elastic half-space. These numerical simulations allow us for the reproduction of several observations at different time scales: the magnitude and recurrence interval of major earthquakes, time series of postseismic displacements from GNSS campaigns, as well as the magnitude, recurrence, and duration of shallow SSEs. Numerical simulations of the seismic cycle along the Izmit segment have helped clarify the frictional properties of the various deep layers of the fault and their influence on the deformation observed at the surface. The recurrence interval and coseismic displacements are controlled by the velocity-weakening layer corresponding to the seismogenic zone as well as by plate loading rates. The overlying velocity-strengthening layer, defined based on the upper boundary of the aftershocks of the 1999 Izmit earthquake, helps explain the postseismic deformation. Finally, the properties of surface frictional heterogeneity control the duration and recurrence time of SSEs. The surrounding steady-state aseismic slip likely provides the background deformation necessary to load localized zones of velocity weakening, leading to recurrent transient slips. The similarity with observations made in California suggests that these structural and hydromechanical conditions could constitute a common mechanism for the occurrence of shallow SSEs on a global scale. Mechanical models reinforce this interpretation by showing that surface friction heterogeneities favor the emergence of recurrent SSEs.

This research focused on the NAF has helped clarify its seismic behavior, particularly along the Izmit segment, revealing the occurrence of shallow SSEs with a return period of approximately 1.3 *years*. However, it is crucial to increase the number of SSE detections in order to enrich existing catalogs and more clearly identify the common characteristics of different SSEs, suggesting the conditions favorable to their development and their role in seismic hazard. The combination of geodetic observations and microseismicity measurements is also essential for better constraining the dynamics of transient creep, highlighting the need for dense seismic and geodetic networks capable of capturing both aseismic and seismic activity. With this in mind, a dense GNSS network to which I contributed, was installed along the Izmit segment in 2024 to acquire geodetic data with high temporal resolution. Combined with the high spatial resolution of InSAR observations, these data will allow for a more detailed characterization of the slip dynamics. Ultimately, comparing the behavior of SSEs along strike-slip faults with the well-documented cycles observed in subduction zones could help identify common mechanisms controlling slow slip in different tectonic contexts.

Résumé court en français

La déformation associée au mouvement relatif des plaques tectoniques est principalement localisée le long de failles inter-plaques qui peuvent être bloquées en profondeur, entraînant l'accumulation de contraintes élastiques. La nucléation et la propagation d'une rupture sismique libèrent la majeure partie de l'énergie de manière quasi instantanée. Une partie de cette énergie peut par ailleurs être libérée de manière asismique, notamment sous la forme de glissements lents produisant peu ou pas de rayonnement sismique.

Au cours des deux dernières décennies, l'amélioration et la disponibilité croissante des observations géodésiques ont conduit à la mise en évidence d'événements de glissements lents transitoires (slow slip events, SSEs). Initialement identifiés dans les zones de subduction, ces événements ont depuis été documentés dans plusieurs contextes tectoniques. Cependant, les mécanismes contrôlant leur occurrence et leurs caractéristiques physiques (localisation, profondeur, durée, taille, amplitude du glissement) restent encore mal compris à ce jour. Certaines études ont néanmoins montré que les SSEs peuvent se produire à différents stades du cycle sismique, parfois en interaction avec des séismes, qu'ils peuvent déclencher ou par lesquels ils peuvent être déclenchés; et d'autres ont suggéré que leur occurrence pouvait être induite par des forçages externes, saisonniers ou non, tels que l'hydrologie. Une meilleure description des SSEs est donc essentielle pour mieux comprendre les mécanismes contrôlant le potentiel sismique et asismique des glissements sur les failles, et par conséquent améliorer l'évaluation de l'aléa sismique.

Parmi les approches disponibles, l'Interférométrie Radar (InSAR), construite à partir d'images satellitaires SAR, constitue un outil particulièrement adapté à l'étude de la déformation de surface. Grâce à sa couverture spatiale et sa sensibilité aux déplacements centimétriques, elle offre un fort potentiel pour la détection et caractérisation de SSEs le long de failles continentales majeures.

La faille nord-anatolienne (NAF) en Turquie représente un cadre d'étude privilégié. Depuis les années 1930, elle a été affectée par une séquence de sept séismes majeurs (magnitude $M_w \geq 7$) se propageant d'est en ouest, les plus récents étant les séismes d'Izmit (M_w 7,6) et de Düzce (M_w 7,2) en 1999. La portion de faille traversant la mer de Marmara, située à proximité d'Istanbul, constitue une lacune sismique majeure, ce qui motive les recherches sur cette zone, dont le segment adjacent d'Izmit. Des études récentes ont mis en évidence l'occurrence de SSEs le long de ce segment 16 à 17 ans après le séisme de 1999. Son contexte géotectonique en fait un laboratoire naturel permettant l'étude du comportement de glissement le long des grandes failles décrochantes continentales, et en particulier les mécanismes contrôlant les SSEs.

Dans ce contexte, l'objectif de cette thèse est de détecter, caractériser et modéliser les glissements lents transitoires le long de la NAF, en combinant observations InSAR permettant de mesurer l'évolution temporelle des mouvements millimétriques de la surface du sol et modélisations mécaniques. Ce travail vise à mieux contraindre les processus à l'origine de la déformation sismique et asismique le long de cette faille.

Pour ce faire, j'ai exploité des séries temporelles de déplacements InSAR couvrant la période 2016-2021, dérivées d'images radar Sentinel-1 et traitées automatiquement dans le cadre du projet FLATSIM (une initiative nationale développée en collaboration entre Formater et le CNES), basée sur une chaîne de traitement "Small Baselines" (NSBAS). Ces produits offrent

une couverture spatiale dense sur les zones continentales et une résolution temporelle de 6 à 12 jours, correspondant au cycle de revisite des satellites Sentinel-1A/B.

Premièrement, j'ai exploité ce jeu de données exceptionnelles couvrant la quasi-totalité de la Turquie afin d'en estimer un champ de déformation tectonique continu InSAR à grande échelle. Une décomposition horizontale et verticale du champ de vitesse moyenne a permis la mettre en évidence de la déformation horizontale majeure liée aux failles nord- et est-anatoliennes, ainsi que des phénomènes plus locaux tels que la subsidence de bassins sédimentaires au sud-ouest de la Turquie ou encore des déformation anthropiques liées à la présence de carrières/mines. Les détails du champ déformation obtenu valident l'existence de glissements asismiques superficiels le long des segments d'Izmit et d'Ismetpasa. De plus, j'ai re-traité des fauchées InSAR incomplètes afin de mesurer le champ de déformation de la partie nord-ouest, et d'étudier la lacune sismique en mer de Marmara. L'analyse jointe de ces données avec des données GNSS, réalisée par des collaborateurs, a pour but d'estimer le couplage le long de l'interface de faille, et ainsi de préciser le risque sismique dans la région de la mégalopole d'Istanbul.

Deuxièmement, j'ai mis en œuvre une méthode de détection automatique des SSEs dans les séries temporelles InSAR. Initialement développée pour des séries GNSS, cette méthode consiste à corréler des modèles physiques de glissement (dislocations) représentant des SSEs synthétiques avec les séries temporelles InSAR afin d'identifier des signaux de déformation transitoire pouvant correspondre à des SSEs et d'en estimer les caractéristiques spatio-temporelles de premier ordre (localisation sur l'interface de faille, temps d'initiation, magnitude équivalente). Cette méthode a été calibrée à l'aide de tests synthétiques incluant un bruit réaliste InSAR, puis appliquée à des données réelles centrées sur les deux segments en glissement asismique de la NAF: Izmit et Ismetpasa. La détection automatique des SSEs à partir des données InSAR a d'abord été évaluée sur des jeux de données présentant différents niveaux de bruit, selon le degré de post-traitement appliqué. Les tests synthétiques intégrant un bruit réaliste ont permis de définir des seuils probabilistes de détection en fonction de la magnitude et de la profondeur des SSEs. Ces tests montrent que la méthode permet de détecter, avec une confiance supérieure ou égale à 90 %, des SSEs superficiels de magnitude supérieure à 4,5 à partir des séries temporelles InSAR horizontales Est-Ouest. Elle permet également de détecter des événements de magnitude supérieure à 4,3 avec une confiance d'au moins 45 %. En appliquant cette méthode aux données réelles, j'ai pu détecter, sans connaissance préalable, trois événements transitoires déjà rapportés le long du segment d'Izmit et deux le long du segment d'Ismetpasa, avec des magnitudes estimées entre 4,0 et 4,5. J'ai pu ainsi valider l'approche méthodologique adaptée aux données spatialisées et confirmer la qualité des séries temporelles InSAR traitées automatiquement. Malgré le niveau de bruit important dans les données géodésiques, elles peuvent en effet être utilisées pour extraire des signaux tectoniques, en particulier les glissements lents de l'ordre de quelques millimètres, représentant ainsi des jeux de données indispensables pour comprendre les cycles sismiques le long des failles décrochantes continentales. L'application de cette approche à l'échelle mondiale pourrait permettre une détection rapide et une caractérisation de premier ordre des événements de glissement transitoire.

Dans le troisième chapitre, je me suis concentrée sur les SSEs détectés le long du segment d'Izmit. J'ai développé une chaîne de post-traitement afin d'extraire le signal tectonique des séries InSAR, incluant un référencement basé sur les données GNSS, la correction des composantes saisonnières et une séparation de différentes sources par analyse en composantes indépendantes (ICA). Les séries temporelles ainsi traitées ont ensuite été utilisées dans des modèles inverses pour reconstruire la distribution du glissement en profondeur sur ce segment de faille, intégré dans un demi-espace élastique stratifié. Ces observations ont été combinées à des données de creepmeters afin de mieux caractériser la dynamique temporelle des SSEs. Une analyse détaillée des deux derniers événements détectés sur le segment d'Izmit, en mars 2018 et novembre 2019, révèle des magnitudes comprises entre 4,3 et 4,4. Le glissement associé est

localisé à faible profondeur, au sein du bassin sédimentaire quaternaire. J'ai également identifié un glissement asismique continu, majoritairement situé entre 2 et 5 km de profondeur, juste sous le bassin sédimentaire, et contribuant probablement au chargement des aspérités responsables des SSEs. Les enregistrements de deux creepmeters lors de l'événement de 2019 confirment l'occurrence du SSE et permettent d'estimer une vitesse de propagation latérale de 6,4 km/jour. L'analyse des SSEs le long de la NAF confirme alors l'occurrence périodique de SSEs environ 20 ans après le séisme d'Izmit de 1999. Ces observations soutiennent un modèle conceptuel dans lequel les SSEs superficiels se développent préférentiellement dans des portions de faille entourées de zones de glissement asismique continu, et au sein de bassins sédimentaires, où se combinent hétérogénéité frictionnelle, matériaux plus déformables et effets des fluides, produisant un glissement conditionnellement stable.

Enfin, j'ai utilisé des modèles mécaniques pour reproduire le cycle sismique du segment d'Izmit dans le cadre du formalisme de friction "rate-and-state". Des simulations numériques ont été réalisées à l'aide d'une approche quasi-dynamique, avec une faille décrochante unidimensionnelle intégrée dans un demi-espace élastique bidimensionnel. Ces simulations numériques permettent de reproduire plusieures observations à différentes échelles temporelles: l'amplitude et le temps de récurrence des séismes majeurs, les séries temporelles de déplacements post-sismiques issues de campagnes GNSS, ainsi que l'amplitude, la récurrence et la durée des SSEs superficiels. Les simulations numériques du cycle sismique le long du segment d'Izmit ont permis de préciser les propriétés frictionnelles des différentes couches en profondeur de la faille et leur influence sur la déformation observée en surface. Le temps de récurrence et les déplacements co-sismiques sont contrôlés par la couche en velocity weakening correspondant à la zone sismogène ainsi que par la vitesse des plaques. La couche sus-jacente en velocity strengthening, définie à partir de la limite supérieure des répliques du séisme d'Izmit de 1999, permet d'expliquer la déformation post-sismique. Enfin, les propriétés de l'hétérogénéité frictionnelle superficielle permettent de contrôler la durée et le temps de récurrence des SSEs. Le glissement asismique continu environnant fournit probablement la déformation de fond nécessaire pour charger des zones localisées en velocity weakening, conduisant à des glissements transitoires récurrents. La similarité avec des observations réalisées en Californie suggère que ces conditions structurales et hydromécaniques pourraient constituer un mécanisme commun à l'occurrence des SSEs superficiels à l'échelle globale. Les modèles mécaniques viennent renforcer cette interprétation en montrant que des hétérogénéités frictionnelles superficielles favorisent l'émergence de SSEs récurrents.

Ces travaux focalisés sur la NAF ont permis de préciser son comportement asismique, en particulier le long du segment d'Izmit, révélant ainsi l'occurrence de SSEs superficiels avec un temps de retour d'environ 1,3 années. Cependant, il est crucial de multiplier les détections de SSEs afin d'enrichir les catalogues existants et d'identifier plus clairement les caractéristiques communes des différents SSEs, suggérant des conditions préférentielles à leur développement et leur rôle dans l'aléa sismique. La combinaison d'observations géodésiques et de mesures de microsismicité est également essentielle pour mieux contraindre la dynamique du glissement transitoire, soulignant le besoin de réseaux sismiques et géodésiques denses capables de capturer à la fois l'activité asismique et sismique. Dans cette optique, un réseau GNSS dense, auquel j'ai contribué, a été installé le long du segment d'Izmit en 2024 afin d'acquérir des données géodésiques à haute résolution temporelle. Combinées à la haute résolution spatiale des observations InSAR, ces données permettront une caractérisation plus fine de la dynamique du glissement. À terme, la comparaison du comportement des SSEs le long des failles décrochantes avec les cycles bien documentés observés dans les zones de subduction pourrait permettre d'identifier des mécanismes communs contrôlant le glissement lent dans différents contextes tectoniques.

Résumé long en français

La déformation associée au mouvement relatif des plaques tectoniques est principalement localisée le long de failles inter-plaques qui peuvent être bloquées en profondeur, entraînant l'accumulation de contraintes élastiques. La nucléation et la propagation d'une rupture sismique libèrent la majeure partie de cette énergie de manière quasi instantanée. Une partie de cette énergie peut par ailleurs être libérée de manière asismique, notamment sous la forme de glissements lents produisant peu ou pas de rayonnement sismique.

Depuis les premières observations de glissement asismique sur la faille de San Andreas par Steinbrugge et al. (1960), nous disposons aujourd'hui d'un nombre croissant d'observations géodésiques qui ont considérablement affiné notre compréhension du cycle sismique et de ses implications pour l'évaluation de l'aléa sismique. Le glissement asismique intermittent — sous forme d'épisodes de glissement lent, ou Slow Slip Events (SSEs) — a ainsi été documenté dans de nombreux contextes tectoniques, aussi bien dans les zones de subduction que le long des failles décrochantes continentales, où la plupart des SSEs observés se produisent dans la partie superficielle de la faille et ne produisent qu'une zone de déformation en surface large de quelques kilomètres, avec des déplacements centimétriques. Outre les *creepmeters*, qui permettent de détecter des décalages millimétriques en des points précis, l'interférométrie radar (InSAR) s'est également révélée précieuse pour détecter les SSEs superficiels le long des failles décrochantes. Cependant, les mécanismes physiques associés à ces événements restent encore aujourd'hui en partie incompris.

La faille Nord-Anatolienne (NAF) est une faille décrochante dextre en Turquie qui accommode l'essentiel du mouvement relatif de 24 ± 1 mm/an entre les plaques anatolienne et eurasienne. Depuis les années 1930, elle a été le siège d'une séquence de sept séismes de magnitude $M_w \geq 7$, migrant progressivement d'Est en Ouest depuis Erzincan jusqu'au segment d'Izmit, et jusqu'au segment offshore sous la mer de Marmara qui demeure aujourd'hui une lacune sismique menaçant directement l'agglomération d'Istanbul. Les deux derniers séismes de cette séquence, d'Izmit (M_w 7,6) et de Düzce (M_w 7,2), ont rompu en 1999. La déformation cosismique du séisme principal d'Izmit a été largement étudiée. La rupture bilatérale depuis l'épicentre a produit un glissement allant jusqu'à 8 m au niveau de deux à trois aspérités principales. La phase post-sismique qui a suivi comporte classiquement deux étapes: un *afterslip* profond rapide durant les 2,5 premières années, puis une relaxation viscoélastique de la croûte inférieure et du manteau supérieur se prolongeant sur plusieurs décennies. Au-delà de cet *afterslip* profond et de la relaxation viscoélastique, la partie superficielle du segment d'Izmit glisse de manière asismique depuis le séisme, ce qui pose la question de savoir si ce comportement relève encore de la phase post-sismique ou s'il correspond déjà à une déformation intersismique pérenne. Des travaux antérieurs (Cakir et al., 2012; Hussain et al., 2016; Aslan et al., 2019b; Özarpacı et al., 2020) ont confirmé, à partir de données InSAR, GNSS et de *creepmeters*, la persistance de ce glissement jusqu'en 2017, avec une profondeur de blocage estimée entre 10 et 18 km selon les études et un glissement stable superficiel de 5 à 10 mm/an entre la surface et 8 km de profondeur. Aslan et al. (2019b) avaient par ailleurs mis en évidence un épisode de glissement lent (ou SSE) d'un mois en décembre 2016, provoquant un déplacement relatif de surface de 10 mm, et Özarpacı et al. (2020) un autre épisode transitoire en septembre 2015. De ce fait, le segment d'Izmit constitue un laboratoire naturel privilégié à l'étude du

glissement asismique.

Le travail de thèse qui suit exploite le jeu de données InSAR fourni par FLATSIM, produit automatiquement à partir d'images Sentinel-1 sur la période 2015 – 2021 dans le cadre d'un projet national porté conjointement par le CNES et FormaTerre, et reposant sur la chaîne de traitement NSBAS (New Small Baseline Subset) (Doin et al., 2011; Thollard et al., 2021). L'un des avantages de l'utilisation de ce type de données est leur haute résolution spatiale. Les objectifs de ces travaux sont alors multiples:

- construire, à l'échelle de l'ensemble de la Turquie, un champ de vitesse en régime permanent (*steady-state*) permettant de caractériser la déformation tectonique associée aux failles nord- et est-anatoliennes (NAF et EAF), et approfondir, à une échelle plus locale, l'étude du déficit de glissement le long de l'interface de faille sous la mer de Marmara, région constituant une lacune sismique majeure à proximité immédiate de la mégalopole d'Istanbul;
- adapter une méthode de détection automatique des événements transitoires, initialement développée pour des données GNSS, à des observations InSAR dans le contexte de failles décrochantes;
- étendre la fenêtre d'observation le long du segment d'Izmit par rapport aux études précédentes et caractériser plus finement sa dynamique de glissement — glissement continu et épisodes transitoires confondus — en la comparant à des enregistrements de *creepmeters* à plus haute résolution temporelle;
- utiliser des modèles numériques de cycle sismique pour tester l'hypothèse d'une hétérogénéité frictionnelle superficielle associée au bassin sédimentaire d'Izmit pouvant expliquer l'occurrence des SSEs tout en préservant les caractéristiques principales du cycle sismique.

Analyse du champ de déformation à grande échelle de la Turquie

Le premier volet scientifique de cette thèse porte sur l'analyse à grande échelle de 14 fauchées InSAR (7 ascendantes et 7 descendantes) couvrant l'essentiel de la Turquie, avec pour objectif la production d'un champ de vitesse Est-Ouest en régime permanent et d'un champ de déformation (*strain*) associé. Un second volet (associé au premier) se concentre sur la région de la mer de Marmara, où les données InSAR sont combinées à un réseau GNSS densifié afin de contraindre, par inversion bayésienne conjointe, la distribution du glissement le long de l'interface de faille principale de Marmara (*Main Marmara Fault*, MMF). Ce second travail, mené en collaboration avec Émilie Klein (CNRS, ENS Paris) et plusieurs collègues turcs et français, est encore en préparation en vue d'une publication.

Méthode

Contrôle qualité des données. Le jeu de données FLATSIM fournit, pour chacune des 14 fauchées, des produits standards (vitesses moyennes dans la ligne de visée du satellite (*Line of Sight*, LOS), séries temporelles, données de contrôle qualité) issus d'un traitement automatique optimisé pour un usage générique. Une première étape a consisté à contrôler la qualité de ces produits: identification d'erreurs de déroulement de phase (visibles par des sauts de phase nets), et évaluation de la cohérence de l'inversion des séries temporelles au moyen de plusieurs métriques de *Root Mean Square Error* (RMSE, erreur quadratique moyenne par date, par interférogramme, par pixel), qui traduisent la fermeture des boucles de phase au sein du réseau interférométrique. Ces RMSEs présentent une saisonnalité marquée (valeurs plus élevées en hiver), attribuable à la décorrélation liée à l'enneigement et à la croissance de la végétation sur les zones agricoles. Un masquage des pixels selon le nombre d'interférogrammes utilisés dans

l'inversion (en fonction de la moyenne et de l'écart-type de cette quantité par fauchée) permet de limiter les artefacts liés à un faible rapport signal/bruit.

Retraitement de certaines fauchées. Deux fauchées situées à l'ouest de la zone, affectées par la présence de la mer de Marmara qui empêche le déroulement de phase continu entre les rives nord et sud, ont été partiellement retraitées avec la chaîne NSBAS afin d'étendre la couverture à la rive nord. Ce retraitement a nécessité une adaptation des paramètres de filtrage (filtre « SW ») pour compenser la forte décorrélation liée aux cultures sur l'une des fauchées.

Correction du biais de phase. Une attention particulière est portée au phénomène de *fading signal*, un biais de phase lié au moyennage spatial (*multilooking*) qui modifie les propriétés statistiques du signal et se traduit par une subsidence apparente sur les cultures et un soulèvement apparent sur les forêts et zones urbaines, en particulier pour les interférogrammes à courte ligne de base temporelle. L'ajout d'interférogrammes à longue ligne de base temporelle (jusqu'à un an) atténue sensiblement cet artefact.

Estimation du champ de vitesse en régime permanent. La séquence de post-traitement comprend: (i) une décomposition saisonnière et linéaire des séries temporelles de déplacement LOS par ajustement par moindres carrés (terme linéaire et termes périodiques annuels, avec soustraction d'une surface polynomiale d'ordre 4 pour retirer les biais de grande longueur d'onde); (ii) un référencement des vitesses par rapport au champ GNSS dense de Kurt et al. (2023), selon la méthode de Hussain et al. (2018), qui consiste à estimer et soustraire un plan $2D$ correspondant à l'écart entre vitesses InSAR et GNSS projetées en LOS; (iii) une estimation des incertitudes à partir des zones de recouvrement entre fauchées adjacentes, conduisant à des incertitudes LOS de l'ordre de 1 à 2 mm/an; (iv) une décomposition horizontale (Est-Ouest) et verticale du champ de vitesse à partir des composantes ascendante et descendante, en négligeant la composante Nord-Sud, mal contrainte par la géométrie des orbites des satellites SAR.

Estimation du glissement et de la profondeur de blocage. Le long de profils perpendiculaires à la faille, la vitesse Est-Ouest est modélisée selon le formalisme classique de Savage and Burford (1973), qui décrit le champ de vitesse en fonction de la distance à la faille par une fonction arctangente dépendant du taux de glissement en profondeur et de la profondeur de blocage d_1. Ce modèle est étendu, suivant Hussain et al. (2016), par l'ajout d'une fonction de *Heaviside* représentant un glissement superficiel de type *back-slip*, caractérisé par un taux de glissement C et une profondeur de glissement d_2.

Calcul du champ de déformation. Le tenseur de déformation (*strain*) est calculé à partir du gradient spatial de la vitesse Est-Ouest InSAR (la composante Nord-Sud étant négligée), permettant de dériver le cisaillement maximal, la rotation et la dilatation, à des résolutions de 1 et 2 km.

Inversion bayésienne au niveau de la mer de Marmara. Quatre fauchées InSAR (deux ascendantes, deux descendantes) couvrent la zone d'étude. La préparation des données suit une séquence similaire à celle présentée précédemment, appliquée sur une période temporelle harmonisée à partir du 9 octobre 2016: harmonisation temporelle des vitesses moyennes, référencement par rapport au champ GNSS augmenté de Özkan et al. (2025) (combiné à celui de England et al. (2016)), contrôle qualité par masquage selon le nombre d'interférogrammes par pixel (avec des seuils propres à chaque fauchée), puis décomposition horizontale-verticale. Le champ de vitesse Est-Ouest obtenu est ensuite fourni, avec le champ GNSS, en entrée d'une inversion bayésienne du taux de glissement le long de l'interface de faille (travail réalisé par Émilie Klein), permettant de comparer les modèles obtenus à partir des données GNSS seules, InSAR seules, et des deux jeux de données combinés.

Résultats et discussion

Ce travail constitue la production, à partir du jeu FLATSIM, d'un champ de vitesse Est-Ouest à haute résolution spatiale sur cinq ans avec un post-traitement limité, validant ainsi

l'intérêt des chaînes de traitement automatiques et massives pour l'étude de signaux tectoniques à grande échelle — une conclusion cohérente avec les travaux antérieurs menés à partir d'une autre chaîne automatique (LiCSAR; Weiss et al., 2020).

Le champ de vitesse Est-Ouest révèle nettement l'extrusion vers l'ouest de la plaque anatolienne, accommodée par les deux systèmes de failles NAF et EAF; un signal tectonique fort est également visible le long de l'EAF, associé au séisme d'Elazığ de 2020 (M_w 6,8). Le champ de vitesse verticale ne présente en revanche aucun signal net directement lié aux deux failles principales, confirmant leur caractère essentiellement décrochant à grande échelle; des signaux locaux sont néanmoins associés à des bassins sédimentaires en extension (bassin de Bursa, avec une subsidence atteignant 5 cm/an, cohérente avec un pompage des eaux souterraines lié à l'agriculture) ou à des activités anthropiques (exemple de la mine de Tunçbilek/Tavşanlı/Kütahya). La carte de déformation (cisaillement maximal) met en évidence trois segments présentant des taux élevés ($\geq 20 \times 10^{-8}$ an^{-1}): Izmit, Ismetpasa et Elazığ. Des profils perpendiculaires à la faille, appliqués le long de la NAF, permettent d'estimer les profondeurs de blocage (7 à 30 km selon les segments, en accord avec les études précédentes) et de confirmer deux segments en glissement asismique bien connus:

- **Segment d'Izmit**: taux de glissement jusqu'à $7,5$ mm/an, profondeur de glissement de $2-3$ km, profondeur de blocage d'environ 7 km — cohérente avec des estimations post-1999 plus faibles que la valeur pré-sismique (~ 21 km) rapportée par (McClusky et al., 2000), suggérant que le blocage ne serait pas encore revenu à sa valeur pré-sismique.

- **Segment d'Ismetpasa**: taux de glissement de $7,5$ à 11 mm/an sur environ 90 km de long, profondeur de glissement de $4-5$ km, profondeur de blocage d'environ 10 km.

L'analyse identifie deux segments supplémentaires présentant des signatures similaires (gradient net de vitesse Est-Ouest, cisaillement et rotation élevés) et donc potentiellement en glissement asismique: le segment de Düzce (offset d'au moins 9 mm/an) et le segment Est-Ouest d'Ezinepazari (offset d'environ 5 mm/an), ce dernier suggérant un partitionnement du glissement entre la branche principale de la NAF et des failles secondaires liées aux bassins en *pull-apart* de Tasova-Erbaa et Niksar.

L'analyse des profils perpendiculaires à la faille confirme des variations latérales de l'accumulation de déformation le long de la NAF, en cohérence avec des variations locales de la profondeur de blocage et avec une relation, au premier ordre, entre l'orientation de la faille et la longueur des ruptures sismiques historiques — ce qui souligne le rôle de la segmentation structurale de la NAF dans la distribution de l'accumulation de contrainte et la propagation des ruptures. Au total, bien que l'essentiel des 1600 km de la NAF reste verrouillé, environ 95 à 100 km de la faille glisseraient asismiquement, contribuant ainsi à la libération partielle de la contrainte accumulée. Le partitionnement du glissement entre la branche principale et des failles secondaires (Ezinepazari) pourrait par ailleurs être sous-estimé dans les modèles existants.

Le champ de vitesse Est-Ouest InSAR confirme un gradient marqué de déformation interséismique le long de la NAF sous la mer de Marmara, avec un gradient net sur le segment d'Izmit (à l'Est) contrastant avec des gradients plus doux sur les segments de Sapanca-Akyazi et de Ganos (à l'Ouest). Le champ vertical révèle localement des signaux non tectoniques (subsidence de bassins, activités minières) ainsi qu'un signal lié à la séquence sismique modérée de 2017 sur la péninsule de Biga. La comparaison des inversions de glissement obtenues à partir des données GNSS seules, InSAR seules, et combinées, montre que le segment central glisse dans les trois cas, mais que la combinaison des deux jeux de données réduit les incertitudes en surface et révèle une augmentation du glissement sous le segment d'Izmit, grâce à la résolution spatiale fine de l'InSAR. Le modèle final de taux de glissement obtenu par inversion jointe (Klein et al., en préparation) apporte un résultat notable: le segment de Kumburgaz (KB), classiquement considéré comme verrouillé ou en transition dans les études antérieures

(Ergintav et al., 2014; Schmittbuhl et al., 2016b; Özkan et al., 2025), apparaît ici en glissement, ce qui n'était pas capturé par les modèles précédents. Ce résultat, contraint principalement par les stations GNSS côtières du nord, s'avère robuste selon des tests synthétiques. Le segment resterait cependant globalement verrouillé jusqu'à environ 12 *km* de profondeur sur sa portion orientale (segment des Îles des Princes), avec un potentiel de rupture de magnitude $M_w > 7$.

S'agissant du déficit de glissement sous la mer de Marmara, cette étude s'inscrit dans une longue lignée d'études visant à contraindre le comportement interséismique du segment central et de ses segments adjacents (GPS terrestre, sismicité répétitive, géodésie acoustique sous-marine, extensométrie). Le résultat d'un segment de Kumburgaz non totalement bloqué, s'il est confirmé, impliquerait un segment verrouillé plus court que précédemment estimé, tout en maintenant un risque sismique significatif au large d'Istanbul en raison du potentiel de rupture du segment des Îles des Princes, dernière portion à ne pas avoir rompu depuis 1766. Le séisme M_w 6,2 du 23 avril 2025, survenu sur le segment central, illustre l'actualité et l'importance de ces questions pour l'évaluation de l'aléa sismique régional.

Méthode de détection automatique des SSEs à partir de données InSAR

Face au volume croissant de données InSAR, développer des méthodes automatiques — ou quasi automatiques — de détection des SSEs devient essentiel pour densifier les catalogues mondiaux de ces événements. Plusieurs familles d'approches ont déjà été proposées dans la littérature pour extraire la déformation transitoire des données géodésiques:

- des méthodes pilotées par les données, recherchant des sauts dans les séries temporelles (par exemple Nishimura (2014), qui sélectionne entre un modèle linéaire simple et un modèle avec décalage via le critère d'information d'Akaike);

- des décompositions statistiques, telles que l'analyse en composantes principales (PCA), l'analyse spectrale singulière (SSA) et sa variante multicanal (M-SSA), ou l'analyse en composantes indépendantes (ICA) et ses variantes probabilistes (vbICA), toutes largement employées pour séparer les sources de déformation dans les séries temporelles géodésiques;

- des méthodes de représentation parcimonieuse, qui supposent que la déformation transitoire peut être capturée par un petit nombre de fonctions de base (par exemple Riel et al. (2014), avec des splines cubiques parcimonieuses);

- des méthodes fondées sur des modèles physiques, comme le filtre d'inversion en réseau de Segall and Matthews (1997), qui modélise les séries temporelles GNSS comme une combinaison de vitesses séculaires, de glissement de faille et d'erreurs, via un filtre de Kalman; ou encore le filtre adapté géodésique (*geodetic matched filter*) de Rousset et al. (2017), fondé sur des corrélations entre séries temporelles synthétiques et données GNSS continues, déjà appliqué à plusieurs zones de subduction (Mexique, Alaska, Nankai, nord du Japon, Pérou-Chili) et à la faille de San Andreas;

- plus récemment, des approches d'apprentissage profond, entraînées sur des séries temporelles synthétiques incluant du bruit réaliste et des SSEs, et appliquées ensuite à différents contextes tectoniques, y compris au segment d'Ismetpasa de la NAF.

Dans ce travail, nous adaptons le filtre adapté géodésique, initialement développé pour les données GNSS (Rousset et al., 2017), à des observations InSAR dans le contexte des failles décrochantes. Cette méthode tire parti de la redondance spatiale de l'information collectée en de multiples points pour abaisser le seuil de détection des SSEs de faible amplitude — un

avantage particulièrement pertinent pour l'InSAR, dont la densité spatiale est bien supérieure à celle du GNSS. Notre démarche comporte quatre modules: nous analysons d'abord les caractéristiques du bruit des séries temporelles InSAR afin de construire des séries synthétiques réalistes; nous évaluons ensuite les limites de la méthode et estimons les seuils de corrélation permettant de détecter d'éventuels SSEs; nous caractérisons, une fois détectés, les principales propriétés de ces événements (durée, magnitude); enfin, nous appliquons cette méthode à deux segments de la NAF où de tels événements ont déjà été documentés par des études antérieures.

Méthode

L'approche du filtre adapté géodésique, développée par Rousset et al. (2017), repose sur une mise en correspondance de gabarits physiques (*template matching*): elle détecte les SSEs en analysant les coefficients de corrélation entre des séries temporelles de déplacement de surface issues des données géodésiques et des gabarits, correspondant à des modèles synthétiques de dislocation associés à des SSEs. La méthode se structure en quatre grandes étapes, correspondant aux quatre modules de notre chaîne de traitement: (a) préparation des données d'entrée (analyse du bruit InSAR, construction des gabarits); (b) Module 1 — analyse de séries temporelles synthétiques pour estimer les seuils de détection; (c) Module 2 — application aux données réelles pour détecter d'éventuels SSEs, avec une étape de validation des détections; (d) Module 3 — caractérisation des SSEs détectés (temps d'initiation, glissement en profondeur).

Préparation des données d'entrée:

Analyse du bruit InSAR. Pour construire des séries temporelles synthétiques permettant d'estimer les seuils de détection, nous analysons d'abord le contenu du bruit présent dans les séries temporelles InSAR réelles, en ligne de visée (LOS) comme en composante Est-Ouest (EW). Nous supposons que ce bruit est corrélé spatialement mais non corrélé temporellement, la dynamique atmosphérique évoluant beaucoup plus vite que la période de revisite des acquisitions Sentinel-1. Nous générons donc un bruit spatialement corrélé en filtrant un bruit blanc gaussien dans le domaine de Fourier, de sorte que son spectre de puissance suive une loi de puissance négative, dont nous estimons trois paramètres à partir des données réelles: la pente du spectre de puissance (caractérisant la corrélation spatiale), l'amplitude moyenne du bruit et son écart-type.

Définition d'un gabarit. La fonction source temporelle s des SSEs synthétiques est définie à partir de mesures de *creepmeters* sur le segment d'Izmit, sous la forme d'une exponentielle saturante $s(t_1) = m(1 - e^{(-t_1/\tau)})$, où m est l'amplitude de glissement, t_1 le temps et τ le temps de relaxation; la durée de l'événement est estimée à 5τ. La série temporelle de déplacement du gabarit est ensuite obtenue en multipliant cette fonction source par le déplacement de surface associé à chaque pixel, déduit de fonctions de Green statiques. Pour limiter les fausses détections liées à des pics de courte durée, nous prolongeons cette série par deux paliers constants avant et après le signal transitoire. Les fonctions de Green sont calculées pour un demi-espace élastique multicouche (Zhu and Rivera, 2002), à partir de modèles de vitesse et de densité locaux propres aux segments d'Izmit et d'Ismetpasa. La faille est discrétisée en mailles de $0,33\ km \times 0,33\ km$, de la surface jusqu'à $10\ km$ de profondeur.

Module 1 – détection sur données synthétiques:

Nous construisons des cubes de séries temporelles synthétiques en combinant le bruit réaliste caractérisé précédemment à un ou plusieurs SSEs synthétiques. Pour atténuer les signaux atmosphériques résiduels, nous utilisons systématiquement des séries temporelles de déplacement relatif entre paires de pixels situées de part et d'autre de la faille — une approche qui élimine les résidus d'amplitude similaire entre pixels voisins et renforce le signal tectonique. Nous décimons également les pixels initiaux (relation exponentielle avec la distance à la faille pour Izmit, quadratique pour Ismetpasa) afin de réduire le temps de calcul, sans dégrader significativement les valeurs de corrélation obtenues (réduction du temps de calcul d'environ 96 %

pour une variation de corrélation inférieure à $\pm\ 0,035$).

Fonctions de corrélation. Suivant Rousset et al. (2017), nous calculons les fonctions de corrélation à partir des dérivées temporelles des séries relatives du gabarit et des données InSAR, normalisées, puis pondérées par l'amplitude des fonctions de Green à chaque paire de pixels — donnant davantage de poids aux pixels les plus susceptibles d'être affectés par le SSE. Le coefficient de corrélation final retenu pour la détection est la moyenne de ces coefficients pondérés sur l'ensemble des paires de pixels considérées.

Estimation des seuils. Nous estimons les seuils optimaux de détection à partir d'un cube synthétique composé de 100 événements sur 6000 pas de temps, chaque SSE synthétique ayant une zone de glissement d'environ 6 *km* de long sur 1 *km* de large et un temps de relaxation d'environ 6 jours — des paramètres calibrés sur les caractéristiques de SSEs superficiels déjà observés (Rousset et al., 2016; Neyrinck et al., 2024; Özdemir et al., 2025). Nous quantifions la fiabilité des détections à l'aide du produit précision-rappel (PRP), défini comme le produit du rapport vrais positifs sur positifs totaux (précision) et du rapport vrais positifs sur positifs réels (rappel). Un $PRP = 1$ signifierait une détection parfaite, sans faux positif ni faux négatif. En combinant l'ensemble des mailles de faille testées, nous estimons ainsi, pour chaque profondeur, la magnitude minimale détectable correspondant à un $PRP \geq 0,4$ — le seuil que nous retenons pour la suite de l'étude. Ces tests montrent qu'à faible profondeur, des SSEs de magnitude aussi faible que $M_w\ 4-4,5$ peuvent être détectés de façon fiable, la magnitude minimale détectable augmentant avec la profondeur, comme attendu compte tenu de l'atténuation du déplacement de surface avec la profondeur de la source.

Module 2 – détection sur données réelles:

Pour maximiser la détection de SSEs de faible magnitude, nous choisissons volontairement un PRP relativement bas, ce qui augmente le nombre de fausses détections potentielles. Nous introduisons donc deux critères de validation, calibrés sur les données synthétiques:

- le nombre de mailles glissantes voisines déclenchant une détection positive: compte tenu de la différence entre la taille de la zone de glissement synthétique et la discrétisation de l'interface de faille, un véritable SSE doit être détecté sur plusieurs mailles voisines dans la direction horizontale. Nous rejetons donc les détections associées à une seule maille isolée;

- un empilement pondéré des séries temporelles de déplacement, centré sur le temps de détection, pondéré par les fonctions de Green associées au gabarit de corrélation maximale, afin d'améliorer le rapport signal sur bruit. Nous validons une détection si le décalage (différence des moyennes calculées sur des fenêtres de 6 mois avant et après la détection) est supérieur à l'écart-type de la série empilée calculé sur une période de 5 mois centrée sur la détection.

Cette étape de validation permet de séparer les vrais positifs des vrais négatifs, même si certaines fausses détections subsistent, généralement associées à de faibles amplitudes de décalage. Elle nous permet en outre d'abaisser le PRP retenu tout en conservant une confiance élevée (rapport vrais positifs sur positifs réels supérieur à 90 % à la magnitude minimale détectable), ce qui réduit encore la magnitude minimale détectable par rapport à un simple seuillage sans validation.

Module 3 – caractérisation des événements:

Après validation, nous caractérisons chaque SSE détecté en termes de localisation le long de la faille et en profondeur (maille présentant l'amplitude de corrélation maximale), de temps d'initiation, de temps de relaxation et de magnitude équivalente. Pour cela, nous ajustons la série temporelle empilée pondérée par la fonction temporelle du gabarit, en minimisant l'erreur quadratique moyenne (davantage pondérée au centre de la série pour privilégier le signal transitoire). Les tests synthétiques montrent que le temps d'initiation est bien résolu

(erreur de $\pm$ 5 jours, cohérente avec le temps de revisite de Sentinel-1), tandis que le temps de relaxation est systématiquement surestimé d'environ 6 jours, en raison de la résolution temporelle limitée de l'InSAR par rapport aux temps de relaxation typiques des SSEs. Pour le segment d'Izmit, la taille du gabarit est fixée à 6 *km* de long par 1 *km* de large, sur la base d'études antérieures ayant correctement contraint l'aire de glissement (Neyrinck et al., 2024); nous montrons qu'une maille plus petite tend à sous-estimer la magnitude et une maille plus grande à la surestimer, avec une erreur d'estimation pouvant atteindre 0,17 unité de magnitude même dans le meilleur des cas. Le moment sismique M_0 et la magnitude de moment équivalente M_w sont enfin calculés à partir du module de cisaillement, de la surface glissante et de l'amplitude de glissement (relations de Hanks and Kanamori (1979)), la précision de cette estimation restant bonne jusqu'à 5 *km* de profondeur et légèrement surestimée au-delà.

Résultats

Deux segments de la NAF se distinguent par la présence d'un glissement asismique superficiel et de SSEs épisodiques, documentés par *creepmeters*, GNSS et InSAR: le segment d'Izmit, qui a rompu lors du séisme de 1999 (M_w 7,6), et le segment d'Ismetpasa, qui a rompu lors du séisme de 1944 (M_w 7,3). Ces deux segments ont hébergé plusieurs SSEs superficiels depuis leur dernière rupture majeure, ce qui fournit des contraintes indépendantes pour valider nos détections.

Afin d'évaluer l'influence de la réduction du bruit et de l'extraction du signal sur la capacité de détection, nous testons plusieurs niveaux de post-traitement: les séries brutes en ligne de visée (LOS), les séries de déplacement Est-Ouest obtenues après décomposition géométrique et retrait des signaux saisonniers (EW-Raw), et les séries EW encore débruitées par ICA (EW-ICA).

Application au segment d'Izmit. Nous appliquons d'abord la méthode au segment d'Izmit, précisément pour étudier l'effet du post-traitement InSAR sur les performances de détection. Trois jeux de données sont testés: (1) les séries LOS brutes de la trace ascendante *A058*, (2) les séries EW-Raw et (3) les séries EW-ICA, ces deux derniers jeux de données étant construits selon la méthode décrite par Neyrinck et al. (2024). Sur la base des tests synthétiques, nous adoptons un PRP initial $\geq 0,4$ pour ce segment. Les magnitudes minimales détectables déduites des expériences synthétiques montrent que les jeux LOS et EW-Raw présentent des seuils de détection comparables, avec une sensibilité légèrement meilleure aux faibles profondeurs pour l'EW-Raw, tandis que le jeu EW-ICA permet systématiquement de détecter des événements de plus faible magnitude à toutes les profondeurs — démontrant le bénéfice d'un débruitage avancé. En appliquant le filtre adapté aux données réelles, aucun SSE n'est détecté à partir du jeu LOS, ce qui indique que les signaux atmosphériques et non tectoniques résiduels dominent encore les séries temporelles à ce niveau de traitement. Le jeu EW-Raw permet de détecter deux SSEs, en 2018 et en 2019. Le jeu EW-ICA permet en outre de détecter un événement supplémentaire en 2016, avec des coefficients de corrélation systématiquement plus élevés pour l'ensemble des événements détectés, confirmant l'amélioration du rapport signal/bruit. Les trois événements ainsi détectés correspondent aux trois épisodes déjà documentés dans la littérature (Aslan et al., 2019b; Neyrinck et al., 2024). Nous caractérisons ensuite ces événements selon la procédure décrite plus haut. Pour l'événement de 2019, les coefficients de corrélation les plus élevés correspondent à une maille glissante centrée à environ $E30,05°$ et à 1 *km* de profondeur, à l'intérieur du bassin sédimentaire d'Izmit. La série empilée pondérée présente un décalage transitoire net, bien ajusté par notre fonction source temporelle, et les enregistrements indépendants des *creepmeters* d'Izmit-Seller et de Tepetarla montrent des déplacements transitoires contemporains, ce qui constitue une validation externe de la détection. Pour les trois événements détectés à partir du jeu EW-ICA, les magnitudes estimées vont de M_w 4,1 à M_w 4,35, avec des temps de relaxation compris entre environ 1 et 5,3 jours. Nous

observons une bonne cohérence avec les données de *creepmeters* pour le temps d'initiation (décalage Δt_0 d'environ 4 à 11 jours). Le temps de relaxation (ou durée) obtenu par notre méthode est plus élevé pour les épisodes de 2018 et 2019 que pour celui de 2016, probablement en raison de variations du rapport signal sur bruit entre les trois séries empilées. Les mailles glissantes inférées restent peu profondes (≤ 2 *km*) et montrent une légère migration vers l'est au cours du temps, cohérente avec les analyses InSAR antérieures.

Application au segment d'Ismetpasa. Nous appliquons ensuite la méthode au segment d'Ismetpasa, afin de tester sa robustesse dans un contexte de bruit différent. Pour ce segment, nous utilisons uniquement le jeu EW-Raw, les tentatives de débruitage par ICA n'ayant pas abouti. Les caractéristiques du bruit sont recalculées localement pour ce segment, ce qui conduit à retenir un PRP plus faible ($\sim 0,2$) compte tenu du niveau de bruit plus élevé, ainsi qu'une taille de gabarit plus petite (3 *km* de long sur 1 *km* de large), sur la base des modèles de glissement inverse publiés antérieurement (Rousset et al., 2016). L'application initiale produit 55 détections candidates, réduites à seulement deux détections retenues après validation: en août 2017 et en décembre 2019. Ces événements présentent des magnitudes estimées entre M_w 4,0 et M_w 4,4, à des profondeurs superficielles comprises entre environ 0,4 et 2 *km*, avec des temps de relaxation entre 3 et 12 jours — des estimations globalement cohérentes avec les observations InSAR, GNSS et *creepmeters* publiées antérieurement, malgré des incertitudes plus élevées que pour le segment d'Izmit. La première détection (août 2017) semble correspondre à l'événement connu de 2017 sur ce segment, malgré un décalage d'environ 58 jours du temps d'initiation par rapport à l'enregistrement du *creepmeter* — une différence qui se répercute logiquement sur le temps de relaxation estimé. L'événement de 2019 est détecté avec seulement un jour de décalage, mais avec des différences plus marquées sur le temps de relaxation (jusqu'à 3 jours par rapport aux *creepmeters*) et la durée (jusqu'à 30 jours par rapport aux données GNSS), ainsi qu'une magnitude légèrement inférieure à celle calculée à partir du GNSS. Globalement, l'application à Ismetpasa confirme que le filtre adapté géodésique parvient à identifier des SSEs dans des jeux de données indépendants, même dans des conditions de bruit moins favorables, tout en soulignant l'importance d'une caractérisation locale du bruit et d'un post-traitement InSAR adapté pour maximiser la sensibilité et la fiabilité de la détection automatique.

Discussion

Validation de l'approche et de ses hypothèses. Les résultats obtenus, aussi bien sur données synthétiques que sur données réelles, démontrent que notre adaptation du filtre adapté géodésique est capable de détecter et de caractériser des SSEs superficiels à partir de séries temporelles InSAR. Les tests synthétiques montrent que, dans des conditions de bruit réalistes, des SSEs de magnitude aussi faible que M_w $4-4,5$ peuvent être détectés à faible profondeur avec un niveau de confiance supérieur à 90 % après l'étape de validation, la magnitude minimale détectable augmentant avec la profondeur. L'application aux segments d'Izmit et d'Ismetpasa confirme la robustesse de l'approche: le long du segment d'Izmit, les trois événements déjà documentés sont retrouvés avec le jeu EW-ICA, avec des magnitudes (M_w $4,1-4,3$), des profondeurs (≤ 2 *km*) et des temps de relaxation cohérents avec les analyses InSAR et *creepmeters* antérieures; le long du segment d'Ismetpasa, deux événements sont détectés après validation, avec des magnitudes et des durées comparables aux observations géodésiques antérieures, quoique avec des incertitudes plus importantes. La cohérence entre les événements détectés, leur caractérisation par empilement pondéré et les enregistrements indépendants des *creepmeters* constitue une validation externe de la méthode. Un résultat central de cette étude est la forte dépendance de la capacité de détection au niveau de bruit et à la stratégie de post-traitement: alors qu'aucun événement n'est détecté à partir des séries LOS brutes, le jeu EW-Raw permet d'en détecter deux, et le jeu EW-ICA permet d'en détecter un troisième, plus petit,

avec des pics de corrélation systématiquement plus élevés — ce qui indique que la sensibilité du filtre adapté est avant tout contrôlée par le rapport signal sur bruit des séries d'entrée.

Ces résultats encourageants s'accompagnent néanmoins de plusieurs limites, liées aux hypothèses retenues:

- **Taille fixe du gabarit.** L'extension spatiale du gabarit utilisé pour la caractérisation est fixe, ce choix étant motivé par la difficulté de résoudre les dimensions de la source à partir des seules données InSAR, compte tenu de la forte covariance spatiale du bruit atmosphérique à l'échelle kilométrique (≤ 5 *km*), qui peut produire des motifs de déformation en partie similaires à un signal de SSE superficiel. Les pentes de densité spectrale de puissance estimées ($\sim\ 2,5-4$) sont d'ailleurs cohérentes avec une turbulence atmosphérique et impliquent un spectre dominé par les grandes longueurs d'onde, comparables aux dimensions attendues des sources de SSEs superficiels.

- **Temps de relaxation fixe du gabarit** ($\tau = 6$ *jours*), calibré à partir d'observations antérieures sur des failles décrochantes continentales. Un temps de relaxation trop différent de celui de l'événement réel réduit l'amplitude de corrélation et peut décaler le temps de détection; la valeur retenue représente un compromis maximisant la sensibilité aux SSEs de quelques semaines tout en limitant les corrélations parasites en période de bruit pur.

- **Hypothèse de bruit non corrélé temporellement mais corrélé spatialement**, justifiée par l'échelle de temps caractéristique de la variabilité atmosphérique par rapport à la période de revisite de Sentinel-1, mais qui peut laisser subsister des signaux corrélés temporellement (par exemple des effets hydrologiques). L'amélioration observée avec l'ICA illustre bien qu'une séparation incomplète des signaux non tectoniques affecte directement la magnitude minimale détectable.

- **Résolution temporelle de l'InSAR** (6 jours pour Sentinel-1A/B), qui limite intrinsèquement la précision des estimations de temps d'initiation et de relaxation: les tests synthétiques montrent une surestimation systématique du temps de relaxation d'environ 6 jours, et la comparaison avec les *creepmeters* révèle des écarts pouvant atteindre un intervalle d'acquisition SAR pour les temps d'initiation.

Ces limites doivent être prises en compte avant toute application à d'autres contextes tectoniques, mais l'ensemble — validation synthétique et récupération réussie de SSEs déjà documentés indépendamment — démontre que notre approche constitue un cadre fiable et systématique pour la détection des SSEs superficiels dans les séries temporelles InSAR.

Comparaison avec les observations géodésiques indépendantes le long de la NAF: Segment d'Izmit. Les trois événements retrouvés avec le jeu EW-ICA correspondent aux SSEs de 2016, 2018 et 2019 déjà documentés (Aslan et al., 2019b; Neyrinck et al., 2024). Les magnitudes ($M_w \sim 4,1-4,3$) et les profondeurs superficielles (≤ 2 *km*) sont cohérentes avec les modèles de glissement de Neyrinck et al. (2024), dans lesquels la section de glissement reste confinée au bassin sédimentaire. La localisation spatiale des mailles glissantes inférées à partir des coefficients de corrélation maximaux se situe bien dans les zones de glissement significatif de ces modèles, ce qui montre que notre approche par gabarit capture la géométrie de premier ordre des événements sans nécessiter une inversion complète. Les temps d'initiation concordent avec les *creepmeters* à un ou deux intervalles de revisite de Sentinel-1 près ($6-12$ *jours*); les temps de relaxation estimés par le filtre adapté sont légèrement plus longs que ceux inférés des *creepmeters*, une différence systématique probablement liée à la résolution temporelle plus grossière de l'InSAR par rapport à l'échantillonnage des *creepmeters* (30 secondes), et au fait que les *creepmeters* enregistrent le glissement sur quelques dizaines de mètres en surface, tandis que l'InSAR intègre la déformation sur des zones de faille kilométriques.

Comparaison avec les observations géodésiques indépendantes le long de la NAF: Segment d'Ismetpasa. Les deux événements retenus peuvent être comparés aux analyses InSAR, GNSS et *creepmeters* antérieures. L'événement de 2019, caractérisé en GNSS par Özdemir et al. (2025) avec une magnitude équivalente d'environ 4, 8 et une durée d'environ 26 *jours*, est également identifié par notre approche, à faible profondeur (≤ 2 *km*) mais avec une durée plus longue (environ 60 *jours*); notre magnitude légèrement plus faible peut en partie s'expliquer par la taille de gabarit fixe utilisée lors de la caractérisation, qui peut sous-estimer le moment si la véritable surface de glissement dépasse les dimensions prescrites. Özdemir et al. (2025) notent d'ailleurs que le rapport signal sur bruit des déplacements de surface GNSS est trop faible pour permettre une inversion fiable — une conclusion à laquelle nous parvenons également avec les observations InSAR. L'événement de mi-2017 est plus faiblement contraint: bien qu'un pic de corrélation soit identifié, le temps d'initiation inféré présente un écart allant jusqu'à trois mois par rapport à l'enregistrement du *creepmeter N. Wall*, ce qui reflète vraisemblablement le niveau de bruit plus élevé du jeu de données InSAR sur ce segment et la plus faible amplitude de signal de cet événement; la gamme de profondeur inférée reste néanmoins globalement compatible avec les interprétations géodésiques antérieures.

Comparaison avec les observations géodésiques indépendantes le long de la NAF: Synthèse. Il est important de noter qu'aucun événement supplémentaire n'est détecté en abaissant encore le PRP, ce qui suggère que le niveau de bruit InSAR actuel empêche probablement l'identification de SSEs plus petits, millimétriques, déjà documentés par les *creepmeters* (par exemple mi-2018 sur Ismetpasa). La cohérence globale entre nos détections par gabarit et les contraintes géodésiques indépendantes indique que la méthode capture avec succès les caractéristiques physiques de premier ordre des SSEs superficiels sans nécessiter d'inversion complète du glissement; les écarts sur les temps d'initiation et de relaxation restent dans les limites imposées par l'échantillonnage temporel et le niveau de bruit de l'InSAR. Cela étant, lorsque le rapport signal sur bruit le permet, une inversion dédiée du glissement reste préférable pour caractériser plus finement la distribution spatiale du glissement et affiner l'estimation du moment.

Mécanismes physiques des glissements lents: Contrôles structuraux et mécaniques. Les SSEs superficiels identifiés le long des segments d'Izmit et d'Ismetpasa se produisent tous deux au sein de sections de faille déjà caractérisées par du glissement asismique. Sur le segment d'Izmit, ce glissement semble principalement localisé sous les SSEs, tandis que sur le segment d'Ismetpasa, il est observé de part et d'autre des SSEs, et peut-être aussi en dessous. Cette observation suggère qu'un régime de glissement asismique préexistant et persistant pourrait constituer un contexte mécanique nécessaire à l'occurrence de SSEs superficiels transitoires. Dans le cadre des modèles de frottement dits *rate-and-state*, les zones à renforcement en vitesse sont classiquement associées à un glissement stable, mais des hétérogénéités spatiales au sein de ces zones peuvent conduire à un comportement conditionnellement stable et à l'émergence d'épisodes de glissement transitoire. Le fait que seuls les segments d'Izmit et d'Ismetpasa, parmi l'ensemble des segments de la NAF, hébergent à la fois du glissement et des SSEs récurrents, alors que la plupart des autres segments n'en présentent pas, appuie l'hypothèse qu'un régime de glissement asismique préexistant constitue une condition préalable au glissement lent transitoire. Au-delà de la présence de glissement, les deux segments partagent un trait géologique intéressant: les SSEs s'y trouvent systématiquement localisés au sein de bassins sédimentaires — le bassin d'Izmit, dont la limite inférieure se situe à environ 2 *km* de profondeur, pour le premier; une couverture sédimentaire superficielle analogue pour le second. Les bassins sédimentaires se caractérisent typiquement par des matériaux riches en argile, peu résistants et potentiellement en surpression, susceptibles de favoriser un glissement stable ou conditionnellement stable. Le contexte géologique de la NAF est complexe, la faille suivant d'anciennes zones de suture séparant des unités lithologiques distinctes; cependant, seuls deux segments connus présentent à la fois du glissement superficiel et des SSEs récurrents, ce qui

suggère que les contrastes lithologiques seuls ne suffisent pas à expliquer leur occurrence. La coïncidence spatiale entre SSEs et bassins sédimentaires pointe plutôt vers l'importance des propriétés des matériaux superficiels — une association déjà documentée sur d'autres failles décrochantes continentales, notamment les failles Imperial et Superstition Hills en Californie, ce qui va dans le sens de l'hypothèse selon laquelle la présence de matériaux compliants et riches en argile pourrait favoriser des conditions frictionnelles propices au glissement asismique transitoire.

Mécanismes physiques des glissements lents: Rôle de la pression de fluide interstitiel. Une pression de fluide interstitiel élevée joue vraisemblablement un rôle central dans la nucléation et l'évolution des SSEs superficiels identifiés sur les deux segments. Une pression de pore élevée réduit la contrainte normale effective s'exerçant sur la faille, abaissant ainsi la contrainte de cisaillement nécessaire au glissement et favorisant la déformation asismique. Dans les sections qui glissent, recouvertes par des bassins sédimentaires ou situées en leur sein, les contrastes de perméabilité, les lithologies riches en argile et le piégeage de fluides peuvent favoriser des surpressions locales. Des études théoriques et numériques ont montré que les variations de pression de fluide peuvent significativement modifier la stabilité du glissement dans les systèmes *rate-and-state*; des modèles hydromécaniques couplés montrent notamment que la diffusion de pression de pore peut générer des impulsions de glissement lent même en régime de renforcement en vitesse, dès lors que la contrainte normale effective est suffisamment réduite — un couplage poroélastique susceptible de déstabiliser un glissement autrement stable et de produire des SSEs transitoires de durée et de magnitude comparables à celles observées géodésiquement. La dilatance module par ailleurs ce comportement: lors du cisaillement, la dilatation de la zone de faille réduit localement la pression de pore, augmentant temporairement la contrainte normale effective et stabilisant le glissement; la diffusion ultérieure des fluides restaure la pression de pore, permettant au glissement de reprendre. Cette rétroaction dilatance-diffusion, proposée comme mécanisme clé du glissement lent épisodique en contexte de subduction, pourrait opérer de façon similaire dans les environnements continentaux superficiels. La faible profondeur des événements détectés ($\leq 2\ km$) est cohérente avec des zones où les hétérogénéités de perméabilité et la circulation de fluides sont susceptibles d'être marquées, en particulier au sein des bassins sédimentaires. Une modulation saisonnière du glissement, attribuée à un chargement hydrologique, a par ailleurs été suggérée sur la faille de San Andreas, soulignant la sensibilité potentielle du glissement superficiel de faille aux variations de contrainte effective. Bien qu'aucune modulation saisonnière nette du glissement ne soit résolue dans notre étude, le fait que les SSEs du segment d'Izmit se produisent systématiquement en hiver suggère que des transitoires de pression pourraient jouer un rôle dans leur déclenchement.

Mécanismes physiques des glissements lents: Relation moment-durée. Les SSEs détectés se situent dans le domaine moment-durée déjà identifié pour les SSEs continentaux superficiels. Reportés sur un diagramme d'échelle adapté de Ide and Beroza (2023) et de Materna et al. (2024), les événements d'Izmit et d'Ismetpasa se regroupent dans la région dite « cachée » pour les zones de subduction — c'est-à-dire les événements de faible magnitude et de courte durée, détectables uniquement sur les failles décrochantes en raison de leur faible profondeur. Leur position sur ce diagramme, avec des magnitudes d'environ $M_w\ 4-4,3$ et des durées de quelques jours à quelques semaines, s'aligne sur les observations faites sur d'autres failles décrochantes continentales glissantes de manière asismique. Bien que le nombre limité d'événements empêche une estimation robuste de la loi d'échelle, le regroupement des SSEs de la NAF dans une portion étroite de cet espace suggère l'existence de conditions mécaniques communes gouvernant leur occurrence. La similarité entre Izmit et Ismetpasa, malgré leurs positions différentes dans le cycle sismique (peu après la rupture de 1999 pour l'un, environ 80 ans après la rupture de 1944 pour l'autre), indique que les propriétés frictionnelles et hydromécaniques locales pourraient l'emporter sur l'évolution de la contrainte à grande échelle

dans le contrôle du comportement des SSEs superficiels.

Mécanismes physiques des glissements lents: Implications pour la mécanique des failles continentales. Pris ensemble, ces éléments soutiennent un modèle conceptuel dans lequel les SSEs superficiels se développent préférentiellement sur des portions de faille entourées de segments en glissement asismique et situées au sein de bassins sédimentaires, où hétérogénéité frictionnelle, matériaux compliants et effets de fluides se combinent pour produire un glissement conditionnellement stable. Un glissement asismique persistant environnant pourrait fournir la déformation de fond nécessaire pour charger de petites zones à affaiblissement en vitesse ou conditionnellement stables, conduisant à un glissement transitoire récurrent. La similarité de ces caractéristiques avec celles documentées en Californie suggère que de telles conditions structurales et hydromécaniques pourraient constituer un ingrédient commun à l'occurrence de SSEs superficiels à l'échelle mondiale. L'élargissement des catalogues de SSEs grâce à des approches systématiques comme le filtre adapté géodésique sera essentiel pour tester si cette association entre glissement, couverture sédimentaire et glissement lent superficiel se vérifie dans des contextes tectoniques plus larges.

Comportement de glissement asismique le long du segment d'Izmit

Ce volet a pour but d'étudier précisément les épisodes transitoires de glissement asismique qui ont affecté le segment d'Izmit, afin d'étendre la période d'étude au niveau de ce segment et d'améliorer la caractérisation de son comportement de glissement.

Méthode

Nous exploitons les données acquises par les satellites Sentinel-1 A et B, dont le temps de revisite de 6 jours nous permet de caractériser la déformation du segment d'Izmit avec une résolution temporelle plus fine que les études antérieures. Les interférogrammes et séries temporelles InSAR utilisés ont été produits dans le cadre du service FLATSIM (*FormaTerre LArge-Scale Multi-Temporal Sentinel-1 InterferoMetry Service*), opéré par le CNES, selon l'approche NSBAS (*New Small Baseline*): sélection des *bursts*, co-registration et corrélation des images, évaluation de la diversité spectrale, correction altimétrique par rapport au Modèle Numérique de Terrain (MNT) et corrections orbitales précises. Les réseaux d'interférogrammes sont construits en minimisant les lignes de base perpendiculaires et temporelles, et les contributions atmosphériques sont corrigées à partir des réanalyses météorologiques globales ERA-5 du Centre européen pour les prévisions météorologiques à moyen terme (ECMWF).

Nous utilisons trois fauchées couvrant le segment d'Izmit: deux ascendantes (A058 et A160) et une descendante (D138), sur une période commune allant de février 2015 à avril 2021. Pour ne conserver que les pixels de bonne qualité, nous filtrons ceux dont l'incohérence de fermeture (RMS) dépasse $1,5$ *rad* par interférogramme, et exigeons au moins 900 interférogrammes par pixel — ce qui conserve environ 63 à 68 % des pixels initiaux.

Plusieurs étapes de post-traitement sont ensuite nécessaires pour isoler le signal tectonique:

- **Référencement par rapport au GNSS.** Nous référençons les vitesses InSAR en ligne de visée (LOS) par rapport au champ de vitesses GNSS de England et al. (2016), exprimé dans un référentiel Eurasie fixe.

- **Extraction des signaux saisonniers.** La plupart des séries temporelles LOS sont affectées par de forts signaux saisonniers, que nous modélisons par une tendance linéaire et des termes périodiques annuels (sinus/cosinus), estimés indépendamment pour chaque pixel.

- **Décomposition horizontale/verticale.** En fixant la direction moyenne de la faille à $N90^\circ$ et en combinant les séries temporelles des fauchées ascendantes et descendante

(après interpolation sur une base spatio-temporelle commune), nous décomposons le signal en déplacement horizontal Est-Ouest et déplacement vertical, en supposant les déplacements Nord-Sud négligeables.

- **Correction des signaux non tectoniques à grande longueur d'onde** (erreurs d'orbite, marées, résidus atmosphériques), par retrait puis réintroduction d'une tendance linéaire par pixel combinée à un aplatissement des cartes de déplacement résiduelles — ce qui réduit l'écart-type moyen des séries temporelles de $1,71$ *cm* à $1,05$ *cm*.

- **Débruitage du bassin sédimentaire par analyse en composantes indépendantes (ICA).** La trace de surface du segment d'Izmit traverse un bassin quaternaire où les séries horizontales présentent un fort bruit haute fréquence. En appliquant une séparation de sources aveugle (ICA, algorithme *FastICA*), nous retirons deux composantes sans tendance linéaire, ce qui réduit de 83 % la variance moyenne des séries temporelles dans le bassin, sans affecter le signal tectonique (vérifié par comparaison de séries différentielles entre pixels situés de part et d'autre de la faille).

Vitesses moyennes et modulation saisonnière. La carte des vitesses Est-Ouest moyennes fait apparaître un fort gradient de part et d'autre de la NAF, cohérent avec la déformation intersismique accommodant le mouvement dextre des plaques. Les profils perpendiculaires à la faille, sur 80 *km*, donnent un mouvement relatif en champ lointain de $2,26 \pm 0,1$ cm/an, en accord avec les estimations antérieures (McClusky et al., 2000; Reilinger et al., 2006; Nocquet, 2012). Le gradient de vitesse est plus marqué et plus resserré à proximité du segment d'Izmit — confirmant l'existence d'un glissement superficiel — qu'au niveau du segment d'Adapazari voisin, où le gradient est plus lisse et où la faille apparaît bloquée jusqu'à une plus grande profondeur. Sur le champ de vitesse verticale, seuls les bassins quaternaires (Adapazari, Gölcük, Izmit) présentent une subsidence significative ($0,5$ à 5 cm/an dans le bassin d'Adapazari); à proximité immédiate du segment d'Izmit, aucun mouvement vertical n'est observé, hormis dans d'étroites zones de 3 *km* de large situées au sud de la faille et affectées par une subsidence probablement d'origine hydrologique locale. Enfin, les termes saisonniers extraits des composantes ascendante et descendante, une fois convertis en champs Est-Ouest et vertical, ne présentent aucune modulation saisonnière du glissement sur la faille elle-même: les signaux saisonniers identifiés (grande échelle et bassin sédimentaire) ne contiennent donc pas de signal tectonique.

Dynamique du glissement le long du segment d'Izmit. Nous comparons les déplacements relatifs InSAR de part et d'autre de la faille aux enregistrements de deux *creepmeters* installés sur le segment: le *creepmeter* d'Izmit à l'ouest, et celui de Tepetarla à l'est, tous deux disponibles de façon discontinue entre 2015 et 2020.

Détection des épisodes transitoires. En calculant la différence des séries temporelles moyennes de part et d'autre de la faille (fenêtres de $600\ m \times 600\ m$, centrées à $700\ m$ de la trace de faille), nous obtenons des séries de déplacement relatif le long de la faille présentant une tendance linéaire moyenne de $5,3$ à $6,7$ mm/an selon la localisation. Une fois cette tendance retirée, ces séries font apparaître des accélérations transitoires nettes début 2018 et fin 2019, avec des déplacements cumulés atteignant 10 *mm*. Le second de ces épisodes coïncide avec un signal enregistré par les deux *creepmeters* (2 *mm* à Izmit, 4 *mm* à Tepetarla). En étudiant l'extension latérale de ces signaux le long de l'ensemble du segment, nous confirmons que les épisodes de mars 2018 et de novembre 2019 s'étendent sur environ 13 *km*, entre la mer de Marmara et la longitude $E030,10°$. Un troisième épisode, émergeant à peine du bruit, est également identifié en 2016; il coïncide avec un signal de 1 *mm* enregistré par le *creepmeter* d'Izmit et avait déjà été documenté par Aslan et al. (2019b), qui l'estimaient à environ 10 *mm* de déplacement Est-Ouest par InSAR.

Comparaison des périodes transitoires et inter-transitoires. En définissant deux cycles complets (un épisode transitoire principal encadré par les périodes de déplacement stable

qui le précèdent et le suivent), nous montrons que l'extension spatiale des trois épisodes transitoires diffère: celui de 2016 rompt surtout la partie ouest du segment sur environ 8 *km*, tandis que ceux de 2018 et 2019 affectent la partie centrale sur environ 13 *km*, avec une forme globalement symétrique centrée sur un maximum d'amplitude. Sur la partie centrale du segment, environ 50 % de la déformation cumulée provient des épisodes transitoires, contre seulement $25-30$ % aux extrémités — ce ratio dépendant toutefois de la distance à la faille choisie pour le calcul. Les *creepmeters*, situés directement sur la faille, ne capturent d'ailleurs que les épisodes transitoires et aucun déplacement relatif entre ceux-ci, ce qui suggère que seul le glissement transitoire atteint réellement la surface, le glissement inter-transitoire se produisant plus en profondeur.

Inversion du glissement en profondeur. Nous estimons la distribution du glissement le long de l'interface de faille à partir des séries temporelles de déplacement Est-Ouest, en inversant séparément le déplacement statique associé aux épisodes transitoires et la vitesse linéaire associée au glissement stable inter-transitoire, dans un formalisme de moindres carrés généralisés. Les fonctions de Green sont calculées pour un demi-espace élastique multicouche, en tenant compte d'un modèle de vitesses sismiques régional et d'un modèle de densité intégrant le bassin sédimentaire d'Izmit (contraint par les données de gravimétrie de Özalaybey et al. (2011)) et les structures plus profondes (*Crust 1.0*). Cette stratification permet d'éviter un biais d'estimation du glissement superficiel lié aux faibles vitesses et densités du bassin sédimentaire. Le maillage de la faille est resserré (mailles de 333 *m*) sous le segment d'Izmit jusqu'à 5 *km* de profondeur, puis s'élargit progressivement en profondeur et latéralement.

Inversion du glissement en profondeur: Glissement stable. En retirant les déplacements associés aux épisodes transitoires des séries temporelles et en ajustant une régression linéaire, nous inversons une série de modèles à profondeur de blocage variable (0 à 30 *km a priori*), le glissement sous cette profondeur étant fixé au mouvement relatif des plaques (24 mm/an). Les profondeurs de blocage inférieures à 10 *km* produisent des résidus trop importants et ne peuvent expliquer le déplacement en champ lointain; en dessous de 15 *km*, des zones de glissement profondes non réalistes apparaissent pour compenser une profondeur de blocage trop grande. Nous retenons ainsi une profondeur de blocage optimale de 11 *km*, qui permet à la fois d'ajuster les données et d'obtenir une distribution homogène du glissement en dessous. Le modèle final révèle un glissement superficiel principalement compris entre 2 et 4 *km* de profondeur, avec des taux de glissement de 2 cm/an, atteignant localement 6 cm/an à la longitude $E029,99^\circ$ — juste sous le bassin sédimentaire. La résolution latérale du glissement superficiel reste en revanche mal contrainte par les données, plusieurs modèles avec des lissages spatiaux différents expliquant également bien les observations; la distribution en profondeur, elle, est bien contrainte, avec des taux de glissement élevés systématiquement situés entre 2 et 4 *km*.

Inversion du glissement en profondeur: Épisodes transitoires de 2018 et 2019. Après retrait de la composante linéaire inter-transitoire, nous calculons le déplacement total associé à chaque épisode transitoire (moyenne des déplacements un mois avant et après l'épisode). Les cartes de déplacement statique obtenues pour 2016, 2018 et 2019 montrent des amplitudes croissantes (environ 5, 8 et 9 *mm* respectivement), les épisodes de 2018 et 2019 présentant des lobes positifs et négatifs nets de part et d'autre de la faille, contrairement au signal de 2016, plus bruité. Nous inversons le glissement en profondeur associé aux épisodes transitoires de 2018 et 2019 en ne considérant que l'interface entre la surface et 5 *km* sous le segment d'Izmit. Les principales zones de glissement se concentrent au-dessus de 2 *km* de profondeur, à l'intérieur ou à proximité immédiate de la limite inférieure du bassin sédimentaire, et se situent toutes deux sur la partie centrale du segment, avec un déplacement Est-Ouest moyen d'environ 3 *cm*. Nous identifions deux aspérités principales — l'une plus petite à l'ouest (~ 3 km^2), l'autre plus grande au centre de l'interface (~ 8 km^2) — toutes deux situées dans ou juste sous le bassin sédimentaire, ce qui suggère que les mêmes zones ont rompu lors des

deux épisodes. En utilisant un module de cisaillement moyen de 18 *GPa* sur les 4 premiers kilomètres de l'interface et des surfaces de glissement de $11,4$ et $9,3$ km^2 pour les épisodes de 2018 et 2019 respectivement, nous obtenons des magnitudes de moment équivalentes de $4,4$ et $4,3$. Les déplacements Nord-Sud prédits par ces modèles restent inférieurs à $0,1$ *mm*, ce qui valide *a posteriori* l'hypothèse d'un déplacement Nord-Sud négligeable retenue dans la décomposition initiale.

Discussion

Un glissement stable toujours actif 22 *ans* **après le séisme d'Izmit.** Nos résultats confirment que le segment d'Izmit continue de glisser de manière asismique 22 *ans* après le séisme de 1999. En combinant nos séries temporelles avec des mesures GNSS de campagne (stations SISL et SMAS) et des séries InSAR publiées antérieurement, nous estimons un taux de glissement post-sismique superficiel d'environ $7,5$ mm/an sur la période 2016-2021, cohérent avec la décroissance logarithmique proposée par Özarpacı et al. (2020) (temps de relaxation de 60 *ans*), qui suggère que la phase post-sismique est toujours en cours. En combinant l'ensemble des estimations disponibles depuis 1999 avec l'observation que les deux tiers de la relaxation se sont produits dans les deux premières années, nous obtenons une estimation grossière du glissement post-sismique superficiel cumulé d'environ 35 *cm* — soit moins de 10 % du déficit de glissement cosismique estimé dans les cinq premiers kilomètres (4 à 5 *m*). Cette faible proportion, entachée d'une grande incertitude, pourrait signifier soit qu'une partie importante de l'*afterslip* précoce manque aux modèles publiés, soit que le déficit cosismique a été surestimé, soit que le rattrapage du déficit par glissement post-sismique peut se poursuivre sur plusieurs décennies encore — à l'image du segment d'Ismetpasa de la NAF, qui glisse toujours en surface environ quatre-vingts ans après le séisme de Bolu-Gerede de 1944.

La profondeur de blocage de 11 *km* que nous estimons pour la période 2016-2021 est cohérente avec les études post-sismiques antérieures ($10-12$ *km*), mais nettement plus superficielle que celle estimée avant le séisme de 1999 (21 *km*, McClusky et al., 2000), ce qui va dans le sens d'un *afterslip* toujours actif sous la zone sismogène, avec un approfondissement progressif de la profondeur de blocage au fil du cycle sismique — un schéma également observé sur le segment d'Ismetpasa.

Le cycle des glissements lents sur le segment d'Izmit. En comptant l'épisode de septembre 2015 (Özarpacı et al., 2020) et celui de décembre 2016 (confirmé ici et par Aslan et al. (2019b)), nous portons à quatre le nombre d'épisodes transitoires recensés sur le segment d'Izmit, pour une période de retour moyenne d'environ $1,3$ *an* — un ordre de grandeur comparable à celui observé sur d'autres failles décrochantes californiennes à épisodes transitoires superficiels (faille de Superstition Hills, San Andreas près de San Juan Bautista) ainsi que sur le segment d'Ismetpasa de la NAF. Cet intervalle de récurrence pourrait se raccourcir si le segment d'Izmit demeure en phase post-sismique, ou rester stable s'il est déjà revenu à un régime intersismique.

Entre les épisodes transitoires, le glissement stable observé en profondeur n'est pas parfaitement constant dans le temps, ce qui pourrait indiquer la présence d'épisodes transitoires de plus faible amplitude — sans que nous puissions les distinguer clairement du niveau de bruit. Seuls les épisodes de 2018 et 2019 disposent d'un signal suffisamment complet pour une inversion du glissement en profondeur; celui de 2015 n'a été capté que par le *creepmeter* d'Izmit ($1,6$ *mm* de déplacement dextre), et celui de 2016 par le *creepmeter* ($1,1$ *mm*) et par InSAR (5 *mm* dans notre analyse, contre 10 *mm* chez Aslan et al. (2019b)). Le déplacement maximal de l'épisode de 2016 est localisé à l'ouest du segment, tandis que ceux de 2018 et 2019 se concentrent sur sa partie centrale — ce qui pourrait indiquer une migration progressive de la zone source. Les amplitudes de glissement estimées, de $1-2$ *cm* (jusqu'à 6 *cm* selon le lissage spatial retenu), et les magnitudes de moment ($4,3-4,4$) sont cohérentes avec d'autres événe-

ments transitoires superficiels documentés sur des failles décrochantes continentales (segment d'Ismetpasa, faille de Superstition Hills). Ces événements permettent de relâcher 48 à 51 % du taux de chargement tectonique de la même zone.

Grâce à l'échantillonnage à 30 secondes des *creepmeters*, nous estimons une durée d'environ 9 jours pour l'épisode de 2019 (9 jours 23 h à Izmit, 8 jours 21 h à Tepetarla), une durée compatible avec celle d'autres épisodes transitoires superficiels sur failles décrochantes continentales, mais plus courte que celle de nombreux SSEs de subduction, bien que de magnitude comparable — plaçant ces événements dans une zone peu documentée du diagramme durée/magnitude, comme le suggèrent Ide and Beroza (2023). Le décalage temporel de 2,26 jours entre le début de l'épisode aux deux *creepmeters*, séparés d'environ $14,5$ *km*, nous permet d'estimer, sous l'hypothèse d'une propagation unilatérale à vitesse constante, une vitesse de propagation latérale d'environ $6,4$ *km*/*jour* — comparable aux vitesses observées sur la faille de San Andreas ainsi qu'aux vitesses de propagation latérale de SSEs de subduction (Nankai, Cascadia, Alaska). Une propagation bilatérale, initiée entre les deux *creepmeters*, resterait toutefois également compatible avec nos observations, avec une vitesse comprise entre 0 et $6,4$ *km*/*jour* selon le point d'initiation retenu.

Mécanismes possibles du glissement stable et des SSEs. Notre analyse révèle deux régimes de glissement superficiels distincts: un glissement stable entre 2 et 4 *km* de profondeur, et des épisodes transitoires entre la surface et 2 *km*. Le glissement asismique superficiel dans les quatre premiers kilomètres compense vraisemblablement le déficit de glissement laissé par le glissement cosismique du séisme de 1999 à des profondeurs sismogènes. Les deux régimes pourraient résulter de variations, avec la profondeur, des propriétés frictionnelles de la faille, les SSEs superficiels se situant précisément à proximité de la limite inférieure du bassin sédimentaire. Le glissement continu entre 2 et 4 *km* pourrait constituer une condition nécessaire au déclenchement des SSEs superficiels, en augmentant continûment la contrainte de cisaillement sur les premiers kilomètres de la faille.

Dans le cadre des modèles de frottement *rate-and-state*, la dépendance en profondeur des paramètres frictionnels permet d'expliquer les différents régimes de glissement sismique et asismique des failles décrochantes: une couche instable à affaiblissement en vitesse (*velocity-weakening*) à profondeur sismogène surmontant une couche à renforcement en vitesse (*velocity-strengthening*) plus profonde explique les cycles de grands séismes; l'ajout d'une zone à renforcement en vitesse dans les premiers kilomètres explique le glissement asismique superficiel; et l'introduction d'une couche supplémentaire à comportement neutre en vitesse, ou conditionnellement stable, permet de reproduire l'émergence de SSEs transitoires superficiels. Dans le cas particulier du segment d'Izmit, deux caractéristiques doivent être expliquées simultanément: la décroissance logarithmique de l'*afterslip* post-sismique et l'émergence d'épisodes transitoires. Les modèles de Wei et al. (2013), incluant une fine couche conditionnellement stable près de la surface, parviennent à reproduire ces deux observations, et prédisent un raccourcissement des intervalles de récurrence des SSEs au cours de la phase post-sismique — une évolution que le nombre encore limité d'événements observés sur le segment d'Izmit ne nous permet pas de tester.

Le contrôle exact de la répartition entre segments en glissement asismique (Ismetpasa, Izmit) et segments bloqués le long de la NAF reste incertain, bien qu'un contrôle minéralogique soit souvent évoqué. Au niveau d'Izmit, la branche nord de la NAF sépare des calcaires paléozoïques-mésozoïques (au nord) de plusieurs unités métamorphiques (au sud), déposés sur un socle métamorphique commun — un contraste lithologique compatible avec les conditions favorisant le glissement asismique selon Kaduri et al. (2017), qui ont montré que les unités volcaniques au niveau de la gouge d'Ismetpasa sont plus sujettes au glissement sismique et asismique que les calcaires. Les sédiments superficiels, généralement riches en argile, peuvent également favoriser le développement du glissement asismique, et une étude tomographique antérieure (Taylor et al., 2019) montre que la zone endommagée de la croûte s'étend jusqu'à 5 *km* sous

la trace du segment d'Izmit — une profondeur compatible avec celle de la zone de glissement identifiée ici.

Une forte pression de fluide interstitiel pourrait également favoriser le glissement asismique transitoire, comme le suggèrent des contextes géothermiques ou des zones de subduction à fort rapport Vp/Vs propices aux SSEs. Sur les failles décrochantes, des événements pluvieux intenses ont été proposés comme un facteur favorisant des épisodes de glissement transitoire, et une modulation saisonnière du glissement a été observée sur certaines failles (San Andreas). Sur le segment d'Izmit, notre analyse des composantes saisonnières ne révèle toutefois aucune preuve claire d'une telle modulation. En croisant les occurrences des trois épisodes transitoires avec les données de température et de précipitations ERA-5 Land sur 2016-2021, nous ne trouvons pas de relation nette, si ce n'est une coïncidence entre l'épisode de 2016 et une période de précipitations accrues, qui pourrait influencer la pression de pore sur l'interface — la topographie en creux du bassin d'Izmit et la présence du bassin sédimentaire pouvant par ailleurs favoriser une pression de pore globalement élevée dans cette zone.

Enfin, la comparaison avec le catalogue sismique AFAD sur 2016-2021 ne révèle aucun lien évident entre la sismicité locale et les SSEs: la distribution temporelle des séismes apparaît aléatoire sur la période étudiée, et la partie centrale du segment — où l'amplitude de glissement des SSEs est la plus importante — apparaît au contraire comme une zone de quiescence sismique, suggérant une ségrégation spatiale entre sismicité et glissement asismique transitoire. Nous n'observons par ailleurs aucun séisme régional susceptible d'avoir déclenché l'un des trois SSEs superficiels identifiés, ce qui suggère qu'il s'agit d'épisodes spontanés.

Modèles de cycle sismique appliqués au segment d'Izmit

Ce dernier volet propose une modélisation mécanique du cycle sismique du segment d'Izmit de la NAF, fondée sur le formalisme de friction *rate-and-state* (RSF), afin de tester si une structure frictionnelle unique et physiquement plausible peut simultanément reproduire l'ensemble des observations disponibles sur ce segment: l'amplitude et le temps de récurrence du glissement cosismique du séisme d'Izmit de 1999 (M_w 7,6), la relaxation postsismique (*afterslip*) enregistrée sur plusieurs décennies, ainsi que l'amplitude, le temps de récurrence et la durée des glissements lents transitoires (*Slow Slip Events*, SSEs) superficiels détectés le long de ce segment. Ce travail fait suite à des discussions lors de l'AGU Fall Meeting 2024 avec Matt Wei (University of Rhode Island) et Yoshihiro Kaneko (Kyoto University), auteurs d'une modélisation similaire pour la faille de Superstition Hills en Californie (Wei et al., 2013), où une hétérogénéité frictionnelle superficielle intégrée dans le cadre RSF permettait déjà d'expliquer l'occurrence de SSEs au cours du cycle sismique.

Le cycle sismique classique décrit une zone sismogène qui accumule la déformation élastique en période interséismique et la libère lors des séismes. Au-dessus et en dessous de cette zone instable, la faille peut glisser de manière asismique, en continu ou de façon transitoire. Ce cadre conceptuel doit toutefois être enrichi de zones de transition à comportement frictionnel conditionnellement stable ou hétérogène dans l'espace, seules capables d'expliquer la coexistence, sur un même segment, de glissement sismique, de glissement superficiel continu, d'*afterslip* postsismique et de glissements transitoires. Si les SSEs ont d'abord été documentés en contexte de subduction, un nombre croissant d'observations géodésiques démontre qu'ils affectent également des failles décrochantes continentales (San Jacinto, Hayward, Imperial/San Andreas, Superstition Hills, Haiyuan, et plusieurs segments de la NAF dont Ismetpasa et Izmit). Le long des failles décrochantes, ces SSEs superficiels sont généralement circonscrits aux premiers kilomètres sous la surface et pourraient être favorisés par la présence de bassins sédimentaires, de contrastes lithologiques superficiels, de fluides, de complexités géométriques ou de zones endommagées héritées.

Le segment d'Izmit constitue un laboratoire naturel privilégié: il a rompu lors du séisme

de 1999, produisant plusieurs mètres de glissement cosismique, avec des temps de récurrence historiques et paléosismologiques de l'ordre du siècle à plusieurs siècles; il a ensuite fait l'objet d'un suivi géodésique continu ayant révélé un *afterslip* postsismique décennal (stations GNSS de campagne SMAS-SISL) ainsi que plusieurs SSEs superficiels en 2015, 2016, 2018 et 2019, localisés dans la partie peu profonde de la zone de rupture de 1999 et recoupant partiellement le bassin sédimentaire quaternaire d'Izmit. Ces observations soulèvent une question centrale: quelle structure frictionnelle peut simultanément expliquer de larges ruptures cosismiques, un *afterslip* persistant sur plusieurs décennies, et des SSEs superficiels récurrents sur ce même segment? Pour y répondre, ce chapitre utilise le cadre numérique RSF développé par Wei et al. (2013), en testant si une hétérogénéité frictionnelle superficielle associée au bassin sédimentaire d'Izmit peut expliquer l'occurrence des SSEs tout en préservant les caractéristiques principales du cycle sismique de 1999.

Méthode

Formalisme rate-and-state. Les simulations numériques reposent sur une approche quasi-dynamique appliquée à une faille décrochante unidimensionnelle intégrée dans un demi-espace élastique bidimensionnel (Rice, 1993; Lapusta et al., 2000; Liu and Rice, 2007; Wei et al., 2013). Dans ce cadre, la contrainte de cisaillement τ dépend de la vitesse de glissement V et d'une variable d'état θ décrivant l'historique de glissement de la faille, selon la loi classique de friction *rate-and-state* (avec les paramètres frictionnels a et b, la distance caractéristique de glissement D_c, le coefficient de friction de référence f_0 et la contrainte normale effective σ). L'évolution de θ suit la loi de vieillissement (*aging law*). La taille de nucléation caractéristique h^* est définie à partir de ces paramètres et du module de cisaillement μ. Pour les très faibles vitesses de glissement, la loi de friction est régularisée sous une forme en arcsinus, justifiée par une description thermiquement activée du glissement au niveau des contacts frictionnels.

Définition des modèles mécaniques. Deux modèles mécaniques limites (*end-members*) sont construits, partageant une même structure profonde mais différant par la couche la plus superficielle:

- **Couche profonde commune**: une couche en *velocity-weakening*, correspondant à la zone sismogène et contrôlant la nucléation des séismes et la rupture cosismique; une seconde couche plus profonde, en *velocity-strengthening*, représentant la portion stable inférieure de l'interface de faille, où les conditions de pression-température inhibent la rupture sismique.

- **Couche superficielle — Modèle 1**: une couche homogène conditionnellement stable en *velocity-weakening*, surmontant une couche stable.

- **Couche superficielle — Modèle 2**: un gradient vertical de propriétés frictionnelles dans la couche superficielle, censé représenter un changement progressif de stabilité frictionnelle apparente, par exemple lié à des variations de pression de pore ou d'endommagement au sein du bassin sédimentaire.

Les paramètres explorés sont la distance caractéristique de glissement D_c, la contrainte normale effective σ (croissant linéairement avec la profondeur selon un gradient lithostatique-hydrostatique de 13 MPa/km), le paramètre frictionnel $(a-b)$, et les largeurs des différentes couches. Plusieurs bornes de profondeur sont contraintes indépendamment par les observations géologiques et sismologiques: la base de la couche superficielle est fixée à la profondeur moyenne du socle du bassin sédimentaire d'Izmit ($\sim 1,2\ km$, Özalaybey et al. (2011)); la base de la couche stable est contrainte par la limite supérieure de la séquence de répliques du séisme de 1999 ($\sim 5-6\ km$); la base de la couche sismogène est contrainte par les estimations de

profondeur de blocage post-1999 ($11-15$ *km*). Le taux de chargement tectonique est fixé à 24 mm/an (McClusky et al., 2000).

Contraintes observationnelles le long du segment d'Izmit. Les simulations sont confrontées à un ensemble de contraintes observationnelles: amplitude du glissement cosismique de 1999 ($\sim 5,5 \pm 0,5$ *m*) et temps de récurrence des grands séismes ($\sim 140 \pm 30$ *ans*, d'après les données paléosismologiques et historiques); constantes temporelles de l'*afterslip* postsismique décennal ($c \sim 4,88$ *cm* et $d \sim 25,23$ an^{-1}) déduites des enregistrements GNSS de campagne SMAS-SISL (Özarpacı et al., 2020); et propriétés des SSEs environ 20 *ans* après le séisme principal — amplitude ($\sim 2 \pm 0,5$ *cm*), temps de récurrence ($\sim 1,35 \pm 0,05$ *an*) et temps de relaxation ($\sim 6 \pm 1$ *jours*), contraints respectivement par les inversions InSAR (Neyrinck et al., 2024) et les enregistrements de *creepmeters* (Aslan et al., 2019b; Neyrinck et al., 2024).

Comparaison entre simulations numériques et observations. Chaque simulation est évaluée selon six observables: amplitude et temps de récurrence du glissement cosismique, temps de relaxation postsismique, amplitude, temps de récurrence et durée des SSEs. Les séismes principaux sont identifiés à partir des pics de vitesse maximale de glissement sur la faille (critère $log_{10}(Vmax/Vpl) \geq 5,44$). Le déplacement postsismique simulé est comparé aux observations GNSS via le calcul de fonctions de Green pour un demi-espace élastique homogène (Okada, 1985), la série temporelle résultante étant ajustée par une fonction logarithmique $(a + bt + c \cdot log(1 + dt))$ au moyen d'une inversion de Levenberg-Marquardt (*SciPy*), suivie du calcul de RMSE entre modèle et observations. Les SSEs sont identifiés par un critère de vitesse maximale sur la cellule la plus superficielle ($0,5 \leq log_{10}(V/Vpl) \leq 6,85$), à l'exclusion des périodes de rupture cosismique.

Résultats

Observations cosismiques. L'amplitude du glissement cosismique et le temps de récurrence des séismes varient avec les propriétés de la couche sismogène. Le paramètre $(a-b)$ exerce le contrôle le plus fort sur l'amplitude: pour $(a-b) \geq -0,001$, le modèle ne produit pas de grand séisme; lorsque $(a-b)$ décroît de $-0,002$ à $-0,007$, le glissement cosismique maximal augmente jusqu'à ~ 9 *m*, cette augmentation s'accompagnant de variations non linéaires du temps de récurrence d'environ 100 *ans* (des paramètres frictionnels plus négatifs tendant à produire des séismes plus grands avec des temps de récurrence plus courts). La distance caractéristique D_c et la largeur de la couche affectent principalement le temps de récurrence (variations d'environ 130 *ans*), l'amplitude cosismique variant plus modérément ($0,5-2$ *m*); l'augmentation de D_c accroît à la fois l'amplitude et le temps de récurrence, tandis que l'élargissement de la couche sismogène augmente l'amplitude mais diminue le temps de récurrence.

Observations d'afterslip. La comparaison entre l'*afterslip* simulé et les observations GNSS SMAS-SISL montre que les deux paramètres testés pour la couche stable (largeur et $(a-b)$) contrôlent conjointement le RMSE: l'augmentation de l'un ou de l'autre tend à augmenter le RMSE en produisant un déplacement postsismique cumulé excessif. Bien que la solution ne soit pas unique, des valeurs de $(a-b)$ proches de $0,005$ associées à une épaisseur de couche stable de $3,7$ *km* représentent une combinaison cohérente avec les déplacements postsismiques observés.

Observations de SSEs. Les deux configurations superficielles (Modèles 1 et 2) permettent de générer des SSEs environ 20 *ans* après le séisme principal, mais avec des proportions et une diversité de simulations réussies différentes. Les tailles de nucléation h^* compatibles avec l'apparition de SSEs sont de $1,3-1,6$ *km* pour le Modèle 1 et de $1,4-1,9$ *km* pour le Modèle 2 — ce dernier autorisant donc une gamme plus large de tailles de nucléation et de paramètres, bien que h^* seul ne détermine pas totalement l'occurrence des SSEs.

En termes d'amplitude et de temps de récurrence, les deux familles de modèles produisent

des SSEs du même ordre de grandeur que les observations: le Modèle 1 produit des amplitudes de 1 à $5,2$ *cm* avec des temps de récurrence de 0,5 à $5,2$ *ans*, le Modèle 2 des amplitudes de 1 à $3,5$ *cm* avec des temps de récurrence de 0,5 à $3,5$ *ans*. Le paramètre frictionnel minimal de la couche superficielle influence à la fois l'amplitude et le temps de récurrence: des valeurs moins négatives produisent généralement des événements plus petits et plus fréquents, la relation n'étant toutefois pas strictement monotone (en particulier pour le Modèle 2 avec $D_c = 0,3$), ce qui indique une dépendance couplée entre stabilité frictionnelle et distance caractéristique.

L'analyse détaillée de l'évolution en profondeur du glissement au cours d'un SSE (pour les modèles optimaux finaux) révèle trois phases communes aux deux configurations: (1) une initiation du glissement à une profondeur intermédiaire ($\sim 650-725$ *m*), avec une augmentation quasi linéaire du glissement sur environ 10 jours (vitesse maximale de $13,7$ *cm*/*an* pour le Modèle 1 et $11,2$ *cm*/*an* pour le Modèle 2); (2) une propagation du glissement vers la surface, avec une accélération rapide des cellules les plus superficielles sur environ un jour, libérant jusqu'à $42,9$ % (Modèle 1) et $37,5$ % (Modèle 2) du déplacement total; (3) une décélération sur au moins 10 jours, de forme logarithmique pour le Modèle 1, plus complexe (avec une accélération secondaire) pour le Modèle 2. La profondeur d'initiation est décalée de ~ 75 *m* plus en profondeur pour le Modèle 2 par rapport au Modèle 1.

Discussion

Limites du modèle et approximation quasi-dynamique. La principale limite du travail réside dans l'usage d'une approximation quasi-dynamique plutôt que d'une résolution pleinement dynamique de la propagation des ondes sismiques: bien que cette approximation réduise fortement le coût de calcul, elle peut affecter les détails de la propagation de rupture, la vitesse de glissement maximale, l'arrêt de la rupture et la redistribution de contrainte associée aux ondes dynamiques. Cette limitation concerne principalement la phase cosismique, et affecterait peu les caractéristiques de l'*afterslip* et des SSEs. Les comparaisons antérieures entre approches quasi-dynamiques et pleinement dynamiques (notamment pour Superstition Hills, Wei et al. (2013)) suggèrent que les motifs de glissement globaux restent similaires, bien que certains paramètres optimaux puissent être décalés entre les deux approches. Les valeurs rapportées dans ce chapitre doivent donc être interprétées comme des paramètres effectifs au sein du cadre quasi-dynamique adopté, plutôt que comme des propriétés frictionnelles uniques.

Contrôles sur la rupture cosismique et l'afterslip postsismique. Le comportement cosismique et postsismique est principalement contrôlé par la géométrie et les propriétés frictionnelles des couches intermédiaire et sismogène, les contraintes externes sur les profondeurs de ces couches étant essentielles pour réduire l'espace des modèles acceptables. Au sein de cette structure, le paramètre $(a-b)$ et la distance D_c de la couche sismogène contrôlent l'amplitude et la récurrence des grands séismes, tandis que la déformation postsismique est principalement gouvernée par la couche stable en *velocity-strengthening*. Les estimations obtenues pour ces deux couches sont du même ordre de grandeur que celles inférées par Wei et al. (2013) pour la faille de Superstition Hills, suggérant que des structures frictionnelles comparables pourraient expliquer la déformation du cycle sismique sur différentes failles décrochantes continentales.

Ingrédients frictionnels nécessaires aux SSEs superficiels. L'occurrence de SSEs superficiels dans les modèles nécessite une couche superficielle conditionnellement instable surmontant la zone stable de l'*afterslip* postsismique: en son absence, la faille glisse de manière stable ou reste trop fortement couplée pour générer des transitoires épisodiques — un résultat cohérent avec les modèles antérieurs pour les failles décrochantes (Wei et al., 2013; Tymofyeyeva et al., 2019). Dans le cas d'Izmit, la couche superficielle requise s'étend approximativement sur la même gamme de profondeur que le bassin sédimentaire, suggérant un lien mécanique entre structure du bassin et glissement transitoire superficiel.

Les deux architectures testées reproduisent les principales propriétés observées des SSEs, mais avec des sensibilités paramétriques différentes: le Modèle 1 homogène ne produit des SSEs que dans une gamme relativement étroite de tailles de nucléation et de paramètres frictionnels, nécessitant un réglage fin, tandis que le Modèle 2, à gradient vertical, autorise des SSEs sur une gamme de paramètres plus large — ce gradient pouvant lisser la transition entre les glissements stable et instable, ralentissant la propagation de la rupture et permettant des événements de plusieurs jours. Les deux modèles optimaux prédisent par ailleurs une phase de nucléation longue (environ 10 jours) précédant le glissement transitoire visible en surface par la géodésie.

Implications pour les processus physiques des SSEs. La coïncidence spatiale entre la source modélisée des SSEs superficiels et le bassin sédimentaire d'Izmit (composé de dépôts alluviaux — sables, argiles, graviers — et de dépôts plio-pléistocènes) suggère que les propriétés du bassin (contrastes lithologiques, gouge argileuse, endommagement, variations de perméabilité) jouent un rôle clé dans le comportement frictionnel superficiel. La pression de pore constitue un autre mécanisme plausible: une pression de pore élevée ou variable avec la profondeur réduit la contrainte normale effective et modifie ainsi la résistance frictionnelle et la taille de nucléation; le Modèle 2 peut être interprété comme une représentation simplifiée de cet effet, imposant une stabilité frictionnelle apparente dépendant de la profondeur sans expliciter les processus hydrologiques sous-jacents.

Enfin, la similitude entre les modèles d'Izmit et les modèles antérieurs développés pour les failles décrochantes californiennes suggère que les SSEs superficiels sur failles continentales pourraient partager des ingrédients mécaniques communs — une couche superficielle conditionnellement instable entre la surface et une région stable plus profonde —, les bassins sédimentaires constituant des environnements particulièrement favorables (faible contrainte effective, lithologie variable, fort endommagement, circulation de fluides possible), sans que cela implique que tout bassin sédimentaire doive nécessairement héberger des SSEs. Sur le plan de l'aléa sismique, ces résultats indiquent que les SSEs superficiels, bien qu'ils libèrent une partie du déficit de glissement près de la surface, ne réduisent pas nécessairement le risque associé à la zone sismogène plus profonde: les modèles reproduisant les SSEs superficiels nécessitent toujours une couche profonde en *velocity-weakening* capable de produire de grands séismes avec des temps de récurrence comparables aux estimations paléosismologiques. Le glissement superficiel asismique doit donc être interprété comme une composante du cycle sismique, et non comme la preuve que l'ensemble du segment serait mécaniquement stable.

Conclusion générale

Ces travaux focalisés sur la NAF ont permis de préciser son comportement asismique, en particulier le long du segment d'Izmit, révélant ainsi l'occurrence de SSEs superficiels avec un temps de retour d'environ $1,3$ *an*. Cependant, il est crucial de multiplier les détections de SSEs afin d'enrichir les catalogues existants et d'identifier plus clairement les caractéristiques communes des différents SSEs, ce qui permettrait de dégager des conditions préférentielles à leur développement et de mieux cerner leur rôle dans l'aléa sismique. La combinaison d'observations géodésiques et de mesures de microsismicité est également essentielle pour mieux contraindre la dynamique du glissement transitoire, soulignant le besoin de réseaux sismiques et géodésiques denses capables de capturer à la fois l'activité asismique et sismique. Dans cette optique, un réseau GNSS dense, auquel j'ai contribué, a été installé le long du segment d'Izmit en 2024 afin d'acquérir des données géodésiques à haute résolution temporelle. Combinées à la haute résolution spatiale des observations InSAR, ces données permettront une caractérisation plus fine de la dynamique du glissement. À terme, la comparaison du comportement des SSEs le long des failles décrochantes avec les cycles bien documentés observés dans les zones de subduction pourrait permettre d'identifier des mécanismes communs

contrôlant le glissement lent dans différents contextes tectoniques.

Remerciements ii

Abstract vi

Résumé court en français x

Résumé long en français xiv

Liste des figures xlviii

Liste des tableaux xlix

Acronyms l

General introduction 2

1 Seismic Cycle and Geodesy in Türkiye 5
1.1 History of earthquake science . . . 8
1.2 Seismic cycle . . . 10
1.2.1 Seismic hazard, seismic risk and vulnerability . . . 10
1.2.2 Simplified seismic cycle sequence . . . 10
1.2.3 Diversity of the observations . . . 12
1.2.3.1 Seismological data . . . 12
1.2.3.2 Geodetic data . . . 13
1.2.3.3 Geological observations . . . 16
1.3 Types of aseismic fault slip behavior . . . 18
1.3.1 Historical discovery . . . 18
1.3.2 Definitions of seismic, aseismic and fault coupling . . . 19
1.3.3 Seismic cycle models . . . 21
1.3.3.1 Constitutive friction laws . . . 21
1.3.3.2 Rate-and-state friction law . . . 22
1.3.3.3 Application to seismic cycle simulation . . . 24
1.3.4 Slow slip events . . . 25
1.3.4.1 Identification of slow slip events around the world . . . 25
1.3.4.2 Observations of Slow Slip Events . . . 26
1.3.5 Mechanisms governing the occurrence of Slow Slip Events . . . 28
1.3.5.1 Frictional control . . . 28
1.3.5.2 Lithological control . . . 30
1.3.5.3 Fluids and pore pressure . . . 30
1.3.5.4 Structural control . . . 30
1.3.5.5 Synthesis on the moment-duration scaling laws . . . 31
1.3.6 Related open challenges . . . 32
1.4 Interferometry Synthetic Aperture Radar (InSAR) processing . . . 33
1.4.1 Definition of SAR Interferometry . . . 33
1.4.1.1 The SAR images acquisitions . . . 33
1.4.1.2 Diversity of missions and their applications . . . 37
1.4.1.3 The interferometric phase measurement . . . 38
1.4.2 InSAR processing overview . . . 43
1.4.2.1 Selection of SAR images and interferogram computation . . . 44
1.4.2.2 Phase unwrapping . . . 44
1.4.2.3 Time series analysis . . . 46
1.4.3 Presentation of the main processing chains . . . 47

1.4.3.1 Persistent Scatterers Interferometry (PSI) . . . 47
1.4.3.2 Small Baseline Subset (SBAS) . . . 48
1.4.3.3 The New Small Baseline Subset chain (NSBAS) . . . 49
1.4.4 The development of an automatic processing chain - the FLATSIM project 50
1.4.4.1 FLATSIM architecture . . . 51
1.4.4.2 The incorporation of the NSBAS chain . . . 51
1.4.4.3 Presentation of the delivered products . . . 53
1.4.5 Related open challenges . . . 53
1.5 The North Anatolian Fault in Türkiye . . . 55
1.5.1 Geological and Tectonic contexts . . . 55
1.5.1.1 The formation of the Anatolian land mass . . . 55
1.5.1.2 The tectonic context . . . 57
1.5.2 The North Anatolian Fault over the last century . . . 60
1.5.2.1 Seismic sequence on the North Anatolian Fault . . . 60
1.5.2.2 The 1999 Izmit-Düzce earthquakes . . . 63
1.5.3 Related open Challenges . . . 74
1.6 Problematics and outline of the manuscript . . . 76
1.6.1 Main research questions of the thesis . . . 76
1.6.2 Outline of the manuscript . . . 76

2 The steady-state deformation across Türkiye inferred from the *FLATSIM* dataset 79
2.1 Introduction . . . 82
2.2 Large scale analysis . . . 83
2.2.1 Data and Methods . . . 83
2.2.1.1 Analysis of the quality of the data . . . 83
2.2.1.2 Reprocessing of InSAR tracks . . . 85
2.2.1.3 Estimate of the steady-state velocity field . . . 87
2.2.1.4 Creep rates and locking depths along the North Anatolian fault . . . 91
2.2.1.5 Computation of the strain field . . . 92
2.2.2 Results . . . 94
2.2.3 Discussion . . . 95
2.2.3.1 Contribution of the InSAR data . . . 95
2.2.3.2 Continuous deformation related to the North Anatolian Fault 97
2.2.3.3 Creeping segments of the North Anatolian fault . . . 97
2.2.4 Conclusion . . . 99
2.3 Slip deficit below the Marmara Sea from joint InSAR and GNSS velocity fields 100
2.3.1 Introduction . . . 100
2.3.2 Preparation of the InSAR data . . . 100
2.3.2.1 Harmonization of the dataset . . . 100
2.3.2.2 GNSS referencing of the interseismic LOS velocity field . . . 100
2.3.2.3 Quality control of the InSAR processing . . . 101
2.3.2.4 Horizontal-Vertical decomposition . . . 102
2.3.3 Results . . . 102
2.3.4 Discussion . . . 103
2.3.4.1 Contributions of the InSAR data on the slip inversions . . . 103
2.3.4.2 Remarks on the slip predictions . . . 104
2.3.5 Conclusion . . . 107

3 Automated Detection of Slow Slip Events from InSAR: Application to the North Anatolian Fault **109**
3.1 Introduction . . . 112
3.2 Method . . . 114
3.2.1 Method's inputs . . . 114
3.2.1.1 Analysis of realistic noise . . . 115
3.2.1.2 Definition of a template . . . 115
3.2.2 Module 1: Detection of synthetic slow slip events . . . 116
3.2.2.1 Building the synthetic data . . . 116
3.2.2.2 Correlation functions . . . 116
3.2.2.3 Thresholds estimates . . . 118
3.2.3 Module 2: Real data peak detection . . . 119
3.2.3.1 Validation of the detections . . . 119
3.2.4 Module 3: Characterization of the events . . . 121
3.2.4.1 Location of the events . . . 122
3.2.4.2 Initiation time and relaxation time . . . 122
3.2.4.3 Magnitude . . . 122
3.3 Application to the North Anatolian Fault . . . 123
3.3.1 Tectonic context and InSAR data processing . . . 123
3.3.2 Application to the Izmit segment: influence of InSAR post-processing 123
3.3.3 Application to the Ismetpasa segment . . . 125
3.4 Discussion . . . 127
3.4.1 Validation of the approach and assumptions . . . 127
3.4.2 Comparison with independent geodetic observations along the NAF . 128
3.4.2.1 Izmit segment . . . 128
3.4.2.2 Ismetpasa segment . . . 129
3.4.2.3 Synthesis across techniques . . . 129
3.4.3 Slow slip events physical mechanisms . . . 130
3.4.3.1 Structural and mechanical controls on shallow SSE occurrence 130
3.4.3.2 Role of pore-fluid pressure . . . 130
3.4.3.3 Moment-duration scaling . . . 131
3.4.3.4 Implications for continental fault mechanics . . . 131
3.5 Conclusion . . . 132

4 Creep behavior along the Izmit segment **135**
4.1 Introduction . . . 138
4.2 Tectonic context . . . 139
4.3 InSAR analysis . . . 141
4.3.1 Interferograms and time series processing . . . 141
4.3.2 InSAR referencing relative to GNSS velocities . . . 141
4.3.3 Extraction of seasonal signals . . . 142
4.3.4 Horizontal and vertical decomposition . . . 142
4.3.5 Extraction of the tectonic signal . . . 143
4.4 Mean velocities and seasonal signals analysis . . . 144
4.4.1 Mean horizontal East-West signal . . . 144
4.4.2 Mean vertical signal . . . 144
4.4.3 Seasonal signals . . . 144
4.5 Creep dynamics along the Izmit segment . . . 146
4.5.1 Fault relative displacement . . . 147
4.5.2 Slip inference at depth . . . 149
4.6 Discussion . . . 152

4.6.1 Steady creep along the Izmit segment . . . 152
4.6.2 Izmit slow slip event cycle . . . 154
4.6.3 Possible mechanisms promoting creep and SSEs along the Izmit segment 156
4.7 Conclusions . . . 157

5 From coseismic rupture to shallow slow slip: seismic-cycle modeling of the Izmit segment of the North Anatolian Fault 161
5.1 Introduction . . . 164
5.2 Methods . . . 166
5.2.1 Rate-and-state formalism . . . 166
5.2.2 Definition of the mechanical models . . . 166
5.2.3 Observational constraints along the Izmit segment . . . 168
5.2.4 Comparison between numerical simulations and observations . . . 169
5.3 Results . . . 170
5.3.1 Coseismic observations . . . 170
5.3.2 Afterslip observations . . . 171
5.3.3 SSE observations . . . 171
5.4 Discussion . . . 174
5.4.1 Model limitations and quasi-dynamic approximation . . . 174
5.4.2 Controls on coseismic rupture and postseismic afterslip . . . 174
5.4.3 Frictional ingredients required for shallow SSEs . . . 175
5.4.4 Implications for slow slip events physical precesses . . . 175
5.4.5 Broader implications for strike-slip faults . . . 176
5.5 Conclusions . . . 176

6 Discussion, perspectives et conclusions 179
6.1 Insights of geodetic data monitoring: focus on InSAR . . . 180
6.2 Perspectives on the behavior of the North Anatolian Fault (NAF) in Türkiye . 183
6.3 Slow slip events: toward a unified framework? . . . 186

A Supplementary Materials: The steady-state deformation all over the Türkiye deduced from the *FLATSIM* dataset 189
A.1 FLATSIM raw data . . . 190
A.2 Seasonal terms . . . 193
A.3 Mean East-West profiles . . . 195

B Supplementary Materials: Automated Detection of Slow Slip Events from InSAR: Application to the North Anatolian Fault 197
B.1 Method . . . 198
B.1.1 Method's inputs . . . 198
B.1.1.1 Analysis of real InSAR noise . . . 198
B.1.1.2 Definition of a template . . . 200
B.1.1.3 Fault interface properties . . . 201
B.1.1.4 Decimation of the data . . . 202
B.1.2 Synthetic tests . . . 203
B.1.2.1 Effects of the template's parameters on correlation functions 203
B.1.2.2 Validation of the detections . . . 205
B.1.2.3 Accuracy of SSEs estimates . . . 206
B.2 Application to real data . . . 208
B.2.1 Presentation of the segments . . . 208
B.2.2 Izmit results . . . 209
B.2.3 Creepmeters records . . . 211

C Supplementary Materials: The slow slip event cycle along the izmit segment of the north anatolian fault 213
C.1 InSAR analysis . . . 214
C.1.1 InSAR data presentation . . . 214
C.1.2 Extraction of the tectonic signal by Independent Component Analysis (ICA) . . . 216
C.1.3 Mean velocities and seasonal signals analysis . . . 219
C.1.4 Fault relative displacement . . . 224
C.1.5 Slip inference at depth . . . 226
C.2 Discussion materials . . . 234

D Supplementary Materials: Postseismic and shallow slow slip events on the Izmit segment of the North Anatolian Fault controlled by depth-dependent frictional variations 237
D.1 Inputs of the simulation . . . 238
D.1.1 Fixed parameters . . . 238
D.1.2 Tests on the cohesion value at the surface . . . 238

List of Figures

1.1 Map of the first proposed tectonic plates . . . 9
1.2 Global seismic hazard map . . . 10
1.3 Scheme of a strike-slip fault at different stages of the seismic cycle . . . 11
1.4 Seismological records of the 1999 Izmit earthquake from Bouchon et al. (2001): East-West acceleration and velocity at two stations, and map of the epicenter, surface break, and aftershock . . . 12
1.5 GNSS displacement time series at station *TUB100TUR*, showing the coseismic offset of the 1999 M_w 7.6 Izmit earthquake . . . 14
1.6 Scheme of a creepmeter . . . 15
1.7 Field photos of surface deformation from the 2023 M_w 7.8 Kahramanmaraş earthquake at Hassa/Hatay, showing the surface rupture and a coseismic offset at a gate . . . 16
1.8 Creepmeter record along the Ismetpasa segment . . . 18
1.9 GPS data along the Cascadia subduction zone by Rogers and Dragert (2003). . . . 19
1.10 Interseismic coupling inferred from InSAR and GPS data, from Bletery et al. (2020). . . . 20
1.11 Force-displacement curve on a Westerly granite sample from Brace and Byerlee (1966), illustrating stick-slip behavior up to fracture . . . 21
1.12 Shear stress response to velocity variations in Westerly granite, comparing the Aging and Slip evolution laws, after Linker and Dieterich (1992) . . . 23
1.13 Scheme illustrating the rate-and-state friction law from An et al. (2018). . . . 23
1.14 Stability diagram related to the velocity jump ΔV and the effective normal stress $\overline{\sigma}$ for velocity-weakening layers, from Scholz (1998). . . . 24
1.15 Synoptic model of the frictional stability on a strike-slip fault modified from Marone (1998). . . . 25
1.16 Map of the currently known fault systems affected by SSEs, modified from Jolivet and Frank (2020). . . . 26
1.17 Evidence of a slow slip event along the Ismetpasa segment of the NAF from Rousset et al. (2016): interferogram, fault-perpendicular LOS displacement profiles, and transient signal . . . 27
1.18 Examples of slow-slip signals recorded by various geodetic and seismological tools, including tremor, VLFEs, LFEs, GNSS, and strainmeter data, after Peng and Gomberg (2010) . . . 28
1.19 Fault structure and slip behavior of strike-slip faults, from Bürgmann (2018) . . . 29
1.20 Scaling law of fast and slow earthquakes proposed by Ide and Beroza (2023) . . . 31
1.21 Cover of the journal *nature* in 1993 showing the first co-seismic interferogram produced by Massonnet et al. (1993) . . . 33
1.22 Scheme of a SAR image acquisition . . . 34
1.23 Amplitude and phase of a *Sentinel-1* single look complex image and interferogram over Istanbul and surroundings . . . 34
1.24 The frequency bands in SAR techniques . . . 35

1.25 Scheme of the Doppler effect . . . 36
1.26 Timeline of previous and current SAR missions since 1980, according to their frequency bands . . . 37
1.27 Scheme of the SAR acquisitions of two successive images . . . 39
1.28 Raw interferogram of the 2003 Bam earthquake showing total interferometric phase, and schematic of orbital contributions . . . 40
1.29 Interferogram after orbital correction of the 2003 Bam earthquake showing total interferometric phase, and schematic of topographic contribution . . . 40
1.30 Example of interferometric phase correction for stratified atmospheric contribution and residual orbital ramp in Mexico, adapted from López-Quiroz et al. (2009) . . . 41
1.31 Interferogram of the 2003 Bam earthquake after orbital and topographic corrections, after filtering and unwrapping, and schematic of the deformation contribution . . . 42
1.32 Acquisition modes of the Sentinel-1 satellites (from the European Space Agency, `https://earth.esa.int/eogateway/documents/20142/37627/PolSAR-2013-Sentinel-1-System-Data.pdf`, accessed on December 2025). . . . 43
1.33 Example of products delivered by *FLATSIM* . . . 45
1.34 Phase profile AA' extracted from the wrapped, wrapped-filtered, and unwrapped interferograms . . . 46
1.35 Scheme showing the characteristics of the permanent and distributed scatterers from Tamburini et al. (2014). . . . 48
1.36 Illustration of the variability of the SBAS algorithms on a synthetic test, published by Jolivet (2011) . . . 49
1.37 Global map showing the sites operated in the framework of the FLATSIM project 51
1.38 Processing sequence from raw SAR images to unwrapped interferograms used by FLATSIM from Thollard et al. (2021). . . . 52
1.39 Türkiye tectonic map . . . 55
1.40 Earthquake hazard, active faults, and historical seismicity map of Türkiye . . . 58
1.41 Tectonic reconstruction of the NAFZ onset . . . 59
1.42 Seismic sequence distribution along the NAF . . . 61
1.43 Coulomb failure stress (CFS) evolution map sequence . . . 63
1.44 Spatio-temporal evolution of seismicity in the Marmara–Izmit region . . . 64
1.45 Foreshock sequence of the 1999 Izmit earthquake . . . 65
1.46 Coseismic deformation of the 1999 Izmit earthquake: InSAR interferogram from ERS-2 images and East-West displacement from SPOT images, showing surface and fault ruptures . . . 66
1.47 Surface rupture and slip distribution of the 1999 Izmit earthquake. . . . 67
1.48 Variability of coseismic slip distributions of the 1999 Izmit earthquake from kinematic source models, after Duputel et al. (2014). . . . 68
1.49 Coulomb stress change before and after the 1999 Izmit earthquake, from Lorenzo-Martín et al. (2006) . . . 68
1.50 Seismicity distribution before, between, and after the 1999 Izmit and Düzce earthquakes, from Bohnhoff et al. (2016) . . . 70
1.51 Temporal evolution of aftershock activity following the 1999 Izmit earthquake, from Bayrak and Öztürk (2004) . . . 71
1.52 Kinematic afterslip models of the Izmit earthquake at 7 *days*, 180 *days*, and 6 *years* after the mainshock, from Ergintav et al. (2009) . . . 72
1.53 Slip dynamics along the Izmit-Akyazi segment after Cakir et al. (2012) . . . 73

1.54 Fault-perpendicular InSAR time series across the Izmit segment (2014–2017) compared to creepmeter records, showing interseismic creep and a transient acceleration in late 2016, after Aslan et al. (2019b) 74

2.1 Map of the 7 ascending and 7 descending *Sentinel-1* tracks used in the FLATSIM dataset of Türkiye 82
2.2 Mean LOS velocities of the track $A087$ before and after the reprocessing . . . 84
2.3 Quality control of the FLATSIM dataset: RMSE per date, interferogram count histograms, and coverage maps for ascending and descending tracks 85
2.4 Evidence of fading signals on the track $A131$ 87
2.5 Mean velocity of the southern part of the track $A131$ before and after GNSS referencing 89
2.6 Histograms of phase differences in overlapping areas for ascending and descending tracks, from West to East, with Gaussian fits 90
2.7 Mean East-West and vertical velocity maps 91
2.8 Locked-fault and rigid-block models for fault motion, after Savage and Burford (1973) 92
2.9 Large-scale strain field: mean InSAR East-West velocity and maximum shear strain rate at 1 km and 2 km resolution 93
2.10 East-West velocity, maximum shear strain rate, and rotation estimates for three areas of interest: the Izmit-Düzce, Ismetpasa, and Alaca-Ezine segments 94
2.11 Focus of the mean vertical velocity on the Bursa basin. 95
2.12 Estimate of along-strike fault parameters 96
2.13 Fault-perpendicular velocity and shear strain profiles across the Izmit, Düzce, Ismetpasa, and Ezinepazari segments 98
2.14 Mean LOS velocity after GNSS referencing for the ascending and descending tracks 101
2.15 Mean East-West and vertical velocities over the Marmara region 102
2.16 InSAR interferogram of track $A131$ (31/01/2017˜18/02/2017) centered on the Biga Peninsula, showing seismic deformation from the 2017 Ayvacık (Çanakkale) earthquakes 102
2.17 Slip rate estimates and uncertainties from GNSS only, InSAR LOS only, and combined GNSS and InSAR datasets 104
2.18 Final slip rate model from joint GNSS and InSAR inversion, with seismic context, segment classification, earthquake distribution, and associated uncertainties along the NAF and MMF 105

3.1 Flow chart presenting the main steps of the method 114
3.2 Synthetic template corresponding to surface displacements induced by a sliding area on the fault interface 115
3.3 Examples of synthetic InSAR time series and correlation functions 117
3.4 Precision-recall products (*PRP*) estimated for various synthetic SSE depths and event magnitudes, compared to the thresholds used for the detection 119
3.5 Example of a weighted stack (black line) of synthetic displacement time series including an SSE of M_w 4.65, located at 0.67 km-depth 120
3.6 Final detections of synthetic SSEs after the validation step 121
3.7 Final peak detection obtained for the Izmit and Ismetpasa segments 124
3.8 Example of the 2019 SSE detected along the Izmit segment 126
3.9 Moment-duration scaling plot modified from Ide and Beroza (2023) and Materna et al. (2024) 132

4.1 Tectonic settings and coverage of the InSAR data 139

4.2 InSAR LOS, horizontal and vertical velocity fields . . . 145
4.3 Spatial and temporal evolution of the East-West relative displacements along the Izmit segment . . . 146
4.4 Relative cumulative displacement recorded during and in between three transient events . . . 148
4.5 East-West velocity field during the continuous creep periods and East-West static offsets during the transient slow slip events . . . 149
4.6 Fault slip models for the steady creep and the 2018 and 2019 slow slip events . 151
4.7 2D fault interface of the Izmit segment with the slip distributions at distinct phases of the seismic cycle . . . 153
4.8 Creepmeter records from Izmit and Tepetarla during the 2019 event . . . 155

5.1 Tectonic context of the Izmit segment of the North Anatolian Fault (NAF) in Türkiye . . . 165
5.2 Schematic representation of the depth-dependent frictional structure used to analyze the seismic cycle along the Izmit segment . . . 167
5.3 Model predictions of fault slip through time for the optimal *Model 2* . . . 169
5.4 Sensitivity of modeled mainshock amplitude and recurrence time to the frictional parameter, critical slip distance, and width of *Layer 3*, compared to observational estimates . . . 170
5.5 Comparison of simulated and observed afterslip following the 1999 Izmit earthquake: RMSE as a function of *Layer 2* width and frictional parameter, with two model prediction examples . . . 171
5.6 Density histograms of models producing slow slip events 20 *years* after the mainshock, for *Model 1* and *Model 2*, as a function of h^* . . . 172
5.7 Amplitude and recurrence time of modeled SSEs 20 *years* after the mainshock for *Model 1* and *Model 2*, compared to observational estimates along the Izmit segment . . . 172
5.8 Depth-dependent slip evolution during a SSE for *Model 1* and *Model 2* configurations, showing frictional structure, slip with depth, and slip time series at three depths . . . 173

6.1 Creepmeters records at Ismetpasa. . . . 186

A.1 Interferogram networks delivered by FLATSIM corresponding to the ascending tracks from (a) west to (g) east. . . . 191
A.2 Interferogram networks delivered by FLATSIM corresponding to the descending tracks from (a) west to (g) east. . . . 192
A.3 Amplitude of the sinus and cosine terms of the seasonal and linear decomposition computed on the ascending tracks . . . 193
A.4 Amplitude of the sinus and cosine terms of the seasonal and linear decomposition computed on the descending tracks . . . 194
A.5 Perpendicular to the fault profile at longitude 29.4°E of the mean East-West velocity map . . . 195
A.6 Perpendicular to the fault profile at longitude 32.7°E of the mean East-West velocity map . . . 195
A.7 Perpendicular to the fault profile at longitude 37.3°E of the mean East-West velocity map . . . 196

B.1 Noise statistics (PSD slope, amplitude, standard deviation) of InSAR displacement time series for LOS, East-West, and post-processed East-West datasets covering the Izmit segment . . . 198

B.2 Histograms of the PSD slope, amplitude and standard deviation of the real InSAR noise covering the Ismetpasa segment . . . 199
B.3 Creepmeter record at Seller during the 2019 event . . . 200
B.4 P-, S-wave velocity and density values profile . . . 201
B.5 Impacts of the data decimation on the correlation computation . . . 202
B.6 Effects of the patch size on the correlation coefficient . . . 203
B.7 Effects of the relaxation time on the correlation coefficient . . . 204
B.8 Detection performance metrics: minimum detectable moment and magnitude, precision-recall ratios, and magnitude thresholds as a function of depth, for a PRP threshold of 0.2 . . . 205
B.9 Sensitivity of SSE magnitude estimates to template patch size, comparing characterized and true magnitudes for three synthetic events of increasing magnitude at 500 *m* depth . . . 206
B.10 Estimates errors during the characterization of the detected SSEs . . . 207
B.11 Mean East-West velocity maps after GNSS referencing covering the Izmit and Ismetpasa segments . . . 208
B.12 Mean East-West velocity maps after GNSS referencing covering the Izmit and Ismetpasa segments, focused on the cropped areas . . . 208
B.13 Final SSE detections along the Izmit segment. . . . 209
B.14 Final SSE detections along the Ismetpasa segment. . . . 210
B.15 Creepmeters records along the Izmit segment. . . . 211
B.16 Creepmeters records along the Ismetpasa segment. . . . 211

C.1 Interferogram networks . . . 214
C.2 Number of interograms per pixel for each track . . . 215
C.3 Comparison of the variance of the reconstructed data based on the ICA sources with the variance of the InSAR time series, as a function of the number of components used for the ICA . . . 216
C.4 Three sources extracted by the FastICA algorithm . . . 217
C.5 Examples of residual time series before and after subtraction of the IC components . . . 218
C.6 Mean horizontal and vertical velocities of the cropped zone computed after HV decomposition of the tracks A160 and D138, and after GNSS referencing . 219
C.7 Mean horizontal and vertical velocities of the cropped zone computed after HV decomposition of the tracks A058 and D138, and after GNSS referencing . 220
C.8 Mean East-West horizontal and vertical surface velocities on the Izmit basin computed after the HV decomposition of the tracks A058 and D138, and after GNSS referencing . . . 221
C.9 East-West and vertical seasonal amplitudes obtained from the *TA058-D138* decomposition . . . 222
C.10 East-West and vertical seasonal amplitudes obtained from the *TA160-D138* decomposition . . . 223
C.11 Map centered on the Izmit basin with the location of the pixels used for the calculation of the relative displacement rates . . . 224
C.12 Cumulative relative displacement using the data from the *TA160-D138* HV decomposition recorded during and in between the three transient events . . . 225
C.13 East-West velocity field during the steady creep periods and East-West static offsets during the transient slow slip events from the *TA160-D138* HV decomposition . . . 226
C.14 P-, S-wave velocity and density values profile . . . 227

C.15 Perpendicular to the fault profiles of displacements based on different Green's functions, for homogeneous slip with amplitude of 1 *cm* starting from 5 *km*-depth 227
C.16 RMS errors as a function of the *a priori* locking depth. The red dotted lines show the *a priori* locking depth for the preferred model. 228
C.17 Slip distributions obtained using several *a priori* models with locking depths of (A) 5 *km*, (B) 11 *km* and (C) 16 *km*. 228
C.18 Comparison between the East-West steady creep velocity field and three model predictions obtained from the inversions 229
C.19 L-curves obtained for the steady creep, the 2018 and 2019 slow slip events, respectively 230
C.20 Slip distributions obtained from the inversions of the mean inter-transient velocity, for several parameters 231
C.21 Comparison between the InSAR East-West displacements recorded during the 2018 and 2019 transient events with the model predictions 231
C.22 Slip distributions obtained from the inversions of the 2018 transient event displacements, for several parameters 232
C.23 Slip distributions obtained from the inversions of the 2019 transient event displacements, for several parameters 233
C.24 Comparison between the GNSS SMAS-SISL baseline and the InSAR results . . 234
C.25 Meteorological data over the period 2016 – 2021 within the Izmit basin 235
C.26 Seismic events from the AFAD catalog, from the January 1st, 2016 to the March 1st, 2021 236

D.1 Impact of the cohesion value σ_0 in *MPa* on the predictions of the cumulative displacement times series at the top cell 238

List of Tables

1.1 Table gathering the applications associated with each frequency band. 38
1.2 Table of the $M_w \geq 6.7$ earthquakes of the last century Anatolian seismic sequence 62
1.3 Table gathering the slip dynamics features estimated on the western part of the Izmit segment. 75

2.1 Characteristics of the tracks processed in the framework of the *FLATSIM* project on the Turkish site presented in Figure 2.1 from West to East. 82
2.2 Percentage of total pixels kept after applying the mask based on the number of interferograms for each track. 101

3.1 Results of the characterization of the five SSEs detected using the geodetic matched filter approach along the Izmit and Ismetpasa segments, compared to previous works. IZ and IS stand for Izmit and Ismetpasa, and Cm. stands for Creepmeters. The references are the following ones: [1] for Aslan et al. (2019b), [2] Jolivet et al. (2023), [3] Neyrinck et al. (2024) and [4] Özdemir et al. (2025). $*$ indicates results from this study, and $-$ indicates that no information is available for this feature. 125

5.1 Table gathering the parameters values tested for the input model and the final estimates corresponding to the optimal models. 168
5.2 Table gathering the Izmit observations of its seismic cycle. 168

D.1 Model simulation parameters. 238

Acronyms

DAS Distributed Acoustic Sensing. 13

DEM Digital Elevation Model. 13, 39, 41, 87

EAF East Anatolian Fault. 21, 57, 94–96, 184

FLATSIM ForM@Ter LArge-Scale Multi-Temporal Sentinel-1 InterferoMetry. xxxix, xli, xlv, xlvi, xlix, 2, 3, 76, 79, 80, 82–84, 88, 96, 99, 100, 102, 109, 123, 135, 141, 152, 158, 180, 181, 189, 191, 192

GNSS Global Navigation Satellite System. xxxix, xl, xliii, xlv, 2, 13–15, 19, 27, 28, 66, 71–73, 76, 79–81, 88, 89, 97, 100–107, 109, 110, 112, 113, 123, 126, 128, 129, 135, 137, 139–142, 145, 153, 156, 162, 164, 165, 169, 171, 174, 175, 180, 181, 183, 185, 187

GPS Global Positioning System. xliii, 14, 19, 20, 104, 106

ICA Independent Component Analysis. 135, 143, 152, 181

IGS International GNSS Service. 14, 15

InSAR Interferometry Synthetic Aperture Radar. xxxviii–xli, xliii–xlv, 2, 3, 6, 13, 14, 20, 26, 33, 35, 37, 39, 41–45, 47–51, 53, 54, 66, 71–76, 79–81, 83, 85–89, 92–97, 99–107, 109–120, 122–129, 132, 135, 136, 138–141, 143, 145, 147, 149, 152–155, 157, 158, 162, 164, 165, 169, 179–181, 183, 185

InWF Wrapped and Filtered Interferogram. 83, 84, 102

ITRF International Terrestrial Reference Frame. 88

LFE low frequency earthquake. 27, 28, 32

LiDAR Light Detection and Ranging. 13, 17

LOS Line Of Sight. xxxix, xliii, xlv, xlvi, 27, 41, 42, 53, 81, 83, 84, 86–91, 100, 101, 103, 104, 119, 123, 124, 127, 141–145, 182, 193, 194

LVDT Linear Variable Differential Transformer. 15, 16

MMF Main Marmara Fault. xlv, 83, 104–107, 180, 181, 183

NAF North Anatolian Fault. xl, xli, xliii–xlv, 2, 3, 17, 21, 26, 27, 30, 57, 58, 60, 61, 63, 65, 68, 69, 74, 76, 77, 79, 83, 94–100, 102, 103, 105, 109, 111, 113, 123, 125, 128, 130, 131, 135, 138, 140, 141, 144, 149, 150, 152, 154–157, 161, 179, 183–185, 187

NSBAS New Small Baseline. 79, 85, 109

OIC Optical Image Correlation. 16

PGA Peak Ground Acceleration. 10

RADAR Radio Detection and Ranging. 13

RMSE Root-Mean-Square Errors. xlv, xlvi, 83–85

RSF rate-and-state friction. xliii, 22, 23, 25, 29, 77, 161

SAF San Andreas Fault. 26, 30, 91, 182, 186, 187

SAR Synthetic Aperture Radar. xxxviii, xliii, xliv, 2, 6, 27, 33–46, 49, 50, 52, 73, 76, 79, 86, 92, 103, 109, 180, 181

SHF Superstition Hills Fault. 181

SRTM Shuttle Radar Topography Mission. 40

SSE Slow Slip Event. xxxviii, xl, xli, xliii, xlv, xlvi, xlix, 2, 3, 6, 18–20, 25–32, 53, 54, 74, 76, 77, 97, 109–133, 135–138, 140, 149–152, 154–157, 161–166, 169–177, 179–187

VLFE very-low frequency earthquake. 28, 31

VS velocity-strengthening. 24, 25, 29

VW velocity-weakening. xliii, 24, 25, 29, 30, 135

General introduction

Although the largest earthquakes occur along subduction zones, most of the deadliest earthquakes in history have occurred in continental interiors or along continental plate boundaries (England and Jackson, 2011). On February 6, 2023, just six days after the start of my PhD, two major earthquakes struck the south-eastern part of Türkiye within a 9-hour interval. Located in the Kahramanmaraş region with magnitudes of 7.8 and 7.5, these twin events led to catastrophic human and economic losses from central Türkiye to north-west Syria (e.g. Goldberg et al., 2023). This crisis serves as a stark reminder of the high seismic hazard over continental regions and underscores the need to intensify studies along these fault segments to enhance our knowledge of the processes occurring under our feet.

The north-western part of Türkiye is likewise not spared by earthquakes. Indeed, a $\sim$ 1600 *km*-long strike-slip fault system, called the North Anatolian Fault (NAF), splits northern Türkiye from east to west and accommodates the relative motion between the Anatolia and Eurasia plates (Şengör et al., 2005). Since the 1930s, a westward-propagating sequence of 10 magnitude $M_w \geq 6.7$ earthquakes has ruptured $\approx$ 1200 *km* of the fault system. However, the westernmost part of the fault beneath the Marmara Sea remains a seismic gap at the time of writing, threatening the megalopolis of Istanbul.

To better assess this threat, understanding the fault's mechanical behavior during the interseismic period is crucial. Inter-plate earthquakes traditionally result from a period of strain accumulation along a fault interface locked at depth. However, recent studies along two segments of the NAF (Izmit and Ismetpasa) reveal an aseismic creep behavior (e.g. Rousset et al., 2016; Aslan et al., 2019b) —- i.e., a slow, continuous displacement along the fault that radiates little to no seismic waves, making it practically imperceptible on classic seismometers. Evidence of such slow displacements has been documented since the last century (e.g. Altay, 1991). Furthermore, the development of geodetic data (e.g., Global Navigation Satellite System (GNSS), Interferometry Synthetic Aperture Radar (InSAR)) over the last two decades has allowed scientists to distinguish between steady-state and transient aseismic creep (e.g. Dragert et al., 2001). The latter, known as Slow Slip Event (SSE)s, correspond to transient accelerations of aseismic creep lasting from days to years (Bürgmann, 2018). By releasing a portion of the accumulated elastic strain, creep and SSEs directly reduce the slip deficit (the energy budget available for future large earthquakes). Today, SSEs have been identified in various tectonic contexts worldwide (Jolivet and Frank, 2020). Yet, detecting these events and unraveling their driving mechanisms —- which remain unclear -— is critical to refining seismic hazard assessments (Avouac, 2015).

Following this idea, the aim of this work is to focus on the North Anatolian Fault to detect, characterize, and model slow slip events using InSAR observations. This satellite imaging technique allows us to monitor surface deformation with high spatial resolution (Bürgmann et al., 2000) by building displacement time series from SAR images (here, *Sentinel-1*). Using automatically processed InSAR data provided by the ForM@Ter LArge-Scale Multi-Temporal Sentinel-1 InterferoMetry (FLATSIM) project (a collaboration between CNES and FormaTerre)

covering Türkiye over the 2016–2021 period, I aimed to: (i) characterize the creep dynamics along the NAF, especially along the Izmit segment which ruptured in 1999 east of the Marmara Sea seismic gap, (ii) enrich SSE catalogs by proposing new extraction and detection strategies, and (iii) analyze potential common features with worldwide SSEs to better constrain the relationships between aseismic and seismic slip.

This work is consequently articulated into four main chapters following an introduction. The first one is a study of the mean surface deformation at large scale observed in Türkiye using the FLATSIM InSAR dataset, with a focus on the Marmara Sea. The second chapter describes an automatic method of SSEs detection implemented for InSAR data, in order to facilitate the identification of SSEs along continental faults and estimates of the first-order parameters (e.g., the location on the fault interface, the initiation time, the relaxation time and the magnitude). Then, in the third chapter I analyze the Izmit segment and propose a specific post-processing sequence of the InSAR data to extract the tectonic signal with the aim of using inverse methods to infer for the slip distribution along the fault interface during single SSE. Finally, the fourth chapter shows mechanical models based on the Izmit seismic cycle observations, allowing us to discuss the potential role of the frictional heterogeneity at depth on the fault on the occurrence of shallow SSEs.

Ultimately, focusing on the NAF highlights the value of studying continental strike-slip faults. Because the deformation often reaches the surface, near-field observations provide unprecedented sensitivity to small fault displacements, offering new insights into the driving mechanisms of aseismic slip worldwide.

Chapter 1

State of the Art: Seismic cycle, Slow Slip Events, Space Satellite measurements of ground deformation and Tectonics in Türkiye

1.1 History of earthquake science . . . 8
1.2 Seismic cycle . . . 10
1.2.1 Seismic hazard, seismic risk and vulnerability . . . 10
1.2.2 Simplified seismic cycle sequence . . . 10
1.2.3 Diversity of the observations . . . 12
1.2.3.1 Seismological data . . . 12
1.2.3.2 Geodetic data . . . 13
1.2.3.3 Geological observations . . . 16
1.3 Types of aseismic fault slip behavior . . . 18
1.3.1 Historical discovery . . . 18
1.3.2 Definitions of seismic, aseismic and fault coupling . . . 19
1.3.3 Seismic cycle models . . . 21
1.3.3.1 Constitutive friction laws . . . 21
1.3.3.2 Rate-and-state friction law . . . 22
1.3.3.3 Application to seismic cycle simulation . . . 24
1.3.4 Slow slip events . . . 25
1.3.4.1 Identification of slow slip events around the world . . . 25
1.3.4.2 Observations of Slow Slip Events . . . 26
1.3.5 Mechanisms governing the occurrence of Slow Slip Events . . . 28
1.3.5.1 Frictional control . . . 28
1.3.5.2 Lithological control . . . 30
1.3.5.3 Fluids and pore pressure . . . 30
1.3.5.4 Structural control . . . 30
1.3.5.5 Synthesis on the moment-duration scaling laws . . . 31
1.3.6 Related open challenges . . . 32
1.4 Interferometry Synthetic Aperture Radar (InSAR) processing . . . 33
1.4.1 Definition of SAR Interferometry . . . 33
1.4.1.1 The SAR images acquisitions . . . 33
1.4.1.2 Diversity of missions and their applications . . . 37
1.4.1.3 The interferometric phase measurement . . . 38
1.4.2 InSAR processing overview . . . 43
1.4.2.1 Selection of SAR images and interferogram computation . . . 44
1.4.2.2 Phase unwrapping . . . 44

1.4.2.3 Time series analysis . . . 46
1.4.3 Presentation of the main processing chains . . . 47
1.4.3.1 Persistent Scatterers Interferometry (PSI) . . . 47
1.4.3.2 Small Baseline Subset (SBAS) . . . 48
1.4.3.3 The New Small Baseline Subset chain (NSBAS) . . . 49
1.4.4 The development of an automatic processing chain - the FLATSIM project 50
1.4.4.1 FLATSIM architecture . . . 51
1.4.4.2 The incorporation of the NSBAS chain . . . 51
1.4.4.3 Presentation of the delivered products . . . 53
1.4.5 Related open challenges . . . 53
1.5 The North Anatolian Fault in Türkiye . . . 55
1.5.1 Geological and Tectonic contexts . . . 55
1.5.1.1 The formation of the Anatolian land mass . . . 55
1.5.1.2 The tectonic context . . . 57
1.5.2 The North Anatolian Fault over the last century . . . 60
1.5.2.1 Seismic sequence on the North Anatolian Fault . . . 60
1.5.2.2 The 1999 Izmit-Düzce earthquakes . . . 63
1.5.3 Related open Challenges . . . 74
1.6 Problematics and outline of the manuscript . . . 76
1.6.1 Main research questions of the thesis . . . 76
1.6.2 Outline of the manuscript . . . 76

1.1 History of earthquake science

Many theories have been proposed since the dawn of time to explain the origin of earthquakes. Initially, the proposals revolved around gods or giant animals, which, depending on their moods, caused tremors. One of these theories, drawn from Japanese folklore, evokes the presence of a giant catfish named Namazu, living just below the surface of the ground. When the gods were unable to control it, Namazu would start moving around, causing earthquakes. Other civilizations, such as China, associated these events with divine messages, even leading to punishments or dismissals of high-ranking individuals following natural disasters, as was the case during the Qin and Han dynasties (221 BC - 220 AD). It was during the latter dynasty that the first device for observing earthquakes was invented, Zhang Heng's seismoscope dating from 132.

These beliefs persisted until around the 18th century in Europe, at the dawn of one of the deadliest European earthquakes. On November 1, 1755, an earthquake devastated Lisbon, killing more than 50,000 people, with a magnitude estimated retrospectively at 8.5-9. This earthquake drastically changed the knowledge and views of the Age of Enlightenment, leading in particular to revisions of philosophical ideas as described by Voltaire and Jean-Jacques Rousseau. Kant, a Prussian philosopher, dedicated three essays to this earthquake, proposing theories on the origin of earthquakes based on the presence of underground cavities filled with hot gases. For scientists, this earthquake was the first in a long list that led the scientific community to question the cause of earthquakes. From then on, attempts were made to list all disasters, resulting in accurate databases from the 19th century onwards, notably Alexis Perrey's archive, which compiled all earthquakes and volcanic activity that had occurred over more than 40 years. The first commissions were organized, testimonies were gathered, and earthquake intensity scales were proposed. The first measuring instruments began to appear with Luigi Palmieri (first seismometer), Filippo Cecchi (first seismograph), and John Milne (first measurements of distance to epicenters) in the 1850s and 1880s. These new technologies made it possible to propose new theories about the causes of earthquakes.

In 1858, Robert Mallet completed one of the most comprehensive maps of historical seismicity, marking seismic zones in shades of orange. Lines can be seen forming, particularly the arc around the Pacific Ocean. However, it would take several years before this map could be interpreted more accurately. In 1912, German scientist Alfred Wegener first proposed his theory of continental drift. He explained that, in his opinion, there was a time when all the continents were interlocked, forming a supercontinent called Pangaea. Despite presenting various arguments based on fossils, glaciers, geological units, and other evidence, Wegener was unable to convince his peers due to a lack of explanation for the force that caused Pangaea to break apart. He died in 1930 upon returning from a mission to Greenland. It was not until 1960, with the discovery of ocean ridges and paleomagnetism, that the theory gained traction. The military needs of World War II led to the exploration of the seabed with the discovery of sonar.

In 1957, the first bathymetric map was completed by Marie Tharp and Bruce Heezen, revealing the presence of underwater mountains, ocean trenches, underwater volcanoes, and fractures. In 1960, Harry Hess described certain large underwater mountain ranges dividing the oceans into two parts as ocean ridges, where ocean floor rocks are formed. A little later, the study of these ridges revealed oceanic expansion, consisting of an increase in the size of the oceans resulting from the formation of new rocks within the ridges, a theory supported by the dating of ocean floor rocks using paleomagnetism. The discovery of ridges therefore explains the formation and expansion of the oceans, and consequently the continental drift proposed

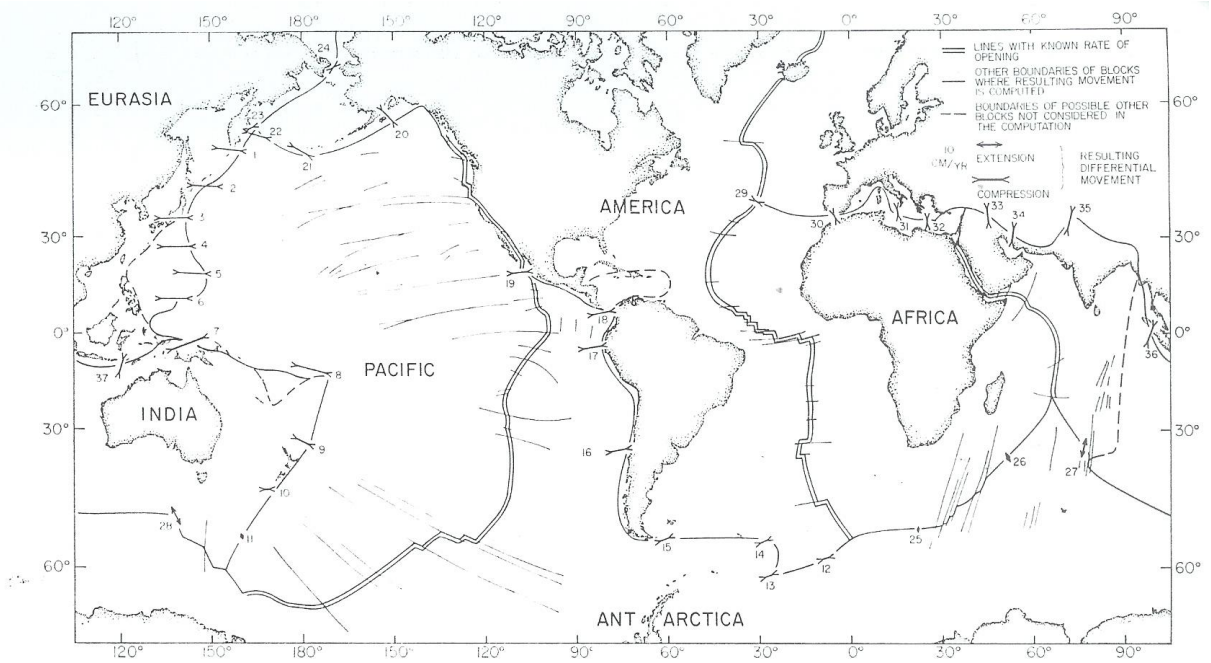

Fig. 6. The locations of the boundaries of the six blocks used in the computations. The numbers next to the vectors of differential movement refer to Table 5. Note that the boundaries where the rate of shortening or slippage exceeds about 2 cm/yr account for most of the world earthquake activity.

Figure 1.1: Map of the six first tectonic plates proposed by Le Pichon (1968).

by Alfred Wegener 50 years earlier. In 1968, the theory of plate tectonics was proposed by a group of around twenty researchers, including Harry Hess, Fred Vine, Drummond Matthews, Tuzo Wilson, Dan McKenzie, and Jason Morgan. In 1968, French scientist Xavier Le Pichon proposed the first global quantitative model of the relative movements of the six main tectonic plates proposed at the time (fig. 1.1). A comparison of these three maps, which were created more than 100 years apart, reveals common lines, such as the Pacific arc and the boundaries between India and Asia or Africa and the Middle East, which are marked by tectonic plate boundaries and areas of high seismicity. These common lines made it possible to identify one of the causes of earthquakes, which is plate tectonics.

1.2 Seismic cycle

1.2.1 Seismic hazard, seismic risk and vulnerability

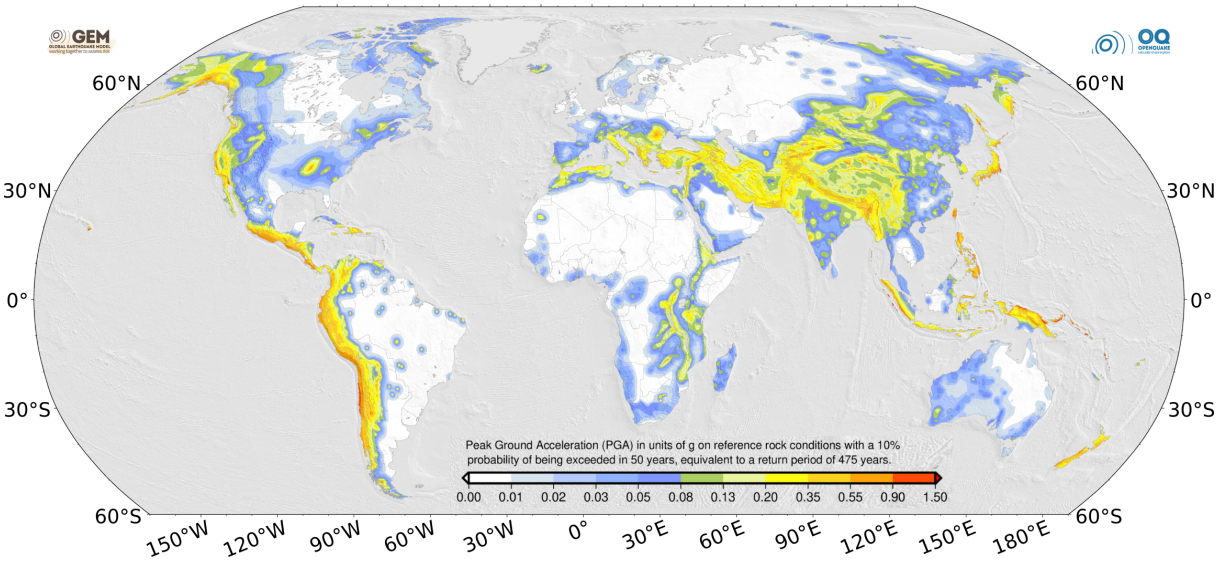

Figure 1.2: Global seismic hazard map (version 2023.1) produced by Johnson et al. (2023), showing the Peak Ground Acceleration (PGA) spatial distribution. The colored areas correspond to medium-high seismic hazard.

To characterize the seismic threat to populations, scientists estimate maps of **seismic hazard**, pointing out areas where an earthquake is likely to occur. The seismic risk which includes the potential damages is made of two different features:

$$Seismic\ Risk = Seismic\ Hazard \times Vulnerability$$

so that the **seismic hazard** is related to the probability of an earthquake to rupture within the region and the **vulnerability** is related to the amount of damages that can cause the rupture within the region. Figure 1.2 shows the estimate of the seismic hazard in 2023, highlighting several high risk areas such as the Circum-Pacific Belt with western coasts of the American continent and East-Asian coasts, as well as the Alpine-Himalayan belt with the Mediterranean sea shores (including Türkiye) and the Himalayas mountains. To improve these estimates, a better understanding of the mechanisms governing and influencing earthquake processes is needed. As explained before, most of the earthquakes occurred at the interface of tectonic plates, due to their relative motions. Indeed, **tectonic plate relative motions** are accommodated by **faults** at their boundaries, accumulating energy along their interface due to the **friction** between the plates. Part of this elastic energy can be released in a quasi-instantaneously way by **earthquakes** that can have disastrous consequences for the surrounding populations. The succession of elastic strain **loading** and **release** along a fault interface in time corresponds to the **seismic cycle** - also called earthquake cycle (Reid, 1910). Studying seismic cycles is necessary to improve the estimates of the seismic risk and prevent the populations.

1.2.2 Simplified seismic cycle sequence

The Figure 1.3a shows a simple scheme corresponding to a left-lateral strike-slip fault separating two blocks, at different stages of the seismic cycle. It can be divided into three or four main steps.

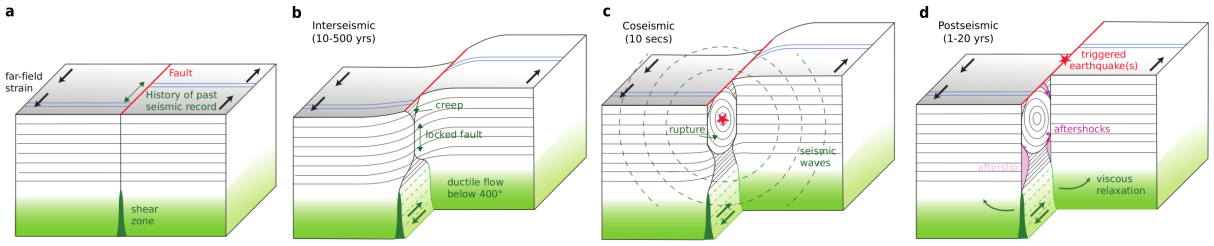

Figure 1.3: Scheme of a strike-slip fault at different stages of the seismic cycle (Dalaison, 2021).

The first and longer stage is the **interseismic** phase (Figure 1.3b). During this period, the fault interface is partially or fully locked at seismogenic depths, and the stress is accumulating along the locked interface because of the far field motion of the blocks and the deep motion along the fault interface (i.e. along the shear zone, Figure 1.3a). This stage can last for centuries or even decades. When the strain loading reaches a threshold (corresponding to a threshold failure or friction), an earthquake occurs, releasing a large amount of strain by a metric scale fault slip that occurs in a few seconds, corresponding to the **coseismic** phase (Figure 1.3c, Reid, 1910). This elastic energy release is accompanied by seismic waves which travel at the surface and within the Earth's layers, represented by the green dotted lines. The surface waves are responsible of the main damages at the surface. The mainshock is followed by weaker seismic events called aftershocks. These events represented in pink in Figure 1.3d happen during the **postseismic** stage, period lasting for years to decades, and which allows for the supplementary release of strain remaining along the fault interface. The frequency of aftershocks after a mainshock decays with time following a power law first described by Omori (1894) or a stretched exponential (Mignan, 2015). Thatcher and Rundle (1979) described different steps of the postseismic period by highlighting (i) an aseismic afterslip releasing shallow strain along the fault interface during the first years after the mainshock, followed by (ii) a visco-elastic relaxation of the deeper part of the crust/upper mantle surrounding the rupture zone (Figure 1.3d - green arrows). Afterslip is often spatially correlated with postseismic seismicity (Barbot et al., 2009), and localized at depth within the crust below the coseismic displacement and/or close to the surface (above the coseismic displacement), as detected after the 2017 M_w 7.3 Zarpol-e-Zahab earthquake in Iran by Wang and Bürgmann (2020). The visco-elastic relaxation of the upper mantle and/or lower crust is related to the stress diffusion within the medium (Pollitz, 1997). Finally, poro-elastic rebound within the upper crust relative to pore pressure diffusion in response of the coseismic stress can also affect the postseismic phase, such as highlighted after the 1992 M_w 7.3 Landers earthquake by Peltzer et al. (1998).

In some cases, a fourth stage known as the preseismic stage can be distinguished, preceding the coseismic rupture. This phase, which can last from hours to days, is characterized by precursory activities that eventually trigger the mainshock. The 2011 M_w 9.1 Tohoku-Oki earthquake (Japan) stands as a landmark case, where precursory seismicity was clearly identified through the migration of repeating earthquakes toward the hypocenter (Kato et al., 2012). While geodetic evidence for Tohoku remains debated due to signal-to-noise limitations, more explicit geodetic transients indicating aseismic slow-slip have been documented for other events. These include the 2014 M_w 8.1 Iquique and 2015 M_w 8.3 Illapel earthquakes in Chile (Schurr et al., 2014; Ruiz et al., 2016), and notably the 2014 M_w 7.3 Papanoa earthquake in Mexico, which was directly triggered by a large-scale slow slip event (Radiguet et al., 2016).

Improvements of observation techniques led to the highlight of a new type of fault slip which is called **aseismic** or **slow slip**. This slip occurs at lower velocity than coseismic earthquake slip and is not associated with the radiation of seismic waves. It has been first pointed out during the **postseismic stage**, with Reid (1910) mentioning a slow displacement occurring at some locations on the fault after the earthquake. . Aseismic slips have also been identified

within the **interseismic period**, as shown by Steinbrugge et al. (1960) along the San Andreas Fault. We will describe the distinct aseismic behaviors later (part 1.3.4), but it is clear that they play an important role for the seismic cycle understanding and estimate.

The previous definitions are simplified, and all of the previous studies show that the seismic cycle along one fault segment is an individual case, meaning that there is a large diversity of fault behaviors. To clarify this diversity, we need to combine various datasets, to better differentiate and estimate the governing mechanisms at different time and spatial scales.

1.2.3 Diversity of the observations

In this section, I will briefly describe some tools which allow us to study the seismic cycle. This list is non-exhaustive.

1.2.3.1 Seismological data

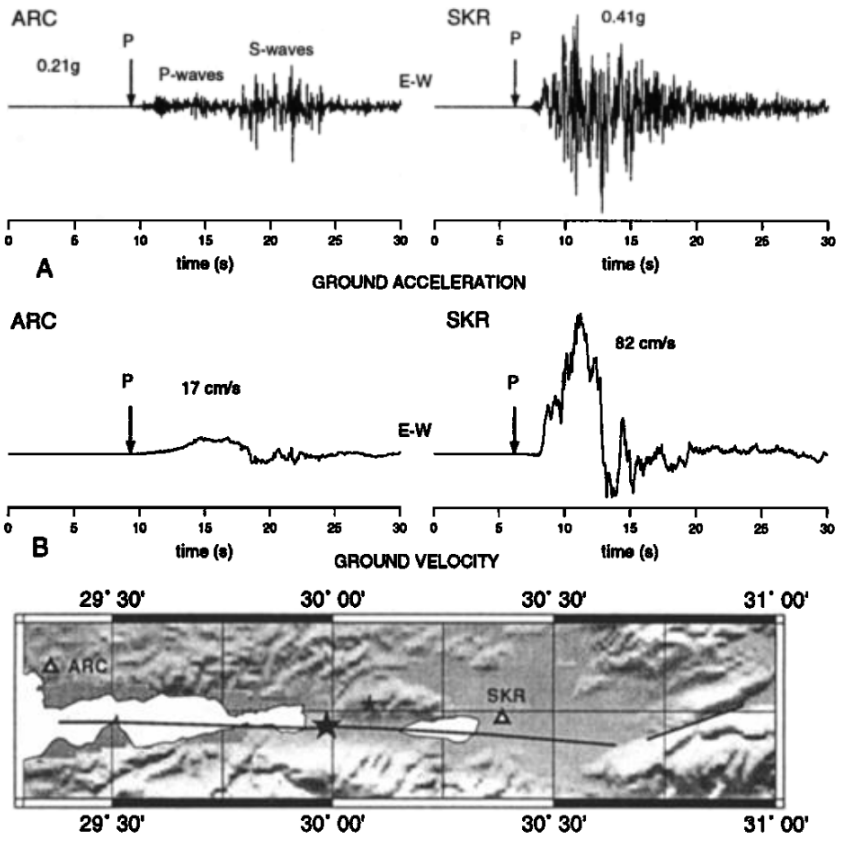

Figure 1.4: Seismological records of the 1999 M_w 7.6 Izmit earthquake reported by Bouchon et al. (2001). (A) East-West accelerations recorded at the two stations *ARC* and *SKR* located about 55 *km* west and 40 *km* east of the hypocenter. (B) Velocity records. (A,B) P-wave arrivals are highlighted by the vertical arrows. (C) Map with the epicenter located by the large black star, the surface break in solid line, both seismic stations (triangles) and the strongest aftershock from 13 September (small star).

The first and most obvious dataset used to study earthquakes is the seismological one. Seismic waves radiated from earthquake hypocenters are recorded by seismometers, as shown in Figure 1.4. They can capture the displacement, velocity, and accelerations caused by the

seismic waves. Figure 1.4 – A,B shows the acceleration and velocity recorded at two sites during the 1999 Izmit mainshock in Türkiye.

Ground motion during an earthquake results from the interplay of three distinct factors: the source effect (rupture mechanics), the path effect (attenuation during travel), and the site effect (local geological amplification). By decoupling these components, researchers can infer critical parameters such as magnitude, source-to-station distance, and local soil response, as well as complex source mechanisms like fault geometry and stress drop. However, the recorded signal also incorporates the instrumental response and ambient noise. Consequently, rigorous filtering and correction steps are required to isolate the pure earthquake-related information.

Several features of interest are used to better understand the characteristics of the rupture: the **arrival times** of the different wave types (see Figure 1.4 – A,B), the maximum **amplitude** of the waves, and the **waveforms**. By using multiple wave arrival times from different locations, we can invert for the precise **hypocenter location**. Taking into account the station-to-epicenter distance, the maximum amplitude of the waves allows for the **magnitude** estimate. Finally, the waveforms recorded on seismograms lead to information about the **focal mechanism** and the **geometry** of the fault rupture. Full-waveform inversion is also employed to retrieve the **Source Time Function (STF)**, which details the temporal evolution of the energy release and the rupture complexity (e.g. Vallée and Douet, 2016). Additionally, **rupture velocity** is a product derived from S-P travel times and waveform modeling.

Nowadays, the location and energy (estimated magnitudes and intensity) of large earthquakes are computed almost immediately thanks to global seismometer networks such as those provided by the International Seismological Centre (ISC, `https://www.isc.ac.uk/about/`, accessed on March 27, 2026), the U.S. Geological Survey (USGS, `https://www.usgs.gov/programs/earthquake-hazards`, accessed on March 27, 2026). National networks enable to monitor smaller events, such as the *Bureau Central Sismologique Français - Réseau National de Surveillance Sismique* (BCSF-Rénass) located in Strasbourg, and monitoring the seismic activity in Metropolitan France (`https://renass.unistra.fr/en/zones/`, accessed on March 27, 2026).

1.2.3.2 Geodetic data

Geodesy gathers several techniques used to study the shape of the Earth. I will detail only those mostly used in earthquake sciences. We can divide these methods into two categories:

- space: Interferometry Synthetic Aperture Radar (InSAR), Global Navigation Satellite System (GNSS);
- terrestrial: creepmeters.

Other types of geodetic data can also be used, such as strainmeters, tiltmeters, theodolites for distance meter and leveling, Light Detection and Ranging (LiDAR) and Distributed Acoustic Sensing (DAS); however we will not detail them in details because they are not used in this work.

Interferometry Synthetic Aperture Radar (InSAR)

Interferometry Synthetic Aperture Radar (InSAR) uses acquisition obtained by active RADAR system. They result from the measurements of phase changes of backscattered electromagnetic waves with *mm* to *cm* wavelength. This technique is used to built Digital Elevation Model (DEM) over large areas. It also allows the measurements of *mm*-scale displacements

of the ground (Bürgmann et al., 2000). It is widely used for surface deformation analysis to monitor volcanoes, tectonic activities, landslides, ground subsidence and glaciers. This type of data has a high spatial resolution ($10-30$ *m* for *Sentinel-1* data) and a moderate temporal resolution ($6-12$ *days* for *Sentinel-1* data). The upcoming Section 1.4 presents in detail InSAR acquisition, processing in the context of this thesis.

Global Navigation Satellite System (GNSS)

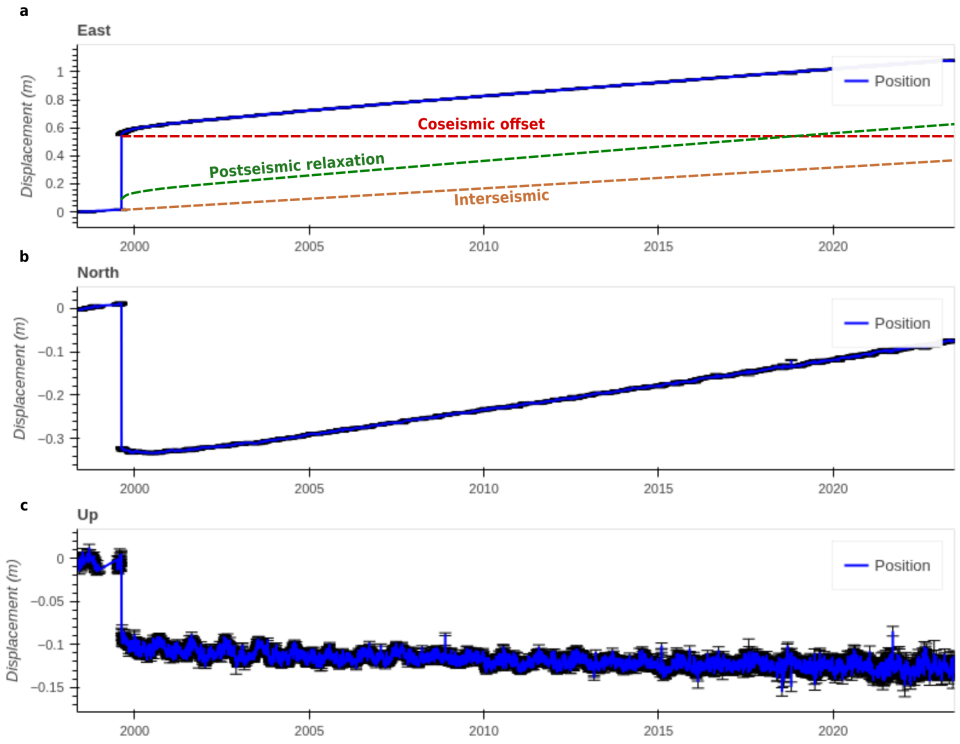

Figure 1.5: Time series of displacement recorded at the station *TUB100TUR* operated by Tubitak located about ~ 44 *km* north-west of the 1999 Izmit epicenter. Data are plotted by FormaTerre, provided by the International GNSS Service (IGS) (Johnston et al., 2017, `https://www.poleterresolide.fr/geodesy-plotter/`, accessed on 27 March, 2026). The offset in 1999 highlighted by the red dotted line (top graph) corresponds to the coseismic displacement of the 1999 M_w 7.6 Izmit earthquake.

GNSS data are acquired by using a receiver on the Earth's surface, and a transmitter in space. Several constellations of satellites from different agencies are associated behind the name GNSS and are available today, e.g. Global Positioning System (GPS) from the USA, GLONASS from Russia, Galileo from ESA (European Union), and BeiDou from the China Satellite Navigation Office. Satellites emit continuously modulated microwaves. GNSS receivers on Earth capture the signals and record the date and identification of the satellite. By using the exact satellite pathways, the travel-times and therefore the distance between the satellite and receiver can be estimated. Combining at least four records from different satellites by a single GNSS station enables the estimation of its precise location. This technique allows for time series of displacement records by computing the previous task at different times. In reality, positioning computation is not so straightforward and requires some additional steps to avoid errors, such as additional time delays associated with signal propagation (e.g., travel through the ionospheric layer) or clock synchronization. I don't detail the full GNSS processing here since I only used published GNSS velocity fields in my work.

GNSS data enable obtaining displacement time series in three components at different frequencies (e.g., sub-daily, daily). In the example shown in Figure 1.5, we can see the daily displacement of a station located between Istanbul and Izmit, over 1998 – 2026 provided by the IGS. This type of data can be used to estimate the interseismic first-order stationary motion – shown by the orange dotted line on the top graph. Global analysis of the absolute or relative displacements can be used to analyze tectonic plate motions and measure interseismic deformation at global (e.g. Kreemer et al., 2014) and large scale (e.g. Nocquet, 2012; Castro-Perdomo et al., 2025). Static coseismic displacements can also be retrieved. In Figure 1.5a, the red dotted line highlights the offset due to the 1999 M_w 7.6 Izmit earthquake, also impacting the other components. The postseismic relaxation following the earthquake is visible, shown by the green dotted line on the top graph. Other signals can be noted, such as for example strong seasonal variations within the vertical displacement time series shown in Figure 1.5c.

Another type of GNSS data recorded at one-second sampling rate named high-rate GNSS data can also be used in earthquake science, since they record seismic surface waves at epicentral distances exceeding 3000 *km* (up to 3800 *km* as shown by Larson et al. (2003)), without experiencing the saturation typical of standard velocimeters during large earthquakes. These data can therefore be used to measure large coseismic motion, and therefore be integrated on the sets of real time data for earthquakes or tsunamis early-warning (e.g. Hoechner et al., 2013).

The main limitation of these data stems from their point-like nature, meaning that spatial resolution is strictly governed by the density and distribution of the station network.

Creepmeters

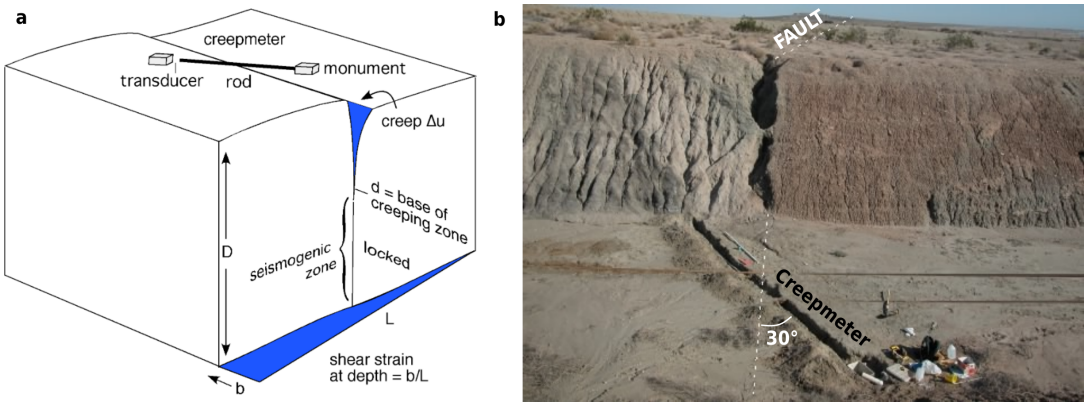

Figure 1.6: Principle of a creepmeter. (a) Scheme of a creepmeter monitoring fault slip between two monuments on either side of a fault as the varying displacement of the free end of an inextensible rod (Bilham et al., 2004). (b) Photography of a creepmeter installed on the San Andreas fault highlighted by the white dotted line (R. Bilham).

A scheme of a creepmeter is shown in Figure 1.6a. It consists of an instrument settled across a fault trace, which monitors the shallow fault slip. A rod with a fixed length is installed between two monuments anchored on either side of the fault. The rod is fixed at one monument, and has a free end on the second monument, allowing for displacement. A Linear Variable Differential Transformer (LVDT) is used at this extremity as a transducer to convert the rectilinear motion into an electrical signal. It allows for displacement records larger than 1 μm. As drawn in Figure 1.6a and shown in the picture in Figure 1.6b, the creepmeter is installed obliquely across the fault, with the initial angle of the rod with the fault (Ω) of about

$\sim 30°$. The displacement measured by the LVDT is therefore relative to this angle, so it needs to be corrected by $1/cos(\Omega)$. The rod is installed 30 *cm* to 1 *m* underground as shown in Figure 1.6b on the San Andreas fault. Data are acquired every 1 to 10 *min*. This type of data enables to detect and study the temporal evolution of aseismic creep. The main limitation of this technique is the spatial extent, the creepmeter being sensitive only to very shallow slip. A series of several creepmeters along a same segment can enable to evidence potential propagation of creep/slip (Gittins and Hawthorne, 2022).

1.2.3.3 Geological observations

Observations of surface ruptures

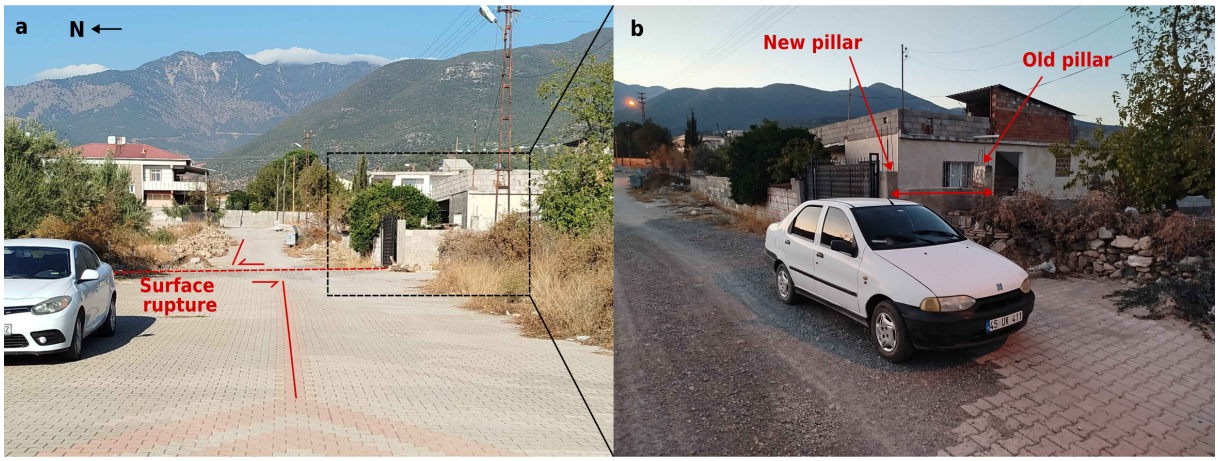

Figure 1.7: Annotated photos taken by C. Lacroix on 17 October 2025 at Hassa/Hatay in Türkiye (precise location: $36°48'03.8''N - 36°31'06.9''E$). The visible surface deformations are relics from the 2023 M_w 7.8 Kahramanmaraş earthquake. (a) The surface rupture is highlighted by the red dotted line. By following the middle red paving stones on the middle of the road, we can observe the coseismic offset and the relative motion. (b) A zoom on the gate shows the new building of a pillar, due to the displacement of the old one by the earthquake, revealing a local shift of the gate of about 2 meters.

Field observations correspond to data directly collected *in situ* after an earthquake. It enables to estimate coseismic offsets, as presented in Figure 1.7 where we can clearly see a gate offset by the 2023 M_w 7.8 Kahramanmaraş earthquake. These photos were taken during a field trip we made in October 2025, i.e. up to ~ 2.7 *years* after the earthquake. The precise horizontal offset has been estimated a few months after the earthquake, as the ones presented in the study of Provost et al. (2024), used to validate OIC observations, and provide precise surface rupture mapping. Even if the growing number of methods based on remote sensing data tends to decrease the amount of studies based only on field observations, these data are crucial to constraining models and providing precise local information that can help to understand the complexity of the rupture.

Long-term geological and geomorphic records

Beyond historical and instrumental catalogs, characterizing the seismic cycle over thousands of years relies on long-term geological archives along the North Anatolian Fault. Tec-

tonic **geomorphology** utilizes landscape features—such as offset river channels, alluvial terraces, and cumulative fault scarps—to infer long-term slip rates and regional deformation history, as documented along the Izmit rupture segment (e.g. Rockwell et al., 2002; Klinger et al., 2003). However, interpreting these landforms remains challenging as geomorphic signals inherently convolute tectonic deformation, climate variations, and surface erosion. To look directly into the subsurface, **paleoseismology** reconstructs past earthquake histories by analyzing sediment deformation and fault geometry within excavated trenches. On the Izmit segment, trenching campaigns have been crucial for constraining the recurrence intervals of large historical events preceding the 1999 rupture (e.g. Rockwell et al., 2009). Today, high-resolution topography (e.g., LiDAR) and 3D trench imaging are increasingly combined with these traditional field methods (e.g. Karabacak et al., 2011), bridging the gap between long-term geological evolution and short-term instrumental observations. This multi-disciplinary integration is essential to refine local seismic hazard assessments, particularly along highly active structures like the North Anatolian Fault (NAF).

1.3 Types of aseismic fault slip behavior

As described above, we can distinguish two main types of fault slip behaviors: **seismic** and **aseismic** slips. Both fault slip behaviors play a role in the seismic potential of faults, and it is crucial to understand their driving mechanisms in order to refine seismic cycle models and, therefore, **seismic hazard** estimates (Avouac, 2015). In this Section, I will present the historical evidence of aseismic fault slip. Then, I focus on Slow Slip Event (SSE) which is the main target of my work. Finally, I will present the impact of aseismic fault slip on seismic cycle modeling.

1.3.1 Historical discovery

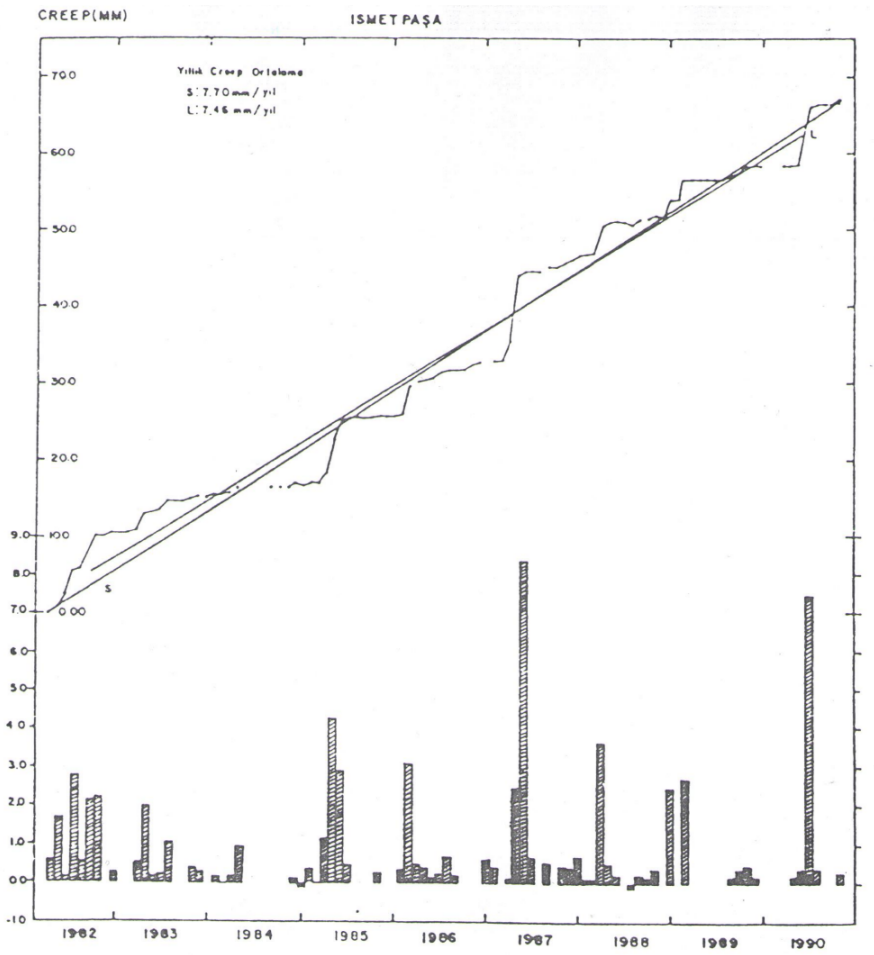

Figure 1.8: Creepmeter record (40°52'25"N, 32°37'24"E) along the Ismetpasa segment of the North Anatolian Fault (Türkiye), from 1982 to 1990, associated with two linear regressions, from Altay (1991). The bottom histogram shows the monthly surface creep.

Even if aseismic fault slip has been pointed out earlier in seismic cycle studies (e.g., evidence of slow shearing in serpentinites along the Hayward Fault (USA) by Louderback (1942)), the discoveries of transient aseismic motions remain recent. Steinbrugge et al. (1960) analyzed **creepmeters records** (cf. part 1.2.3.2) installed along creeping segments of the San Andreas Fault (USA). They highlighted periods of rapid creep, some related to surrounding earthquakes, and some unrelated to any surrounding seismic event. These observations have been confirmed by other publications using offset records from the **field** (e.g. Tocher, 1960;

Rogers and Nason, 1971) and also **strainmeters** (Goulty and Gilman, 1978).

Ten years later, Ambraseys (1970) published an analysis of the dynamics of the North Anatolian Fault (Türkiye) close to the city of Ismetpasa, which reveals that this central segment is aseismically creeping, as shown by several offsets in the field, such as displaced walls. Several years later, Altay (1991) confirmed this aseismic creep and clarified it by using creepmeter records. The Figure 1.8 shows the displacement recorded from 1982 to 1990 with linear regressions of the cumulative displacement. They analyzed the mean creep rate and mentioned a seasonal variation in the creep velocity, without interpreting those transient variations. However, this record nicely shows that the creep behavior along the Ismetpasa segment is modulated by the occurrence of **transient creep events**, with steady-state creep between two successive events or no motion, as observed between the 1985 and 1986 events.

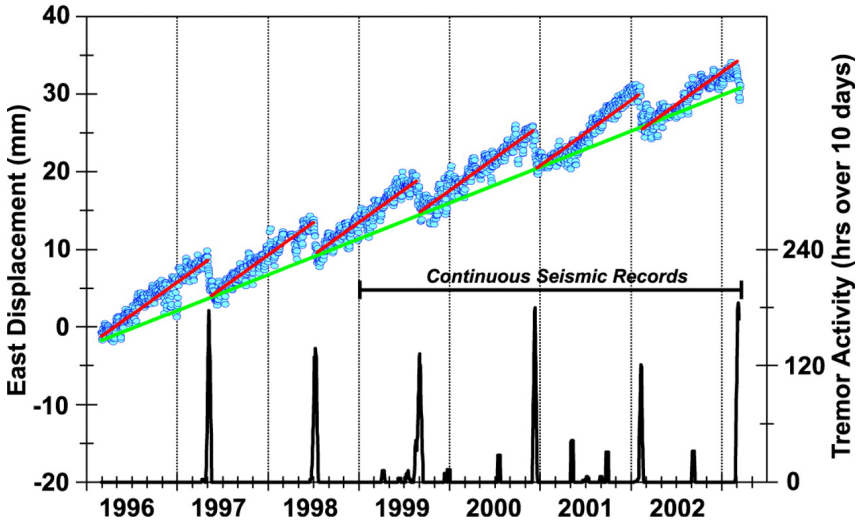

Figure 1.9: Evidences of creep events along the Cascadia subduction zone by Rogers and Dragert (2003). The blue circles correspond to GPS data, compared with the tremor activity shown by the bottom graph.

At the end of the 20th century, the **improvements in geodetic techniques** have enabled us to refine the temporal analysis of surface displacement, especially with the deployment of large GNSS networks along subduction zones like those in the USA. The analysis of these displacement time series, reveals some periods when the direction of surface displacements recorded by GNSS is reversed. In their key publication, Dragert et al. (2001) highlighted this dynamic along the Cascadia subduction zone, deducing the occurrence of a **Slow Slip Event (SSE)** in the summer 1999 releasing a part of the accumulated strain on the subduction interface corresponding to an equivalent magnitude of 6.7. Two years later, Rogers and Dragert (2003) demonstrated that these events can be periodic and associated with **tremor activities**, as revealed by Figure 1.9. Since then, SSE detections have multiplied in both subduction zones and strike-slip faults, allowing for more precise information on their occurrence conditions.

1.3.2 Definitions of seismic, aseismic and fault coupling

Seismic fault slip is related to the propagation of seismic waves, in opposition to **aseismic slip**, which is slow enough to produce few or no seismic radiations. Both behaviors enable the release of energy. During a seismic event, the slip rate on the fault typically ranges from cm/s to m/s (while the rupture front propagates at km/s). Conversely, transient aseismic phenomena such as SSEs exhibit much slower slip rates, typically ranging from mm/day to cm/day,

while steady aseismic creep matches the long-term tectonic loading of a few centimeters per year. Slip durations also differ significantly, with a mean duration of seismic slip of a few seconds, whereas SSEs can last for days to even decades (Bürgmann, 2018).

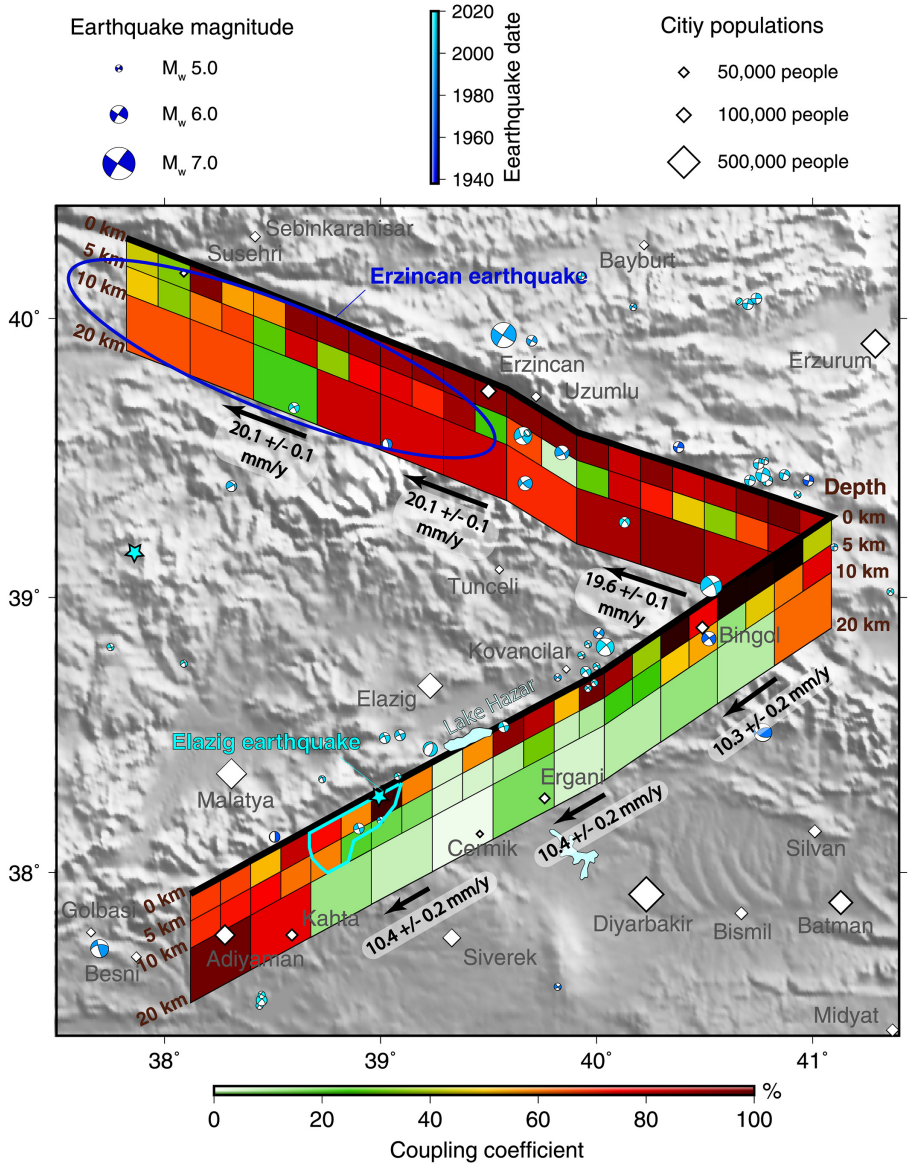

Figure 1.10: Interseismic coupling inferred from InSAR and GPS data, from Bletery et al. (2020).

The partitioning of slip along faults between seismic and aseismic modes can be estimated by using the **fault coupling**. The **interseismic coupling** χ_i corresponding to the ratio of the deficit of slip in the interseismic period to long-term slip, can be expressed as following (Avouac, 2015):

$$\chi_i = \chi_s + \chi_a \tag{1.1}$$

with χ_s and χ_a the seismic and aseismic coupling, respectively. The **seismic coupling** estimates the fraction of the cumulative seismic slip over the long-term slip, while the **aseismic coupling** estimates the fraction of the cumulative aseismic transients (i.e. afterslip and SSEs). These ratios, ranging from 0 to 1, enable the evaluation of the fault's slip budget relative to the tectonic loading rate. An interseismic coupling of 0 means that there is no slip deficit, indicating that the fault interface creeps steadily at the tectonic loading rate without accumulating strain. In contrast, an interseismic coupling of 1 means that the fault interface is fully locked during the interseismic period. However, a high seismic hazard is only expected if this accumulated deficit is released through seismic slip ($\chi_s = 1$), whereas it poses no seismic threat

if predominantly balanced by aseismic transients ($\chi_a = 1$). The equation 1.1 highlights the need to study aseismic slip, in order to avoid an overestimation of the coupling. An example is shown in Figure 1.10 with the interseismic coupling estimated along the eastern part of the NAF and EAF (Türkiye). Bletery et al. (2020) highlight high coupling along the NAF, especially the Erzincan segment which ruptured in 1939 with a M_w 7.7 earthquake, and is currently accumulating strain. However, the coupling is lower along the eastern part of the EAF, with the rupture of the 2020 M_w 6.8 Elazig earthquake and previous ones (e.g. the 2003 M_w 6.3 Bingol and 2010 M_w 6.1 Kovancilar earthquakes) coinciding with areas of high coupling.

1.3.3 Seismic cycle models

The physical mechanisms of earthquakes, and more broadly, the various processes characterizing the seismic cycle along the faults have been specified using both **laboratory experiments** and **real earthquake-related observations**. The challenge is to explain slip rate variations observed along fault planes, leading either to sudden slips at seismic velocities ($\sim m/s$) or to aseismic slow slips ($\sim cm/yr$).

1.3.3.1 Constitutive friction laws

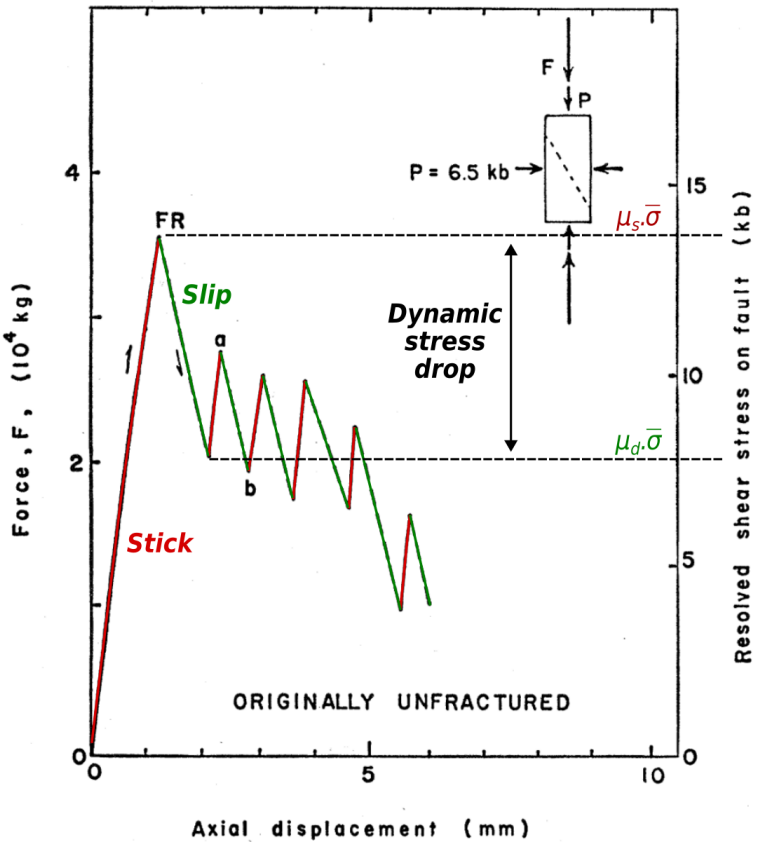

Figure 1.11: Experimental results modified from Brace and Byerlee (1966) showing the force-displacement curve on a Westerly granite sample. *FR* highlights the fracture of the sample. Red and green annotations distinguish stick and slip periods, respectively. As mentioned by Brace and Byerlee (1966), the curve evolution during the slip periods is not known here.

From laboratory results, Brace and Byerlee (1966) proposed **stick-slip** as one possible mechanism for earthquakes. They used a spring-slider model with the pulling force of the

slider representing the plate motion and the spring representing the elasticity of rocks. The application of a tangent force leads to (i) an elastic strain accumulation to a certain level along the contact surface ("stick"), and then (ii) a stress drop accompanied by a slip enabling the release of a portion of the stress loaded ("slip"). Two distinct behaviors can be distinguished: **stable stick** and **unstable slip**.

The bases of the stick-slip theory are shown in Figure 1.11 and detailed below:

1. **Stick:** strain accumulation due to the applied force F (red lines – Figure 1.11),
2. **Initiation of slip:** initiation of slip and start of the sliding occur when the following equation is verified at the surface:

$$\frac{F_{fric}}{F_n} = \frac{\tau}{\overline{\sigma}} \geq \mu_s, \tag{1.2}$$

   with F_{fric} and F_n as the friction and normal forces, respectively, τ as the shear stress, $\overline{\sigma}$ as the effective normal stress, and μ_s as the static friction coefficient (FR – Figure 1.11).
3. **Slip:** decrease of F_{fric} until reaching the dynamic friction coefficient μ_d, leading to a dynamic stress drop (green lines – Figure 1.11).

These experiments highlight that earthquakes do not only result from structural fracturing, but can also be dictated by the frictional control of nucleation.

Following this idea, **constitutive laws** have been developed to explain laboratory experiments and model seismic cycles based on the spring-slider analogy and the fundamental laws of Amonton-Coulomb on friction. First, several models relying on **weakening friction** have been proposed (i.e., a decrease in resistance with slip rate). These models explain well the stress drop leading to the transition from μ_s to μ_d and therefore to the nucleation of an earthquake (e.g. Rabinowicz, 1958; Ida, 1972). The main issue with these laws is that they do not allow for the occurrence of successive earthquakes (or seismic cycles) since they do not explain stress recovery. The concept of **fault healing** or slip memory has been introduced to model the increase and recovery of the friction coefficient, allowing to produce new earthquakes. In particular, Dieterich (1972) highlighted the time-dependent behavior of the static friction coefficient, followed by the introduction of a **state variable** by Dieterich (1981) and Ruina (1983).

1.3.3.2 Rate-and-state friction law

This improvement, along with others not detailed here from the previous models, led to the formulation of a **rate-and-state friction (RSF) constitutive law**. One of the most famous expressions is the Dieterich-Ruina or "slowness" law defined as (Marone and Scholz, 1988; Scholz, 1998):

$$\tau = \left[\mu_0 + a.ln\left(\frac{V}{V_0}\right) + b.ln\left(\frac{V_0.\theta}{D_c}\right)\right]\overline{\sigma} \tag{1.3}$$

with τ the shear stress, V the slip rate, V_0 a reference velocity, μ_0 the steady-state friction at $V = V_0$, θ the state variable, D_c the critical slip distance, $\overline{\sigma}$ the effective normal stress, and (a,b) empirical constants. This equation is related to a state law, which describes the time evolution of θ, such as:

$$\frac{d\theta}{dt} = 1 - \frac{\theta V}{D_c}, \tag{1.4}$$

$$\frac{d\theta}{dt} = -\frac{\theta V}{D_c}.ln\left(\frac{\theta V}{D_c}\right) \tag{1.5}$$

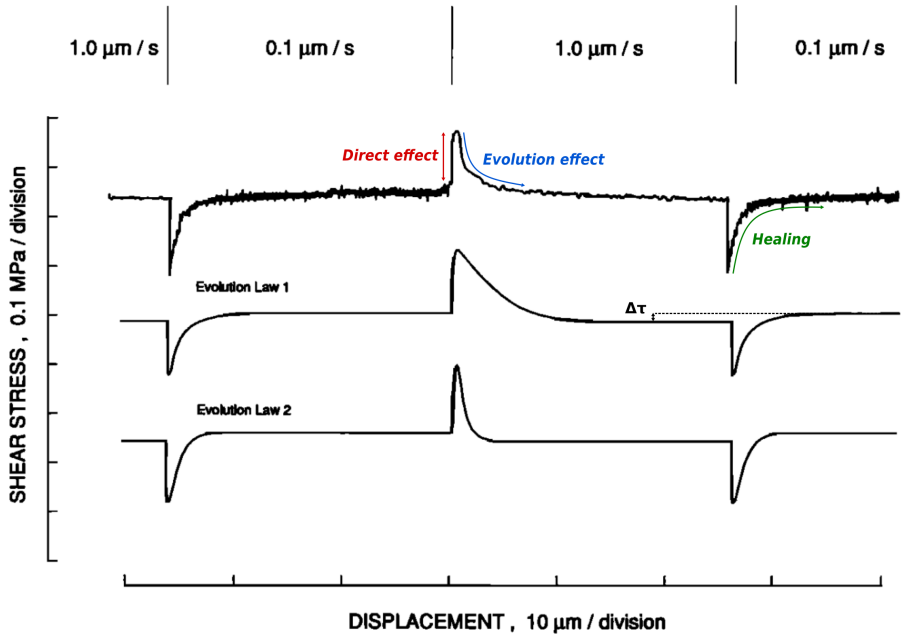

Figure 1.12: Comparison of the shear stress evolution related to velocity variations of a Westerly granite with two evolution laws (1: Aging law – equation 1.4; 2: Slip law – equation 1.5) from Linker and Dieterich (1992). $\Delta\tau$ corresponds to the difference between the static and dynamic shear stresses.

corresponding to the **aging** (Dieterich, 1981) and **slip evolution** (Ruina, 1983) laws, respectively. An example of these state laws is shown in Figure 1.12, where we can also see the global good coherence between observations (top) and models. Other laws have been developed to improve the fit with experimental data, even if no law enables to perfectly reproduce all lab experiments (e.g. Linker and Dieterich, 1992; Perrin et al., 1995; Kato and Tullis, 2001; Bhattacharya et al., 2015).

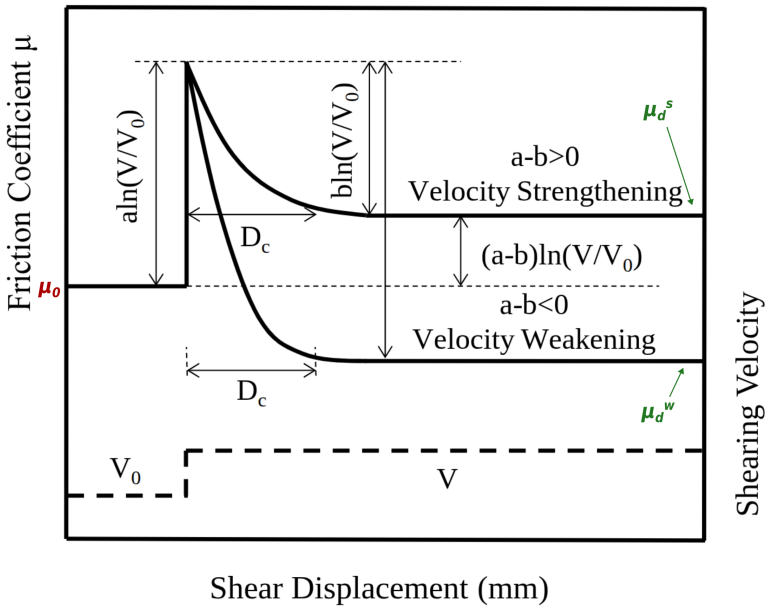

Figure 1.13: Scheme illustrating the rate-and-state friction law from An et al. (2018).

At steady-state friction ($V = V_0$), the RSF law presented in equation 1.3 becomes:

$$\tau = \left[\mu_0 + (a-b).ln\left(\frac{V}{V_0}\right)\right]\overline{\sigma}, \tag{1.6}$$

with the velocity-dependent frictional parameter $(a-b)$ used to describe the frictional stability regime. The Figure 1.13 illustrates the change in friction related to the equation 1.3 following a shearing velocity offset. After the direct effect of the velocity change, two different scenarios are possible depending on the values of $(a-b)$ leading to two distinct values of the friction coefficient called μ_d^w and μ_d^s. The first regime shows an increase of the frictional resistance with slip velocity so that $\mu_d^w > \mu_0$. This behavior is called **velocity-strengthening (VS)** and is associated with $(a-b) \geq 0$. This regime is frictionally **stable**, and can reproduce slow aseismic creep. The second regime showing a decrease of the frictional resistance with slip velocity ($\mu_d^s < \mu_0$) is called **velocity-weakening (VW)** and is associated with $(a-b) < 0$. This regime can be **unstable** or **conditionally stable** depending on a critical value of the effective normal stress $\overline{\sigma_c}$, as shown in Figure 1.14. The conditionally stable state means that the layer is stable under quasi-static loading. However, a small velocity increase can modify the current regime into an unstable one. In this case, earthquakes can nucleate within this regime, due to the unstable behavior. Ruptures can propagate through unstable and conditionally stable fault segments, but will be stopped by stable layers.

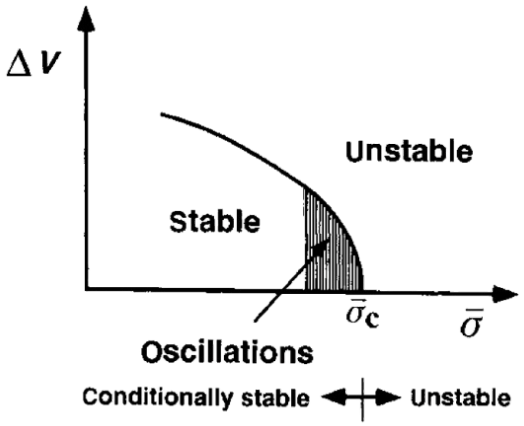

Figure 1.14: Stability diagram related to the velocity jump ΔV and the effective normal stress $\overline{\sigma}$ for velocity-weakening layers, from Scholz (1998).

1.3.3.3 Application to seismic cycle simulation

Different behaviors of the frictional resistance can be explained by the rock properties and the temperature-pressure conditions. Several laboratory studies highlighted the relationships between the frictional parameters $(a-b)$ and the temperature; for instance, they explained the behaviors of the layers at depth (Blanpied et al., 1995, 1998). Another dependence can also be pointed out, between the frictional parameters and the normal stress, showing a decrease in the frictional parameters with the increase in normal stress (Marone and Scholz, 1988).

Laboratory results compared to field observations led to synoptic models of stability for subduction zones and crustal faults, as shown for a strike-slip fault in Figure 1.15. The presence of unconsolidated gouge in the shallow part of crustal faults may enhance the stability of the fault, as indicated by the top stable layer in Figure 1.15 – in blue. Conversely, VW layers will be found where the gouge is consolidated, as shown by the transition from VS to VW layers above a few *km*-depth – in yellow and red. At greater depth ($> 15-20$ *km* for crustal faults, below the synoptic model), the high temperature will lead to the onset of plasticity of quartz (Qz) at $300°C$, stabilizing the slip behavior. Obviously, specific conditions along faults may modify this reference model (e.g. local thermal gradient or fluid pore pressure). The geology of the zones can also influence the frictional stability (Moore and Rymer, 2007). As proposed by Marone and

Scholz (1988), the upper boundary of the VW layer can be estimated using the seismicity depth distribution along the fault (e.g. histogram of the seismicity of the Imperial Fault - Figure 1.15). They correlated the bottom of sedimentary basins (i.e., unconsolidated sediments related to VS behavior) with an upper cutoff on the depth distribution of the seismicity (e.g., ~ 3 *km*-depth along the Imperial Fault; Figure 1.15), revealing a negative stress drop at these depths and highlighting a transition between a VW layer below and a VS layer above.

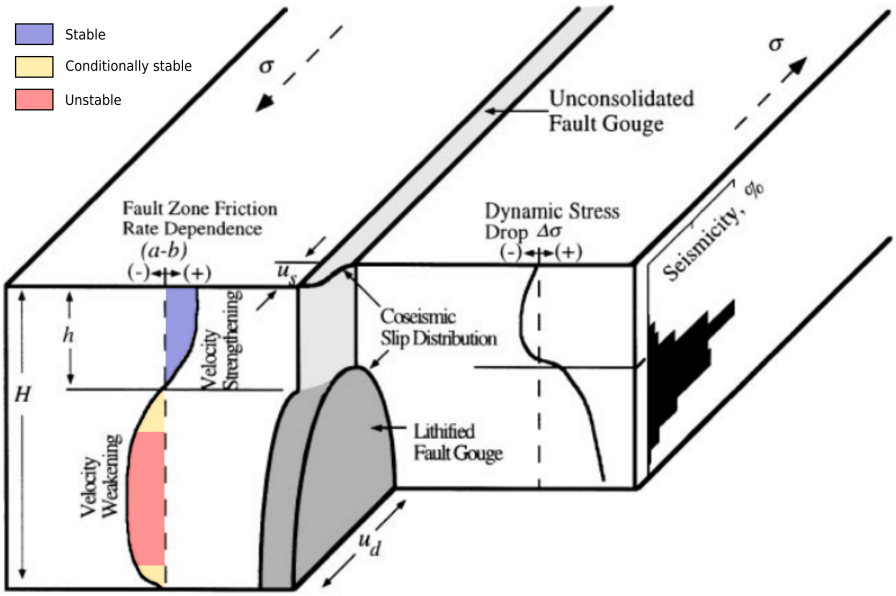

Figure 1.15: Synoptic model of the frictional stability on a strike-slip fault modified from Marone (1998).

The RSF formalism can therefore be used to model seismic and aseismic slips on faults during the seismic cycle (Barbot et al., 2012): fault loading, nucleation and propagation of earthquakes (e.g. Kaneko et al., 2010; Ong et al., 2019), postseismic relaxation (e.g. Barbot et al., 2009) and interseismic creep (e.g. Kaneko et al., 2013). Indeed, the seismogenic VW layer is unstable and therefore can nucleate earthquakes, whereas the top VS layer is stable and may be responsible of the postseismic creep following an earthquake. By modifying the layers' widths and all the parameters involved in the RSF equation, the slip behavior throughout the seismic cycle will vary, allowing us to explain the ensemble of surface observations.

However, some questions remain regarding the modeling of steady-state shallow aseismic creep or the occurrence of SSEs on the upper part of the fault which are not illustrated here (see Figure 1.19A). Several mechanisms have been proposed to explain SSEs within the rate-and-state friction framework, as presented in Section 1.3.5.1. All of these methods proposed a variety of conditions which can explain the emergence of SSEs rather than a seismic rupture (in case of VW layer) or steady-state creep (in case of VS layer), based on laboratory experiments and real observations. By making those models more detailed, it may provide insights into the conditions and mechanisms required to generate SSEs.

1.3.4 Slow slip events

1.3.4.1 Identification of slow slip events around the world

As briefly described above (Section 1.3.1), aseismic slip can have different dynamics. It can be **steady** (e.g. during the interseismic period), or **transient** (e.g. afterslip or Slow Slip

Event). Since their discovery, SSEs have been identified in various tectonic settings, as shown by Figure 1.16 from Jolivet and Frank (2020) who gathered SSE detections in 2020.

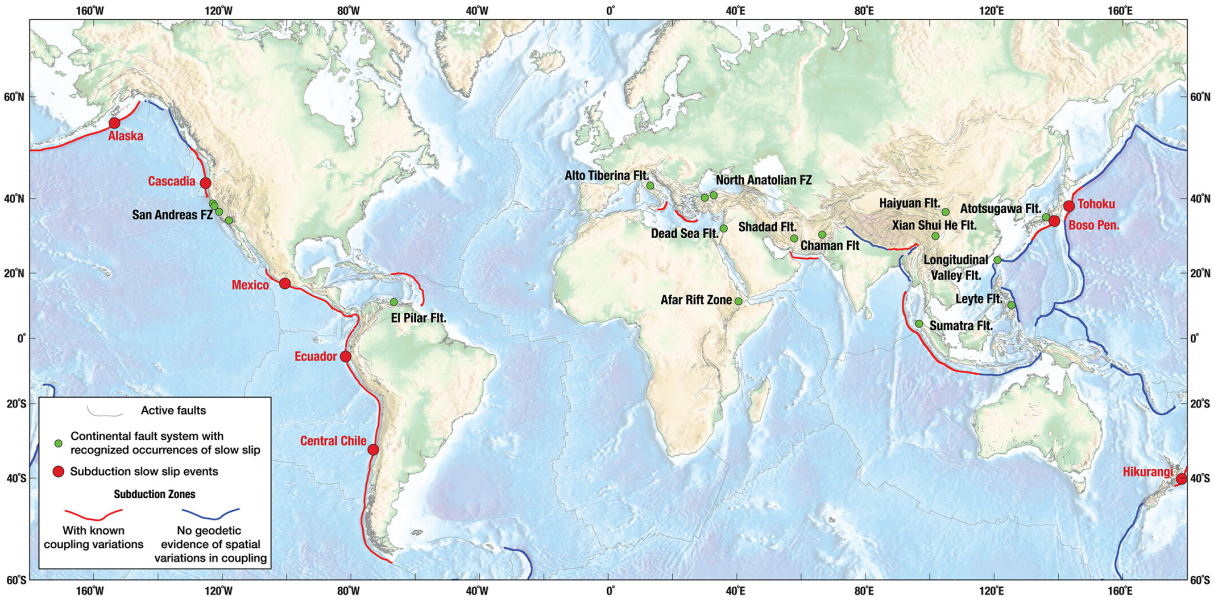

Figure 1.16: Map of the currently known fault systems affected by SSEs, modified from Jolivet and Frank (2020).

First, evidences have been found on **subduction zones** (red dots – Figure 1.16) like in Alaska (Rousset et al., 2019b), the Cascadia subduction zone (e.g. Dragert et al., 2001), in Mexico (Radiguet et al., 2011, e.g.), Costa Rica (e.g. Jiang et al., 2012), Ecuador (e.g. Vaca et al., 2018), in Chile (e.g. Klein et al., 2018), the Nankai subduction zone in Japan (e.g. Obara et al., 2004) and the Hikurangi subduction zone in New Zealand (e.g. Wallace et al., 2012). Meanwhile, evidences have also been found along **continental fault systems** (green dots – Figure 1.16), such as along **strike-slip faults** like the San Andreas Fault (SAF) (e.g. Rousset et al., 2019a; Gittins and Hawthorne, 2022), the San Jacinto Fault (e.g. Inbal et al., 2017), the Superstition Hills Fault (e.g. Wei et al., 2011), the North Anatolian Fault (NAF) in Türkiye (e.g. Rousset et al., 2016; Aslan et al., 2019b; Jolivet et al., 2023), the Chaman Fault in Pakistan and Afghanistan (e.g. Bilham et al., 2019), the Longitudinal Valley Fault in Taiwan (e.g. Murase et al., 2013) and more recently along the West Caspian Fault in Azerbaijan (Bayramov et al., 2025). Active **normal faults** can also be affected by this slow deformation such as the Alto Tiberina Fault in the Apennines in Italy (e.g. Gualandi et al., 2017) and in Djibouti within the Afar Rift Zone (e.g. Doubre and Peltzer, 2007). Along some fault segments, the transient nature of slow slip has yet to be unambiguously established, and the distinction between episodic SSEs and steady aseismic creep remains unclear. A *Slow Earthquake Database* (`http://www-solid.eps.s.u-tokyo.ac.jp/~sloweq/?page=map`, accessed on 16 April 2026) has been created to gather most of the available data related to SSE in order to help their studies (Kano et al., 2018).

1.3.4.2 Observations of Slow Slip Events

While first observations of SSEs were made by studying manmade structures (Louderback, 1942; Steinbrugge et al., 1960; Ambraseys, 1970), several tools are now suitable to detect space and time evolutions of such events. The Figure 1.17 shows an example of a detected SSE along the Ismetpasa segment of the NAF made by Rousset et al. (2016) by using InSAR data (see Section 1.2.3.2). The use of InSAR data enables to estimate the spatial extent of the event

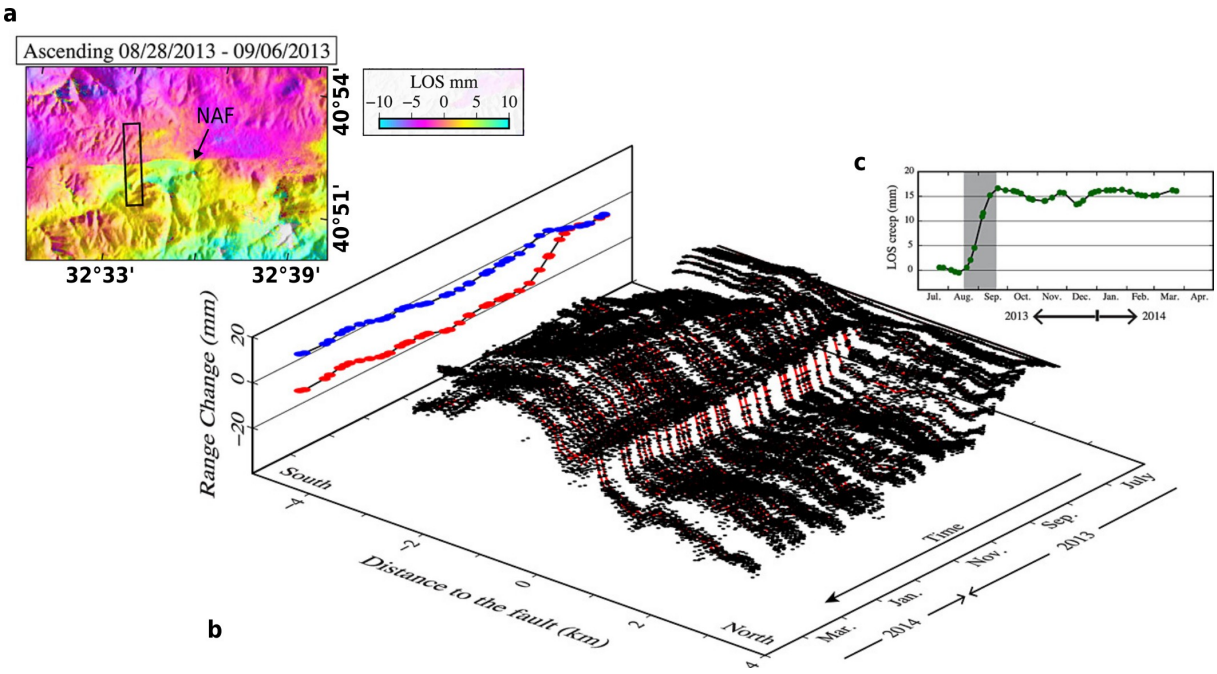

Figure 1.17: Evidences of a SSE along the Ismetpasa segment of the NAF in Türkiye, from Rousset et al. (2016). (a) Interferogram built from ascending Cosmo-Sky Med images acquired the 28 August 2013 and 6 September 2013. The black arrow shows the location of the NAF, coinciding with a sharp gradient of displacement. (b) Fault perpendicular profiles of LOS displacement in time. Blue and red lines correspond to average change taken from pixels located on the south and north of the fault, respectively. (c) Difference between the blue and red curves, highlighting a transient event (SSE) shown by the gray rectangle.

corresponding to the length of the sharp displacement gradient on time series (Figure 1.17a). Additionally, analyzing the amplitude of the surface deformation, when integrated into slip inversion models, allows for the determination of the event's magnitude, as well as its overall duration (Figure 1.17c). However, the return time of SAR acquisitions can be a limitation to estimate temporal characteristics of SSEs. Other tools can complement the observations along continental strike-slip faults, such as creepmeters (e.g. Linde et al., 1996; Bilham et al., 2016) sensitive to millimeter-scale offsets at specific locations, near-field GNSS (Figure 1.18e; e.g. Özarpacı et al., 2020; Özdemir et al., 2025), strainmeters (Figure 1.18f; e.g. Dragert and Wang, 2011; Hawthorne et al., 2016; Inbal et al., 2017) and tiltmeters (e.g. Hirose and Obara, 2005; Yabe et al., 2023). SSEs can also be associated with seismic signals such as tremors and low frequency earthquake (LFE) (Figure 1.18 – a,b,c; e.g. Obara et al., 2004; Shelly et al., 2006), enabling a finer characterization of SSEs dynamics (Frank et al., 2018).

The growing number of identified SSEs provides insight into their spatio-temporal characteristics and common features. As explained above, SSEs have been discovered along faults with different tectonic settings. In this work, we are interested on SSEs along continental strike-slip faults. In this context, SSEs are mostly shallow, located within the first kilometers of the fault interface and usually above the seismogenic zone. The resulting displacement is about a few millimeters to centimeters, leading to equivalent moment magnitudes up to $4-5$ (e.g. Wei et al., 2009; Rousset et al., 2016; Materna et al., 2024; Vavra et al., 2024; Özdemir et al., 2025). Slow slip can last for hours to weeks (e.g. Bilham et al., 2016; Rousset et al., 2016; Aslan et al., 2019b; Özdemir et al., 2025). These events can be periodic, with a return time of a few months to decades (e.g. Wei et al., 2013; Bilham et al., 2016; Gittins and Hawthorne, 2022; Vavra et al., 2024), and can shift from shorter to longer periods if they are related to the postseimsic stage (Wei et al., 2013).

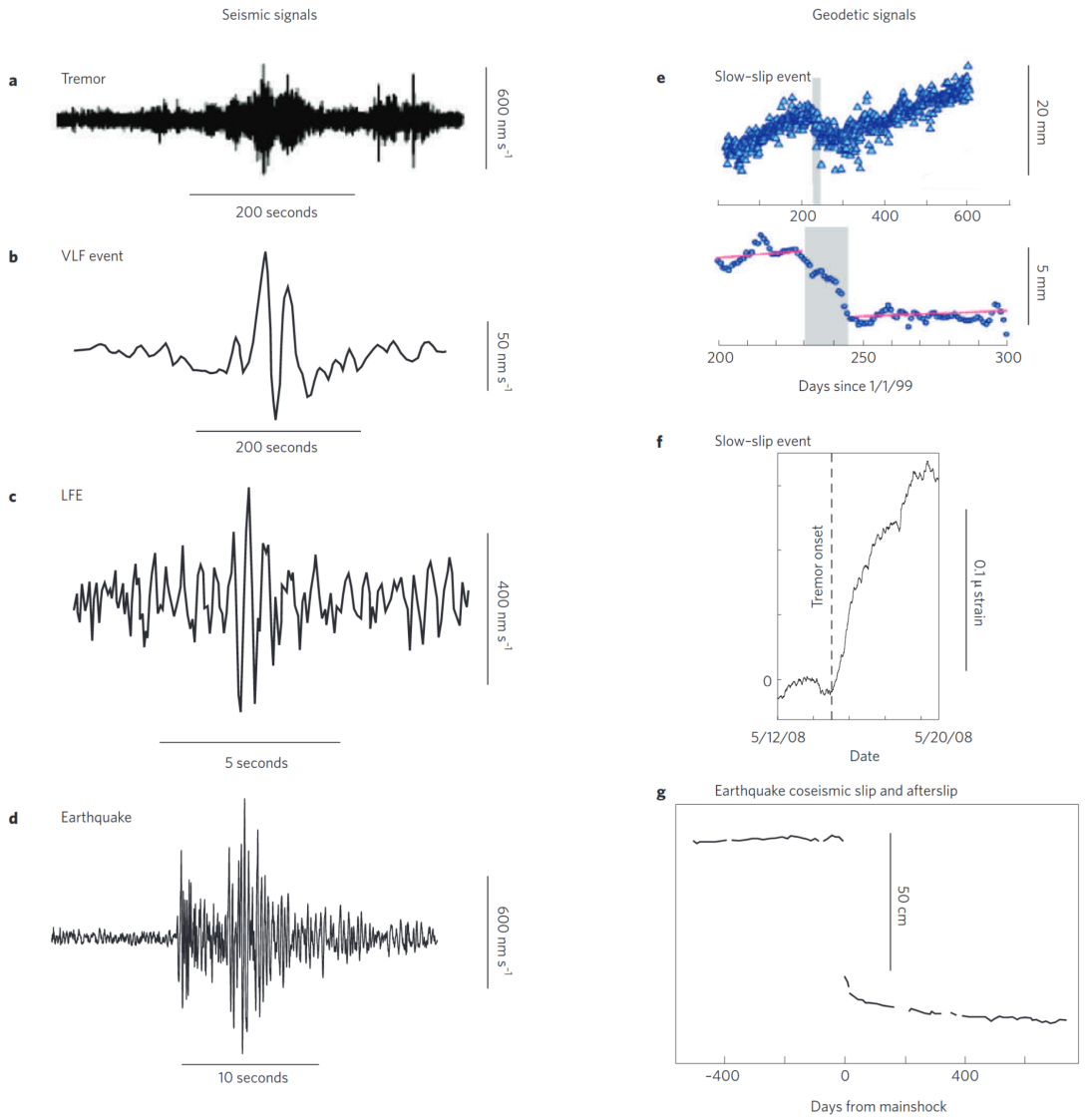

Figure 1.18: Examples of slow-slip signals recorded by using various tools, from Peng and Gomberg (2010). Here are the references therein: (a) tremor and (b) very-low frequency earthquake (VLFE) recorded in Japan (Ide et al., 2008), (c) low frequency earthquake from Japan (Shelly et al., 2006), (d) M_w 1.9 earthquake recorded in western Washington, (e) GNSS data in Cascadia (Dragert et al., 2001), (f) record from a strainmeter in western Washington (McCausland et al., 2008) and (g) coseismic and postseismic displacement fields recorded by GNSS from the 2001 M_w 8.4 Peru earthquake (Perfettini et al., 2005).

1.3.5 Mechanisms governing the occurrence of Slow Slip Events

Combining worldwide observations of SSEs using different types of data (see Section 1.2.3), several mechanisms have been identified as potential driving mechanisms of SSEs (Figure 1.19; Bürgmann, 2018). We will present in the sections below the three main physical processes promoting the occurrence of SSEs.

1.3.5.1 Frictional control

A last explanation for the occurrence of SSEs is related to the friction variations along the fault interface, corresponding to the mechanical control. This effect can be estimated

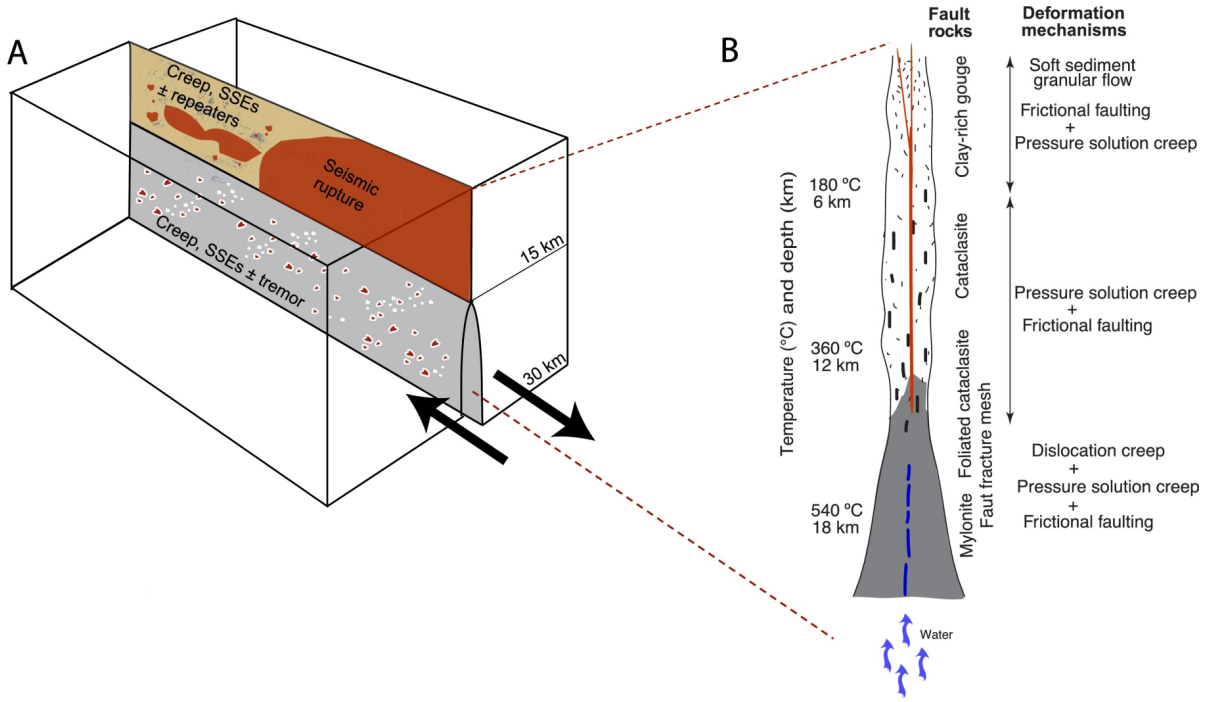

Figure 1.19: Fault structure and slip behavior of strike-slip faults, from Bürgmann (2018). (A) Schematic illustration of the distribution of seismic, aseismic slip and tremor on the partially coupled San Andreas Fault near Parkfield (modified from original image by Kaj Johnson, written comm., 2017). (B) Conceptual section across strike-slip fault illustrating depth distribution of fault zone rocks and deformation mechanism accommodating slow slip (based on Fagereng and Toy (2011)).

by using rate-and-state friction law, that I detail below (see Section 1.3.3.2). In short, frictional variations at depth dictate distinct slip behaviors. The decrease of the friction with slip (velocity-weakening) may lead to a rupture due to the strain accumulation like an earthquake, however the increase of the friction with slip (velocity-strengthening) may lead to a slow slip (e.g. Kaneko et al., 2013). By adding more complexities to the frictional variations, especially within the first kilometers of the fault, it is possible to explain the emergence of SSEs (e.g. Wei et al., 2013; Tymofyeyeva et al., 2019). Changes in friction properties according to the slip can also provide instability allowing for the emergence of SSEs. Im et al. (2020) used velocity dependent parameters within the rate-and-state friction equations along subduction zone fault plane to model the occurrence of SSEs at the interface between velocity-weakening/low slip rate and velocity-strengthening/high slip rate. Some studies showed that frictional-viscous heterogeneities can also explain the occurrence of SSEs. Skarbek et al. (2012) quantified the mixture ratio of velocity-weakening and velocity-strengthening materials at depth allowing for the occurrence of deep SSEs and tremors along the subduction interface. Coupled models incorporating hydrological and mechanical forcing, such as a pore pressure diffusion within a velocity-strengthening layer can also generate SSEs. By accounting for poroelastic effects and elastic bimaterial contrasts (i.e., different elastic properties across the fault), Heimisson et al. (2019) demonstrated that SSEs can be generated within a mildly velocity-strengthening layer along a subduction zone fault plane.

1.3.5.2 Lithological control

The lithological composition of fault gauges may also influence the slip behavior along faults. As detailed by Bürgmann (2018), the analysis of outcrops from exhumed fault zones highlighted a potential mineralogical cause to the development of aseismic slip along some segments of major faults. The study of the geology along several segments of the NAF by Kaduri et al. (2017) reveals the presence of low-friction and clay-rich minerals along the Ismetpasa segments which can promote aseismic slip. Similar studies along the reverse Longitudinal Valley Fault (Taiwan) also highlighted similar minerals (Thomas et al., 2014a). Moreover, serpentinized outcrops have been found along the creeping section of the SAF by Moore and Rymer (2007). The presence of talc associated with serpentinite, probably resulting from a reaction with silica-saturated hydrothermal fluids, decreases the frictional strength of the serpentinites alone, and therefore enhances slow creep.

1.3.5.3 Fluids and pore pressure

The presence of fluids and therefore the variations of pore pressure are other factors expected to promote the occurrence of SSEs. We can express the effective normal stress σ_n' as:

$$\sigma_n' = \sigma_n - P \tag{1.7}$$

with the normal stress σ_n and the pore pressure P. The increase of pore pressure leads to a decrease of the effective normal stress, followed by a decrease of the friction. By lowering the shear stress required for slip, aseismic creep and more particularly SSEs are likely to occur (Sibson, 1992). For instance, Liu and Rice (2007) successfully model SSEs along subduction zones by applying a stress perturbation related to pressure change caused by high pore-fluid pressure conditions in regions affected by dehydration.

Correlations between SSEs and fluid accumulation have been pointed out in various settings. While surficial and localized triggers include intense rain events (e.g., Roeloffs, 2001) or anthropic fluid injections in geothermal contexts (e.g., Guglielmi et al., 2015), deeper evidence comes from seismic imaging. In subduction zones, seismic tomography frequently reveals a strong spatial correlation between SSE locations and zones characterized by high V_p/V_s ratios, which directly image high-pressure fluid reservoirs along the plate interface (e.g., Shelly et al., 2006).

Another phenomenon related to the presence of fluids is the dilatancy (Segall et al., 2010). The hydrological dilatancy (or dilatant strengthening) corresponds to the decrease of the porosity corresponding to the rearrangement of the materials due to slip. This effect leads to an increase of the effective normal stress, and therefore stabilizes the slip. Segall et al. (2010) highlighted the stress perturbation caused by the dilatancy associated with fault slips and therefore reducing the pore pressure. By testing two laws, they showed that this resulting instability can produce SSEs.

1.3.5.4 Structural control

A first factor expected to promote transient aseismic creep is the fault geometry. For instance, Romanet et al. (2018) used a velocity-weakening mechanical model and applied it on two overlapping faults in order to simulate fault geometrical complexities due to complex stress interactions. These conditions allow for SSEs generations according to the distance between both fault segments and their lengths. More recently, Sun and Cattania (2025) showed

that fault roughness induces slip variations along the fault, and therefore can model the generation of SSEs that can be clustered.

1.3.5.5 Synthesis on the moment-duration scaling laws

Ide and Beroza (2023) proposed an update of the previous scaling law from Ide et al. (2007), built using the duration and moment magnitude estimates of SSEs. Because most of the detections are related to subduction zones, this scaling law is mostly based on detections along the Nankai, Cascadia and Mexico. The proposed scaling law is shown in Figure 1.20. In comparison with the cubic moment-duration scaling law attributed to earthquakes ("Fast EQ" in Figure 1.20), Ide et al. (2007) suggests a linear moment-duration scaling law for the SSEs ("Slow EQ" in Figure 1.20). As the ranges of estimates are constrained by the data resolution ("Hidden zone" less resolved by the current approaches) and therefore the current techniques accuracies, the update from Ide and Beroza (2023) point out that this scaling law should be considered as an upper limit of the propagation velocity of SSEs related to diffusional processes. Some complete estimates of continental SSEs allow for new points that can be added to this Figure 1.20, as proposed by Materna et al. (2024), highlighting SSEs localized within the hidden region, and therefore in agreement with the idea of the upper-bound.

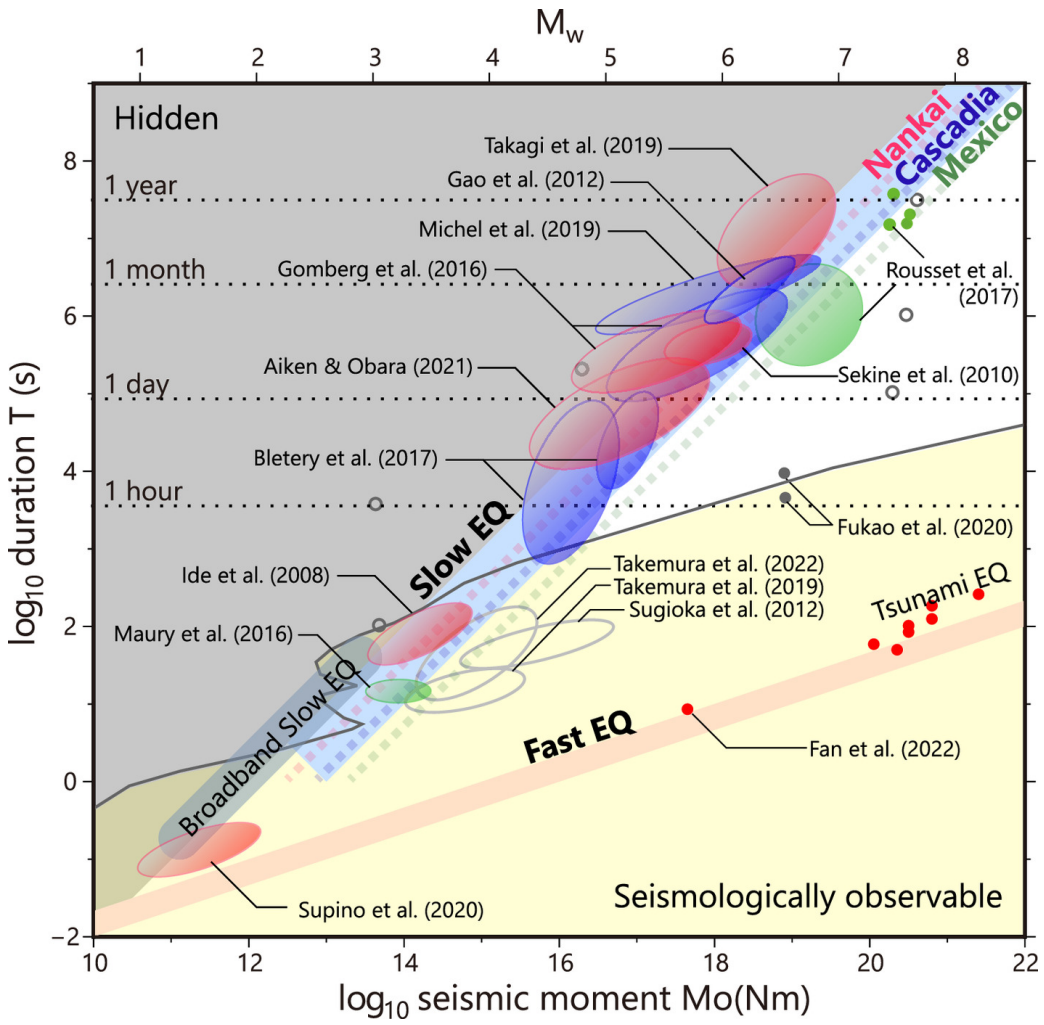

Figure 1.20: Scaling law of fast and slow earthquakes proposed by Ide and Beroza (2023). Red, blue and green ellipses and points correspond to estimates from Nankai, Cascadia, and Mexico, respectively. Gray ellipses correspond to estimates for VLFE.

However, some studies proposed that SSEs can also follow a cubic moment-duration scal-

ing law, as the earthquakes, suggesting a common behavior between slow and fast earthquakes. Frank and Brodsky (2019) used a complete LFE catalog along the Mexican subduction zone to calibrate and precise subdaily slip events. They suggest that by using LFE catalog, they get rid of the clustering processes merging slow transients into a larger one, and therefore that the slow rupture process can be compared to the earthquakes ones, modeled by a common scaling law. Then, Michel et al. (2019) extended a SSEs catalog along the Cascadia subduction zone using a shorter cut-off period than Ide et al. (2007), and therefore highlighted that SSEs may follow a cubic moment-duration scaling law. Again, they suggest that the discrepancies of the scaling laws rely on the scaling of the SSEs, being assembled or not. These different studies highlight the importance of the scaling in SSEs studies, considering large event or potential smaller bursts that define the large event.

Following this idea, Costantino et al. (2026) used a deep learning model to denoise geodetic time series and enhance SSEs detections along the Cascadia subduction zone. By comparing the impact of various detection thresholds, they show that it influences the inferred scaling laws. The use of high thresholds leads to the detection of events following a linear scaling law, rather than low thresholds lead to events following a cubic scaling law, related to a sampling bias and highlighting the impact of the signal-to-noise ratio of the data and the chosen detection threshold.

Finally, Gomberg et al. (2016) tested the hypothesis that distinct driving mechanisms govern slow and fast earthquakes, which had previously been used to justify their different scaling laws. Using a single dislocation model for both slip behaviors, they successfully demonstrated that both behaviors can be explained by bounded slip zones. Specifically, they showed that a cubic scaling law arises when the slip area grows in two dimensions, whereas a linear scaling law emerges when growth is confined to a single dimension. Nevertheless, as highlighted by the work of Ide and Beroza (2023) mentioned earlier, significant uncertainties remain regarding the universal validity of these scaling laws and their physical implications. This ongoing debate underscores the critical need for more high-resolution data to conclude on the effects of observational bias from true fault physics.

1.3.6 Related open challenges

The previous sections presented the slip dynamics during the seismic cycle, and especially the discovery of Slow Slip Events modifying our understanding of the strain release. The main current challenge is to precisely estimate the spatio-temporal characteristics of the SSEs, particularly along continental strike-slip faults for which the catalogs of events remain smaller than those established for subduction zones. The growing amount of detected SSEs may provide insights on their driven mechanisms, and therefore on the slip dynamics and seismic hazard over the seismic cycle.

The main scientific questions targeted by this work are the following:

1. What are the relationships between **aseismic** and **seismic slips**?
2. What are the **mechanisms** governing the occurrence of the SSEs?
3. In what extent aseismic creep modifies our estimates of **seismic hazard**?

1.4 Interferometry Synthetic Aperture Radar (InSAR) processing



Figure 1.21: Cover of the journal *nature* in 1993 showing the first co-seismic interferogram produced by Massonnet et al. (1993). This interferogram has been produced using two *ERS-1* SAR images acquired before and after the 1992 Landers earthquake.

In 1993, the first *"Image of an earthquake"* was produced by Massonnet et al. (1993), illustrating the surface displacement caused by the 1992 Landers earthquake (Figure 1.21). This study was the first to successfully use this geodetic technique called **Interferometry Synthetic Aperture Radar (InSAR)** to analyze earthquakes, and it highlighted several advantages of this technique that I present below. This method, based on the measurement of the displacement field with high spatial coverage over large areas, has opened new doors to the study of tectonics and is widely used today.

1.4.1 Definition of SAR Interferometry

Interferometric Synthetic Aperture Radar, or **SAR interferometry**, is based on the "comparison" of SAR images acquired by satellites in near-polar orbit around the Earth. The regular acquisition of images enables the study of surface displacement evolution over time, for almost all regions of the world, and over periods on the order of a decade.

1.4.1.1 The SAR images acquisitions

The **radar system** (RAdio Detection And Ranging) development experienced its boom during the World War II (WWII), enabling the detection of aircraft or ships from miles away, at night and in cloudy conditions. The principle of this technique is to use the travel-time of **back-scattered electromagnetic waves** on a surface or an object, to determine its position. By recording not only the travel-time but also the amplitude of these backscattered signals,

researchers could map variations in surface roughness and material properties, transitioning the technology from a simple positioning tool to an imaging system. Following this idea, an American engineer and physicist named Carl Wiley invented the **SAR technology** in the 1950s. His idea was to simulate a larger antenna aperture by using a sensor in motion, like an aircraft. This enables an increase in data resolution which is related to the length of the antenna. Later, this technology started to be carried by satellite, which enables regular imaging of the Earth's surface.

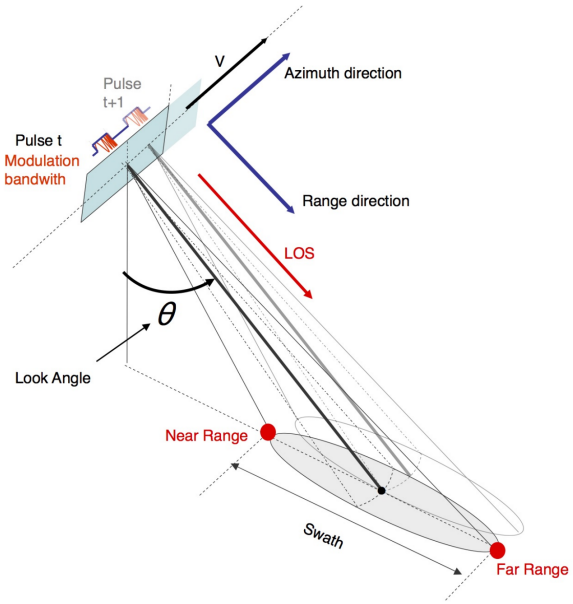

Figure 1.22: Scheme of a SAR image acquisition (Daout, 2016). The satellite is represented by the light blue rectangle, with the range and azimuth directions shown by the blue arrows. The Line Of Sight (LOS) direction is shown by the red arrow. The acquisition ellipse is represented by the grey area, with the near and far ranges distinction.

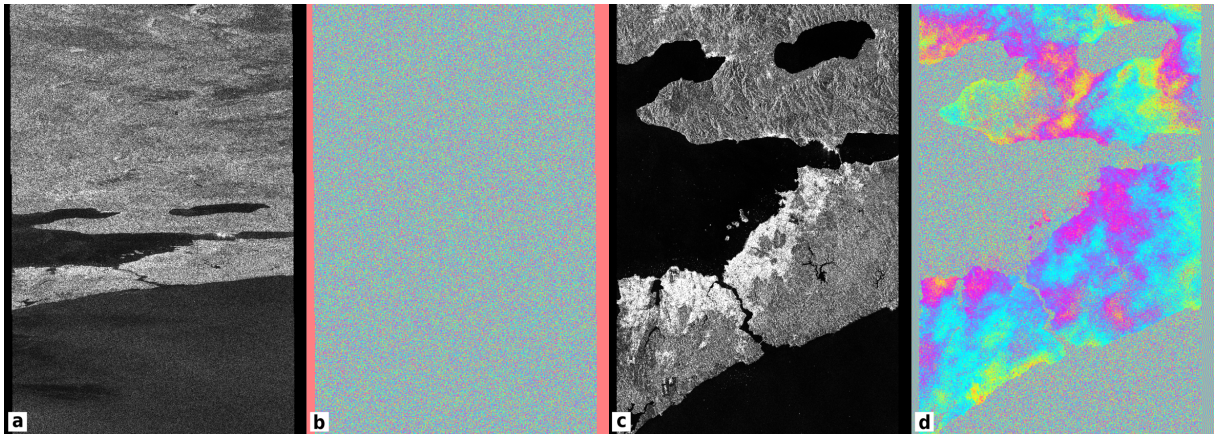

Figure 1.23: Examples of the amplitude (a,c) and the phase (b,d) of a single look complex image (a,b) and an interferogram (c,d), built from *Sentinel-1* images. The images correspond to Istanbul and its surroundings, Türkiye.

The **side-looking radars**, carried by satellites, transmit an electromagnetic wave by pulses in the direction of the Earth according to a certain look angle θ and record the back-scattered wave after its interaction with the Earth (Figure 1.22). The recorded signal corresponds to the amount of energy reflected toward the satellite and the travel-time of the wave. This signal corresponds to a **complex value** defined by an **amplitude** and a **phase** (Figure 1.23 – a and b, respectively). The near and far ranges indicate the shorter and longer arrival times of the

echoes, respectively, defining the width of the swath. As the satellite flies in the azimuth direction, other pulses of waves are sent and other echoes are recorded at $t + 1$, leading to new acquisition points and eventually a **two-dimensional SAR image**.

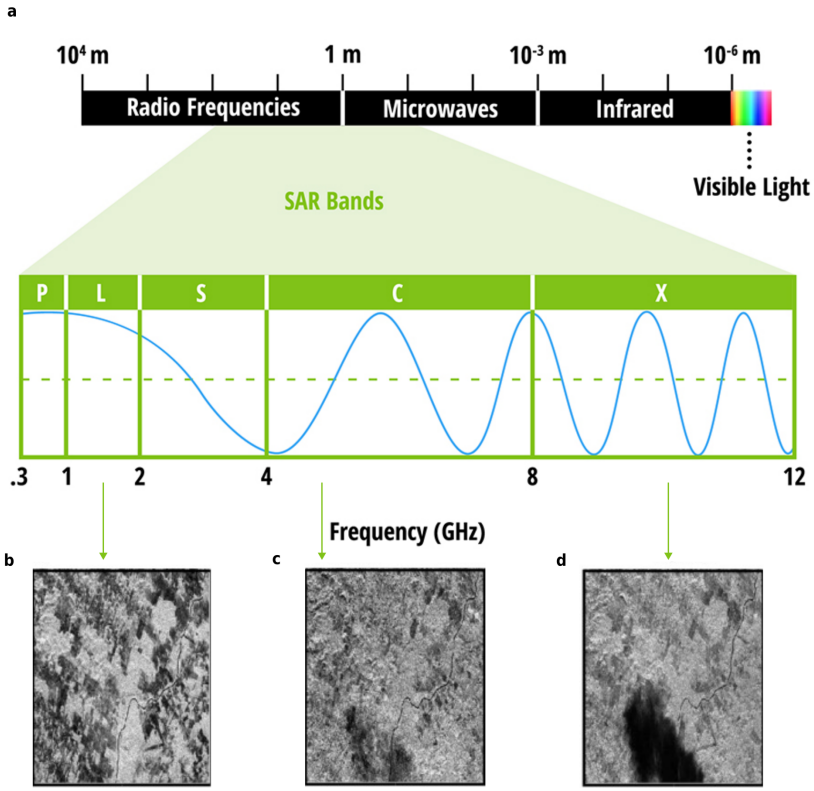

Figure 1.24: The frequency bands in SAR techniques. (a) The electromagnetic spectrum with a focus on the SAR bands (NASA, `https://www.earthdata.nasa.gov/learn/earth-observation-data-basics/sar`, accessed on 8 December 2025). The frequency and the wavelength of the waves are expressed on the bottom and top, respectively. (b,c,d) Effects of the frequency band on the SAR images, shown by several SIR-C/X acquisitions taken over a tropical forest (Ferro-Famil and Pottier, 2016).

According to the characteristics of the waves, the data will be sensitive to distinct objects. One basic classification of electromagnetic waves is based on their **wavelength** λ, which is inversely proportional to the **frequency** f. Figure 1.24a shows the electromagnetic spectrum, with the SAR bands frequencies within the green inset. The advantage of using **microwaves** is that they are not (or are less) sensitive to clouds, water, or oxygen, and therefore propagate easily through the atmosphere. It enables the acquisition of SAR images regardless of the weather or the hour of the day (independent of sunlight). The wavelength also impacts the penetration into vegetation cover, so a wave with a high wavelength will penetrate more, allowing for imaging objects deep within forests, for example. The Figure 1.24 illustrates this principle by comparing three SAR acquisitions over the same area – a tropical forest – made using three different frequency bands: the X, C, and L-bands. On the L-band image shown in Figure 1.24b, the textures of distinct vegetation are distinguishable due to the low frequency of the wave allowing for high penetration into the vegetation and soil. However, the waves with high frequency in the X-band (Figure 1.24d) do not pass through the vegetation, leading to a canopy reflectivity that appears more homogeneous. This will prevent applications for ground measurements in vegetated regions, especially if the plants are changing with the season, inducing changes in the reflectivity properties in each image, leading to the loss of interferometric coherence. The presence of a cloud is, however, identifiable by the dark zone

in the X-band image, allowing for weather monitoring, for example. The moderate frequency C-band (Figure 1.24c) appears to be a compromise between good penetration into vegetation and soils, enabling good coherence and good sensitivity, allowing the detection of millimeter-scale ground surface deformation. Alternatively, recent dual-frequency missions like *NISAR* bypass this trade-off by combining L and S-bands simultaneously, optimizing both vegetation penetration and deformation sensitivity (see `https://science.nasa.gov/mission/nisar/about-the-satellite/`, last accessed on 17 May 2026).

Another useful characteristic is the **polarization** of the wave, i.e., the plane orientation of the oscillations of the electromagnetic waves. The transmit and receive signal polarization can be controlled by the radar sensors. Horizontal and vertical polarizations are denoted *H* and *V*, respectively. For example, *HV* stands for a sensor that transmits a horizontal signal and receives a vertical one. Rough surfaces (e.g. vegetation) are highlighted by *VV* polarization, whereas double-bounce scattering (e.g. buildings) is more highlighted by *HH* polarization. The choice of polarization enables distinguishing different types of scattering of the surface.

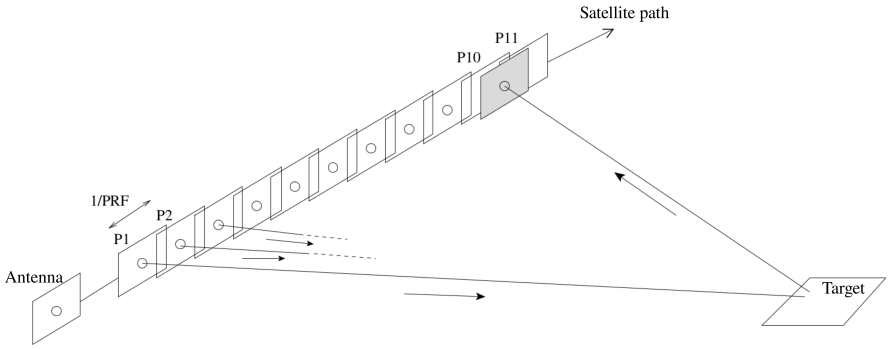

Figure 1.25: Scheme of the Doppler effect (Hanssen, 2001). The successive positions of the satellite are shown by the rectangles named *Pi*.

The **spatial resolution** of SAR images is defined according to its two dimensions in **range** and **azimuth** (Figure 1.22). The range resolution is constrained by the pulse length of the electromagnetic wave. This resolution is increased by modulating the pulse in frequency, which is called a **chirp**. The range of frequencies of the chirp corresponds to the range bandwidth of the radar. The azimuth resolution depends on the **antenna opening**, constrained by the satellite capacities (elevation, antenna length, wavelength, incidence angle). The synthetic aperture method enables us to overcome this limit and increase the azimuth resolution, thanks to the motion of the radar. As mentioned before, this resolution can be increased by using the **Doppler frequencies** as shown in Figure 1.25. The same area is illuminated by several pulses that come from different positions of the satellite during its travel. It creates a Doppler shift in frequency according to the distance between the sensor and the target. The proper sampling of these Doppler frequencies is governed by the **Pulse Repetition Frequency (PRF)**. If the PRF is too low, it leads to frequency aliasing, which degrades the image. Using this Doppler effect enhances the distinction of two sources in azimuth due to slight differences in the shift. The Doppler frequencies enable an increase in the azimuth resolution to half of the **antenna length**.

The signal received by the satellite corresponds to the back-scattered wave, which can be expressed using a complex number with its amplitude and phase, as mentioned before. The **amplitude** of the SAR image (example shown in Figure 1.23a) is related to the sensor characteristics (e.g. the wavelength, the incidence angle) and to the ground properties (e.g. the presence of water, buildings, vegetation, the local topography, the ground roughness, the dielectric property of the ground).

The **phase** of the signal (example shown in Figure 1.23b) is related to three main factors: (i) the distance between the satellite and the ground that the wave travels, (ii) the variations in the propagation velocities of the wave through the atmosphere, and (iii) the contributions of the various reflectors on the ground within the pixel. This last contribution is random across the image due to the random spatial distribution of the scatterers within the pixel. It leads to a signal that is not coherent. The phase signal of one SAR image is therefore not meaningful, as shown in Figure 1.23b. However, by comparing the phase of two SAR images covering the same zone but acquired on two different dates, the phase difference highlights changes that occurred between those two dates by removing this random backscattered phase contribution, as shown in Figure 1.23d.

1.4.1.2 Diversity of missions and their applications

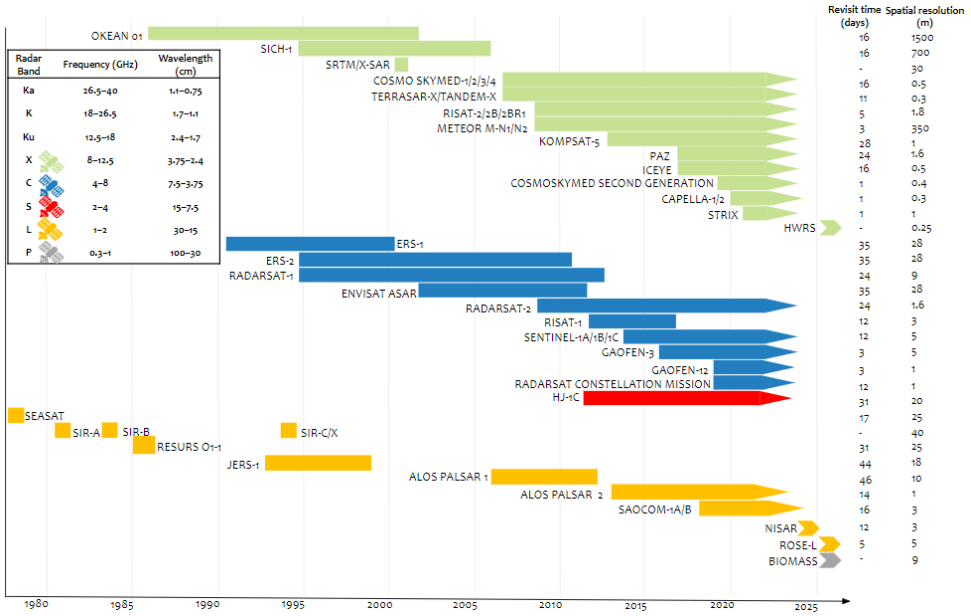

Figure 1.26: Timeline of previous and current SAR missions since 1980, according to their frequency bands (`https://detektia.com/en/sar-synthetic-aperture-radar/`, accessed on 9 December 2025). NISAR mission should be also noted in S-band.

The most important SAR missions are presented in Figure 1.26 according to their frequency bands. As explained above, the frequency band impacts the sensitivity and resolution of the acquisition. Depending on the radar band, the data can be used for various applications, as detailed in Table 1.1. Other applications (e.g., topographic or atmospheric delay mapping) are also conducted using SAR images. The applications dealing with the Earth surface motion due to tectonics, such as earthquakes and volcanoes, are mainly conducted using X- to L-bands.

The **C-band** SAR data are widely used because of their global coverage, short revisit time, and good balance between penetration into vegetation/soils and spatial resolution. Moreover, most of the data archives usually cover one decade, leading to a large number of images for each sensor. The ***Sentinel-1*** data operated by the European Space Agency (ESA) are in open access provided by the Copernicus program. Data from this mission is used in this thesis.

The ***Sentinel-1*** constellation was initially made up of twin satellites carrying a C-band SAR, named *Sentinel-1A* and *Sentinel-1B*, launched on April 3, 2014, and April 25, 2016, respectively. The use of two satellites in the same orbit but 180° apart enables a shorter revisit time of 6 *days*. On August 3, 2022, *Sentinel-1B* was officially decommissioned due to anomalies.

Band	Frequency (GHz)	Wavelength (cm)	Characteristics	Typical Applications
X 	8 – 12	3.8 – 2.4	High resolution, low penetration, fast coherence decay in vegetated areas	Urban and infrastructures monitoring, ice and snow
C 	4 – 8	7.5 – 3.8	Medium resolution, medium penetration, higher coherence	Global mapping, change detection, ice, ocean, maritime navigation, glaciers
S 	2 – 4	15 – 7.5	Experimental SAR, high penetration	Agriculture monitoring
L 	1 – 2	30 – 15	Medium resolution, high penetration	Geophysical monitoring, biomass, vegetation mapping, soil moisture
P 	0.3 – 1	100 – 30	Experimental SAR, susceptible to ionosphere	Biomass, vegetation mapping, soil moisture

Table 1.1: Table gathering the applications associated with each frequency band.

A third satellite, *Sentinel-1C* was launched on December 5, 2024, with the first cross-satellite interferogram computed in February 2025. This new mission reestablished the six-day repeat-pass observations. The last satellite of the constellation, *Sentinel-1D*, was also launched on November 4, 2025. The latter will replace the original one – *Sentinel-1A*, to ensure the continuity of the acquisitions. At time of writing, the Copernicus dashboard counts more than 34 *PB* of published products from the *Sentinel-1* mission. This huge amount of data is also challenging for both the archive/distribution and the processing, as I will discuss below (part 1.4.4).

1.4.1.3 The interferometric phase measurement

An **interferogram** is generated by computing the complex conjugate product of two SAR images, S_1 and S_2, as follows:

$$I = S_1 \cdot S_2^* = |A_1| \cdot |A_2| \cdot e^{j(\phi_1 - \phi_2)} = |I| \cdot e^{j\Delta\phi} \tag{1.8}$$

where A_i and ϕ_i are the amplitude and phase of the respective acquisitions, $|I| = |A_1| \cdot |A_2|$ is the interferometric amplitude, and $\Delta\phi = \phi_1 - \phi_2$ is the **interferometric phase**. The latter corresponds to the phase difference between the two images and is wrapped modulo 2π. Figure 1.23d corresponds to the interferometric phase $\Delta\phi$ computed from the phase of a first SAR image ϕ_1 and the phase of a second SAR image ϕ_2 acquired 12 *days* later and shown in Figure 1.23b. The interferometric phase measurement enables the removal of the random backscattered phase contribution at each pixel (Figure 1.23b), and therefore to study a potential variation of the two-way propagation phase delay of the electromagnetic wave between the satellite and the ground, between two different dates, with millimeter precision (Figure 1.23d).

The sketch in Figure 1.27b shows the geometry of the two acquisitions used to compute one interferogram. In practice, the orbit used by the satellite varies from one pass to another pass, inducing a difference in geometry for both images. The distance between the two satellite positions, perpendicular to the look direction, is called the **perpendicular baseline** ($B_\perp$

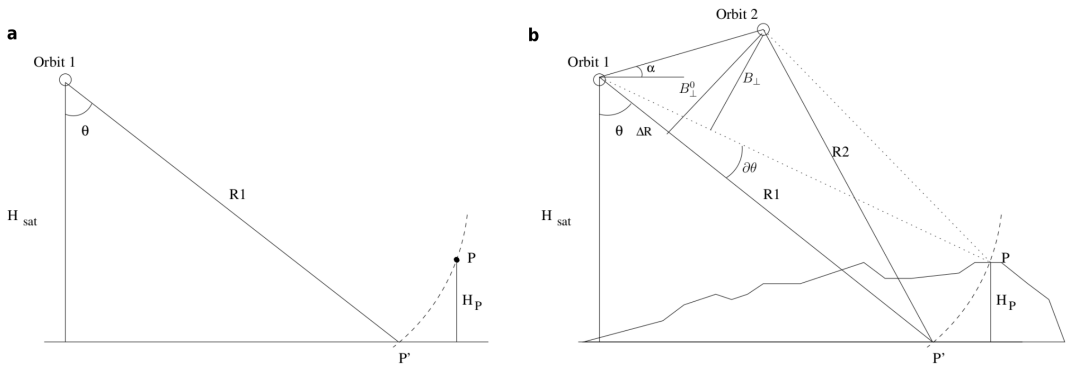

Figure 1.27: Scheme of the SAR acquisitions of a first image (a) compared with a second image acquisition (b) (Hanssen, 2001; Cavalié, 2007). *Ri* corresponds to the distance to the satellite at the acquisition *i*, H_{sat} the elevation, and $B_\perp$ the perpendicular baseline.

in the sketch). This non-zero baseline causes a signal throughout the entire image (the orbital contribution) and a topography-related signal (the topographic contribution) within the interferometric phase. In the example of Massonnet et al. (1993) shown in Figure 1.21, the orbital and topographic contributions are removed from the differential interferogram using the acquisition geometries provided by the spatial agencies (or other institutions) and external topographic data (Digital Elevation Model) in order to eliminate those effects and highlight the deformation signal.

Other contributions are included in the interferometric phase:

$$\Delta\phi_{ij} = \Delta\phi_{orb} + \Delta\phi_{topo} + \Delta\phi_{atmo} + \Delta\phi_{defo} + \Delta\phi_{noise} \tag{1.9}$$

with $\Delta\phi_{orb}$ corresponding to the orbital contribution (also called *flat Earth*), $\Delta\phi_{topo}$ the topographic one (mentioned above), $\Delta\phi_{atmo}$ the atmospheric one inducing variations in the trajectories and velocities of the wave propagation in the troposphere (mainly for X and L bands) and the ionosphere (mainly for L band), $\Delta\phi_{defo}$ the deformation of the Earth's surface, and $\Delta\phi_{noise}$ the residual noise. According to the objectives of the thesis, we may need to isolate one unique contribution, by modeling and removing the others. We are interested in the **deformation signal** $\Delta\phi_{defo}$, in order to study the ground deformation related to tectonic activity. Before describing the InSAR processing steps for the extraction of the deformation signal, I will briefly explain the contributions mentioned earlier.

The orbital contribution

$\Delta\phi_{orb}$ is related to the difference between the two orbits corresponding to each acquisition of the two SAR images, as shown in Figure 1.27b. If we consider a single point on the ground illuminated in both acquisitions, the travel-time of the waves will vary according to the perpendicular baseline, i.e. the difference between the two orbits (viewed from the point on the ground). At the interferogram scale, it means that all pixels are affected by this effect, inducing a phase delay for every pixel, as drawn in Figure 1.28b. This is visible in the interferogram as fringes mainly parallel to the azimuth direction, as shown in Figure 1.28a. The width of the fringes is proportional to the perpendicular baseline, highlighting the spatial difference between the two orbits. To remove this effect, we correct for the phase delay induced by the travel-time difference:

$$\Delta\phi_{orb} = \frac{4\pi}{\lambda} B_\perp \delta\theta \tag{1.10}$$

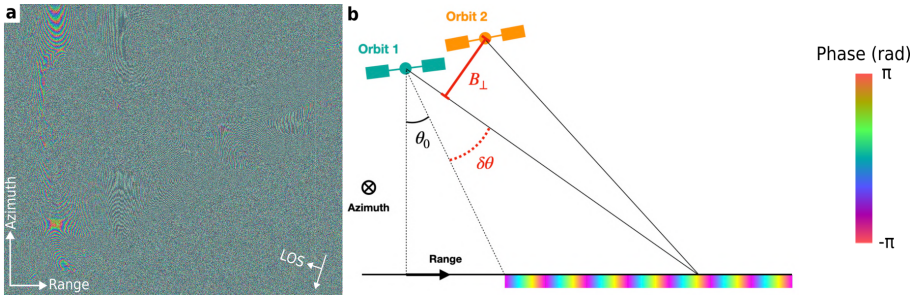

Figure 1.28: (a) Raw interferogram of the 2003 M_w 6.5 Bam earthquake (Iran) built using *ENVISAT* SAR images, i.e., the total interferometric phase $\Delta\phi$. (b) Scheme of the orbital contributions (in the vertical plane) made by Marconato (2024).

with $\delta\theta$ the look angle difference between the two acquisitions. This contribution is also called *flat Earth* because by removing the orbital effects, we eliminate the impacts of the Earth's curvature. The correction of this component is done by using precise orbits delivered by space agencies (e.g., the *Sentinel-1* accuracy of the orbits is below 1 *cm*).

The topographic contribution

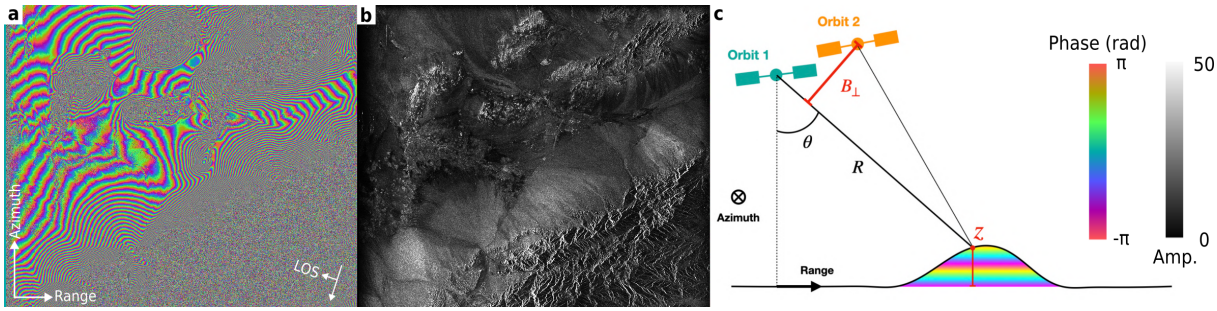

Figure 1.29: (a) Interferogram of the 2003 M_w 6.5 Bam earthquake (Iran) built using *ENVISAT* SAR images after the orbital correction. (b) Amplitude of the SAR image acquired before the earthquake. (c) Scheme of the topographic contribution (in the vertical plane) made by Marconato (2024).

$\Delta\phi_{topo}$ corresponds to the phase delay induced by the variations of the view angle between the two acquisitions, caused by a non-zero perpendicular baseline, as sketched in Figure 1.29c. This phase delay can be expressed as follows:

$$\Delta\phi_{topo} = \frac{4\pi}{\lambda}\frac{B_\perp}{R.sin(\theta)}z \tag{1.11}$$

The example in Figure 1.29a shows the interferometric phase after removal of the orbital component. The comparison between the amplitude image (Figure 1.29b) and the phase (Figure 1.29a) reveals a link between the orientation of the fringes and the presence of reliefs, such as alluvial fans in the foreground of the image. By using external Digital Elevation Model (DEM), such as from the Shuttle Radar Topography Mission (SRTM) (Farr et al., 2007) with 1 *arc* resolution ($\sim$ 30 *m*), we can estimate and remove the topographic contribution.

The atmospheric contribution

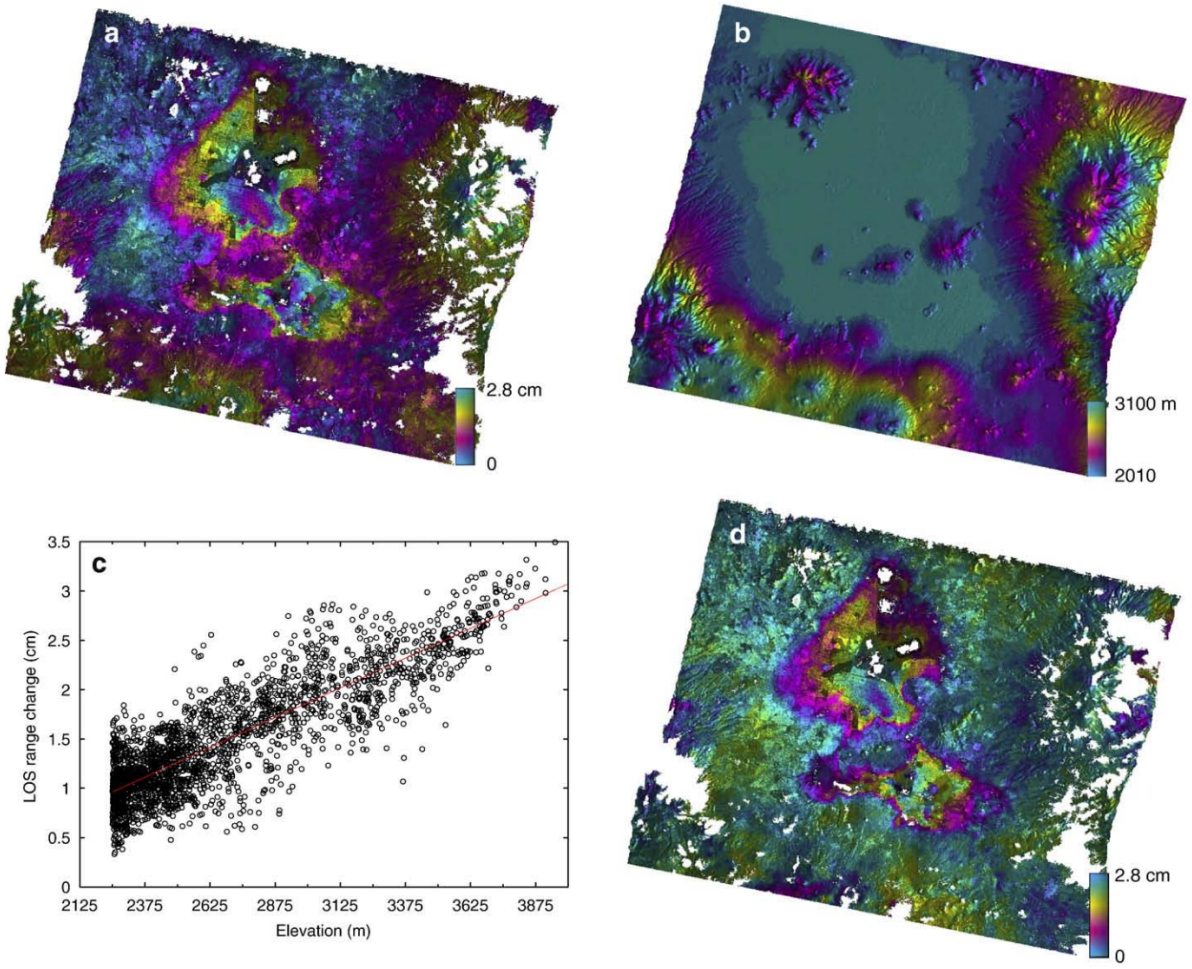

Figure 1.30: Example of interferometric phase correction for stratified atmospheric contribution and residual orbital ramp in Mexico, adapted from López-Quiroz et al. (2009). (a) Original interferometric phase computed from *ENVISAT* SAR images acquired on 26 November 2004 and 31 December 2004. (b) Digital Elevation Model (DEM) covering the area. (c) Line Of Sight (LOS) phase plotted versus elevation. The red line shows the linear regression used to correct for this correlation. (d) Interferometric phase after removal of the linear relationship shown in panel (c).

$\Delta\phi_{atmo}$ is related to the phase delays caused by the propagation of waves throughout the atmosphere. Two main atmosphere layers are responsible for this contribution: the troposphere and the ionosphere. First, the troposphere is the lowest layer of the atmosphere ($\leq$ 15 *km*-height). The phase delay from this layer can be decomposed into a stratified layer, affected by strong variations of temperature, pressure and water content, and a turbulent part.

The phase delay is proportional to the thickness of the water vapor of the atmosphere crossed by electromagnetic waves. Therefore, in the case of a stratified atmosphere, these variations of the interferometric phase are correlated with elevation, as shown in Figure 1.30c. By computing the linear correlation between the interferometric phase and the elevation, this contribution is modeled and then removed (Doin et al., 2009; López-Quiroz et al., 2009). Another part of the troposphere contribution can be turbulent, corresponding to complex spatio-temporal patterns that cannot easily be corrected. In the best cases, these effects on time series or mean velocity analysis are limited due to their random characteristic in space and time, which are so different from one acquisition to another. Several methods have been proposed to correct the stratified tropospheric phase delays, one of which is based on global meteorological models, enabling the computation of a prediction of the delays and then correcting

them in the data (Jolivet et al., 2011). However, the resolution of these models is lower than the resolution of SAR images even with multilooking.

The ionospheric contribution (i.e. related to the upper group of layers above the Stratopause, from 80 to 1000 *km*-height) is due to the concentration of gas ionized by solar radiation, leading to variations in the Total Electronic Content (TEC). The ionization of the gasses (also called photoionization because of the main role of solar radiation) induces strong spatial variations in the TEC due to the Sun's exposure. This effect can be modeled and corrected using the following equation:

$$\Delta\phi_{iono} = \frac{4.\pi.K}{c.f_0}\Delta TEC \tag{1.12}$$

with K a constant, c the speed of light in a vacuum, f_0 the frequency of the wave and ΔTEC the TEC difference between the two acquisitions from the model (Belcher, 2008). The inversely proportional aspect of the relationship between $\Delta\phi_{iono}$ and f_0 indicates that this contribution is relatively large or small within the interferogram, depending on the chosen band, allowing for the neglect of these effects according to the study area and the chosen band.

The deformation contribution

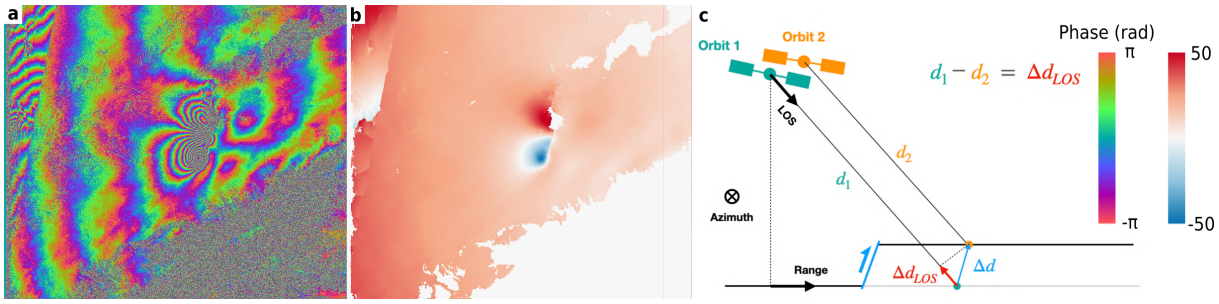

Figure 1.31: (a) Interferogram of the 2003 M_w 6.5 Bam earthquake (Iran) built using *ENVISAT* SAR images after orbital and topographic corrections. (b) Same interferogram than (a) after filtering and phase unwrapping. The colorbars are shown on the right. (c) Scheme of the deformation contribution made by Marconato (2024).

$\Delta\phi_{defo}$ corresponds to the phase delays induced by ground displacements between both acquisitions. The example of the Bam earthquake is shown in Figure 1.31 – before and after phase unwrapping, highlighting two lobes of deformation in opposite directions related to the strike-slip motion of the Bam fault. The amount of deformation is relative to the LOS direction as shown in Figure 1.31c. It can be used to express the deformation contribution using the following relation:

$$\Phi_{defo} = -\frac{4\pi}{\lambda}\Delta d_{LOS} \tag{1.13}$$

with Δd_{LOS} the deformation in the LOS direction. The combination of ascending and descending tracks obtained via different acquisition geometries can help retrieve the horizontal (essentially East-West) and vertical components of the displacement. By projecting the 3D displacement vector onto the respective LOS unit vectors of each orbit, a system of geometric equations can be solved. Although InSAR remains largely insensitive to North-South movements due to its quasi-polar orbit, combining opposite viewing angles allows for the mathematical separation of the vertical and East-West components.

The residual noise

The final contribution of the interferometric phase is $\Delta\phi_{noise}$. An example is shown in Figure 1.31a on the bottom right of the interferogram, where the phase seems random. This is the result of the decorrelation due to the presence of mountains inducing geometric decorrelation. In the case of the Bam earthquake, the presence of mountains leads to decorrelation, which can be triggered by both geometric and temporal baselines. On the one hand, high slopes exacerbate geometric decorrelation, which occurs when a non-zero perpendicular baseline distorts the look angle over steep topography. On the other hand, the presence of snow introduces temporal decorrelation, as the scattering properties of the ground surface change significantly between the two acquisition dates.

Other reasons can lead to the presence of noise in the interferograms, which can be split into instrumental and ground causes. Within the instrumental causes, there can be alignment errors of the SAR images or effects associated with too large baselines (affecting mountains areas for example). Ground changes may impact the signal-to-noise ratio of the interferograms, with vegetation cover variations, the presence of snow or soil moisture.

1.4.2 InSAR processing overview

In this part, I will briefly describe the most important steps of InSAR processing, for both the computation of interferograms and time series inversions. I focus on the *Sentinel-1* acquisitions that I used in this thesis. The acquisition mode of *Sentinel-1* is the interferometric wide swath mode (IW), for which the images include three consecutive sub-swaths as shown in Figure 1.32, and cover 250 *km*-wide areas. Available raw data delivered by the satellite agencies are focused complex SAR data (also called Single-Look Complex (SLC) data) or raw unfocused data. In the following, I describe the main steps of the interferograms calculation from the SAR images to the time series.

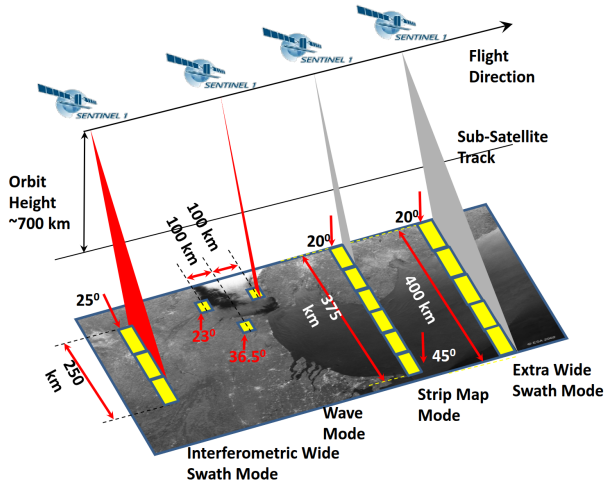

Figure 1.32: Acquisition modes of the Sentinel-1 satellites (from the European Space Agency, `https://earth.esa.int/eogateway/documents/20142/37627/PolSAR-2013-Sentinel-1-System-Data.pdf`, accessed on December 2025).

1.4.2.1 Selection of SAR images and interferogram computation

As briefly mentioned above, the objectives of the study guide the **selection of SAR images**, depending on both the sensor characteristics and the local terrain conditions. For example, the analysis of coseismic deformation benefits from selecting interferometric pairs with short perpendicular baselines in order to minimize residual topographic, orbital, and noise-related effects, as well as short temporal baselines to better isolate the deformation associated with the earthquake.

In the case of raw unfocused images, the next step corresponding to a two-dimensional compression of pixels (in range and azimuth) is called **focusing**, and it enables the production of **SLCs**.

Then, the SLCs have to be **co-registered** to correct for the acquisition geometries. More precisely, it corresponds to sub-pixel registration between the SLCs, which can be performed by different algorithms. The method remains similar, i.e. the computation of the relative shifts between both SAR images. In order to reduce the number of calculations and the time needed for the coregistration of several SLCs, a common single primary date is chosen, and the coregistration is done on this primary date. All secondary SLCs will be aligned with the primary geometry and then resampled. The geometry of all interferograms remains the same at the end.

Interferogram networks are built based on the perpendicular baseline and the temporal one (time between acquisitions). To mitigate phase bias due to fading signals (Ansari et al., 2021) and to ensure high coherence, the network was constructed using a maximum perpendicular baseline of 200 m and temporal baselines extending up to ~ 1 *year*. The phase differences for each interferogram are then calculated between both corresponding co-registered SLCs. An example of an interferogram is shown in Figure 1.33a, with in panel b the product of the two image's amplitudes.

Interferograms can be **multi-looked** by computing the average of the signal from a group of nearby pixels to reduce the speckle, which is visible for example in Figure 1.23. Figure 1.23a corresponds to a single look image of amplitude from a SLC. By averaging nearby pixels, we downsample the image. Figure 1.23c shows the multi-looked amplitude image, based in part on the acquisition in Figure 1.23a. In this case, using FLATSIM products (see Section 1.4.4.2), the data are multi-looked by a factor of 8×2 in range and azimuth. This asymmetric window is applied to compute the signal average and compensate for the non-square pixel aspect ratio inherent to most raw SAR images. For *Sentinel-1* images, this pixel aspect ratio is close to 4. Indeed, while the single-look ground resolution is approximately 5 $m \times 20$ m (in range and azimuth, respectively), the data is distributed with a pixel spacing of about 4 $m \times 14$ m. Applying an 8×2 multilooking factor perfectly compensates for this geometry, resulting in a nearly square final ground pixel size of approximately 30 m. As observed in Figure 1.23, this process effectively reduces speckle noise and increases the coherence of the image, although the spatial resolution is reduced.

1.4.2.2 Phase unwrapping

The phase is calculated modulo 2π and needs to be unwrapped to obtain continuous spatial variations of the phase delay over the studied zone. One of the major steps of the InSAR processing is the **phase unwrapping**, which consists of resolving the 2π ambiguity by integrating the phase difference starting from a group of pixels where the phase is chosen to be zero.

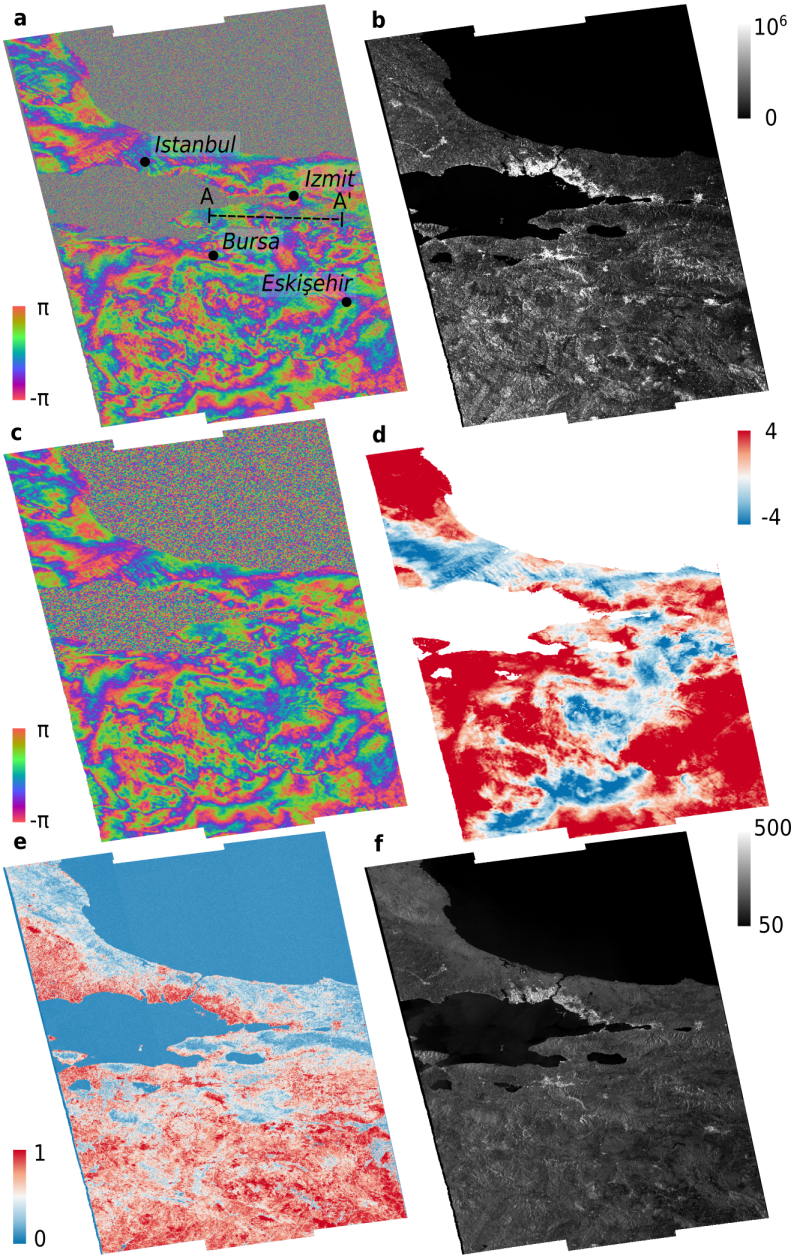

Figure 1.33: Example of products delivered by *FLATSIM*, corresponding to a 6 *days* interferogram of the track *A*058 in Türkiye built from Sentinel-1 images acquired in 1st and 7 September 2020. (a) The wrapped phase of the interferogram (InW). The dashed line corresponds to a profile used in Figure 1.34. (b) The product of the two image's amplitudes. (c) The filtered wrapped phase of the interferogram (InWF). (d) The unwrapped phase of the interferogram (InU). (e) The spatial coherence of the interferogram. (f) The average amplitudes of the two SAR images used to form the interferogram.

An example of a wrapped interferogram of the track *A*058 in Türkiye is shown in Figure 1.33a. The blue curve in Figure 1.34 corresponds to the profile *AA'* of this interferogram. We can see that the phase is affected by high-frequency variations due to several factors, that makes the unwrapping step difficult. The most important factor is the decorrelation of the data. This effect is measured by the **interferometric coherence**, which is estimated to be between 0 and 1, where 0 means that pixels have random phases, making it impossible to determine a displacement for such pixels. As seen below, different parameters can reduce the coherence such as the presence and change of vegetation or snow (temporal coherence loss) or a large baseline between both satellite locations in areas with relief (geometric coherence loss).

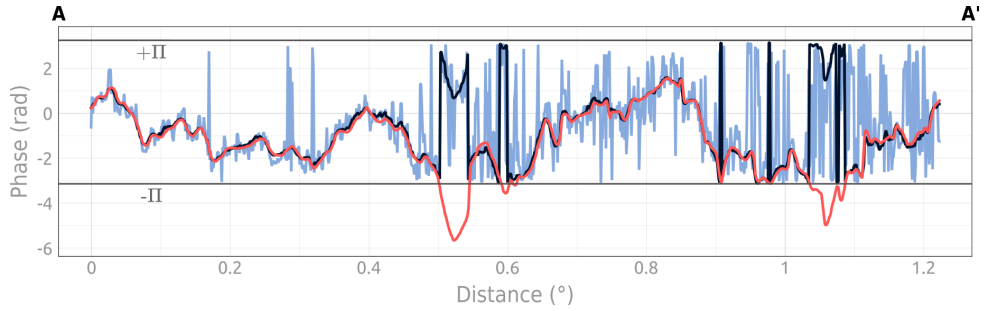

Figure 1.34: Profile *AA'* extracted from the wrapped interferogram (in blue – Figure 1.33a), the wrapped and filtered interferogram (in black – Figure 1.33c) and the unwrapped interferogram (in red – Figure 1.33d). The horizontal lines show the limit values $\pm\pi$.

An example is shown in Figure 1.33e, compared with the average amplitudes of the two SAR images used to form the interferogram shown in Figure 1.33f. Pixels with a high amplitude have a higher signal-to-noise ratio and, therefore, higher coherence values. We can see in this example that the most accurate zones are the cities (Istanbul in the north, Bursa in the middle, and Eskişehir in the east), while the less coherent ones are mostly located in mountain areas (e.g., the Samanli range between Izmit and Iznik Lake). By defining a coherence threshold, we can remove those zones of less coherence to avoid phase offsets after unwrapping due to incoherent signals.

Other factors make phase unwrapping complex, such as strong phase gradients due to topography variations which can induce layovers, atmosphere, high ground displacement gradients and residual noise. Another intermediate step enhancing unwrapping is to **filter** the interferometric phases. Several filtering methods can be used (e.g. Qing et al., 2004). An example of the filtered version of the wrapped interferogram made using an average wrapped filter (*SW* filter) shown in Figure 1.33a is presented in panel c. The black curve in Figure 1.34 corresponds to the *AA'* profile. The remaining variations are smooth, facilitating unwrapping.

Then, the phase can be unwrapped by using different algorithms (Goldstein et al., 1988; Chen and Zebker, 2001). Again, the unwrapped version of the wrapped filtered interferogram shown in Figure 1.33c is presented in panel d, with a non-cyclic colorbar. The red profile in Figure 1.34 corresponds to the unwrapped phase of the *AA'* profile.

1.4.2.3 Time series analysis

Time series are deduced from a set of interferograms, to quantify the evolution of the surface displacement in time. To do so, an inversion is performed using the phase delays of the interferograms for all acquisition pairs to retrieve an interferometric phase varying with time.

The cumulative phase delay is calculated for each pixel using the following set of equations. First, we define the phase delay per pixel Φ corresponding to the difference between two absolute phases ϕ acquired at different times (i, j):

$$\Phi^{i,j} = \phi^j - \phi^i \tag{1.14}$$

This is also defined by the sum of the phase increments $\delta\phi$ between the two acquisition times:

$$\Phi^{i,j} = \sum_{k=1}^{j-1} \delta\phi^k \tag{1.15}$$

To retrieve the displacement time series, this formulation is extended to all computed interferograms to build a linear system of equations, expressed in matrix form as:

$$\Phi = A\delta\phi \tag{1.16}$$

where Φ is the vector containing the interferometric phase values for a given pixel across all M interferograms, $\delta\phi$ is the vector of the $N-1$ unknown phase increments between consecutive acquisitions, and A is a design matrix of size $M \times (N-1)$ filled with 0 and 1 according to the network configuration. This linear system can then be solved using inversion methods such as Least-Squares or Singular Value Decomposition (SVD) (Doin et al., 2011). A phase time series cube is built, with the cumulative phase at each pixel corresponding to cumulative phase at each acquisition date.

1.4.3 Presentation of the main processing chains

Time series inversions are challenging due to the temporal and spatial decorrelation of the phase and the presence of atmospheric disturbances reducing the signal-to-noise ratio.

Since 2000's, several methods have been developed to tackle this challenge and to provide time series of deformation. In the following, I detail two end-members of the processing chains widely used today in these various algorithms: the ***Persistent Scatterers Interferometry*** (PSI) and ***Small Baseline Subset*** (SBAS) methods.

1.4.3.1 Persistent Scatterers Interferometry (PSI)

The aim of the ***Persistent Scatterers Interferometry*** (PSI) methods is to rely on stable pixels over the study period, in order to enhance the accuracy of the time series inversion. The main challenge of this method is to define how to choose those coherent pixels.

The first implementation of *Permanent Scatterer* (PS) approach came from Ferretti et al. (2000, 2001), who proposed a selection of stable pixels using a dispersion index D_A calculated from the amplitude as a criterion corresponding to the ratio of the mean and standard deviation of the time series of the amplitude values per pixel. They showed that this method enables the selection of pixels with a stable phase over time, mostly corresponding to urban areas and rocky terrains. Similar methods have been developed using different pixel selection criteria, e.g., coherence maps with a delicate tradeoff between the choice of the coherence threshold and the threshold estimate window size or analysis of the phase stability (Hooper et al., 2004), leading later to the StaMPS algorithm (Hooper et al., 2012). These methods are robust, enabling high accuracy on the selected PSs; however, the spatial resolution is reduced due to the pixel selection.

To improve the spatial resolution, new methods combine the processing of PSs and DSs, i.e. *Distributed Scatterers* (DS) (e.g. Ferretti et al., 2011). The latter corresponds to reflectors that are also stable over time but are characterized by several small scattered objects affecting a group of pixels (rather than one main object per pixel for the PSs). The scheme in Figure 1.35 shows the difference between both scatterer groups, indicating the main nature of both, such as the PSs being mostly linked to walls or corners of a building, electric pylons for example, whereas the DSs are mostly related to crops, homogeneous rocky slopes, etc. This strategy is used within the SqueeSAR algorithm implemented by Ferretti et al. (2011). In this case, we talk about *Persistent Scatterers* because the selection includes pixels that are not ideal

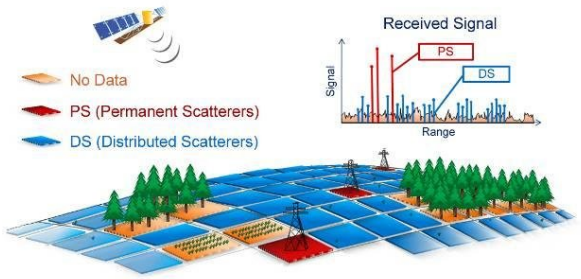

Figure 1.35: Scheme showing the characteristics of the permanent and distributed scatterers from Tamburini et al. (2014).

but statistically stable over time. Abuse of terms leads to a generic term of ***Persistent Scatterers Interferometry*** (PSI), gathering all *Permanent Scatterers* methods (e.g. Ferretti et al., 2000, 2001), *Persistent Scatterers* (e.g. Ferretti et al., 2011), and hybrid methods, as developed by Crosetto et al. (2016).

1.4.3.2 Small Baseline Subset (SBAS)

A second type of method used to compute time series inversions is called **Small Baseline Subset (SBAS)**. It was first mentioned by Berardino et al. (2003) in their study of deformations related to the Campi Flegrei caldera and the city of Naples in Italy. These methods are based on the minimization of the decorrelation of the interferograms, by selecting only short spatio-temporal baselines as shown in the example in Figure 1.36a.

In order to maintain the good coherence achieved through the specific selection of interferograms, subsets are built corresponding to a group of closely related interferograms. The inversions are independently computed on each subset, which reduces noise and enhances the target signal. The main challenge of this method is to merge the several resulting time series to produce a unique time series covering the entire period, such as the one presented in Figure 1.36b. Figure 1.36 – c,d,e shows an example of the effects of different algorithms on a same dataset illustrated by Jolivet (2011). Without going into details, three different strategies exist:

c. a least square method with a linear interpolation of the time series within the overlap periods (Usai, 2003),

d. a singular value decomposition (SVD) method with a quantification of the variation rate of the phase allowing for a merge of the overlap periods (Berardino et al., 2003),

e. and the use of constraints to the inversion based on a polynomial function denoted the evolution of the phase applied with a weight to reduce the artifacts due to the the method used (López-Quiroz et al., 2009).

The resulting time series is different and highlights the importance of the choice of the algorithm related to the objectives of the studies.

The examples detailed in Figure 1.36 do not show all SBAS methods, as pointed out by Li et al. (2022) for instance. Their goals are to overcome issues of the classic SBAS method, such as data coherence or the accuracy of the deformation estimates. In this thesis, I use InSAR data processed using the NSBAS method from Doin et al. (2011), which I present in the following section.

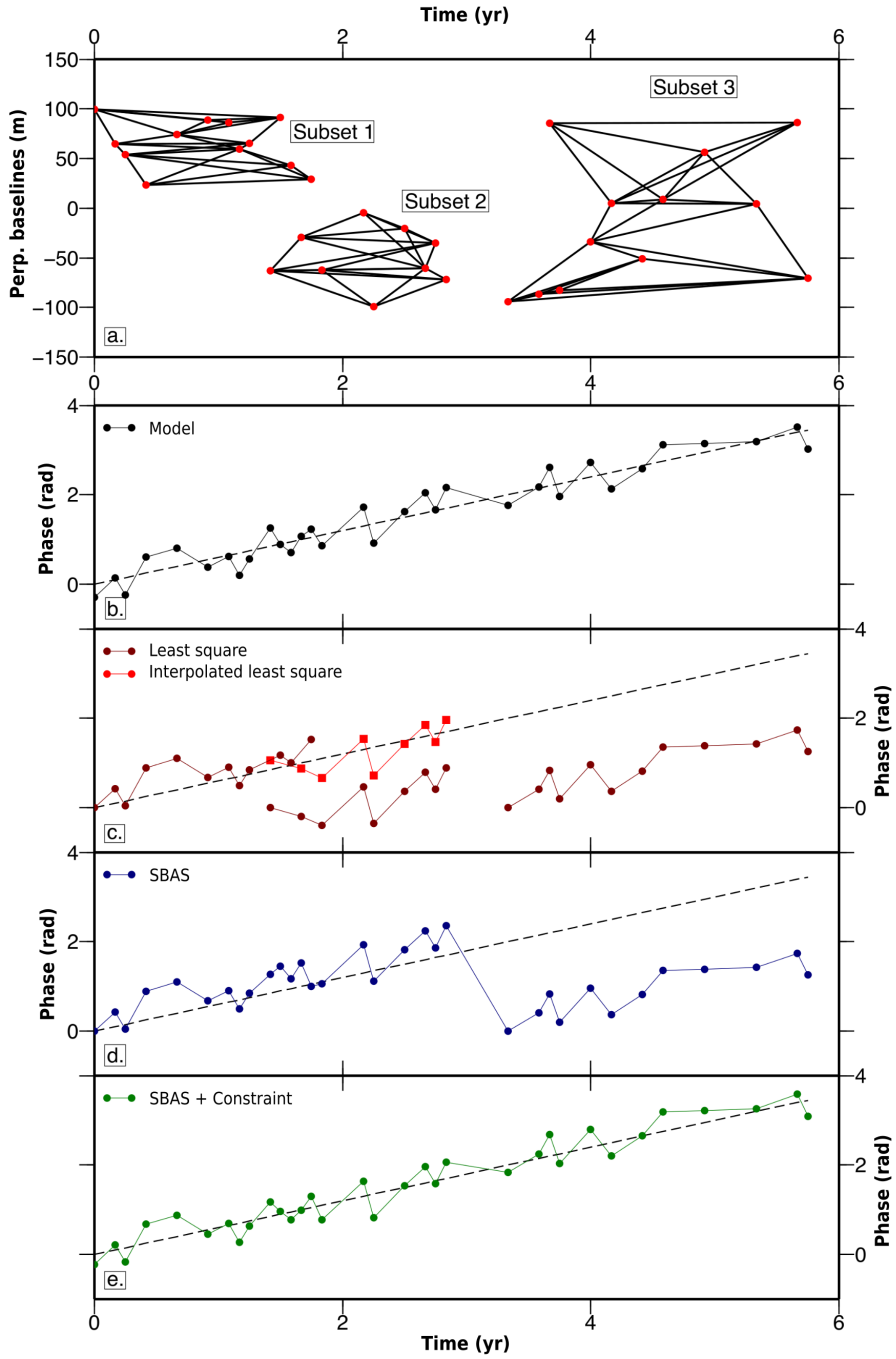

Figure 1.36: Illustration of the variability of the SBAS algorithms on a synthetic test, published by Jolivet (2011). (a) Interferogram network. (b) Synthetic time series of a pixel (black line) built using white noises in addition with a synthetic linear deformation of the ground (dotted line). (c) Resulting time series obtained used the approach developed by Usai (2003) based on a least square method. (d) Resulting time series obtained using the initial SBAS method developed by Berardino et al. (2003) based on a SVD approach. (e) Resulting time series obtained by using the algorithm developed by López-Quiroz et al. (2009), based on a SBAS approach enhanced by the use of constraints.

1.4.3.3 The New Small Baseline Subset chain (NSBAS)

The **New Small Baseline and Subset (NSBAS)** chain (Doin et al., 2011) corresponds to a fully automatic processing chain to compute time series of displacements from raw SAR im-

ages. It was initially developed for ENVISAT images, with the aim of overcoming the growing number of available SAR images (ERS, ENVISAT, RADARSAT) and has therefore been adapted for use with *Sentinel-1* images (Grandin, 2015).

The NSBAS processing chain is based on Repeat Orbit Interferometry PACkage (ROIPAC) modules (Rosen et al., 2004). Without going into the details of each step of the workflow, I focus on the key aspects of the method. The greatest asset of this method is the enhancement of interferogram coherence, especially in areas with moderate or high topography and areas covered mostly by vegetation.

Such improvements are possible thanks to some processing steps. First, during the early steps of the processing, the SLCs are computed using a common Doppler band systematically to increase the coherence by fixing the azimuthal spectral coverage. They are co-registered to a "super master image", i.e., the coregistration of all the SLCs is relative to one chosen geometry, reducing the computation time. Then, the use of Digital Elevation Models (DEM) early in the processing enables consideration of the variations in topography and, therefore, limits the loss of coherence due to geometrical distortions related to a non-zero perpendicular baseline (see Section 1.4.1.3). This is done by the local slope adaptive range filtering (Guillaso et al., 2008). The most significant impacts are observed in long-temporal baseline interferograms. By successfully incorporating pairs with longer temporal spans than traditional techniques like SBAS, this approach effectively mitigates long-term phase biases and improves the retrieval of slow, steady displacement rates. Corrections and filtering are then applied before the unwrapping of the phase based on the coherence to optimize the unwrapping path and limit unwrapping errors (Grandin et al., 2012). Atmospheric corrections are also applied to reduce their phase delays. This is done by applying model-based corrections of stratified atmospheric delays using global meteorological models (e.g., with ERA-I from ECMWF, Jolivet et al., 2011) and/or orbit corrections re-estimation (Cavalié et al., 2008; Jolivet et al., 2012). Finally, the last step is the time series inversion, according to two different strategies, which are the constrained inversion as explained before (see Section 1.4.3.2, López-Quiroz et al., 2009; Jolivet et al., 2012) and the smoothed inversion, in which we do not assume that the time series follows a polynomial function but that the temporal evolution is smooth.

1.4.4 The development of an automatic processing chain - the FLATSIM project

With the growing number of *Sentinel-1* data, automatic processing methods have been developed to provide surface displacement time series over large areas and long time periods. As explained in Section 1.4.3, various processing chains have been implemented, leading to the building of some workflows able to automatically process InSAR data and compute time series, e.g. LiCSBAS which is an open-source Python package developed by Morishita et al. (2020) as part of the COMET consortium in the United Kingdom. In France, a similar project has been settled in the framework of the **FLATSIM** *FormaTerre LArge-Scale Multi-Temporal Sentinel-1 InterferoMetry* project detailed by Thollard et al. (2021), in collaboration with the French *Centre National d'Études Spatiales* (CNES). The aim is to provide interferograms, mean velocities, and phase time series (which can be converted into ground displacement) obtained using *Sentinel-1* data and based on the NSBAS processing chain detailed before (Section 1.4.3.3, Doin et al., 2011)). The following section is a summary of the FLATSIM project based on Thollard et al. (2021). The FLATSIM data has been used in this thesis.

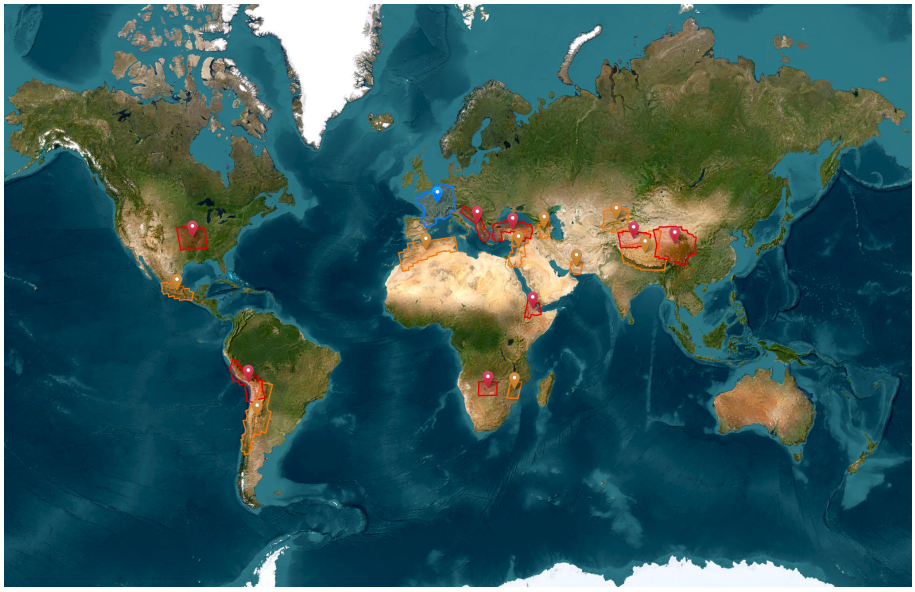

Figure 1.37: Global map showing the sites operated in the framework of the FLATSIM project (`https://flatsim.cnes.fr/doi/`, accessed on December 10, 2025). Red and orange areas correspond to chosen areas from the first and second calls for projects, respectively (a third call has been launched in 2026, with the kickoff of the processing in April 2026). The blue one corresponds to the French site, the FITS-FR collection of the Service National d'Observation ISDeform.

1.4.4.1 FLATSIM architecture

FLATSIM architecture is split into two main components: (1) a production module enabling the automatic processing of the InSAR data, and (2) a delivery module allowing for the distribution of the products to the users.

The **production module** is designed to incorporate the NSBAS chain into the CNES high performance computing (HPC) infrastructure. First, this strategy takes advantage of the *Sentinel-1* data from ESA locally copied and stored by the CNES. Then, the NSBAS chain has been adapted to run within the HPC infrastructure, and the main processing steps are parallelized to decrease the computation time. The collaboration with CNES also enables high storage. As an example, the processing of a 5.5 °-long swath with 8 *looks* resolution over 5 *years* requires 10000 *hours* of CPU (i.e., Central Processing Unit) time and therefore 60 *hours* of real time. To be more efficient, the production module is itself divided into two sub-components: (1.1) the FLATSIM application server corresponding to the catalogs and orchestrator capabilities, and (1.2) the FLATSIM unitary treatments corresponding to the processing jobs sent to the HPC infrastructure.

After processing interferograms and time series for a given region, each track is checked by the Principal Investigator (PI) of the project site to validate the products. This is part of the **delivery module**, which provides scientific experts with direct access to the final products. After validation, the data are available to the users.

1.4.4.2 The incorporation of the NSBAS chain

Figure 1.38 gathers the main steps used by the FLATSIM project based on the NSBAS processing chain, allowing for the computation of unwrapped interferograms, then used for the

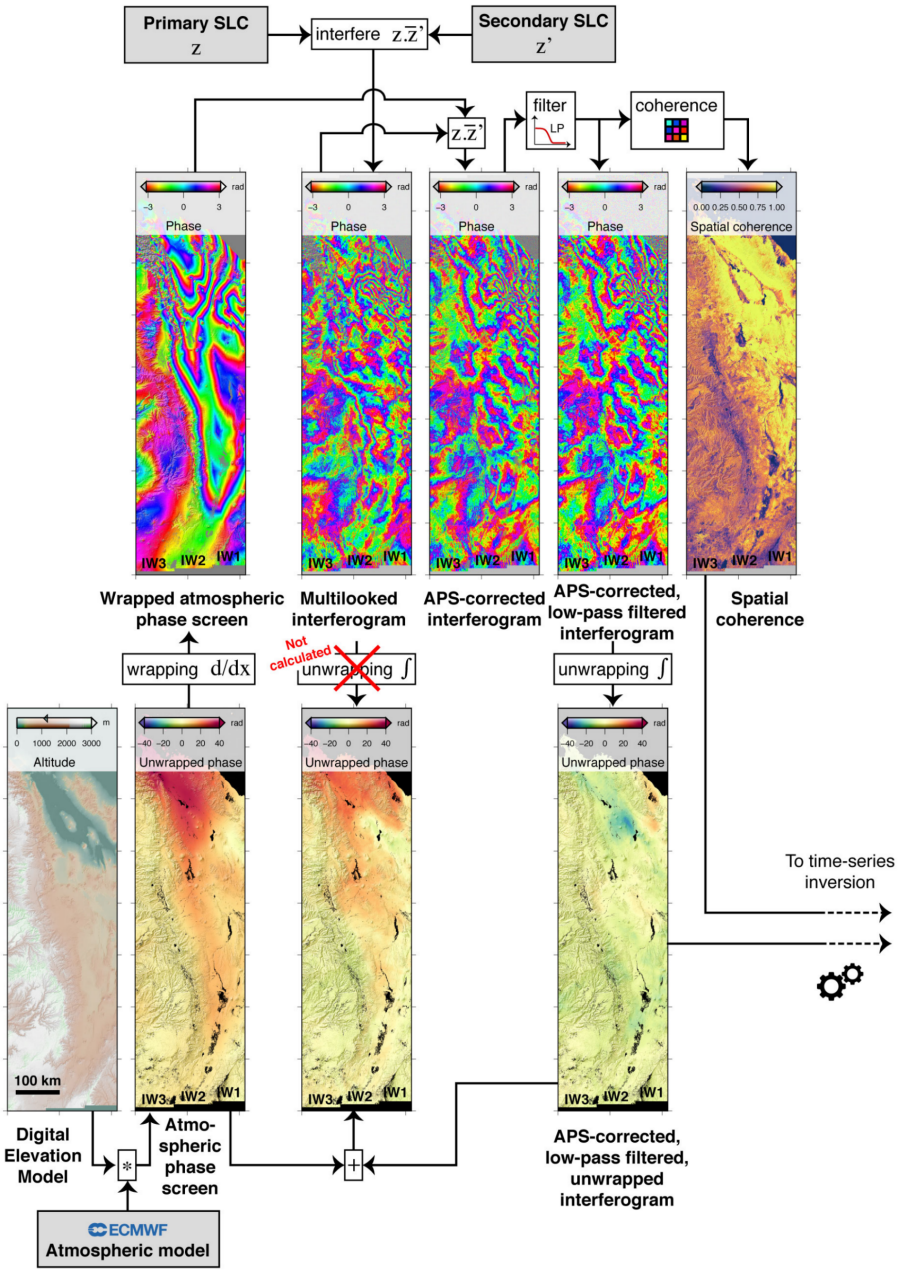

Figure 1.38: Processing sequence from raw SAR images to unwrapped interferograms used by FLATSIM from Thollard et al. (2021).

time series inversion. All of these steps are done using the radar geometry. As described in Section 1.4.3.3, interferograms are selected based on their temporal and spatial baselines. SLCs are co-registered using a master SLC, and then interferograms are computed and multi-looked. Atmospheric phase screen (APS) correction is applied based on a DEM simulation and an atmospheric model. A filter is applied to the APS-corrected wrapped interferograms, before unwrapping based on the spatial coherence and the DEM of the latter.

The final APS-corrected low-pass filtered and unwrapped interferograms are used for the time series inversion after validation of the interferograms based on their unwrapping fractions and the residual phase standard deviations per interferograms and dates. The total phase delay time series and a temporally smoothed time series are jointly inverted, the first product being delivered to the users and the second one being used as a regularization in case of disconnections in the interferogram network. The time series inversion algorithm also uses an iterative process, which allows for the correction of unwrapped errors (Cavalié et al., 2007;

López-Quiroz et al., 2009; Doin et al., 2015). Finally, different quality control (QC) features are computed based on the inversion, and the mean LOS velocity is produced based on a linear least-square regression in time of the time series, iteratively improved by using weights on data presenting high deviations from the displacement temporal evolution trend.

Some processing parameters are automatically chosen, such as the type of filter used for the wrapped phases, the spatial coherence threshold used to mask the data before unwrapping or the threshold of the unwrapping fraction per interferogram used to select the validated interferograms for the time series inversion. These choices have an impact on the final interferograms and time series. Users have the possibility to download the 2-looks wrapped interferograms (or 8-looks) and pursue the processing manually and/or compute the time series. In the following part, I will detail the delivered outputs from FLATSIM.

1.4.4.3 Presentation of the delivered products

The access of the products is made via the CNES data portal called GEODES (`https://geodes-portal.cnes.fr/`, accessed on March 2, 2026). The delivered products are divided into three categories with the list of the main important files:

- **Interferogram based products**: wrapped (InW), filtered wrapped (InWF), unwrapped (InU) interferograms, spatial coherence (Coh) and atmospheric phase screen (APS) data,
- **Time Series**: time series cube of phase (DTs), mean velocity (MV-LOS), network misclosures (Net) data, and list of the interferograms,
- **Auxiliary Data**: LOS components (CosENU), digital elevation model (DEM), lookup tables (LuT, for the conversion from radar to ground geometry) and temporal coherence (TCoh).

These products are provided in radar and geographic geometries at different resolutions according to the related step in the processing. The interferogram based products are available for all pairs of acquisitions used in the final time series however they are heavy (~ 2.2 *Gb* per interferogram for the zipped folder) due to the 2 *looks* resolution. An example of some products of the interferogram package is shown in Figure 1.33. In comparison, the zipped folder of the time series is about ~ 6.7 *Gb* for 100 processed images, with a data cube of about ~ 6.1 *Gb* and ~ 4.1 *Gb* in ground and radar geometries, respectively.

1.4.5 Related open challenges

The presentation of InSAR technique shows the opportunities to study displacement time series along worldwide continental fault systems over decades with a high spatial resolution. The use of these data has already proved its efficiency in detecting small displacements (down to a few millimeters), allowing for the study of slow deformation.

As a complement to the previous open challenges related to the discovery of SSEs (Section 1.3.6), here are additional challenges related to the use of the InSAR technique:

1. What new insights or added values into **fault creep dynamics** can be gained from **continuous**, **long-term InSAR monitoring** at regional to global scales?

2. How can the increasing volume of **automatically processed InSAR products** be systematically exploited to better constrain the **spatio-temporal variability of creep** along **continental strike-slip faults**?

3. How robust are **automated InSAR processing chains** in preserving **low-amplitude deformation signals**, and how do processing choices affect the detection of SSEs?

4. How can **large-scale, automatically processed InSAR datasets** be used to build systematic **inventories of transient deformation events** along global fault systems?

5. What are the current limitations in terms of **sensitivity, spatial resolution, and noise amplitude** of the InSAR data?

1.5 The North Anatolian Fault in Türkiye

1.5.1 Geological and Tectonic contexts

1.5.1.1 The formation of the Anatolian land mass

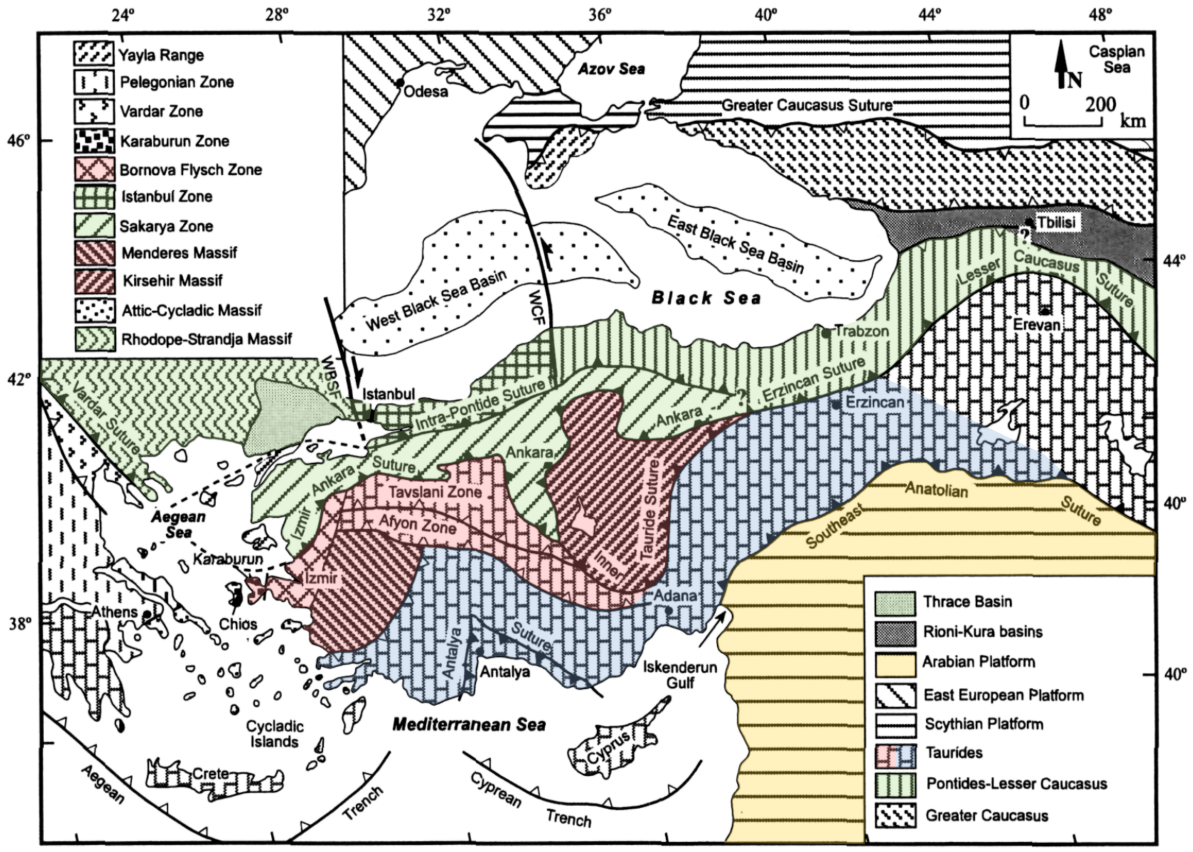

Figure 1.39: Simplified tectonic map showing major structures and provinces modified from Bozkurt and Mittwede (2001). Abbreviations: WBSF = Western Black Sea fault, and WCF = West Crimean fault. The sutures are shown by the lines with filled triangles, so that the tips of triangles indicate polarity. Thrust belts are shown by the lines with open triangles, so that triangles point toward the vergence direction. Strike-slip faults are shown by the lines with half arrows, so that the half arrows show relative movement along these faults. The Pontides and Lesser Caucasus form the eastern extension of the Sakarya Zone. The colors correspond to four main tectonic blocks: the Pontides in green, the Anatolides in red, the Taurides in blue and the Arabian Plate in yellow.

Türkiye can be split into four main tectonic blocks as represented in Figure 1.39:

1. the **Pontides** on the Northern side (green),
2. the **Anatolides** on the central part (red),
3. the **Taurides** on the Southern side (blue),
4. the **Arabian plate** on the South-Eastern side (yellow).

The second and third blocks are sometimes grouped as the Anatolide-Tauride block. All of these pieces are tied by several sutures shown by the black lines, traces of the past geology, which point to ocean closures and continental collisions. This land mass is surrounded by three

seas - the **Black sea** (North), the **Aegean sea** (West) and the **Mediterranean sea** (South); and contains one sea on its North-Western side - the **Marmara sea**. These blocks are witnesses of Paleozoic and Mesozoic times, assembled during the Triassic and completely reworked during the Neogene, mostly due to the Alpine orogeny, leading to the current Türkiye with its complex tectonic and geological contexts. As shown in Figure 1.39, this complex geological history has shaped the country with many relics from the ancient Tethyan oceanic basins closures (e.g. sutures, metamorphic and volcanic massifs, accretionary complex). The next paragraphs provide an overview of the major geological events leading to the formation of these different suture zones.

More than 350 *Ma* ago during the Carboniferous period, the closure of one of the most significant Paleozoic oceans, the **Rheic ocean**, led to the collision of the two supercontinents Gondwana and Laurussia during the Variscan or Hercynian orogeny (Carbonifeous-Permian). The Rheic ocean separated the Avalonia and Armorica terranes (Gondwana side), two micro-continents detached from Baltica-Laurussia and Gondwana. Two areas in Türkiye come from those continents (Figure 1.39): the Istanbul zone was part of Avalonia (e.g. Okay et al., 2011b), and the Sakarya and the Strandja zones were part of Armorica (e.g. Okay et al., 2008b; Ustaömer et al., 2012). The closing of the Rheic ocean forms the first suture in current Türkiye within the Pontides zone, represented in purple in Figure 1.39, called the **Rheic Suture** (Akdoğan et al., 2021). Due to the Alpine orogeny, which reworked a lot of this region, the precise origin of the Rheic suture is still debated, with some papers suggesting that this suture may rather be a Neo-Tethyan suture (e.g. Marroni et al., 2020).

The subduction of the Rheic ocean led to the **Variscan orogeny** with the continental collision of Gondwana and Laurussia, which formed **Pangea** during the early Permian. At least two oceans existed during this period: the superocean Panthalassa, and the **Paleo-Tethys** ocean. Some studies suggest that the Paleo-Tethys can be the result of a back-arc basin of the northward subduction of the Rheic ocean lithosphere (Karsli et al., 2020), but this is still debated. Indeed, some studies suggest that the Paleo-Tethys opened during the late Ordovician - Silurian, meaning that the Rheic and Paleo-Tethys oceans were coeval at this period (Topuz et al., 2020). Nevertheless, the Paleo-Tethys ocean was separating the young Pontides zone (part of the previous Laurussia, mostly the current Eurasia) with the Anatolide-Tauride block (part of the previous Gondwana, mostly the current Africa). The closure of the latter by dual subduction north- and south-ward started in the late Paleozoic (Candan et al., 2016), and continued for the northward subduction under Laurasia during the **Cimmeride (or Cimmerian) orogeny** in Late Triassic forming the **Izmir-Ankara suture** (Şengör et al., 1984; Okay et al., 2011a). The Karakaya complex within the Sakarya zone (north of the Izmir-Ankara suture, in orange in Figure 1.39) corresponds to the accretionary complex of the Paleo-Tethys subduction (Okay et al., 1996, 2011a; Aysal et al., 2018).

Meanwhile, the breakup of Pangea also started in the late Triassic, with the opening of an ocean called the **Neo-Tethys**. This ocean is composed of several branches separating micro-continents, such as the Anatolide-Tauride locked between the Northern and Southern branches of the Neo-Tethys. The Northern branch of the Neo-Tethys is also made of different branches, with the Intra-Pontide ocean on the North, the Izmir-Ankara-Erzincan ocean separating the Sakarya zone with the Anatolide-Tauride block, and Inner Tauride oceans (Şengör and Yilmaz, 1981). Those oceans opened following the rifting initiation during the early Triassic, suggesting that Paleo- and Neo-Tethys may have been coeval (e.g. Göncüoğlu et al., 2003; Robertson et al., 2004; Tüysüz and Tekin, 2007).

Those oceans closed due to the North-South convergence between the Africa-Arabia and Eurasia blocks during the **Alpine orogeny**. The subduction of the Neo-Tethys started in late Cretaceous (Maffione et al., 2017). The end of the full Neo-Tethys closure is still debated but

some studies suggest that it lasts at least until the beginning of the Eocene like for the Intra-Pontide ocean (e.g. Cengiz, 2023; Kuş et al., 2025). The closure of the latter shaped the **Intra-Pontide suture** (IPS - in blue Figure 1.39) between the Istanbul zone and the Sakarya terranes. The closure of the central branch of the Neo-Tethys led to the collision of the Pontides and the Anatolide-Tauride block, forming the **Izmir-Ankara-Erzincan suture** (in red - Figure 1.39) (e.g. Sarıfakıoğlu et al., 2017; Mueller et al., 2019). The **Black Sea** formed as a response of the subduction of the northern branch of the Neo-Tethys during the Cretaceous, corresponding to an oceanic back-arc basin (e.g. Stephenson and Schellart, 2010). The continental collision led to the uplift of the Pontides and Tauride mountain ranges, and also to volcanism activities.

The southern branch of the Neo-Tethys also closed during this period. The eastern subductions continued probably until the Miocene (Gülyüz et al., 2020). It led to the exhumation of metamorphic complexes, such as the Kirsehir massif (central Anatolia) (e.g. Cinku et al., 2016). The incomplete closure of the southern branch of the Neo-Tethys formed the **Mediterranean sea** (Le Pichon et al., 2019a). $\sim 15\ Ma$ (Miocene), the **Hellenic subduction zone** in the Mediterranean sea has formed to accommodate this convergence (Le Pichon et al., 2019b). The result of this subduction is a North-South extensional tectonics west of the Anatolia block, which formed the **Aegean sea**. Simultaneously on the east of the Anatolian block, the Arabian plate entered in collision, leading to the **Bitlis-Zagros suture** (e.g. Okay et al., 2008b; Cavazza et al., 2018) (in brown - Figure 1.39). Again, associated metamorphism and volcanism appeared in response of the subduction and collision zones.

All of these successive events shaped the Anatolian land mass that we know today. This block is made of Gondwana and Laurussia pieces, assembled by several sutures - relics of ancient oceans, which have been metamorphosed and covered by new layers. This land mass remains affected by active deformation, that I described below.

1.5.1.2 The tectonic context

Türkiye is composed of **three major distinct tectonic plates**: the Anatolian plate (central and major one), the Eurasian plate (north and east) and the Arabian plate (south-east). Two major faults currently cross the country (Figure 1.40): the **North Anatolian Fault** (NAF) and the **East Anatolian Fault** (EAF). The NAF was first described by Ketin (1948) after the 1930's earthquakes in eastern Türkiye, starting with the 1939 Erzincan earthquake (Barka, 1996). By studying the displacements along the ruptures, he concluded that one major right-lateral strike-slip fault on the north-east side of the country explains the observations. To accommodate the westward displacement of the Anatolian block, a second fault (corresponding to the EAF) was needed in the South (Arpat and Saroglu, 1972). While this two-fault configuration forms the backbone of the Anatolian extrusion engine, modern block models now incorporate several secondary fault systems such as western grabens and central splays, to fully account for the internal deformation of the plate.

During the Neogene period, all the micro-plates gathered forming the current land mass that we know, and impacting the tectonics. The **Arabian plate** is pushing the Anatolian and Eurasian plates on the eastern side, and the **Hellenic subduction** is pulling the Anatolian plate on the western side. The onset of the NAF and EAF has been largely debated. Indeed, the dating of syntectonic sediments along the North Anatolian Fault Zone (NAFZ) reveals that the eastern part may have initiated $13 - 11\ Ma$, against $200\ ka$ within the Marmara Sea on the western part (Şengör et al., 2005). These observations suggest a westward propagation of the NAF initiation, with an average velocity of $11\ cm/yr$, based on an analysis of the North Anatolian Shear Zone (NASZ) provided by Şengör et al. (2005), and based on general observations

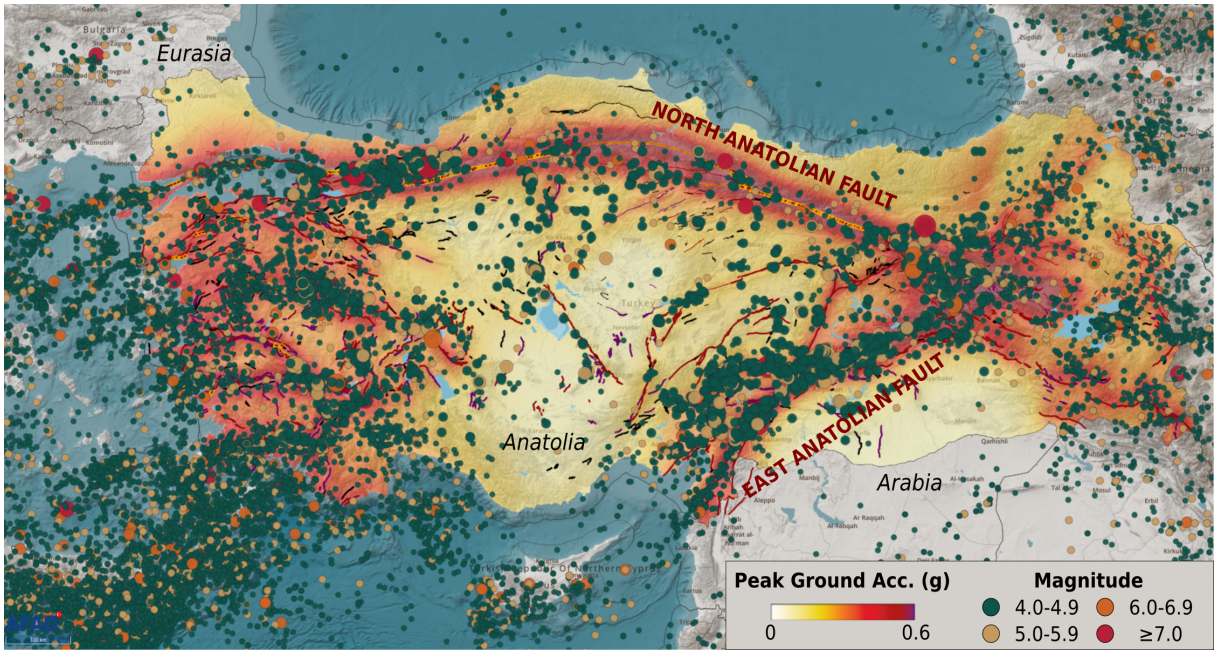

Figure 1.40: $Mw \geq 4.0$ earthquakes over the period $1900 - 2026$ from the AFAD catalog, overlayed by the Türkiye earthquake hazard map (i.e. peak ground acceleration). The red lines show the faults network, and the superimposed yellow dots highlight the earthquake surface ruptures since 1900. The major tectonic plates are written in italic, and the two major faults are written in bold red.

made by Tchalenko (1970). However, new datings highlight the presence of older syntectonic sediments on the western part of the NASZ, along the southern branches of the NAF , south of the Marmara Sea. Karabacak et al. (2022) found that the earliest age within this area is about 500 *ka*, consistent with the onset of the southern branch of the NAF before the northern branch crossing the Marmara Sea. New studies also revealed older ages of syntectonic sediments along the central part of the NAF , such as Nuriel et al. (2019) who found evidence of extensional normal faulting active 42 *Ma* ago, and reactivated 11 *Ma* ago as strike-slip faulting. It appears that the idea of a one directional propagation of the NAF is not so simple, and that it may instead be a succession of several **episodes of reactivation** of preexisting fault structures and the establishment of links between them. The distinct dates recorded along the NAF suggest a temporal sequence of the fault onset and reactivation along the NAF since the middle Eocene (~ 40 *Ma* ago) (Uysal et al., 2025). Figure 1.41 corresponds to the proposition made by Uysal et al. (2025) concerning the formation of the NAFZ.

As mentioned above, two main forces may explain the westward extrusion of the Anatolian plate: the **Arabian-Eurasian-Anatolian collision** and the **Hellenic subduction retreat**. Some studies found evidence of strike-slip faulting in the western part of Türkiye (Aegean region) active during the Oligocene, pre-dating the Arabia-Eurasia collision in the Miocene, suggesting a predominant role of the Hellenic subduction (Okay et al., 2008a). Even the continental collision may be driven by the subduction, as proposed by Reilinger et al. (2006) in their block model study. Other studies focused on the evolution of the Bitlis-Hellenic subduction zone and show that it may have played an important role in the formation of the NAF (e.g. Faccenna et al., 2006; Govers and Fichtner, 2016; Memiş et al., 2020). By using tomography analysis, Faccenna et al. (2006) highlighted two distinct mechanisms along the subduction zone: (i) a continuous subduction in the western part (Hellenic zone) and (ii) a broken slab in the eastern part (Bitlis zone). They suggest that the **break-off of the slab** beneath the Bitlis zone in the Middle-Late Miocene led to the **Arabian indentation** in the eastern part and a **retreat of**

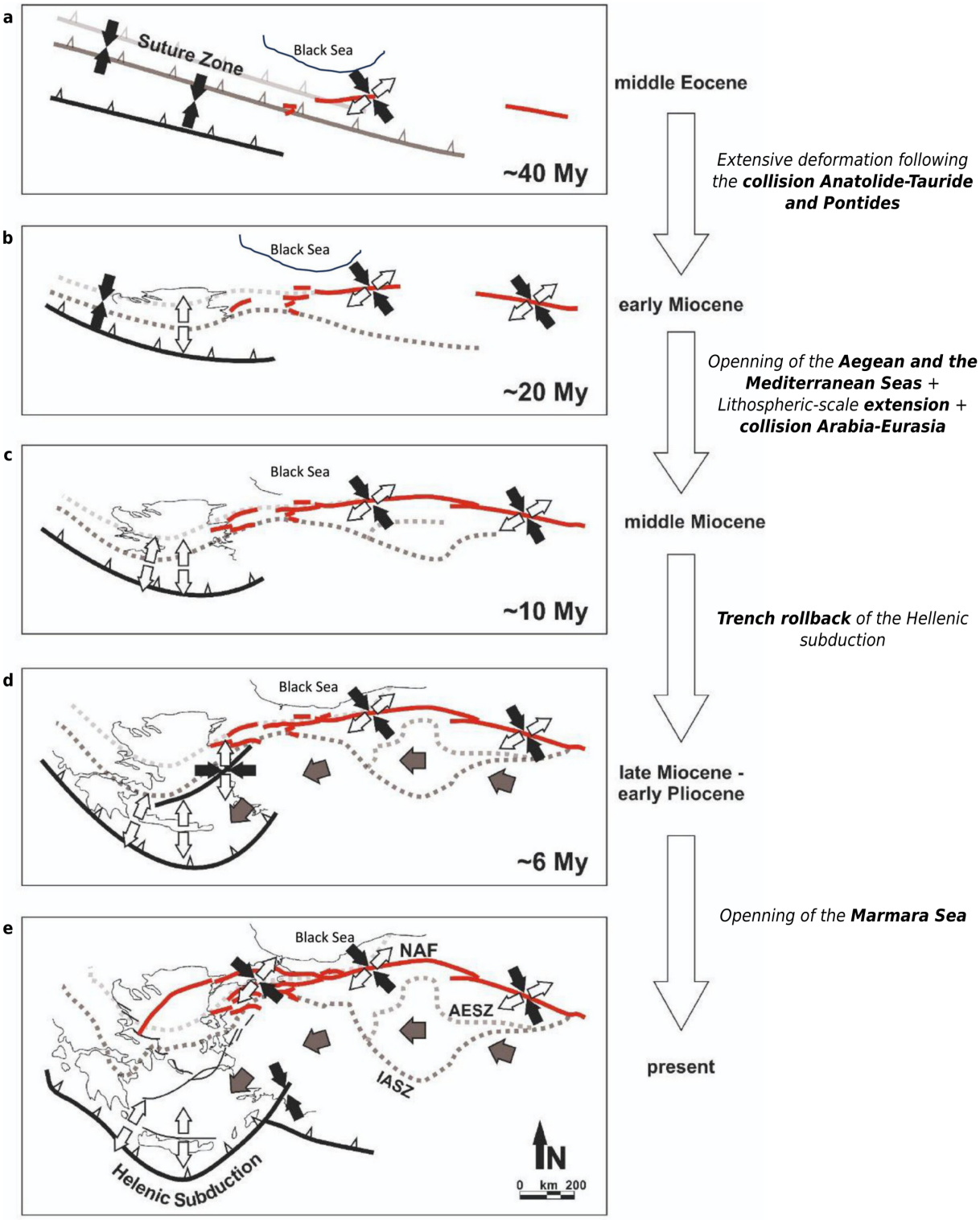

Figure 1.41: Simplified reconstruction of the NAFZ onset proposed by Uysal et al. (2025). The dashed lines show the Neo-Tethys suture zones, and the solid line shows the Hellenic subduction. Notes on the right side remind the main synchronous tectonic events.

the Hellenic subduction zone in the western part. Both of these effects may have pulled the Anatolian plate, and initiated most of the NAFZ segments. Full-wave inversion methods provided precision on the slab fragmentation, separating the western (Aegean-Hellenic) side and the eastern (Cyprus-Bitlis) side. Govers and Fichtner (2016) propose that this fragmentation occurred during the Eocene, and led to (i) a slab roll-back of the Hellenic subduction enhancing its SW-ward retreat (Jolivet et al., 2013), and (ii) a horizontal subduction on the Cyprus-Bitlis

zone. By studying the uplift affecting eastern Türkiye (North of the Cyprus-Bitlis subduction zone), Memiş et al. (2020) propose that the break-off of a slab is a possible scenario (Faccenna et al., 2006), but not mandatory to explain the observations. The most important feature is the **slab peel-back**, which started $\sim 18\ Ma$ ago, i.e., after the Arabian-Eurasian collision, leading to the uplift of the overriding plate and the presence of an asthenospheric upwelling zone. This model, which positions the southwestward retreat of the Hellenic subduction as the primary tectonic driver, provides a clear mechanism for the westward extrusion of the Anatolian block.

The Figure 1.41e shows the formation of the Marmara Sea, with the development of the **Main Marmara Fault (MMF)** as a western prolongation of the NAF . The Marmara Sea opened $4.5 - 3.5\ Ma$ ago, in an extensional context related to the **Aegean subduction** (Le Pichon et al., 2016). The onset of the MMF occurred no earlier than $2.5\ Ma$ ago, with a westward propagation until reaching the Aegean subduction zone. Grall et al. (2012) analyzed the subsidence episodes within the Marmara Sea basins and showed that the 200 *ka* onset estimate of the MMF may be rather related to readjustments of the fault system (e.g. connection with other fault segments or fault interactions). As mentioned earlier, precise dating of the onset of the faults is difficult to estimate due to the evolution of the tectonic context.

As defined by Şengör et al. (2005), the North Anatolian complex strike-slip fault can be defined as a **keirogen**[1], which can be divided into several branches and secondary faults accommodating the block motions. By looking at the North Anatolian keirogen extent, it appears that the fault has progressed within the **tethyside accretionary complex**, following older sutures such as the Intra-Pontide suture (west) and the Izmir-Ankara-Erzincan suture (east). The width of the shear zone varies significantly, increasing from east to west. In eastern Türkiye, the deformation is localized along a narrow corridor of less than 10 to 20 *km*. In contrast, toward the west, the keirogen widens into a broad deformation zone exceeding 100 to 150 *km* in width, as it splits into multiple strands within the Marmara region and merges with the extensional regime of the Aegean Sea. Therefore, the formation of the NAF seems related to weak areas corresponding to older sutures. The NAF extends along a bimaterial interface covered by tethyside subduction-accretion materials and quaternary sediments (e.g. Şengör et al., 2005).

1.5.2 The North Anatolian Fault over the last century

In this thesis, we focus on the NAF crossing the norther part of Türkiye. We will detail in the following sections the current tectonic context of the NAF , especially during the last century when several earthquakes happened on that fault. Finally, we will focus in details on the 1999 Izmit earthquake, which is the my main study area.

1.5.2.1 Seismic sequence on the North Anatolian Fault

In 1939, a M_w 7.7 earthquake ruptured the eastern part of the NAF near the city of Erzincan, killing more than 32 000 people and therefore being one of the largest earthquakes in Türkiye. Since then, 10 $M_w \geq 6.7$ earthquakes have shaken the country and are listed in Table 1.2. The associated ruptures are shown in the map in Figure 1.42. Their spatio-temporal distribution suggests a **westward propagation of the earthquakes**, leading to the rupture of most of the

[1] "A keirogen (from ancient Greek $\kappa\varepsilon\iota\rho\omega$ = shear) is abroad strike-slip shear zone in which more than one major strike-slip fault and associated structures take up the shear and it is the strike-slip counterpart of the shortening orogens and extending taphrogens." Sengor and NATAL'IN (1996), endnote 8.

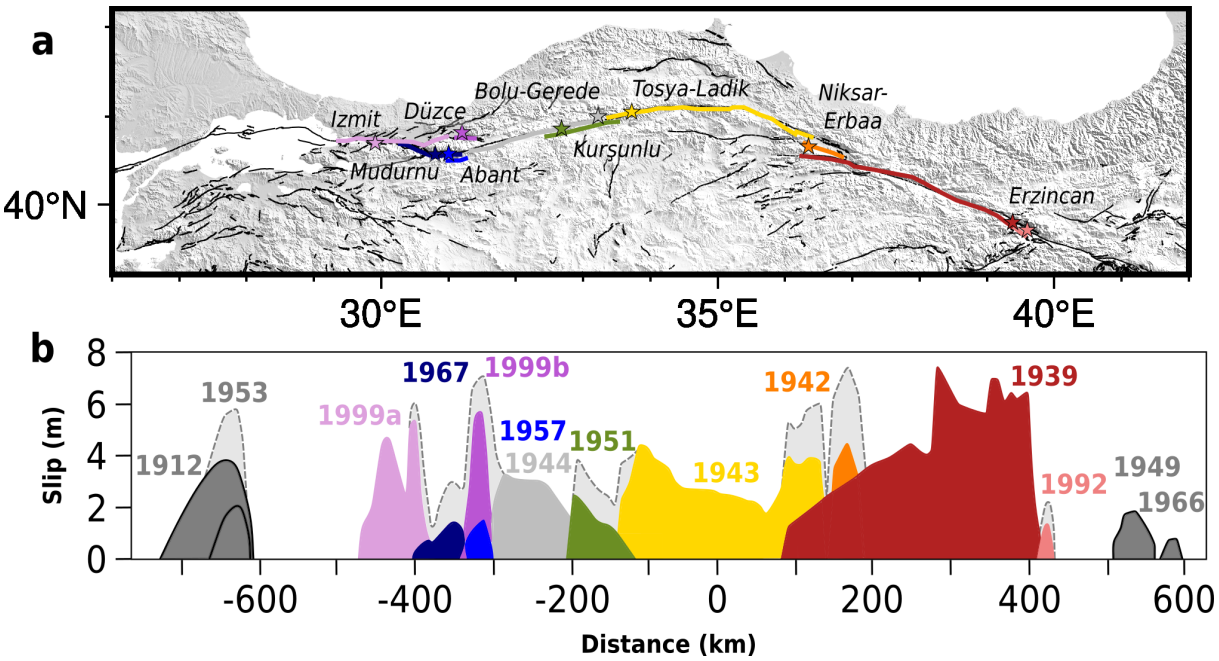

Figure 1.42: The seismic sequence distribution along the NAF . (a) Map showing the surface ruptures from Armijo et al. (2000). The surface ruptures corresponding to the 1951 and 1957 earthquakes have been shifted by −0.07°N to be visible. The colored stars show the locations of the epicenters gathered in Table 1.2. (b) Slip distribution along the NAF of the $Mw \geq 6.7$ earthquakes from the last century modified from Stein et al. (1997) and Armijo et al. (2000). The dark gray events correspond to earthquakes not shown on the upper map. The light gray areas indicate the cumulative slip values of the earthquakes which ruptured the same segments.

NAF . This propagation can be explained by **stress transfer** between successive earthquakes throughout the seismic sequence.

Indeed, Stein et al. (1997) studied the **Coulomb failure stress change** (ΔCFS) during the period 1939 – 1992 caused by the **static elastic stress changes** induced by the earthquakes. They concluded that 9 of the 10 studied earthquakes were triggered by the preceding event through positive ΔCFS, resulting in subsequent ruptures occurring earlier than expected from steady tectonic loading alone. Analysis of stress triggering along the NAF highlights potential future ruptures zones, including the eastern extent near Erzincan and the western extent near Izmit, where a slip deficit has been observed (Barka, 1996); as well as the western and eastern edges (Stein et al., 1997). Stein et al. (1997) estimated a 30-year probability of 15 % and 12 % for future earthquakes on the eastern and western edges of the fault, respectively, relative to the 1992 state of the seismic sequence. In 1999, the western edge ruptured through the 1999*a* M_w 7.6 Izmit earthquake followed by the 1999*b* M_w 7.2 Düzce earthquake (in red and purple in Figure 1.42a, respectively), further supporting the hypothesis of westward stress transfer along the NAF .

Following the last earthquakes along the NAF , the stress transfer has been reevaluated, with the aim of **refining the seismic hazard estimate** for the **Marmara seismic gap** (Figure 1.42a). New computations of ΔCFS have been done, taking into account a **viscoelastic behavior** of the lower crust, thus defining a time-dependent stress change. The Coulomb failure stress change can be defined as:

$$\Delta CFS = \Delta\tau + \mu' \Delta\sigma_N \tag{1.17}$$

with $\Delta\tau$ corresponding to the shear stress, $\Delta\sigma_N$ the normal stress, and μ' the effective or apparent coefficient of friction. The effective coefficient of friction accounts for the effects of

Date (DD/M-M/YY)	Site	Lat. (°N)	Lon. (°E)	Rupture length (km)	M_o (Nm)	M_w	Ref.
26/12/1939	Erzincan	39.80	39.38	263	4.11×10^{20}	7.7	3,4,6,8
20/12/1942	Niksar-Erbaa	40.66	36.35	44	1.74×10^{19}	6.8	3,4,6,8
26/11/1943	Tosya-Ladik	41.05	33.72	270	2.51×10^{20}	7.6	3,4,6,8
01/02/1944	Bolu-Gerede	41.00	33.22	101	1.48×10^{20}	7.4	3,4,6,8
13/08/1951	Kurşunlu	40.86	32.68	38	2.12×10^{19}	6.9	1,4,5
26/05/1957	Abant	40.58	31.00	31	1.35×10^{19}	6.7	3,4,6,8
22/07/1967	Mudurnu	40.57	30.80	61	2.82×10^{19}	7.0	2,3,4,6,8,15
13/03/1992	Erzincan	39.71	39.60	-	1.14×10^{19}	6.7	6,7,9,10
17/08/1999	Izmit	40.70	29.91	99	2.15×10^{20}	7.4	12,13,14
12/11/1999	Düzce	40.82	31.20	-	4.67×10^{19}	7.2	11,12,16,17

Table 1.2: Table gathering the $M_w \geq 6.7$ earthquakes of the last century Anatolian seismic sequence, from Lorenzo-Martín et al. (2006) and DeVries et al. (2016). References: (1) Pinar (1953), (2) Ambraseys and Zatopek (1969), (3) Ambraseys (1970), (4) Dewey (1976), (5) Barka and Kadinsky-Cade (1988), (6) Şaroğlu et al. (1992), (7) Pinar et al. (1994), (8) Barka (1996), (9) Nalbant et al. (1996), (10) Grosser et al. (1998), (11) Ayhan et al. (2001), (12) Tibi et al. (2001), (13) Wright et al. (2001a), (14) Barka et al. (2002), (15) Muller et al. (2003), (16) Utkucu et al. (2003) and (17) Umutlu et al. (2004).

pore-fluid pressure within the crust, using this equation:

$$\mu' = \mu(1 - B) \tag{1.18}$$

with μ the friction coefficient and B the Skempton coefficient, ranging from 0 to 1.0, such that $B = 0$ corresponds to dry layers (Lorenzo-Martín et al., 2006). By taking into account the viscoelastic behavior, the components of the stress tensor vary with time, and so does the final estimate of ΔCFS.

On top of the elastic stress transfer, it is important to consider the **viscoelastic relaxation of the upper mantle and the lower crust**. As proposed by Lorenzo-Martín et al. (2006) and illustrated in Figure 1.43, CFS can be estimated at different times of the seismic sequence to track stress transfer over time. Each panel displays the stress state immediately after a major earthquake, where red lines highlight the co-seismic rupture and red stars mark the epicenters of subsequent events. After each earthquake, the next segment to rupture is characterized by an increase in CFS, whereas the ruptured segment exhibits a decrease in CFS due to stress release. The last panel in Figure 1.43 highlights the high stress accumulation beneath the Marmara Sea, which still constitutes a seismic gap at the time of writing. Another inelastic contribution to take into account is the **postseismic deformation** following the mainshocks. This can be added to the models by using a Burger rheology rather than a Maxwell one, as proposed by DeVries et al. (2016). All of these models validate the hypothesis of a stress-triggering sequence propagating westward.

The analysis of historical earthquakes reveals potential past sequences, which could be similar to the one presented above (Şengör et al., 2005). Especially, successive earthquakes during the $1668 - 1912$ period seem to also have propagated westward following the large 1668 earthquake along the central segments from Erzincan to Bolu with an estimated magnitude up to 8.0 (Ambraseys and Finkel, 1995). However, due to the poor historical records,

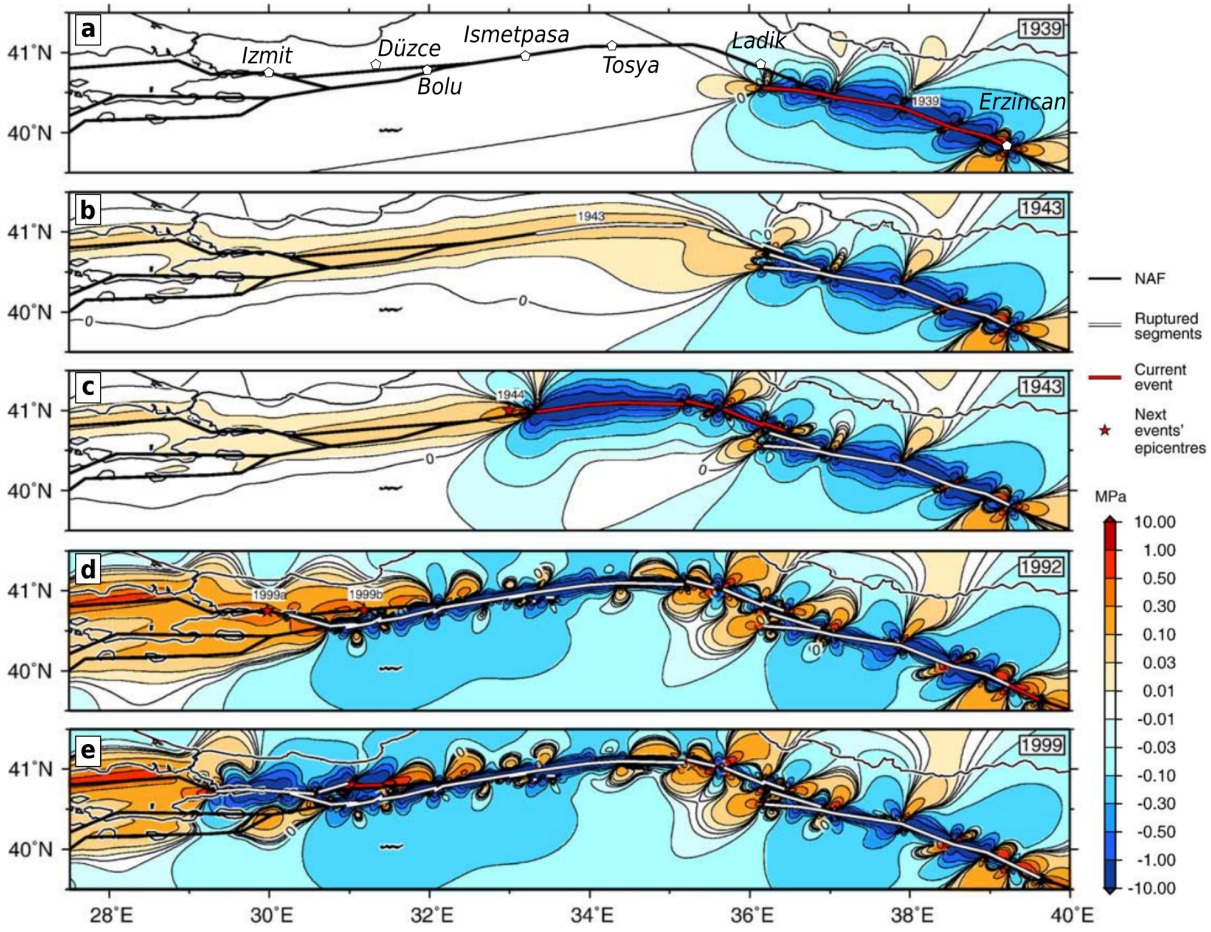

Figure 1.43: Temporal evolution of the Coulomb failure stress (CFS) from Lorenzo-Martín et al. (2006), evaluated for 10 km-depth. (a-e) CFS estimated at different points in time: (a) immediately after the 1939 event, (b) after the 1942 event, (c) after the 1943 event, (d) after the 1992 event, and (e) after the 1999b event. (a) Main cities mentioned in Table 1.2 are located by white pentagons.

previous potential sequences appear incomplete, and it remains challenging to conclude that these seismic sequences along the NAF can be cyclic.

The NAF system composed of *en echelon* fault segments with predominantly linear east-west geometries, appears to favor the development of stress-triggered sequences of major earthquakes rupturing individual segment, rather than the nucleation of a single great earthquake rupturing the entire NAF in one event (e.g., Barka and Kadinsky-Cade, 1988; Stein et al., 1997; Şengör et al., 2005). Understanding stress changes along each segment of the NAF is therefore essential for improving seismic hazard assessment, particularly in the vicinity of the current seismic gap beneath the Marmara Sea.

1.5.2.2 The 1999 Izmit-Düzce earthquakes

On Tuesday 17 August 1999, i.e., two years after the work of Stein et al. (1997) suggesting a high probability of an earthquake located west of the port city of Izmit, the Izmit segment ruptured with a magnitude of about 7.6, followed by a second shock 75 *days* later, near the city of Düzce with a magnitude of about 7.2. In the following part, I detail the timeline of both earthquakes.

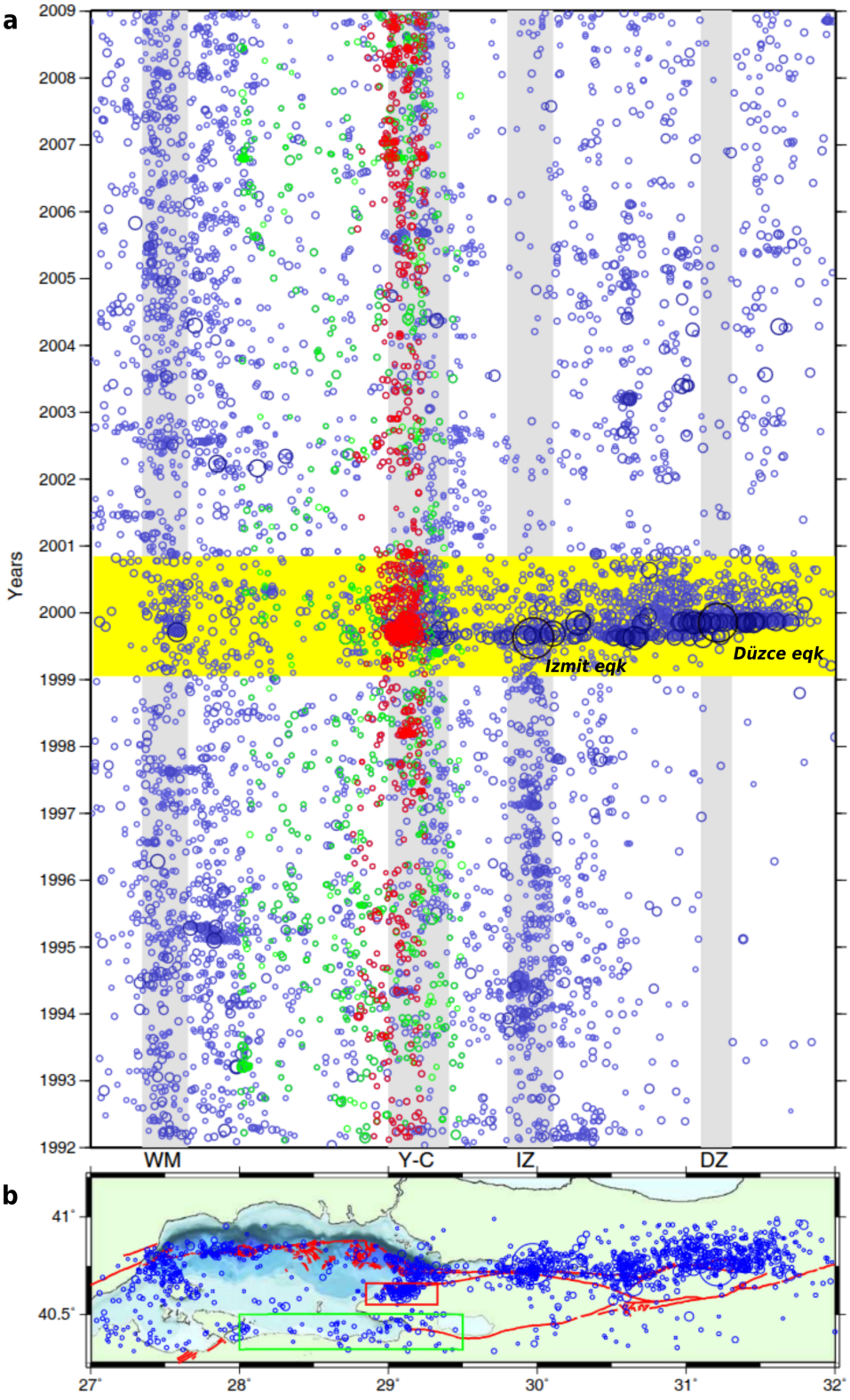

Figure 1.44: Spatio-temporal evolution of the seismicity with $M_w > 2.5$ in the Marmara-Izmit region recorded by the KOERI catalog from Karabulut et al. (2011). (a) Space-time evolution, the yellow region corresponds to the period associated with the Izmit-Düzce earthquakes (2 *years* before and after), and the gray bars highlight four segments: west Marmara region (WM), Yalova-Çinarcik (Y-C), Izmit (IZ) and Düzce (DZ). (b) Seismicity map, with the red lines showing the fault network from Le Pichon et al. (2001), and the red and green boxes highlighting two seismicity clusters.

Before the Izmit earthquake – Preseismic activity: The seismicity analysis before 1999 in the Marmara-Sapanca region, as shown in Figure 1.44, indicates the occurrence of earthquakes within the Marmara Sea and near the Izmit segment (Ozalaybey et al., 2002; Karabulut et al., 2011; Bohnhoff et al., 2016). In comparison, the Düzce segment seems to be locked with few earthquakes. It also highlights a non-negligible activity along the southern branches of the NAF (see the green dots related to the southern part of the region in Figure 1.44). This clustered seismicity in time appears to be diffuse in space as well , because the seismicity is not concentrated along the fault traces.

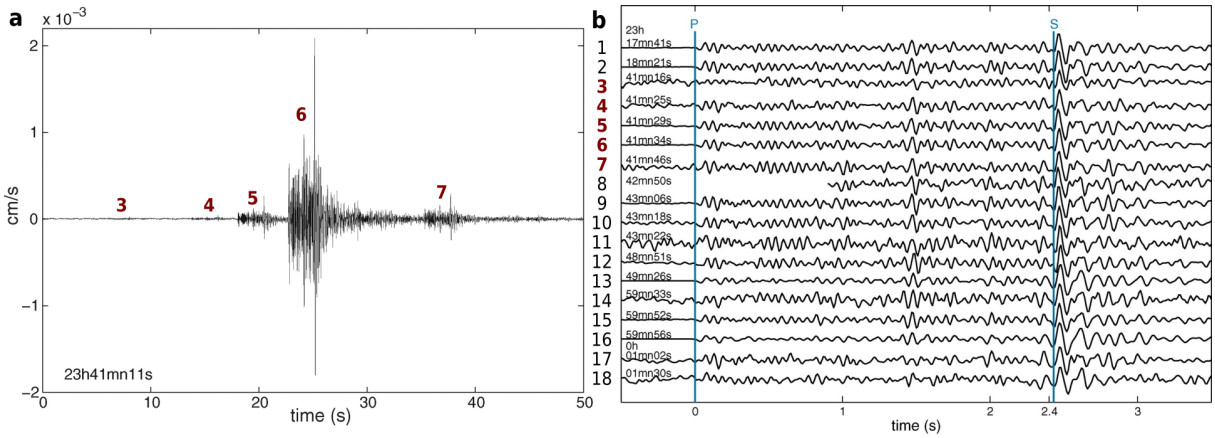

Figure 1.45: Evidence of foreshocks preceding the 1999 M_w 7.6 Izmit earthquake, from Bouchon et al. (2011). (a) Vertical ground motion recorded 20 *min* before the mainshock at the station *UGC* located 14 *km*-away from the epicenter. (b) Waveforms of 18 foreshock events with magnitudes from 0.3 to 2.7 preceding the mainshock.

44 *min* before the Izmit earthquake, several **foreshocks** have been recorded near the Izmit segment, as reported in Figure 1.45. This foreshock sequence consists of several successive bursts, with an increase of released energy and an acceleration that is slow at first and then rapid in the 2 *min* preceding the mainshock (Ozalaybey et al., 2002; Bouchon et al., 2011; Bohnhoff et al., 2016; Ellsworth and Bulut, 2018). Two mechanisms have been proposed to explain this sequence.

First, Bouchon et al. (2011) proposed that this sequence can be the result of a **precursory aseismic driven process**. Foreshocks are repeating seismic events resulting from the same seismic asperity of the fault interface at depth, which is reloading between each event. The asperity is reloaded by transient aseismic slip surrounding it, i.e., in this case, at the lowermost boundary of the seismogenic zone, near the brittle-ductile transition.

The limitation of the previous explanation is to find direct evidence of this deep transient aseismic slip. Ellsworth and Bulut (2018) proposed a second possible mechanism, corresponding to a **triggered cascade of foreshocks**. Using template matching, they highlighted new foreshock events, up to a total of 26 events. Then, they applied a clustering of those events and associated them into four groups of foreshocks. The relocation of the hypocenters of the four clusters showed an eastward propagation of the events at depth, toward the final mainshock hypocenter on the eastern edge. They explained these results as a 'triggered cascade' of foreshocks, i.e. each foreshock triggers another by loading the adjacent asperity with its stress perturbation. In this theory, the mainshock corresponds to the fifth asperity of the triggered cascade of events.

These two explanations are still being debated. Another observation before the earthquake has been made by Langridge et al. (2002), and consists of a period of **seismic quiescence** $\sim$ 18 *days* before the foreshocks and the mainshock. These studies highlighted the preseismic

period before the Izmit earthquake, although the associated physical mechanisms are not yet clearly identified.

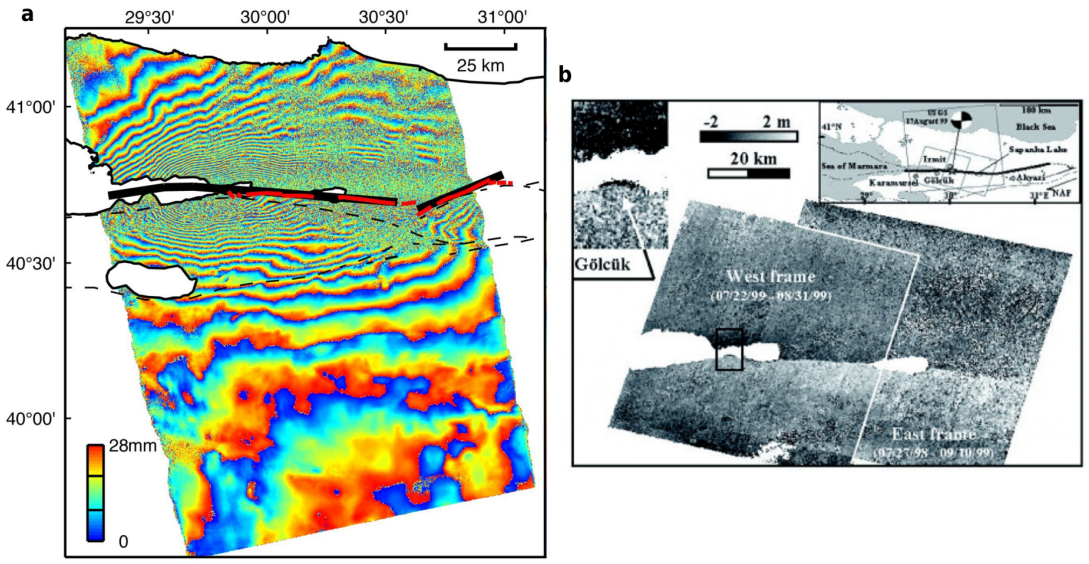

Figure 1.46: (a) Coseismic interferogram of the 1999 M_w 7.6 Izmit earthquake (NASA/JPL-Caltech, 2001). This interferogram has been built using *ERS-2* images acquired before (13 August 1999) and after (17 September 1999) the earthquake. The red lines correspond to the surface ruptures. The thick black lines correspond to the fault ruptures inferred by InSAR. (b) East-West displacement related to the Izmit earthquake computed using *SPOT* images before (22 and 27 July 1999) and after (31 August and 16 September 1999, west and east frames respectively) the earthquake from Michel and Avouac (2002).

The Izmit earthquake – Coseismic analysis The interferogram shown in Figure 1.46a corresponds to the coseismic displacement field due to the 1999 M_w 7.6 Izmit earthquake observed by InSAR. Its epicenter has been estimated to be locate at 40.76°N – 29.97°E (Toksöz et al., 1999; Delouis et al., 2002), within the Kocaeli region. The rupture characteristics and dynamics related to this earthquake have been widely studied by using regional seismic data (e.g. Bouchon et al., 2001), teleseismic data (e.g. Tibi et al., 2001), geodetic data (e.g. Delouis et al., 2002; Feigl et al., 2002; Michel and Avouac, 2002), and field observations (e.g. Barka et al., 2002; Rockwell et al., 2002).

This earthquake is a bilateral rupture from the epicenter (Delouis et al., 2002; Ozalaybey et al., 2002), causing the rupture of a $\sim$ 145 *km*-long segment from Yalova (west) to Düzce (east), as shown in Figure 1.47a. Using a joint inversion with InSAR, GNSS and teleseismic data, Delouis et al. (2002) found a mean rupture propagation velocity of about 3.5 $km.s^{-1}$, below the supershear speed. However, Bouchon et al. (2001) used near field strong motion data and showed that the rupture propagation velocity reached locally 5 $km.s^{-1}$, corresponding to supershear speeds. This has been observed in the eastward propagation of the 50 *km*-long central segment corresponding to the Izmit-Sapanca Lake segment and the western part of the Sapanca-Akyazi segment (Figure 1.47a), whereas both the western and eastern extremities of the rupture were slower, at a sub-Rayleigh velocity (Bouchon et al., 2002). These observations are consistent with the geometry of the fault rupture observed by field studies (Figure 1.47a – Barka et al. (2002)) and optical image correlation such as the *SPOT* coseismic displacement field obtained by Michel and Avouac (2002) and presented in Figure 1.46b. The supershear segment corresponds to a linear fault segment, compatible with a rapid propagation of the rupture.

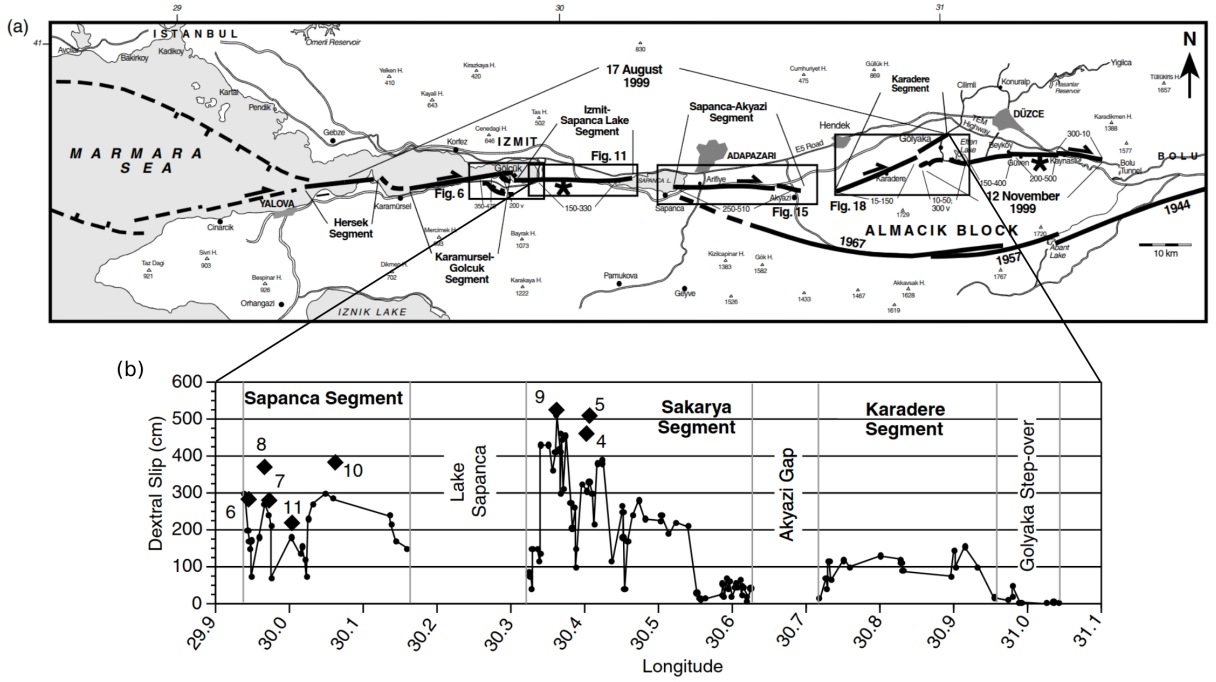

Figure 1.47: (a) Map of the 1999 Izmit rupture from Barka (2002). Stars show the epicenters of the 1999 Izmit and Düzce earthquakes. (b) Slip distribution along the Izmit earthquake rupture. Survey results from Rockwell et al. (2002) are shown by diamonds with corresponding site numbers, superposed on the slip distribution curve based on field measurements from Barka (2002).

Understanding the relationship between fault geometry and rupture propagation velocities is important to obtain better estimates of the seismic hazard.

Analysis of the surface slip distribution reveals lateral heterogeneities in the coseismic offset amplitudes along the fault. The geometry of the fault inferred from the ruptures mapped at the surface indicates that the fault rupture can be divided into five main segments separated by step-over zones, as shown in Figure 1.47a. The bottom panel shows the surface offsets measured on the field by Barka et al. (2002) and Rockwell et al. (2002) along these five segments. A bimodal slip distribution is observed with a background amplitude and some segments with higher offsets such as along the Sapanca-Akyazi segment where the offset reaches 5.2 *m*. Rockwell et al. (2002) also highlighted the importance of off-fault deformation, with an estimate of about 15% of the total lateral slip accommodated by deformation distributed within a zone up to 30 *m* wide across the fault.

As mentioned before, the Izmit earthquake is one of the most documented continental earthquakes of the late 90's, leading to a large number of coseismic slip models. Duputel et al. (2014) compared some of these models, presented in Figure 1.48, and highlighted the variability of the results (e.g., slip distribution, geometry of the interface) related to the inversion approaches and used datasets. Other coseismic models can be found in the literature (e.g. Reilinger et al., 2000; Feigl et al., 2002; Çakir et al., 2003). The main characteristic common to all slip models is that the slip distribution seems to be divided into two or three main slip patches centered on Gölcuk, Sapanca-Akyazi and Karadere, with maximum slip amplitudes up to $6-8$ *m*. Coseismic models from Delouis et al. (e.g. 2002); Feigl et al. (e.g. 2002) also suggest that 23 *m* of slip occurs in the shallower 5 *km* along the Izmit earthquake, leading to a shallow slip deficit on that part of the rupture.

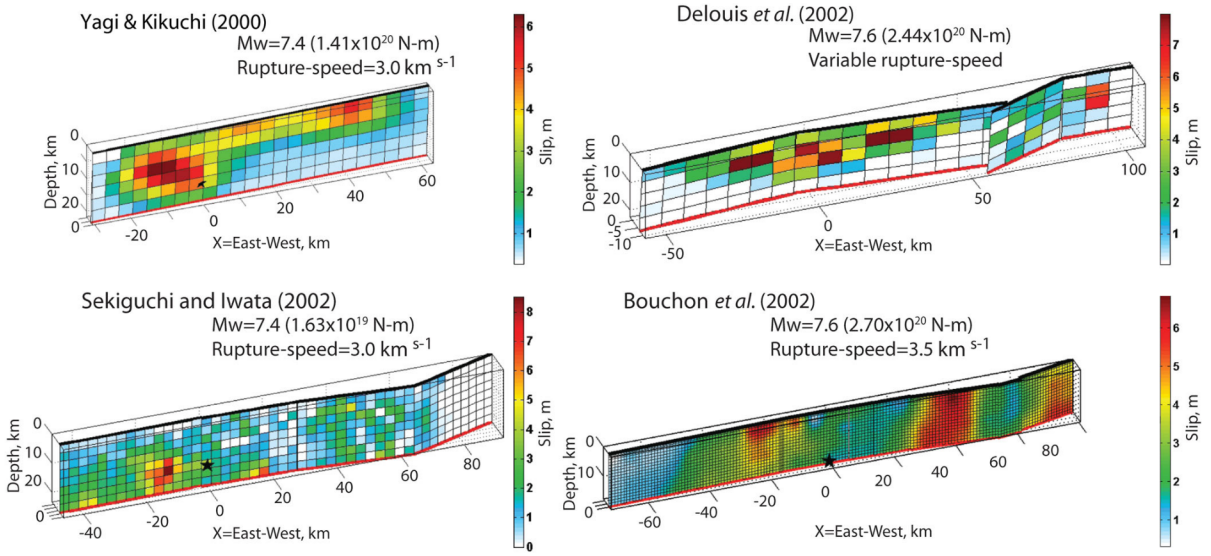

Figure 1.48: Several coseismic slip distributions of the 1999 Izmit earthquake gathered by Duputel et al. (2014) and showing the variability of kinematic earthquake source models. The references are the following: Yagi and Kikuchi (2000); Delouis et al. (2002); Sekiguchi and Iwata (2002); Bouchon et al. (2002).

Between the Izmit and Düzce Earthquakes: nucleation of a second rupture As shown in Figure 1.49a, the Izmit rupture propagated along fault segments subjected to increased Coulomb stress following the 1992 earthquake, but did not extend onto the eastern segment of the northern branch of the NAF located around between longitudes 31° and 31.5°E. As a result, Coulomb stress further increased on this unruptured segment, as illustrated in Figure 1.49b. A second earthquake subsequently occurred in Düzce on 11 November 1999, only 75 *days* after the Izmit rupture.

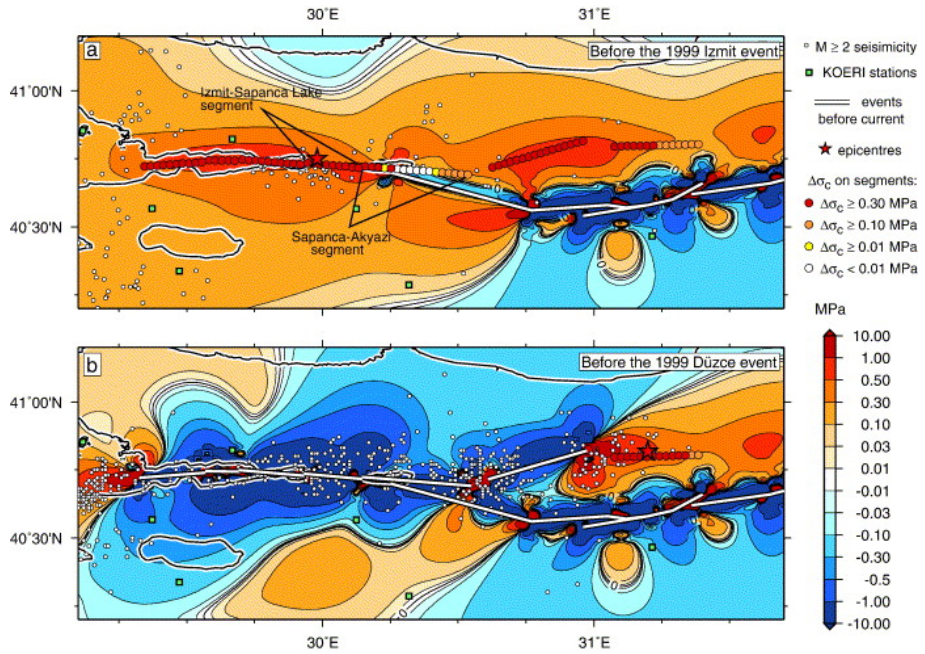

Figure 1.49: Coulomb stress change estimated at 10 *km*-depth (a) before the 1999 Izmit earthquake and (b) before the 1999 Düzce earthquake, by Lorenzo-Martín et al. (2006).

After the Izmit earthquake, new seismic stations have been installed within the Marmara-Izmit-Bolu region as illustrated by the green triangles in Figure 1.50c to record the aftershock

sequence. It enables us to precisely capture the nucleation of the Düzce earthquake on the eastern segment. As described above, the Gölcük-Izmit-Sapanca segments exhibited background microseismicity prior to the Izmit rupture, as illustrated in Figures 1.44, and 1.50 – a,b; and the rupture nucleated close to a swarm of foreshocks. Following this rupture, microseismicity migrated eastward, with an intense activity along the Sapanca-Akyazi-Karadere segments, especially in the vicinity of the triple junction of the NAF and along the Karadere-Düzce segment, as shown by Figure 1.50 – c,d. The latter is located close to the epicenter of the Düzce earthquake, increasing the stress loading along the Düzce segment. The Gölcük-Izmit-Sapanca remains active during the first months following the earthquake.

The nucleation and propagation of the 1999 M_w 7.2 Düzce earthquake again led to a migration of seismicity, with an eastward migration as shown by Figure 1.50 – e,f. We note that some of the western segments of the 1999 Düzce surface rupture were already involved during the 1999 Izmit earthquake (Akyuz et al., 2002). Following this earthquake, the seismicity is constrained east of the triple junction. This is also seen in a larger timescale plot (Figure 1.44), where the seismicity along the Izmit segment significantly decreased right after the Düzce earthquake, with a new rate lower than the background seismicity rate before 1999. Analysis of the stress orientation of the different clusters along the NAF during these three periods also reveals variations, with a rotation of the maximum principal stress axis (σ_1) along the Izmit segment after the earthquake. This rotation can be explained by the regional geology (in particular the presence of pull-apart basins) and the high Coulomb stress change, which may induce stress rotations following the release of large amount of strain (Bohnhoff et al., 2006; Ickrath et al., 2015).

Because I mostly study the Izmit segment in my thesis, I detail only the postseismic deformation related to the 1999 Izmit earthquake in the following.

First decade of postseismic deformation following the 1999 Izmit earthquake As mentioned above, most aftershocks of the 1999 Izmit earthquake clustered around the NAF triple junction along the Akyazi–Karadere segments, and at the eastern rupture termination, loading the Düzce segment (Figure 1.50d). They initiated immediately after the mainshock (Ito et al., 2002; Ozalaybey et al., 2002) and persisted until the Düzce earthquake, after which the seismicity spatially redistributed eastward. To study the temporal distribution and the rate of their decay, we can look at their temporal evolution and fit a modified Omori law defined as (e.g., Utsu et al., 1995):

$$n(t) = \frac{K}{(t+c)^p} \tag{1.19}$$

with $n(t)$ being the number of aftershocks at time t, K is the total number of events, c the rate of activity at the beginning of the sequence and p the decay parameter. Figure 1.51 shows the results obtained using the 1999 Izmit aftershocks and proposed by Bayrak and Öztürk (2004), leading to an estimate of the decay parameters of about ~ 0.86, which is small compared to other aftershock sequences and suggests a low decay of the aftershocks. We may also note that the Düzce earthquake probably disturbed the Omori-type aftershock decay (Bohnhoff et al., 2016).

The aftershocks are located along the coseismic rupture plane but also off-fault, resulting in a 40 *km*-wide band around the Izmit earthquake rupture (Ozalaybey et al., 2002). Along the central Izmit-Sapanca-Akyazi segment, a smaller number of aftershocks are recorded and are mainly located on secondary faults, as shown in Figure 1.50d. This off-fault deformation and quiescence along the main rupture segment agree with the assumption of a supershear segment releasing for of the accumulated stress (Bouchon and Karabulut, 2008). This segment also shows no aftershock on the top 5 *km* of the interface (see Figure 1.50d – asperity A). This

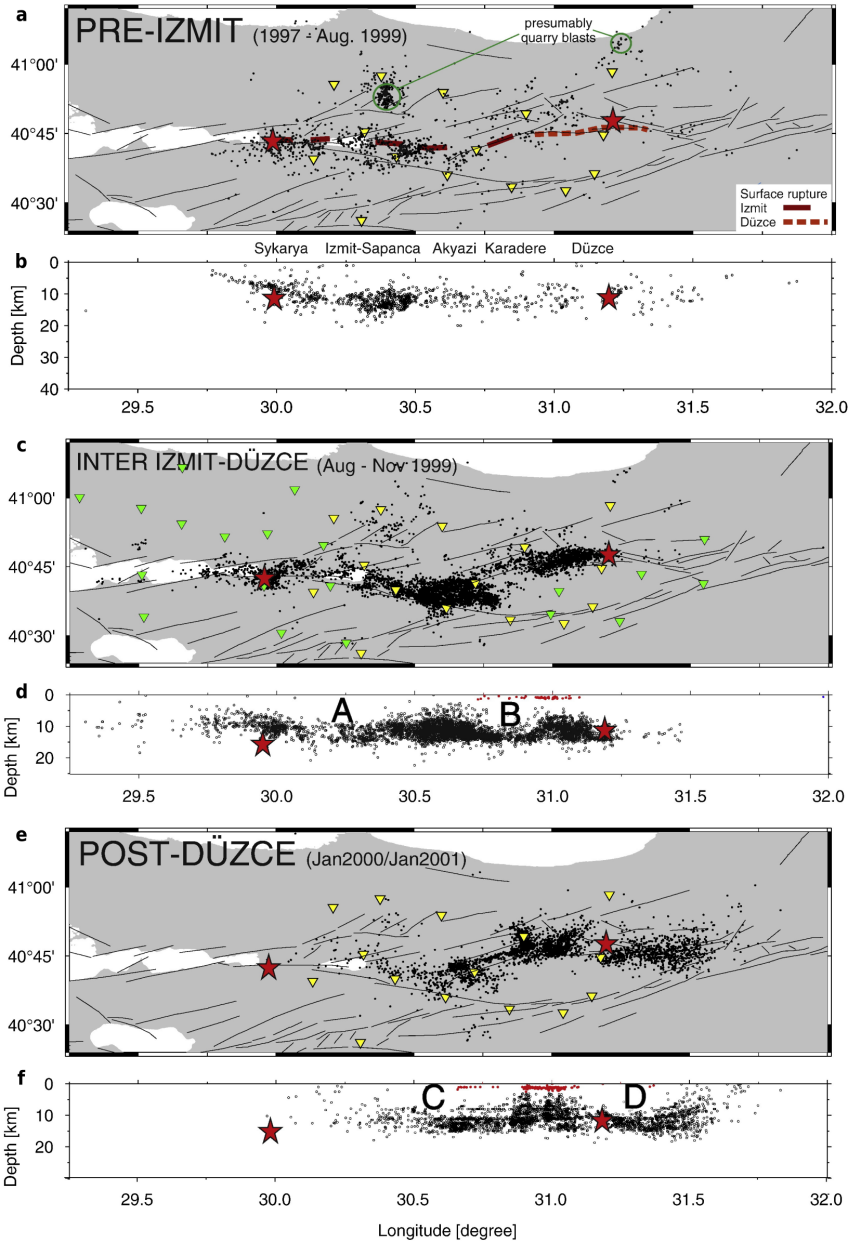

Figure 1.50: Seismicity distribution (a,b) before the 1999 Izmit earthquake (from 1997 to 1999), (c,d) between the Izmit and Düzce events (from the 17 August 1999 and 11 November 1999), and (e,f) after the 1999 Düzce earthquake (from January 2000 to January 2001), from Bohnhoff et al. (2016). (a,c,e) The yellow and green triangles show the locations of the stations of the SApanca-BOlu NETwork (SABONET) and the additional stations deployed after the earthquake by GFZ Potsdam (Bulut et al., 2007), respectively. The two red stars correspond to the 1999 Izmit (west) and Düzce (east) epicenters, with their surface ruptures highlighted in (a) by the dotted lines. The fault network is shown by the black lines. (b,d,f) Seismicity distributions along depth sections. (d,f) Red dots correspond to shallow earthquakes along the Karadere-Düzce segment. A, B, C and D correspond to highlighted areas which are seismically inactive during those periods.

is related to the presence of low-velocity sedimentary basins (Izmit and Adapazari basins, Karabulut, 2025) and suggests a narrow fault zone with homogeneous frictional properties (Bouchon et al., 2002), probably associated with aseismic deformation.

Associated with the aftershocks, a rapid afterslip started along the rupture plane. First,

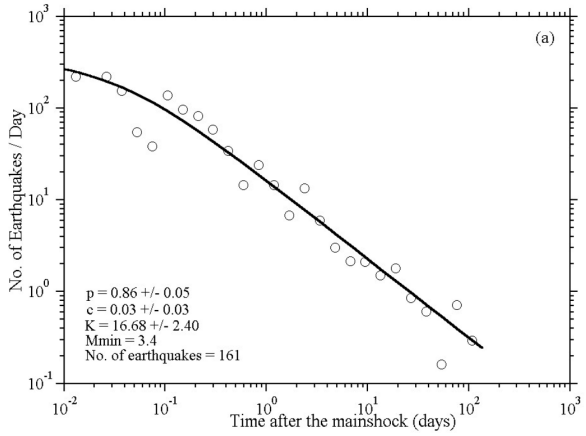

Figure 1.51: Temporal evolution of the number of aftershocks following the 1999 Izmit earthquake with a magnitude of completion of about 3.4, from Bayrak and Öztürk (2004).

Çakir et al. (2003) extracted a large, early and deep afterslip 29 *days* after the mainshock using InSAR data. They concluded that half of the afterslip probably occurred in the first 2 *days* after the mainshock at $16-18$ *km*-depth, with a remarkably high slip amplitude of 1 *m* in 2 *days*. These observations suggest that all the strain accumulated within the seismogenic layer has not fully been released by the mainshock. Using GNSS alone, this large afterslip was not observable, due to its rapidity and the absence of near-field permanent GNSS sites. However, these studies also identified a shallow and rapid afterslip occurring mostly between regions of high coseismic displacement (see Figure 1.52a, Burgmann, 2002; Hearn et al., 2002; Ergintav et al., 2009). This afterslip rapidly initiated at the base of the seismogenic layer and below after ≈ 40 *days* and led later to a slip distribution similar to the one shown in Figure 1.52b. Two patches are distinct: one located below the epicenter, and a second located along the Karadare segment. Shallow deformations close to Yalova and Gölcuk (western part) associated with the activation of secondary faults, as highlighted by the development of the Yalova–Çinarcik seismic cluster (Çakir et al., 2003; Karabulut et al., 2011). Several years later, the deeper afterslip has decreased and shallow deformation is observed as shown in Figure 1.52c (the deeper patch at 30 *km*-depth probably being an artifact according to the authors).

Different models have been proposed to determine the mechanisms governing the 1999 Izmit postseismic deformation. In particular, Hearn et al. (2009) compared the observations to a velocity-strengthening frictional afterslip model, a viscous fault zone creep using a Newtonian viscosity below 10 *km*-depth, a lower crust viscoelastic relaxation model (between 22 and 32 *km*-depth), and finally a dual-process models taking into account both the frictional faults and various viscosities in the lower crust and upper mantle layers. They found that the velocity-strengthening frictional afterslip mechanism corresponding to stress-driven afterslip explains well the early postseismic deformation, but after one year a viscoelastic relaxation component with a viscosity of 2 to 5×10^{19} *Pa.s* needs to be taken into account to explain the deformation. Some studies such as Wang et al. (2009), based on GNSS observations, suggest that the contribution of viscoelastic relaxation to the observed postseismic deformation became dominant as early as $\sim$3 months after the mainshock, earlier than previously estimated. Uncertainties remained about the relative amplitude of the viscoelastic relaxation of the lower crust and/or upper mantle. However these dual processes have been confirmed by numerous studies (e.g., Burgmann, 2002; Ergintav et al., 2002; Hearn et al., 2002; Çakir et al., 2003; Ergintav et al., 2009; Hearn et al., 2009; Wang et al., 2009).

Late postseismic deformation of the 1999 Izmit earthquake Recent geodetic measurements of the surface deformation along the Izmit segment provided insights on the late postseismic stage. Using InSAR data before and after the 1999 Izmit earthquake, Cakir et al. (2012) highlighted the onset of shallow aseismic creep along the Izmit-Akyazi segment since

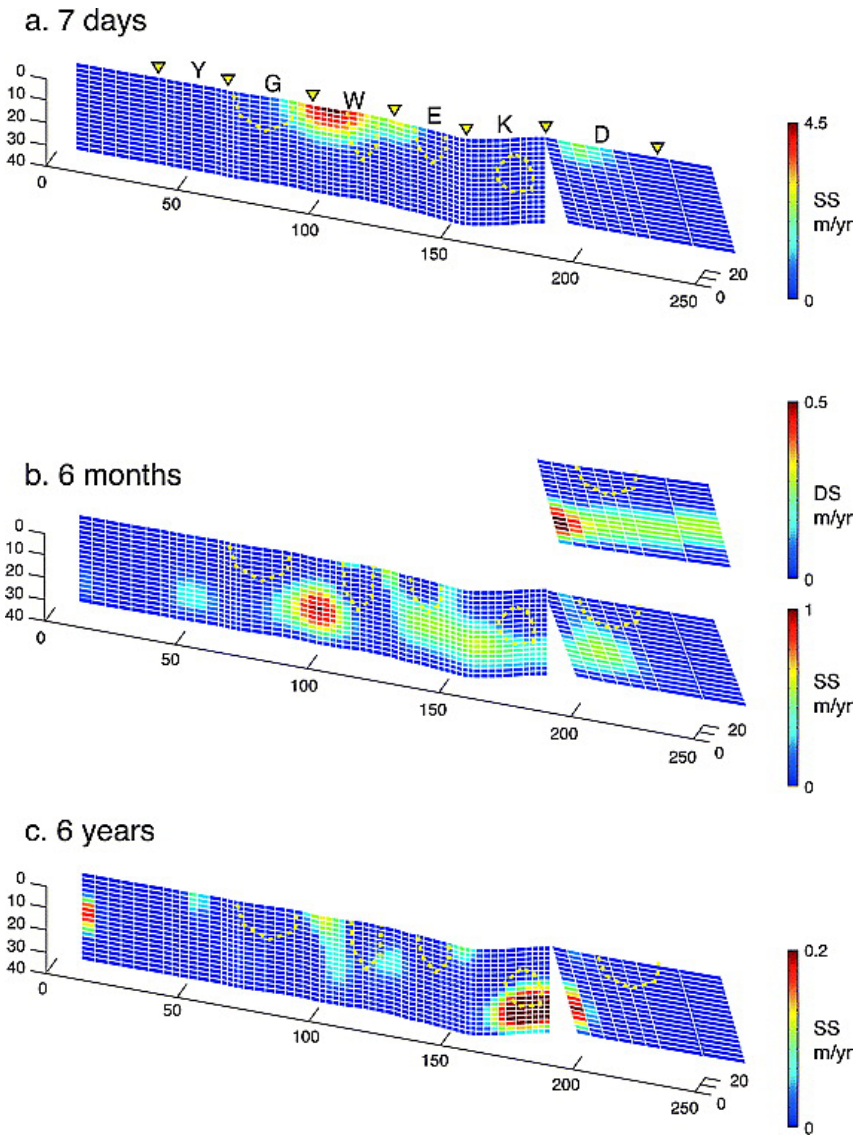

Figure 1.52: Kinematic afterslip models produced by Ergintav et al. (2009) at (a) 7 *days*, (b) 180 *days* and (c) 6 *years* after the Izmit earthquake. SS and DS stand for strike slip and dip slip. Y, G, W and E, K, and D indicate the Yalova, Golcuk, East and West Sapanca, Karadare, and Düzce segments, respectively. Yellow dashed lines show outlines of coseismic slip from Reilinger et al. (2000).

the mainshock. They suggest that this fault creep is an evolution of the postseismic afterslip, and might last for decades to centuries, according to the apparent steady-state behavior shown by the time series of GNSS campaign measurements at both SMAS and SISL stations since $\sim$ 2006 (Figure 1.53E). Indeed, the observed relative rate is still higher than the one recorded before the Izmit earthquake. Figure 1.53 – C,D shows the lateral evolution of the creep dynamics, with especially the presence of creep along the Adapazari segment, calculated from fault-perpendicular profiles of InSAR horizontal displacements.

Hussain et al. (2016) confirmed aseismic creep along the Izmit-Adapazari segments by analyzing InSAR data over the period 2002 – 2010. They estimated a mean fault-parallel creep rate of up to 5 mm/yr along the Izmit segment with a maximum of 11 mm/yr reached near the city of Izmit. Aslan et al. (2019b) provided a detailed analysis of the surface deformation inferred from InSAR data over the subsequent period 2011 – 2017. They also highlighted aseismic creep along the Izmit segment, with a creep rate of up to 8 mm/yr close to the city of Izmit, slightly smaller than the estimates made by Hussain et al. (2016).

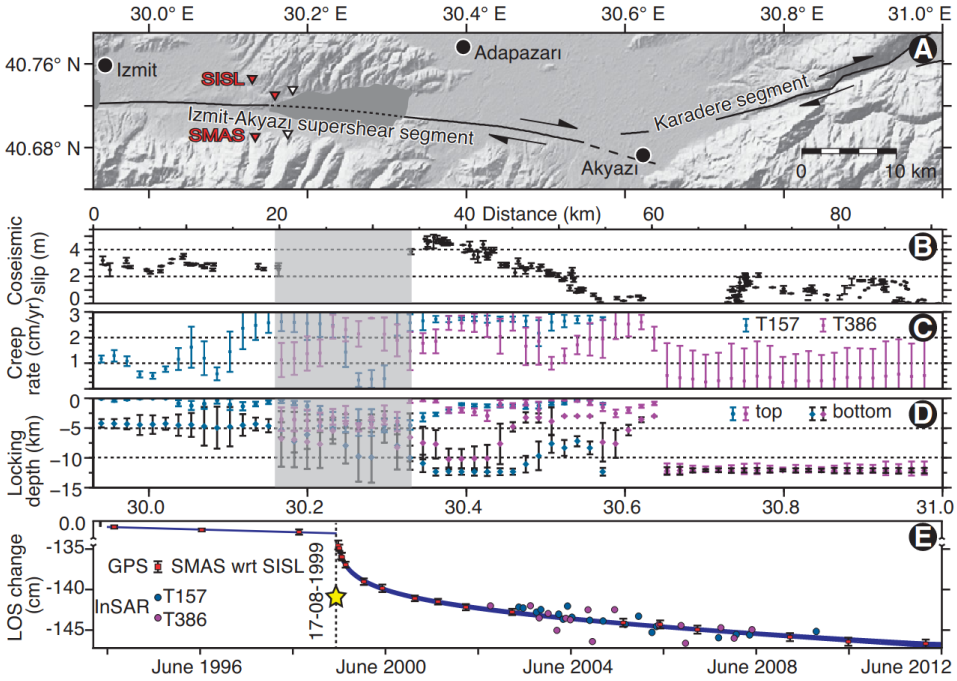

Figure 1.53: Slip dynamics estimated along the Izmit-Akyazi segment by Cakir et al. (2012). (A) Map of the Izmit surface rupture in black lines with the locations of the GNSS stations SISL and SMAS marked by the red triangles. (B) Coseismic surface slip from Emre et al. (2003). (C,D) Creep rates and depths of the creeping fault deduced from elastic dislocation modeling of InSAR data, using two different tracks distinguished by the colors. (E) Time series of fault-parallel component of baseline change between both SMAS and SISL GPS stations, with a fit shown in a blue curve.

However, the main result of their study is the identification of a transient accelerating creep event in December 2016, correlated with a transient slip event recorded by a creepmeter installed on the fault, and associated with 10 *mm* of surface slip in one month. This acceleration is shown in Figure 1.54a, corresponding to a slow slip event on the Izmit segment. A previous event was recorded on the creepmeter record in September 2015, however the noise of the InSAR data during this period does not allow for its detection. This is mainly due to the acquisition of SAR images done by only one satellite (*Sentinel-1A*), leading to a revisit time of 12 *days* and therefore an increase of atmospheric contribution within the time series (Figure 1.54b). A year later, Özarpacı et al. (2020) characterized the 2015 slow slip event, using GPS campaign data acquired close to the Izmit fault segment. Their update of the GNSS campaign measurements at both stations SMAS and SISL shows that the afterslip was still on-going in 2020 and that the preseismic rate was not yet recovered.

All the previous observations and others made along the Izmit segment are gathered in Table 1.3. It shows several main results:

- The presence of a **shallower locking depth** below the Izmit segment after the mainshock in comparison with before the earthquake.
- **Shallow aseismic creep** (5 first km) reaching the surface along the Izmit segment since the mainshock, with larger amplitudes near the city of Izmit.
- A slight decrease of the creep rate over time.
- The occurrence of **transient accelerating creep events** (i.e. slow slip events), at least

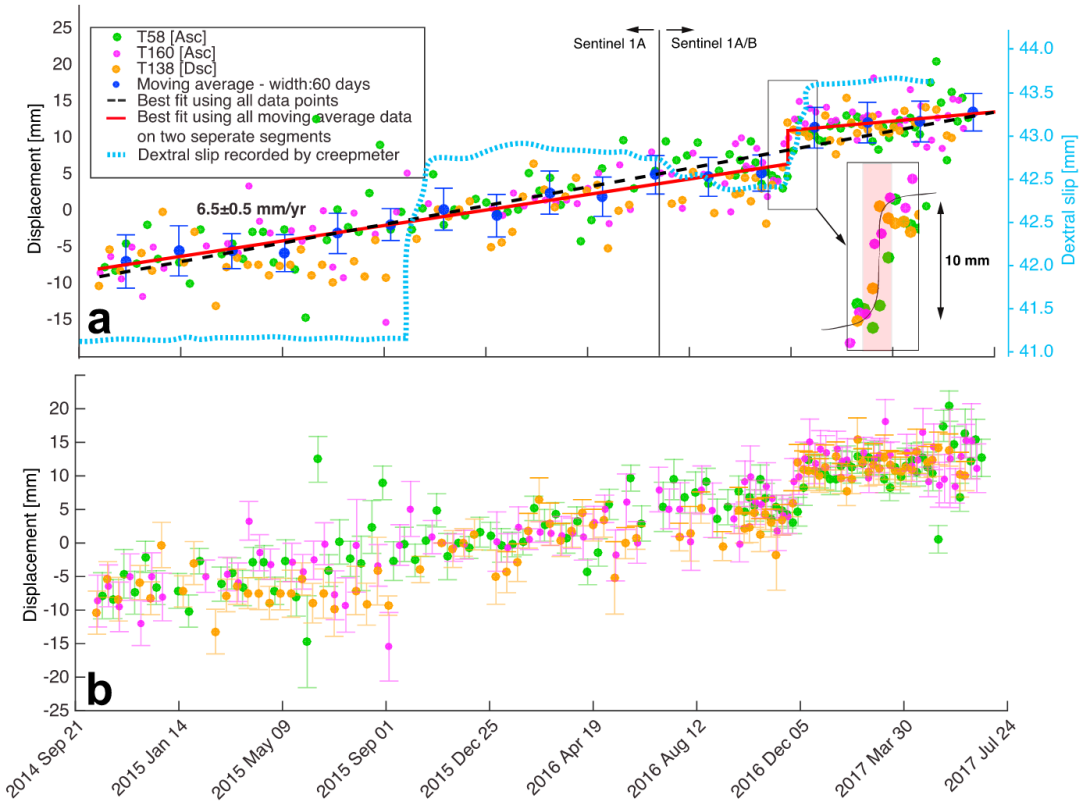

Figure 1.54: Horizontal InSAR time series extracted from a 15 *km*-long fault-perpendicular profile located at 29.975°E across the Izmit segment over the period 2014 – 2017, from Aslan et al. (2019b). (a) InSAR data are compared to a creepmeter record shown by the dotted blue line. The inset focus on the transient creep acceleration at the end of 2016. (b) Raw InSAR data showing estimated creep displacement with error bars.

since 2015 with a return time longer than 1 *year*.

1.5.3 Related open Challenges

As presented above, the North Anatolian Fault in Türkiye has been widely studied since the westward propagation of major and devastating earthquakes during the last century. This $\sim$ 1600 *km*-long segmented fault system, with different slip dynamics along its different segments, appears as an ideal natural laboratory to address the open questions outlined previously (see Sections 1.3.6 and 1.4.5).

By focusing on the Izmit segment where two SSEs close in time have been identified, I define new challenges:

- What is the **temporal creep behavior** of the Izmit segment 20 *years* after the earthquake?
- What are the temporal bounds of **shallow afterslip** along the Izmit segment, and how does the partitioning of the **postseismic slip budget** between aseismic creep and locked patches inform the seismic hazard of the western NAF?

References	Data	Study period	Creep rate	Creep depth	Slip rate	Locking depth
McClusky et al. (2000)	GPS	1988 – 1997	-	-	24 mm/yr	21 km
Ergintav et al. (2014)	GPS	1994 – 2014	-	-	25 mm/yr	5 km
Çakir et al. (2003)	InSAR (LOS)	1992 – 1999	-	-	27 mm/yr (Reilinger et al., 2006)	12 km
Çakir et al. (2003)	InSAR (LOS)	2002 – 2009	10 mm/yr	5 km	27 mm/yr	12 km
Hussain et al. (2016)	InSAR (EW)	2002 – 2010	11 mm/yr	8 km	20 mm/yr	18 km
Aslan et al. (2019b)	InSAR (EW)	2011 – 2017	7.7 mm/yr	4.3 km	26.2 mm/yr	12 km
Özarpacı et al. (2020)	GPS	2013 – 2020	12.7 mm/yr	1.3 km	25.1 mm/yr	12 km

Table 1.3: Table gathering the slip dynamics features estimated on the western part of the Izmit segment.

1.6 Problematics and outline of the manuscript

1.6.1 Main research questions of the thesis

In the state-of-the-art section, I raised several scientific questions related to the **occurrence of SSEs** (see Section 1.3.6), the contribution of **InSAR data** (see Section 1.4.5), and finally the specific tectonic context of the **North Anatolian Fault in Türkiye** (see Section 1.5.3). The purpose of this work is to complement the state-of-the-art of SSEs deformation in Türkiye using SAR interferometry. Here are the main scientific questions targeted in this manuscript and resulting from the open challenges proposed previously:

1. What new insights or added values into **fault creep dynamics** can be gained from **continuous**, **long-term InSAR monitoring** at local (the Izmit segment) to regional scales (the NAF), and to what extent does this provide new insights into **seismic hazard**?

2. How can **large-scale, automatically processed InSAR datasets** be used to build **inventories of transient slip events** along global fault systems ? What are the current limitations in terms of **sensitivity, spatial resolution, and noise discrimination**?

3. How can the detailed analysis of slip behavior along the Izmit segment associated with seismic cycle models provide insights into the **mechanisms** governing the occurrence of shallow SSEs?

1.6.2 Outline of the manuscript

This thesis is divided into five chapters following the present introduction. The manuscript is structured around a progressive approach, starting with a large-scale study of the whole NAF, then focusing on the creeping segments identified in the first analysis to detect SSEs. Finally the thesis investigates the detected SSEs of the Izmit segment in greater details to better understand the seismic cycle of this segment and to propose potential mechanisms driving their occurrence.

Chapter 2 presents a large scale on-going work, in which I use the FLATSIM InSAR data throughout Türkiye to estimate the average velocity field. In a first section, I present InSAR post-processing methods to compute the velocity field and strain maps, a discussion of the lateral variations observed along the entire ~ 1600 *km*-long NAF and the importance of the segmentation of the fault for the seismic hazard assessment. In a second section, I focus on the Marmara region by presenting joint slip inversions with GNSS and InSAR data in order to characterize the slip deficit of this segment at the location of the current seismic gap.

Chapter 3 is an article currently submitted, in which I present an automatic method of detection of SSEs using InSAR data and based on comparisons with physics based slow slip models. The aim is to develop a detection method requiring minimal post-processing while remaining sensitive to small deformation signals. The validation of this approach is carried out by applying it to the Izmit and Ismetpasa segments of the NAF.

Chapter 4 is a published work, in which I focus on the Izmit segment. I extract static displacements related to three SSEs in 2016, 2018 and 2019, detected using InSAR data. In this chapter, I propose a specific post-processing sequence to remove most of the non-tectonic signals and extract SSE-related tectonic signals. The slip distribution along the fault segment

at depth during the two latest SSEs is then inferred with inverse models. This work provides insights of the seismic cycle of the Izmit segment, by describing the slip dynamics 20 *years* after the mainshock.

Chapter 5 presents on-going work, focusing on the Izmit segment, in which I use numerical simulations of earthquake cycles in the framework of rate-and-state friction. It provides mechanical models in order to suggest potential frictional control of the slip dynamics at different depths.It allows the reproduction of all the observed timescales, from coseismic recurrence intervals to postseismic relaxation and shallow short-term SSEs.

Chapter 6 concludes this thesis, summarizing the observations made along the NAF and comparing those with other results and observations worldwide. I also discuss the various methodologies developed and applied in this work. Finally, I discuss the perspectives opened by this thesis in combination with other recent results.

Chapter 2

The steady-state deformation across Türkiye inferred from the *FLATSIM* dataset

The growing amount of geodetic data covering decades of deformation such as InSAR data provides a perfect tool to study steady-state deformation over large continental areas. In addition, the development of automatic processing methods overcomes the limitation of InSAR for processing large areas over long time periods.

In this chapter, I present a study based on automatically processed InSAR time series inferred from *Sentinel-1* SAR images over the period $2016-2021$ provided by the French project FLATSIM created by the CNES and FormaTerre, based on the NSBAS processing chain (Doin et al., 2011; Thollard et al., 2021). I focus on the deformation in Türkiye and especially around the North Anatolian Fault (NAF). As described in the previous section, this ~ 1600 *km*-long strike-slip fault system is one of the most active in the world, with its seismic sequence made of 7 $M_w \geq 7$ earthquakes since the 1930s. Moreover, the presence of a seismic gap along the branches beneath the eastern side of the Marmara Sea, currently threatening the megalopolis of Istanbul highlights the need to specify the slip deficit along this major fault system and the related seismic hazard to better prepare an eventual disaster.

By merging InSAR velocity fields from distinct tracks and estimating the East-West component, I produce a first version of the steady-state velocity field covering Türkiye from FLATSIM data, highlighting the high deformation along the North and East Anatolian Faults, accommodating the westward extrusion of the Anatolian plate. The resulting strain map shows lateral variations of the strain accumulation along the major NAF branch, with the presence of several creeping segments releasing a part of the strain. This velocity field is also used in another work presented in this chapter, focusing on the Marmara Sea. This work led by Émilie Klein (CNRS Research Engineer at the Laboratoire de Géologie, École Normale Supérieure, Paris, France), in collaboration with other scientists presented later, aims at analyzing the slip rate along the fault interface beneath the Marmara Sea, to better estimate the current seismic hazard. She computed Bayesian joint inversions based on InSAR data and GNSS records provided by Özkan et al. (2025). It confirms that the central segment is creeping, and suggests that this creeping segment may be larger than previously estimated. This work is still on-going and further tests may specify the uncertainties related to the slip rate models, and therefore to the estimated seismic hazard.

Abstract

The North and East Anatolian Faults dividing Türkiye on the northern and eastern parts are ones of the most active continental strike-slip faults in the world. For now, the westward propagation of major earthquakes along the North Anatolian Fault since the 1930's ended with the 1999 M_w 7.6 and 7.2 Izmit and Düzce earthquakes, leading to a remaining seismic gap beneath the Marmara Sea, currently threatening the megalopolis of Istanbul. To specify the seismic hazard in Türkiye, focused on the North Anatolian Fault, we use automatically processed InSAR time series from *Sentinel-1* images built in the framework of the FLATSIM project. We compute a steady-state East-West velocity field over the Türkiye by merging 14 ascending/descending tracks, and infer for a strain map. The unprecedented quality of the FLATSIM dataset allows us to specify the locations and length of the creeping segments, and therefore to specify lateral variations of the strain loading and releasing. Local deformations can also be pointed out, such as subsidence deformation related to large basins. In addition to the InSAR data, a dense GNSS network (Özkan et al., 2025) surrounding the Marmara Sea gives new insights on the strain accumulation of the region. By computing joint inversions based on InSAR and GNSS data, Émilie Klein et al. provide an update of the slip rate along the Main Marmara Fault, revealing a creeping central segment between longitudes 27.5 and 28.6°E, surrounding by two locked segments, suggesting a high seismic hazard related to the Çınarcık Basin segment located south of Istanbul and west of the 1999 Izmit rupture. The latter locked segment may have accumulated sufficient strain to potentially produce an earthquake with $M_w > 7$.

Keywords: North Anatolian Fault, InSAR, FLATSIM, Marmara sea, interseismic deformation



- Automated InSAR processing from *Sentinel-1* images provide data with high accuracy over large areas.
- Shear strain is reported along the North and East Anatolian Faults, with some segments slipping aseismically.
- Strain accumulation along the Çınarcık Basin segment, capable of generating a $M_w > 7$ earthquake.

Contents

2.1 Introduction . . . 82

2.2 Large scale analysis . . . 83

2.2.1 Data and Methods . . . 83

2.2.1.1 Analysis of the quality of the data . . . 83

2.2.1.2 Reprocessing of InSAR tracks . . . 85

2.2.1.3 Estimate of the steady-state velocity field . . . 87

2.2.1.4 Creep rates and locking depths along the North Anatolian fault . . . 91

2.2.1.5 Computation of the strain field . . . 92

2.2.2 Results . . . 94

2.2.3 Discussion . . . 95

2.2.3.1 Contribution of the InSAR data . . . 95

2.2.3.2 Continuous deformation related to the North Anatolian Fault 97

2.2.3.3 Creeping segments of the North Anatolian fault . . . 97

2.2.4 Conclusion . . . 99

2.3 Slip deficit below the Marmara Sea from joint InSAR and GNSS velocity fields 100

2.3.1 Introduction . . . 100

2.3.2 Preparation of the InSAR data . . . 100

2.3.2.1 Harmonization of the dataset . . . 100

2.3.2.2 GNSS referencing of the interseismic LOS velocity field . . . 100

2.3.2.3 Quality control of the InSAR processing . . . 101

2.3.2.4 Horizontal-Vertical decomposition . . . 102

2.3.3 Results . . . 102

2.3.4 Discussion . . . 103

2.3.4.1 Contributions of the InSAR data on the slip inversions . . . 103

2.3.4.2 Remarks on the slip predictions . . . 104

2.3.5 Conclusion . . . 107

2.1 Introduction

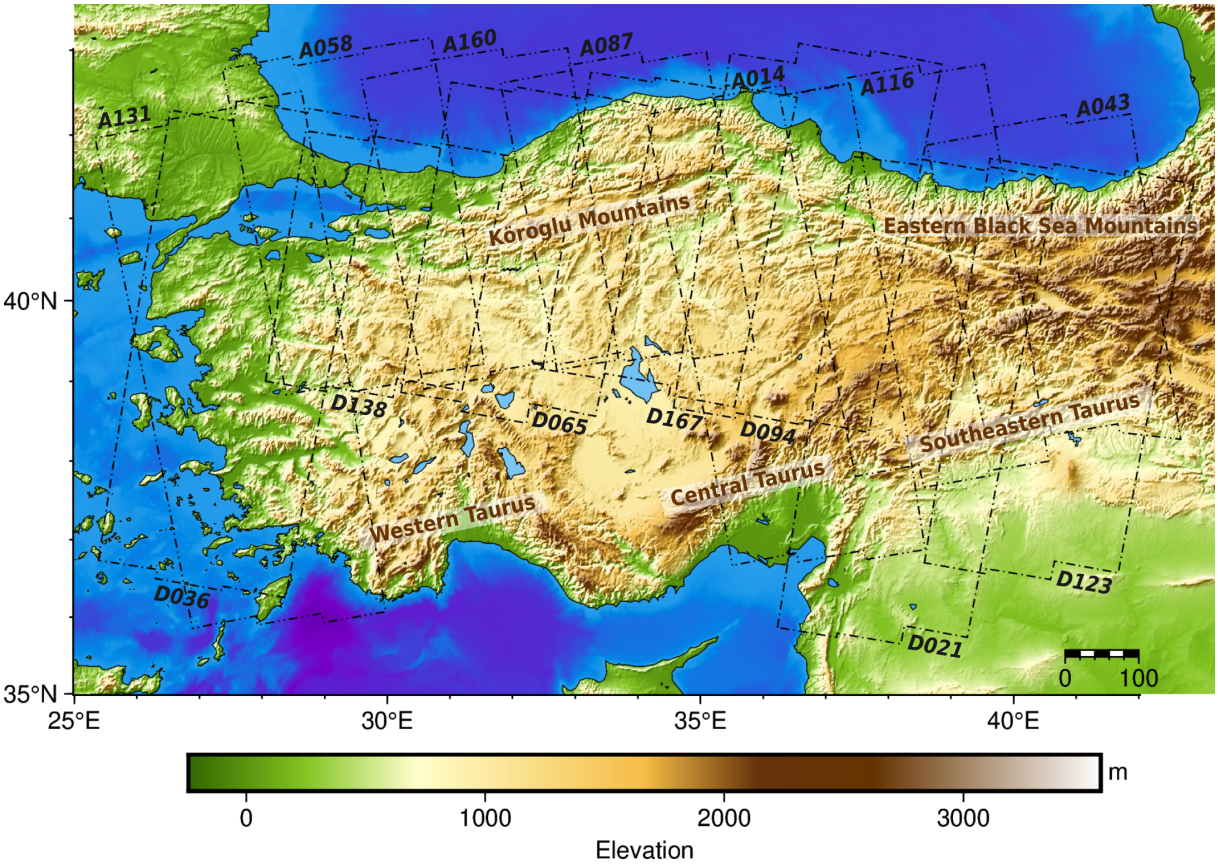

Figure 2.1: Map of the 7 ascending and 7 descending tracks coverages included in the *FLATSIM* dataset of Türkiye. *A* and *D* stand for ascending and descending, respectively. The most important mountain ranges are marked in brown on the map.

Orbit direction	No. track	Nb. ifg.	Nb. dates	Date min	Date max
Ascending	131	1552	322	14/10/2014	28/04/2021
	058	1447	315	13/01/2015	29/04/2021
	160	1485	315	13/02/2015	30/04/2021
	087	1422	311	22/12/2014	25/04/2021
	014	1520	329	18/10/2014	26/04/2021
	116	1350	298	13/10/2014	27/04/2021
	043	1237	326	20/10/2014	28/04/2021
Descending	036	1561	327	20/10/2014	28/04/2021
	138	1471	328	15/10/2014	29/04/2021
	065	1480	326	10/10/2014	30/04/2021
	167	1447	322	17/10/2014	25/04/2021
	094	1279	279	01/09/2015	26/04/2021
	021	1412	310	11/01/2015	27/04/2021
	123	1371	298	14/10/2014	28/04/2021

Table 2.1: Characteristics of the tracks processed in the framework of the *FLATSIM* project on the Turkish site presented in Figure 2.1 from West to East.

During this work, we used the Turkish *FLATSIM* dataset, that I will present in the following parts. The Turkish project takes part on the first call for projects, and its main purpose is to study the tectonic activity affecting Türkiye, which is mostly due to the presence of the North and East Anatolian Faults (cf. part 1.5.1.2). With their coverages shown in Figure 2.1, 14 tracks (7 ascending and 7 descending tracks) have been automatically processed. The main characteristics of each track (orbit direction, number of interferograms, dates and temporal extent) are detailed in Table 2.1. The mean temporal extent is $2014 - 2021$, taking advantage of the 6 *days* revisit time of the *Sentinel-1* data since May 2016.

InSAR processing for this region leads to several challenges, especially due to vegetation and topographic elements. As presented in Figure 2.1, Türkiye is mainly covered by mountains, the highest being in the eastern part (Eastern Black Sea Mountains and Southeastern Taurus). In addition of the seasonal presence of ice/snow in mountains inducing loss of coherence, significant topographic variations also affect the signal-to-noise ratio of the displacement/velocity measurements. Strong variations of the atmospheric signals can lead to the presence of atmospheric residual signals. Finally, the northwestern area surrounding the Marmara Sea is predominantly covered by croplands, whose seasonal growth cycles induce significant temporal decorrelation and can generate spurious phase signals that bias the estimated displacement and velocity fields. The automatic processing chain enables to process a large set of data, but the results can suffer from the fact that the processing parameters have been optimized for a generic use and not for the specific study areas.

In the following parts, I first analyze the large scale dataset by merging the several tracks in order to study deformation in the whole Türkiye. Then, I focus on the study of the lands surrounding the Marmara Sea in order to investigate the slip deficit along the Main Marmara Fault (MMF).

2.2 Large scale analysis

The aim of this project is to study the **steady-state deformation in Türkiye** using all the InSAR data processed in the framework of the *FLATSIM* project and covering Türkiye (Figure 2.1). In the following, I detail the quality control of the automatic processing of these 14 tracks, the reprocessing of some of the tracks and the tectonic signal extraction. Then, I present the strain field computation and propose interpretations of the results.

2.2.1 Data and Methods

2.2.1.1 Analysis of the quality of the data

The mean LOS velocities

As presented in Section 1.4.4.2, the automatic processing delivers different outputs, such as the mean LOS velocities per track. An overview of the latter helps for the detection of strong **unwrapping errors** highlighted by sharp phase jumps, as observed on the middle part of the central ascending track (*A*087) shown in Figure 2.2a. First, I reprocessed partially this track in order to remove the unwrapping errors, which are on the eastern part close to the NAF, and therefore can be misinterpreted. I used the Wrapped and Filtered Interferogram (InWF) delivered by *FLATSIM* and I remove the first interferograms affected by high Root-Mean-Square

Errors (RMSE). It produces a new mean LOS velocity shown in Figure 2.2b, and the difference between both velocities is shown in Figure 2.2c, highlighting the main unwrapping errors.

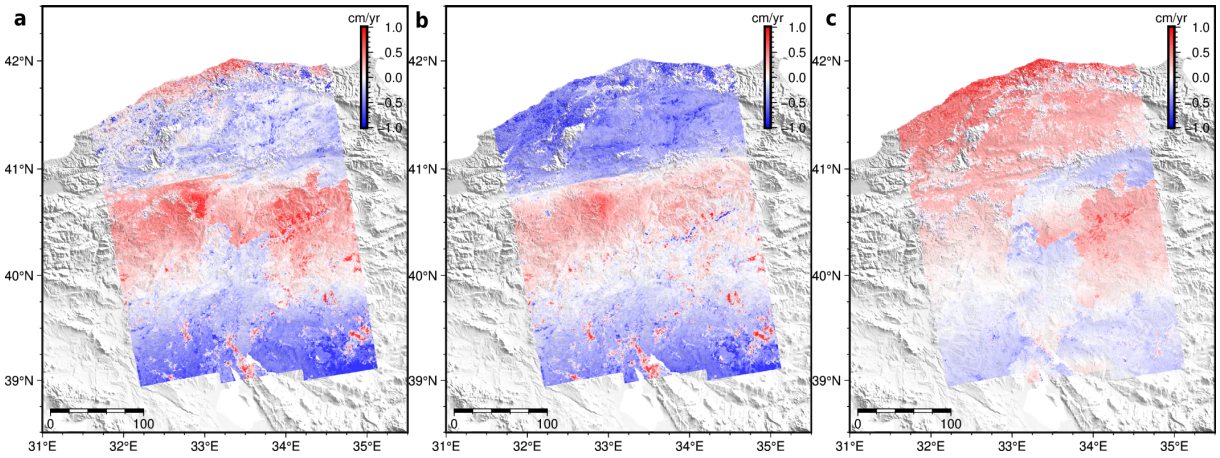

Figure 2.2: Mean LOS velocities of the track *A*087, (a) computed by *FLATSIM* and (b) after the reprocessing. (c) Difference of both mean velocities.

I reprocessed the **two western tracks** (*A*131 and *D*036) as well. Because of the presence of the Marmara Sea, the unwrapping (cf. Section 1.4.2.2) could not be done between the southern and the northern shores. Indeed, only the southern part of these tracks has been unwrapped by *FLATSIM*. I used the InWF delivered by *FLATSIM* and did the unwrapping and subsequent processing steps fo the northern shore as well.

Time series inversion quality controls

Other outputs delivered by the automatic processing enable **quality control of the time series inversion**, some of which are shown in Figure 2.3. Several **RMSE** metrics are computed to assess the consistency of the inversion (López-Quiroz et al., 2009). These metrics evaluate the **network misclosure**, i.e. the degree to which the sum of phase differences along closed loops of interferograms deviates from zero, a condition that should theoretically be satisfied in the absence of noise and unwrapping errors. This misclosure can be quantified per pixel, per interferogram, or per date, providing complementary diagnostics of the inversion quality at different levels. The **RMSE** per date, shown in Figure 2.3a, corresponds to the network misclosure averaged over all interferogram loops for each acquisition date, and thus reflects the overall reliability of the displacement estimate at that epoch. We see that the RMSE per date are seasonal, with higher values in winter. This can be explained by seasonal decorrelation effects, namely snow cover in winter and vegetation growth on croplands in spring and summer (cf. Figure 2.1). Another important information is the **number of interferograms** used in the inversion per pixel. The corresponding maps are shown in Figure 2.3 – c,d, and the related histograms in panel b. A lower number of interferograms covering the eastern part is probably due to the presence of several major mountain ranges. To avoid artifacts due to low signal-to-noise ratio in the final interseismic velocity field, we mask the pixels where $N_{ipp} < \mu_{N_{ipp}} - \sigma_{N_{ipp}}$ with N_{ipp} corresponds to the number of interferograms per pixel, and (μ, σ) the mean and standard deviation of N_{ipp}, respectively. The dashed lines in Figure 2.3b show the various thresholds used per track.

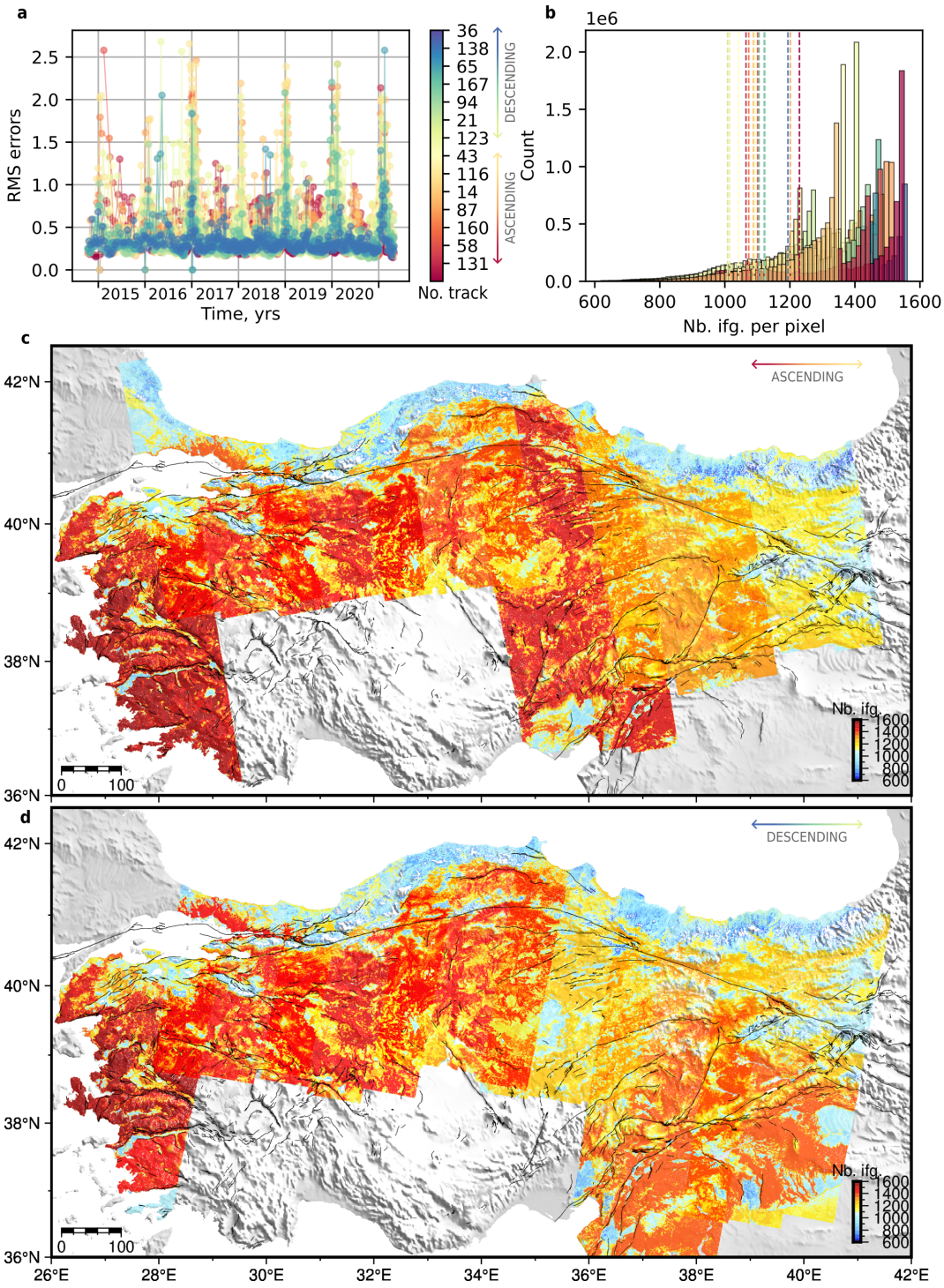

Figure 2.3: Quality control of the data. (a) Root-Mean-Square Errors (RMSE) per date for all tracks. The ascending and descending tracks are ordered so that red to yellow goes from the western to the eastern ascending tracks, and from blue to yellow goes from the western to the eastern descending tracks. (b) Histograms of the number of interferograms per pixel for each track with the same colorbar. The vertical dashed lines correspond to the thresholds used for the masks. (c,d) Maps of the number of interferograms per pixel for the (c) ascending and (d) descending tracks. The fault network is shown by the black lines (Emre et al., 2018).

2.2.1.2 Reprocessing of InSAR tracks

I used the NSBAS processing chain presented in Section 1.4.3.3 to process data for the northern side of the tracks *A*131 and *D*036 (Doin et al., 2011). This is done using the High

Performance Computing infrastructure of the University of Strasbourg (`https://hpc.pages.unistra.fr/`) to deal with the large amount of data. I started the processing with 1596 and 1607 wrapped 2-looks interferograms for the tracks $A131$ and $D036$, respectively. Due to strong decorrelation of the *one year* interferograms of the track $D036$ related to the presence of crops, I modified the filtering parameters corresponding to an average wrapped filter (*SW* filter) in order to enhance the signal-to-noise ratio and increase the unwrapping fraction.

The unwrapping reference points have been chosen on the northern shore of the Marmara Sea. We removed the first acquisitions (until 1st October 2016) to take advantage of the 6 *days* return time of *Sentinel-1* SAR images and to obtain a dense interferogram network. Due to the poor coherence within this area and our period selection, I kept only 920 and 885 unwrapped interferograms for the tracks $A131$ and $D036$, respectively. Then, from each track, I derived the InSAR time series and obtained the LOS cumulative phase/displacement field at each date and the LOS mean velocity field.

Overview of the phase bias

The study area reprocessed here is a good illustration of the presence of phase bias within the interferometric phase, and more specifically the presence of **fading signals**. As proposed by Ansari et al. (2021), the fading signal is a feature observed in multilooked interferograms, due to the spatial averaging of the signal which leads to modifications of the statistical properties of the data. It corresponds to a variation of the temporal coherence of the signal, due to differences of the scattering properties of the ground between the acquisitions. Therefore, the fading signal is most readily identified in short temporal baseline interferograms, where other contributions to the interferometric phase (such as deformation and atmospheric delays) remain largely stable between acquisitions. However, this artifact is not exclusive to short baselines, as it depends primarily on the spatial averaging of the signal and the statistical properties of the scatterers, which can vary over any temporal separation.

One method to decrease the effect of fading signals on the mean velocity is to use long-temporal baseline interferograms (such as *one*-year interferograms). However, in some areas such as in the north of the Marmara sea, the spatial coherence of the *one*-year interferograms can be low preventing the unwrapping and therefore limits the amount of long-temporal baseline interferograms.

The Figure 2.4 highlights the presence of fading signals within the mean velocity. The triplets of panels (c,e,f) and (d,g,h) gather the distribution of the mean velocity values inferred from time series analysis resulting from only short-temporal baseline interferograms (from $6-12$ days of return time) and from both short- and long-temporal baseline interferograms (up to one year of revisit time), respectively. In the case of short baselines, the crops appear to be affected by an apparent subsidence (motion away from the satellite), whereas forests and urban areas appear to be affected by an apparent uplift (Figure 2.4d). Possible effects of the topography can also be assumed but are less clear (Figure 2.4c), particularly along river beds forming sharp elevation gradient. By adding longer-temporal baseline interferograms within the dataset, these apparent motions are less visible (Figure 2.4f), and the effects of different land cover on the the mean velocity decrease, as shown in Figure 2.4 – c,d.

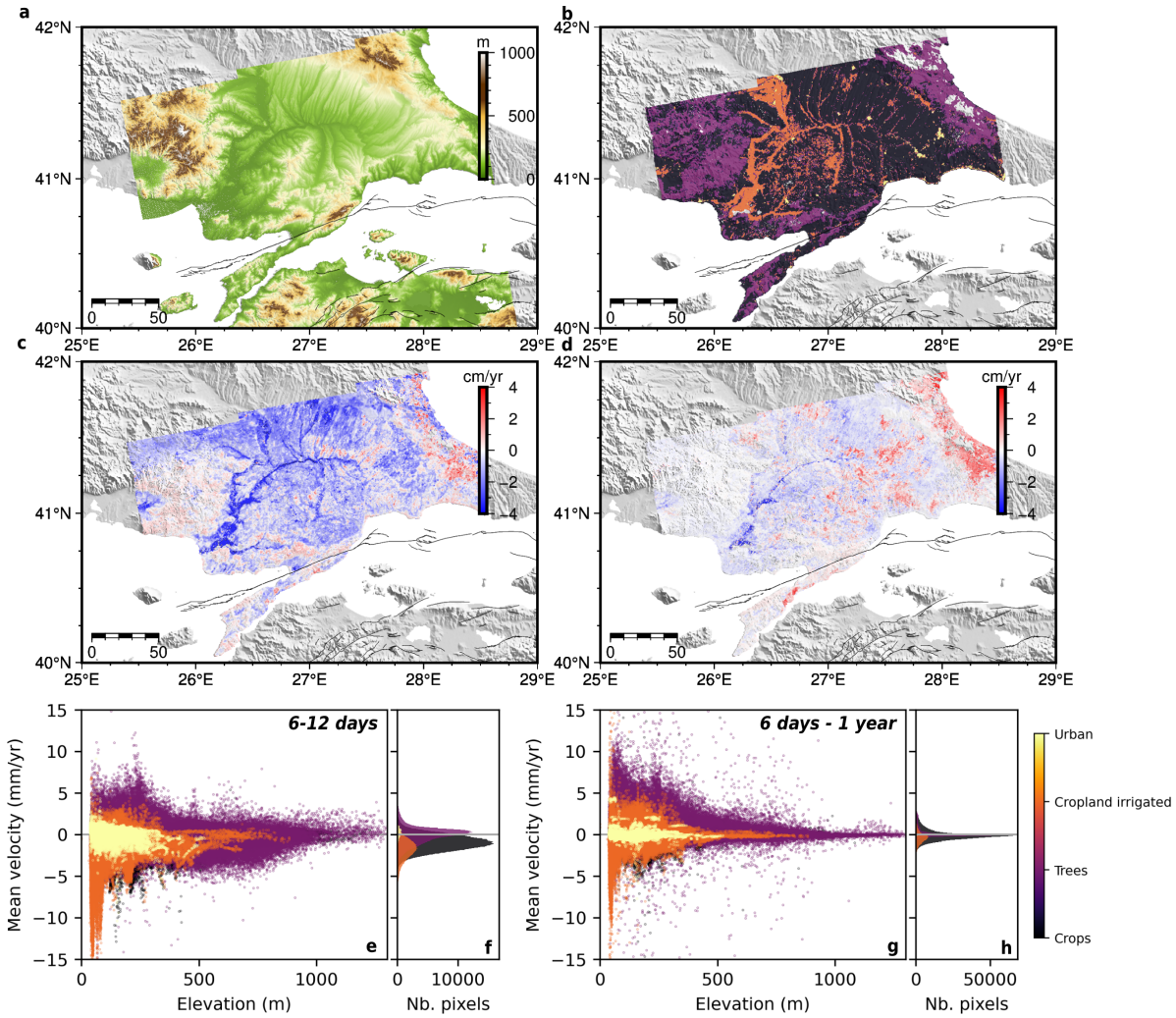

Figure 2.4: Evidences of fading signals on the track *A*131. (a) Digital Elevation Model (DEM) covering the area. (b) Land cover from `https://cds.climate.copernicus.eu/` (accessed on December 2025). The corresponding color scale is in the bottom right corner. (c,d) Mean LOS velocity based on (c) short-temporal baseline interferograms and (d) long-temporal baseline interferograms. Red and blue correspond to surface motion towards and away from the satellite. (e,g) Mean velocity values related to the pixels elevations and the land covers for (e) short- and (g) long-temporal baseline interferograms. (f,h) Histograms of the mean velocity values related to land covers for (f) only short-temporal baseline interferograms and (h) for both short and long-temporal baseline interferograms.

2.2.1.3 Estimate of the steady-state velocity field

The large scale study of the steady-state velocity field inferred from InSAR data faces several challenges. First, the InSAR deformation signal includes various signals that can be tectonic, hydrological, atmospheric, or even residual noise. We need to **extract the tectonic signal** by estimating and removing obvious other sources such as the seasonal signal (e.g. mostly due to hydrological effects or seasonal coherence variations). Then, the association of several independently processed tracks requires an homogeneous **referencing** of the mean velocities to allow for comparison. Finally, in order to precisely analyze of the tectonic signal due to two main strike-slip fault systems (see Section 1.5.1.2), we aim to retrieve the **horizontal signal**.

The post-processing sequence I followed to estimate the steady-state velocity field is the following one: (i) a seasonal and linear decomposition of the LOS displacement time series, (ii) the referencing of the velocity field with uncertainties estimates, and (iii) the decomposition of the LOS velocity fields into the horizontal east-west and vertical components.

Seasonal and linear decomposition

Because I combine the *FLATSIM* velocities with the reprocessed tracks located north of the Marmara Sea (see Section 2.2.1.2), the processing sequences are homogenized by constraining all time series to start on 9 October 2016.

Then, I calculate the mean velocity B by fitting the time series with a **linear term and annual periodic terms**:

$$x(t) = x_R + B.(t - t_0) + C.sin(2\pi(t - t_0)) + D.cos(2\pi(t - t_0)) \tag{2.1}$$

with $x(t)$ the cumulative LOS displacement at each pixel at time t, t_0 the initial time (chosen here to January 1st, 2016) and x_R a constant term. B represents the linear trend of the signal. C and D correspond to seasonal amplitudes with periods of one year (cosine and sine correspond to the summer/winter and spring/autumn cycles). The best parameters are estimated independently for each pixel of each track in a least-square sense. Since the seasonal amplitude components (C and D) are sensitive to the signal amplitude at the unwrapping reference point, a 4th order polynomial surface is subtracted to remove any long-wavelength bias and ensure that the estimated amplitudes reflect local variations only.

GNSS referencing of the velocity field

Overview of the different methods: In order to merge different InSAR velocities, we need to homogenize the **reference frame** of all the tracks. Several approaches can be used to achieve this step. The first type of approaches consists of using external data well referenced such as a **GNSS velocity field**. The referencing consists in estimating and removing a systematic offset between the InSAR LOS measurements and the GNSS displacements projected onto the LOS direction. This offset is modeled either as a high-pass filtered signal (Tong et al., 2013) or as a polynomial surface fit (Hussain et al., 2018; Weiss et al., 2020) to the difference between the two datasets. A second type of approach consists of identifying and removing long-wavelength signals of non-tectonic origin (such as residual atmospheric delays, tidal loading, and orbital errors) in order to retrieve the surface deformation in the International Terrestrial Reference Frame (ITRF). This method has been first developed by Lemrabet et al. (2023) in Tibet, where they estimated and removed the residual atmospheric delays and tidal loading. The benefit of this second type of approach is to avoid the dependence on GNSS data.

Application to the Turkish dataset: In the case of Türkiye, I take advantage of the dense network of GNSS observations combined by Kurt et al. (2023) and resulting in a precise velocity field covering the country. I therefore referenced the InSAR LOS velocities relative to GNSS velocities. The referencing method, described by Hussain et al. (2018), enables to remove possible ramps between the different tracks, and to obtain a LOS velocity field relative to fixed Eurasia. I project the GNSS velocities into the LOS components for each track, only using the horizontal eastward and northward GNSS components. I then extract the mean InSAR LOS velocities within a 1 *km*-diameter circle surrounding each GNSS station to compare them

with the GNSS velocities. I compute a 2D plane corresponding to the difference between the estimated mean InSAR LOS velocities and the GNSS velocities. By subtracting the 2D plane to our InSAR velocities, I obtain a LOS velocity field relative to fixed Eurasia. An example is shown in Figure 2.5 with the southern part of the track $A131$. GNSS referencing enables the merging of the northern and southern parts of the western tracks ($A131$ and $D036$), which are processed independently and may exhibit a relative offset due to differences in their unwrapping reference points. This step is done for both velocity fields resulting from ascending and descending tracks.

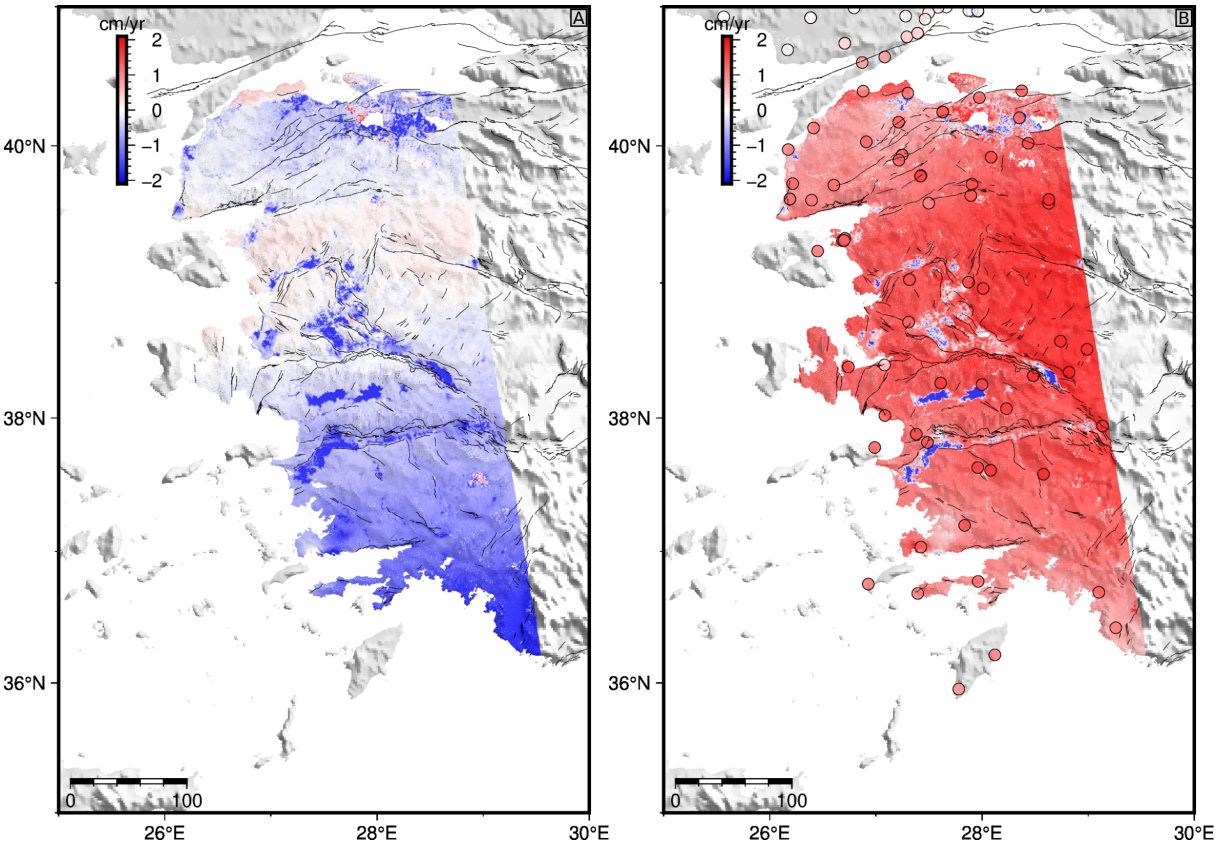

Figure 2.5: Mean velocity (A) before and (B) after GNSS referencing of the southern part of the track $A131$. The dots correspond to the GNSS velocities projected into the LOS of the corresponding track.

Uncertainties estimates: As proposed in previous large scale InSAR studies (e.g. Hussain et al., 2018; Weiss et al., 2020), **overlapping areas** between adjacent tracks can be used to estimate the uncertainties on the velocity measurements, by comparing independent LOS velocity estimates from adjacent tracks over the same pixels. The Figure 2.6 shows histograms corresponding to the velocity RMS misfit computed within the 12 overlapping areas (from ascending and descending tracks). The misfit is estimated by computing the velocity of adjacent tracks after GNSS referencing to avoid potential large scale fringes due to the referencing and projection into horizontal velocities. By approximating the misfits by a Gaussian, I obtain mean RMS misfits of the difference between the horizontal component of two independent adjacent tracks of about 4.41 mm/yr and 3.77 mm/yr for the ascending and descending tracks, respectively. I can deduce the horizontal errors for an individual track, with amplitudes of 3.12 mm/yr and 2.67 mm/yr for the ascending and descending tracks, respectively. Finally, by using an incidence angle between $20-40°$, the LOS uncertainties are estimated to be between $1.07-2.00$ mm/yr and $0.91-1.72$ mm/yr for the ascending and descending tracks respectively. These values are consistent with previous studies (Hussain et al., 2018).

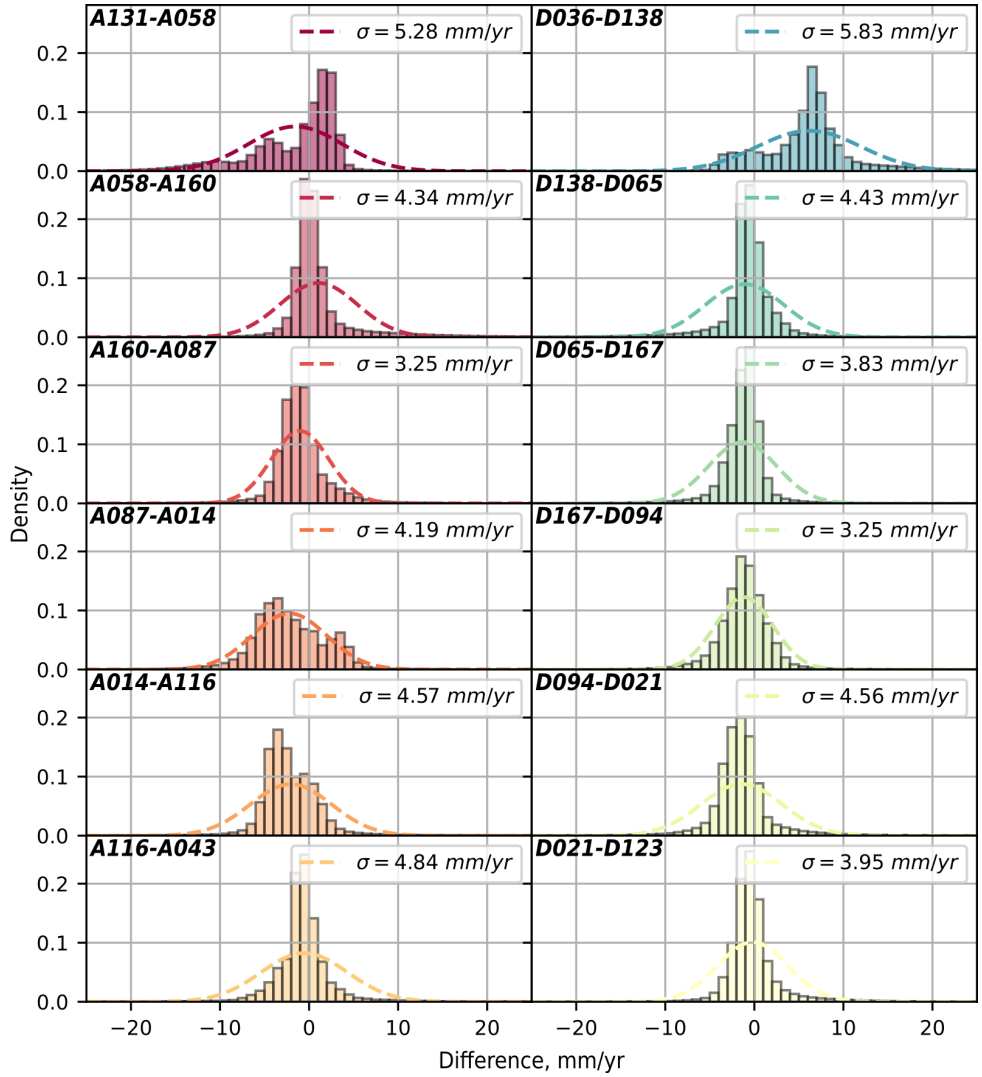

Figure 2.6: Histograms of the phase differences computed within the overlapping areas, for the (left) ascending and (right) descending tracks, (top) from West to (bottom) East. The dashed lines correspond to the fit of a Gaussian function, with its standard deviation noted in each legend.

Horizontal-Vertical decomposition

Finally, I decompose the horizontal and vertical components of the velocity field, neglecting the North-South displacement. To do so, I first need to spatially interpolate the descending velocity field in order to use the same spatial grid between the ascending and descending tracks. I then use the following equations to project the mean LOS ascending and descending velocities along the fault-parallel (horizontal – East-West) and vertical directions (e.g. Fialko et al., 2002):

$$P = \begin{pmatrix} e_{asc}sin\alpha + n_{asc}cos\alpha & u_{asc} \\ e_{desc}sin\alpha + n_{desc}cos\alpha & u_{desc} \end{pmatrix} \tag{2.2}$$

$$\begin{pmatrix} v_f \\ v_z \end{pmatrix} = P^{-1} \begin{pmatrix} v_{asc} \\ v_{desc} \end{pmatrix} \tag{2.3}$$

with P a rotation matrix, α the mean strike of the displacement (in this case, the east-west direction, 90°), (e_i, n_i, u_i) the Cartesian components of the satellite look vectors for the ascending and the descending tracks (noted *asc* and *desc*, respectively), v_i the mean LOS velocity, and (v_f, v_z) the component of the mean velocity along the fault-parallel direction and the vertical direction, respectively. The results are presented in Figure 2.7.

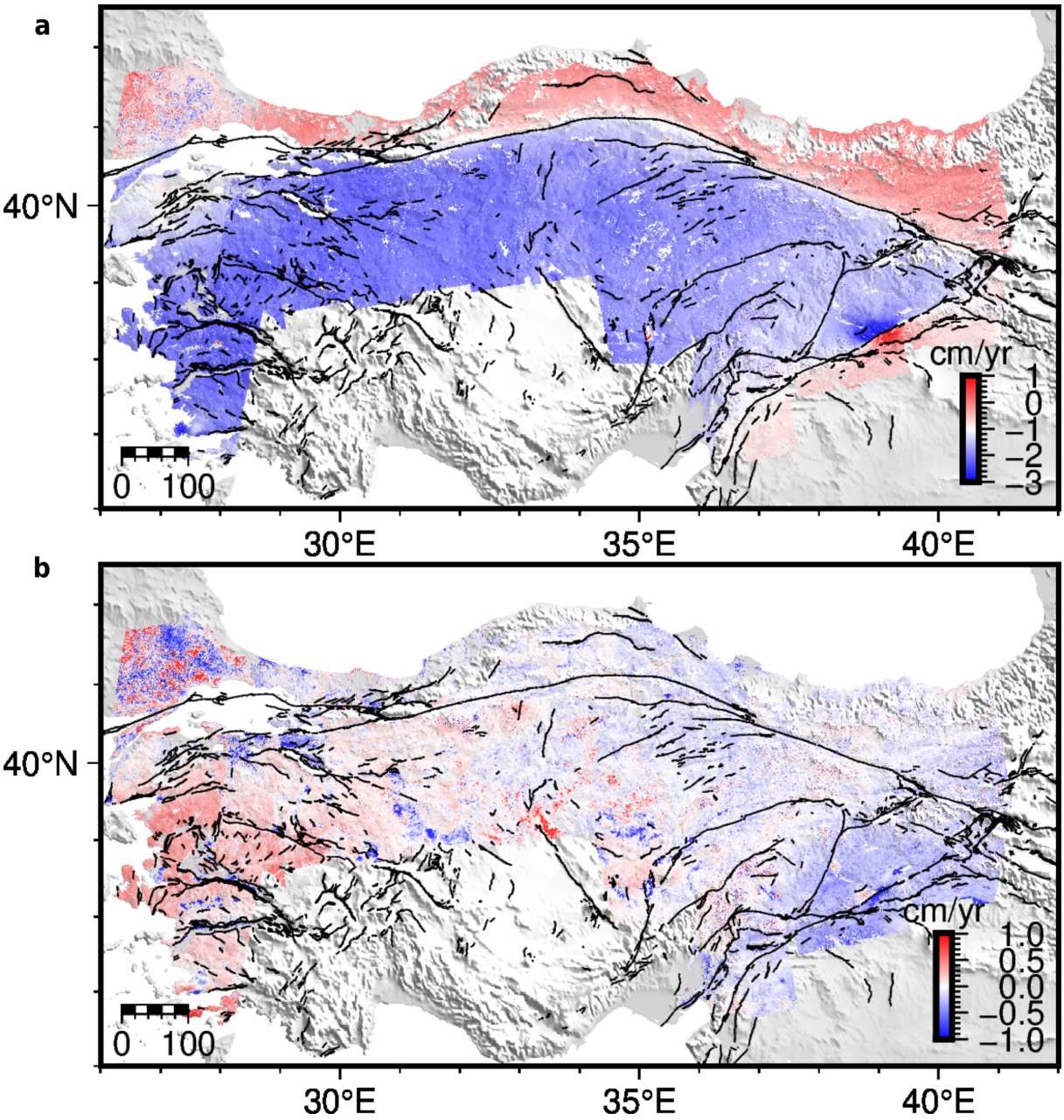

Figure 2.7: (a) Mean East-West and (b) vertical velocity maps obtained after the decomposition. The fault network is shown by the black lines (Emre et al., 2018).

2.2.1.4 Creep rates and locking depths along the North Anatolian fault

By using geodetic data, I can infer the locking depths and creep rates along the fault interface by analyzing profiles perpendicular to the fault. This approach has been first proposed by Savage and Burford (1973) along the San Andreas Fault (SAF), by making the hypothesis of a screw dislocation embedded in a homogeneous linear elastic half-space.

Based on that, Savage and Burford (1973) expressed the velocity across the fault V as a

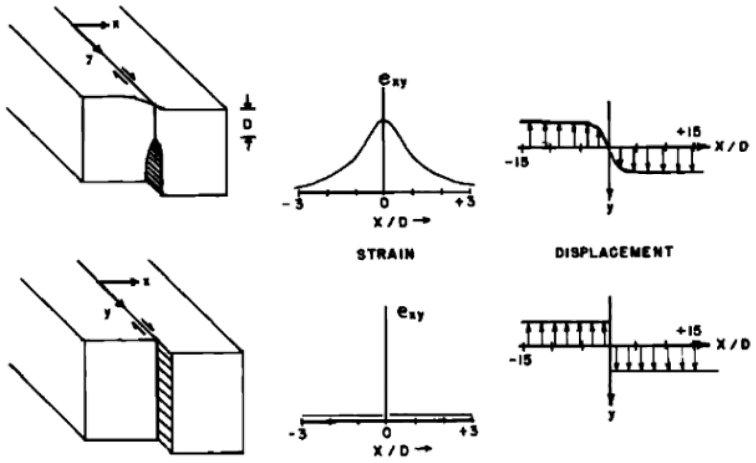

Figure 2.8: Simple models for fault motion from Savage and Burford (1973). Top sketches refer to a locked-fault model, in which slip on the fault occurs only at depths greater than D. Bottom sketches refer to the rigid-block model, in which slip is approximately uniform with depth.

function of the distance to the fault trace x such as (Weertman and Weertman, 1964):

$$V(x) = \frac{S}{\pi} arctan\left(\frac{x}{d_1}\right) \tag{2.4}$$

with S the slip rate at depth and d_1 the locking depth. This equation enables to model the interseismic slip on a fault plane below the locking depth (Figure 2.8).

To take into account shallow creep, Hussain et al. (2016) proposed to model it by using a back slip approach with (i) a Heaviside function $H(x)$ corresponding to shallow creep (i.e. the sum of slip on the entire fault plane) and (ii) a screw dislocation in the opposite sense to plate motion at creeping depth d_2:

$$V(x) = -\frac{S}{\pi} arctan\left(\frac{x}{d_1}\right) + C\left[\frac{1}{\pi} arctan\left(\frac{x}{d_2}\right) - H(x)\right] + a \tag{2.5}$$

with C the creep rate, and a a constant.

2.2.1.5 Computation of the strain field

In order to investigate horizontal deformation in the context of regional tectonic plate motions, I compute the strain field, which quantifies the spatial deformation associated with the accumulation and release of tectonic stresses, as follows:

$$\begin{bmatrix} \varepsilon_{11} & \varepsilon_{12} \\ \varepsilon_{21} & \varepsilon_{22} \end{bmatrix} = \begin{bmatrix} \frac{\delta V_x}{\delta x} & \frac{1}{2}\left(\frac{\delta V_x}{\delta y} + \frac{\delta V_y}{\delta x}\right) \\ \frac{1}{2}\left(\frac{\delta V_x}{\delta y} + \frac{\delta V_y}{\delta x}\right) & \frac{\delta V_y}{\delta y} \end{bmatrix} \tag{2.6}$$

with ε corresponding to the strain, V the velocity field, and (x,y) the East-West and North-South components. Different components can be deduced from the strain field, such as the shear strain (ε_{12}), the rotation (ω_{12}), the dilatation and the maximum shear strain (γ_{max}). To estimate these strain rates, I first calculate the InSAR East-West velocity gradient directly from the velocity field (Figure 2.7a). The North-South component, which is poorly constrained by InSAR data due to the near-polar orbital geometry of SAR satellites, was neglected in this

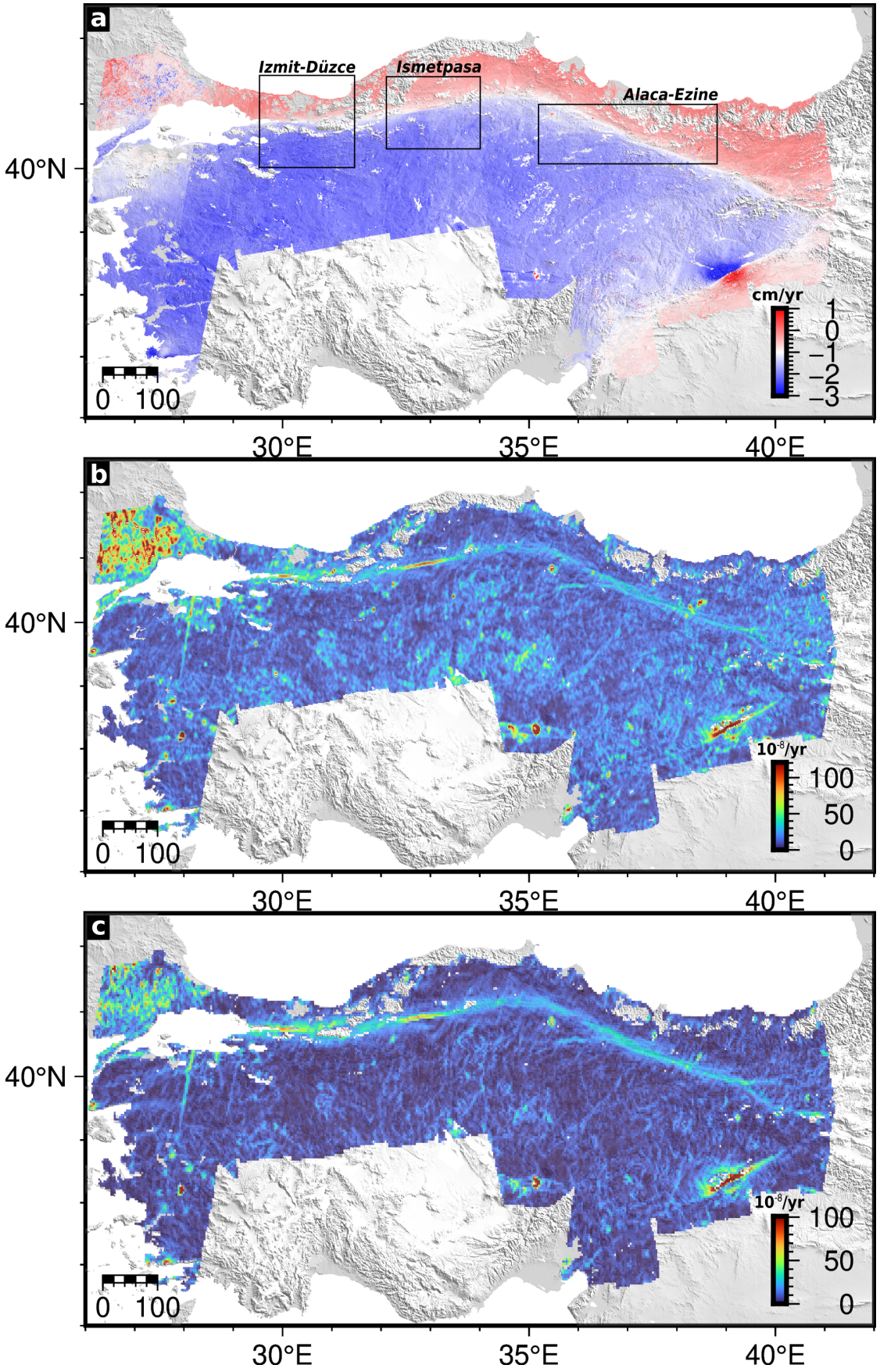

Figure 2.9: Results of the strain field computation at large scale. (a) Mean InSAR East-West velocity. The black rectangles highlight the zooms shown in Figure 2.10. (b-c) Maximum shear strain rate estimated at (b) 1 *km*-resolution and (b) 2 *km*-resolution.

analysis. However, this omission has a significant impact on the strain rate computation, as the fault-perpendicular component of deformation along the East-West striking NAF is primarily expressed in the North-South direction. The rotation is therefore equal to the shear in this case. Then, I compute the various components using the following equations:

$$\omega_{12} = \frac{1}{2}\left(\frac{\delta V_x}{\delta y} - \frac{\delta V_y}{\delta x}\right) \tag{2.7}$$

$$dilatation = \frac{\varepsilon_{12} + \varepsilon_{22}}{2} \tag{2.8}$$

$$\gamma_{max} = \frac{1}{2}\sqrt{(\varepsilon_{11} - \varepsilon_{22})^2 + 4\varepsilon_{12}^2} \tag{2.9}$$

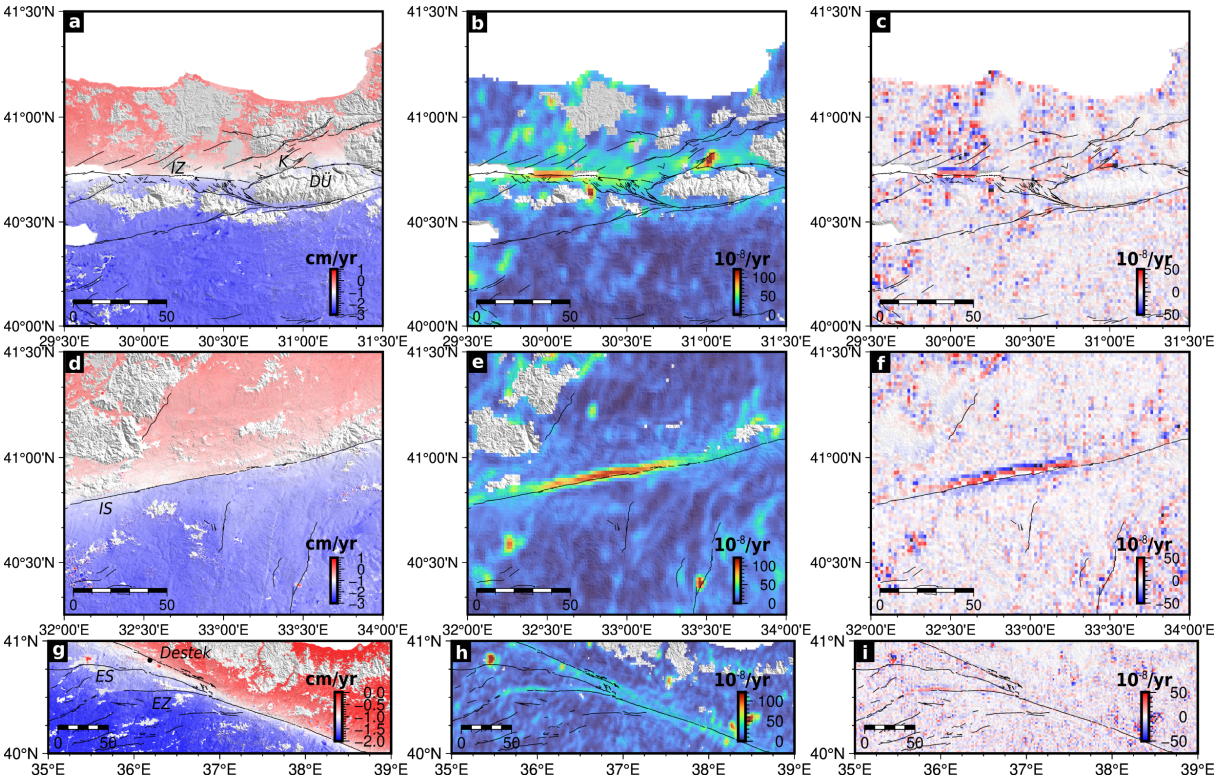

Figure 2.10: Focus on the three areas of interest: (a-c) the Izmit-Düzce segment, (d-f) the Ismetpasa segment and (g-i) the Alaca-Ezine segment. (a,d,g) Mean InSAR East-West velocity. (b,e,h) Maximum shear strain rate estimated at 1 *km*-resolution. (c,f,i) Rotation estimates. (a-i) The fault network is shown by the black lines (Emre et al., 2018). (a,d,g) Italic letters correspond to names of fault segments: *IZ*: Izmit, *K*: Karadere, *DÜ*: Düzce, *IS*: Ismetpasa, *ES*: Esencay, and *EZ*: Ezinepazari.

The Figure 2.9 shows the results at large scale, and the Figure 2.10 shows zooms of several regions of interest.

2.2.2 Results

On the mean East-West velocity map (Figure 2.7a), we can see the westward extrusion of the Anatolian plate accommodated by two major fault systems: the NAF and EAF. A strong tectonic signal is also visible along the EAF, corresponding to the 2020 M_w 6.8 Elazığ earthquake (e.g. Pousse-Beltran et al., 2020). This signal could have been attenuated by estimating

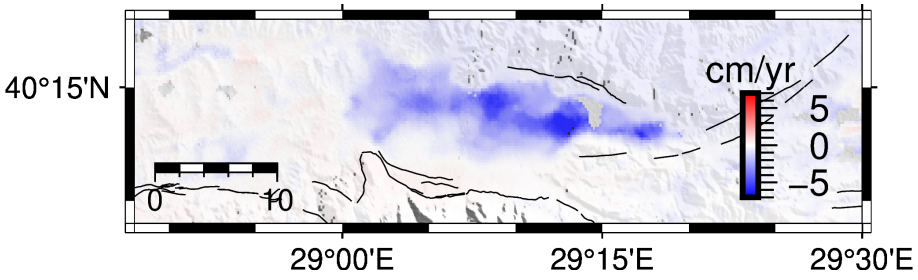

Figure 2.11: Focus of the mean vertical velocity on the Bursa basin.

and removing the coseismic offset of displacement for each pixel. The north-western part of Türkiye appears noisier, preventing precise analysis of the steady-state deformation.

The mean vertical velocity map (Figure 2.7b) shows no obvious signal, if any, related to the two main fault systems, suggesting that both faults are mostly strike-slip faults at a large scale. However, some signals can be related to the tectonic activity, such as the large sedimentary basins located in the western part of Türkiye (Western Anatolian Extensional Province), highlighted by the subsidence due to the North-South extension of the area (e.g. Bozkurt, 2003). North of the Konya Basin (central Anatolia), strong uplift with up to 2 cm/yr is measured, which may require further attention to verify whether it could be related to the tectonic deformation, the area being affected by the active Tuz Gölü Fault Zone (Yıldırım, 2014) or to phase bias. More local signatures can be related to the presence of large sedimentary basins and hydrological forcing (e.g. the Adapazari basin on the north-western side, see Figure 2.15b), while other areas are affected by a vertical signal due to anthropogenic activities, e.g. the big mine at Tunçbilek/Tavşanlı/Kütahya (see Figure 2.15b). One interesting example is the Bursa basin shown in Figure 2.11, which exhibits a subsidence rate of up to 5 cm/yr. As proposed by Aslan et al. (2019a) who found a subsidence of up to 2.5 cm/yr, this vertical motion may be related to anthropogenic activities such as agriculture related to groundwater pumping. In this case, the higher subsidence amplitude reported by Aslan et al. (2019a) may reflect the different study period ($2014-2017$), during which subsidence rates could have been more pronounced.

The strain rate map shown in Figure 2.9c also highlights both strike-slip fault systems with maximum shear rates $\geq 20.10^{-8} yr^{-1}$. Three segments are identified by higher values of the shear strain rates: the Izmit, Ismetpasa and Elazığ segments. However, the absolute amplitude of the shear strain rates should be interpreted with caution, as two factors may affect their estimates. First, the spatial smoothing applied during the velocity field interpolation reduces the sharpness of strain rate gradients, likely leading to an underestimation of peak values along the fault. Second, the omission of the North-South displacement component results in an incomplete strain tensor, which may bias the amplitude of the computed shear strain rates. The rupture of the 2020 earthquake along the Elazığ segment explains the high rate estimates. By comparing with the strain rate map at 1 km resolution (Figure 2.9b), the same characteristics are visible with more precise strain variations along the NAF and EAF.

2.2.3 Discussion

2.2.3.1 Contribution of the InSAR data

This work enables the production of a first version of an unprecedentedly detailed East-West velocity field computed over five years using InSAR data. The quality of the velocity field resulting from a low amounts of post-processing (see Section 2.2.1.3) highlights the quality of

the data provided by FLATSIM and validates the use of automatic processing chains to study large-scale tectonic signals. This exercise has been done previously by Weiss et al. (2020) using another automatically InSAR processing chain: LiCSAR (Lazeckỳ et al., 2020) and delivering velocity fields and strain rate fields. Their study highlights the tectonic deformation related to the NAF and EAF. Both studies support the use of automatic and massive processing chains, in order to obtain large-scale velocity fields with a high spatial resolution, allowing for the analysis of large and local deformation signals.

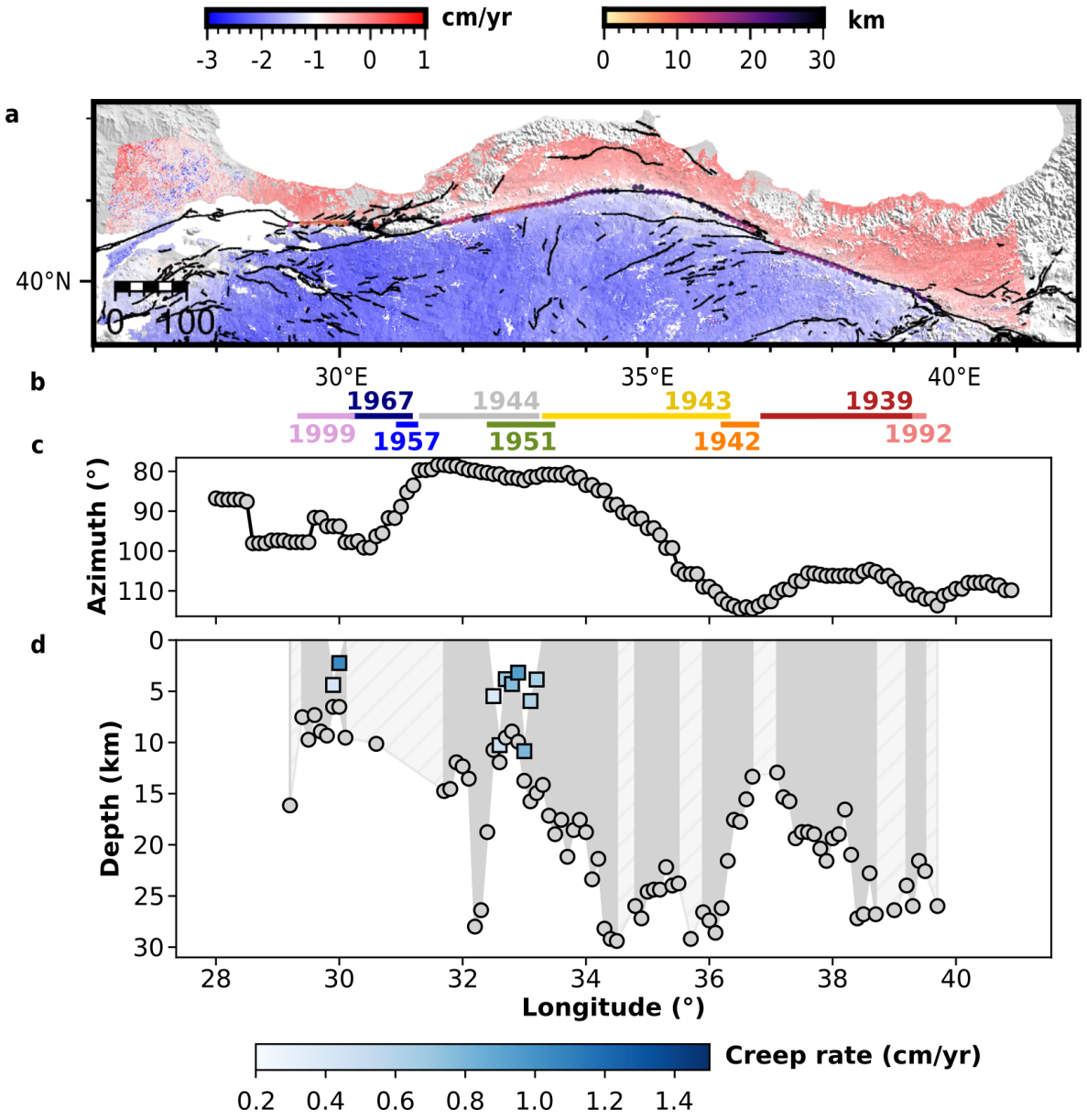

Figure 2.12: Estimate of along-strike fault parameters. (a) Mean East-West velocity map focused on the NAF. Colored dots show values of locking depth estimates on fault-perpendicular profiles. The fault network is represented by the black lines. (b) Length of the surface ruptures from Figure 1.42. (c) Fault azimuths per longitude on the NAF. (d) Estimates of the locking depth, creep rate and creep depth per profile. The locking depth is represented by the gray dots. The creep depth and rate correspond to the squares and the blue colorbar, respectively. Hatching areas correspond to area without data.

2.2.3.2 Continuous deformation related to the North Anatolian Fault

NAF perpendicular profiles across the fault and strain fields suggest lateral variations of the strain accumulation with variations of the East-West velocity gradients and maximum shear strain amplitudes. To better explain these observations, I used 111 *km*-long and 555 *m*-wide fault-perpendicular profiles of the mean East-West InSAR velocity and the method described in Section 2.2.1.4 to estimate locking depths and shallow creep along the main strand of the NAF.

The Figure 2.12 gathers estimates of the creep depth (d_2), the creep rate (C), the locking depth (d_1) and the fault azimuth. The estimates have been obtained by making the hypothesis that the loading rate V is constant and equal to 24 mm/yr (McClusky et al., 2000). First, we observe two segments affected by shallow creep, that I will detail in the next Section 2.2.3.3. Then, we observe discrepancies of the locking depth (Figure 2.12 – a,d) ranging from 7 to 30 *km*, in agreement with previous studies (e.g., Wright et al., 2001b; Cavalié and Jónsson, 2014). Hussain et al. (2018) found the same order of magnitude for the locking depth along the NAF, with some significant differences, such as in the western part (longitude $< 31°E$) where they found locking depths deeper than 15 *km*. However, the trend of the lateral variations of the locking depth is similar to the one that we observe. Lateral variations of loading rate would impact the locking depths estimates.

The comparison between locking depth, fault azimuth, and the surface ruptures associated with the major earthquakes of the last century (Figure 2.12 – b,c,d) suggests, at first order, a relationship between fault orientation and the length of large seismic ruptures. These observations further emphasize the structural segmentation of the NAF, which likely influences the spatial distribution of strain accumulation and earthquake rupture propagation.

2.2.3.3 Creeping segments of the North Anatolian fault

As mentioned above, the Figure 2.12d highlights two creeping segments corresponding to both known Izmit and Ismetpasa around longitude $30°E$ and between 32.5 to $33.4°E$, respectively. Both segments ruptured during the last century, with the 1999 M_w 7.6 Izmit earthquake and the 1944 M_w 7.3 Bolu-Gerede earthquake, respectively. Since then, several analyzes based on creepmeters, GNSS, and InSAR data identified shallow aseismic creep and episodic SSEs affecting both of them (Ambraseys, 1970; Cakir et al., 2005, 2012; Kaneko et al., 2013; Bilham et al., 2016; Cetin et al., 2014; Rousset et al., 2016; Aslan et al., 2019b; Özarpacı et al., 2021; Jolivet et al., 2023; Özdemir et al., 2025). Along the Izmit segment, I estimate a creep rate of up to 7.5 mm/yr, a creep depth of about $2-3$ *km*, and a locking depth close to ~ 7 *km*. This shallow locking depth is in agreement with Cakir et al. (2012); Ergintav et al. (2014); Aslan et al. (2019b); Özarpacı et al. (2020) who found a locking depth ranging from 5 to 12 *km*. Hussain et al. (2016) found a slightly deeper locking depth (18 *km*), which can be related to the uncertainties of their model. In comparison, McClusky et al. (2000) estimated a locking depth of about 21 *km* before the rupture of the segment, suggesting that the locking depth has not yet returned to its pre-earthquake value. The creep parameter estimates are also in good agreement with previous studies. Along the Ismetpasa segment, I estimate a creep rate ranging from 7.5 to 11 cm/yr, for a creep depth close to $4-5$ *km* and a locking depth of about 10 *km*. The first striking observation is the length of the creeping segment, reaching ~ 90 *km*-long (e.g. Cakir et al., 2005; Kaneko et al., 2013; Rousset et al., 2016; Jolivet et al., 2023). Some studies detected SSEs on the western edge of the Ismetpasa segment along a $5-8$ *km*-long portion (Rousset et al., 2016; Jolivet et al., 2023; Özdemir et al., 2025). Moreover, the creep rate, the creep depth, and the locking depth are in the same order of magnitude as previous estimates

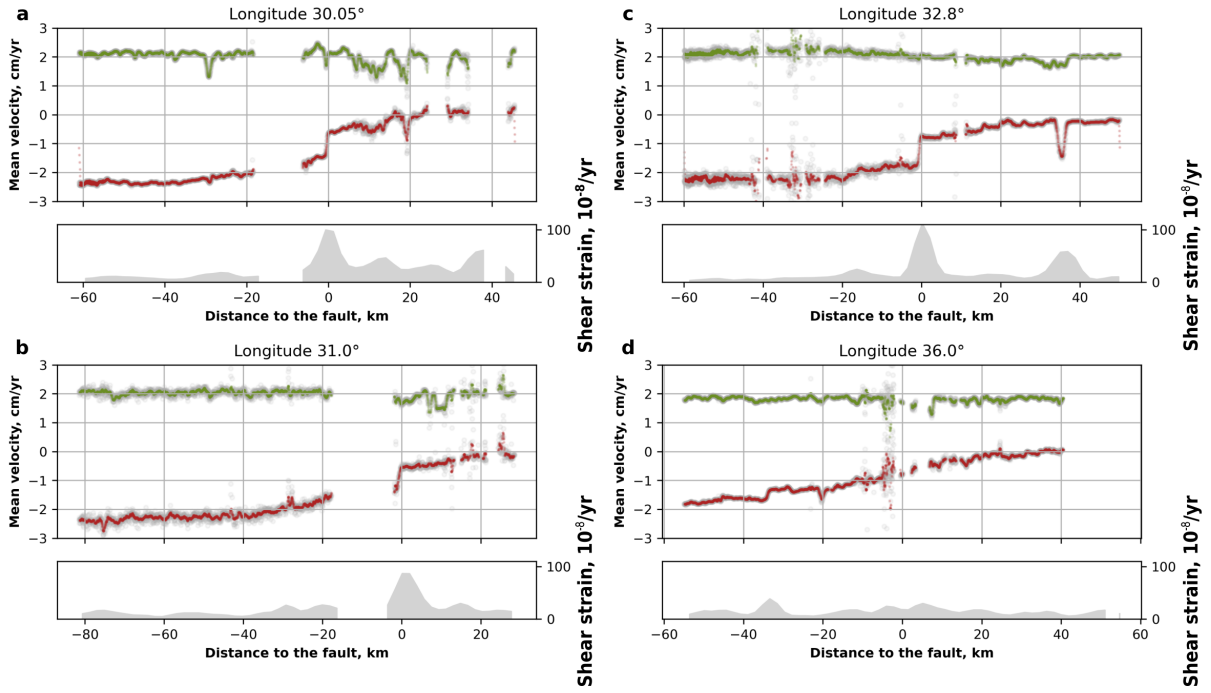

Figure 2.13: Fault-perpendicular profiles across the four following segments: (a) Izmit, (b) Düzce, (c) Ismetpasa and (d) Ezinepazari. (top) Red and green lines correspond to the mean East-West and vertical velocities, respectively. These mean velocities correspond to the average computed by using the gray dots in the background. The vertical data have been shifted by 2 cm/yr in order to improve the visibility. (bottom) Maximum shear strain (see Figure 2.8).

(Jolivet et al., 2023, and references therein). By focusing on these areas in the mean East-West velocity map, the maximum shear strain rate map and the rotation as shown in Figure 2.10 – a-f, we can observe (i) a sharp gradient on the East-West velocity field, (ii) high values of the maximum shear strain rate $\geq 80 \times 10^{-8} yrs^{-1}$, and (iii) high absolute amplitudes of the rotation $\geq 40 \times 10^{-8} yrs^{-1}$ along the creeping sections. Fault-perpendicular profiles centered on each segment are shown in Figure 2.13 – a,c. The co-location of a peak amplitude of the shear rate, the sharp offset of the East-West velocity and the fault trace proves shallow aseismic creep along those segments. The pattern of the rotation amplitudes along the creeping segments reveals a positive fringe on the fault, surrounding by negative fringes. This rotation anomaly is directly related to the East-West velocity gradient perpendicular to the fault, as shown by equation 2.7.

By analyzing in details the segments of the NAF, two additional segments present similar observations: the Düzce segment (Figures 2.10 – a,b,c around $31.00°E - 40.75°N$ and 2.13b) and the Ezinepazari segment (Figures 2.10 – g,h,i around $36.00°E - 40.50°N$ and 2.13d connected to the main strand of the NAF). Liu and Wang (2023) also highlighted the potentially creeping behavior of the Düzce segment and east of Destek, the latter being close to the Ezinepazari segment, further motivating the study of both areas. The profile shown in Figure 2.13b along the Düzce segment highlights a sharp gradient, with an offset of at least 9 mm/yr centered at the fault trace. This segment, which ruptured during the 1999 M_w 7.2 Düzce earthquake, may also be affected by shallow creep. This segment has been affected by smaller coseismic surface offsets of up to 2 m in comparison with the central and eastern parts of the rupture, which reached 5 m (Pucci et al., 2006). In addition, this segment has been affected by shallow earthquakes within the first two kilometers, before and after the mainshock. Further investigations are needed to specify this behavior. This area is characterized by complex fault geometry (junction with the Karadere segment to the West and *en échelon* fault segments, (Pucci et al.,

2008)) and basin-related subsidence. Together with the apparent slip deficit from the earthquake, these factors may promote shallow creep to release part of this energy. The second segment of interest is the East-West Ezinepazari segment, corresponding to a branch of the North Anatolian Shear Zone. Within this area, the main strand of the NAF splits into several segments forming the Tasova-Erbaa and Niksar pull-apart basins (Figure 2.10g). The Niksar one is the younger; its formation may have started during the early Pleistocene (Barka et al., 2000). This pull-apart basin is related to the growth of the East-West Ezinepazari segment, which ruptured during the 1939 M_w 7.7 Erzincan earthquake at its eastern termination (see Figure 1.42a). As proposed by Barka et al. (2000), the joint formation of a new pull-apart basin and fault segment suggests an anticlockwise rotation of the Anatolian plate. Some studies along the western part of this segment (Sungurlu fault) found no or low strain accumulation (e.g. Yavaşoğlu et al., 2011; Karasözen et al., 2014). However, by looking at the eastern part, the InSAR East-West velocity field (Figure 2.10g) reveals a sharp gradient correlating with the segment location, and therefore associated with a high value of shear strain (Figure 2.10h). The analysis of the fault-perpendicular profiles (Figure 2.13d) shows an offset of about ~ 5 mm/yr located at ~ 35 km south from the main strand of the NAF. This result suggests two points: (i) the presence of slip partitioning between the NAF main branch and secondary faults, such as the Ezinepazari segment within this area, and (ii) the presence of shallow creep along this segment, highlighted by a sharp velocity gradient. The red spot located at $35.5°E - 40.8°N$ shows a strong negative vertical velocity and may be due to phase bias because of the presence of crops.

2.2.4 Conclusion

The InSAR data automatically processed in the framework of the *FLATSIM* project covering Türkiye provide an unprecedented high spatial resolution of the steady-state velocity field, with limited post-processing. It allows us to analyze the lateral segmentation of the NAF, and highlight specific segments affected by shallow aseismic creep. As shown by previous studies, the Izmit and Ismetpasa segments are clearly visible within the East-West velocity field, as well as the maximum shear strain rate. Other segments might also be creeping, such as the Düzce and Ezinepazari segments, even if further investigations are required to better describe their slip dynamics (e.g., Liu and Wang, 2023). These results highlight the importance of the segmentation of the main strand of the NAF, with segments affected by distinct behaviors. Even if most of the 1600 km-long fault system is locked, $\approx 95 - 100$ km of the fault is creeping, and therefore releases strain. This new steady-state velocity field also suggests that the slip partitioning between the main strand and secondary faults may be underestimated. This seems to be the case for the Tasova-Erbaa-Niksar pull-apart basins, where the Ezineapazari segment is probably accumulating and releasing strain south of the main strand. Locally, this velocity fields enables us to detect signals related to anthropogenic activities: large subsiding basins, local effects such as resource pumping or mining. As pointed out by Hussain et al. (2018) and Weiss et al. (2020), the contribution of the InSAR is crucial to better estimate the seismic hazard, and the development of automatic processing chains such as *FLATSIM* is obviously facilitating the task.

2.3 Slip deficit below the Marmara Sea from joint InSAR and GNSS velocity fields

2.3.1 Introduction

Some segments of the NAF beneath the Marmara Sea correspond to a **seismic gap**, and threaten the megalopolis of Istanbul (see Section 1.5.2.1). A detailed study of the interseismic behavior of these segments may help to better estimate the seismic hazard of this region. Özkan et al. (2025) recently proposed an augmented GNSS velocity field surrounding the Marmara Sea with densified measurements on the northern shore. Here, I add InSAR data in order to derive a Bayesian inversion of the slip rate beneath the Marmara Sea. This project is led by Émilie Klein (Research Engineer CNRS at the Laboratoire de Géologie, École Normale Supérieure, Paris, France) and in collaboration with Baptiste Rousset, Frédéric Masson (Professor at Université de Strasbourg, ITES, Strasbourg, France), Ali Özkan (Assistant professor at Osmaniye Vocational School, Osmaniye Korkut Ata University, Osmaniye, Turkey), Hasan Hakan Yavaşoğlu (Professor at Department of Geomatics Engineering, Istanbul Technical University, Istanbul, Turkey), Romain Jolivet (Professor at Laboratoire de Géologie, École Normale Supérieure, Paris, France) and Patrice Ulrich (Engineer CNRS, Université de Strasbourg, ITES, Strasbourg, France). I was in charge of the InSAR processing of the tracks overlaying the area, supervised by Cécile Doubre and Baptiste Rousset.

2.3.2 Preparation of the InSAR data

Four tracks are overlaying the Marmara Sea: two ascending ($A131$ and $A058$) and two descending ($D036$ and $D138$) tracks (Figure 2.1). As mentioned previously, the two western tracks ($A131$ and $D036$) needed to be partially reprocessed, due to the incomplete initial unwrapping by *FLATSIM* (see Section 2.2.1.2).

In order to prepare the InSAR data for the joint inversion, we applied the following post-processing sequence: (1) a temporal harmonization of the dataset, (2) GNSS referencing of the InSAR velocity field, (3) quality control of the data, and (4) horizontal-vertical decomposition of the velocity field to enhance the tectonic signal.

2.3.2.1 Harmonization of the dataset

To compare mean velocities computed over the same period, we re-estimate the mean velocities on the *FLATSIM* time series, starting from the same common date: 9th October 2016. We model the mean velocities by retrieving the linear term so that:

$$x(t) = x_R + B.(t - t_0) \tag{2.10}$$

with $x(t)$ the cumulative LOS displacement at each pixel at time t, t_0 the initial time (here 1st January 2016), x_R a constant term and B the linear trend corresponding to the mean velocity.

2.3.2.2 GNSS referencing of the interseismic LOS velocity field

I referenced the InSAR LOS velocities relative to GNSS velocities using the method described in Section 2.2.1.3. The GNSS velocity field used is a combination of data from England

et al. (2016) and Özkan et al. (2025), both relative to fixed Eurasia plate, calculated from survey and continuous measurements. The GNSS data are shown in Figure 2.15 by the green arrows.

2.3.2.3 Quality control of the InSAR processing

I applied a mask based on the number of interferograms per pixels to remove possible artifacts on the mean velocities, similar to the one described in Section 2.2.1.1. Due to the difference in the total number of interferograms per track, I estimated independent thresholds for each track, based on the standard deviation (σ) and the mean (μ) of the number of interferograms. The Table 2.2 gathers the percentage of the total kept pixels after applying the mask. The final mean velocities in LOS for the ascending and descending tracks are shown in Figure 2.14.

Tracks	*A*058	*A*131-South	*A*131-North	*D*138	*D*036-South	*D*036-North
$\mu - 2\sigma$	96.48%	93.48%	94.63%	95.26%	94.02%	95.56%
$\mu - 1\sigma$	78.98%	82.01%	88.55%	81.30%	81.06%	87.78%

Table 2.2: Percentage of total pixels kept after applying the mask based on the number of interferograms for each track.

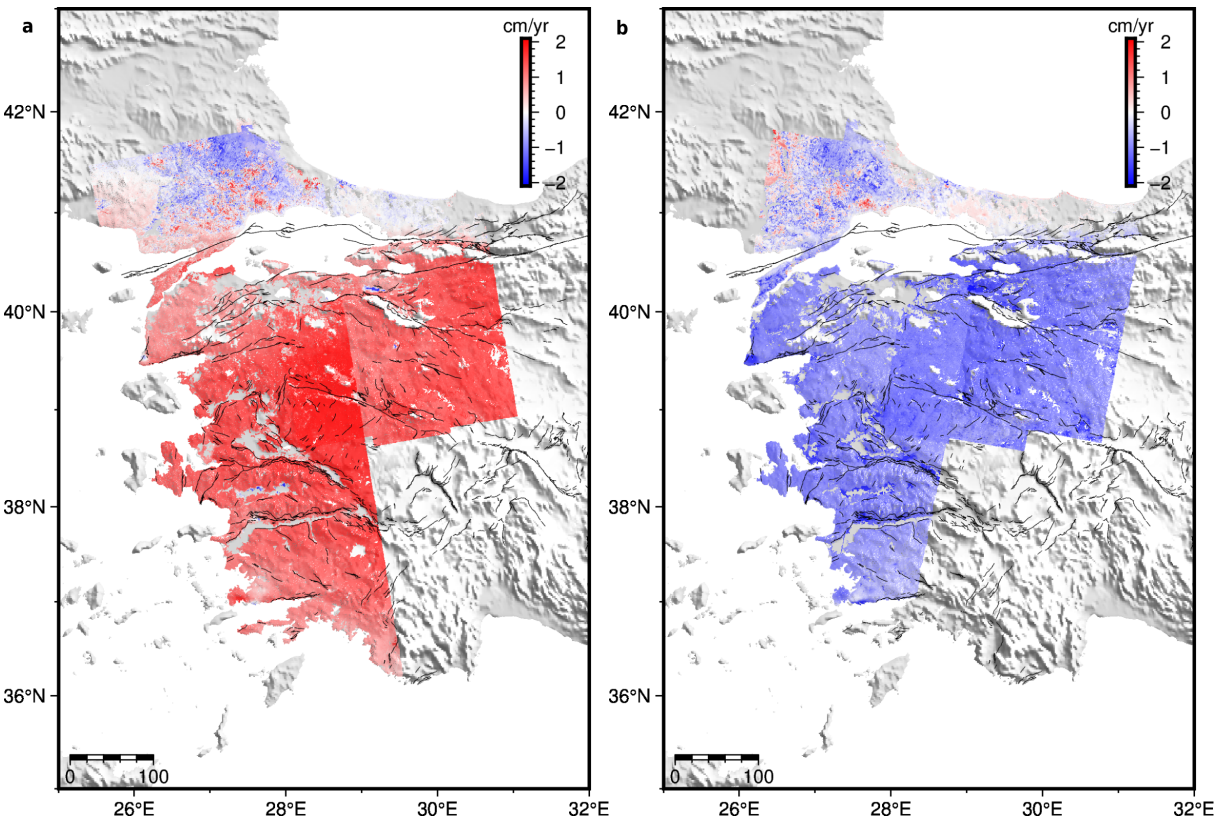

Figure 2.14: Mean velocity in LOS after GNSS referencing and the application of a mask on the number of interferograms per pixel for the (a) ascending and (b) descending tracks.

2.3.2.4 Horizontal-Vertical decomposition

To improve the inversion results, I estimate the mean East-West InSAR velocity field, allowing for the removal of local vertical effects, which are assumed to be non-tectonic. The applied method is described in Section 2.2.1.3. The results are presented in Figure 2.15.

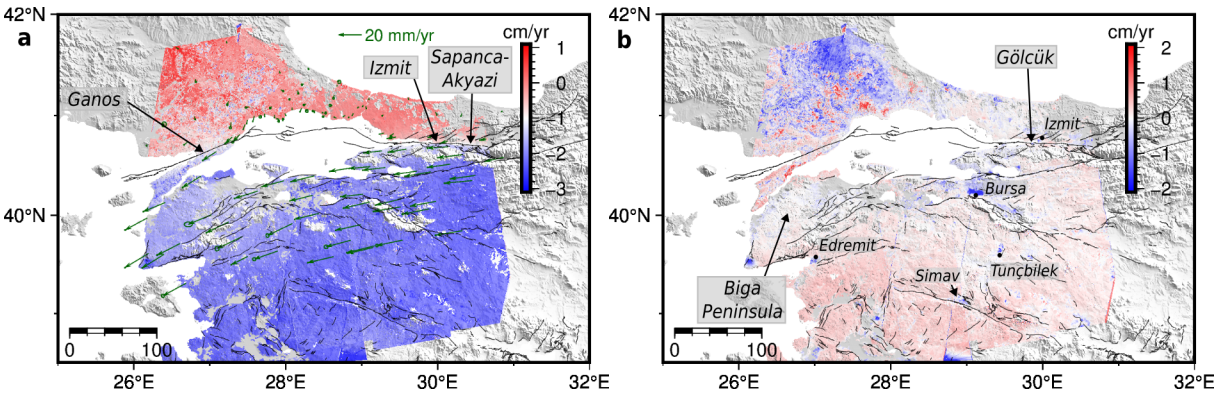

Figure 2.15: Mean (a) East-West and (b) vertical velocities over the study area. (a) The green arrows correspond to the GNSS data from Özkan et al. (2025), relative to the fixed Eurasia.

2.3.3 Results

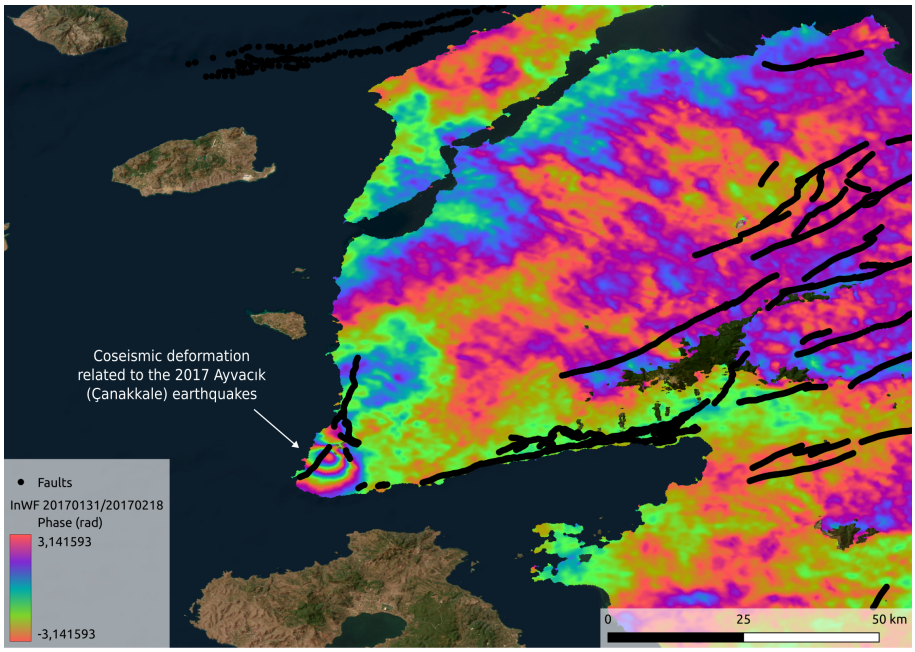

Figure 2.16: Wrapped and Filtered Interferogram (InWF) between dates 31/01/2017 – 18/02/2017 of the track *A*131 computed by *FLATSIM*. The fault network is shown by the black dots. The view is centered on the Biga Peninsula. The concentric fringes in south-west highlight seismic deformations related to the 2017 Ayvacık (Çanakkale) earthquakes.

As detailed in Section 2.2.1.2, the data within the northwestern part of the Marmara Sea are noisy due to residual phase bias, preventing any precise interpretations.

On the mean East-West velocity map (Figure 2.15a), the predominant signal is related to the NAF with a strong gradient along its main strand, consistent with the interseismic deformation accommodating the westward extrusion of the Anatolian plate (see Section 1.5.1.2). The

onshore segments of the NAF reveal a sharp gradient along the Izmit segment (east), compared to the smooth gradients observed along the Sapanca-Akyazi (east) and Ganos (west) segments.

On the mean vertical velocity map (Figure 2.15b), no vertical motion is observed in the vicinity of the NAF. However, local tectonic motions can be pointed out, such as the normal faulting close to Gölcük, and also a strong signal on the south-west of the Biga peninsula ($\approx 39.60°N, 26.40°E$). This latter is related to the seismic sequence of moderate earthquakes that affected the region in 2017 over three months (Özden et al., 2018). A southward propagation of ruptures along normal antithetic faults led to surface deformation visible within InSAR data (e.g. Ganas et al., 2018), as shown in Figure 2.16, which corresponds to a zoom on this area of an interferogram built from $31/01/2017 - 18/02/2017$ SAR images. Then, the large sedimentary basins (e.g. Edremit, Bursa, Izmit and Simav graben) are affected by subsidence with high rate, up to 5 cm/yr in Bursa (see Figure 2.11). More locally, strong signals can also be related to anthropogenic sources, e.g. the big mine at Tunçbilek/Tavşanlı/Kütahya.

2.3.4 Discussion

In this section, I present some preliminary results of slip inversions derived by Émilie Klein, which are part of a publication currently in preparation.

2.3.4.1 Contributions of the InSAR data on the slip inversions

The Figure 2.17 compares different slip inversions obtained by using different datasets: (a) GNSS, (b) InSAR, and (c) GNSS and InSAR jointly. We observe that in both GNSS and InSAR-only models, the central segment is creeping. Its slip rate and uncertainties vary, with the GNSS-only model having higher uncertainties close to the surface, whereas it is more homogeneous for the InSAR-only model. Using both datasets together (Figure 2.17c), the uncertainties decrease close to the surface. The slip rate model also reveals an increase of the slip under Izmit, thanks to the integration of InSAR data with a high spatial resolution close to the fault along this segment. It also gives more precisions at longitude 29.2°, which is poorly constrained due to the low density of GNSS data (see Figure 2.15a). The joint inversion takes advantage of the high spatial resolution of the InSAR data filling potential areas where few GNSS stations are present. It also provides good accuracy along onshore fault segments, despite the downsampling of the data before inversion, explaining that the slip does not reach the surface even if we conclude that this segment is mainly aseismically creeping (see Section 1.5.2.2).

InSAR data used as inputs in Figure 2.17 are the LOS velocity fields shown in Figure 2.14. Using ascending or descending data, the range of uncertainties of the slip models are between -24.7-11.8 mm/yr and -23.32-10.4 mm/yr respectively, i.e. of the same order of amplitude. However, the East-West and vertical decomposition of the velocity model (Section 2.3.2.4) shows a non-negligible contribution of the vertical deformation in the LOS velocity field (Figure 2.15b). Assuming pure strike-slip motion and therefore using only the East-West component of the velocity field as inputs of the joint inversion, the uncertainties are reduced to the range -11.6-9.5 mm/yr.

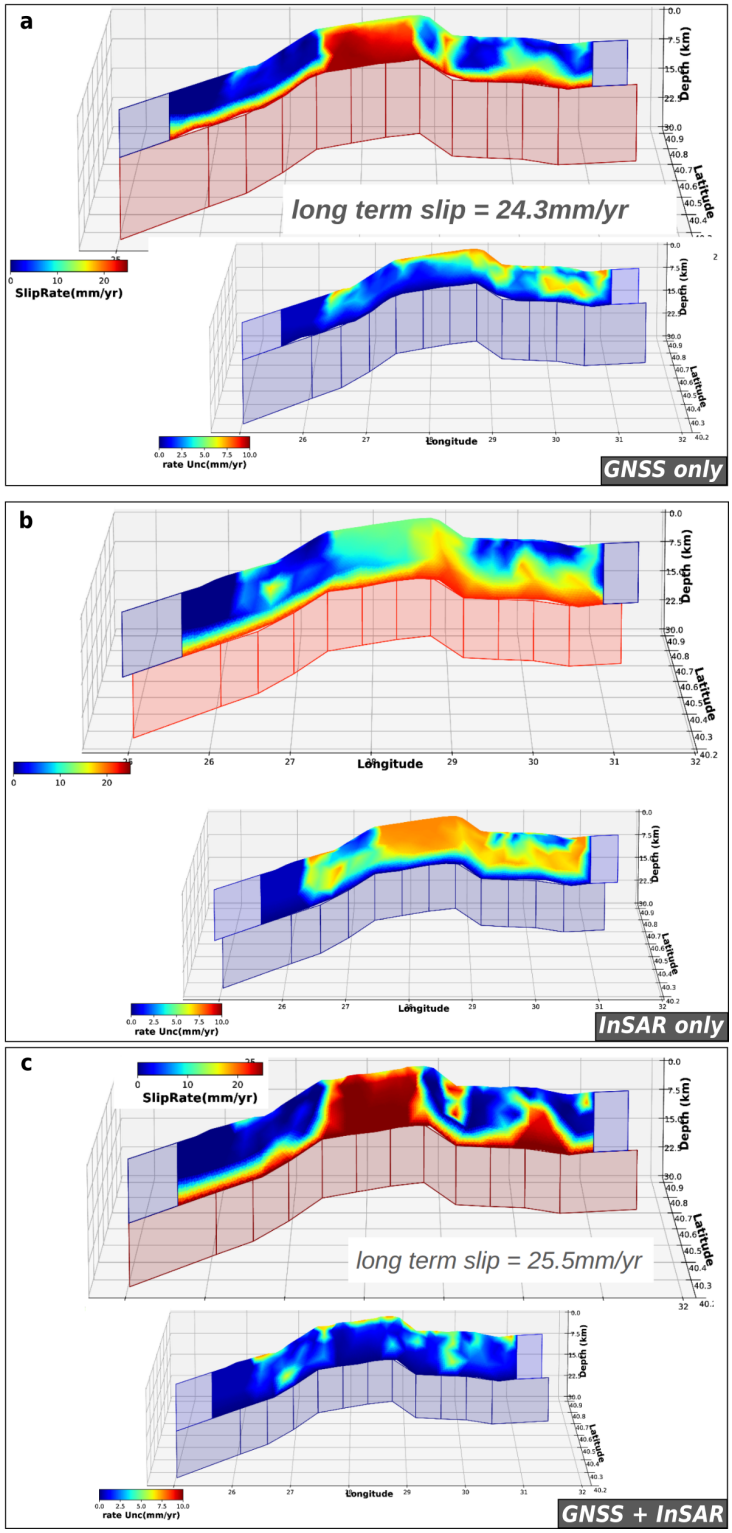

Figure 2.17: Comparison of the estimated slip rates and corresponding uncertainties obtained by using (a) only GNSS data, (b) only LOS InSAR data, and (c) GNSS and InSAR data (Klein et al., in prep.).

2.3.4.2 Remarks on the slip predictions

Using GPS data acquired over 20 *years*, Ergintav et al. (2014) showed that not all of the MMF was accumulating strain, but probably only its eastern segment (Princes Islands segment, PI) with a slip deficit of up to $10-15$ mm/yr, whereas the central segment ($\sim$ Central and Kumburgaz basins, CeB and KB) may be creeping. These observations suggest that only the

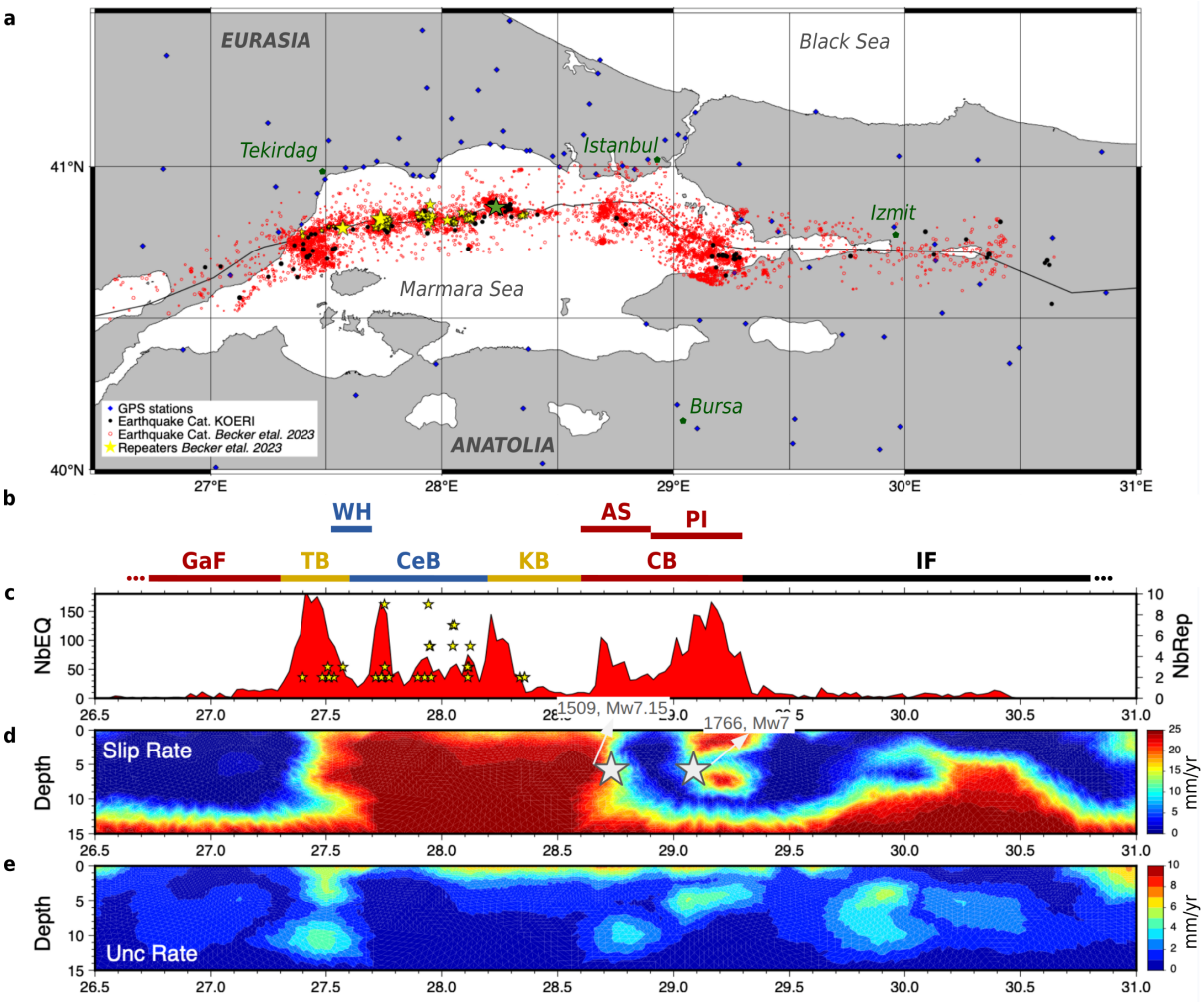

Figure 2.18: Final slip rate model compared to the seismic context (Klein et al., in prep). (a) Tectonic settings with the location of earthquakes recorded along the NAF shown by black and red dots (KOERI and Becker et al. (2023)), including repeaters shown by yellow stars. The green star corresponds to the epicenter of the 2025 M_w 6.2 earthquake. The fault trace used in the inversions is drawn by the black line. Blue dots correspond to the GNSS stations used in this study (Özkan et al., 2025). Green pentagons point out the locations of the main cities. Gray bold and names correspond to the tectonic plates, and italic ones to the seas. (b) Lengths and names of the main segments of the MMF and NAF. Segments abbreviations are: GaF: Ganos Fault, TB: Tekirdağ Basin, WH: Western High, CeB: Central Basin, KB: Kumburgaz Basin, AS: Avcilar Segment, PI: Princes Islands, CB: Çınarcık Basin, IF: Izmit Fault. Segment's colors red, orange and blue correspond to locked, transitional and creeping segments, from Becker et al. (2023). The black segment corresponds to the last rupture from the 1999 M_w 7.6 Izmit earthquake. (c) Histogram showing the number of earthquakes and of repeaters with respect to the longitude of the epicenter in red, and in yellow, respectively. (d) Slip rate model obtained by the joint inversion of GNSS and InSAR data, with both white stars highlighted the two last mainshocks which ruptured the MMF. (e) Corresponding uncertainties rates.

PI fault segment may be able to generate a $M_w > 7$ earthquake; its last rupture being in 1766 (Ambraseys, 2002).

Following this work, new studies in the last decade refined the creeping behaviors of the segments of the MMF, and the implications on the seismic hazard. Schmittbuhl et al. (2016b) proposed that the CeB segment is creeping based on the presence of repeating earthquakes.

However they interpreted the KB and CB (Çınarcık Basin) segments as locked, leading to an estimate of the magnitude of a potential future event to 7.3 on the eastern part. Creep was later confirmed by the detection of long-lasting seismic repeaters along the CB segment and within the seismogenic zone (Schmittbuhl et al., 2016a).

The use of onland geodetic data from the GPS networks can also be helpful to infer the slip distribution along the MMF interface, as proposed by Klein et al. (2017). The building of an interseismic model from a Bayesian approach led to similar interpretations, with a central segment creeping, and the Ganos Fault (GaF) and CB segments being locked. However, the sparsity of the GPS network is a limitation to the resolution of the slip model, adding the fact that the onland data are acquired far from the fault.

To overcome this issue, some studies proposed the use of acoustic ranging techniques, corresponding to seafloor geodesy, and enabling the monitoring of the horizontal deformation with a *mm*-precision over several years. These experiments concluded that the eastern edge of the KB segment is fully locked (Sakic et al., 2016; Lange et al., 2019). In contrast, Yamamoto et al. (2019) used extensometer records on a western segment of the MMF named Western High (WH) segment, and found evidence of creep, in agreement with seismic and onland geodetic data.

The 23 April 2025, a M_W 6.2 earthquake ruptured a $10-20$ *km*-long segment of the central MMF, followed by ≈ 500 aftershocks within 15 days, affecting the KB segment supposed to be a locked or transitional segment (Ertuncay et al., 2025). This new earthquake has led to a need to refine the coupling along those segments. Özkan et al. (2025) took advantage of a denser GPS network and longer data time series to update the slip rate model along the MMF. This new velocity field confirmed that the western part (GaF segment) is locked, similar to the eastern part (KB and CB segments). In order to understand the impact of the segmentation on the seismic cycle, Guvercin and Barbot (2025) proposed numerical simulations based on a 3D rheological model built using heat flow related to the sediment thickness and temperature along the fault, and laboratory-derived frictional properties. They successfully recover seismic sequences similar to historical records along the MMF. They showed that the presence of a rheological barrier within the CeB segment splits the MMF into two distinct parts with different seismic cycles: (i) creeping along the CeB, and (ii) a low probability for the MMF to fully rupture. They also suggest that the eastern part (KB and CB segments) can be affected by full or partial ruptures (such as the 2025 M_w 6.2 earthquake), with creep potentially accommodating the remaining slip deficit on the CeB segment. Finally, Martínez-Garzón et al. (2026) provided precision on the seismic cycle in the eastern part of the MMF by analyzing the seismic activity following the 2025 M_w 6.2 earthquake. They suggested an eastward propagation of ruptures by comparing the properties of the moderate events that occurred over the last two decades. This 15 *year*-long eastward migration of $M_w > 5$ earthquakes is confirmed by historical records (Ambraseys, 2002) and suggests a stress transfer closer to the edge of PI segment. In summary, all the previous studies agreed that the PI segment can host the source of a future $M_w > 7$ earthquake. The question of the slip deficit and the size of the rupture, and therefore the magnitude, is still remaining.

Along these lines, refining the slip rate model and therefore the length of the locked segment located south of Istanbul is crucial to quantify the current high seismic risk in this area. At time of writing, our final slip rate model resulting from the joint inversion of GNSS and InSAR data is presented in Figure 2.18c. The striking observation concerns the KB segment, which appears to be creeping, a behavior not captured by previous models. This result is primarily constrained by the northern coastal GNSS stations, and synthetic tests demonstrate that our dataset has sufficient resolution to resolve the slip behavior on this segment. If confirmed, this implies that the locked segment is smaller than previously estimated, though our

model still suggests a significant risk of a large earthquake offshore Istanbul, with a maximum magnitude of M_w 7 – 7.3.

2.3.5 Conclusion

This on-going study provides insights on the seismic hazard along the Main Marmara Fault in Türkiye. The joint analysis of the interseismic velocity field built from GNSS and InSAR data takes advantage of both the high spatial resolution of the InSAR data and the high accuracy of the GNSS velocity measurements. The slip inversion shows that the central segment is creeping, in contrast to the surrounding segments, which are locked. The length of the creeping segment is ~ 133 *km*-long. The related uncertainties and tested forward modeling indicate that the data robustly resolve the slip behavior along this segment. We still note a strain accumulation of up to ~ 10 mm/yr in to the shallow part, which can generate moderate earthquakes ($M_w \sim 5$). The eastern segment close to Istanbul and the Princes Islands is locked down to ~ 12 *km*-depth, and has accumulated sufficient strain to potentially produce a $M_w > 7$ earthquake.

Chapter 3

Automated Detection of Slow Slip Events from InSAR: Application to the North Anatolian Fault

In the previous section, we have seen that the InSAR data processed in the framework of the *FLATSIM* project from *Sentinel-1* SAR images based on the NSBAS processing chain and over the period $2016 - 2021$ allows us to produce a precise steady-state East-West velocity field with an unprecedented high spatial resolution. This work points out lateral variations of the creep dynamics along the whole NAF from fully locked segments to aseismically creeping segments. Previous studies highlighted in Section 1.5.2.2 identified slow slip events (SSEs) along those creeping segments. Looking at details in our data, we aim to identify new or known SSEs. However InSAR time series contain distinct contributions as presented in the Section 1.4, and therefore a post-processing sequence may be needed in order to extract the tectonic signal.

After the application of a simple and basic post-processing sequence, I propose here an automatic method to detect SSEs from InSAR data without any prior knowledge. This method has been adapted from the initial one developed for GNSS time series by Rousset et al. (2017). It correlates physics-based dislocation slip models representing synthetic SSEs with InSAR time series to detect transient deformation signals and estimate their first-order spatio-temporal characteristics (e.g., location, initiation time and equivalent magnitude). First, this method is calibrated using synthetic tests including InSAR realistic noise, and then applied to real data centered on two aseismically creeping segments of the NAF: Izmit and Ismetpasa. Synthetic tests including InSAR realistic noise provided probabilistic detection thresholds as a function of SSE magnitude and depth. These tests show that this method enables the detection with ≥ 90 % confidence of shallow SSEs with magnitudes larger than 4.5 using horizontal East-West InSAR time series. Events with magnitude larger than 4.25 are detected with ≥ 45 % confidence. Second, applying this method to InSAR data along both creeping segments of the NAF, we detected without any prior knowledge three previously reported transient events along Izmit and two ones along Ismetpasa. The estimated magnitudes range from 4.0 to 4.5. Despite the level of noise within the InSAR time series, the detection tests performed using the geodetic matched filter approach demonstrate strong potential for the systematic detection of transient slow slip signals. Applying this method on worldwide strike-slip fault segments could enable rapid detection and a first order characterization of transient slip events.

This chapter is an article submitted in *JGR: Solid Earth*, and has been published as a Preprint:

Neyrinck, E., Rousset, B., Doubre, C., Rivera, L. (2026). *Automated Detection of Slow Slip Events from InSAR: Application to the North Anatolian Fault.* Preprint. https://doi.org/10.31223/X5K77R.

Abstract

The growing volume of InSAR time series offers new opportunities to systematically detect transient aseismic deformation, but identifying low-amplitude slow slip events (SSEs) remains challenging due to noise and limited temporal resolution. Here, we adapt the geodetic matched filter, originally developed for GNSS data, to InSAR displacement time series in the context of shallow strike-slip faults. The method relies on correlations between physics-based templates and relative displacement time series constructed between pixels located on either side of the fault, enhancing the signal-to-noise ratio and mitigating atmospheric artifacts. Using synthetic experiments with realistic noise, we quantify detection thresholds and show that SSEs with magnitudes as small as M_w $4-4.5$ can be reliably detected at shallow depths. A validation strategy based on spatial coherence and weighted stacking of displacement time series significantly reduces false detections. We apply this approach to the Izmit and Ismetpasa segments of the North Anatolian Fault using multi-level processed InSAR datasets. The method successfully retrieves previously documented SSEs and shows that advanced post-processing improves detection capability. Detected events have magnitudes M_w $4.0-4.3$, shallow depths ($<$ $2-4$ km), and durations of days to weeks, consistent with independent geodetic observations. These results demonstrate that physics-based template matching provides a robust and scalable framework for automatic SSE detection in InSAR time series.

Keywords: slow slip events, North Anatolian Fault, SAR interferometry, strike-slip fault



- We developed a geodetic matched filter approach on InSAR data that enables to detect shallow slow slip events along strike-slip faults.
- Based on synthetic tests, it can detect shallow events larger than M_w 4.5 with 90 % confidence using horizontal East-West time series.
- Application along creeping segments of the North Anatolian Fault validates the method by detecting and characterizing five slow slip events.

Contents

3.1 Introduction . . . 112
3.2 Method . . . 114
3.2.1 Method's inputs . . . 114
3.2.1.1 Analysis of realistic noise . . . 115
3.2.1.2 Definition of a template . . . 115
3.2.2 Module 1: Detection of synthetic slow slip events . . . 116
3.2.2.1 Building the synthetic data . . . 116
3.2.2.2 Correlation functions . . . 116
3.2.2.3 Thresholds estimates . . . 118
3.2.3 Module 2: Real data peak detection . . . 119
3.2.3.1 Validation of the detections . . . 119
3.2.4 Module 3: Characterization of the events . . . 121
3.2.4.1 Location of the events . . . 122
3.2.4.2 Initiation time and relaxation time . . . 122
3.2.4.3 Magnitude . . . 122
3.3 Application to the North Anatolian Fault . . . 123
3.3.1 Tectonic context and InSAR data processing . . . 123
3.3.2 Application to the Izmit segment: influence of InSAR post-processing 123
3.3.3 Application to the Ismetpasa segment . . . 125
3.4 Discussion . . . 127
3.4.1 Validation of the approach and assumptions . . . 127
3.4.2 Comparison with independent geodetic observations along the NAF . 128
3.4.2.1 Izmit segment . . . 128
3.4.2.2 Ismetpasa segment . . . 129
3.4.2.3 Synthesis across techniques . . . 129
3.4.3 Slow slip events physical mechanisms . . . 130
3.4.3.1 Structural and mechanical controls on shallow SSE occurrence 130
3.4.3.2 Role of pore-fluid pressure . . . 130
3.4.3.3 Moment-duration scaling . . . 131
3.4.3.4 Implications for continental fault mechanics . . . 131
3.5 Conclusion . . . 132

3.1 Introduction

Since the first observations of aseismic creep along the San Andreas Fault (SAF) by Steinbrugge et al. (1960), numerous observations have been made worldwide, refining our understanding of the seismic cycle and its implications for seismic hazard estimates (Avouac, 2015). Due to the increase in geodetic measurements and improvements in their temporal resolution, the intermittent occurrence of aseismic slip has been documented in several tectonic contexts, including subduction zones and strike-slip faults (Bürgmann, 2018). In subduction zones, large transient slow slip events (SSEs) of M_w up to 7.5 and producing up to several centimeters of surface displacement, are mostly detected with Global Navigation Satellite System (GNSS) observations (Dragert et al., 2001), although strainmeters (Hawthorne and Rubin, 2013) and tiltmeters (Hirose and Obara, 2005) can also capture them. Along strike-slip faults, most observed SSEs occur in the shallow parts of faults, producing surface deformation footprints only a few kilometers wide with centimetric displacements. Whereas creepmeters can detect SSEs with millimeter-scale offsets at specific locations (Linde et al., 1996; Bilham et al., 2016), Interferometric Synthetic Aperture Radar (InSAR) time series have also proven valuable for detecting shallow SSEs along strike-slip faults (e.g. Rousset et al., 2016; Materna et al., 2024).

Developing automatic - or quasi-automatic - methods for SSE detection along strike-slip faults is essential to cope with the rapidly growing volume of InSAR measurements and to densify worldwide SSE catalogs. Several approaches have been proposed to extract transient deformation in geodetic data, including deformation due to SSEs.

Given that transient SSEs produce permanent offsets in displacement time series observed at the surface, one way to detect them is to use data-driven methods, searching for steps in geodetic time series. Nishimura (2014) scanned moving windows of GNSS time series in Nankai and fitted each segment either with a linear trend or with a linear trend plus an offset associated with potential SSEs. The preferred model was then selected using the Akaike Information Criterion (AIC, Akaike (1974)), allowing a statistical evaluation of the robustness of the models.

Principal Component Analysis (PCA) is also commonly used to separate distinct deformation sources within geodetic data. It assumes that the different physical processes contributing to the signal are orthogonal and can therefore be separated into a small number of dominant eigenmodes. This method has been widely applied to geodetic time series to highlight tectonic transients superimposed on long-term trends or seasonal components (e.g. Kositsky and Avouac, 2010).

Other decompositions are based on Singular Spectrum Analysis (SSA) and its multichannel extension (M-SSA). These techniques decompose time series into periodic signals, trend, and noise components while accounting for temporal correlations, making them particularly suited to extract repeating processes such as seasonal signals. Their ability to recover smooth transient signals from InSAR time series has been demonstrated in various contexts. For instance, Jasir et al. (2024) used SSA to isolate the post-seismic deformation of the 2019 M_w 6 Mirpur earthquake, while Walwer et al. (2025) applied M-SSA to identify volcanic deformation transients at Pacaya volcano.

A more flexible decomposition is provided by Independent Component Analysis (ICA) and its probabilistic variants such as variational Bayesian ICA (vbICA, Gualandi et al., 2016). Unlike PCA, ICA aims to separate statistically independent, non-Gaussian sources, making it particularly effective when deformation processes are not orthogonal. Maubant et al. (2020) used ICA on InSAR time series to extract the transient signal associated with the 2017–2018 Guerrero

SSE in the Mexico subduction zone. Similarly, Gualandi and Liu (2021) showed that vbICA can robustly separate tectonic loading from seasonal hydrological deformation in InSAR time series in the San Joaquin Valley and the central San Andreas Fault.

Finally, sparse-representation methods assume that transient deformation can be captured by a sparse set of basis functions. The approach of Riel et al. (2014), based on sparse B-spline coefficients, automatically identified repeating SSEs of varying duration in GNSS time series along the Cascadian subduction zone.

A second group of methods used to detect and extract transient deformation within geodetic data is based on physical models of SSEs. The network inversion filter, proposed by Segall and Matthews (1997), models GNSS displacement time series as a combination of secular velocities, fault slip, benchmark motions, reference frame errors, and estimation errors. It uses a Kalman filter to provide a stochastic description of these components over time, allowing for the separation of transient slip signals from background noise. It provides a kinematic modeling of large SSEs. By adapting the method to InSAR data, Bekaert et al. (2016) analyzed the 2006 SSE in Guerrero, Mexico.

Another approach specifically designed to detect and characterize small-amplitude SSEs is based on correlations between synthetic dislocation-based time series and continuous GNSS data (Rousset et al., 2017). Using a network-based method, it allows the extraction of coherent slow slip surface deformation patterns and provides estimates of the main SSE parameters. The first application was on the Mexican subduction zone (Rousset et al., 2017), and subsequent applications have been performed in various tectonic contexts, including the San Andreas Fault (Rousset et al., 2019a), the Nankai subduction zone (Okada et al., 2022), the northern Japan subduction zone (Marill et al., 2024), the South-Central Alaska subduction zone (Okada and Nishimura, 2023), and the southern Peru–northern Chile subduction zone (Jara et al., 2024).

More recently, deep learning approaches have been applied to denoise geodetic time series to better highlight transient deformation signals (Rouet-Leduc et al., 2021; Costantino et al., 2024). These models are trained on synthetic time series that include realistic noise and SSEs and are then applied to different tectonic contexts. Rouet-Leduc et al. (2021) applied such a method to the Ismetpasa segment of the North Anatolian Fault (NAF) in Türkiye, which allowed the extraction of surface deformation due to a known SSE affecting in 2013 (Rousset et al., 2016). Similarly, Costantino et al. (2024) applied this approach to GNSS time series and recovered denoised signals highlighting transient deformation potentially associated with low-amplitude SSEs.

In this study, we adapt the geodetic matched filter, originally developed for GNSS observations (Rousset et al., 2017), for application to InSAR observations in the context of strike-slip faults. Indeed, this method takes advantage of the redundancy of information collected at multiple locations to reduce the detection threshold for low-amplitude SSEs. Given the high spatial density of InSAR observations, it therefore has the potential to detect low-amplitude events compared to the noise amplitude. First, we consider relative displacement time series between pixels located on either side of the fault to mitigate large-scale atmospheric propagation delays. Second, we analyze the noise characteristics of the InSAR time series to construct synthetic time series with realistic noise, which allows us to assess the limitations of our method and to estimate correlation coefficient thresholds for the detection of potential SSEs. Third, following detection, we characterize the main features of the identified SSEs, including their duration and magnitude. Finally, we apply this method to two creeping segments of the NAF, where such events have been documented in previous studies.

3.2 Method

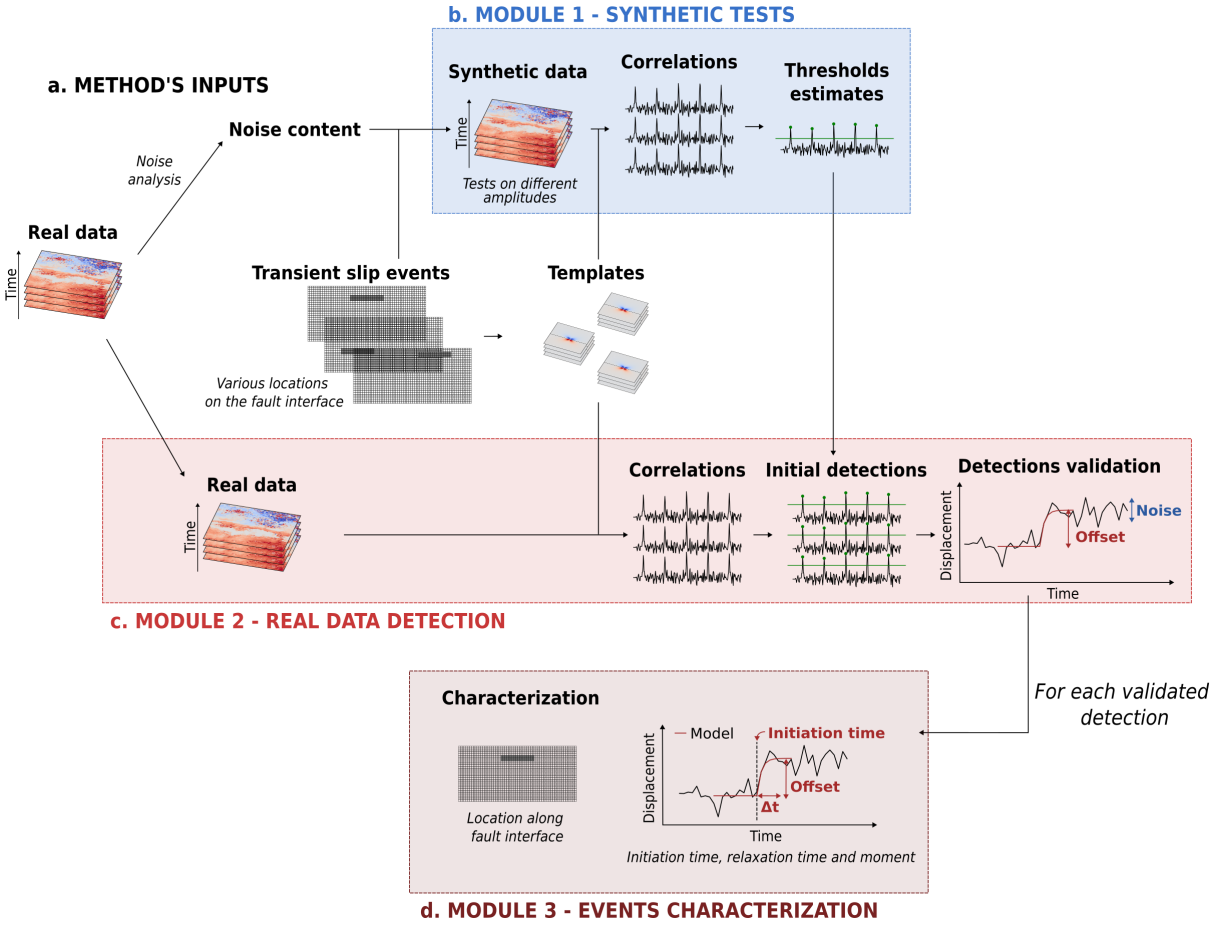

Figure 3.1: Flow chart presenting the main steps of the method. (a) Method's inputs including analysis of the InSAR noise and construction of the templates. (b) *Module 1*: analysis on synthetic data to determine detection thresholds for SSE identification. (c) *Module 2*: Processing workflow applied to real data, including initial detections and validations. (d) *Module 3*: estimation of the main characteristics of the detected SSEs from real data.

The geodetic matched filter approach developed by Rousset et al. (2017) is based on physics-based template matching. It enables the detection of SSEs on fault zones by analyzing correlation coefficients between time series of surface displacements derived from geodetic data and templates, corresponding to synthetic dislocation models of SSEs. The main phases of the approach presented in Figure 3.1 are: (a) the preparation of the inputs of the method, (b) the analysis of synthetic time series including realistic noise and synthetic SSEs to estimate detection thresholds, (c) the application to real data to detect potential SSEs with a detections validation step, and (d) the characterization of the SSEs in terms of initiation time and slip amplitude on the fault interface.

3.2.1 Method's inputs

In this section, we explain the preliminary steps of the method shown in the Figure 3.1a, leading to the preparation of the method's inputs.

3.2.1.1 Analysis of realistic noise

To build synthetic displacement time series allowing for thresholds estimates before, we need to analyze the noise content present within the real InSAR displacement time series (Figure 3.1a). We made the analysis on Line Of Sight (LOS) and East-West (EW) displacement time series, in order to estimate the impact of the noise level on the detectability of the method and evaluate the benefits of post-processing methods.

We assume that the InSAR noise is spatially correlated but temporally uncorrelated, as atmospheric dynamics typically evolve much faster than the revisit period of Sentinel-1 acquisitions. Spatially correlated noise is generated by filtering white Gaussian noise in the Fourier domain so that its power spectrum follows a negative power-law. Three parameters are estimated from noise extracted from real InSAR time series: (1) the slope of the power spectrum, (2) the mean noise amplitude, and (3) its standard deviation. The slope of the power spectrum is estimated by fitting a linear function in log-log space, which characterizes the spatial correlation of the noise. The mean and standard deviation of the noise amplitude observed in real data are then used to define parameter distributions, ensuring that the synthetic noise reproduces the dispersion within the synthetic data. Histograms representing the distributions of each parameter derived from the real data are shown in Appendix B (Figures B.1 and B.2).

3.2.1.2 Definition of a template

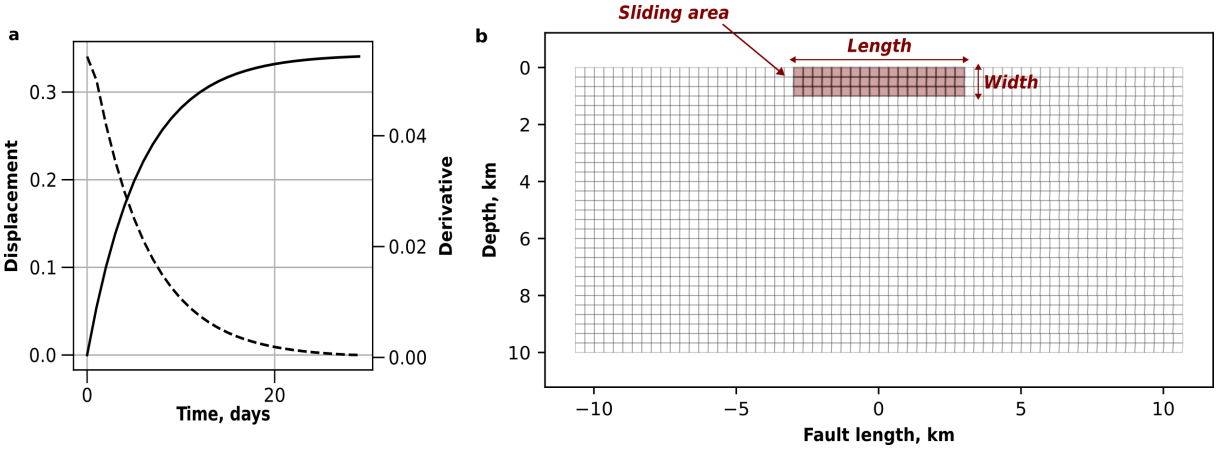

Figure 3.2: Synthetic template corresponding to surface displacements induced by a sliding area on the fault interface. (a) Relative time series (solid line) of the template computed for the pair of pixels shown in Figure 3.3a, assuming a relaxation time of 6 *days*. The dotted line corresponds to its temporal derivative. (b) Mesh of the fault interface, with the sliding patches used to build the template shown in red. The fault is meshed with patches of $0.33\ km \times 0.33\ km$, from the surface down to 10 *km*.

The temporal source function s of synthetic SSEs is defined based on creepmeter measurements on the Izmit segment (Figure B.3):

$$s(t_1) = m(1 - e^{-\frac{t_1}{\tau}}) \tag{3.1}$$

with s the cumulative slip, m the slip amplitude, t_1 the time and τ the relaxation time. The duration of events is estimated by 5τ. The template displacement time series w^i is then obtained by using the following equation:

$$w^i(t_1) = w^i_s.s(t_1) \tag{3.2}$$

with w_s^i the surface displacement at pixel i deduced from static Green's functions.

An example of a template time series and its temporal derivative is shown in Figure 3.2a. To reduce spurious detections associated with short-lived spikes, the template displacement time series defined in equation 3.2 is extended by adding two constant plateaus before and after the transient signal. Each plateau corresponds to a constant value with a duration comparable to that of the transient event. Green's functions, relating slip on a given fault patch to surface displacement, are computed assuming a multi-layered elastic half-space (Zhu and Rivera, 2002), using local velocity and density models for the Izmit and the Ismetpasa segments (detailed in Figure B.4, Özalaybey et al. (2011); Laske et al. (2013); Rousset et al. (2016); Karabulut (2025)). An example of the mesh of the fault interface is shown in Figure 3.2b.

3.2.2 Module 1: Detection of synthetic slow slip events

The following parts explain the steps of the *Module* 1 shown in the Figure 3.1b, leading to the analysis on synthetic displacement time series.

3.2.2.1 Building the synthetic data

We use the real InSAR noise characteristics (Section 3.2.1.1) to build synthetic displacement time series cubes. To sample the full range of parameter combinations according to their associated probabilities in the synthetic time series, parameters are randomly drawn from these empirical distributions. To mitigate residual atmospheric signals present within InSAR displacement time series, we decided to use relative displacement time series between all pairs of pixels located on either side of the fault. It has the advantage to remove similar amplitudes of the residuals at nearby pixels and to enhance the tectonic signal by taking pixels on either side of the fault. The relative surface displacement between the pair of pixels i and j noted $w^{i,j}$ is estimated by:

$$w^{i,j}(t_1) = w^i(t_1) - w^j(t_1) \tag{3.3}$$

The final synthetic displacement time series cubes are constructed by combining realistic noise with one or several synthetic SSEs using equation 3.3. Examples of synthetic time series are presented in Figure 3.3 – a,b,c,d, with panel 3.3d showing the relative displacement time series (in black) between two displacement time series from a pair of pixels on either side of the fault (panel 3.3c).

We also decimate the initial pixels using an exponential relationship with the distance from the fault for the Izmit segment and a quadratic one for Ismetpasa (smaller study area), to decrease the number of pixels, as shown by the black dots in Figure 3.3 – a,b. We will show the influence of decimation on our results in the next part (see section 3.2.2.2).

3.2.2.2 Correlation functions

The correlation functions $C^{i,j}$ used to detect the SSEs are computed between the template relative displacement time series $w^{i,j}$ and the InSAR relative displacement time series $d^{i,j}$ of each pair of two pixels i and j located on either side of the fault. As described by Rousset et al.

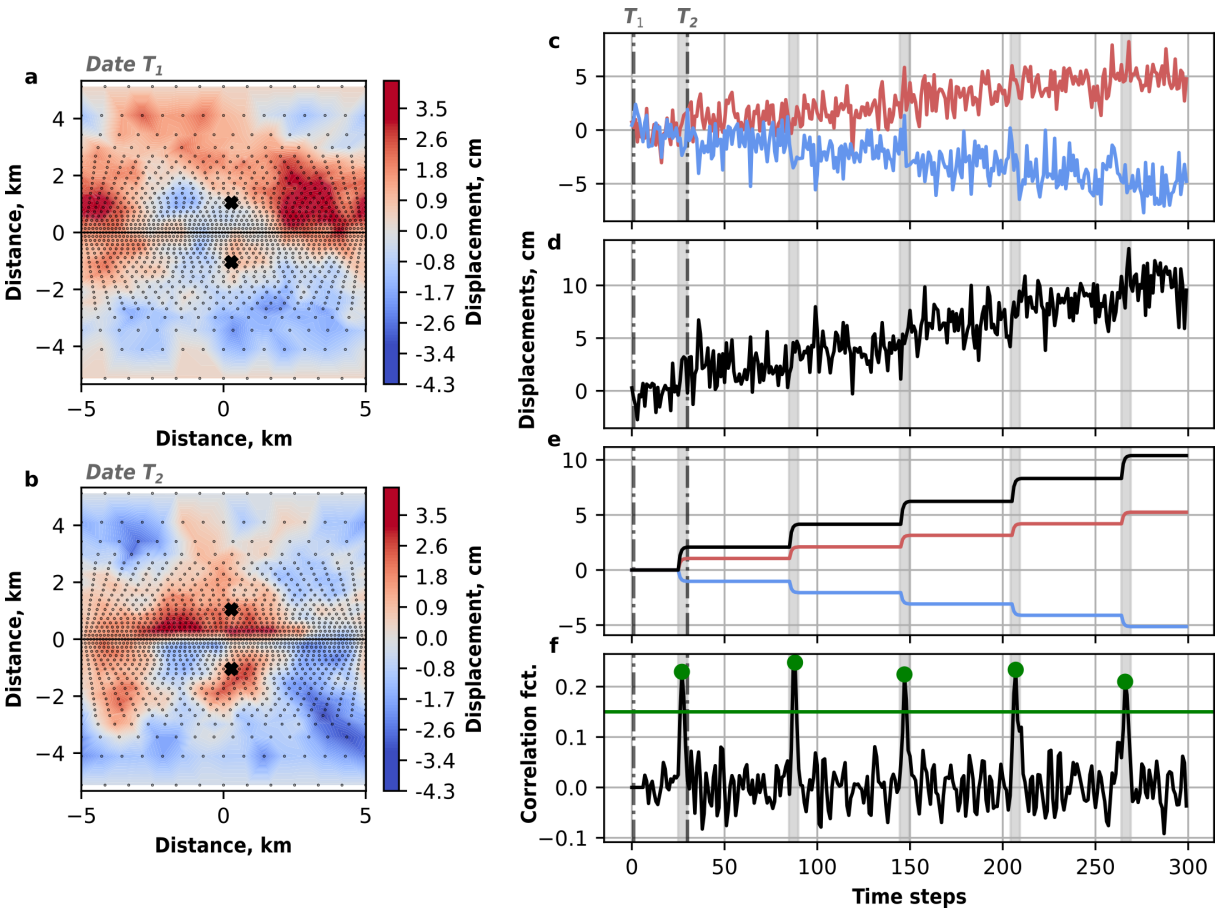

Figure 3.3: Examples of synthetic InSAR time series and correlation functions. (a,b) Synthetic cumulative surface displacement fields including (a) only realistic synthetic noise at a date T_1 and (b) realistic noise and a SSE located in the middle of the fault trace (shown in black) at a date T_2. SSEs are built using a sliding patch of 6 *km*-length and 1 *km*-width, centered at a depth of 0.67 *km*, with a magnitude of 4.55. Black dots indicate pixel locations after decimation. (c) Synthetic time series for the two pixels marked by black crosses in panels (a, b), located on either side of the fault. The blue curve corresponds to the northern pixel and the red curve to the southern pixel. (d) Relative time series obtained by differencing the two time series shown in (c). (e) Synthetic SSE templates inserted into the time series, for the two pixels and for their relative time series. (f) Correlation functions associated with the sliding patch used to build the synthetic SSEs. The green line and dots show the detection threshold and the detected peaks, respectively. (c-f) Thick gray vertical lines correspond to the occurrence and duration of the synthetic SSEs added to the time series. Vertical dash-dotted lines indicate the two dates used to plot the maps (a,b).

(2017), we use the temporal derivative of $w^{i,j}$ (Figure 3.2a) and $d^{i,j}$ so that:

$$C^{i,j}(t) = \frac{< \dot{w^{i,j}}(t_1), \dot{d^{i,j}}(t_2) >_{N,\Delta t}}{\sqrt{< \dot{w^{i,j}}(t_1), \dot{w^{i,j}}(t_1) >_{N,\Delta t} < \dot{d^{i,j}}(t_2), \dot{d^{i,j}}(t_2) >_{N,\Delta t}}} \tag{3.4}$$

with N the number of time steps of the template ($N = ||t_1|| = ||t_2||$) and Δt the temporal sampling. $< w^{i,j}(t_1), d^{i,j}(t_2) >_{N,\Delta t}$ the inner product is defined as:

$$< w^{i,j}(t_1), d^{i,j}(t_2) >_{N,\Delta t} = \sum_{k=0}^{N-1} w^{i,j}(t_1 + k\Delta t) d^{i,j}(t_2 + k\Delta t). \tag{3.5}$$

The correlation is then weighted by the amplitude of the Green's function at each pair of pixels (i, j):

$$C_w^{i,j}(t) = (|w_s^i|.|w_s^j|)C^{i,j}(t). \tag{3.6}$$

A more important weight is given to pixels that are supposed to be the most affected by the SSE.

Finally, the correlation coefficients used for SSE detections are the mean average of all $C_w^{i,j}$ computed for every pair of pixels (i, j). An example of correlation coefficients are shown in Figure 3.3f.

Comparison of the maximum values of the correlation functions estimated for the same displacement time series cube one shallow slow slip event (SSE) (depth 500 m – M_w 4.8) and a realistic InSAR noise but applying different decimation ratios shows that the correlation values are similar ($\pm$ 0.035), however it enables to significantly reduce the computation time by $\sim 96\%$ (see Figure B.5).

3.2.2.3 Thresholds estimates

The occurrence of potential SSEs in the data is highlighted by high values of the correlation coefficients, relative to a given threshold. An example is shown in green in Figure 3.3f. To estimate the optimal thresholds and to analyze the sensitivity of the method, we first use synthetic displacement time series built in the previous section (Section 3.2.2.1). We use a synthetic displacement time series cube composed of 100 events over a period of 6000 time steps. Each synthetic SSE has a slip area of ~ 6 km in length and ~ 1 km in width, with a relaxation time of ~ 6 $days$. These parameters have been calibrated according to the characteristics of observed shallow SSEs reported in previous studies (Rousset et al., 2016; Neyrinck et al., 2024; Özdemir et al., 2025). The influence of both the template area and the relaxation time on the correlation functions is analyzed in the Appendix B: a template length that is twice as long or twice as short as the real SSE length decreases the correlation coefficient by ~ 2 (Figure B.6); a relaxation time that is too long will both decrease the correlation coefficient and shift the detection in time (Figure B.7).

To analyze the reliability of the detections on synthetic displacement time series, we compute the precision-recall product PRP, defined as:

$$PRP = \frac{TP}{AP}.\frac{TP}{RP}, \tag{3.7}$$

with TP corresponding to the true positive detections (i.e. the number of detections corresponding to synthetic SSEs added to the displacement time series), RP the real positive detections (i.e. the initial number of SSEs in the synthetic displacement time series) and AP all the positive detections (i.e. true and false positive detections). PRP lies between 0 and 1, with $PRP = 1$ indicating that all the SSEs in the synthetic displacement time series are detected, with no false detection. The first ratio TP/AP estimates the fraction of true detections (i.e. the precision), while the second ratio TP/RP estimates the number of detected events relative to the number of events in the time series (i.e. the recall). This product is estimated by combining all the detections associated with the ensemble of fault patches along the fault interface. Figure 3.4 – a,b shows PRP as a function of the selected threshold for two given depths of the synthetic SSEs. By using this precision-recall product, we can estimate the minimum magnitude of the events that can be detected by this method as a function of the depth of the synthetic SSEs, and the corresponding threshold for a given $PRP \geq p$, with p representing the confidence of the detections. The final results for this synthetic displacement time series with

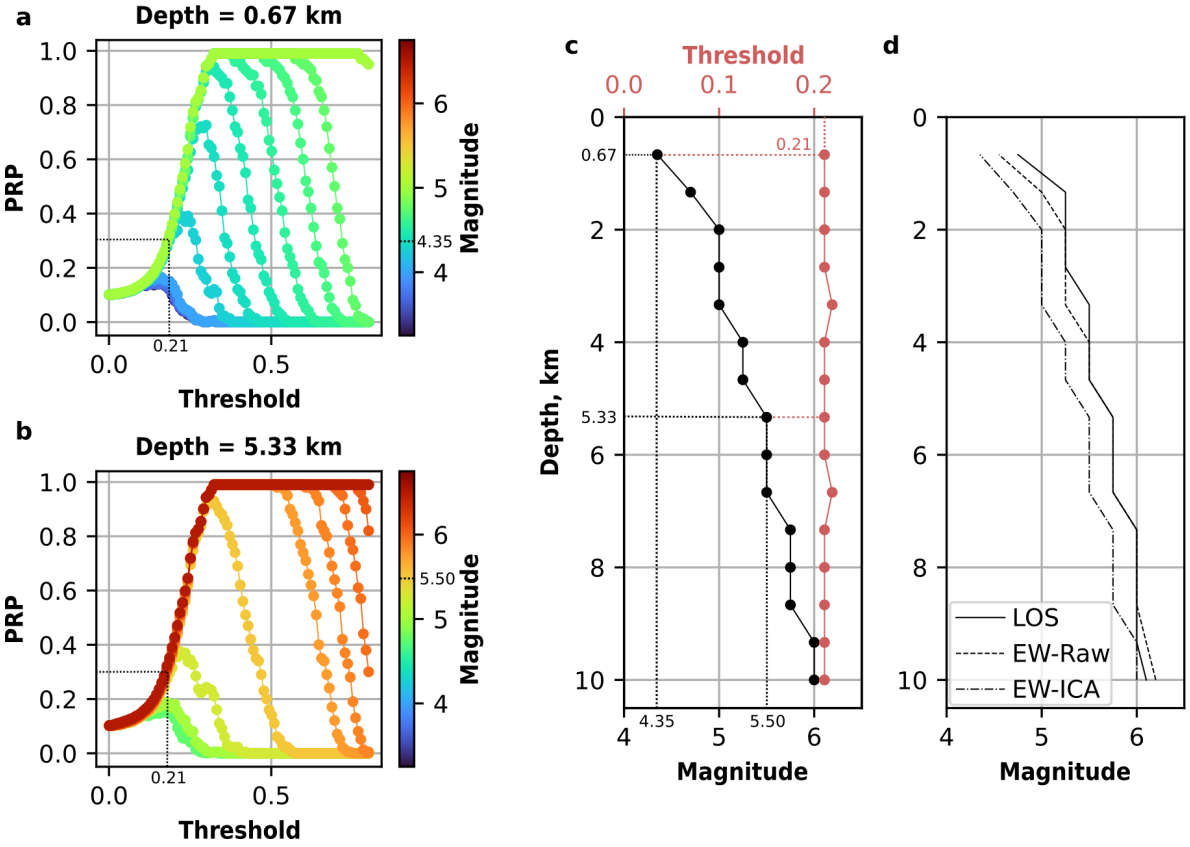

Figure 3.4: Precision-recall products (*PRP*) estimated for various synthetic SSE depths and event magnitudes, compared to the thresholds used for the detection. (a,b) *PRP* obtained for events at depths of 0.67 *km* (a) and 5.33 *km* (b). Each colored line corresponds to a given magnitude. (c) Minimum detectable magnitudes (black) and associated thresholds (pink) for $PRP \geq 0.4$ as a function of depth. The dotted lines show the selected minimum magnitude and threshold corresponding to $PRP \geq 0.4$ at both depths shown on panels (a,b). (d) Comparison of the minimum magnitudes estimated using synthetic noise from three different datasets: LOS (solid line), EW-Raw (dotted line) and EW-ICA (dash-dotted line).

$PRP \geq 0.4$ are shown in Figure 3.4c. By applying these thresholds to the correlation functions, we detect potential SSEs.

3.2.3 Module 2: Real data peak detection

The following parts explain the steps of the *Module* 2 shown in the Figure 3.1c, leading to the detection of SSEs with the real InSAR displacement time series. Some parts have already been explained in the previous section (Section 3.2.2).

3.2.3.1 Validation of the detections

In order to detect small magnitudes SSEs, we need to choose a relatively low *PRP* to decrease the minimum magnitudes of SSEs detectable using this approach (Figure 3.4c) and according to the InSAR noise present in the data (Figure 3.4d – test of three different types of noise). Therefore, we define two conditions tested beforehand using synthetic displacement time series, that allow us to select the detections obtained from the correlation functions, and

remove false detections due to the choice of a low *PRP*.

The first condition is based on the number of neighboring sliding patches triggering a positive detection. Due to the difference between the synthetic SSE sliding patch size and the discretizations of the fault interface (areas of 0.33 x 0.33 km^2), a SSE must be detected on several neighboring sliding patches in the horizontal direction. We therefore discard detections associated with a single horizontal sliding patch.

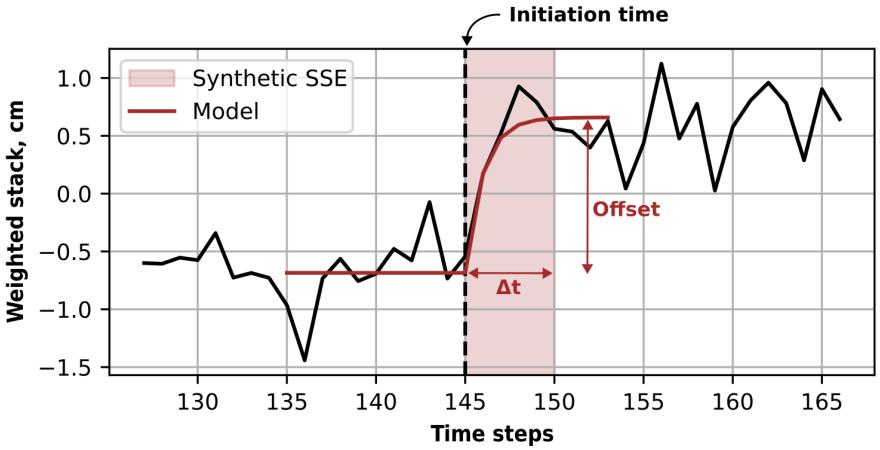

Figure 3.5: Example of a weighted stack (black line) of synthetic displacement time series including an SSE of M_w 4.65, located at 0.67 *km*-depth. The red rectangle shows the duration of the synthetic SSE. The red curve corresponds to the model obtained during the characterization step, allowing the estimate of the initiation time (dotted line), offset and relaxation time (related to the duration Δt).

The other condition is based on a weighted stack of displacement time series at each pixel centered on the detection time. The aim of the stack is to enhance the signal-to-noise ratio by stacking the raw displacement time series, weighted by the Green's functions w_s^i associated with the template that exhibits the maximum correlation coefficient. An example of a synthetic stacked time series is shown in Figure 3.5. The offset associated with the SSE is related to the source slip and the slipping area. To validate the detection, we compute the offset by taking the difference between the averages over $6-months$ time windows before and after the detection. We validate the detection if this offset is larger than the standard deviation of the stacked time series computed on a period of 5 *months* centered on the detection.

Figure 3.6 – a,b shows the effect of the validation for two synthetic displacement time series including SSEs at two distinct depths, with $PRP \geq 0.4$. It shows that the validation step allows to separate well true positive detections from true negative ones. Some false positive detections remain, usually corresponding to low offset amplitudes.

Figure 3.6d shows TP/RP and TP/AP ratios before and after the validation step, obtained with different initial *PRP* values for synthetic SSEs located at 0.67 *km*-depth (Figure B.8 presents a similar figure for the Ismetpasa configuration). The TP/AP ratio (in green) is significantly improved by the validation step for low *PRP*. We also observe a decrease in the TP/RP ratio (in blue), which is important for $PRP = 0.1$ and of approximately ~ 0.1 for larger *PRP*. This can be explained by the fact that for low *PRP*, the tested magnitudes are lower (as shown by panel 3.6c), leading to SSE offsets that are close to the noise level.

In order to maximize the probability of capturing SSEs while maintaining a confidence of getting true positive detections larger than 0.9, we chose an initial $PRP \geq 0.4$ for the real InSAR data, corresponding to $TP/RP \geq 90\%$ at the minimum detectable magnitude. The val-

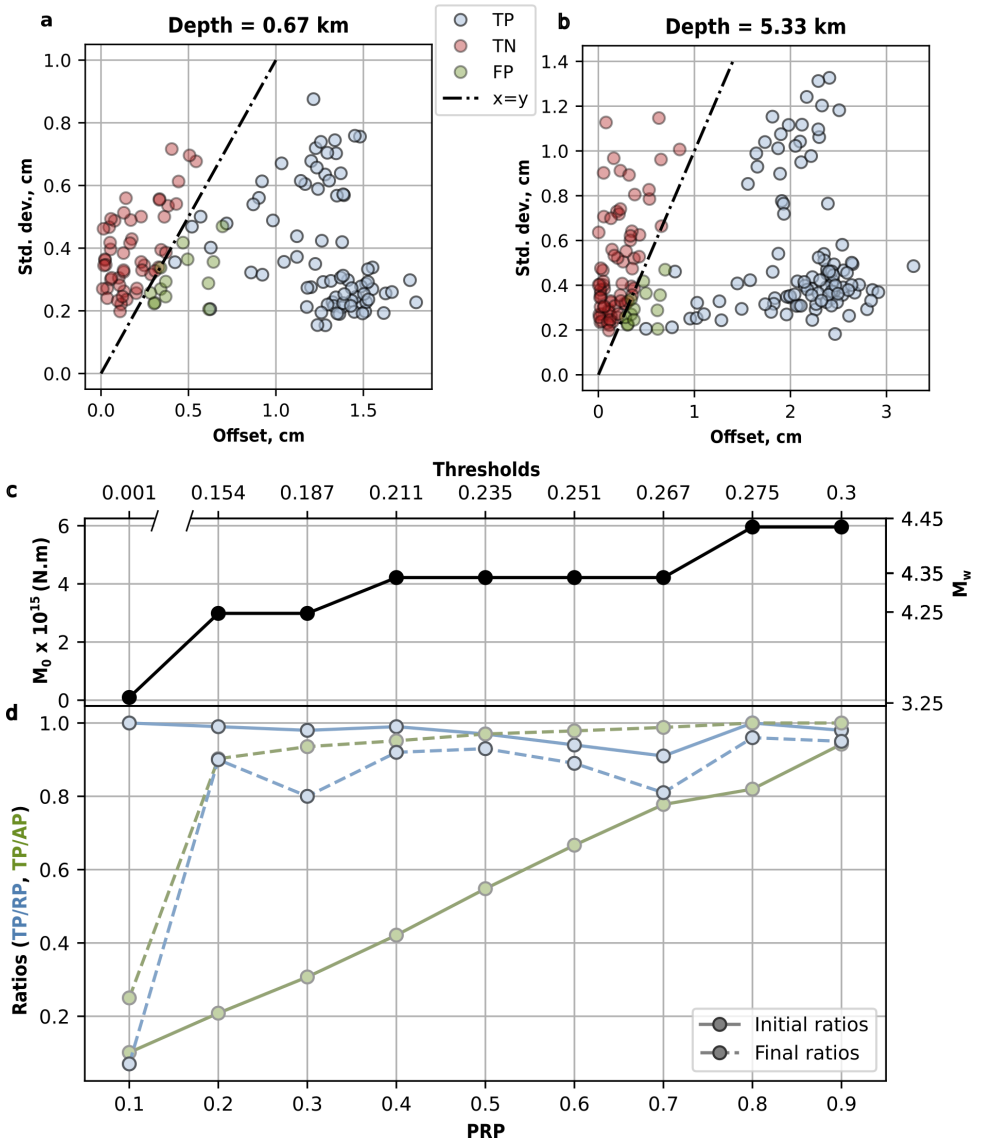

Figure 3.6: Final detections of synthetic SSEs after the validation step. (a,b) Comparison between the estimated offsets and the standard deviation of the weighted stacks for each detection for synthetic SSEs at a depth (a) of 0.67 *km* and (b) of 5.33 *km*. TP, TN, and FP denote true positives, true negatives and false positives, respectively. The dash-dotted line indicates the threshold where the offset equals the standard deviation, which is used to separate positive from negative detections. (c) Minimum moments M_0 (and corresponding magnitudes M_w) detected as a function of PRP and estimated before the validation step. (d) TP/RP and TP/AP ratios as a function of PRP, shown in blue and green, respectively. Solid and dotted lines correspond to the ratios before and after the validation step, respectively. Panels (c) and (d) correspond to synthetic SSEs at a depth of 0.67 *km*.

idation step makes it possible to choose a lower PRP while keeping a high probability of detecting true events, and thus further reduce the minimum detectable magnitude.

3.2.4 Module 3: Characterization of the events

The following section explains the steps of the *Module 3* shown in Figure 3.1d. After the validation of the detections, we estimate several characteristics of the detected SSEs, including

their location along the fault and at depth, the initiation time, the relaxation time and the equivalent magnitude of the event.

3.2.4.1 Location of the events

For the Izmit segment, the spatial extent of the sliding patch is fixed to 6 *km*-length by 1 *km*-width, based on previous studies properly extracting slip area (Neyrinck et al., 2024). The along-fault and depth locations for a given location correspond to the patch with maximum correlation amplitude. The Figure B.9 shows the impact of the chosen size of the sliding patch on the final magnitude estimates of the events by comparing the estimated moments with the initial ones, for different sizes and different magnitudes. By using a smaller patch, we tend to underestimate the magnitude, whereas a larger patch overestimates it. However, even by using the smaller patch, the magnitude estimate error is up to ~ 0.17. The accuracy of the location along the fault and at depth estimates of the sliding patch is shown in Figure B.10 – a,b, at a function of depth and *PRP*. High *PRP* improves the estimate accuracies, and we see a decrease of the depth estimate accuracy for deeper sliding patches due to a larger spatial extent of the related surface deformation reaching the edges of the study area.

3.2.4.2 Initiation time and relaxation time

As for the validation step of the detection (section 3.2.3.1), we use the stacked displacement time series weighted by the Green's functions coefficients w_s^i associated with the patch of larger correlation coefficient (Rousset et al., 2017). The stacked time series is then fitted by the temporal function used to describe the template time evolution (equation 3.2) and is set to zero beforehand. The initiation time and relaxation time are estimated by minimizing the root-mean-square error (RMSE) between the model and the weighted stacked time series. An example of the best model is shown in Figure 3.5. The RMSE calculation is weighted, with more weight at the center of the time series, to emphasize the transient signal. The accuracy of the relaxation time and initiation time estimates based on synthetic tests are presented in Figure B.10 – c,d as a function of depth for 3 values of *PRP*. The relaxation time is overestimated by ~ 6 *days*, due to the low InSAR return time, which is comparable with the relaxation times of SSEs. However, the initiation time is well resolved, with an error of ± 5 *days*, consistent with the return time of the InSAR data obtained from Sentinel-1 images.

3.2.4.3 Magnitude

By using the offset surface displacement of the modeled SSE to compute the temporal parameter, and the fixed template slip dimensions of the sliding patch, we compute the moment M_0 and the associated moment magnitude M_w using the following equations:

$$M_0 = \mu.S.\Delta u, \tag{3.8}$$

$$M_w = \frac{2}{3}.(log_{10}M_0 - 9.1), \tag{3.9}$$

with μ the shear modulus, S the slipping surface and Δu the slip amplitude. The accuracy of magnitude estimate from synthetic tests shows that the magnitude is well recovered for sliding patches down to a depth of 5 *km* and is slightly overestimated at greater depths (Figure B.10e).

3.3 Application to the North Anatolian Fault

3.3.1 Tectonic context and InSAR data processing

The NAF is a major continental right-lateral strike-slip fault system accommodating the westward extrusion of Anatolia relative to Eurasia (Şengör et al., 2005). Two segments are characterized by shallow aseismic creep and episodic SSEs, documented using creepmeters, GNSS, and InSAR observations (Ambraseys, 1970; Cakir et al., 2005; Çakir et al., 2012; Bilham et al., 2016; Rousset et al., 2016; Jolivet et al., 2023; Neyrinck et al., 2024).

In this study, we apply the geodetic matched filter approach to the two creeping segments: the Izmit segment (Figures B.11a and B.12a), which ruptured during the 1999 M_w 7.6 earthquake (Barka, 1999), and the Ismetpasa segment (Figures B.11b and B.12b), which ruptured during the 1944 M_w 7.3 earthquake (Stein et al., 1997). Both segments have hosted multiple shallow SSEs since their last major ruptures (Aslan et al., 2019b; Neyrinck et al., 2024; Özdemir et al., 2025), providing independent constraints for validation of our detections. Because of their strike direction close to 90°, the locations along the fault is also expressed in the following parts by the longitudes.

The InSAR displacement time series are automatically processed within the FLATSIM framework (Thollard et al., 2021), using a Small Baseline Subset approach (NSBAS, Doin et al., 2011). In order to assess the influence of noise reduction and signal extraction on SSE detectability, we consider several levels of post-processing. These include raw Line-Of-Sight (LOS) displacement time series, East-West (EW) displacement time series obtained after geometric decomposition and seasonal signal removal, and further post-processed EW displacement time series in which non-tectonic components are isolated and removed using Independent Component Analysis (ICA).

3.3.2 Application to the Izmit segment: influence of InSAR post-processing

We first apply the method to the Izmit segment to investigate how InSAR post-processing affects SSE detection performance. Three datasets are tested: (1) raw LOS displacement time series from Sentinel-1 ascending track $A058$, (2) EW displacement time series after horizontal-vertical decomposition and removal of seasonal signals (EW-Raw), and (3) EW displacement time series further denoised using ICA (EW-ICA). The detailed post-processing method used for the datasets (2) and (3) is described by Neyrinck et al. (2024), consisting in a seasonal and linear decomposition of the signal to remove the non-tectonic annual periodic terms, a horizontal-vertical decomposition of the LOS displacement time series using ascending and descending tracks (producing the EW-Raw dataset) and the application of an Independent Component Analysis (ICA) on the pixels of the previous EW-Raw displacement time series within the sedimentary basin (producing the EW-ICA dataset).

Based on the synthetic tests presented in Section 3.2, we adopt an initial precision-recall product of $PRP \geq 0.4$ for the Izmit segment. The minimum detectable magnitudes inferred from the synthetic experiments (Figure 3.4d) indicate that LOS and EW-Raw datasets yield comparable detection thresholds, with slightly improved sensitivity at shallow depths for the EW-Raw case. In contrast, the EW-ICA dataset consistently allows the detection of lower–magnitude events at all depths, highlighting the benefit of advanced noise reduction.

When applying the matched filter to the real data (Figure 3.7a), no SSE is detected using

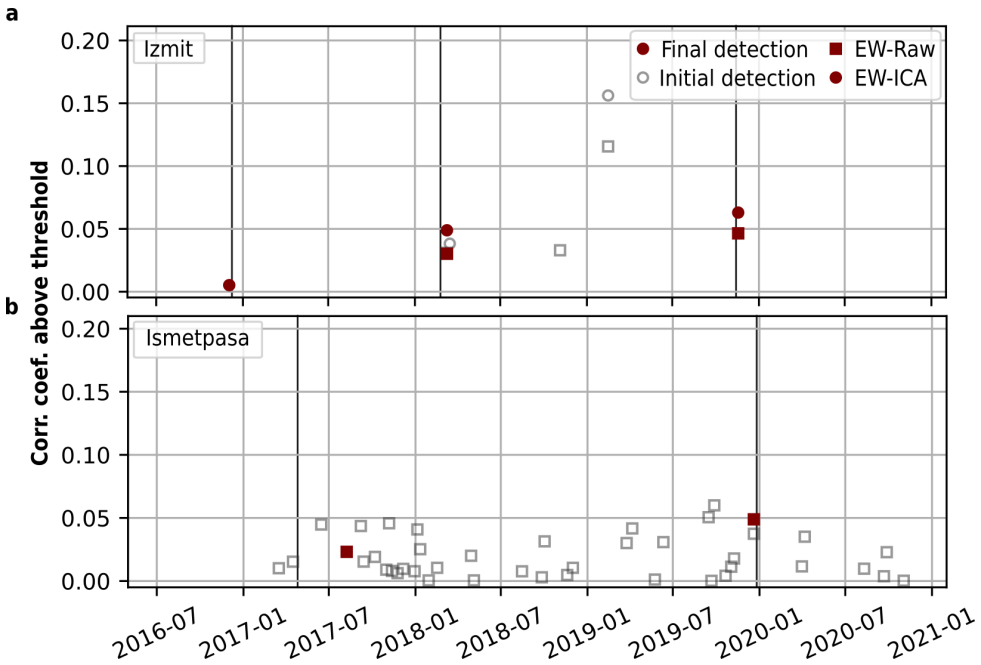

Figure 3.7: Final peak detection obtained for the Izmit segment (a) and the Ismetpasa segment (b). The peaks are shown by their difference between the correlation coefficients and the thresholds. Filled red circles highlight final validated detections (after the validation step – Section 3.2.3.1), whereas empty gray circles are considered as false detections. Two datasets from different post-processing sequences are considered: the EW-Raw (squares) and EW-ICA (circles) datasets (cf. the description of the datasets in part 3.3.2; the LOS dataset resulting in zero detection is therefore not shown here). The vertical lines correspond to initiation times of SSEs recorded along both segments by creepmeters (Figures B.12, B.15 and B.16).

the LOS dataset, indicating that residual atmospheric and non-tectonic signals dominate the displacement time series at this processing level. Using the EW-Raw dataset, two SSEs are detected in 2018 and 2019. The EW-ICA dataset enables the detection of an additional event in 2016 and yields systematically higher correlation coefficients for all detected events, demonstrating an improved signal-to-noise ratio. The three events detected are consistent with the three event already documented in published articles (Aslan et al., 2019b; Neyrinck et al., 2024).

The detected events are subsequently characterized following the procedure described in Section 3.2.4. Figure 3.8 illustrates the characterization of the 2019 event. The highest correlation coefficients correspond to a sliding patch centered at approximately $30.05°E$ and at about 1 *km* depth, within the Izmit sedimentary basin (Özalaybey et al., 2011). The corresponding weighted stack displacement time series (Figure 3.8b) exhibits a clear transient offset that is well fitted by the adopted temporal source function. Independent creepmeter records from the Izmit-Seller and Tepetarla sites show contemporaneous transient displacements (Figure 3.8c), providing an external validation of the InSAR-based detection. Similar figures for the characterization of other detections using EW-Raw and EW-ICA datasets are shown in Figure B.13.

For the three events detected using the EW-ICA dataset, the estimated magnitudes range between M_w 4.1 and M_w 4.35, with relaxation times between ~ 1 and 5.3 *days*, all estimates being gathered in Table 3.1. Previous InSAR and creepmeters analyses of SSEs along the Izmit segment already provided some estimates, and are also gathered in Table 3.1. We observe a good consistency with the creepmeters data of the initiation time with $\Delta t_0 \approx 4 - 11$ *days*. The duration or relaxation time obtained by the geodetic matched filter approach leads to higher values for the 2018 and 2019 SSEs, whereas the estimates corresponding to the 2016

Table 3.1: Results of the characterization of the five SSEs detected using the geodetic matched filter approach along the Izmit and Ismetpasa segments, compared to previous works. IZ and IS stand for Izmit and Ismetpasa, and Cm. stands for Creepmeters. The references are the following ones: [1] for Aslan et al. (2019b), [2] Jolivet et al. (2023), [3] Neyrinck et al. (2024) and [4] Özdemir et al. (2025). $*$ indicates results from this study, and $-$ indicates that no information is available for this feature.

Seg.	**Initiation time**	**Lon.** (°)	**Depth** (*km*)	**Relaxation time** (*days*)	**Duration** (*days*)	M_w	**Ref.**
IZ	30/11/2016	-	-	-	-	-	Cm.
	$-$/12/2016	29.98	-	-	21	-	[1]
	$-$/12/2016	29.85	-	-	-	-	[3]
	03/12/2016	30.025	1.00	1.0		4.16	$*$
IZ	$-$/03/2018	30.03	0.5	-	21	4.4	[3]
	10/03/2018	30.038	1.00	6.4		4.29	$*$
IZ	25 $-$ 29/11/2019	-	-	$1.4-3$	9	-	Cm.
	$-$/11/2019	30.04	1.00	-	21	4.3	[3]
	18/11/2019	30.05	1.00	5.1	-	4.29	$*$
IS	11/06/2017	-	-	9.7	-	-	Cm.
	mid 2017	32.62	-	-	-	-	[2]
	08/08/2017	32.58	2.10	2.8	-	4.41	$*$
IS	21/12/2019	-	-	9.3	-	-	Cm.
	late 2019	32.62	-	-	-	-	[2]
	21/12/2019	32.65	< 2	-	26	4.8	[4]
	20/12/2019	32.61	0.43	11.9	-	3.98	$*$

event is much lower, probably due to the variations of the signal-to-noise ratios between the three weighted stack displacement time series (Figure B.13). A comparison of the tectonics (Figure 3.8 – b,c) for the 2019 event shows smaller duration of the event according to the creepmeters data. The inferred sliding patches are shallow (≤ 2 *km* depth) and display a slight eastward migration with time, consistent with previous InSAR analyses of SSEs along the Izmit segment (Aslan et al., 2019b; Neyrinck et al., 2024).

3.3.3 Application to the Ismetpasa segment

We next apply the geodetic matched filter approach to the Ismetpasa segment in order to test its robustness in a different location along the NAF with a distinct noise environment. For this segment, we use the EW-Raw dataset only, ICA attempts being unsuccessful on that segment. The noise characteristics are recomputed locally (Figure B.2) to derive segment-specific detection thresholds (Figure B.8). Due to the higher noise level, a lower precision-recall product ($PRP \approx 0.2$) is adopted. Based on previous geodetic observations and inverse slip models (Rousset et al., 2016), we also use a smaller template size (3 *km* length and 1 *km* width).

The initial application yields to 55 candidate detections (Figure 3.7b). After applying the

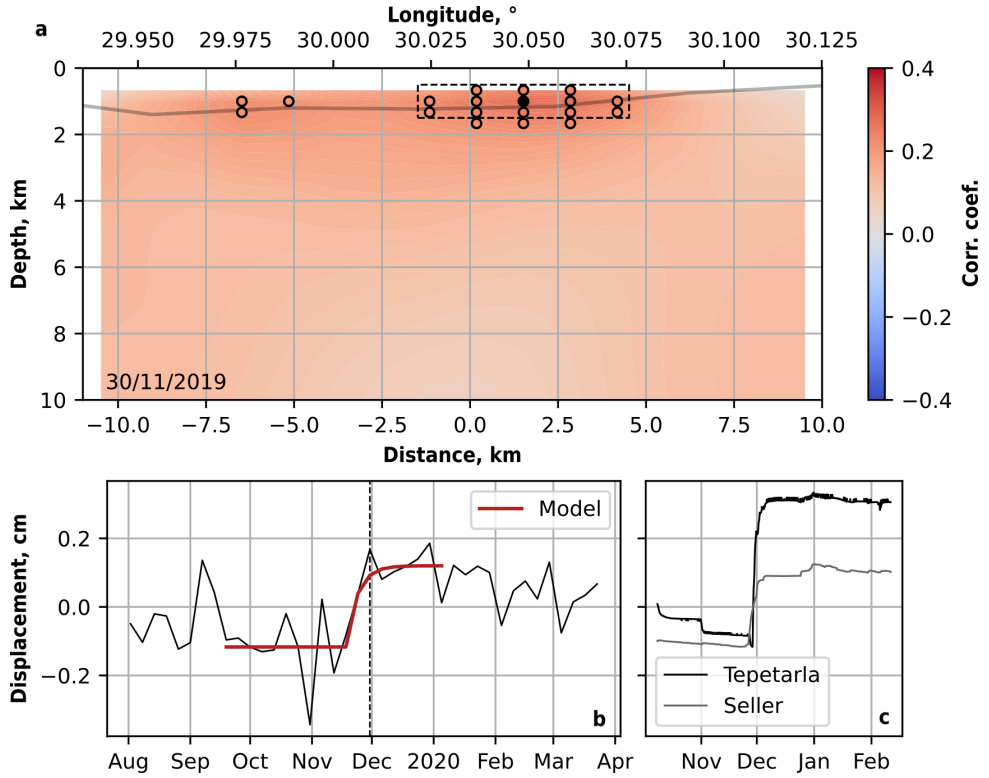

Figure 3.8: Example of the 2019 SSE detected along the Izmit segment (Figure 3.7a). (a) Correlation coefficients along the fault interface at the date of the detection for the EW-ICA dataset. Dots indicate spatial detections, with the black one marking the patch with the highest amplitude, corresponding to the center of the template (dotted black line). The gray line shows the downdip boundary of the sedimentary basin (Özalaybey et al., 2011). (b) Weighted stack displacement time series for the template highlighted in (a) by the dotted black line. The best fitting model is shown in red. The vertical dotted line shows the time of highest correlation amplitude. (c) Creepmeter records in Izmit-Seller and Tepetarla sites, showing cumulative displacement over the same period. The locations of both creepmeters are shown in Figures B.11a and B.12a (Bilham et al., 2016; Emre et al., 2018).

validation criteria based on spatial coherence and weighted stack displacement time series (Section 3.2.3.1), only two detections remain, occurring in August 2017 and December 2019 (Figure B.14).

The retained events have estimated magnitudes between M_w 4.0 and M_w 4.4 and are located at a shallow depth ranging from $\sim$ 0.4 to 2 *km* (Table 3.1). The inferred relaxation time ranges between 3 and 12 *days*. Despite larger uncertainties than for the Izmit segment, these estimates are consistent with previous InSAR, GNSS, and creepmeter observations along the Ismetpasa segment (Table S1; Bilham et al., 2016; Jolivet et al., 2023; Özdemir et al., 2025). The first detection in August 2017 seems related to the 2017 SSE recorded along the Ismetpasa segment (Figure 3.7b), despite a difference of $\sim$ 58 *days* of the intiation time with the creepmeter record (Figure B.16). The relaxation time is therefore also lower than observed on the creepmeter data, due to the temporal shift of the detection. The 2019 event is detected with only one-day delay, but large differences of the estimates: a relaxation time difference up to 3 *days* compared to the creepmeters records, and a duration difference up to 30 *days* compared to GNSS data. We also obtain a lower magnitude than the one calculated using the GNSS data.

Overall, the application of our method to the Ismetpasa segment confirms that the geodetic matched filter approach can successfully identify SSEs in independent datasets, even under less

favorable noise conditions. The comparison between the Izmit and Ismetpasa segments highlights the importance of local noise characterization and appropriate InSAR post-processing to maximize the sensitivity and reliability of automatic SSE detection.

3.4 Discussion

3.4.1 Validation of the approach and assumptions

The results obtained from both synthetic tests and real-data applications demonstrate that the adapted geodetic matched filter approach is capable of detecting and characterizing shallow SSEs using InSAR time series. Synthetic experiments (Figures 3.4 and 3.6) show that, for realistic noise conditions, SSEs with a magnitude down to $M_w \sim 4 - 4.5$ can be detected at shallow depths with a confidence level exceeding 90 % after the validation step (Figure 3.6 – c,d). The minimum detectable magnitude increases with depth, as expected from the decay of surface displacement with increasing source depth (Figure 3.4c).

The application to the Izmit and Ismetpasa segments further confirms the robustness of the approach. Along the Izmit segment, the three previously documented events (Aslan et al., 2019b; Neyrinck et al., 2024) are successfully retrieved when applying the method to the EW-ICA dataset (Figures 3.7a, 3.8 and S13), and their estimated magnitudes (M_w $4.1 - 4.3$), depths (≤ 2 *km*), and relaxation times are consistent with previous InSAR and creepmeter analyses (Aslan et al., 2019b; Neyrinck et al., 2024). Along the Ismetpasa segment, two events are detected after validation (Figure 3.7b and Figure B.14), with magnitudes and durations comparable to earlier geodetic observations (Rousset et al., 2016; Özdemir et al., 2025), although with larger uncertainties. The agreement between detected events, weighted stack characterization (Figure 3.8b), and independent creepmeter records (Figure 3.8c and Figures B.15 and B.16) provides an external validation of the method.

A key outcome of this study is the strong dependence of detection capability on the noise level and post-processing strategy. The comparison between LOS, EW-Raw, and EW-ICA datasets along the Izmit segment (Section 3.3.2; Figure 3.4d) shows that post-processing substantially lowers the detection threshold. While no event is detected using raw LOS time series, the EW-Raw dataset enables the recovery of two events, and the EW-ICA dataset allows the detection of an additional, smaller event with systematically higher correlation peaks. These results highlight that the sensitivity of the matched filter is primarily controlled by the signal-to-noise ratio of the input time series.

Despite these encouraging results, several assumptions we made impose limitations. First, the spatial extent of the template used during the SSE characterization (Section 3.2.4) is fixed. This choice is motivated by the difficulty of resolving source dimensions from InSAR data alone, given the strong spatial covariance of atmospheric noise at kilometer scale (≤ 5 *km*), which can generate deformation patterns partially mimicking shallow SSE signals. Indeed, the estimated PSD slopes (≈ 2.5˜4; Figures B.1 and B.2) are consistent with atmospheric turbulence and imply a steep power-law spectrum dominated by long wavelengths. Such spectral behavior indicates substantial spatial correlations at scales comparable to the expected dimensions of shallow SSE sources.

Second, the temporal evolution of the template is defined by a fixed relaxation time ($\tau =$ 6 *days*), calibrated from previous observations along continental strike-slip faults (Rousset et al., 2016; Neyrinck et al., 2024; Özdemir et al., 2025). As shown in Figure B.7, using a re-

laxation time significantly different from that of the real event reduces correlation amplitudes and may shift detection times. The adopted value represents a compromise: it maximizes sensitivity to SSEs with durations of a few weeks while reducing spurious correlations during noise-only periods. However, events with relaxation times substantially different from the assumed template value would produce lower correlation amplitudes and therefore be detected with reduced efficiency.

Third, the method assumes temporally uncorrelated but spatially correlated noise when generating synthetic time series (Section 3.2.1.1). Although this assumption is justified by the short characteristic timescale of atmospheric variability relative to the Sentinel-1 revisit period, residual temporally correlated signals (e.g., hydrological loading) may still affect detection performance. The improvement observed when applying ICA (Section 3.3.2) illustrates that incomplete separation of non-tectonic signals directly impacts the minimum detectable magnitude.

Finally, the temporal resolution of InSAR (6 *days* for Sentinel-1A/B) inherently limits the precision of initiation time and relaxation time estimates. Synthetic tests (Figure B.10 – c,d) indicate a systematic overestimate of the relaxation time by ~ 6 *days*, and comparisons with creepmeter records (Section 3.4.2) show discrepancies of up to one SAR acquisition interval for initiation times. These differences reflect both the coarse temporal sampling of InSAR and the different spatial sensitivities of creepmeters and InSAR observations.

Overall, the combined synthetic validation and successful retrieval of independently documented SSEs demonstrate that the proposed approach provides a reliable and systematic framework for detecting shallow SSEs in the InSAR time series. At the same time, its performance remains conditioned by noise characteristics, template assumptions, and the intrinsic spatial and temporal resolution of the data. These aspects should be carefully considered when applying the method to other tectonic contexts.

3.4.2 Comparison with independent geodetic observations along the NAF

A detailed comparison with previously published creepmeter, GNSS, and InSAR studies provides an independent assessment of the robustness of the geodetic matched filter approach along the Izmit and Ismetpasa segments of the NAF. We focus here on the consistency of the inferred spatiotemporal parameters and on the origin of remaining discrepancies.

3.4.2.1 Izmit segment

Along the Izmit segment, the three events retrieved with the EW-ICA dataset correspond to the 2016, 2018, and 2019 SSEs previously documented using InSAR time series and slip inversions (Aslan et al., 2019b; Neyrinck et al., 2024). The estimated magnitudes ($M_w \sim 4.1 - 4.3$) and shallow depths (≤ 2 *km*) are consistent with the slip models inferred by Neyrinck et al. (2024), in which the creeping section is confined within the sedimentary basin (Figures 3.8a and S13). The spatial location of the sliding patches inferred from the maximum correlation coefficients falls within the areas of significant slip in those models, indicating that the template-based approach captures the first-order geometry of the events without performing a full inversion.

Temporal parameters derived from the weighted stack analysis (Figure 8b and S13) are also comparable to independent creepmeter observations (Figure 3.8c and Figure B.15). The

initiation times agree within approximately one to two Sentinel-1 revisit time ($6-12$ *days*). Relaxation times estimated from the matched filter approach (e.g., ~ 5.3 *days* for the 2019 event) are slightly longer than those inferred from creepmeters ($1.4-3$ *days*). This systematic difference likely reflects (i) the coarse temporal resolution of InSAR compared to the $30s$ sampling of creepmeters, and (ii) the fact that creepmeters record slip over a few tens of meters at the surface, whereas InSAR integrates deformation over kilometer-scale fault areas.

3.4.2.2 Ismetpasa segment

Along the Ismetpasa segment, two events are retained after validation and can be compared with previous InSAR, GNSS, and creepmeter analyses (Jolivet et al., 2023; Özdemir et al., 2025). The 2019 event, characterized by GNSS by Özdemir et al. (2025) with an equivalent magnitude of ~ 4.8 and a duration of ~ 26 *days*, is also identified by our approach with a shallow depth (< 2 *km*) and a duration of a few months (~ 60 *days*). Although our magnitude estimate is slightly smaller, this discrepancy can be partly attributed to the fixed template size used in the characterization step (Figure B.9), which may underestimate the moment if the true slipping area exceeds the prescribed dimensions. As described in Özdemir et al. (2025), the signal-to-noise ratio of the GNSS surface displacements is too low to permit a reliable inversion. We reach a similar conclusion using the InSAR observations.

The mid-2017 event is more weakly constrained. While a correlation peak is identified (Figure 3.7b), the inferred initiation time differs by up to three months from the N. Wall creepmeter record (Figure B.16). An increase in the stacked displacement time series (Figure S14a) is also observed in July, consistent with the timing of the creepmeters, followed by a decrease likely related to atmospheric noise. The delayed detection likely reflects the higher noise level of the Ismetpasa InSAR dataset and the lower signal amplitude of this event. Nevertheless, the inferred depth range remains broadly compatible with previous geodetic interpretations (Jolivet and Frank, 2020; Özdemir et al., 2025), suggesting that the detection is physically meaningful even if its temporal characterization is less precise.

More generally, the comparison with GNSS observations highlights the complementary strengths of the datasets. GNSS provides higher temporal resolution but sparse spatial sampling, whereas InSAR offers dense spatial coverage but limited temporal resolution. The matched filter approach leverages the spatial redundancy of InSAR to compensate for its lower temporal sampling, enabling the recovery of shallow, kilometer-scale events that may be only partially resolved by GNSS networks.

3.4.2.3 Synthesis across techniques

Importantly, no additional events are detected when lowering the *PRP*, suggesting that the current InSAR noise level likely prevents the identification of smaller, millimetric SSEs documented by creepmeters (e.g., mid-2018 along Ismetpasa; Figure B.16a).

The overall consistency between the template-based detections and independent geodetic constraints indicates that the method successfully captures the first-order physical characteristics of shallow SSEs without requiring a full slip inversion. Differences in initiation times and relaxation times remain within the limits imposed by the temporal sampling and noise level of the InSAR data. These comparisons demonstrate that the geodetic matched filter approach provides a robust framework for systematic SSE detection while remaining consistent with high-resolution *in situ* observations. Nevertheless, when the signal-to-noise ratio allows

it, a dedicated slip inversion would provide a more detailed characterization of the spatial distribution of slip and a refined estimate of the moment (Rousset et al., 2016; Neyrinck et al., 2024).

3.4.3 Slow slip events physical mechanisms

3.4.3.1 Structural and mechanical controls on shallow SSE occurrence

The shallow SSEs identified along the Izmit and Ismetpasa segments occur within fault sections that are already characterized by aseismic creep. On the Izmit segment, aseismic creep appears to be localized primarily downdip of the SSEs (Neyrinck et al., 2024), whereas along the Ismetpasa segment it is observed on both sides of the SSEs and possibly beneath them as well (Jolivet and Frank, 2020). This observation may indicate that surrounding persistent aseismic creep constitutes a necessary mechanical background for the occurrence of shallow SSEs. In rate-and-state friction frameworks, velocity-strengthening regions are typically associated with stable creep (Kaneko et al., 2013), but spatial heterogeneities within such regions may lead to conditionally stable behavior and the emergence of transient slip episodes (Wei et al., 2013). The fact that both Izmit and Ismetpasa host SSEs within creeping sections, while most other NAF segments do not, supports the hypothesis that a pre-existing aseismic slip regime may be a prerequisite for transient slow slip.

In addition to the presence of creep, both segments share a striking geological feature: the SSEs are systematically located within sedimentary basins. Along the Izmit segment, the detected events are confined within the Izmit basin (Figure 3.8a), whose downdip boundary lies at about two kilometers depth (Özalaybey et al., 2011). Along the Ismetpasa segment, the events are also located within a shallow sedimentary cover (Jolivet et al., 2023; Özdemir et al., 2025). Sedimentary basins are typically characterized by clay-rich, weak, and potentially overpressurized materials, which may favor stable or conditionally stable slip (Bürgmann, 2018).

The geological context of the NAF is complex, as the fault follows former suture zones separating distinct lithological units (Şengör et al., 2005). However, only two segments exhibit both shallow creep and recurrent SSEs, suggesting that lithological contrasts alone are insufficient to explain their occurrence. The spatial coincidence between SSEs and sedimentary basins instead points toward the importance of shallow material properties. Similar associations between shallow slow slip and sedimentary or altered materials have been documented along other continental strike-slip faults, including the Imperial and Superstition Hills faults in California (Materna et al., 2024; Vavra et al., 2024). These analogies suggest that the presence of compliant, clay-rich may promote frictional conditions favorable to transient aseismic slip.

3.4.3.2 Role of pore-fluid pressure

Elevated pore-fluid pressure likely plays a central role in the nucleation and evolution of the shallow SSEs identified along both the Izmit and Ismetpasa segments. High pore pressure reduces the effective normal stress acting on the fault, thereby lowering the shear stress required for slip and promoting aseismic deformation (Sibson, 1992). In creeping fault sections overlain by or within sedimentary basins, permeability contrasts, clay-rich lithologies, and fluid trapping may favor locally elevated pore pressures. Such conditions are commonly invoked to explain stable or conditionally stable slip behavior in both subduction zones and

continental strike-slip faults (e.g. Bürgmann, 2018).

Theoretical and numerical studies have shown that fluid pressure variations can significantly modify slip stability in rate-and-state systems. Coupled hydromechanical models demonstrate that pore-pressure diffusion may generate slow slip pulses even in velocity-strengthening regimes, provided that effective normal stress is sufficiently reduced (Segall and Rice, 1995; Segall and Matthews, 1997; Liu and Rice, 2007; Heimisson et al., 2019). In particular, Heimisson et al. (2019) showed that poroelastic coupling can destabilize otherwise stable sliding and produce transient SSEs with durations and magnitudes comparable to those observed geodetically.

Dilatancy further modulates this behavior. During shear, fault zone dilatation reduces pore pressure locally, temporarily increasing effective normal stress and stabilizing slip. Subsequent fluid diffusion restores pore pressure, allowing slip to resume. This dilatancy–diffusion feedback has been proposed as a key mechanism governing episodic slow slip in subduction settings (Segall and Rice, 1995; Liu and Rice, 2007) and may similarly operate in shallow continental environments. The shallow depth of the detected events (≤ 2 *km*) is consistent with zones where permeability heterogeneities and fluid circulation are expected to be strong, particularly within sedimentary basins.

Seasonal modulation of creep attributed to hydrological loading suggested by Li et al. (2023) on the San Andreas fault highlights the potential sensitivity of shallow fault slip to effective stress variations. Although no clear seasonal modulation of slip is resolved here, the fact that SSEs on the Izmit segment consistently occur in winter suggests that pressure transients may play a role in triggering the SSEs.

3.4.3.3 Moment-duration scaling

The detected SSEs fall within the moment-duration domain previously identified for shallow continental SSEs (Figure 3.9). When plotted on the scaling diagram adapted from Ide and Beroza (2023) and Materna et al. (2024), the Izmit and Ismetpasa events cluster within the so-called "hidden" region for subduction zones, corresponding to low-magnitude, short-duration events that are only detectable on strike-slip faults because of their shallow depth.

Their position on the diagram is consistent with moment magnitudes $M_w \sim 4 - 4.3$ and durations of days to a few weeks. These values align with observations from other continental creeping faults (Materna et al., 2024; Vavra et al., 2024) and suggest that shallow SSEs obey a scaling shifted from that of fast earthquakes and subduction SSEs. Although the limited number of events prevents robust scaling estimation, the clustering of the NAF SSEs within a narrow portion of the scaling space suggests that common mechanical conditions govern their occurrence. The similarity between Izmit and Ismetpasa, despite their different positions within the seismic cycle (post-1999 rupture versus ~ 80 *years* after the 1944 rupture), indicates that local frictional and hydromechanical properties may dominate over large-scale stress evolution in controlling shallow SSE behavior.

3.4.3.4 Implications for continental fault mechanics

Taken together, the observations support a conceptual model in which shallow SSEs preferentially develop on fault portions surrounded by creeping segments and within sedimentary basins, where frictional heterogeneity, compliant materials, and fluid effects combine to produce conditionally stable slip. Persistent aseismic surrounding creep may provide the

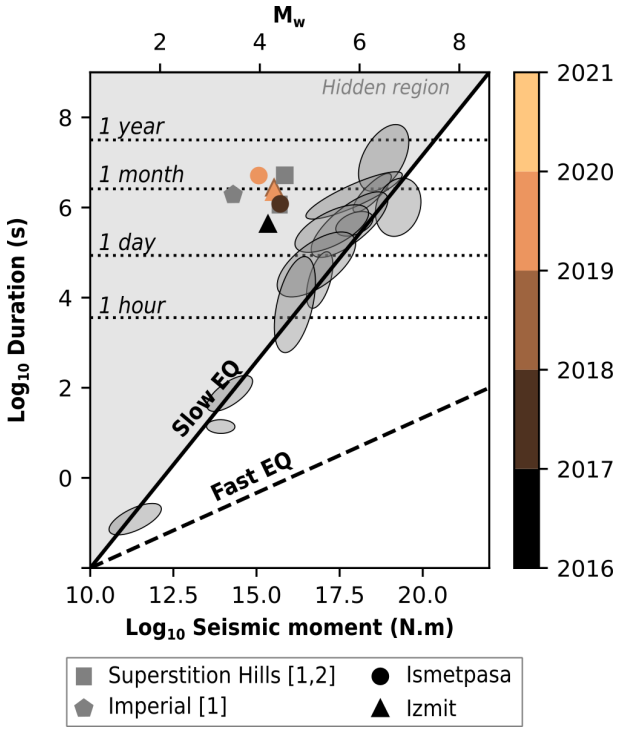

Figure 3.9: Moment-duration scaling plot modified from Ide and Beroza (2023) and Materna et al. (2024). Results from this study are shown by the colored circles and triangles. The references 1 and 2 used for the Imperial Valley results correspond to Materna et al. (2024) and Vavra et al. (2024), respectively. Gray ellipses correspond to estimates made on subduction zones (Ide and Beroza, 2023).

background deformation necessary to load small velocity-weakening or conditionally stable patches, leading to recurrent transient slip.

The similarity of these features with those documented in California suggests that such structural and hydromechanical conditions may represent a common ingredient for shallow SSE occurrences worldwide. Expanding SSE catalogs using systematic approaches, such as the geodetic matched filter, will be essential to test whether this association between creep, sedimentary cover, and shallow slow slip holds across broader tectonic contexts.

3.5 Conclusion

The adaptation of the geodetic matched filter approach to InSAR time series enables the detection of shallow SSEs along continental strike-slip fault segments, under assumptions that are consistent with previous observational and modeling studies. Applied to two distinct creeping segments of the North Anatolian Fault, this method demonstrates its ability to automatically detect and characterize SSEs without requiring extensive post-processing or full slip inversions. Over the 2016-2021 period, we identify three events along the Izmit segment and two along the Ismetpasa segment, with moment magnitudes ranging from $M_w \sim 4$ to 4.4, compatible with previous estimates, all located within the upper few kilometers of the fault interface. The geodetic matched filter provides a systematic screening tool for large InSAR datasets, guiding more detailed analyses when the signal-to-noise ratio permits. With the continuous increase in SAR acquisitions, improvements in automated InSAR processing, and the development of advanced post-processing techniques, such approaches open the possibility

of systematically documenting aseismic transient deformation along continental faults over decadal time scales. Expanding SSE catalogs is essential for better constraining the kinematics and mechanics of shallow fault slip, improving our understanding of fault zone processes, and refining seismic hazard assessments in regions hosting creeping strike-slip faults.

Acknowledgments

We thank Cécile Lasserre, Marie-Pierre Doin and Philippe Durand for stimulating discussions. The InSAR data is based on the FLATSIM service (doi: 10.24400/253171/FLATSIM2020), developed as part of the ForM@Ter Solid Earth data and services center and supported and operated by CNES. Creepmeters data come from the GAGE/UNAVCO dataset (`https://www.unavco.org/data/strain-seismic/creep-data/creep-data.html`). Baptiste Rousset has benefited funding for this study from the CNRS PNTS and the IdEx University of Strasbourg.

Supplementary Materials

The Supplementary Materials are shown in Appendix B.

Chapter 4

Creep behavior along the Izmit segment

In the previous chapter, I proposed an automatic method of detection of SSEs adapted to InSAR data, in order to increase the amount of SSEs detected along continental faults. The first-order estimates of the event magnitudes reveal smaller magnitudes for an equivalent duration in comparison with SSEs identified along subduction zones, and therefore included within the "hidden region" defined by Ide and Beroza (2023). The occurrence of these SSEs along continental strike-slip faults in addition to the unprecedented data quality of the *FLATSIM* products offer an opportunity to study in details these events.

In this chapter, I focus on the Izmit segment of the NAF, with the objective of extracting the tectonic signal related to the three previously detected SSEs. I develop a post-processing workflow to extract the tectonic signal from InSAR time series, including GNSS-based referencing, removal of seasonal components, and blind source separation using Independent Component Analysis (ICA). The post-processed time series were then used in inversion models to infer the slip distribution at depth on a two-dimensional fault interface embedded in a layered elastic half-space. These observations were combined with creepmeter data recorded on the fault in order to better characterize the SSEs. A detailed analysis of the last two detected events along the Izmit segment occurring in March 2018 and November 2019 revealed moment magnitudes of $4.3 - 4.4$. The inferred slip is located at shallow depth within the sedimentary basin. I also identified continuous creep between these events, with most of the slip occurring between 2 and 5 *km*-depth, just below the sedimentary basin, likely participating in loading SSE asperities. Creepmeters records during the 2019 event confirm the occurrence of the SSE and enables a lateral propagation velocity estimate of 6.4 km/day. These observations support a conceptual model in which shallow SSEs preferentially develop on fault portions surrounded by creeping segments and within sedimentary basins, where frictional heterogeneity, compliant materials, and fluid effects are combined to produce conditionally stable slip. Persistent aseismic surrounding creep may provide the background deformation necessary to load small velocity-weakening or conditionally stable patches, leading to recurrent transient slip.

This chapter is an article published in *Earth and Planetary Science Letters (EPSL)*, as:

Neyrinck, E., Rousset, B., Doubre, C., Rivera, L., Lasserre, C., Doin, M.-P., Durand, P., Bilham, R., Çakir, Z., FLATSIM Working Group (2024). *The slow slip event cycle along the izmit segment of the North Anatolian fault.* Earth and Planetary Science Letters, 648 , 119104. https://doi.org/10.1016/j.epsl.2024.119104.

Abstract

The occurrence of aseismic creep along seismogenic faults significantly impacts seismic hazard assessment by releasing accumulated stress and reducing the slip deficit. Since the 1999 M_w7.6 Izmit earthquake on the North Anatolian Fault in Türkiye, while aseismic creep has been observed as a postseismic response to the Izmit rupture, additional slow slip events were detected in 2015 and 2016, accommodating several millimeters of relative displacement over periods of approximately one month. By automating Interferometry Synthetic Aperture Radar time series processing from 2016 to 2021 (FLATSIM project) and applying specific post-processing, we extract the tectonic signal to estimate the slip dynamics of the Izmit segment, including the detection and characterization of slow slip events. Modeling the slip distribution at depth on a 2D fault interface within a layered elastic half-space, we estimate a locking depth of 11 *km* and steady creep between 2 and 5 *km*. Above the steady creep zone, we identify two new shallow slow slip events in March 2018 and November 2019, with moment magnitudes of 4.3 and 4.4, respectively. Based on creepmeter measurements, we estimate a lateral propagation velocity of 6.4 km/day for the 2019 event. The location of these shallow slow slip events above the sedimentary-bedrock interface suggests a critical role of variations in frictional properties in the occurrence of transient slip events.

Keywords: shallow aseismic creep, slow slip events, seismic cycle, strike-slip fault, SAR interferometry, North Anatolian Fault.



- Aseismic creep along the Izmit segment includes a steady creep from 2 to 5 km-depth, and episodic SSEs at shallower level.
- From InSAR time series, we detect three SSEs (December 2016, March 2018, November 2019).
- The return period of the SSEs along the segment is quantified to ~ 1.3 *years*.
- The moment magnitude of the 2018 and 2019 SSEs is $\sim 4.3 - 4.4$.

Contents

4.1 Introduction . . . 138
4.2 Tectonic context . . . 139
4.3 InSAR analysis . . . 141
4.3.1 Interferograms and time series processing . . . 141
4.3.2 InSAR referencing relative to GNSS velocities . . . 141
4.3.3 Extraction of seasonal signals . . . 142
4.3.4 Horizontal and vertical decomposition . . . 142
4.3.5 Extraction of the tectonic signal . . . 143
4.4 Mean velocities and seasonal signals analysis . . . 144
4.4.1 Mean horizontal East-West signal . . . 144
4.4.2 Mean vertical signal . . . 144
4.4.3 Seasonal signals . . . 144
4.5 Creep dynamics along the Izmit segment . . . 146
4.5.1 Fault relative displacement . . . 147
4.5.2 Slip inference at depth . . . 149
4.6 Discussion . . . 152
4.6.1 Steady creep along the Izmit segment . . . 152
4.6.2 Izmit slow slip event cycle . . . 154
4.6.3 Possible mechanisms promoting creep and SSEs along the Izmit segment 156
4.7 Conclusions . . . 157

4.1 Introduction

The growing number of seismological and geodetic observations has enabled to refine the seismic and aseismic slip behaviors of worldwide active faults (e.g. Bürgmann, 2018). A large diversity of aseismic behaviors is observed, ranging from steady-state creep to slow slip events (SSEs), also referred to as transient creep events, that can last from minutes to years. The first observations of aseismic creep came from Steinbrugge et al. (1960) who highlighted the existence of shallow creep on a continental strike-slip fault by analyzing distortions on constructions in the cities above San Andreas Fault (SAF) zone. Since these observations, aseismic deformation on faults has been extensively studied using various geodetic techniques including Global Navigation Satellite System (GNSS), strainmeters, creepmeters and Interferometry Synthetic Aperture Radar (InSAR). Transient SSEs have mostly been detected on subduction zones including the Cascadia subduction zone (Dragert et al., 2001), the Nankai subduction zone (Obara et al., 2004), in Mexico (Radiguet et al., 2011), New Zealand (Wallace et al., 2016), Alaska (Rousset et al., 2019b), Costa Rica (Jiang et al., 2012), Ecuador (Vaca et al., 2018), and more recently in Chile (Klein et al., 2017). They have been observed at both the deep (e.g. Dragert et al., 2001; Obara et al., 2004) and shallow (McCaffrey et al., 2008; LaBonte et al., 2009, e.g.) ends of the seismogenic zone. Several continental strike-slip faults appear to also be affected by SSEs such as the SAF (e.g. Rousset et al., 2019b; Gittins and Hawthorne, 2022), the San Jacinto Fault close to the Anza gap (Inbal et al., 2017), the Superstition Hills Fault (Wei et al., 2009), the Haiyuan Fault (Jolivet et al., 2012) and the North Anatolian Fault (NAF) (Rousset et al., 2016; Aslan et al., 2019b; Jolivet et al., 2023).

On continental strike-slip faults, SSEs predominantly occur within the upper few kilometers, exhibiting slip amplitudes ranging from millimeters to centimeters and equivalent moment magnitudes from 4 to 5 where estimable (e.g. Wei et al., 2009; Rousset et al., 2016; Materna et al., 2024). These events recur every few months to years or decades (Wei et al., 2013; Bilham et al., 2016; Vavra et al., 2024) and recurrence intervals can transition from shorter to longer periods during the postseismic phase (Wei et al., 2013). The SSEs timing can also be influenced by dynamic stresses from nearby large earthquakes (Wei et al., 2011).

The primary explanation for shallow creep on strike-slip faults is the presence of poorly consolidated sediments close to the surface (Scholz, 1998). Lateral alternations of creeping and locked segments could be due to lateral variations in mineralogical composition of the gouge, with talc and serpentine for example, deforming and transforming into low-friction minerals, favoring creep (e.g. Bürgmann, 2018; Kaduri et al., 2017). The presence of high pore fluid pressure on some segments may also enhance aseismic slip, as evidenced in geothermal contexts (e.g. Guglielmi et al., 2015). In the framework of rate-and-state friction seismic cycle models for purely elastic media, shallow creep can be reproduced with a shallow velocity-strengthening layer (Kaneko et al., 2013). The emergence of transient SSEs can arise by adding a layer of velocity-neutral friction also referred to as conditionally stable (Wei et al., 2013). However, the small number of SSE observations on strike-slip fault contexts limits our understanding of the underlying physical processes and key mechanical parameters. A better description of the mechanisms governing the various aseismic slip behaviors on faults and the possible interactions between seismic and aseismic slips throughout the various phases of the seismic cycle is crucial to improve seismic hazard models (Avouac, 2015).

In this paper, we focus on the Izmit segment of the NAF in Türkiye where aseismic creep is observed since the 1999 M_w7.6 Izmit earthquake from geodetic measurements (Cakir et al., 2012; Hussain et al., 2016; Aslan et al., 2019b; Özarpacı et al., 2020). Based on automatically processed Sentinel-1 InSAR time series from 2016 to 2021, we apply a sequence of post-processing

steps to extract the tectonic signal and study the slip behavior of the segment, in comparison with creepmeter records with higher temporal resolution.

4.2 Tectonic context

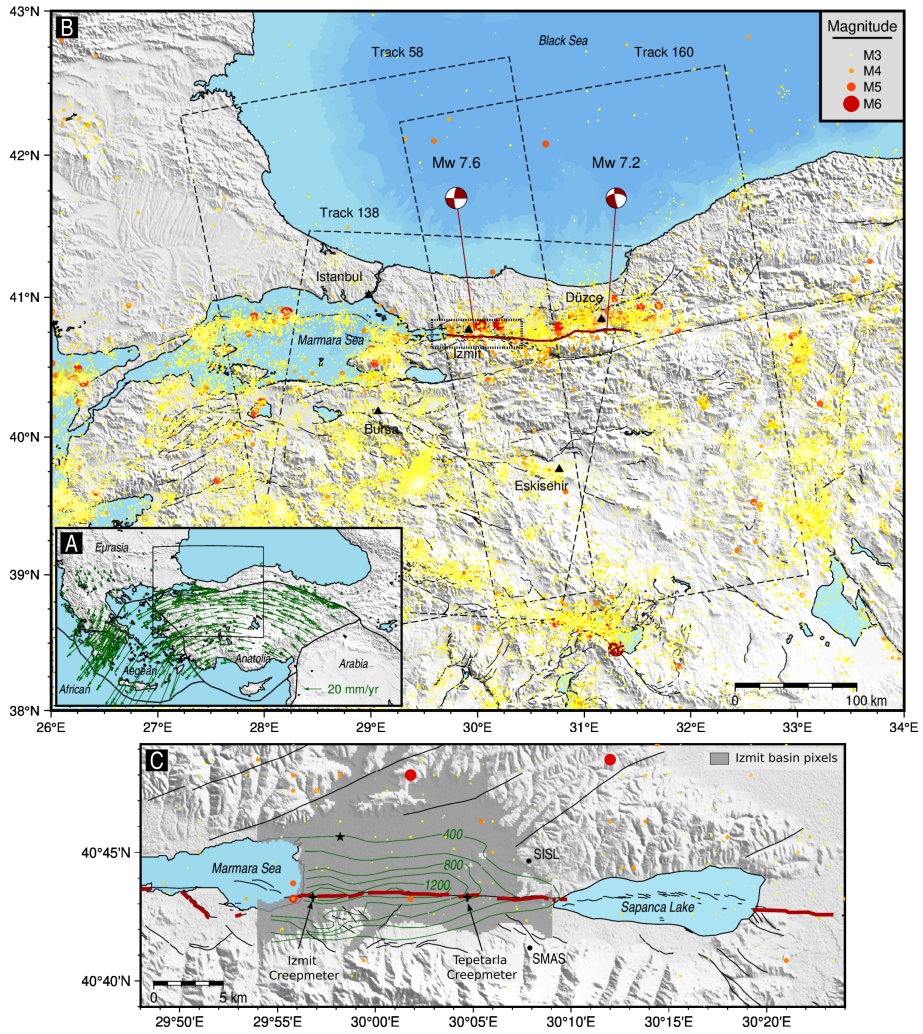

Figure 4.1: Tectonic settings and coverage of the InSAR data. (A) GNSS velocity field from England et al. (2016) of the Anatolia and the Aegean plates relative to Eurasia. The horizontal velocities are represented by the green arrows. The tectonic plates are delineated by the bold dark lines. The black rectangle corresponds to the area shown in B. (B) Earthquakes from the AFAD catalog over the 1999-2021 period are shown by colored dots. The focal mechanisms are for the 1999 M_w7.6 Izmit (West) and the 1999 M_w7.2 Düzce (East) earthquakes. The corresponding surface rupture trace is indicated by the bold red line (Barka, 2002). The geological faults are shown by the black lines (Emre et al., 2018). The dashed rectangles correspond to the three InSAR tracks used in this study, and the dotted rectangle corresponds to the cover of the bottom map. (C) Bedrock depth (green lines) within the Izmit basin based on gravity data from Özalaybey et al. (2011). The gray zone shows the pixels within the Izmit basin, with an elevation lower than 150 m. The black star corresponds to the 1999 Izmit earthquake epicenter. The two black crosses and the two black dots show the locations of two creepmeters installed along the Izmit segment and of the campaign GNSS stations (SISL, SMAS), respectively. The bold red line corresponds to the surface rupture of the Izmit earthquake from Barka (2002).

The right-lateral strike-slip NAF located between the Anatolia and Eurasia plates, with a relative velocity of 24 ± 1 mm/yr (McClusky et al., 2000; Reilinger et al., 2006; Nocquet, 2012), crosses Türkiye from East to West over a length of 1600 km. Since the 1930's, it has been affected by a seismic sequence that includes 7 $M_w \geq 7$ earthquakes, propagating westwards from Erzincan to the Izmit segment (figure 4.1), until the offshore segment below the Marmara Sea which remains a seismic gap and threatens the region of the megalopolis of Istanbul (Stein et al., 1997).

The two last M_w7.6 and M_w7.2 earthquakes of this sequence ruptured in 1999 the Izmit and Düzce segments (red line Figure 4.1B), respectively. The coseismic deformation of the Izmit mainshock has been widely studied, using seismic data (e.g. Bouchon et al., 2001), geodetic data including SAR acquisitions and GNSS data (e.g. Delouis et al., 2002; Feigl et al., 2002) and field observations (e.g. Barka, 2002). The Izmit bilateral rupture from the epicenter (40.76°N, 29.97°E) led to numerous coseismic slip models showing between two and three main slip asperities, with a slip amplitude reaching 8 m (e.g. Delouis et al., 2002; Feigl et al., 2002). The $M_w \geq 3$ aftershocks are concentrated on the rupture segment, leading to the nucleation of the Düzce earthquake 87 $days$ later and a seismic quiescence on the Izmit segment after the Düzce rupture (Karabulut et al., 2011).

Studies of several time periods following the mainshock reveal a postseismic phase in two stages: i) rapid deep afterslip in areas surrounding the coseismic slip during the first ~ 2.5 $years$ (e.g. Bürgmann et al., 2002; Hearn et al., 2002), ii) viscoelastic relaxation of the lower crust and upper mantle over the decades following the earthquake (Ergintav et al., 2009), as shown by Hearn et al. (2009) and Wang et al. (2009) who used various rheological models to compute the postseismic deformation and found a viscosity for the lower crust and the upper mantle of $\sim 2.10^{18} - 5.10^{19}$ $Pa.s$ and $\sim 7.10^{19} - 2.10^{20}$ $Pa.s$, respectively. Comparison of afterslip models indicates a common slip area that rapidly initiated below the Izmit segment at a depth of $12 - 24$ km with a maximum amplitude of 2 m (Çakir et al., 2003).

In addition to the deep afterslip and the viscoelastic deformation, the shallow part of the Izmit segment is slipping aseismically since the mainshock, raising the question whether this on-going segment behavior is related to the postseismic phase or is more perennial and corresponds to the interseismic deformation. Cakir et al. (2012) showed that the Izmit segment started to creep after the 1999 earthquake on the first kilometers of the sub-surface down to depths of $4 - 5$ km with a creeping rate of up to 10 mm/yr computed over the 2003-2009 period. It showed that some portions of this segment can slip both seismically and aseismically. By using InSAR, GNSS, and creepmeters data, the aseismic creep along the Izmit segment has been confirmed until 2017 (Cakir et al., 2012; Hussain et al., 2016; Aslan et al., 2019b; Özarpacı et al., 2020), with a locking depth estimated between 10 and 18 km and shallow steady creep of from 5 to 10 mm/yr, located between the surface and 8 km depth, depending on studies. Recently, Aslan et al. (2019b) highlighted a 1 $month$-long SSE in December 2016 causing a surface relative displacement of 10 mm, by using Sentinel-1 InSAR time series and creepmeter data collected close to Izmit (figure 4.1C). Özarpacı et al. (2020) detected another transient event, also recorded by the Izmit creepmeter in September 2015, as well as with campaign GNSS measurements acquired close to the fault.

4.3 InSAR analysis

4.3.1 Interferograms and time series processing

By exploiting Sentinel-1 A and B SAR acquisitions, which benefit from repeat acquisition times of 6 days, we aim to characterize the deformation on the Izmit segment with a high temporal resolution from 2016 to 2021, i.e. extending the time period with respect to previous studies. The interferograms and InSAR time series used in this work have been processed in the framework of the FLATSIM *ForM@Ter LArge-Scale Multi-Temporal Sentinel-1 InterferoMetry Service* project, operated by the French *Centre National d'Études Spatiales* (CNES) (Thollard et al., 2021). The processing workflow follows the New Small Baseline (NSBAS) approach (Doin et al., 2011): a selection of bursts, image co-registration and correlation, evaluation of the spectral diversity (Grandin, 2015), range estimate relative to the Digital Elevation Model (DEM) and precise orbit corrections. Interferogram networks are built by minimizing the perpendicular and temporal baselines (up to one year to reduce the impact of phase biases). Atmospheric contributions are addressed for each interferogram, based on global atmospheric models, using the ERA-5 meteorological analysis from the European Centre for Medium-Range Weather Forecasts (ECMWF) (e.g. Jolivet, 2011). Finally, the time series are calculated from the inversion of the interferometric phases.

We use the results from three 250 *km*-wide tracks covering the Izmit segment of the NAF (figure 4.1B): two ascending ones (A058 and A160), and a descending one (D138). The Figure C.1 in the Appendix C gives the interferogram networks with the number of SAR images and interferograms used for the time series analysis. The common time period covered by the time series of the three tracks is from February 2015 to April 2021. In order to remove the pixels with abnormal noise levels, we kept only the time series corresponding to the pixels with a Root Mean Square (RMS) misclosure lower than 1.5 *rad* in each interferogram and using at least 900 interferograms per pixel to derive the time series ($63-68\%$ of the initial pixels – Figure C.2). The mean InSAR Line Of Sight (LOS) velocities of the three tracks are shown in Figure 4.2 – A and B.

4.3.2 InSAR referencing relative to GNSS velocities

We use the velocity field centered on the studied area relative to the fixed Eurasia plate calculated from survey and continuous GNSS measurements by England et al. (2016) covering the Anatolia plate (figure 4.1A) to reference the InSAR data. The details are explained below.

Method 1 – Method of InSAR referencing relative to GNSS velocities:

We project the GNSS velocities into the LOS components for each track, only using the horizontal eastward and northward GNSS components. We then extract the mean InSAR LOS velocities within a 1 *km*-diameter circle surrounding each GNSS station to compare them with the GNSS velocities. We compute a 2D plane corresponding to the difference between the estimated mean InSAR LOS velocities and the GNSS velocities. By subtracting the 2D plane to our InSAR velocities, we obtain a LOS velocity field relative to fixed Eurasia.

4.3.3 Extraction of seasonal signals

Most of the LOS displacement time series across the tracks are affected by strong seasonal signals. To isolate the tectonic signal, we model the seasonal signal for each pixel with annual periodic terms. Details of the method including specific referencing of the seasonal terms are described below.

Method 2 – Seasonal signals extraction:

We model the seasonal signal using a linear and annual periodic terms:

$$x(t) = x_R + B.(t - t_0) + C.sin(2\pi(t - t_0)) + D.cos(2\pi(t - t_0)) \tag{4.1}$$

with $x(t)$ the cumulative LOS displacement at each pixel at time t, t_0 the initial time (here January 1st, 2015) and x_R a constant term. B represents the linear trend of the signal. C and D correspond to the seasonal amplitudes with periods of one year (cosine and sine correspond to the summer/winter and spring/autumn cycles for a t_0 on January 1st, respectively). The best parameters are estimated independently for each pixel of each track in a least-square sense. The seasonal amplitudes (C and D components) are locally referenced by subtracting a 4th order fitting surface in order to not be dependent on the signal amplitude of the unwrapping reference point.

4.3.4 Horizontal and vertical decomposition

The mean strike of the Izmit segment being fixed to $N90^{\circ}$, we combine LOS time series corrected from the seasonal effects and referenced by GNSS velocities from the two ascending and the descending tracks, and convert them into horizontal East-West and vertical displacement time series. We consider that the North-South displacements are negligible. The method is described below. Finally, we obtain four time series: the East-West and the vertical cumulative displacement time series for the two ascending/descending couples of tracks. To describe the pairs of tracks used in each decomposition, we specify the set of data with the following terms *TA058-D138* and *TA160-D138*, corresponding to the numbers of the ascending (A) and descending (D) tracks.

Method 3 – Horizontal/Vertical decomposition:

We interpolate the LOS time series to be on the same spatial and temporal basis for the three tracks, by building a new spatial grid using a 0.001°-side square mesh (the initial grids having a 8 *looks* resolution corresponding to a 120 *m* pixel size (Thollard et al., 2021)) and interpolating each time series with it. Then, we define a new time vector with 6 *days*-intervals, minimizing the time between the initial acquisition times of the three tracks and the interpolated one, coinciding with the days of acquisitions of the tracks A058 and D138, acquired the same day but with an interval of 12 *hours* (D1308 is acquired at 4am and A058 is acquired at 4pm). The time interpolation is linear. Since Sentinel-1 acquisitions shifted from 12 *days* revisit times before April 25, 2016 to 6 *days*-intervals afterward, we only use data acquired after May 1st, 2016, for consistency.

We then use the following equations to project the LOS ascending and descending displacements onto the fault-parallel (horizontal) and vertical directions (e.g. Fialko et al., 2002):

$$P = \begin{pmatrix} e_{asc}sin\alpha + n_{asc}cos\alpha & u_{asc} \\ e_{dec}sin\alpha + n_{dec}cos\alpha & u_{dec} \end{pmatrix} \tag{4.2}$$

$$\begin{pmatrix} x_{f,t} \\ x_{z,t} \end{pmatrix} = P^{-1} \begin{pmatrix} x_{asc,t} \\ x_{dec,t} \end{pmatrix} \tag{4.3}$$

with P a rotation matrix, α the mean strike of the fault (in this case 90°), (e_i, n_i, u_i) the Cartesian components of the satellite look vectors for the ascending and the descending tracks (noted *asc* and *dec*, respectively), $x_{i,t}$ the LOS displacement, and $(x_{f,t}, x_{z,t})$ the component of the displacement along the fault-parallel direction and the vertical direction, respectively, at time t.

Because the Izmit segment is located in the far range of the track A058 where sensitivity to vertical displacements is lower than in the near range, we focus in the main text on the East-West time series based on the pair of tracks *TA058-D138*. The results for the second pair *TA160-D138* are shown in the Appendix C.

4.3.5 Extraction of the tectonic signal

To extract small amplitude deformation within the area of interest (figure 4.2 – C and D) related to slip on the top first kilometers of the Izmit segment interface, we apply additional corrections. We first correct for remaining long-wavelength signals that are non-tectonic, possibly due to orbit errors, tides or atmospheric signals. To do so, (i) we remove a linear temporal trend in each pixel time series, then (ii) we flatten each residual epoch displacement map, and finally (iii) we add back the linear trend. This step enables to reduce the mean standard deviation of the time series from 1.71 *cm* to 1.05 *cm*.

As shown in Figure 4.1C, the surface trace of the Izmit segment cuts through a Quaternary basin. Horizontal time series throughout the basin exhibit high-frequency temporal noise. To address this noise, we apply blind source separation using Independent Component Analysis (ICA) (e.g. Maubant et al., 2020). More details on this method are described below. The decomposition is only applied to pixels within the basin selected based on an elevation threshold ($\leq$ 150 *m* – gray area Figure 4.1C), on the temporally detrended horizontal time series. By removing two sources extracted by ICA, we reduce the average time series variances within the Izmit basin by 83%. The spatial distribution of the components (figure C.4 – A and C) corresponds to a ramp within the basin, possibly due to residual low-elevation atmospheric signals.

Method 4 – Independent Component Analysis (ICA):

Independent Component Analysis (ICA) assumes that a signal X can be represented as a mixture of several independent sources S so that $X = A * S$, where A is a mixture matrix. The sources are estimated in order to estimate sources as independent as possible (Hyvärinen and Oja, 2000). We use the *FastICA* algorithm from the *scikit-learn* Python library.

We determine the optimal number of IC components by comparing the InSAR time series variances with the variance of the reconstructed time series using a variable number of IC components (figure C.3). Three components enables to explain almost 80% of the InSAR data variance (shown in Figure C.4), including one component exhibiting a temporal linear trend (figure C.4E). In order not to get rid of potential tectonic signal, we only remove the two

components without temporal linear trends (figure C.4 – D and F). By checking differential time series between two pixels on opposite sides of the fault, we verify that the tectonic signal is unaffected by the removal of the noise components (e.g. Figure C.5).

4.4 Mean velocities and seasonal signals analysis

4.4.1 Mean horizontal East-West signal

On the mean East-West velocity map (figure 4.2D), the main signal is the strong gradient located along the NAF, consistent with the interseismic deformation accommodating the right-lateral relative motion of the plates. By comparing the extracted velocities from 80 *km*-long fault perpendicular profiles (red profile on Figure 4.2E), we estimated a far field relative motion of 2.26 ± 0.1 cm/yr by using far field linear fits, in agreement with previous estimations (McClusky et al., 2000; Reilinger et al., 2006; Nocquet, 2012). Lateral variations of the velocity gradient in the near fault are visible along the NAF, with a stronger gradient across the Izmit segment as shown by the profile Figure 4.2E, and a smoother one across the Adapazari segment (eastern part of the study zone – Figure C.7). These lateral variations confirm that shallow creep is occurring along the Izmit segment, while the fault interface of the Adapazari segment is locked from the surface to a greater depth (Aslan et al., 2019b).

4.4.2 Mean vertical signal

On the mean vertical velocity field (figure 4.2C), the Adapazari, Gölcük and Izmit basins are affected by subsidence (from 0.5 to 5 cm/yr in the Adapazari basin). On the north of the NAF, many pixels located outside of these Quaternary basins also have a negative mean vertical velocity, mostly correlated with westward motion, inconsistent with the expected tectonic deformation. Possible explanations for this signal could be either short-term phase biases or variations of temporal coherence due to soil moisture or vegetation growth, these pixels being located in vegetated areas (e.g. crops, forests). However, we did not succeed to find a good metrics to mask out these pixels. Because the affected pixels are relatively far from the fault, they do not impact the extraction of the tectonic signal in this study.

Along the Izmit segment, no vertical motion is observed in the vicinity of the fault, except within 3 *km*-wide areas located south of the NAF (zoom on Figure C.8A) and affected by subsidence, likely due to local hydrological effects. The fault-perpendicular profile of the mean vertical velocity (the blue profile on Figure 4.2E) reveals no deformation at the location of the fault.

4.4.3 Seasonal signals

Similar to the linear terms, we transform the two LOS displacement fields corresponding to the seasonal terms C and D from the equation 4.1 into horizontal East-West and vertical displacement fields by combining the seasonal terms from ascending and descending tracks (figures C.9 andC.10). The profiles perpendicular to the NAF confirm that the slip on the fault is not modulated by the seasonal oscillations on the Izmit basin. More details are given in section C.1.3 in the Appendix C.

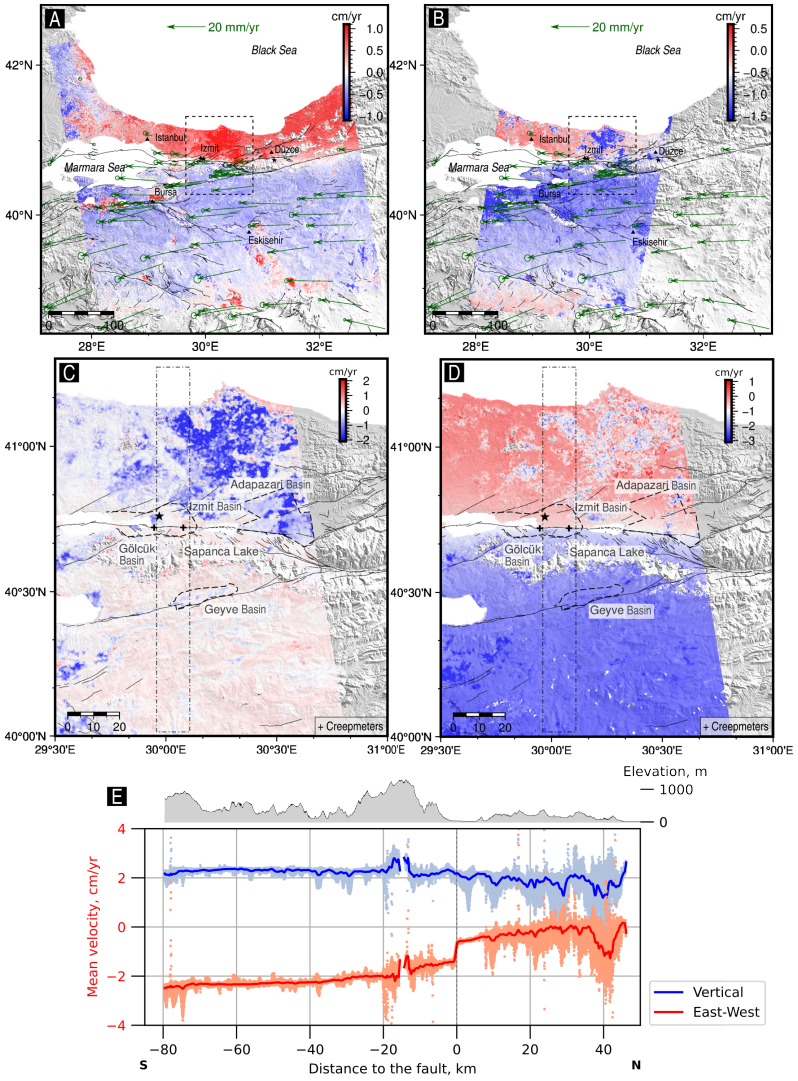

Figure 4.2: InSAR LOS, horizontal and vertical velocity fields. (A,B) Maps of the mean LOS velocities of (A) ascending tracks A058 and A160 and (B) descending track D138. Red and blue values correspond to velocities in cm/yr away and towards the satellite, respectively. The fault network is represented by the black lines from Emre et al. (2018). The green arrows correspond to the GNSS velocities in a fixed Eurasia reference frame, obtained from England et al. (2016), and used to reference the East-West InSAR velocity field. The two black stars correspond to the 1999 Izmit M_w7.6 and the 1999 Düzce M_w7.2 earthquakes epicenters and the main cities are located by black triangles. The dotted rectangle corresponds to the cropped zone used in this study. (C,D) Mean vertical (C) and horizontal East-West (D) velocities after decomposition for tracks A058 and D138, and GNSS referencing. (C) Mean vertical velocities in cm/yr with in red and blue, up and down displacements, respectively. (D) Mean East-West velocities in cm/yr with in red and blue, eastward and westward displacements, respectively. The dotted lines highlight the major Quaternary basins named after the main city within them, Gölcük-Izmit, Adapazari and Geyve. (E) Fault-perpendicular profiles corresponding to the dotted-dashed rectangles on the middle maps of mean vertical (blue) and mean East-West (red) velocities, and the elevation (upper profile in gray). The thick lines correspond to the averaged velocities (smoothed over moving windows of 18 *days*). For graphical reasons, the vertical velocity profile is shifted by $+2$ cm/yr. The corresponding results obtained with the decomposition *TA160-D138* are shown Figure C.6.

4.5 Creep dynamics along the Izmit segment

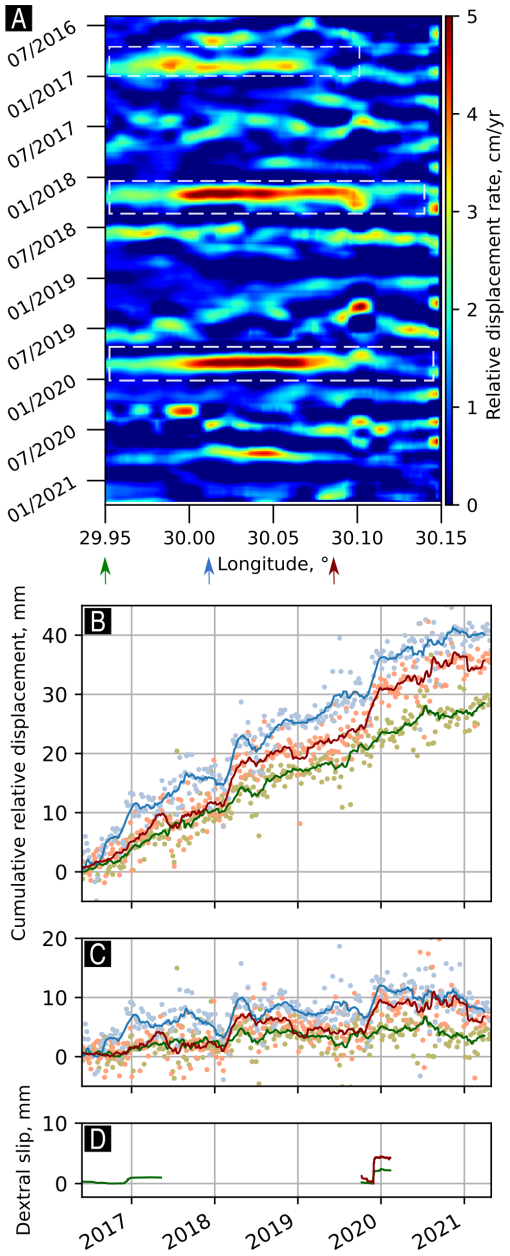

Figure 4.3: Spatial and temporal evolution of the East-West relative displacements along the Izmit segment. (A) East-West relative displacement rate along the Izmit segment estimated by using a 50 *days* average sliding window, using pixels from 400 *m* to 1000 *m* away from the fault. The pixels used are shown in Figure C.11. Three high amplitude periods are delimited by white dotted rectangles, corresponding to an increase of relative displacement rates above 4 cm/yr. The arrows below the Figure correspond to the location of the profiles shown on panels (B) and (C), green and red corresponding to the locations of the Izmit and Tepetarla creepmeters, respectively. (B) Cumulative East-West relative displacement estimated at three longitudes, by using pixels from 600 *m*-width boxes. The lines correspond to the 60 *days* average sliding windows. (C) Corresponding detrended cumulative East-West relative displacement time series obtained after the removal of the linear trend between the transient accelerations. (D) Creepmeter records over the analyzed period of time, green and red corresponding to Izmit and Tepetarla creepmeters, respectively.

In this section, we compare the InSAR relative displacements between pixels on both sides of the fault with the data collected at two creepmeters installed on the Izmit segment: the 'Izmit creepmeter' on its western part (40.7211°N-29.9465°E) and the 'Tepetarla creepmeter' on its eastern part (40.7210°N-30.0784°E) (shown in Figure 4.1C). The temporal coverage of the creepmeters is from 2015 to 2020, but is discontinuous because of technical issues like flooding.

4.5.1 Fault relative displacement

Transient creep events

We analyze the East-West displacement time series corrected from non-tectonic signals close to the fault in order to focus on the shallow creep dynamics of the Izmit segment. We compute the mean time series of the pixels located within two 600 m by 600 m squares, located on each side of the fault and centered 700 m from the fault trace. We then compute the difference of both time series to obtain the Izmit along-strike relative displacement. Figure 4.3B shows three examples of cumulative relative displacement time series obtained at longitudes $E029.95°$, $E030.01°$ and $E030.08°$. All three relative time series exhibit a linear trend corresponding to an average velocity of ~ 5.3 mm/yr at the western location, ~ 6.7 mm/yr at the middle one and ~ 6.0 mm/yr at the eastern one. Superimposed on these positive trends, clear temporal variations are observed in the time series, including transient accelerations in early 2018 and late 2019 at the two eastern locations.

Figure 4.3C shows the detrended cumulative relative displacement time series, where the linear trends computed between the acceleration episodes have been removed. It highlights the relative displacement amplitude during the transient accelerations in March 2018 and in November 2019 of up to 10 mm of cumulative offsets during the two events. The second transient event coincides in time with a transient observed by both creepmeters (figure 4.3D) with transient amplitudes of 2 mm at the Izmit creepmeter and 4 mm at the Tepetarla creepmeter.

To constrain the lateral extent of these transient events, we analyze the relative displacement along the entire Izmit segment (figure 4.3A). The two transient events of 2018 and 2019 are clearly visible, extending along ~ 13 km, from the Marmara sea to latitude $E030.10°$. Another transient event emerging from the noise is also visible in 2016 but with lower amplitude than the two others. It coincides in time with a 1 mm transient recorded by the Izmit creepmeter (figure 4.3D) and has also been documented by Aslan et al. (2019b) who estimated an offset of about 10 mm of East-West displacement with InSAR measurements.

Analysis of transient and inter-transient periods

To compare the total displacements due to the transient events and the periods between them ('inter-transient' periods), we define two complete cycles composed of one main transient event and one inter-transient period. The first cycle starts on January 20, 2017 and ends on May 20, 2018, including the 2018 transient slip event, while the second cycle starts on May 21, 2018 and ends on January 10, 2020, including the 2019 transient slip event.

Figure 4.4 shows the cumulative displacements recorded during each period. The spatial extent of the three transient events is different. The 2016 event (panel A) ruptures mostly the western part of the segment over a ~ 8 km-long distance, and both the 2018 and 2019 events (panels B and C, respectively) happen on the central part of the segment over a ~ 13 km-long distance. The shape of the cumulative displacements during these events is mostly symmetrical, with maximum amplitude at the center. This representation highlights a lack of

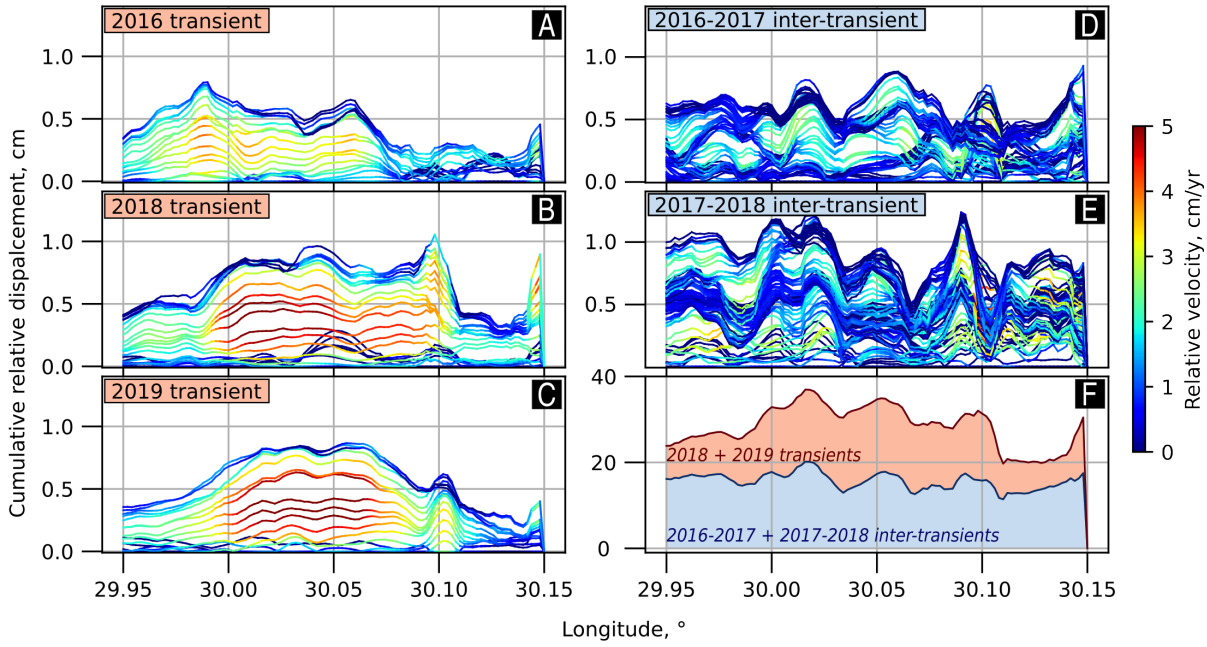

Figure 4.4: Relative cumulative displacement recorded during (A,B,C) and in between (D,E) three transient events highlighted by the white dotted rectangles in the Figure 4.3A: in December 2016, in March 2018 and in November 2019. Two inter-transient periods are therefore defined, between the 2016 (from October 10, 2016 to January 20, 2017) and 2018 (from January 1st, 2018 to May 20, 2018) events and 2018 and 2019 (from October 10, 2019 to January 10, 2020) events. (F) Sum of the relative cumulative displacement during the transient (red) and inter-transient (blue) periods. The pixels used to build this Figure are shown in Figure C.11. Similar results obtained with the pair of tracks *TA160-D138* are shown in Figure C.12.

displacement during the transient events on the eastern part of the segment. The analysis of the cumulative relative displacements during the inter-transient periods (panels D and E) shows a cumulative relative displacement of 1 *cm* on average everywhere along the segment. Lateral variations are evolving between the two inter-transient periods showing a temporal evolution of either local noise or potential other transient slip events producing a signal close to the noise level.

On Figure 4.4F, we sum the relative displacements for the two 2018 and 2019 transient slip events and 2016-2017 and 2017-2018 inter-transient periods. Despite the variations of cumulative relative displacement during the inter-transient periods, the sum is homogeneous over the segment. However, the largest cumulative displacement occurring during the transient periods is located on the central part of the segment, with a difference of at least 10 *mm* of total displacement between the middle and the edges of the segment. The proportion of displacements due to both periods varies along the segment. On the middle of the segment, 50% of the cumulative deformation is due to the transient events, against only $25-30\%$ at the edges. Note that these ratios depend on the distance from the fault trace chosen to compute the relative displacements. For example, the creepmeters located right on the fault capture only the transient events and no relative displacements before or after the events (figure 4.3D), suggesting that only the slip during the transient events reach the surface while the inter-transient slip might be deeper.

4.5.2 Slip inference at depth

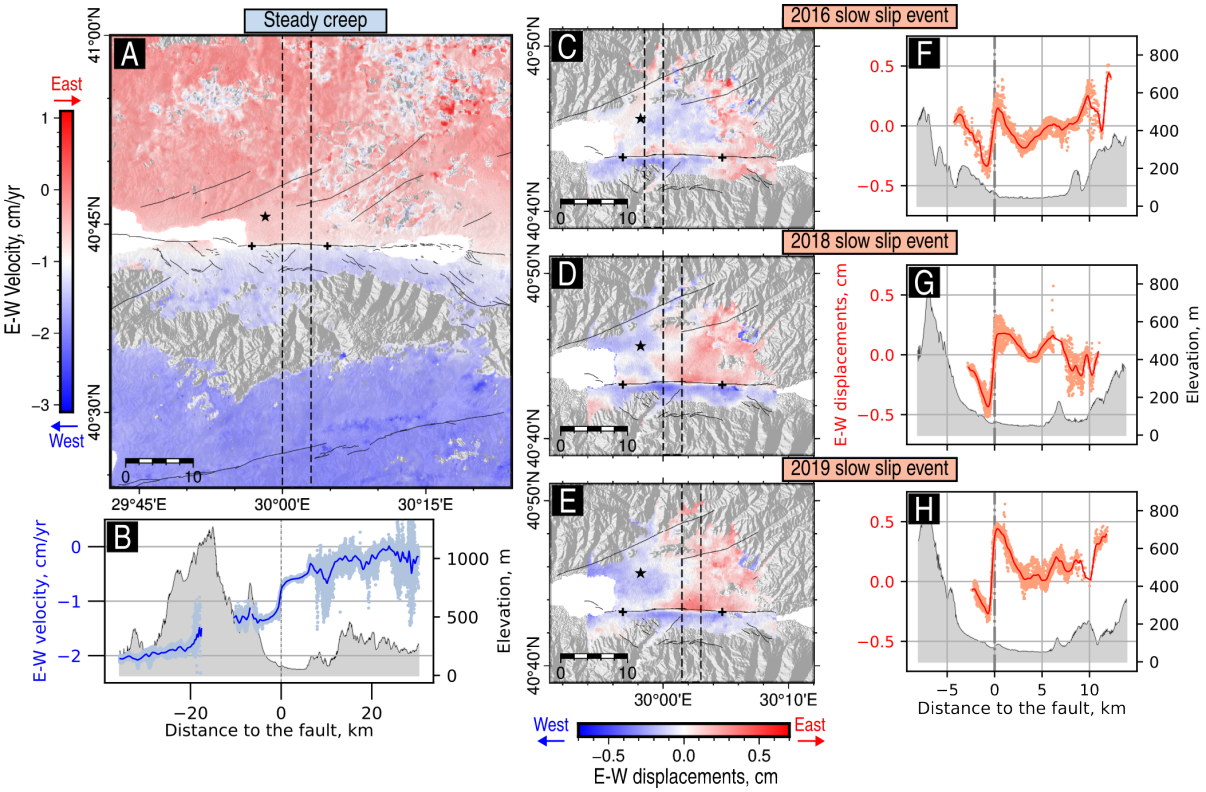

Figure 4.5: East-West velocity field during the continuous creep periods and East-West static offsets during the transient slow slip events. (A) Surface velocity computed during the steady-state creep periods. (B) Fault-perpendicular profile (location on A with the dashed lines) of the East-West velocity and of the mean elevation. (C-E) Static displacements offsets estimated during the three transient slow slip events in 2016 (C), 2018 (D) and 2019 (E). (F-H) Associated fault-perpendicular profiles from each map. The corresponding results obtained with the pair of tracks *TA160-D138* are shown in Figure C.13.

In this section, we estimate the slip distribution along the Izmit segment of the NAF from surface InSAR East-West displacement time series. We perform independent inversions for the static displacement during transient SSEs and for the linear velocity associated with steady creep estimated in between transient events. The inverse models formalism is explained below.

Method 5 – Inverse models formalism:

To estimate the depth and amplitude of slip on the fault interface, we invert the InSAR surface displacement or velocity field by using the generalized least square solution (Tarantola and Valette, 1982):

$$m = m_0 + (G^t.C_d^{-1}.G + C_m^{-1})^{-1}.G^t.C_d^{-1}.(d - G.m_0) \tag{4.4}$$

where m is the strike-slip distribution on the fault plane, m_0 the *a priori* model (non-zero only for the steady creep inversions), G the Green's functions relating unit slip on a given fault patch to the surface displacement field, C_d the data covariance matrix, C_m the model covariance matrix and d the InSAR data. We add a positivity constraint on m of positive right-lateral strike-slip motion by using the non-negative least square algorithm (Lawson and Hanson, 1995). We compute covariograms for each dataset to estimate the spatial covariance C (Sudhaus and Jónsson, 2009):

$$C(h_C) = \frac{1}{2N}\sum_{i=1}^{N}(d(r_i).d(s_i)) \tag{4.5}$$

where r_i and s_i are two pixels, $h_C = ||r_i - s_i||$ is the distance between both pixels, N is the total number of pairs and d the observed displacements per pixel. The matrix C_d is made of the spatial covariance C for each pixel within the study zone. We compute a covariance matrix, using the following equation (e.g. Radiguet et al., 2011):

$$C_m = \left(\sigma_m.\frac{\lambda_0}{\lambda}\right)^2 e^{-\frac{a}{\lambda}} \tag{4.6}$$

with σ_m the standard deviation of the model parameters, λ_0 a scaling factor, λ the correlation distance, and a the distance between fault patches.

To compute the Green's functions G, we consider a multi-layered elastic half-space (Zhu and Rivera, 2002). The velocity model (Karabulut, 2025) as well as the density model for the sedimentary basin (Özalaybey et al., 2011) and for the deeper part (Crust 1.0, Laske et al., 2013)) are shown in Figure C.14. This layered structure is important for the study area to take into account the low velocities and low densities within the Izmit basin, and avoid estimation bias of the shallow slip. The fault is meshed with tight patches of 333 m by 333 m below the Izmit segment down to 5 km. The mesh is coarser around and down to 35 km with patches size increasing from 750 m by 1000 m meters at the surface to 5000 m by 5000 m at depth. For the steady creep estimation between transient SSEs, we estimate tectonic loading from the side by computing Green's functions for 4060 km-long and 35 km-deep fault patches. Below, we use a soft medium with near zero velocities. Such a medium has no resistance against the above-imposed fault motion and thus move together with both plates. A comparison with an infinite fault in an elastic medium shows that this boundary condition produces equivalent deformation amplitudes in the far field at a much reduced computational cost (figure C.15). The scaling factor λ_0 being determined using the mean distance between the patches, we use 1500 m for the continuous creep using the whole mesh and 333 m for the transient creep events inversions using only the tightened mesh.

Steady-state creep

To study the linear trend observed on the time series between transient SSEs, we adjust the time series segments by removing the transient SSE offsets and compute the mean velocity using a linear regression (figure 4.5A). The fault-perpendicular profile shown on the Figure 4.5B is focused closer to the fault than the profile shown Figure 4.2E and enables to confirm the relative long-term velocity of the NAF (McClusky et al., 2000; Reilinger et al., 2006; Nocquet, 2012).

We perform a series of inversions to constrain the locking depth in the deep part of the fault, using as inversion parameters 1500 m for λ_0, 2500 m for λ and 0.5 for σ_m, parameters selected by computing the slip roughness as a function of the RMS and selecting the values with the L-curve criterion (Hansen, 1992) (figure C.19A). We conduct several inversions with varying locking depths in the *a priori* model m_0 ranging from 0 to 30 km, with slip rate below the locking depth fixed to the relative plate motion of 24 mm/yr (McClusky et al., 2000; Reilinger et al., 2006; Nocquet, 2012). We compute the RMS errors as a function of the *a priori* locking depths (figure C.16) and investigate the slip models (figure C.17). For *a priori* locking depths below 10 km, the RMS are large and the slip models cannot explain the displacement away from the fault (figure C.18), because of too shallow locking depths together with the slip positivity constraint preventing to obtain smaller slip amplitudes fitting the data. For lock-

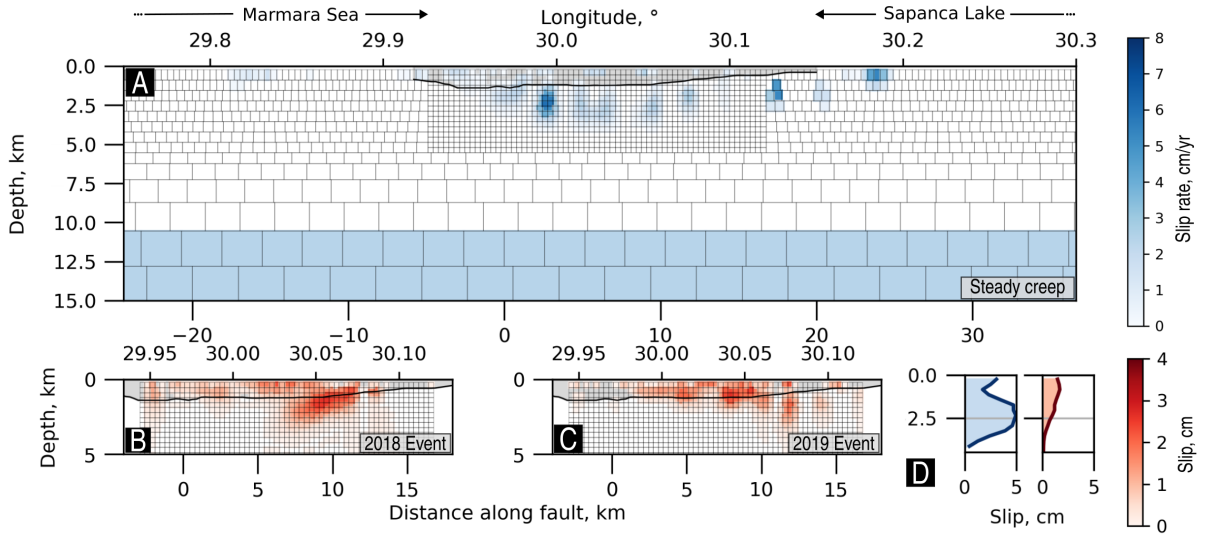

Figure 4.6: Fault slip models for the steady creep and the 2018 and 2019 slow slip events. (A) Preferred slip model obtained for the steady creep, with an *a priori* locking depth at 11 *km*-depth. (B-C) Slip models obtained for the 2018 and 2019 slow slip events. The gray area underlined by a black thick line corresponds to the sedimentary basin obtained from gravity data by Özalaybey et al. (2011). The distance along fault is computed from the 1999 Izmit earthquake epicenter. (D) Depth distribution of the cumulative slip during the two complete cycles of transient and inter-transient periods (from the October 10, 2016 to January 10, 2020). The blue and red parts correspond to the creep during the inter-transient and transient periods, respectively. It has been computed within the tightened mesh, below the Izmit segment.

ing depths below 15 *km*, deep patches with unrealistic slip amplitudes are appearing in the slip models to counterbalance too deep locking depths. We thus estimate the optimal locking depth at 11 *km*, to both fit the data and obtain an homogeneous slip distribution below the locking depth. The corresponding slip distribution is presented in the Figure 4.6A (the deeper part is shown on Figure C.17B), and shows homogeneous slip below the locking depth as well as shallow creep. The residuals between the preferred model prediction and the observations are shown in Figure C.18H.

The final slip distribution (figure 4.6A) shows shallow slip, mostly from 2 to 4 *km*, with slip rates of 2 cm/yr and up to 6 cm/yr at the longitude $E029.99°$. This shallow slip is located right below the sedimentary basin as constrained by gravity measurements (Özalaybey et al., 2011). Other slip patches closer to the surface are located to the east of the Izmit segment, below the Sapanca Lake, at longitude $E030.18°$. The lateral roughness of shallow creep is poorly constrained by the data, which prevents us to study the along-strike slip rate variations. Several models obtained with distinct spatial smoothing in slip rate equally explain the observations (examples Figure C.20). However, the depth distribution is well constrained, independently of the spatial smoothing, with high slip rates between 2 and 4 *km* depth.

Transient slow slip events

After the removal of the linear inter-transient velocity studied previously (figure 4.5A), we compute the total displacement during each SSE by averaging the displacements 1 *month* before and after the transient periods and computing the difference, at each pixel. The three maps on the Figure 4.5 – C,D and E are the total East-West displacement fields obtained for the 2016, 2018, and 2019 events, respectively. The locations of the three fault-perpendicular profiles (figure 4.5 – F,G and H) have been selected at the maximum relative displacements

along the fault for each transient event. The three profiles show a strong gradient with different amplitudes: ~ 5 *mm*, ~ 8 *mm* and ~ 9 *mm* for the 2016, 2018 and 2019 events, respectively. While the signal associated with the 2016 event appears more noisy on the map, the 2018 and 2019 events are characterized by positive and negative lobes on each side of the fault.

We conduct inversions to estimate the slip at depth associated with the 2018 and 2019 SSEs. Taking into account the strong gradients of the East-West displacement fields observed across the fault, we choose to consider only the part of the interface below the Izmit segment from the surface to 5 *km*. The Figure 4.6 – B and C shows the results of the inverse model computation for the 2018 and 2019 transient events, respectively, using as inversion parameters $m_0 = 0$, $\lambda_0 = 333\ m$, $\lambda = 2500\ m$ (2018 event) and $\lambda = 2000\ m$ (2019 event) and $\sigma_m = 0.5$. λ is selected based on the L-curve criterion (Figure C.19B and C.19C). Different models with varying λ are shown in Figures C.22 and C.23. RMS errors obtained when comparing the preferred model predictions to the data are shown in Figure C.21. The main slipping patches are concentrated on the upper part of the fault interface, above 2 *km*-depth, within or close to the downdip limit of the sedimentary basin. In both slip distributions, the slip is mostly localized on the central part of the Izmit segment, with a mean East-West displacement of about ~ 3 *cm*. We observe two main slipping areas, a smaller one on the western part ($\sim 3\ km^2$) and a bigger one on the central part of the interface with a size about $\sim 8\ km^2$. Both are located within or just slightly below the sedimentary basin. It suggests that the same slipping areas ruptured by both SSEs. By using a mean shear modulus of 18 *GPa* for the first 4 *km* of the fault interface and slipping areas of 11.4 and 9.3 km^2 for the 2018 and 2019 transient events, respectively, we obtain equivalent magnitudes of 4.4 and 4.3 (Hanks and Kanamori, 1979). Thus, the predicted North-South displacements related to each slip distribution reveal amplitudes lower than 0.1 *mm*, validating the assumption of a negligible North-South displacement along the Izmit segment.

4.6 Discussion

The InSAR data used in this study results from the automatic processing made in the framework of the FLATSIM project briefly described in section 4.3.1. We applied specific post-processing including referencing, denoising and sources decomposition (section 4.3) allowing us to extract a tectonic signal related to the spatio-temporal evolution of the slip on the Izmit segment of the NAF (section 4.5). Our results confirm that the products of this automatic processing are suitable not only for the analysis of continental deformation (Lemrabet et al., 2023), but also for the analysis of a regional (within a 200 km^2 region) and slow (a few *mm* for the transient events) deformation. Our post-processing analysis enables to correct the InSAR data from seasonal signals, as well as (i) large-scale signals included in the whole tracks, extracted using a trajectory model approach (section 4.4.3) and (ii) local signals located within the Izmit sedimentary basin and extracted using ICA (section 4.3.5). These seasonal signals (figures C.4, C.9 and C.10) can be related to several mechanisms not studied here (e.g. hydrological or atmospheric residuals effects), and their spatial analysis reveal that no clear tectonic signal was contained in both types of signal, meaning that the creep along the Izmit segment is not seasonally modulated.

4.6.1 Steady creep along the Izmit segment

Our results confirm that the Izmit segment is still aseismically creeping 22 *years* after the 1999 Izmit earthquake. To compare the cumulative displacements along the segment before

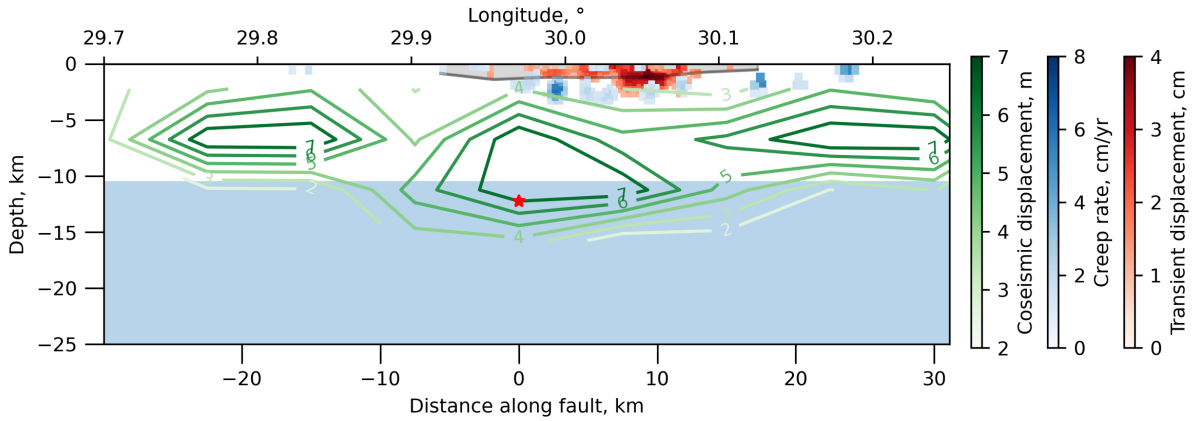

Figure 4.7: 2D fault interface of the Izmit segment with the slip distributions at distinct phases of the seismic cycle. The green lines delimit the coseismic slip distribution from Delouis et al. (2002). The blue colorbar corresponds to the continuous creep with homogeneous creep at 24 mm/yr below 11 km depth and continuous creep patches between 2 and 4 km depth. The red colorbar corresponds to the sum of both slip distributions obtained by inversions of the total displacements during the 2018 and the 2019 slow slip events. The gray area corresponds to the bottom of the sedimentary basin obtained from gravity data by Özalaybey et al. (2011). The red star corresponds to the 1999 Izmit earthquake hypocenter. The distance along fault is computed from the 1999 Izmit earthquake epicenter.

and after the Izmit earthquake, we use two survey GNSS stations SISL and SMAS located 3 km away from the fault (black dots in Figure 4.1C) combined with published InSAR time series (Cakir et al., 2012; Hussain et al., 2016) as well as InSAR time series from this study. The Figure C.24 shows the East-West component of the SMAS-SISL baseline computed for the 1995-2019 period after removing the interseismic linear trend before the earthquake (Özarpacı et al., 2020). We used the logarithmic decay with a relaxation time of 60 yr provided by Özarpacı et al. (2020) based on the SMAS-SISL baseline to model the postseismic phase. As mentioned by Özarpacı et al. (2020), this logarithmic evolution suggests that the postseismic phase is still on-going. The InSAR time series from this study, with ~ 5 mm/yr of baseline increase rate during the period 2015-2021, fit well with the logarithmic decay.

The shallow steady-state creep estimated in this study, occurs within the shallowest 5 km of the fault. Coseismic models of the 1999 Izmit earthquake (Delouis et al., 2002; Feigl et al., 2002) suggest that $2-3$ m of slip occurs in the first 5 km while the slip reached a maximum value of 7 m around 6 to 8 km-depth. This is leading to 4 to 5 m of slip deficit in the shallow section of the fault. Postseismic slip estimates are discontinuous in time in the published literature. Early postseismic models suggest that $5-9$ cm of slip occurred on the first 5 km of the Izmit segment during the first 10 $days$ (Bürgmann et al., 2002; Ergintav et al., 2002). However, we have no constraints on the amplitude of early afterslip that occurred within the first few hours after the earthquake, which could reach up to 10 % of the coseismic slip amplitude (Twardzik et al., 2019). Later estimates of the postseismic creep rate on the first kilometers of the fault (≤ 5 km-depth) are coming from InSAR studies: ~ 10 mm/yr from 2002 to 2010 (Cakir et al., 2012; Ergintav et al., 2014; Hussain et al., 2016), ~ 8 mm/yr from 2011 to 2017 (Aslan et al., 2019b; Özarpacı et al., 2020) and ~ 7.5 mm/yr from 2016 to 2021 estimated by our study. Taking into account all these estimates plus the observation that 2/3 of the relaxation occurred within the first two years based on the logarithmic decay for the baseline between GNSS sites SISL and SMAS (figure C.24), we obtain a rough estimate of a cumulative shallow postseismic slip of ~ 35 cm, representing less than 10% of the coseismic slip deficit, in agreement with the

analysis from Özarpacı et al. (2020). Such a small amount of shallow postseismic slip with large uncertainties could mean that either a large part of the early shallow afterslip is missing in the published models or that the coseismic deficit was overestimated (e.g. due to neglected off-fault yielding) or that postseismic afterlip can still last for several decades to catch-up the deficit, like on the NAF Ismetpasa segment still creeping at the surface about eighty years after the 1944 M_w7.3 Bolu-Gerede earthquake (Jolivet et al., 2023).

Our inverse models with varying *a priori* locking depths (section 4.5.2), suggest an optimal locking depth of ~ 11 *km* along the Izmit segment during the 2016-2021 period. Reilinger et al. (2006) found a locking depth of 21 *km* before the 1999 earthquake, whereas studies for the periods after the earthquake found locking depths from 10 to 12 *km* (Cakir et al., 2012; Aslan et al., 2019b; Özarpacı et al., 2020), in agreement with our result, except for Hussain et al. (2016) who found a deeper locking depth of ~ 18 *km*. The shallow locking depth in the two decades after the Izmit earthquake together with the deeper one estimated before the earthquake is favouring a still active postseismic afterslip below the seismogenic zone, with deepening of the locking depth throughout the seismic cycle. A shallow locking depth is also observed along the Ismetpasa segment of the NAF by Jolivet et al. (2023), who found locking depths of about $8-12$ *km* below the creeping segment and $15-20$ *km* below the locked surrounding segments. As proposed by Jolivet et al. (2023), the shallow locking depth below some segments may potentially be a key factor in terms of stress transfers for the establishment of long-lasting continuous shallow creep during the interseismic phase.

4.6.2 Izmit slow slip event cycle

Up to now, four SSEs have been detected along the Izmit segment: in September 2015 (Özarpacı et al., 2020), in December 2016 (this study and Aslan et al., 2019b), in March 2018 and in November 2019 (this study), corresponding to an averaged return period of ~ 1.3 *years*. Such a recurrence interval is on the same order of magnitude to the ones observed on the California faults segments with shallow SSEs, including the Superstition Hills Fault or the San Andreas Fault near San Juan Bautista (Wei et al., 2013). The recurrence intervals of SSEs on the Ismetpasa creeping section of the NAF was also of ~ 1 *yr* in the 80's and between 2014 and 2016 (Bilham et al., 2016). This recurrence interval might increase in the future if the Izmit segment is still in its postseismic phase or can stay steady if the fault is already back in its interseismic phase (Wei et al., 2013). In between SSEs, we observe steady-state creep that is localized below. When looking at the slip rate variations during these periods of time, they are not steady in time (figure 4.4 – D and E) and might suggest the presence of lower amplitude transient slip events. However, these variations are at the noise level, preventing us to identify smaller amplitude SSEs. All scenarios between end-members continuous slip and successions of small amplitude SSEs are possible for the slip dynamics between 2 and 4 *km*-depth.

Among the four SSEs of the Izmit segment observed so far, only the 2018 and 2019 events have a signal complete enough to get estimates of associated slip at depth. The 2015 event has been observed only with the Izmit creepmeter recording 1.6 *mm* of dextral displacement (Aslan et al., 2019b). The 2016 event has been observed both with the Izmit creepmeter recording 1.1 *mm* of dextral displacement and 10 *mm* of InSAR East-West relative displacement by Aslan et al. (2019b) and 5 *mm* of East-West InSAR relative displacement in our analysis. The maximum relative displacement (figure 4.4A) is located on the western part of the Izmit segment. Slip amplitudes for both 2018 and 2019 SSEs are around 1 to 2 *cm* and can reach up to 6 *cm* depending on spatial smoothing. The slip is mainly located on the central part of the Izmit segment for both of these events, suggesting a potential migration compared to the 2016 event. The associated equivalent moment magnitudes for these two events are 4.4 and 4.3.

The slip characteristics in terms of depth, shape of the slipping asperity and amplitudes are equivalent to other models of shallow SSEs on the Ismetpasa segment of the NAF (Rousset et al., 2016) or on the Supertition Hills Fault (Wei et al., 2009). These SSEs on the Izmit segment allow the release of $48-51\%$ of the plate loading velocity, when computing the loading moment rate on the same area than the one used to compute the equivalent moment of the events.

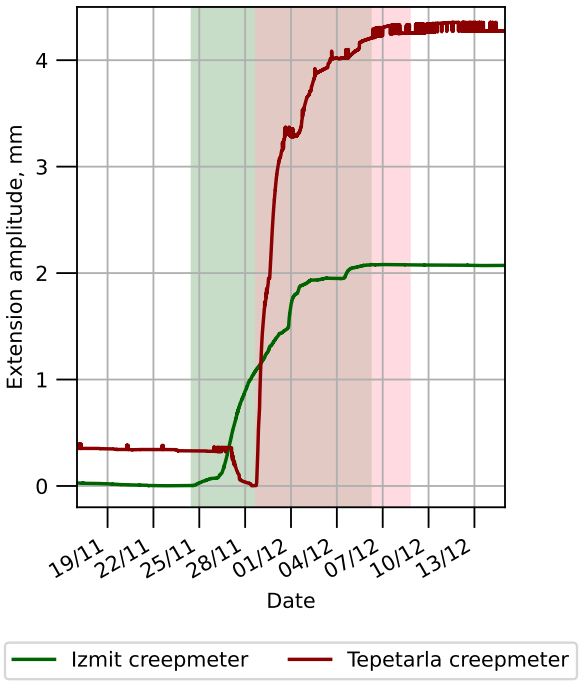

Figure 4.8: Creepmeter records from Izmit (in green) and Tepetarla (in red) during the 2019 event. The lines correspond to the raw records and the rectangles correspond to the transient event periods.

To estimate the durations of the transient events, we analyzed the creepmeters records, the 6 *days* InSAR temporal sampling being too sparse to estimate precisely the durations of the SSEs. The Figure 4.8 shows the records of both creepmeters for the 2019 event, with a sampling of 30 *sec*. The start of the event is obvious with a sharp onset. We estimate the end of an event as the time for which the pre-transient trend is being recovered. For the Izmit creepmeter (figure 4.8 in green), the event started on November 26, 2019 at 10am GMT and ended on December 6, 2019 at 9am GMT, corresponding to a total duration of 9 *days* and 23 *hours*. For the Tepetarla record (figure 4.8 in red), the event started on November 28, 2019 at 5pm GMT and ended the December 7, 2019 at 1pm GMT, corresponding to a total duration of 8 *days* and 21 *hours*.

By using the total duration of about 9 *days* and the equivalent moment magnitude of 4.3 for the 2019 event estimated from the slip models, we can compare these characteristics with other worldwide SSEs. These values are in agreement with shallow continental strike slip faults SSEs on the Ismetasa segment of the NAF (Rousset et al., 2016), on the Superstition Hills Fault (Wei et al., 2009) and the Imperial Fault (Materna et al., 2024). Compared to subduction SSEs, these events have lower moment magnitudes, but the duration that can be equivalent to some short-term subduction events. In a moment magnitude versus duration plot, they fall to the left of the linear relation between duration and moment magnitude obtained by gathering all subduction SSEs and tremors (Materna et al., 2024). As suggested by Ide and Beroza (2023), these events take place within the hidden area due to the a lack of observational results for small magnitude events in subduction zones.

The onset of the 2019 SSE is shifted by 2.26 *days* between both creepmeters. By using the distance of ~ 14.5 *km* between them, and assuming a unilateral rupture with constant velocity, we estimate a propagation velocity from Izmit to Tepetarla of ~ 6.4 km/day, comparable with the ones observed for propagating events on the San Andreas Fault (Gittins and Hawthorne, 2022; Materna et al., 2024). It is also comparable with the along-strike propagation velocities of subduction SSEs in Nankai (Obara and Sekine, 2009), Cascadia (Bartlow et al., 2011) and Alaska (Rousset et al., 2019b). Given that there is only two observation points to estimate the onset of the 2019 Izmit SSE, it is also possible that this event propagated bi-laterally, starting in between the two creepmeters and would lead to a propagation velocity between 0 and 6.4 km/day depending on the initiation location.

4.6.3 Possible mechanisms promoting creep and SSEs along the Izmit segment

Our analysis of the slip rate on the Izmit segment reveals two distinct slip modes: steady creep between 2 and 4 *km* and transient SSEs between the surface and 2 *km* depth. The presence of shallow aseismic slip within the first 4 *km* is likely due to a compensation of slip deficit from the 1999 Izmit earthquake coseismic slip at seismogenic depths. Both slip modes observed at shallow depth are possibly due to depth variations of frictional properties, the shallow SSEs being located within or close to the downdip limit of a sedimentary basin. The continuous creep between 2 and 4 *km* might be a necessary condition to drive the shallow SSEs by continuously increasing the shear stress on the first kilometers of the fault.

In the framework of rate-and-state friction models, the depth-dependence of the frictional parameters explains the various seismic and aseismic slip modes for strike-slip faults. An unstable velocity-weakening layer at seismogenic depth overlaying a velocity-strengthening layer at deeper depths explains cycles of large earthquakes (e.g. Lapusta et al., 2000; Barbot et al., 2012). The addition of a velocity-strengthening zone within the first kilometers of the fault can explain shallow aseismic creep (Kaneko et al., 2013). By adding even more complexities to the frictional variations within the first kilometers of the faults, including variations between conditionally stable velocity-neutral and velocity-strengthening layers, Wei et al. (2013) and Tymofyeyeva et al. (2019) show that the emergence of shallow transient aseismic slip events is possible. In the particular case of the Izmit segment, two key features have to be explained, (i) a logarithmic decay associated to the postseismic afterslip as observed by the pair of GNSS sites SISL and SMAS (figure C.24) and (ii) the emergence of transient slip events. The models derived by Wei et al. (2013) including a small conditionally stable layer close to the surface succeed to explain both of these observations. This model predicts a shortening of the recurrence SSE intervals within the postseismic phase. However, we cannot estimate such an evolution with the limited number of events observed so far on the Izmit segment.

The distribution between creeping segments (e.g. Ismetpasa and Izmit) and locked segments along the NAF remains unclear, although a mineralogical control is often evoked. Within the Izmit area, the northern branch of the NAF splits two bedrocks units composed of (i) limestones from the Paleozoic-Mesozoic sequence on the northern side and (ii) several metamorphic units on the southern side, both deposited on a metamorphic basement (Akbayram et al., 2013; Kaduri et al., 2017; Taylor et al., 2019). The mineralogical analysis of the gouge of the Ismetpasa creeping segment from Kaduri et al. (2017) suggests that the volcanic units are more prone to be affected by both seismic and aseismic slip than the limestone ones. In the case of the Izmit segment, the contrast between the northern and the southern units is in agreement with geological conditions which can promote aseismic creep according to Kaduri et al.

(2017). The shallow sediments are usually clay-rich (e.g. Rockwell et al., 2009), which can also promote the development of creep (Bürgmann, 2018). In addition, a tomography study from Taylor et al. (2019) shows that the damaged zone within the crust goes down to 5 *km* below the Izmit segment surface trace, compatible with the depth of the creeping zone.

High pore fluid pressure can also enhance the presence of transient aseismic slip as evidenced by tomography with high Vp/Vs ratio at subduction zones areas prone to SSEs (Shelly et al., 2006). In geothermal contexts, aseismic slip seems also to be the favored mechanisms to release the accumulated stress on local faults (e.g. Guglielmi et al., 2015). On strike-slip faults, intense rain events have been suggested to favor transient creep events (Roeloffs, 2001). Seasonal modulation of creep have been observed on some faults, like the SAF (Li et al., 2023), which could be due to seasonal variations of either pore pressure or regional hydrological surface loading. On the Izmit segment of the NAF, we analyzed the seasonal components of the time series (section 4.4.3) and found no clear evidence of seasonal modulation of creep. To evidence any potential correlation with meteorological events, we looked at temperature and precipitation data from the ERA-5 Land data during the 2016-2021 period (figure C.25). We do not see clear relationship between temperature variations, cumulative precipitations and the transient event occurrences. However, the 2016 transient event coincides with a period of increased precipitations, which could potentially have an effect on pore pressure of the fault interface. The topographical low of the Izmit basin together with the sedimentary basin may also favor an overall high pore pressure within the basin.

Finally, we looked at the AFAD earthquake catalog over the 2016-2021 period to detect any link between seismicity within the Izmit basin and the SSEs (figure C.26). The temporal distribution of the events seems to be random over the 5 *years*-long period, and no obvious link between these events and the SSEs can be inferred. The location of the events (figure C.26A) reveals a seismically quiescent area corresponding to the central part of the Izmit segment, where the SSEs slip amplitude is the highest (figure 4.4F), suggesting a spatial segmentation between seismicity and transient aseismic SSEs. We also looked for possible triggering by regional large earthquakes and found no events at the times of the shallow SSEs, suggesting that they are spontaneous SSEs.

4.7 Conclusions

By employing automated InSAR time series analysis and subsequent processing, we investigated the slip dynamics of the Izmit segment of the North Anatolian Fault from 2016 to 2021. Our results reveal a locked zone at 11 *km* depth and aseismic creep within the upper 5 *km*, likely compensating for the 1999 Izmit earthquake's slip deficit. The temporal analysis of the creep combined with slip inverse models show that steady creep is occurring $2-4$ *km*-depth while transient slow slip events are happening from the surface to 2 *km*-depth. The depth separation between these two slip modes is likely due to frictional variations, the SSEs being located at the downdip limit of the sedimentary basin and above it. We detected two new SSEs, leading to four SSEs observed along this segment since the 1999 Izmit earthquake: in September 2015, December 2016, March 2018 and November 2019; corresponding to an average return period of 1.3 *years*. The slip models of the 2018 and 2019 events correspond to equivalent moment magnitudes of 4.4 and 4.3, respectively. The creepmeter recordings at two sites allow to extract a propagation velocity of 6.4 km/day for the 2019 event. The presence of a transient slow slip event cycle 22 *years* after the Izmit earthquake might last for decades when comparing to the Ismetpasa segment of the NAF where slow slip events are still happening 80 years after the 1944 Gerede-Bolu earthquake.

Acknowledgments

We thank Hayrullah Karabulut for sharing the velocity model used in this study and for stimulating discussions. The InSAR data is based on the FLATSIM service (doi:10.24400/253171/FLATSIM2020), developed as part of the ForM@Ter Solid Earth data and services center and supported and operated by CNES. Creepmeters data come from the GAGE/UNAVCO dataset (https://www.unavco.org/data/strain-seismic/creep-data/creep-data.html). ERA-5 Land data used for the temperature and precipitation analysis are from the Copernicus Climate Change Service (C3S) Climate Data Store (CDS) (https://cds.climate.copernicus.eu/cdsapp#!/dataset/10.24381/cds.e2161bac?tab=overview, DOI:10.24381/cds.e2161bac). The seismic catalog is available from the AFAD earthquake catalog via https://deprem.afad.gov.tr/event-catalog. Baptiste Rousset has benefited funding for this study from the CNRS PNTS and the IdEx University of Strasbourg.

Supplementary Materials

The Supplementary Materials are shown in Appendix C.

Chapter 5

From coseismic rupture to shallow slow slip: seismic-cycle modeling of the Izmit segment of the North Anatolian Fault

The detection (Section 3) and subsequent detailed characterization of the spatio-temporal properties of two slow slip events (SSEs) occurring along the Izmit segment of the NAF in 2018 and 2019 (Section 4) highlight the important role of these transient slip events within the Izmit seismic cycle. These events enable the aseismic release of part of the residual strain that was not accommodated during the 1999 M_w7.6 Izmit earthquake. The shallow localization of the slip, together with the distinction between the transient shallow SSEs within the sedimentary basin and the steady-state creep observed at depths of 2–5km, suggests that frictional variations with depth may control the slip dynamics along the fault. Following discussions with Matt Wei (Associate Professor at the University of Rhode Island, USA) and Yoshihiro Kaneko (Professor of Geophysics at Kyoto University, Japan) during the 2024 AGU fall meeting, who derived seismic cycle models for the Superstition Hills Fault in California (Wei et al., 2013), we decided to collaborate with them. For the Superstition Hills Fault case, mechanical models incorporating shallow frictional heterogeneity within the framework of RSF successfully reproduced the observations and explained the occurrence of SSEs during the seismic cycle. The objective of this chapter is therefore to test whether similar mechanical models can reproduce the full range of observed time scales along the Izmit segment, including coseismic slip amplitudes and recurrence times, postseismic afterslip relaxation, and the amplitudes and recurrence times of shallow slow slip events, and therefore provide insights into the underlying physical mechanisms. The work of this chapter is currently being prepared as a journal article.

Abstract

Earthquake-cycle models provide a mechanical framework for linking the broad spectrum of slip rates observed on faults, from seismic rupture to interseismic creep, postseismic afterslip, and slow slip events. Yet the parameters controlling shallow slow slip events (SSEs) on continental strike-slip faults remain poorly constrained, mainly because such observations are still rare and because few fault segments are monitored over sufficiently long periods to capture several phases of the seismic cycle. Here, we use one-dimensional quasi-dynamic rate-and-state friction models to investigate the ensemble of geodetic, seismological, and paleoseismological observations available along the Izmit segment of the North Anatolian Fault in Türkiye. This segment ruptured during the 1999 M_w 7.6 Izmit earthquake and has since been extensively monitored, providing constraints on coseismic slip, earthquake recurrence time, logarithmic postseismic relaxation, and shallow SSEs. GNSS, InSAR, creepmeter, seismological, and paleoseismological observations allow us to describe cumulative fault slip during several phases of the seismic cycle. The comparison between model predictions and observed time scales leads to a restricted family of frictional models. First, the maximum coseismic slip of ~ 6 *m* and recurrence times of ≥ 200 *yrs* are reproduced by an unstable seismogenic layer extending below 5.5 *km* depth, with a thickness of ~ 9.5 *km* and frictional parameter $(a-b) \sim -0.004$. Second, the decadal afterslip observed by a pair of campaign GNSS stations located on opposite sides of the fault is mainly controlled by a stable layer between 1.3 and 5.5 *km* depth, whose lower limit is consistent with the upper extent of the aftershock sequence. We compare model slip predictions with GNSS time series by computing Green's functions for a layered elastic half-space. The intermediate layer that best reproduces the observed relaxation time is characterized by $(a-b) \sim 0.005$ and $D_c \sim 8$ *km*. Finally, a shallow layer extending from the surface to ~ 1.3 *km* depth is required to generate shallow SSEs about 20 *yrs* after the mainshock. This layer may either have constant negative frictional parameters or a vertical gradient in apparent frictional properties. Its depth extent is consistent with the Quaternary sedimentary basin beneath the Izmit region, suggesting that sediment properties, pore-pressure variations, or both may promote shallow velocity-weakening behavior and episodic aseismic slip.

Keywords: seismic cycle models, rate and state friction, shallow aseismic creep, slow slip events, strike-slip fault, North Anatolian Fault



- Frictional parameters, critical slip distance, and layer width jointly control coseismic rupture, postseismic relaxation, and shallow slow slip along the Izmit segment.
- A shallow transition from stable to conditionally unstable friction promotes the occurrence of shallow slow slip events.
- Pore-pressure variations or lithological heterogeneity within the Izmit sedimentary basin may generate a frictional gradient that favors episodic shallow slip.

Contents

5.1 Introduction 164

5.2 Methods 166

5.2.1 Rate-and-state formalism 166

5.2.2 Definition of the mechanical models 166

5.2.3 Observational constraints along the Izmit segment 168

5.2.4 Comparison between numerical simulations and observations 169

5.3 Results 170

5.3.1 Coseismic observations 170

5.3.2 Afterslip observations 171

5.3.3 SSE observations 171

5.4 Discussion 174

5.4.1 Model limitations and quasi-dynamic approximation 174

5.4.2 Controls on coseismic rupture and postseismic afterslip 174

5.4.3 Frictional ingredients required for shallow SSEs 175

5.4.4 Implications for slow slip events physical precesses 175

5.4.5 Broader implications for strike-slip faults 176

5.5 Conclusions 176

5.1 Introduction

Faults accommodate plate motion through a wide range of slip modes that vary with depth, frictional properties, effective normal stress, temperature, lithology, and fluid pressure. In the classical view of the seismic cycle, the seismogenic zone accumulates elastic strain during the interseismic period and releases it during earthquakes through rapid seismic slip. Above and below this unstable region, faults may instead slip aseismically, either continuously or transiently. At shallow depth, creep may reach the surface and produce measurable fault-parallel displacement without generating large earthquakes. This shallow aseismic slip may be steady over years to decades, but it may also occur episodically as shallow slow slip events. Around coseismic rupture zones, postseismic afterslip can further accommodate part of the coseismic stress perturbation, often producing logarithmic or power-law surface deformation over months to decades (Avouac, 2015). The coexistence of seismic slip, shallow creep, afterslip, and slow transient deformation therefore indicates that the seismic cycle cannot be described only by locked and fully rupturing fault patches, but must instead include transitional regions with conditionally stable or spatially heterogeneous frictional behavior.

Slow slip events have been most extensively documented in subduction zones, where they often occur near the downdip transition from the locked seismogenic zone to stable sliding (e.g. Bürgmann, 2018). In these settings, SSEs are commonly interpreted as the expression of transitional behavior between frictional to ductile due to temperature increase (Yousfi et al., 2026) with potential high pore pressure effects (Segall et al., 2010). However, SSEs are not restricted to subduction interfaces. Growing geodetic evidence shows that transient aseismic slip also occurs on continental strike-slip faults, including the San Jacinto Fault near the Anza gap (Inbal et al., 2017), the Hayward Fault (Lienkaemper et al., 2001), the Imperial and San Andreas faults (Titus et al., 2006; Gittins and Hawthorne, 2022), the Superstition Hills Fault (Wei et al., 2013), the Haiyuan Fault (Jolivet et al., 2012), and several sections of the North Anatolian Fault, including the Ismetpasa (Rousset et al., 2016; Jolivet et al., 2023) and Izmit segments (Aslan et al., 2019b; Neyrinck et al., 2024). Along strike-slip faults, shallow SSEs are generally inferred within the first kilometers below the surface and may be influenced by sedimentary basins, shallow lithological contrasts, fluids, geometric complexity, or inherited damage zones. These processes can modify effective stress or frictional stability and may allow small shallow patches to fail episodically rather than slip steadily.

The Izmit segment of the North Anatolian Fault provides a particularly favorable natural laboratory for investigating these processes (Figure 5.1). This segment ruptured during the 1999 M_w 7.6 Izmit earthquake, which produced several meters of coseismic slip along the fault (Delouis et al., 2002; Çakir et al., 2003). Historical and paleoseismological data indicate that large earthquakes repeatedly rupture this section of the fault, with recurrence times on the order of one to several centuries (Ambraseys, 2000; Langridge et al., 2002; Rockwell et al., 2009). After the 1999 earthquake, geodetic observations revealed significant postseismic afterslip, including decadal deformation recorded by campaign GNSS stations located on both sides of the fault within the Izmit basin (Özarpacı et al., 2021). More recently, InSAR, GNSS, and creepmeter observations have revealed several shallow SSEs in 2015, 2016, 2018, and 2019, localized within the shallow portion of the 1999 rupture zone and partly overlapping the Quaternary sedimentary basin beneath Izmit (Özarpacı et al., 2020; Aslan et al., 2019b; Neyrinck et al., 2024). These observations raise a central question: which frictional structure can simultaneously reproduce large coseismic ruptures, long-lived afterslip, and shallow SSEs along the same fault segment?

To address this question, we use the rate-and-state friction numerical framework imple-

mented by Wei et al. (2013). We test whether shallow frictional heterogeneity associated with the Izmit sedimentary basin can explain the occurrence of SSEs while preserving the main characteristics of the 1999 earthquake cycle. We first describe the rate-and-state formulation and the two shallow mechanical models considered. We then compare the simulated coseismic slip, postseismic relaxation, and SSE properties with GNSS, InSAR, creepmeter, seismological, and paleoseismological constraints. Finally, we discuss the physical implications of the optimal models, with particular emphasis on the role of shallow sedimentary materials, pore pressure, and frictional gradients in promoting episodic aseismic slip.

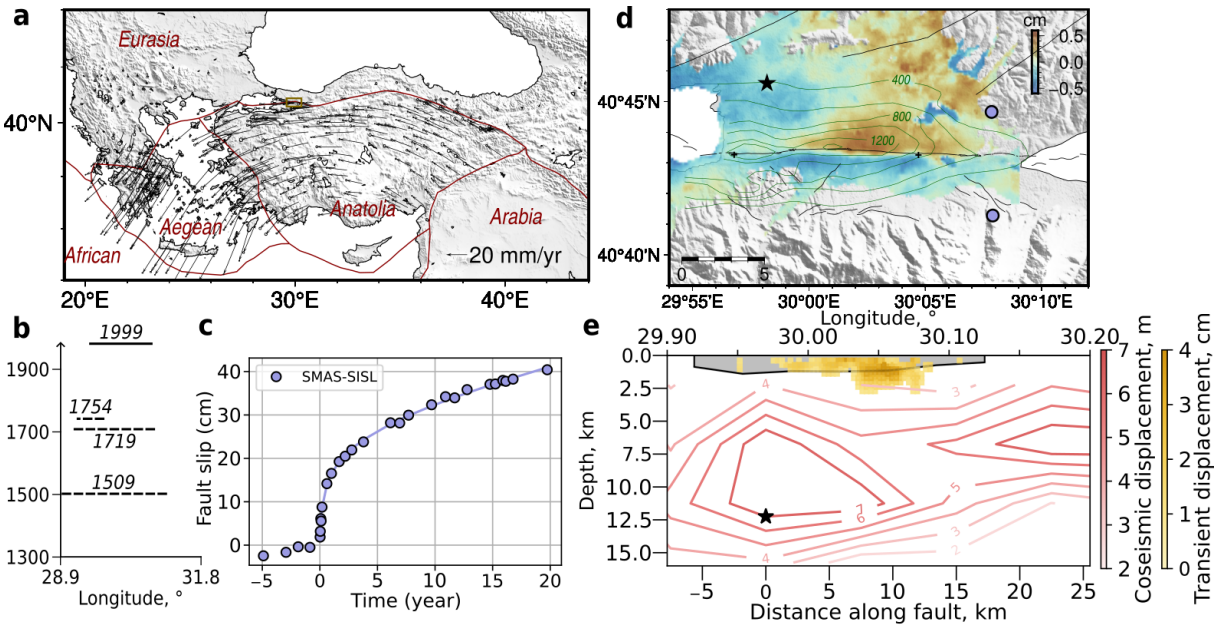

Figure 5.1: Tectonic context of the Izmit segment of the North Anatolian Fault (NAF) in Türkiye. (a) GNSS velocity field from England et al. (2016) of the Anatolia and Aegean plates relative to Eurasia, represented by black arrows. Tectonic plates are delineated by red lines. The brown rectangle corresponds to the area shown in panel (d). (b) Historical earthquakes that may have affected the Izmit segment since A.D. 1300, compiled by Langridge et al. (2002) and references therein. (c) SMAS–SISL GNSS postseismic displacement following the 1999 Izmit earthquake from Özarpacı et al. (2021). The locations of both stations are shown in panel (d) by purple dots. (d) Static displacement offsets estimated during the 2019 SSE from InSAR data within the Izmit basin (Neyrinck et al., 2024). Bedrock depth within the Izmit basin, based on gravity data from Özalaybey et al. (2011), is shown by green contours. The black star corresponds to the 1999 Izmit earthquake epicenter. The two black crosses show the locations of two creepmeters installed along the Izmit segment. (e) Two-dimensional fault interface of the Izmit segment showing the coseismic slip distribution from Delouis et al. (2002) and the sum of the slip distributions inferred from inversions of the 2018 and 2019 SSEs from Neyrinck et al. (2024), corresponding to the red and yellow color bars, respectively. The gray area corresponds to the base of the sedimentary basin from Özalaybey et al. (2011). The black star corresponds to the 1999 Izmit earthquake hypocenter.

5.2 Methods

5.2.1 Rate-and-state formalism

We use numerical simulations based on a quasi-dynamic method for a one-dimensional strike-slip fault embedded in a two-dimensional elastic half-space. Fault slip is modeled over multiple seismic cycles using the rate-and-state friction framework (Rice, 1993; Lapusta et al., 2000; Liu and Rice, 2007; Wei et al., 2013). In this approach, the shear stress τ evolves as a function of slip rate V and of a state variable θ, which describes the slip history of the fault:

$$\tau = \overline{\sigma}\left[f_0 + a\ln\left(\frac{V}{V_0}\right) + b\ln\left(\frac{V_0\theta}{D_c}\right)\right], \tag{5.1}$$

where a and b are friction parameters, D_c is the critical slip distance, f_0 is the friction coefficient at the reference velocity V_0, and $\overline{\sigma}$ is the effective normal stress. We use the aging law to describe the evolution of θ (e.g. Scholz, 1998):

$$\frac{d\theta}{dt} = 1 - \frac{V\theta}{D_c}. \tag{5.2}$$

The nucleation size h^* is defined as

$$h^* = \frac{2\mu b D_c}{\pi(b-a)^2\overline{\sigma}}, \tag{5.3}$$

where μ is the shear modulus (e.g. Rubin and Ampuero, 2005). By prescribing these parameters along a depth profile, we compute the evolution of cumulative slip over several hundreds of years and analyze the resulting seismic-cycle behavior.

The algorithm developed by Wei et al. (2013) is based on the quasi-dynamic relation between shear stress and slip. In discretized form, the shear stress τ_i on the i-th grid point is expressed as (Rice, 1993; Liu and Rice, 2007)

$$\tau_i = -\sum_{j=1}^{N} k_{ij}\left(\delta_j - V_{pl}t\right) - \frac{\mu}{2c_s}V_i, \tag{5.4}$$

where N is the total number of grid points, k_{ij} is the elastic stiffness, V_{pl} is the tectonic loading rate, t is time, δ_j is slip, μ is the shear modulus, c_s is the shear-wave speed, and V_i is the slip velocity on the i-th grid point. For very low slip rates, the friction law is regularized as

$$\tau = a\overline{\sigma}, \operatorname{arcsinh}\left[\frac{V}{2V_0}\exp\left(\frac{f_0 + b\ln\left(V_0\theta/D_c\right)}{a}\right)\right], \tag{5.5}$$

which is justified by a thermally activated description of slip at frictional contacts (Lapusta et al., 2000; Rice et al., 2001). The fixed parameters used in the numerical simulations are given in Table D.1.

5.2.2 Definition of the mechanical models

To explore the development of shallow SSEs during the seismic cycle, we build two end-member mechanical models defined by their depth-dependent frictional properties. Both models share the same deeper structure, but differ in the shallowest layer. Figure 5.2a shows the

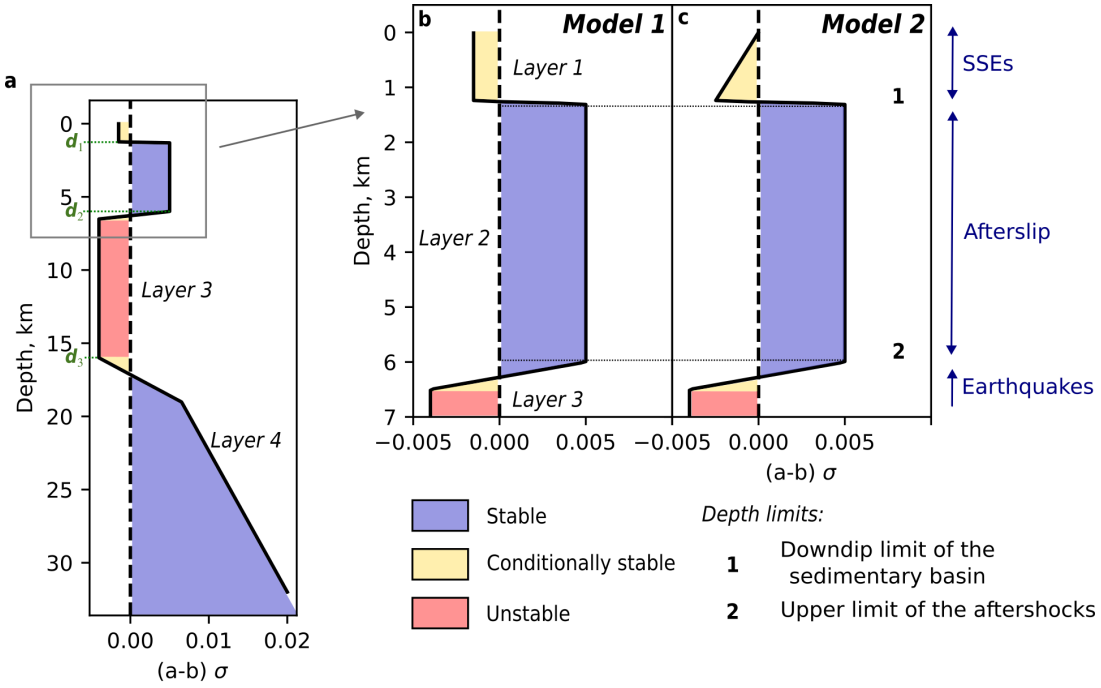

Figure 5.2: Schematic representation of the depth-dependent frictional structure used to analyze the seismic cycle along the Izmit segment. (a) Stable, conditionally stable, and unstable regions are defined from the sign and magnitude of $(a-b)\sigma$. (b,c) Two shallow configurations tested in this study. Blue arrows and annotations indicate the seismic-cycle features most affected by each layer. Horizontal dotted lines indicate the two depth limits used to define the frictional structure. (b) Reference model, hereafter called *Model 1*, with a velocity-weakening top layer. (c) Intermediate model, hereafter called *Model 2*, with a vertical gradient of frictional parameters in the top layer.

common deeper part, composed of *Layers 3* and *4*, following previous rate-and-state modeling studies (e.g. Rice, 1993; Lapusta et al., 2000).

The velocity-weakening *Layer 3* corresponds to the seismogenic zone and controls earthquake nucleation and coseismic rupture. The deeper velocity-strengthening *Layer 4* represents the stable lower portion of the fault interface, where pressure-temperature conditions inhibit seismic rupture. Figures 5.2b,c show the two shallow configurations tested here. In the first model, referred to as *Model 1*, the uppermost layer is a homogeneous conditionally stable velocity-weakening layer overlying a stable *Layer 2*. In the second model, referred to as *Model 2*, the shallow layer contains a vertical gradient in frictional parameters, representing a progressive change in apparent frictional stability with depth. This second configuration is designed to mimic potential gradual changes in pore pressure or damage within the shallow sedimentary basin.

To identify models that best reproduce the surface slip observed along the Izmit segment during the seismic cycle, we explore the influence of the critical slip distance D_c, effective normal stress σ, frictional parameter $(a-b)$, and layer widths (d_i in Figure 5.2a). The tested ranges and final estimates are listed in Table 5.1. The effective normal stress is assumed to increase linearly with depth using a lithostatic-minus-hydrostatic gradient of 13 MPa/km (Wei et al., 2013).

Several parameters are constrained using geological and seismological observations. The depth of *Layer 1* (d_1 in Figure 5.2a) is set to the mean depth of the base of the sedimentary basin beneath Izmit, about 1.2 km (Özalaybey et al., 2011). This choice assumes that shallow

Parameters		Min.	Max.	Final estimates	
				Model 1	*Model 2*
$a-b$	Layer 1	-0.004	-0.001	-0.0015	-0.0025
	Layer 2	0.0035	0.0075	0.005	0.005
	Layer 3	-0.007	-0.001	-0.004	-0.004
D_C	Layer 1	0.1	4.5	0.3	0.3
	Layer 3	5	11	8	8
Width	Layer 2	3.7	6.7	3.7	3.7
	Layer 3	9.5	12.5	10.5	10.5

Table 5.1: Table gathering the parameters values tested for the input model and the final estimates corresponding to the optimal models.

lithology partly controls frictional properties. The depth of *Layer 2* (d_2 in Figure 5.2a) is constrained by the upper limit of the aftershock sequence after the 1999 M_w 7.6 Izmit earthquake, following the interpretation of Marone and Scholz (1988); this limit is approximately 5–6 *km* depth (e.g. Karabulut, 2025). The base of *Layer 3* (d_3 in Figure 5.2a) is constrained by locking-depth estimates after the 1999 earthquake, between 11 and 15 *km* depth (Çakir et al., 2012; Hussain et al., 2016; Aslan et al., 2019b; Neyrinck et al., 2024). Because these depth limits remain uncertain, we test several widths for *Layers 2* and *3*. The tectonic loading rate V_{pl} is fixed to 24 mm/yr, following previous estimates (e.g. McClusky et al., 2000). Finally, because of the lack of direct constraints on shallow cohesion along the Izmit segment, the effective normal stress at the surface is set to zero (Figure D.1; Liu and Rice, 2007).

5.2.3 Observational constraints along the Izmit segment

Coseismic		Afterslip	SSEs 20 *years* after the mainshock		
Amplitude	Return time	Time constants	Amplitude	Return time	Relaxation time
$\sim 5.5 \pm 0.5$ *m*	$\sim$ 140 $\pm$ 30 *years*	$c \sim 4.88$ *cm* and $d \sim 25.23$ yrs^{-1}	$\sim 2 \pm 0.5$ *cm*	$\sim$ 1.35 $\pm$ 0.05 *years*	$\sim 6 \pm 1$ *days*
e.g., Delouis (2002)	Ambraseys (2000); Rockwell et al. (2009)	Özarpacı et al. (2021)	Aslan et al. (2019b); Özarpacı et al. (2021); Neyrinck et al. (2024)	Neyrinck et al. (2024)	Aslan et al. (2019b); Neyrinck et al. (2024)

Table 5.2: Table gathering the Izmit observations of its seismic cycle.

Table 5.2 summarizes the observational constraints used to evaluate the simulations. The 1999 M_w 7.6 Izmit earthquake provides direct constraints on coseismic slip amplitude and rupture depth. Paleoseismological and historical earthquake studies constrain the recurrence of large earthquakes along the Izmit segment (Figure 5.1b; Ambraseys, 2000; Rockwell et al., 2009). Coseismic slip models indicate maximum slip at depth of at least 5 *m* (Çakir et al.,

2003). Postseismic deformation is constrained by the SMAS and SISL campaign GNSS stations, located about 3 *km* from the fault within the Izmit basin (Figure 5.1c,d), and analyzed by Özarpacı et al. (2021). Finally, the properties of shallow SSEs are constrained by four events detected to date: September 2015 (Özarpacı et al., 2021), December 2016 (Aslan et al., 2019b), March 2018, and November 2019 (Neyrinck et al., 2024). The slip amplitude is constrained by slip inversions based on InSAR measurments while the relaxation time is constrained by creepmeter records (Neyrinck et al., 2024). Because no comparable SSE observations are available before, we focus on SSEs occurring about 20 *yrs* after the mainshock.

5.2.4 Comparison between numerical simulations and observations

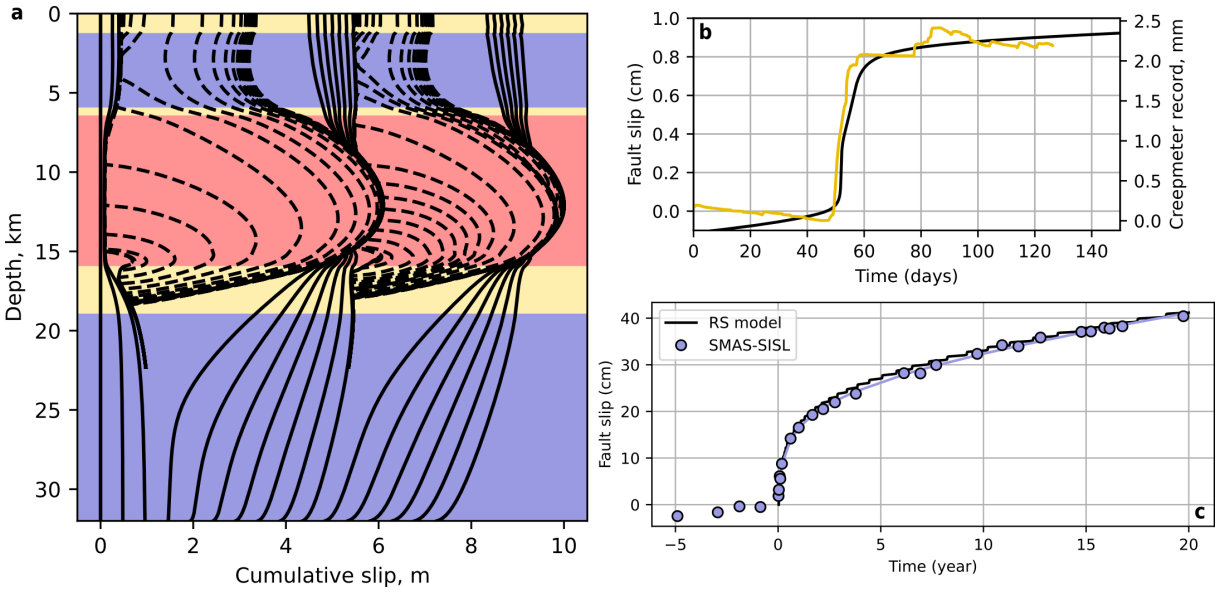

Figure 5.3: Model predictions of fault slip through time for the optimal *Model 2*. (a) Slip history during two seismic cycles. Solid and dashed lines correspond to cumulative slip during the interseismic period, plotted every 40 *yrs*, and during the coseismic period, plotted every 2 *s*, respectively. Colors correspond to the layers shown in Figure 5.2. (b) Example of modeled fault slip during an SSE 20 *yrs* after the earthquake, shown in black, compared with the 2019 Izmit creepmeter record, shown in yellow. (c) Relative surface slip 20 *yrs* after the earthquake from the model predictions compared with the relative surface displacement recorded by the SMAS–SISL GNSS stations along the Izmit segment, shown by blue dots (Özarpacı et al., 2021).

We evaluate each simulation against six observables that characterize the Izmit seismic cycle: coseismic slip amplitude, earthquake recurrence time, postseismic relaxation time, SSE amplitude, SSE recurrence time, and SSE duration. Figure 5.3 illustrates the procedure for one optimal model, showing cumulative slip over two seismic cycles, an SSE extracted 20 *yrs* after the mainshock, and the corresponding surface displacement predicted at the SMAS–SISL GNSS station pair.

Mainshock times are identified from peaks in maximum fault velocity satisfying $\log_{10}(V_{max}/V_{pl}) \geq 5.44$, which selects slip rates high enough to represent dynamic rupture in the quasi-dynamic framework. From these events, we estimate coseismic slip amplitude and recurrence time. Postseismic deformation is then extracted after each mainshock. To compare the simulated afterslip with GNSS observations, we compute Green's functions for a homogeneous elastic half-space (Okada, 1985) and combine them with the modeled depth-dependent slip to predict surface displacement near the two GNSS stations shown in Figure 5.1d. The resulting time

series is fitted with

$$x(t) = a + bt + c\log(1 + dt), \tag{5.6}$$

where a, b, c, and d are fitted constants. The fit is obtained using a Levenberg–Marquardt inversion implemented with the Python library *SciPy*. We then compute root-mean-square errors (RMSEs) between the model predictions and the observations.

SSE starting times are extracted by selecting periods during which the maximum velocity on the shallowest fault cell satisfies $0.5 \leq \log_{10}(V/V_{pl}) \leq 6.85$, while excluding coseismic rupture periods. We then estimate SSE amplitudes and recurrence times throughout the seismic cycle. The duration of each SSE is more difficult to estimate automatically because the end of an event is not sharply defined. We therefore analyze SSE durations in detail only for the final optimal models.

5.3 Results

We now describe how the numerical simulations reproduce three key components of the Izmit seismic cycle: mainshocks, postseismic afterslip, and shallow SSEs occurring about 20 *yrs* after the 1999 earthquake. These comparisons allow us to identify two optimal models, one for each shallow frictional configuration.

5.3.1 Coseismic observations

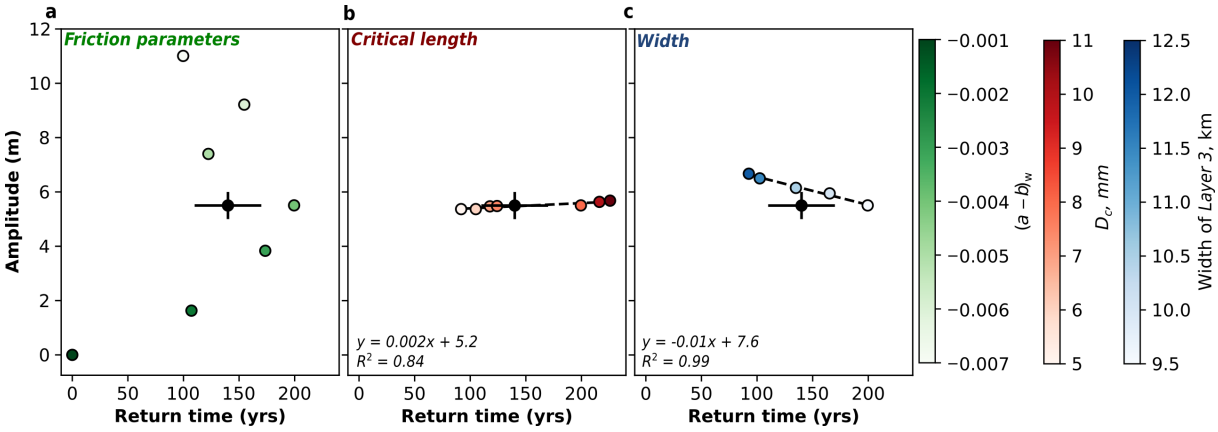

Figure 5.4: Comparison between modeled mainshock amplitude and recurrence time as a function of the properties of *Layer 3*: (a) frictional parameter $(a-b)$, in green; (b) critical slip distance D_c, in red; and (c) layer width, in blue. Shallow-layer properties are fixed. The reference values used for the three tested parameters are $(a-b) = -0.004$, $D_c = 8$ *mm*, and a layer width of 9.5 *km*. Black dots correspond to observational estimates. In panels (b,c), dotted lines show linear regressions, with the corresponding equation and coefficient of determination R^2 indicated in the lower-left corner.

Figure 5.4 shows how coseismic slip amplitude and earthquake recurrence time vary with the parameters of the seismogenic *Layer 3*. The parameter that most strongly controls coseismic slip amplitude is $(a-b)$ (Figure 5.4a). For $(a-b) \geq -0.001$, the model does not produce large mainshocks. As $(a-b)$ decreases from -0.002 to -0.007, the maximum coseismic slip increases up to ~ 9 *m*. This increase is accompanied by variations in recurrence time of about

100 *yrs*, although the relation is nonlinear: more negative frictional parameters tend to produce larger earthquakes with shorter recurrence times.

The critical slip distance D_c and the width of *Layer 3* mainly affect recurrence time, with variations of about 130 *yrs*, while coseismic slip amplitude varies more moderately, by about 0.5–2 *m*. Increasing D_c increases both amplitude and recurrence time. Increasing the width of the seismogenic layer increases coseismic amplitude but decreases recurrence time.

5.3.2 Afterslip observations

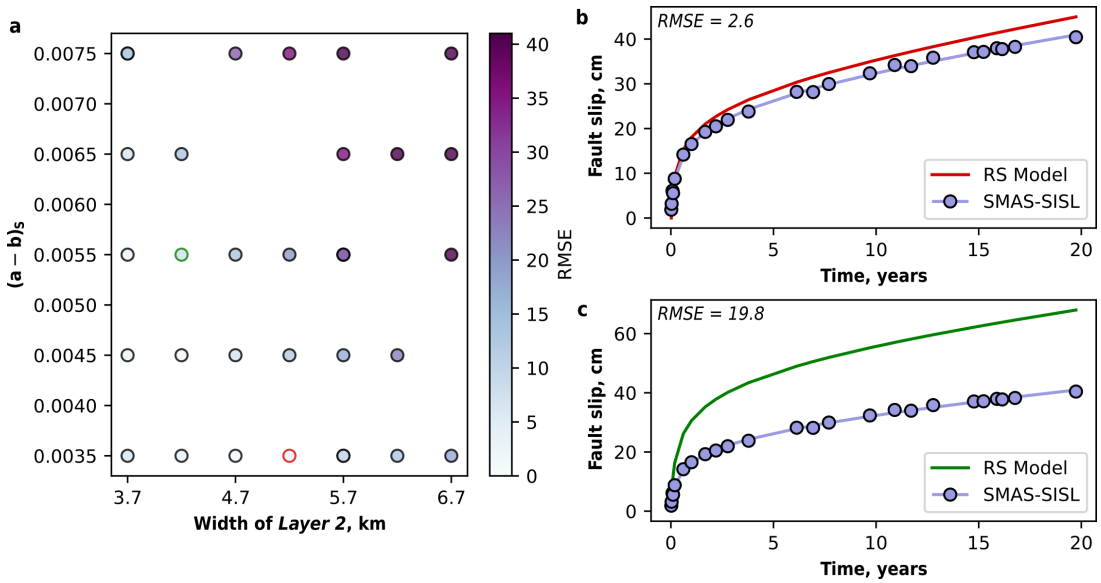

Figure 5.5: Comparison between simulated afterslip and the SMAS–SISL GNSS campaign observations following the 1999 M_w 7.6 Izmit earthquake. (a) Root-mean-square error (RMSE) between the fitted model predictions and the GNSS observations, as a function of two *Layer 2* parameters: layer width and frictional parameter $(a-b)$. Empty cells correspond to simulations that did not converge. Edge colors red and green highlight the two examples shown in panels (b) and (c). (b,c) Examples of two model predictions, shown in red and green, compared with the observations, shown in purple. Parameter pairs ($(a-b)$, width) are (b) 0.0035, 5.2 *km* and (c) 0.0055, 4.2 *km*.

Figure 5.5 shows the RMSE obtained when comparing simulated postseismic deformation with the SMAS–SISL GNSS observations. We vary two parameters of *Layer 2*: its width and frictional parameter $(a-b)$. Both parameters influence the modeled afterslip. Increasing either the width of the layer or $(a-b)$ generally increases the RMSE (Figure 5.5a). The examples shown in Figures 5.5b,c indicate that high RMSE values are associated with excessive postseismic displacement. Thus, larger positive $(a-b)$ values or wider stable layers tend to generate too much cumulative afterslip during the postseismic period. While the solution is non-unique, (ab) values around 0.005 with a stable layer thickness of 3.7 *km* represent one combination consistent with the observed postseismic displacements.

5.3.3 SSE observations

We test the two shallow configurations shown in Figures 5.2b,c to determine whether they can generate shallow SSEs about 20 *yrs* after the mainshock. We focus on three parameters:

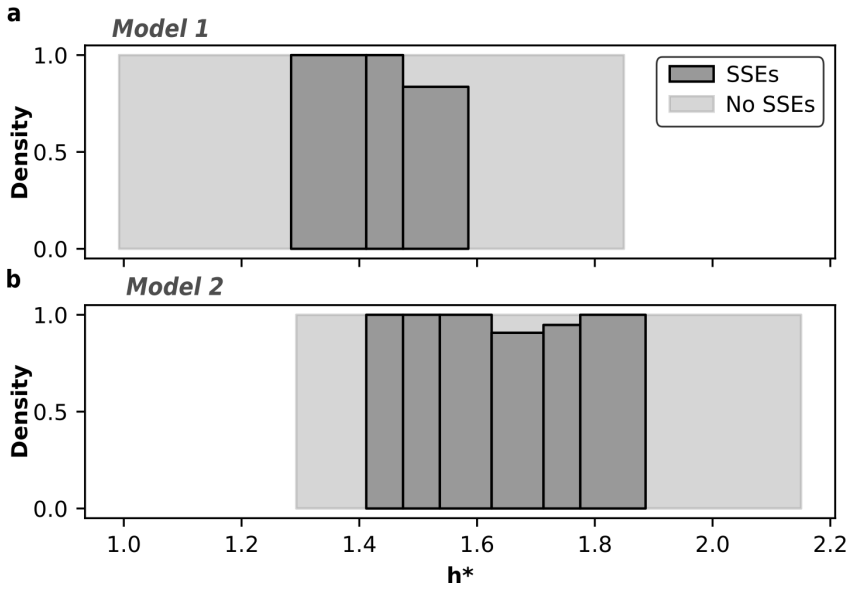

Figure 5.6: Histograms of the density of tested models producing SSEs 20 *yrs* after the mainshock for (a) *Model 1* and (b) *Model 2*. Gray histograms indicate all tested values of h^*, and vertical bars highlight simulations producing SSEs 20 *yrs* after the mainshock.

the type of shallow frictional heterogeneity (either *Models 1* or *2*), the frictional parameter of the top layer $(a-b)\times W$, and the critical slip distance of this layer, $D\times c1$.

Both *Model 1* and *Model 2* can generate SSEs 20 *yrs* after the mainshock, but the fraction and diversity of successful simulations differ between the two configurations (Figure 5.6). Using Equation 5.3, we estimate the range of nucleation sizes h^* that allows SSEs. The successful *Models 1* have h^* values of 1.3–1.6 *km*, whereas the successful *Models 2* have h^* values of 1.4–1.9 *km*. The *Model 2* configuration therefore allows a broader range of nucleation sizes and model parameters. However, h^* alone does not fully determine whether SSEs occur, as shown by the fact that the density of successful models is not always equal to one within these ranges.

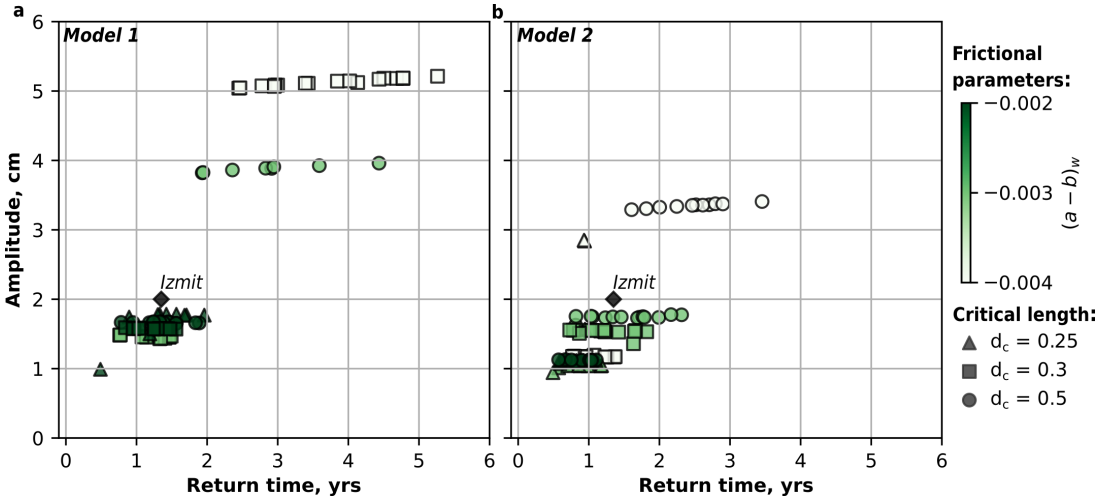

Figure 5.7: Amplitude and recurrence time of modeled SSEs 20 *yrs* after the mainshock for (a) *Model 1* and (b) *Model 2*. Green shading indicates variations in the frictional parameter of *Layer 1*: the constant value for the *Model 1* and the minimum value for the *Model 2*. Marker shapes indicate different values of the critical slip distance of *Layer 1*. The black diamond corresponds to the observational estimates at 1 *km*-depth along the Izmit segment.

Figure 5.7 compares the amplitude and recurrence time of modeled SSEs with the Izmit observations. Both model families produce SSEs within the same order of magnitude as the observed events. The *Models 1* produce amplitudes between 1 and 5.2 *cm* and recurrence times between 0.5 and 5.2 *yrs*. The *Models 2* produce amplitudes between 1 and 3.5 *cm* and recurrence times between 0.5 and 3.5 *yrs*.

The frictional parameter $(a-b)_W$ corresponding to the minimum frictional parameter within the *Layer 1* affects both SSE amplitude and recurrence time. In general, less negative values of $(a-b)_W$ produce smaller and more frequent events. This trend is not strictly monotonic, especially for the *Models 2* with $D_c = 0.3$, indicating that SSE properties depend on coupled variations in frictional stability and critical slip distance. Increasing D_c generally increases both SSE amplitude and recurrence time.

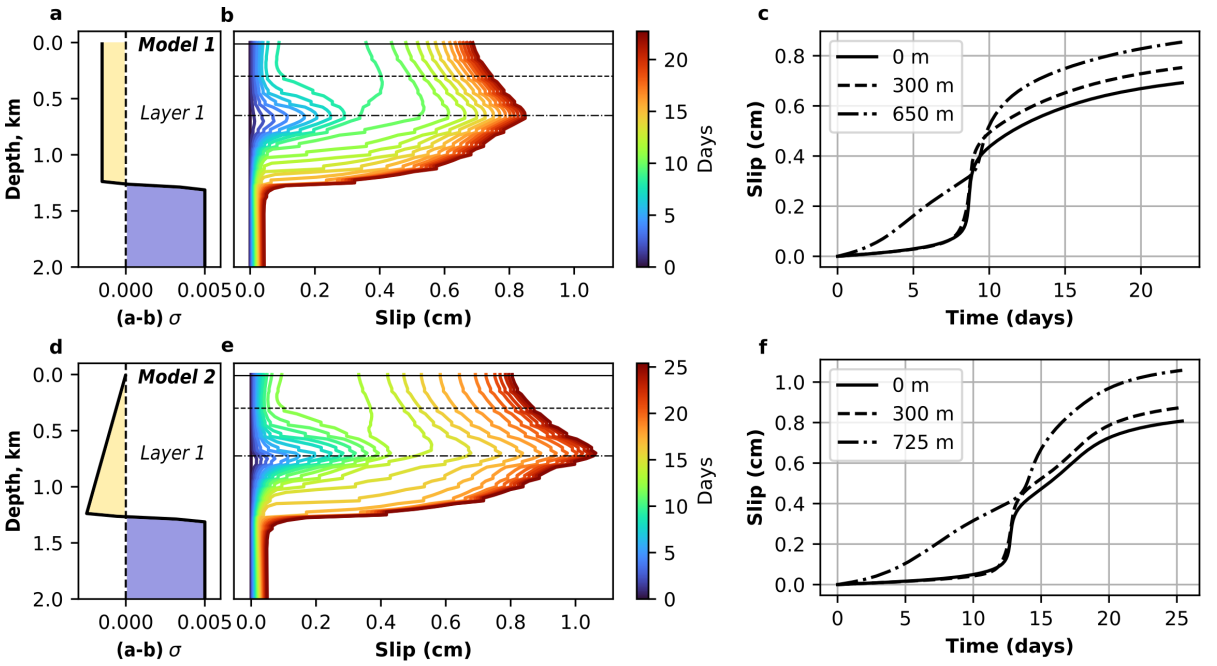

Figure 5.8: Evolution of depth-dependent slip during an SSE for the two shallow model configurations. Top and bottom panels correspond to the *Model 1* and *Model 2*, respectively. (a,d) Zoom on the shallow frictional structure. (b,e) Time evolution of slip with depth. (c,f) Slip time series at three depths: the shallowest cell, 300 *m*, and 725 *m*, indicated by line styles and by vertical lines in panels (b,e).

Because SSE duration is difficult to define automatically, we analyze the time evolution of slip for the final optimal models. Figure 5.8 shows an example of an SSE occurring 20 *yrs* after the mainshock for both model configurations. The two models share three main phases. First, slip initiates at intermediate shallow depth, around 650–725 *m*, with a nearly linear increase in slip during around 10 days. Maximum slip rates during this phase reach 13.7 cm/yr for the *Model 1* and 11.2 cm/yr for the *Model 2*. Second, slip propagates upward toward the surface, producing rapid acceleration of the shallowest cells during about one day. During this phase, the shallowest cell releases up to 42.9% and 37.5% of its total displacement in the *Model 1* and *Model 2*, respectively. Third, slip decelerates over at least 10 *days* with a logarithmic decrease in the *Model 1*, and more complicated temporal variations for the *Model 2*, with a secondary acceleration at the surface.

Despite these similarities, the two model families differ in detail. The initiation depth is shifted downward by about 75 *m* in the *Model 2* relative to the *Model 1*. The initial slip rate is higher in the *Model 1*, reaching 14.2 cm/yr at 650 *m* depth, compared with 11.2 cm/yr at

725 *m* depth in the *Model 2*. In both models, the delay between the onset of shallow slip and the beginning of simultaneous deceleration at all depths is about one day. However, the relaxation phase differs: the *Model 1* displays a more logarithmic deceleration, whereas the *Model 2* shows complex deceleration including a secondary acceleration phase five days after the first one.

5.4 Discussion

5.4.1 Model limitations and quasi-dynamic approximation

The first limitation of this study is the use of a quasi-dynamic approximation rather than a fully dynamic solution. Quasi-dynamic models approximate inertial effects during rupture through a radiation damping term (Rice, 1993), but they do not explicitly solve for the complete propagation of seismic waves (Lapusta et al., 2000). This approximation greatly reduces computational cost and therefore makes it possible to explore a wide parameter space over multiple seismic cycles. However, it may affect the details of rupture propagation, peak slip velocity, rupture arrest, and the stress redistribution associated with dynamic waves. It should primarily affect the coseismic phase, but likely have little to no effect on the characteristics of afterslip and SSEs.

Previous comparisons between quasi-dynamic and fully dynamic models indicate that the broad slip patterns are often similar, but that some model parameters may be shifted between the two approaches (Thomas et al., 2014b). For the Superstition Hills Fault, Wei et al. (2013) found that quasi-dynamic and fully dynamic simulations produce comparable behavior, although the optimal frictional parameters and the width of the velocity-strengthening layer above the seismogenic zone differ slightly. Similar uncertainties may affect our estimates for the Izmit segment. Therefore, the values reported here should not be interpreted as unique frictional properties, but rather as effective parameters within the adopted quasi-dynamic framework. Given the limited constraints on the lithological composition, fluid pressure, and frictional properties of the Izmit fault gouge at depth, this approximation remains appropriate for identifying the first-order ingredients required to reproduce the observed seismic-cycle behavior.

5.4.2 Controls on coseismic rupture and postseismic afterslip

The modeled coseismic and postseismic behavior is primarily controlled by the geometry and frictional properties of the intermediate and seismogenic layers. External constraints on layer depths are essential for reducing the range of acceptable models. The shallowest layer is tied to the depth of the Izmit sedimentary basin (Özalaybey et al., 2011); the base of *Layer 2* is constrained by the upper extent of the aftershock sequence following the 1999 earthquake (Marone and Scholz, 1988; Karabulut, 2025); and the base of *Layer 3* is guided by locking-depth estimates (Hussain et al., 2016; Neyrinck et al., 2024). Within this structure, the frictional parameter $(a-b)$ and the critical slip distance D_c of *Layer 3* control the amplitude and recurrence of large earthquakes. More negative $(a-b)$ values promote larger coseismic slip, whereas D_c and seismogenic-layer width mostly modulate recurrence time.

Postseismic deformation is mainly controlled by the velocity-strengthening *Layer 2*. This layer accommodates stress changes imposed by the 1999 rupture and produces the decadal relaxation observed by the SMAS–SISL GNSS station pair. The best-fitting models require a

stable layer extending from the base of the shallow sedimentary unit to the upper limit of the aftershock sequence. Increasing either the width of this layer or its positive $(a-b)$ value produces excessive postseismic slip and worsens the fit to the GNSS observations. The resulting estimates for *Layers 2* and *3* are of the same order of magnitude as those inferred by Wei et al. (2013) on the Superstition Hills Fault, suggesting that comparable frictional structures may explain earthquake-cycle deformation on different continental strike-slip faults.

5.4.3 Frictional ingredients required for shallow SSEs

The occurrence of shallow SSEs in our models requires a shallow conditionally unstable layer above the stable postseismic afterslip zone. Without this shallow velocity-weakening or transitional layer, the fault either creeps stably or remains too strongly coupled to generate episodic shallow transients. This result is consistent with previous models in which shallow frictional heterogeneity is required to produce SSEs on strike-slip faults (Wei et al., 2013; Tymofyeyeva et al., 2019). In the Izmit case, the required shallow layer extends over approximately the same depth range as the sedimentary basin, suggesting a mechanical link between basin structure and shallow transient slip.

The two tested shallow architectures reproduce the main observed SSE properties, but they do so with different degrees of parameter sensitivity. In the homogeneous *Model 1*, SSEs occur only within a relatively narrow range of nucleation sizes and frictional parameters. This suggests that a uniform shallow velocity-weakening layer requires fine tuning to generate SSEs with amplitudes and recurrence times comparable to the observations. In contrast, the *Model 2* allows SSEs over a broader range of parameters. A vertical gradient in apparent frictional properties therefore provides a more robust mechanism for producing shallow transients. Such a gradient may smooth the transition between stable creep and unstable slip, slowing rupture propagation and allowing days-long events rather than either steady creep or rapid seismic failure.

The duration of the modeled SSEs further illustrates the importance of shallow frictional structure. Both optimal models generate events lasting several days, compatible with the Izmit observations, but the slip histories differ. The homogeneous *Model 1* produces a sharper acceleration and a more logarithmic decay, whereas the *Model 2* produces a more progressive complex temporal pattern with two phases of acceleration. This is compatible with creepmeter observations at Ismetpaşa (Özdemir et al., 2025), where the 2019 recordings show several phases of acceleration within a single SSE. Both models also suggest that the initiation of the SSE start around 10 days before the surface transient slip likely observed by surface geodetic measurements. This important model prediction would suggest that shallow SSEs along strike-slip fault have a long-lasting nucleation phase.

5.4.4 Implications for slow slip events physical precesses

The spatial coincidence between the modeled shallow SSE source region and the Izmit sedimentary basin suggests that basin properties may play a key role in controlling shallow slip behavior. The basin is composed of alluvial deposits, including sand, clay, and gravel, as well as Late Pliocene–Pleistocene deposits (Karakas and Coruk, 2010; Doğan et al., 2021). Such materials may influence friction through lithological contrasts, clay-rich gouge, distributed damage, or variations in permeability. These properties can generate spatially variable frictional behavior along the shallow fault zone, potentially allowing localized conditionally unstable

patches to nucleate slow events.

Pore pressure provides another plausible mechanism for producing an apparent frictional gradient. Elevated or depth-dependent pore pressure reduces effective normal stress and therefore modifies both frictional strength and nucleation size. In a sedimentary basin, permeability contrasts and fluid circulation may produce strong vertical variations in effective stress. Under these conditions, a layer that would otherwise be stable may become conditionally unstable and host episodic slip. The *Model 2* can be interpreted as a simplified representation of this effect: rather than prescribing explicit hydrological processes, it imposes a depth-dependent apparent frictional stability that captures the mechanical consequences of variable effective normal stress.

5.4.5 Broader implications for strike-slip faults

The similarity between the Izmit models and previous models developed for California strike-slip faults suggests that shallow SSEs on continental faults may share common mechanical ingredients. In both cases, a shallow conditionally unstable layer embedded between the surface and a deeper stable region can generate episodic aseismic slip. Sedimentary basins may be particularly favorable environments because they combine low effective stress, variable lithology, high damage, and possible fluid circulation. This does not imply that all sedimentary basins should host SSEs, but rather that basin-related frictional and hydrological heterogeneity may lower the threshold for shallow transient slip.

These results also have implications for seismic hazard. Shallow SSEs may release part of the accumulated slip deficit near the surface, but they do not necessarily reduce the hazard associated with the deeper seismogenic zone. Along the Izmit segment, the models that reproduce shallow SSEs still require a deeper velocity-weakening layer capable of producing large earthquakes with recurrence times comparable to paleoseismological estimates. Therefore, shallow aseismic slip should be interpreted as one component of the seismic cycle, not as evidence that the entire segment is creeping or mechanically stable.

5.5 Conclusions

We used quasi-dynamic rate-and-state friction models to reproduce the main observations of the seismic cycle along the Izmit segment of the North Anatolian Fault: coseismic slip amplitude, earthquake recurrence time, postseismic relaxation, and shallow slow slip events. The results show that these observations can be explained by a layered frictional structure composed of: (1) a velocity-weakening seismogenic layer controlling large earthquakes; (2) an overlying velocity-strengthening layer controlling decadal postseismic afterslip; and (3) a shallow conditionally unstable layer controlling shallow SSEs.

The depth of the shallow layer required to generate SSEs is consistent with the depth extent of the Izmit sedimentary basin. This spatial correspondence suggests that basin-related frictional properties, lithological heterogeneity, or pore-pressure variations may promote episodic shallow slip. A homogeneous velocity-weakening shallow layer can reproduce the observations, but only within a relatively narrow parameter range. A model with a vertical frictional gradient provides a more flexible and physically plausible explanation, as it may represent gradual variations in pore pressure, lithology, or damage within the basin.

The comparison with previous models for other continental strike-slip faults suggests that shallow SSEs may arise from common mechanical conditions: a shallow transitional frictional regime, low effective normal stress, and structural or hydrological heterogeneity. Further observations, especially dense near-fault geodesy, continuous creepmeters, and improved constraints on shallow basin properties, are needed to determine whether shallow SSEs along the Izmit segment are primarily controlled by pore pressure, lithology, or a combination of both. More complex 2D seismic-cycle models would allow the exploration and reproduction of additional details of seismic and SSE ruptures, such as lateral propagation and final rupture lengths.

Chapter 6

Discussion, perspectives et conclusions

In this final chapter, I revisit the main scientific questions that motivated this thesis and discuss the implications of this work along three main axes. First, I discuss the use of InSAR data to monitor tectonic deformation along continental faults, from large-scale processes such as interseismic loading to smaller-scale transient deformation such as slow slip events. Second, I focus on the North Anatolian Fault in Türkiye in order to provide an overview of the current understanding of the tectonic setting and creep dynamics of this fault system, from the regional scale down to individual fault segments. Third, I highlight how constraining the creep dynamics along the North Anatolian Fault may contribute to a broader understanding of other continental strike-slip faults worldwide, and how detailed observations along a single fault segment can help identify common behaviors and key processes controlling seismic cycles. Finally, I take a broader perspective by comparing SSEs observed along continental strike-slip faults with those occurring in subduction zones. The objective is to identify potential common features that may improve our understanding of the mechanisms controlling the occurrence of these transient slip events.

Contents

6.1 Insights of geodetic data monitoring: focus on InSAR 180

6.2 Perspectives on the behavior of the North Anatolian Fault (NAF) in Türkiye . 183

6.3 Slow slip events: toward a unified framework? 186

6.1 Insights of geodetic data monitoring: focus on InSAR

As described in Section 1.4, SAR images cover large regions every 6-12 days with high spatial resolution, making InSAR technique a unique tool to monitor the behavior of large continental faults. Furthermore, the implementation of automatic InSAR processing chains such as FLATSIM (see Section 1.4.4; Thollard et al., 2021) provides a large amount of available displacement time series covering large areas over several years. However, in this work, we aim to study SSEs whose related surface deformation reaches amplitudes on the order of a millimeter, requiring a specific methodology to achieve this precision.

Related questions

Q1. How can **large-scale, automatically processed InSAR datasets** be used to build **inventories of transient slip events** along global fault systems?

Q2. What are the current limitations in terms of **measurement precision and geometry, spatial resolution, and noise discrimination**?

Results

Large-scale monitoring

The study of the steady-state deformation in Türkiye using FLATSIM data (Section 2.2) demonstrates the capability of large-scale, automatically processed InSAR datasets to characterize creep dynamics along major fault systems at high spatial resolution, without heavy post-processing. In particular, it highlights distinct creeping segments with lengths of a few kilometers (e.g., the $\sim$15 km-long Izmit segment). Patterns characteristic of local deformation were also observed, especially within the mean vertical velocity field (Figures 2.7b and 2.11). Although I did not focus on them, they suggest the efficiency of this dataset in resolving deformation affecting kilometer scale areas (e.g., mines, urban subsidence). In addition, the seasonal components of the InSAR displacement time series (Figures A.3 and A.4) reveal spatially distinct patterns, potentially related to hydrology-driven processes (e.g., amplitudes located within valleys) or climate-driven processes (e.g., snow and ice loading on mountain ranges), illustrating the broader potential of such datasets beyond tectonic applications.

Building on this large-scale perspective, the joint inversion of GNSS and InSAR data presented in Section 2.3 further demonstrates the complementarity of these two geodetic observables in constraining interseismic deformation along the Main Marmara Fault. While GNSS measurements provide three-dimensional displacement vectors with high temporal resolution, their inherently sparse spatial distribution leaves the slip rate model under-determined, particularly along continental segments of the fault with shallow creep such as the Izmit segment. The inclusion of InSAR data significantly increases the spatial sampling of surface deformation, adding observational constraints in areas poorly covered by the geodetic network. This densification directly translates into a reduction of the uncertainties associated with the estimated slip rate distribution, allowing more robust discrimination between locked and creeping fault segments.

Regional-scale monitoring

Focusing on the detection and characterization of SSEs brings new challenges related to the small displacement amplitudes associated with these events. The implementation of an automated detection method based on InSAR data (Section 3) quantifies the impact of the noise level on the detectability of SSEs, and highlights the benefits of targeted post-processing — such as horizontal-vertical decomposition of the signal or denoising approaches like ICA — to remove most of the non-tectonic contributions. The extraction of the tectonic displacement associated with SSE occurrences then proves feasible, allowing the inference of slip distributions at depth and providing a more precise understanding of the potential driving mechanisms. In particular, the presence of sedimentary layers in the basin appears to promote the occurrence of SSEs — a factor also identified along other continental strike-slip fault segments such as Ismetpasa (Jolivet et al., 2023) or the Superstition Hills Fault (Materna et al., 2024). Altogether, the application of dedicated post-processing to FLATSIM data enables a significant enhancement of the signal-to-noise ratio, making it possible to study millimeter-scale deformation signals such as those produced by SSEs (Neyrinck et al., 2024).

Perspectives

- **Interseismic loading:**
  - The isolation of the interseismic tectonic signal from non-tectonic contributions (e.g., hydrological loading, urban subsidence) remains a significant challenge when working with long InSAR time series. The application of advanced signal decomposition approaches, including Independent Component Analysis (ICA), or deep learning-based methods, to multi-year InSAR datasets could improve the extraction of the slow tectonic signal, particularly in regions where non-tectonic deformation sources are spatially correlated with fault-parallel structures.
  - The availability of SAR archives spanning several decades (from ERS and Envisat to Sentinel-1) opens the possibility of investigating the temporal variability of interseismic coupling along continental faults. Constructing long InSAR time series over such periods would allow potential temporal variations in the coupling coefficient to be detected, providing a more dynamic view of the interseismic phase of the seismic cycle.
  - In this work, the constraints on interseismic coupling models rely on the joint inversion of GNSS and InSAR data. A natural perspective would be to assess the extent to which InSAR data alone, provided that they offer sufficient spatial coverage and robust atmospheric corrections, could independently constrain fault coupling models. Such an assessment would be particularly valuable in regions lacking dense GNSS networks, where InSAR constitutes the primary available geodetic observable.
  - The multidisciplinary approach combining GNSS and InSAR data, as applied along the Main Marmara Fault, could be extended to other poorly instrumented fault segments where the spatial coverage of geodetic networks remains insufficient to resolve along-strike variations in fault coupling. In particular, integrating seafloor geodetic observations — such as GNSS-Acoustic measurements — with InSAR data would allow coupling models to be better constrained along offshore segments, where surface deformation is not directly observable from space. Furthermore, the increasing availability of multi-track SAR acquisitions from current and forthcom-

ing satellite missions (e.g., NISAR, Sentinel-1 Next Generation) will enhance the three-dimensional decomposition of the mean velocity field, reducing the inherent ambiguity of LOS measurements and improving the resolution of slip rate models.

- **Slow Slip Events:**
  - The automated detection framework developed in Section 3 constitutes a first step toward the systematic construction of SSE catalogs along continental fault systems. Applying this method to other strike-slip fault segments — particularly those sharing comparable geological settings (e.g., sedimentary basins and/or shallow creeping sections) such as the Imperial Valley Fault (e.g., Materna et al., 2024) — would allow a more comprehensive assessment of the spatial distribution and recurrence of transient slip events. Such catalogs are essential to investigate the along-strike variability of fault rheology and its role in modulating the slip behavior.
  - The installation of more sensitive instruments along creeping segments affected by SSEs, such as strainmeters or tiltmeters, could enhance their identification by lowering the detectability threshold, as demonstrated by Linde et al. (1996) along the San Andreas Fault.

6.2 Perspectives on the behavior of the North Anatolian Fault (NAF) in Türkiye

Related questions

Q1. What new insights or added values into **fault creep dynamics** can be gained from **continuous**, **long-term InSAR monitoring** along the North Anatolian Fault at regional to large-scale, and to what extent does this provide new insights into **seismic hazard**?

Q2. What do the fault creep dynamics imply for the **seismic cycle** along the Izmit segment and the **seismic hazard** estimate of the western part of the North Anatolian Fault?

Results

Large-scale monitoring

Analysis of the steady-state horizontal velocity field and strain rate along the NAF (Section 2.2) highlights the influence of fault segmentation on the lateral variations of the creep dynamics behavior. In particular, creeping segments are identified through high strain accumulation and anomalous surface deformation. In addition to the two previously documented creeping segments (Izmit and Ismetpasa, e.g., Cakir et al., 2012; Rousset et al., 2016), two additional segments appear to be creeping: the western part of the Düzce segment and the Ezinepazari segment. The presence of strain accumulation along the latter suggests that this segment, which ruptured in 1939 during the Erzincan earthquake, may be aseismically releasing accumulated strain. This observation is of direct relevance to seismic hazard assessment in the region, where the NAF splits into several branches, forming pull-apart basins in between (e.g., Barka et al., 2000).

Estimates of the locking depth along the NAF derived from fault-perpendicular profiles reveal significant lateral variations. A particularly notable observation is the correlation between shallow locking depth and the presence of shallow aseismic creep, suggesting potential processes at depth that enhance near-surface displacement (e.g., Jolivet et al., 2023).

The heterogeneous interseismic behavior including locked segments, creeping sections and segments affected by SSEs is consistent with the along-strike variability of rupture patterns documented during past earthquake sequences (e.g. Armijo et al., 2000), where abrupt transitions between seismic and aseismic slip have been observed, suggesting the presence of potential structural barriers arresting the displacement along the interface (Kearse and Kaneko, 2026). A key open question concerns the temporal dimension of this segmentation: whether the aseismic deformation observed today along certain segments was already present prior to historical ruptures, or whether it was initiated or enhanced by the coseismic stress changes associated with past earthquakes. Addressing this question would require longer geodetic time series and a more systematic comparison of pre- and post-seismic deformation patterns across the fault system.

Focusing on the Marmara region (Section 2.3) further illustrates the contribution of InSAR data to the monitoring of the steady-state velocity field and the inference of interseismic coupling along the Main Marmara Fault. The joint inversion with GNSS and InSAR data allows the distinction between regions of high strain accumulation, indicative of locked fault segments and regions of strain release associated with aseismic creep, providing critical input for

seismic hazard assessment in one of the most tectonically threatened urban areas in the world.

Regional-scale monitoring

Additional detections of SSEs along the Izmit segment and their spatio-temporal characterization provide new insights into the seismic cycle and the slow slip event cycle. Observations spanning the whole seismic cycle allow the use of inverse and mechanical models to specify the spatial relationships between co- and postseismic slip distributions at depth, linking the 1999 Izmit slip deficit with the current pattern of aseismic creep. Mechanical models further support the potential key role of the sedimentary basin in promoting the occurrence of SSEs within the shallow part of the fault.

Monitoring of SSEs along the Izmit segment since 2015 (Aslan et al., 2019b; Özarpacı et al., 2020) has so far led to the detection of four events, with a recurrence time of $1.3 - 1.4$ *years* and a preferential occurrence in winter. These observations provide a basis for anticipating future detections along the segment and refining the characterization of the slow slip event cycle.

A particularly striking observation is the spatial relationship between SSEs and the surrounding fault kinematics. Along the Izmit segment, the occurrence of SSEs in the shallow part of the fault appears spatially associated with deeper steady-state aseismic creep below. Along the Ismetpasa creeping segment to the east, the asperity producing SSEs is also surrounded by continuous creep. This configuration suggests that the conditionally stable zone where SSEs nucleate may be mechanically loaded by the adjacent aseismic creep. The location of the fault, crossing a sedimentary basin, a characteristic shared with other continental strike-slip systems exhibiting shallow creep, thus appears to be a controlling factor in the occurrence of transient slip events.

Perspectives

- **Interseismic loading:**
  - The identification of new potentially creeping segments along the NAF such as the western Düzce and Ezinepazari segments calls for an updated block modeling approach that accounts for the full complexity of the fault network. Incorporating these segments into kinematic block models would allow the strain budget across the entire fault system to be reassessed, and would provide tighter constraints on the locking state of individual fault branches, with direct implications for regional seismic hazard.
  - The strain map computed in this work exhibits non-tectonic signals arising from small and localized velocity changes far from the fault, which lead to spuriously high strain amplitudes. A Bayesian approach for strain computation (e.g. Métois et al., 2025), combined with an adaptive mesh of higher density surrounding the NAF and EAF, could preserve high spatial resolution in the vicinity of the faults while mitigating non-tectonic signals over the rest of the map.
- **Slow Slip Events:**
  - The two newly identified potentially creeping segments (western Düzce and Ezinepazari) suggest dedicated investigation to determine whether transient slip events occur

along these sections. Applying the automated InSAR-based detection framework developed in Section 3 to these segments would allow their slip behavior to be systematically characterized and would contribute to expanding the current catalog of continental SSEs.

- The recent installation of new GNSS stations along the Izmit segment in 2024 by Baptiste Rousset in collaboration with a Turkish team represents a significant step toward establishing a dense, multi-sensor monitoring network. Combined with InSAR time series, this instrumentation will improve the spatio-temporal characterization of future SSEs and consolidate the Izmit segment as a natural laboratory for the study of transient slip on continental faults. The deployment of seismic nodes could further allow potential links between slow slip and seismicity to be investigated (e.g., Luckie and Choens, 2025).
- The preferential winter occurrence of SSEs along the Izmit segment raises the question of the role of pore fluid pressure in modulating transient slip. Pore pressure variations at depth has been proposed as a potential trigger for transient slip episodes, an hypothesis supported by recent laboratory experiments demonstrating that fluid pressure variations can modulate the frictional stability of fault gouge (e.g., Passelègue et al., 2025). This interpretation is further supported by observations of SSEs in geothermal reservoir settings, where fluid-induced pore pressure changes are known to promote episodic aseismic slip (e.g. Bayramov et al., 2025; Lengliné et al., 2025).
- The preferential occurrence of SSEs along the Izmit segment during winter months further suggests a potential role of seasonal forcing, possibly through hydrological loading or precipitation-induced pore pressure variations. This seasonal modulation is particularly intriguing given that the sedimentary basin hosting the fault should theoretically promote velocity-strengthening frictional behavior, and therefore inhibit unstable slip. Yet, SSEs are systematically observed there. This apparent paradox calls for a more integrated view of the physical conditions governing transient slip, combining frictional, hydrological, and lithological constraints.

6.3 Slow slip events: toward a unified framework?

Related questions

Q1. How can the **creep dynamics** along fault segments provide insights into the **mechanisms** governing the occurrence of **shallow SSEs**?

Q2. To what extent do **SSEs along continental strike-slip faults** share common characteristics with those observed along **subduction zones**, and what does this imply for a **unified understanding** of transient slip?

Results

The comparison of magnitude-duration estimates of SSEs along subduction zones with estimates along the Ismetpasa (Özdemir et al., 2025), Izmit, and San Andreas Fault segments (Materna et al., 2024; Vavra et al., 2024) reveals that SSEs along continental strike-slip faults release less energy for similar duration. Similar geodetic detection methods have been applied in both contexts (Rousset et al., 2017), confirming that the general framework of slow slip as a distinct mode of fault slip applies across tectonic settings (Ide and Beroza, 2023). The availability of near-field geodetic observations along continental faults, closer to the slip source than what is typically achievable above subduction interfaces, reveals slip events at scales that fall within the so-called "hidden region" of subduction zone scaling relations.

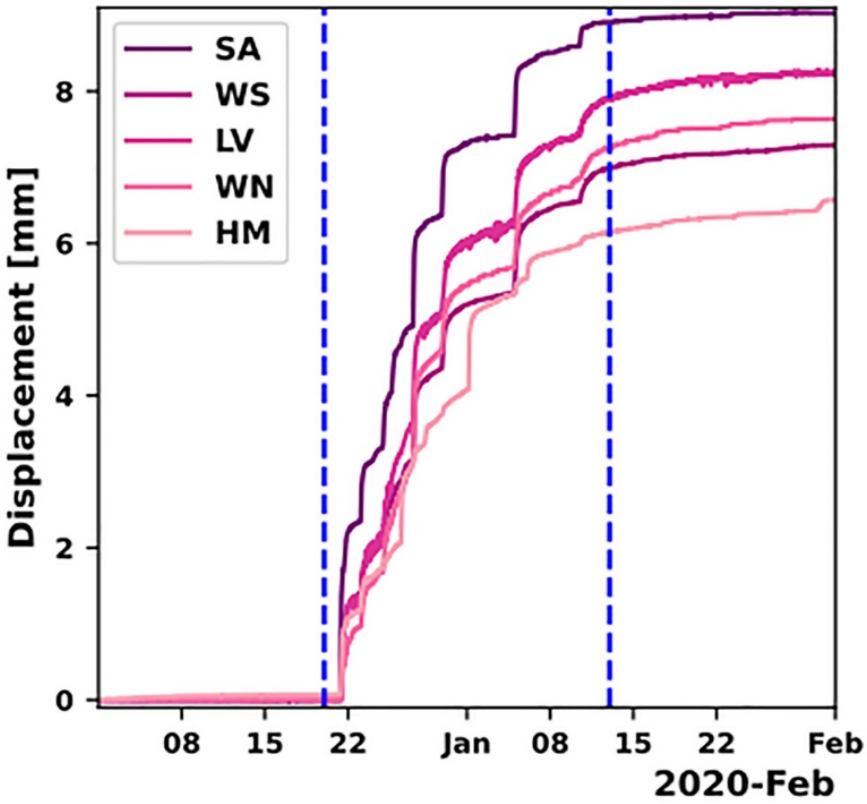

Figure 6.1: Creepmeters records along the Ismetpasa segment during the 2020 SSE published by Özdemir et al. (2025).

Creepmeter records at Ismetpasa, shown in Figure 6.1, reveal that large slow slip events are composed of successive bursts of accelerated slip. This observation raises the question of

whether the scaling relations established for geodetically detected SSEs remain valid at the sub-event scale (Frank et al., 2018). Similarly, the displacement time series along the Izmit segment exhibit smaller-amplitude transients superimposed on the inter-SSE periods, whose origin remains ambiguous. Together, these observations raise the broader question of whether steady-state aseismic creep is truly steady, or it reflects the time-averaged expression of a continuous spectrum of slip transients below the detection threshold.

Along subduction zones, slow slip events are frequently accompanied by low-frequency earthquakes and tectonic tremors, which serve both as indicators of ongoing slip and as constraints on its spatial and temporal evolution (e.g., Dragert et al., 2004). Along continental strike-slip faults, such associations are less systematically documented. Recent work along the San Andreas Fault (Zali et al., 2025) suggests that micro-seismicity may be associated with transient slip episodes, opening new perspectives for the joint analysis of geodetic and seismic signals along continental faults.

Perspectives

- The potential establishment of a moment-duration scaling law for continental fault SSEs remains unclear, primarily due to the limited size of existing catalogs and the scarcity of precise geodetic estimates. Expanding the detection effort to other segments of the NAF and comparable fault systems worldwide would increase the statistical basis required to test and refine such a scaling relation, and to assess whether the lower energy release observed on continental faults reflects a fundamental difference in slip mechanism with respect to subduction zone SSEs.
- Whether observed steady-state aseismic creep is truly steady, or whether it reflects the time-averaged expression of a continuous spectrum of slip transients below the detection threshold, remains an open question. Improving the temporal characterization of events using high-temporal resolution data (e.g., high-rate GNSS records, creepmeters, strainmeters, tiltmeters) and reducing the noise content of the time series may provide key insights into the internal structure of SSEs, that can be compared across tectonic contexts (Frank et al., 2018).
- The combination of geodetic observations with dense seismic networks capable of detecting micro-seismicity may specify the potential relationships between transient slip episodes and microseismicity.
- The automatic detection methods developed in this work can be adapted to other datasets, such as Distributed Acoustic Sensing, or submarine geodesy (e.g., Rolandone et al., 2018), broadening the range of tectonic contexts in which SSEs can systematically be identified and characterized. The combination of these approaches with near-field instrumentation would further lower the detection threshold and improve the spatial resolution of slip models, contributing to a more unified view of transient slip across tectonic settings.

Appendix A

Supplementary Materials: The steady-state deformation all over the Türkiye deduced from the *FLATSIM* dataset

Contents

A.1 FLATSIM raw data 190
A.2 Seasonal terms 193
A.3 Mean East-West profiles 195

A.1 FLATSIM raw data

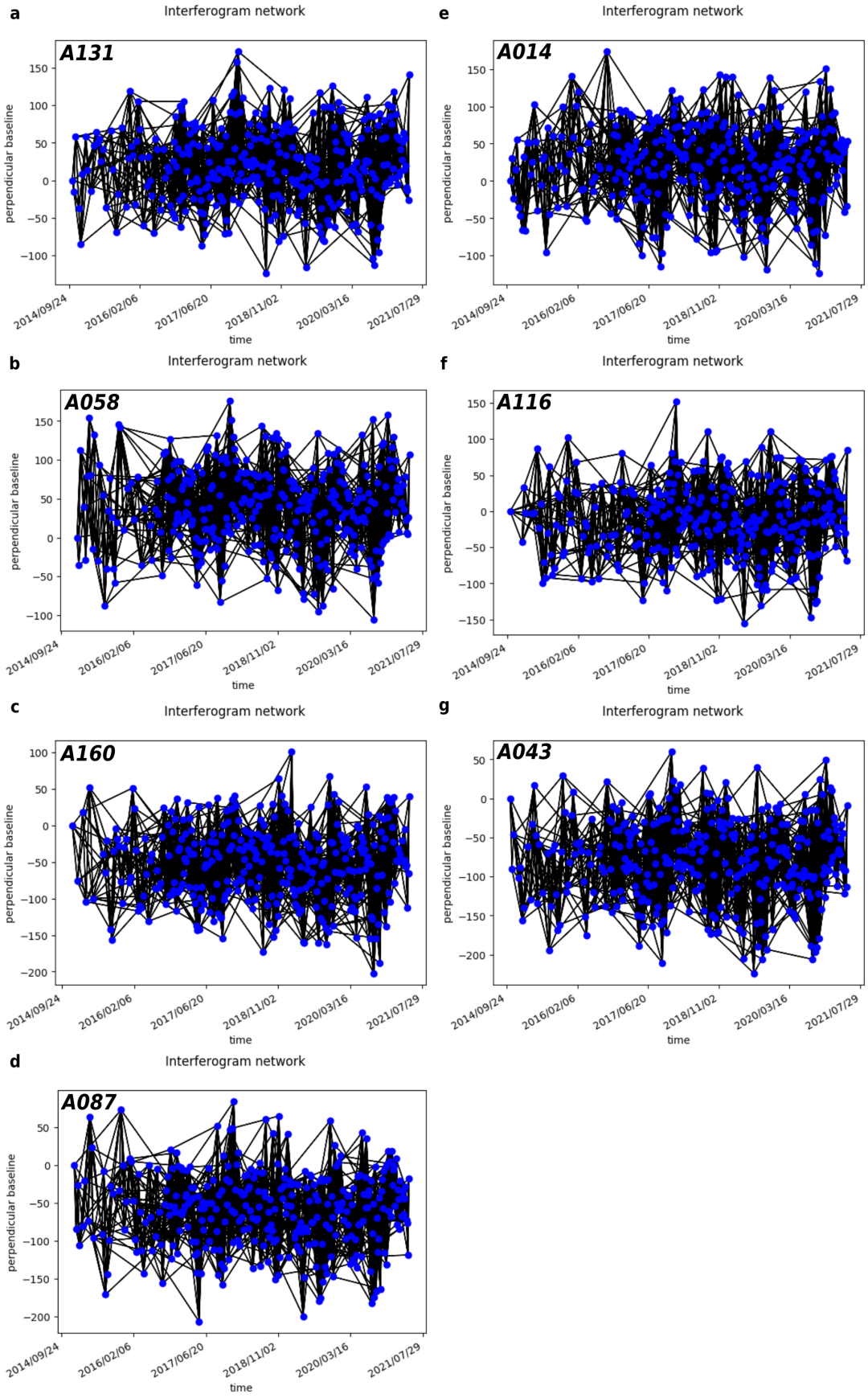

Figure A.1: Interferogram networks delivered by FLATSIM corresponding to the ascending tracks from (a) west to (g) east.

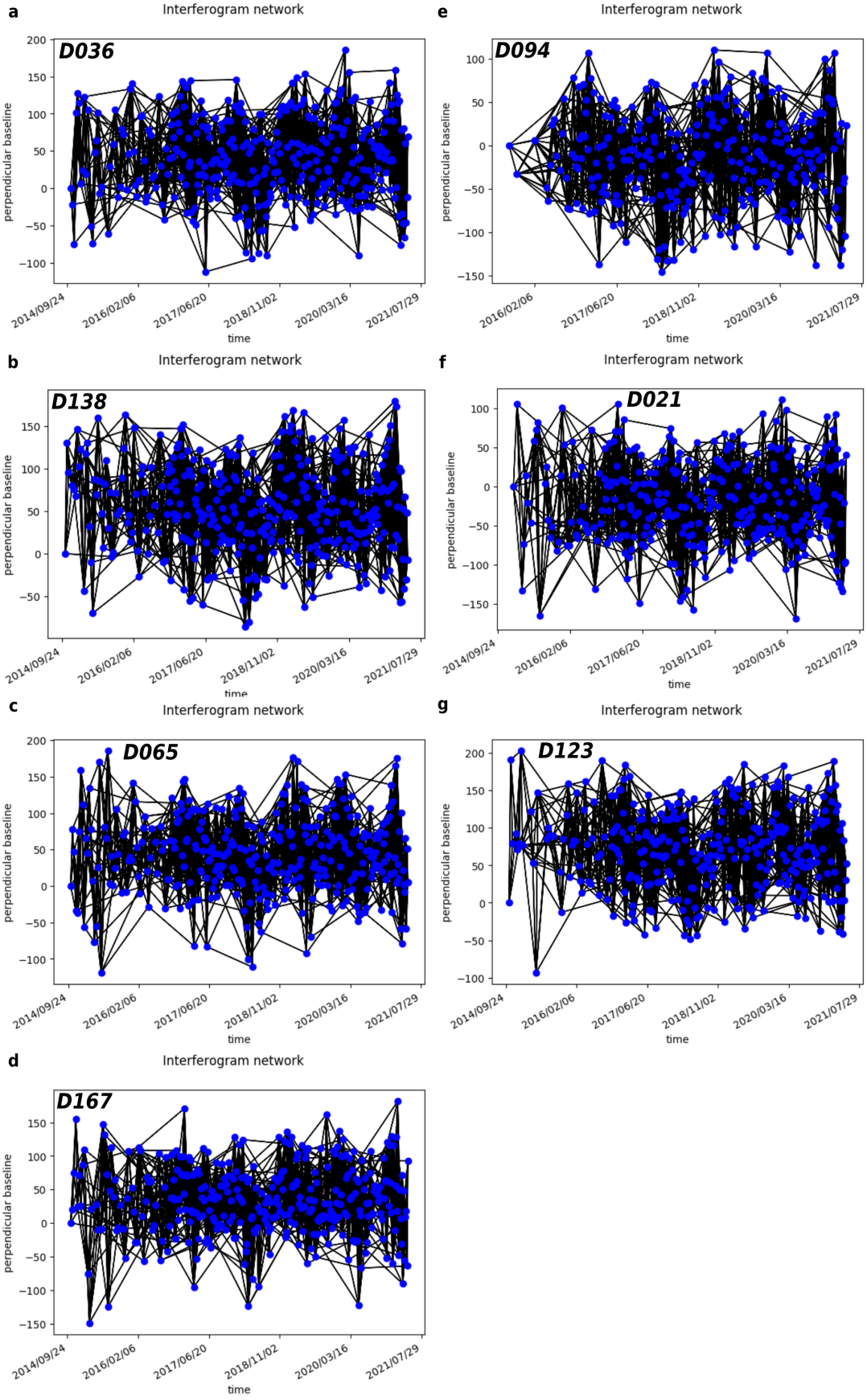

Figure A.2: Interferogram networks delivered by FLATSIM corresponding to the descending tracks from (a) west to (g) east.

A.2 Seasonal terms

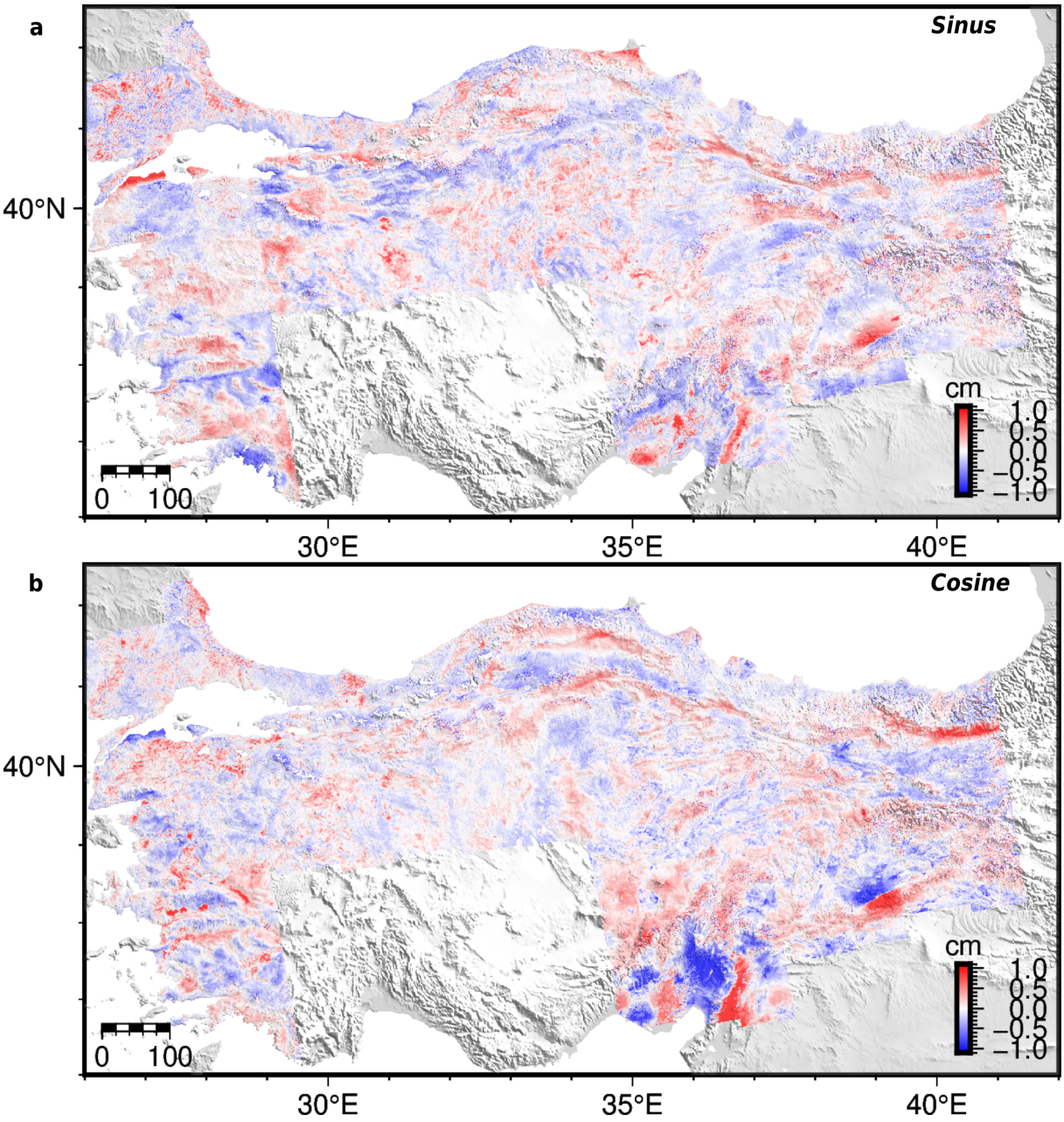

Figure A.3: Amplitude of the sinus and cosine terms of the seasonal and linear decomposition computed on the ascending tracks. The data are in Line Of Sight (LOS) so that red and blue pixels correspond to motions away and toward the satellite, respectively.

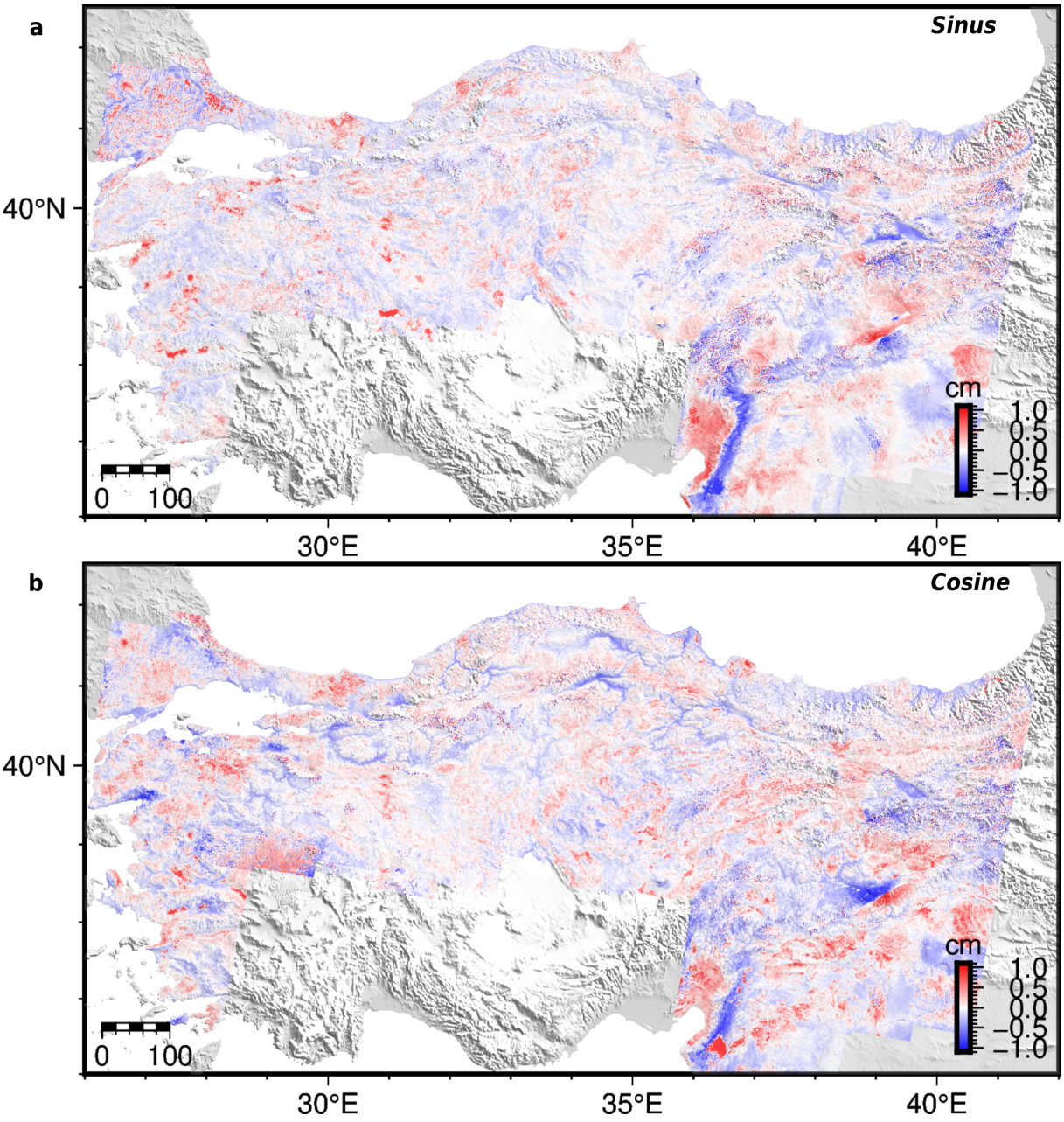

Figure A.4: Amplitude of the sinus and cosine terms of the seasonal and linear decomposition computed on the descending tracks. The data are in Line Of Sight (LOS) so that red and blue pixels correspond to motions toward and away from the satellite, respectively.

A.3 Mean East-West profiles

The following figures (Figures A.5, A.6 and A.7) show three examples of perpendicular to the fault profiles extracted from the mean East-West velocity field, with the best fitted models of the displacement related to the distance to the fault.

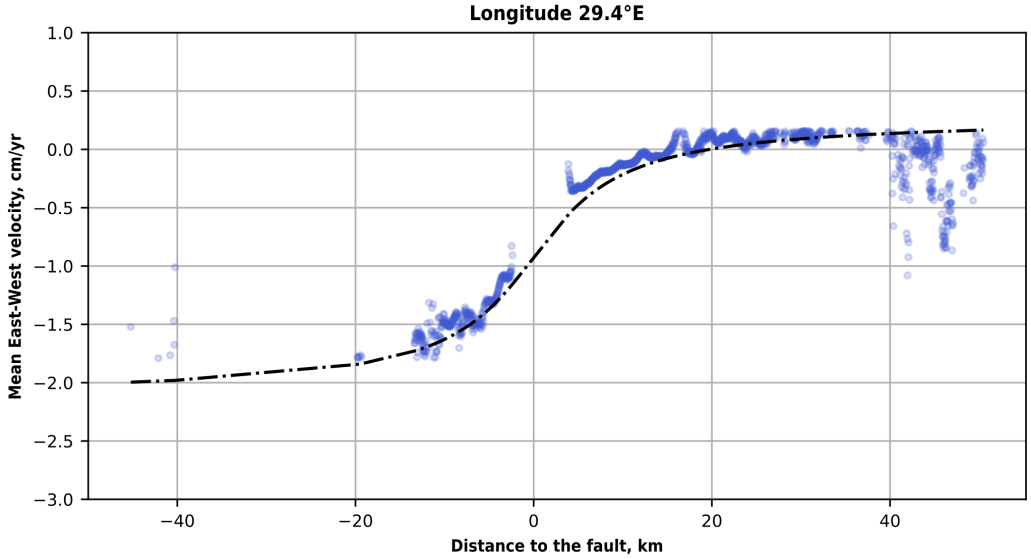

Figure A.5: Perpendicular to the fault profile at longitude 29.4°E of the mean East-West velocity map shown by the blue dots. The dotted black line corresponds to the fitted model of the far field.

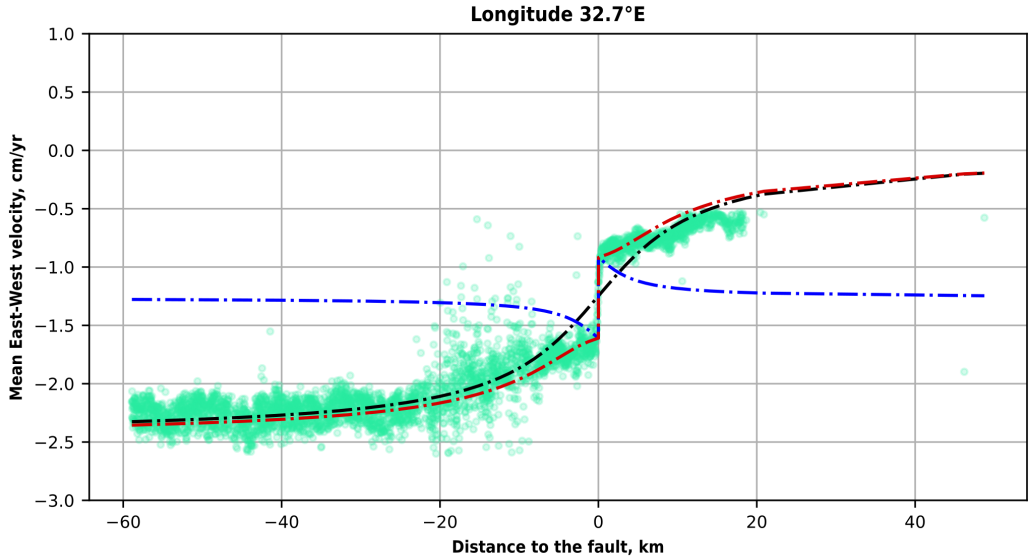

Figure A.6: Perpendicular to the fault profile at longitude 32.7°E of the mean East-West velocity map shown by the green dots. The dotted black line corresponds to the fitted model of the far field, the blue one corresponds to the fit of the aseismic creep and the red one to the sum of both processes.

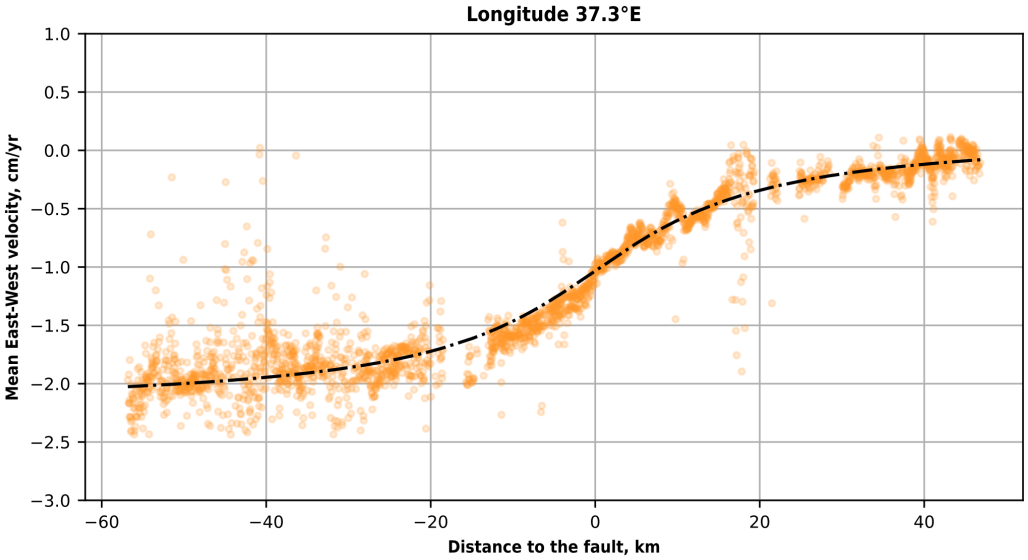

Figure A.7: Perpendicular to the fault profile at longitude 37.3°E of the mean East-West velocity map shown by the orange dots. The dotted black line corresponds to the fitted model of the far field.

Appendix B

Supplementary Materials: Automated Detection of Slow Slip Events from InSAR: Application to the North Anatolian Fault

Contents

B.1 Method . . . 198
B.1.1 Method's inputs . . . 198
B.1.1.1 Analysis of real InSAR noise . . . 198
B.1.1.2 Definition of a template . . . 200
B.1.1.3 Fault interface properties . . . 201
B.1.1.4 Decimation of the data . . . 202
B.1.2 Synthetic tests . . . 203
B.1.2.1 Effects of the template's parameters on correlation functions 203
B.1.2.2 Validation of the detections . . . 205
B.1.2.3 Accuracy of SSEs estimates . . . 206
B.2 Application to real data . . . 208
B.2.1 Presentation of the segments . . . 208
B.2.2 Izmit results . . . 209
B.2.3 Creepmeters records . . . 211

B.1 Method

B.1.1 Method's inputs

B.1.1.1 Analysis of real InSAR noise

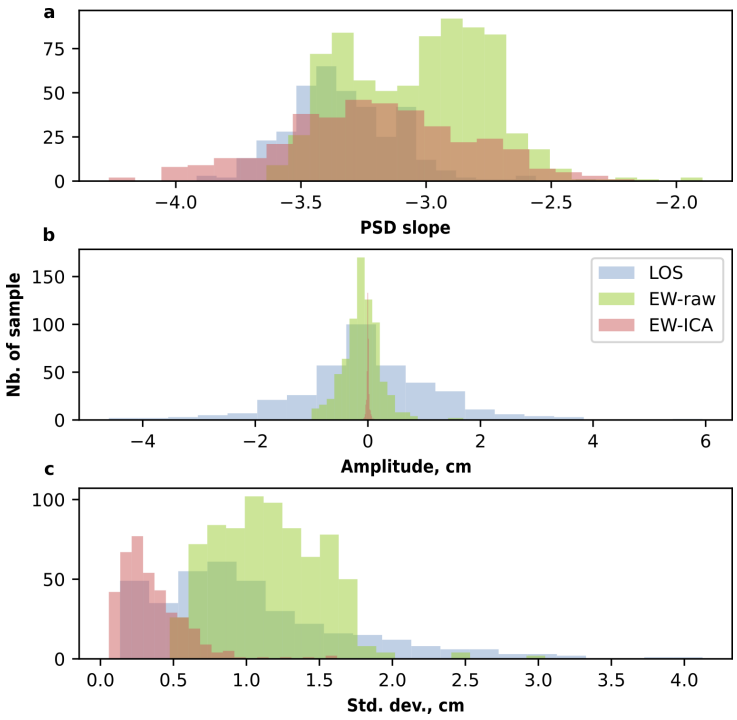

Figure B.1: For the three datasets covering the Izmit segment, histograms of the (a) power spectral density (PSD) slope, (b) amplitude and (c) standard deviation of the real InSAR displacement time series. The blue, green and red colors correspond to noise contents from the Line-Of-Sight (LOS) displacement time series of the ascending track $A058$, the East-West (EW) displacement time series from the horizontal-vertical decomposition of the tracks $A058 - D138$ and the EW displacement time series after post-processing steps detailed in Neyrinck et al. (2024) within the Izmit basin, respectively. The boxes used to compute those features are located within the area located between longitudes $30.0 - 30.6°E$ and latitudes $40.0 - 40.6°N$.

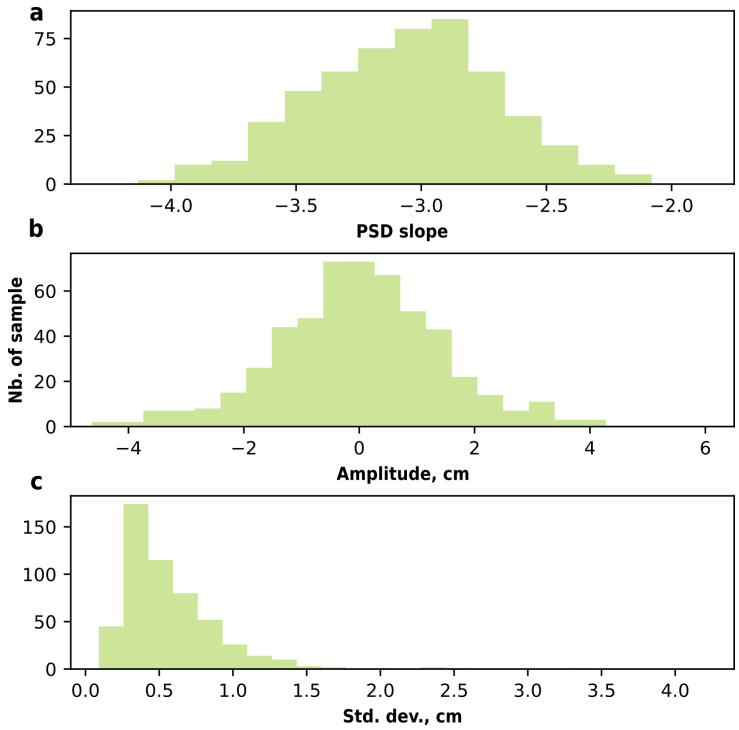

Figure B.2: Histograms of the (a) PSD slope, (b) amplitude and (c) standard deviation of the real InSAR noise gathered from the Ismetpasa East-West displacement time series from the horizontal-vertical decomposition of the tracks $A087 - D065$. The boxes used to compute those features are located within the area longitudes $32.4 - 33.2$°E - latitudes $40.2 - 41.6$°N.

B.1.1.2 Definition of a template

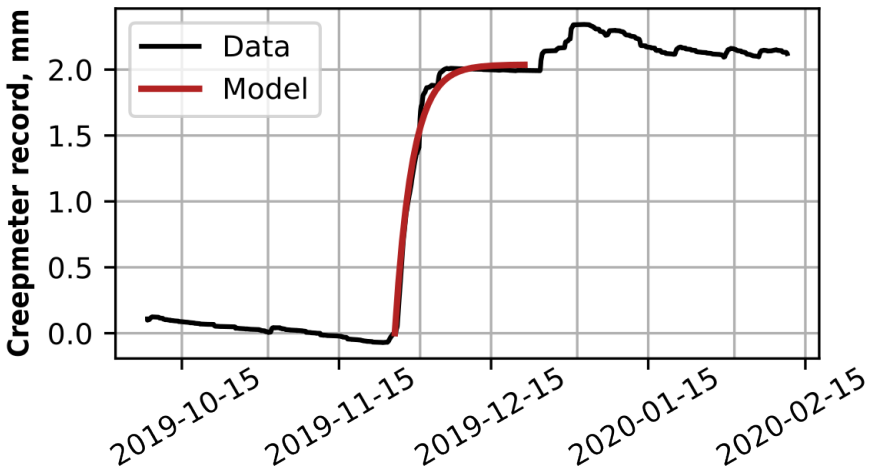

Figure B.3: Creepmeter record at Seller (longitude 29.9720°E - latitude 40.7209°N) during the 2019 event. The red line corresponds to the fit based on the equation $s(t_1) = m(1 - e^{-\frac{t_1}{\tau}})$, with $m = 2.04$ *mm* and $\tau = 3.44$ *days*. Creepmeters data come from the GAGE/UNAVCO dataset (`https://www.unavco.org/data/strain-seismic/creep-data/creep-data.html`).

B.1.1.3 Fault interface properties

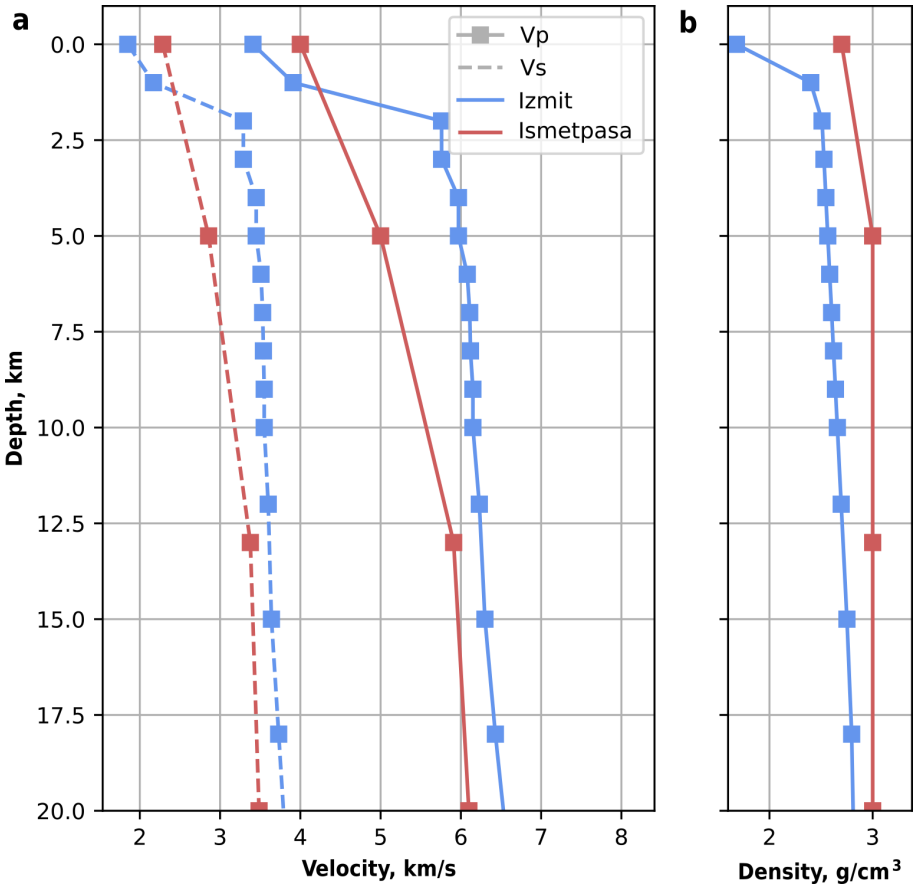

Figure B.4: (a) P-wave velocity Vp , S-wave velocity Vs and (b) density ρ values used for the Green's functions computation for a stratified medium. Blue and red colors correspond to the velocities/densities at the Izmit and Ismetpasa segments, respectively. Along the Izmit segment, Vp and Vs values come from Karabulut (2025), ρ values from the surface down to 1.5 *km*-depth come from Özalaybey et al. (2011), and the other values of ρ are chosen according to Crust 1.0 (Laske et al., 2013). Along the Ismetpasa segment, all of the velocities/densities come from the model published by Rousset et al. (2016).

B.1.1.4 Decimation of the data

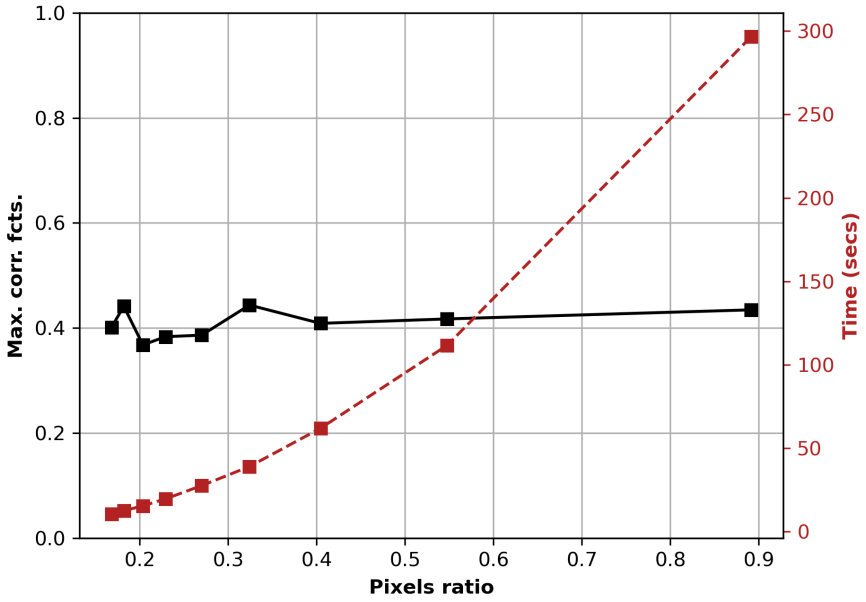

Figure B.5: Impacts of the data decimation on the correlation computation. The correlation function is computed for a single displacement time series cube of 100 *dates* including one shallow slow slip event (SSE) (depth 500 m – M_w 4.8) and a realistic InSAR noise. The pixels ratio is the ratio between the final and initial numbers of pixels after and before decimation. The black line shows the peak of correlation corresponding to the SSE and obtained for each test of decimation. The red line highlights the computation time for each test. Those tests show that the decimation enables to reduce drastically the computation time, without taking into account the impacts on the computation memory.

B.1.2 Synthetic tests

B.1.2.1 Effects of the template's parameters on correlation functions

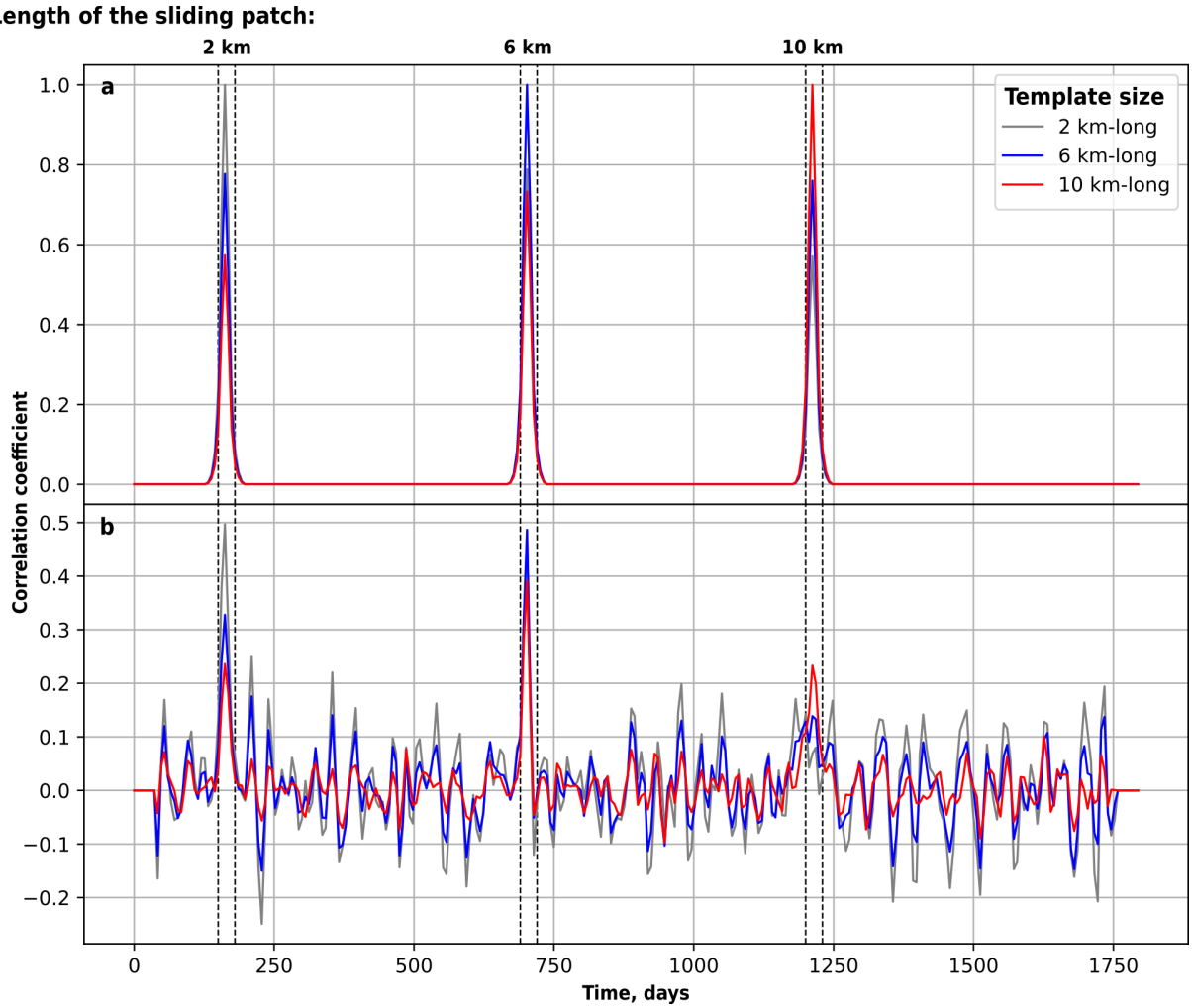

Figure B.6: Effects of the patch size on the correlation coefficient. The correlation function is computed with a displacement time series cube of 300 *dates* containing three shallow SSEs located at depth 500 *m* and with M_w 4.8, computed using three different sliding patch lengths: 2 *km*, 6 *km* and 10 *km*. The width of the sliding patch is fixed of about 1 *km*. The periods affected by a SSE are limited by the vertical dotted lines. The curves show the correlation coefficients obtained by using three different template lengths (2 *km*, 6 *km* and 10 *km*). Sum of the correlation functions for synthetic displacement time series (a) without noise and (b) with realistic noise.

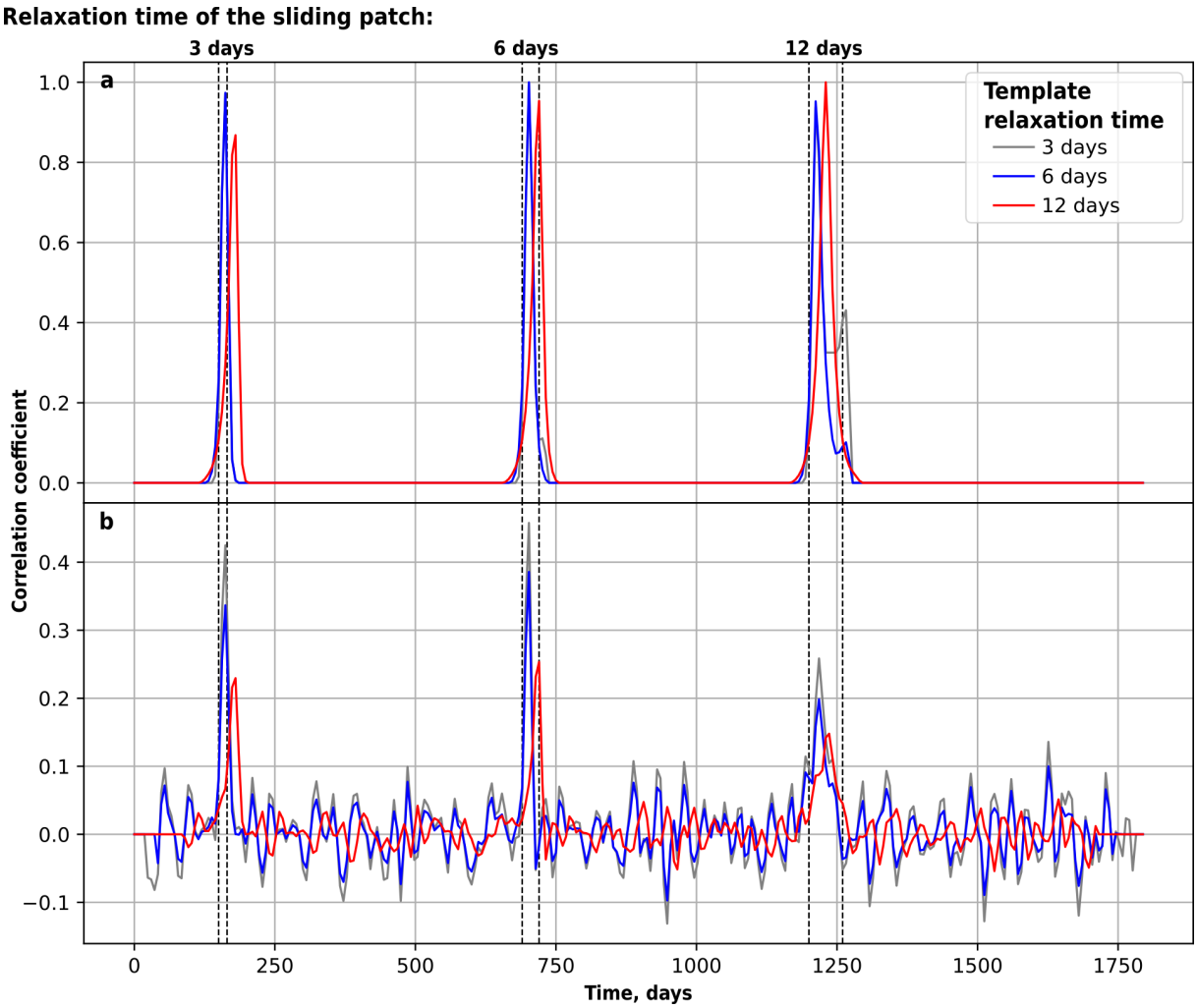

Figure B.7: Effects of the relaxation time on the correlation coefficient. The correlation function is computed with a displacement time series cube of 300 *dates* containing three shallow SSEs located at depth 500 *m* and with M_w 4.8, computed using three different relaxation time: 3 *days*, 6 *days* and 12 *days*. The periods affected by a SSE are limited by the vertical dotted lines. The curves show the sum of the correlation functions computed by using the three previous relaxation time for the template. Sum of the correlation functions for synthetic displacement time series (a) without noise and (b) with realistic noise.

B.1.2.2 Validation of the detections

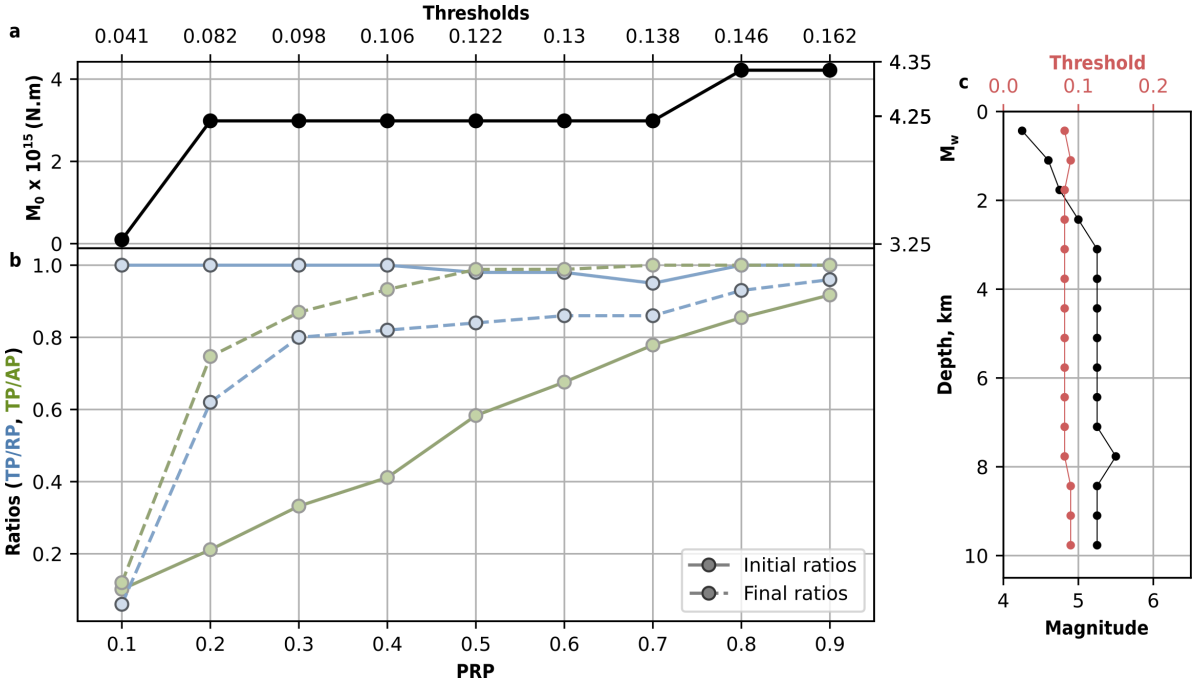

Figure B.8: (a) Minimum moments M_0 (and corresponding magnitudes M_w, respectively) detected as a function of the precision-recall product (PRP). (b) TP/RP and TP/AP ratios as a function of PRP, shown in blue and green, respectively. TP stands for true positive detections, RP for real positive detections and AP for all the positive detections. Solid and dotted lines correspond to the ratios before and after the validation step. (c) Minimum magnitudes (black) and thresholds (pink) relative to $PRP \geq 0.2$ as a function of depth.

B.1.2.3 Accuracy of SSEs estimates

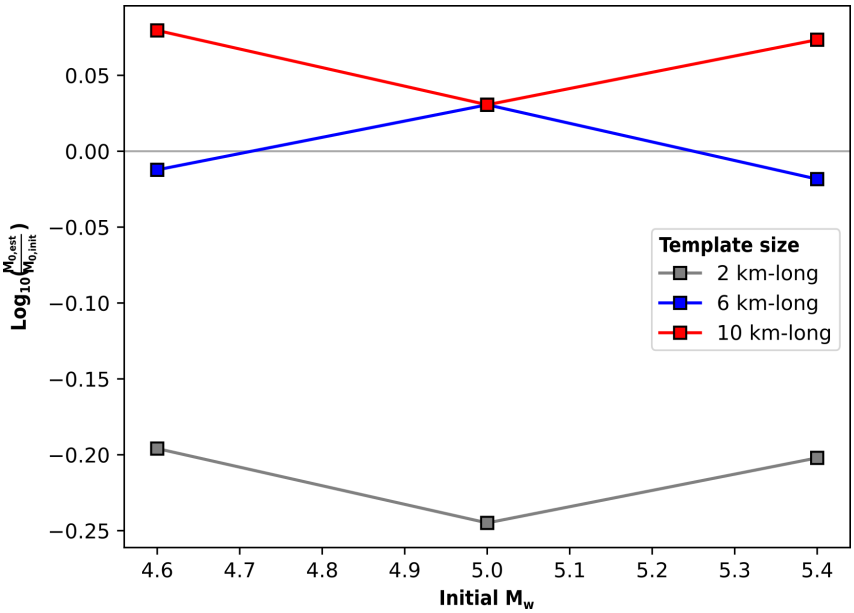

Figure B.9: Comparison of the magnitude estimates during the characterization of the SSEs (*Module 3* – Figure 1d) and the real one chosen to build the synthetic displacement time series, related to the size of the template patch. A displacement time series cube of 300 *dates* including three shallow SSEs (depth 500 *m*) are used for this test, without synthetic noise. The three SSEs have three different magnitudes but a similar sliding patch size of 6 *km*-long and 1 *km*-deep. From the first to the last event, the magnitude is 4.6, 5.0 and 5.4. Three analysis (detection + characterization) are done by using three different lengths of the template patch: 2 *km*, 6 *km* and 10 *km*. The lines show the log of the ratio of the magnitude estimates and to the initial magnitude, obtained with three different template patch.

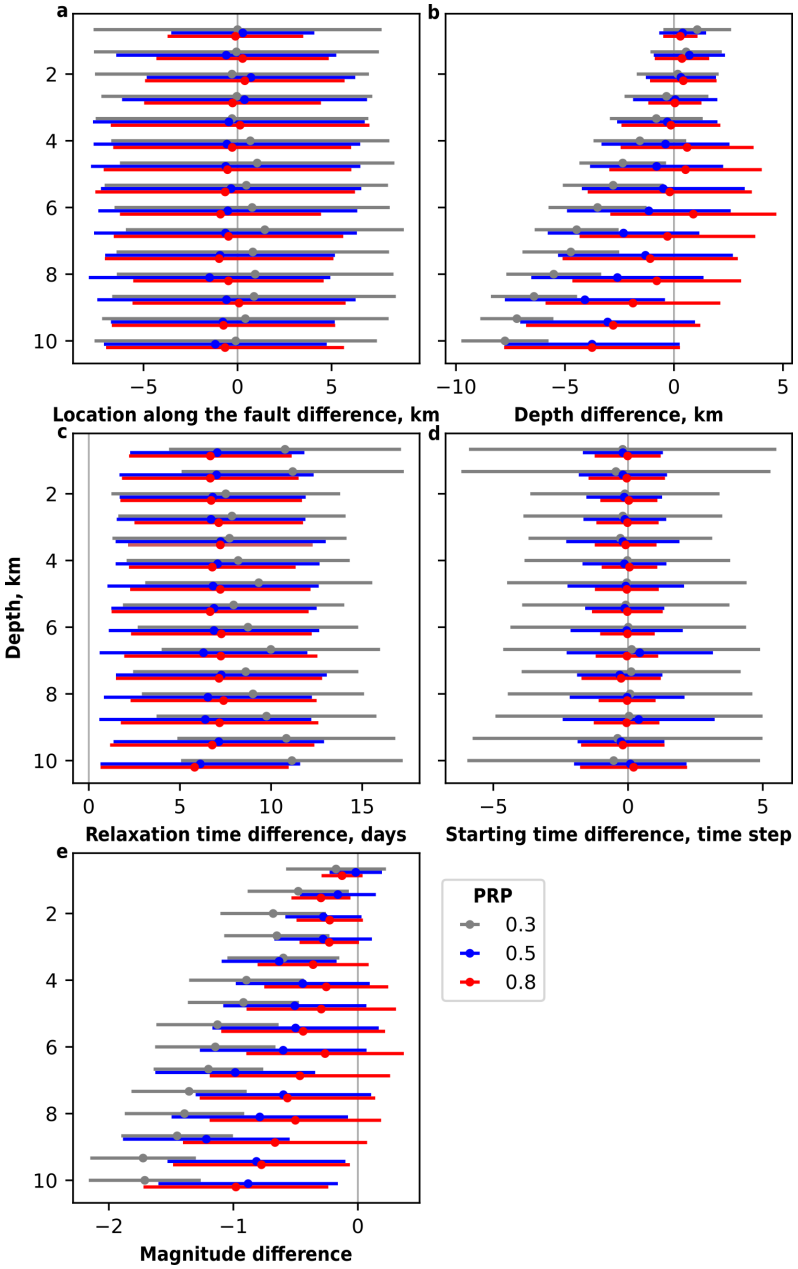

Figure B.10: Estimates errors during the characterization of the detected SSEs. These errors are computed using a synthetic displacement time series made of 100 events, as explained in the main article. (a-b) Differences between the (a) location along the fault and (b) the depth of the sliding patch. (c-d) Differences between the (c) relaxation time and (b) starting time of the SSEs. (e) Differences between the magnitudes of the SSEs.

B.2 Application to real data

B.2.1 Presentation of the segments

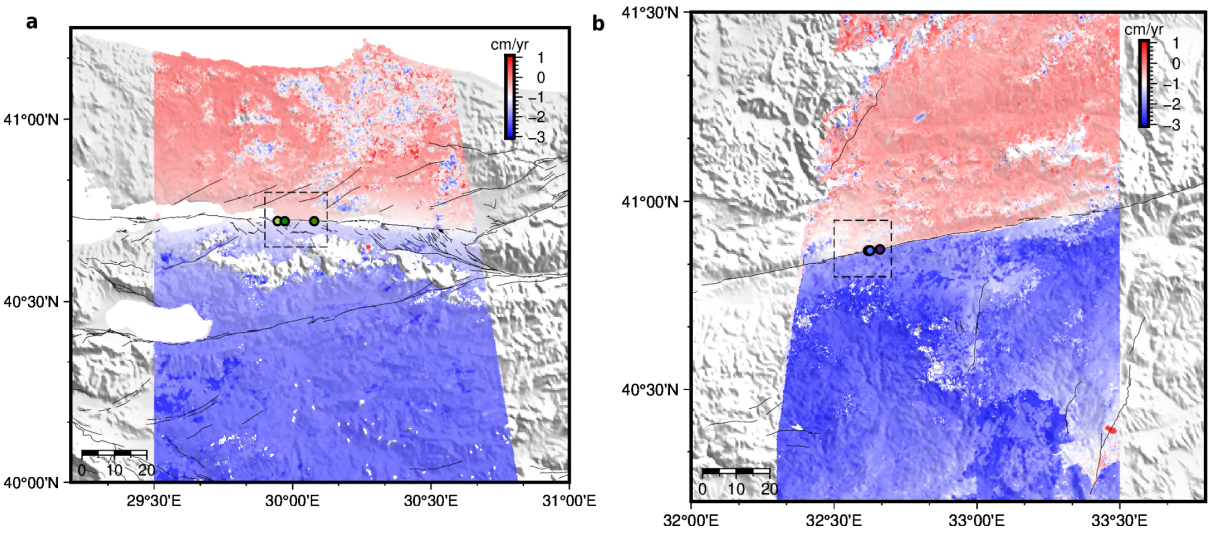

Figure B.11: Mean East-West velocity maps after GNSS referencing covering the (a) Izmit and (b) Ismetpasa segments. The red and blue pixels correspond to eastward and westward motion, respectively. The fault network from Emre et al. (2018) is represented by the black lines. The creepmeters are shown by the colored circles (Bilham et al., 2016). The dashed rectangles show the cropped area surrounding the segments affected by SSEs, and used for the application of the geodetic matched filter approach. A zoom on the cropped areas is shown figure B.12.

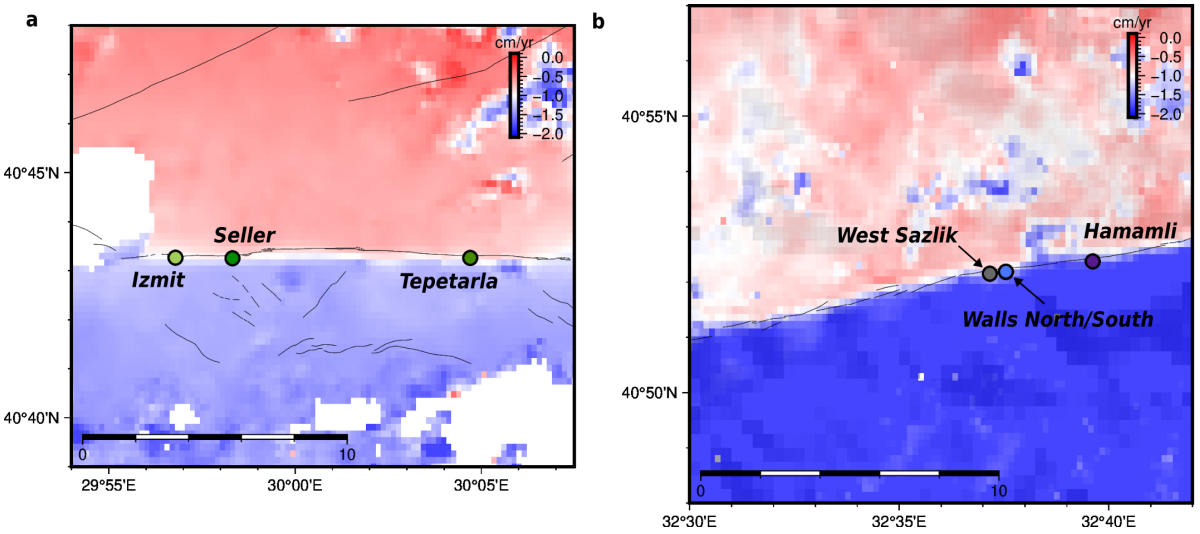

Figure B.12: Mean East-West velocity maps after GNSS referencing covering the (a) Izmit and (b) Ismetpasa segments, focused on the cropped areas shown figure B.11.

B.2.2 Izmit results

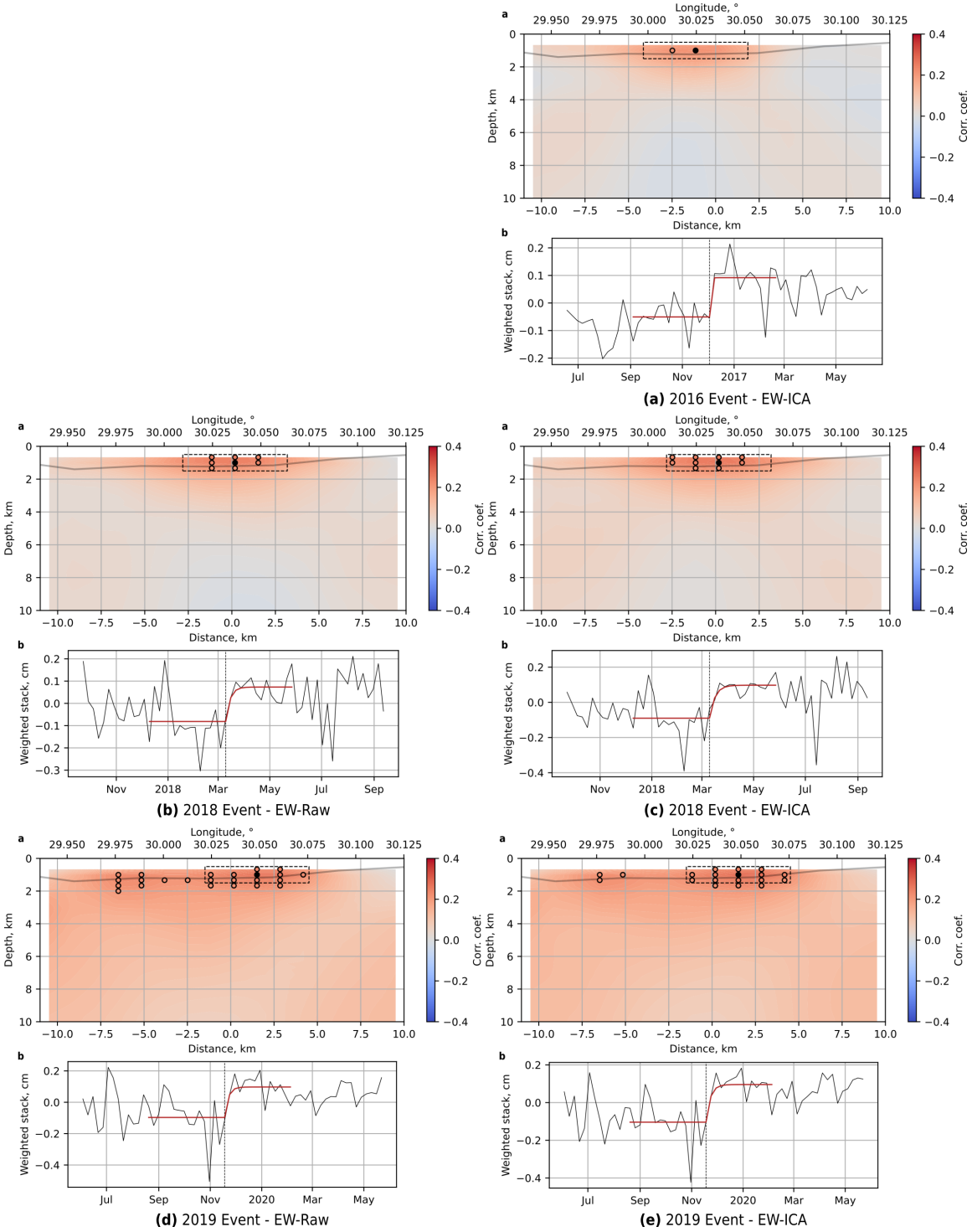

Figure B.13: Final SSE detections along the Izmit segment.

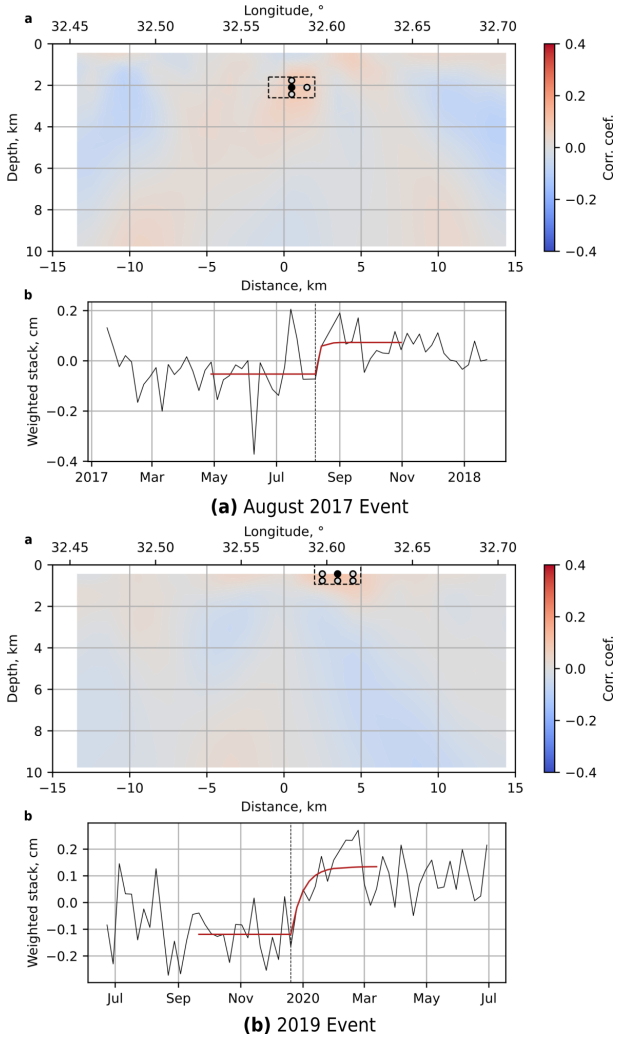

Figure B.14: Final SSE detections along the Ismetpasa segment.

B.2.3 Creepmeters records

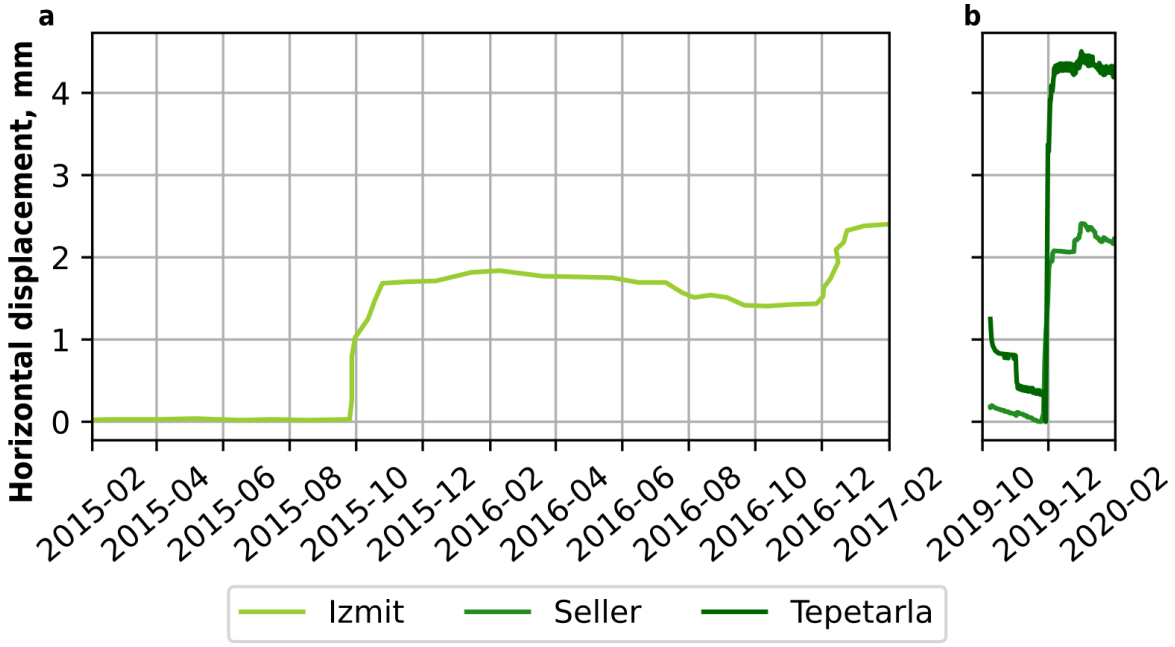

Figure B.15: Creepmeters records along the Izmit segment.

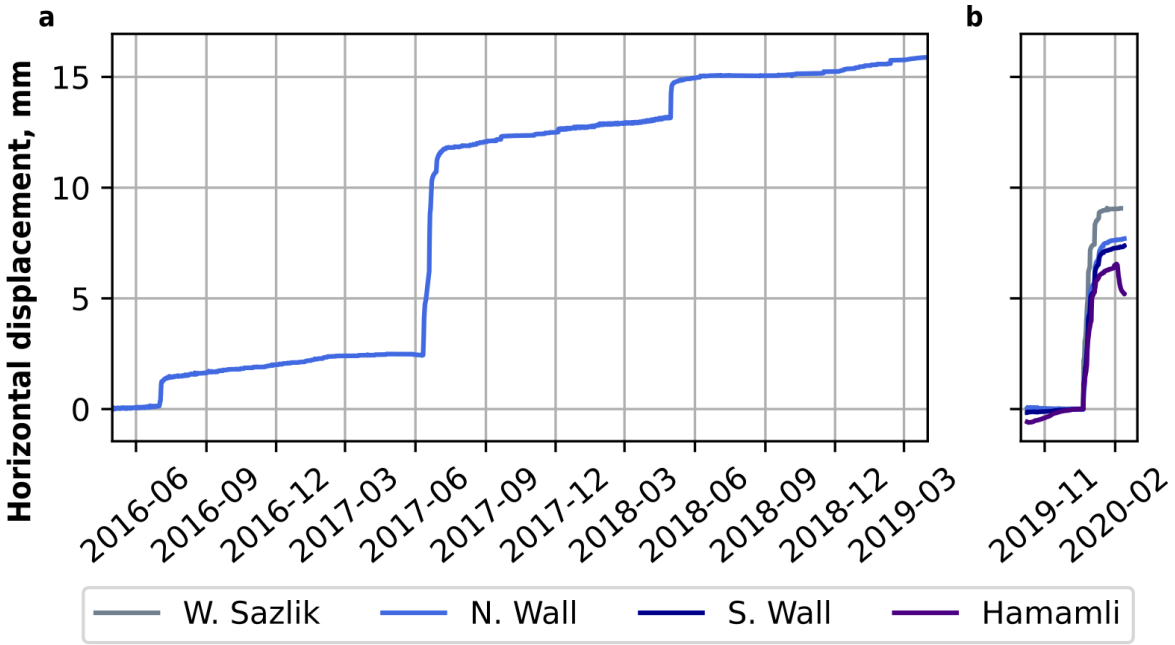

Figure B.16: Creepmeters records along the Ismetpasa segment.

Appendix C

Supplementary Materials: The slow slip event cycle along the izmit segment of the north anatolian fault

Contents

C.1 InSAR analysis 214

C.1.1 InSAR data presentation 214

C.1.2 Extraction of the tectonic signal by Independent Component Analysis (ICA) 216

C.1.3 Mean velocities and seasonal signals analysis 219

C.1.4 Fault relative displacement 224

C.1.5 Slip inference at depth 226

C.2 Discussion materials 234

C.1 InSAR analysis

C.1.1 InSAR data presentation

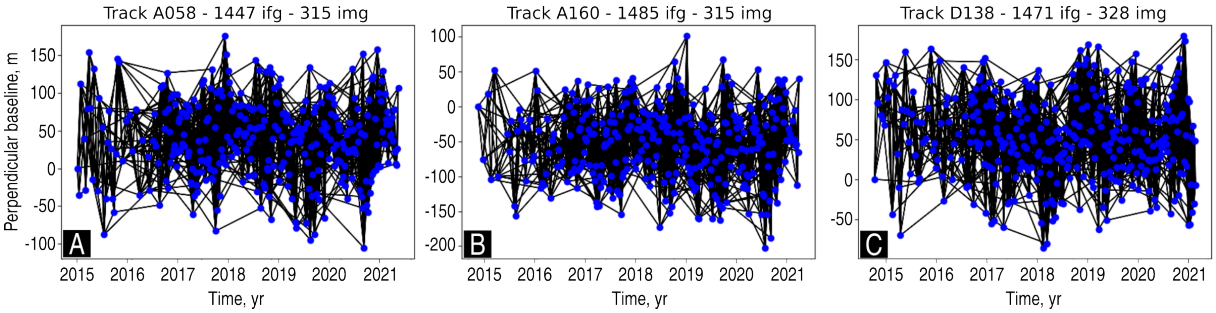

Figure C.1: Interferogram networks for the tracks A058 (A), A160 (B) and D138 (C). *ifg* and *img* stand for interferograms and images, respectively.

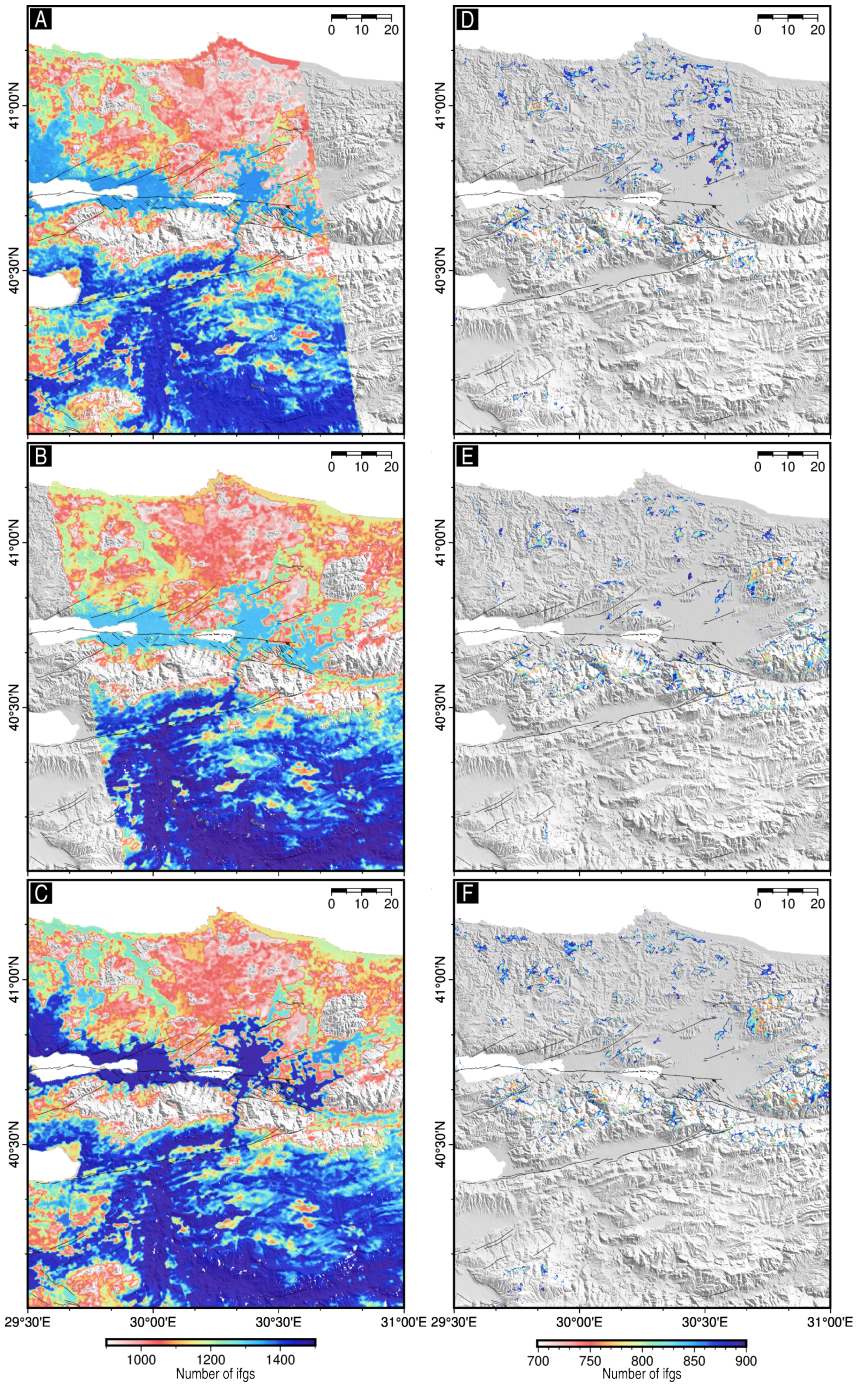

Figure C.2: Number of interferograms (*ifgs*) per pixel for each track above the threshold of 900 interferograms (A-C) and below (D-F). Number of interferograms for the tracks A058, A160 and D138 correspond to the maps (A,D), (B,E) and (C,F), respectively.

C.1.2 Extraction of the tectonic signal by Independent Component Analysis (ICA)

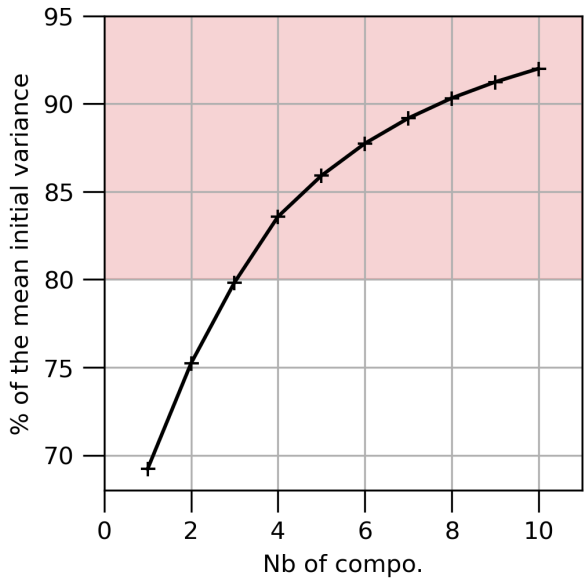

Figure C.3: Comparison of the variance of the reconstructed data based on the ICA sources with the variance of the InSAR time series, as a function of the number of components used for the ICA. The results are given as a percentage of the InSAR variance explained by the ICA sources. The red area corresponds to the area within at least 80% of the InSAR data is explained by the components. In order to get a compromise between the reconstructed variance and the number of IC components, we chose to use three components.

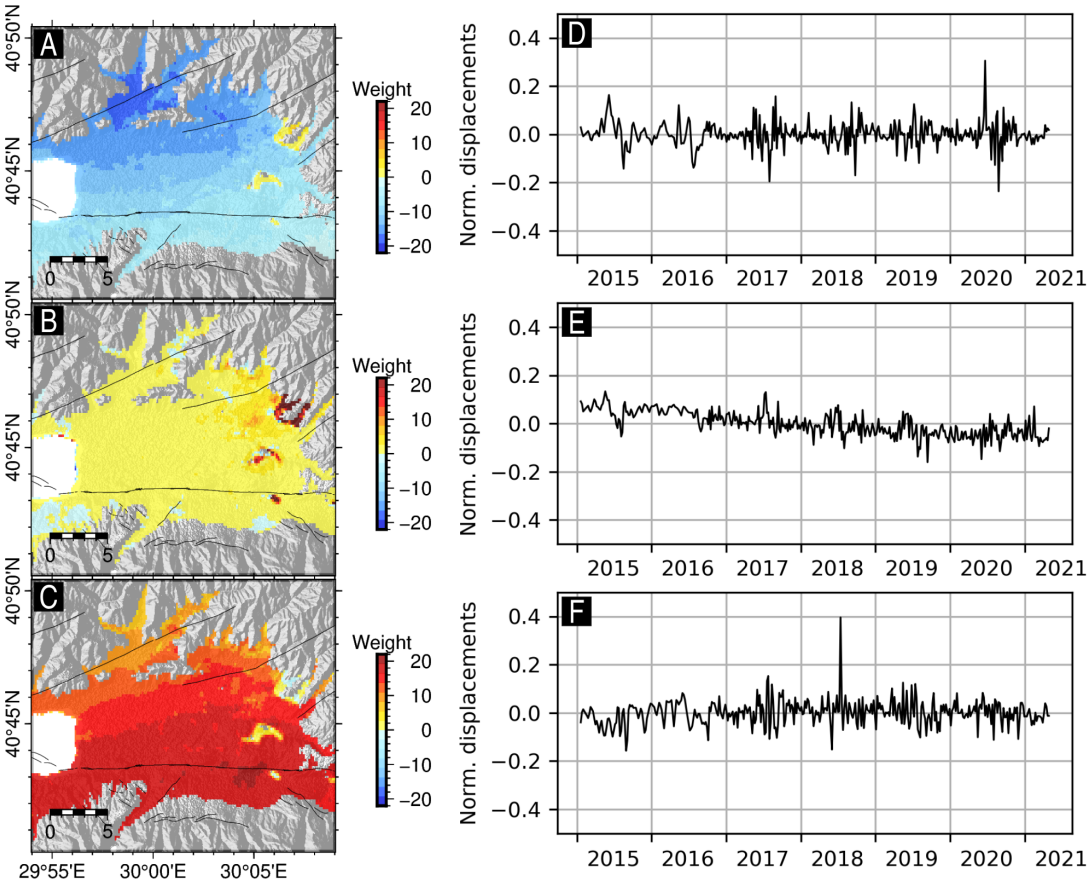

Figure C.4: Three sources extracted by the FastICA algorithm. (A,B,C) Weight per pixels for each sources, corresponding to the mixing matrix. (D,E,F) Temporal sources extracted corresponding to each map. The A and C maps show patterns with high amplitudes associated with high standard deviation on summer (D and F). The maps of these components do not have patterns related to the fault location.

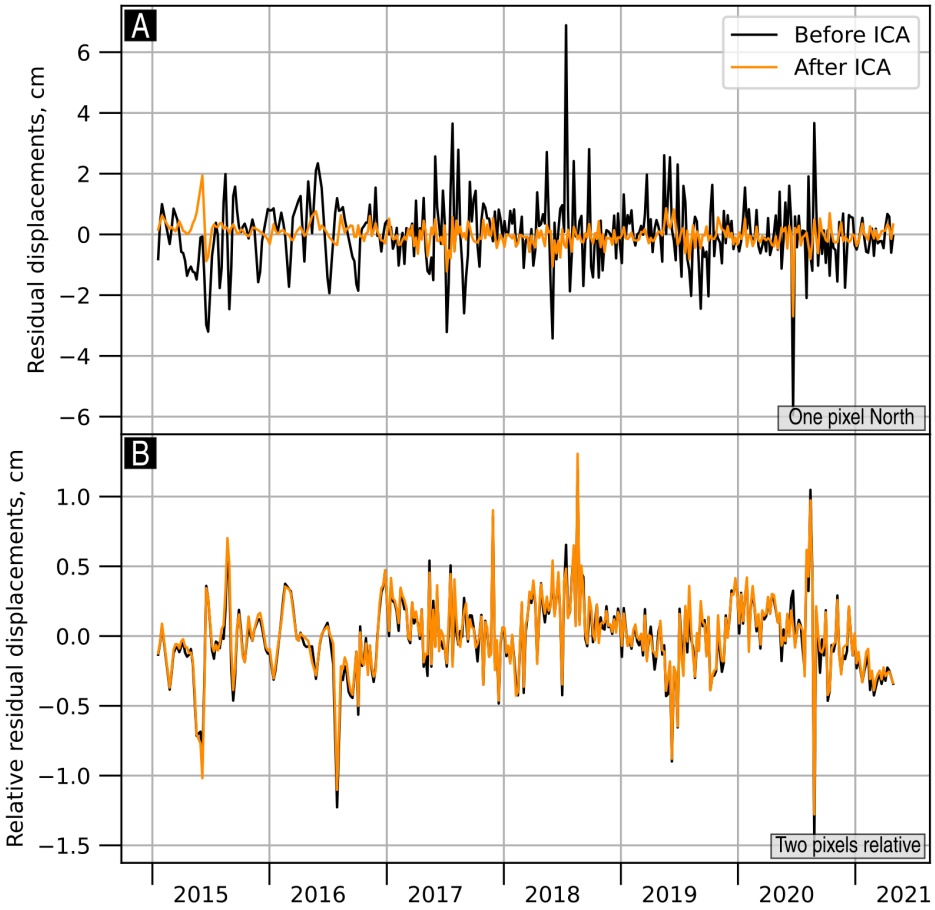

Figure C.5: Examples of residual time series before (in black) and after (in orange) subtraction of the IC components. (A) Residual time series of one pixel located North of the fault (40.73°*N*29.99°*E*). (B) Relative residual time series computed using the previous pixel and a pixel located South of the fault (40.73°*N*29.99°*E*). Note that the ICA enables to reduce the variance of the time series by about 89.6% (A), without decreasing the tectonic signal as shown by the relative analysis close to the fault (B).

C.1.3 Mean velocities and seasonal signals analysis

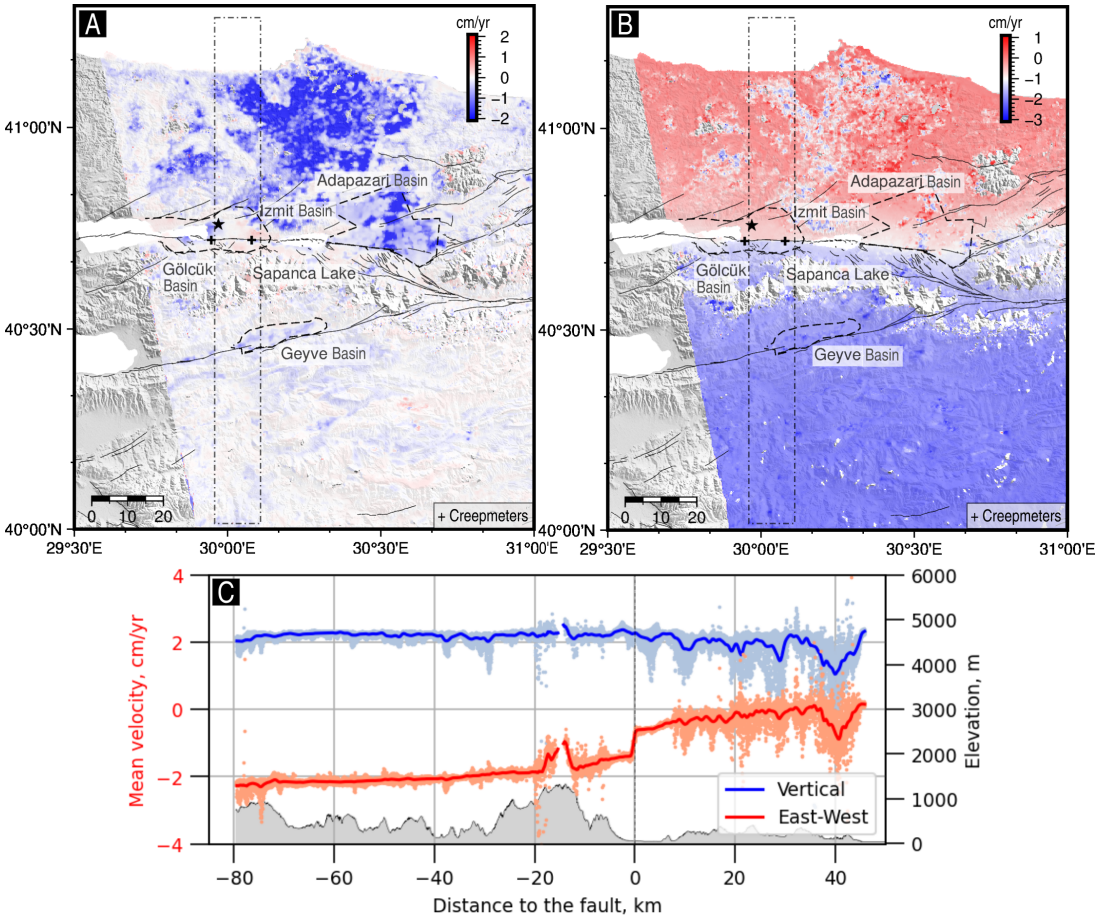

Figure C.6: Mean horizontal and vertical velocities of the cropped zone computed after HV decomposition of the tracks A160 and D138, and after GNSS referencing. (A) Mean vertical velocity with in red and blue up and down displacements, respectively. The dotted lines highlight the major Quaternary basins named by the main city within them, Gölcük, Izmit, Adapazari and Geyve. The fault network is shown by the black lines. The black star is the 1999 Izmit earthquake epicenter and the two black crosses correspond to the Izmit (West) and Tepetarla (East) creepmeters. (B) Mean East-West velocity with in red and blue eastward and westward displacements, respectively. (C) Fault-perpendicular velocity profiles (dot-dashed rectangle in the upper maps) are plotted relatively to the mean elevation of the zone. The lines correspond to the mean average of the data, red and blue corresponding to the East-West and vertical velocities respectively.

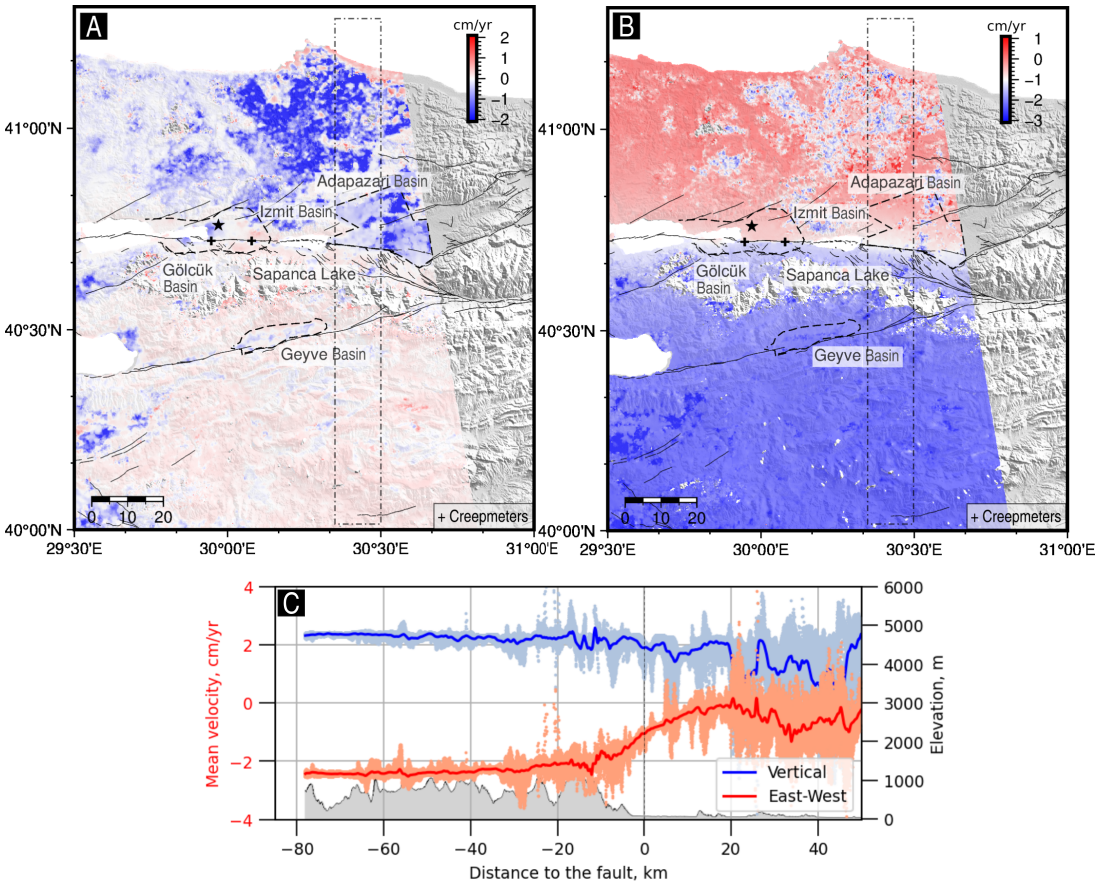

Figure C.7: Mean horizontal and vertical velocities of the cropped zone computed after HV decomposition of the tracks A058 and D138, and after GNSS referencing. (A) Mean vertical velocity with in red and blue up and down displacements, respectively. The dotted lines highlight the major Quaternary basins named by the main city within them, Gölcük, Izmit, Adapazari and Geyve. The fault network is shown by the black lines. The black star is the 1999 Izmit earthquake epicenter and the two black crosses correspond to the Izmit (West) and Tepetarla (East) creepmeters. (B) Mean East-West velocity with in red and blue eastward and westward displacements, respectively. (C) Fault-perpendicular velocity profiles (dot-dashed rectangle in the upper maps) are plotted relatively to the mean elevation of the zone. The lines correspond to the mean average of the data, red and blue corresponding to the East-West and vertical velocities respectively.

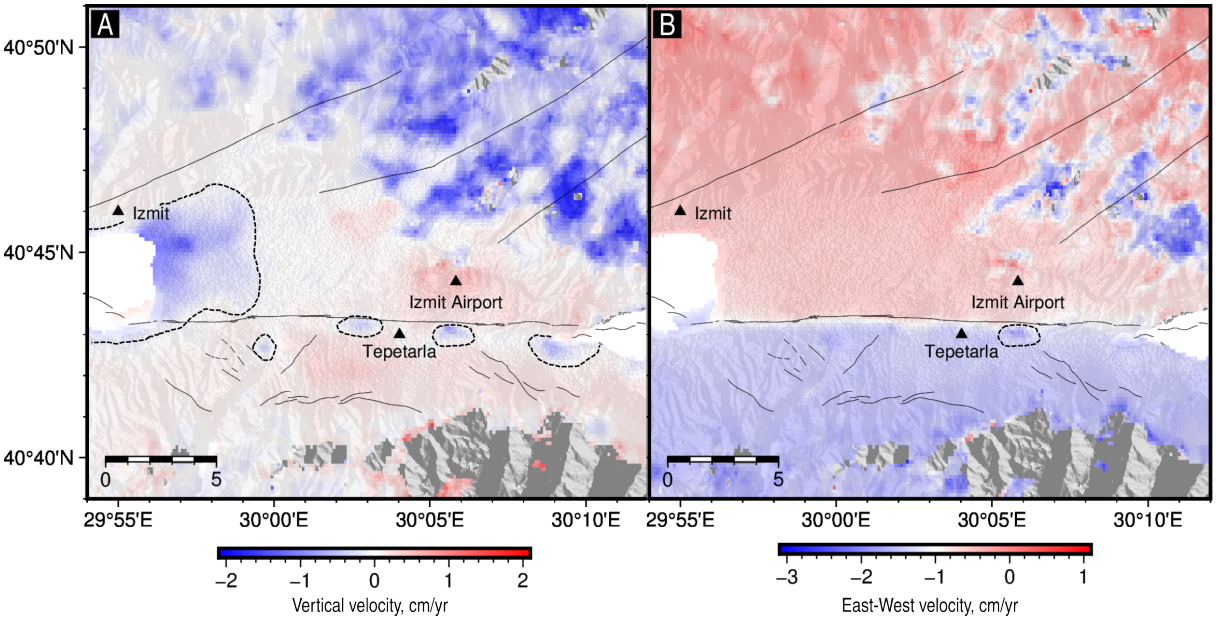

Figure C.8: Mean East-West horizontal and vertical surface velocities on the Izmit basin computed after the HV decomposition of the tracks A058 and D138, and after GNSS referencing. (A) Mean vertical velocity in cm/yr with in red and blue up and down displacements, respectively. The dotted lines highlight areas affected by a strong downward motion. The three eastern areas are correlated with swamps, mapped by Barka (2002). (B) Mean East-West velocity in cm/yr with in red and blue eastward and westward displacements, respectively. The dotted ellipse highlights an area located South of the surface fault trace and affected by a stronger westward motion, corresponding to one of the swamps. The fault network is shown by the black lines.

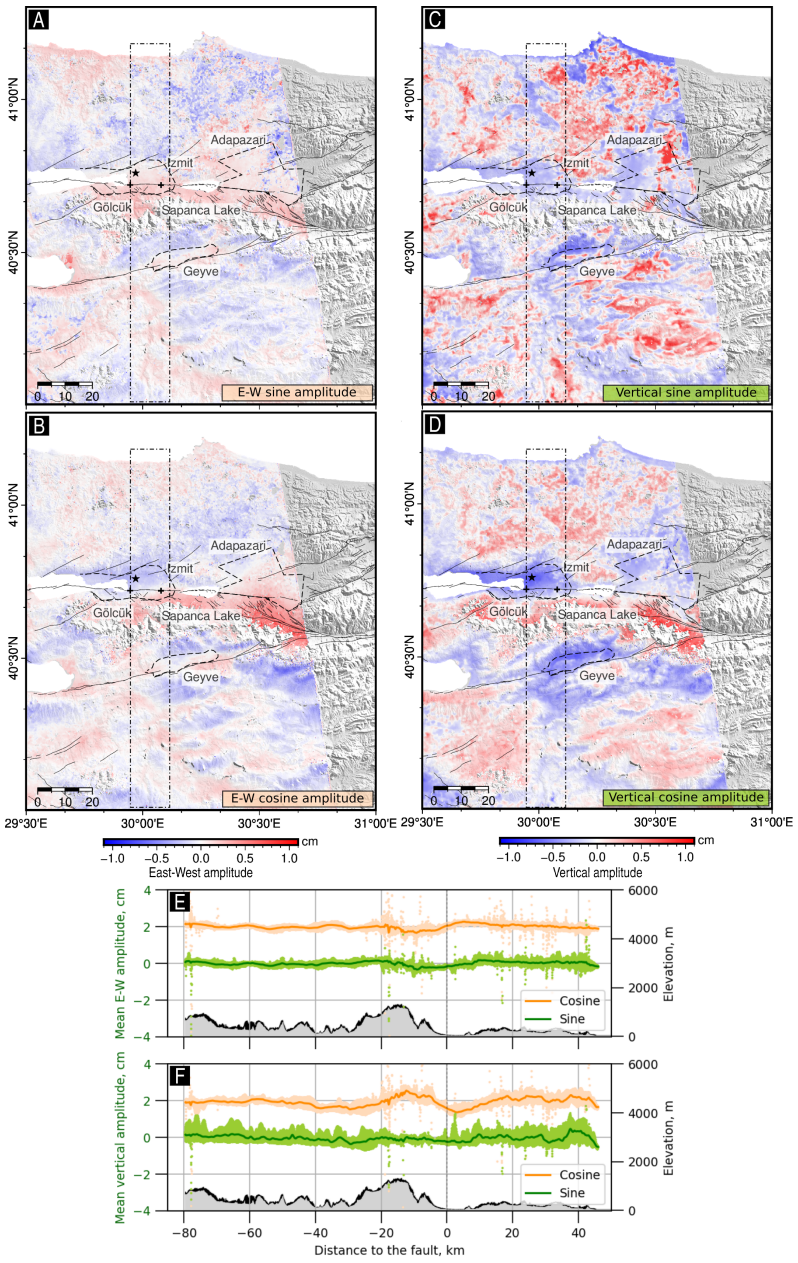

Figure C.9: East-West (A,B) and vertical (C,D) seasonal amplitudes obtained from the *TA058-D138* decomposition. The positive and negative values (red and blue) of the East-West amplitudes correspond to eastward and westward deformation amplitude, respectively, and the positive and negative values of the vertical amplitudes correspond to upward and downward deformation amplitude, respectively. (E,F) Perpendicular to the fault profiles corresponding to the pixels within the dashed rectangle on the above maps.

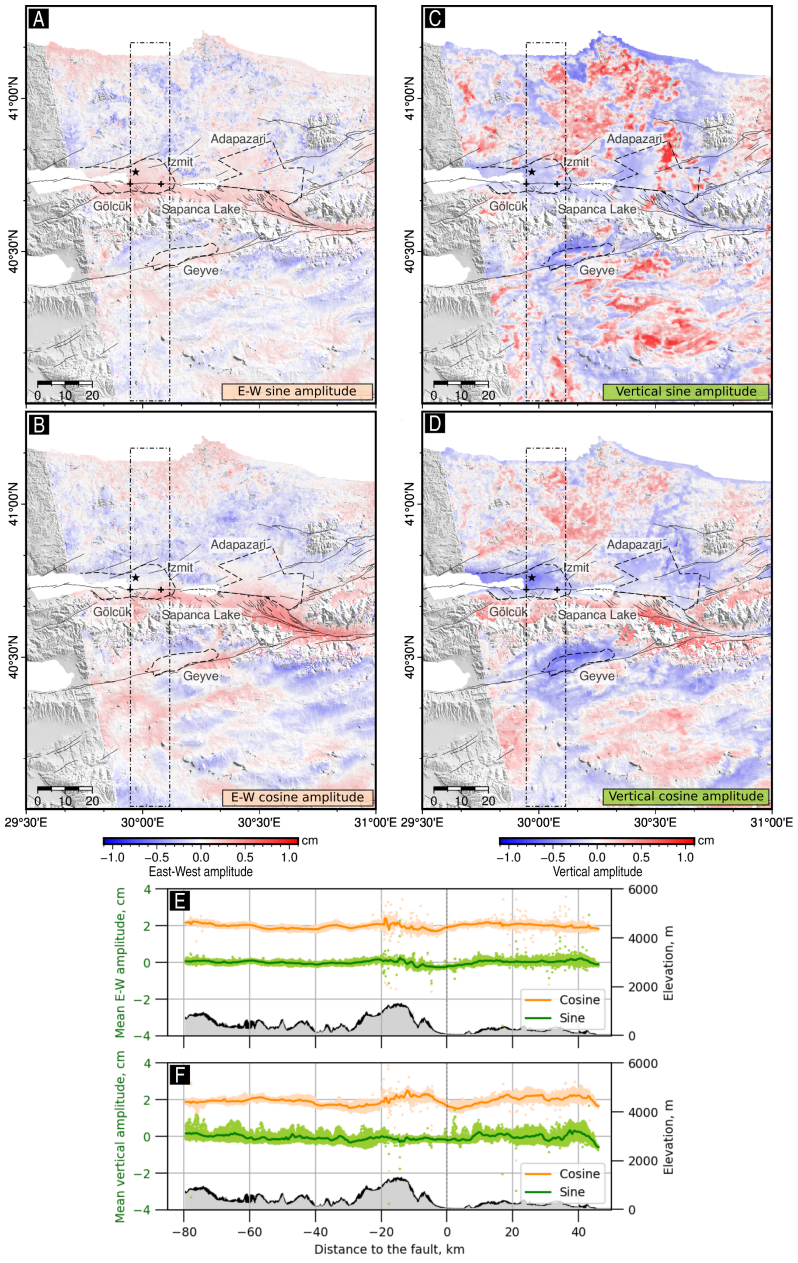

Figure C.10: East-West (A,B) and vertical (C,D) seasonal amplitudes obtained from the *TA160-D138* decomposition. The legend is the same as for figure C.8.

The amplitudes of the seasonal amplitudes (Figures C.8 and C.9) are two to three times larger on the vertical components than on the horizontal East-West ones. The spring/autumn cycles (term *C*) present higher frequency contents than the summer/winter cycles (term *D*), with high amplitudes north of the NAF in crop areas, likely related to surface moisture. The large-scale annual deformation cycles are more pronounced along the cosine components (summer/winter cycles) and are correlated with the topography, with larger amplitudes in the valleys. The three sedimentary basins of Izmit, Adapazari and Geyve have particularly large seasonal vertical deformation.

C.1.4 Fault relative displacement

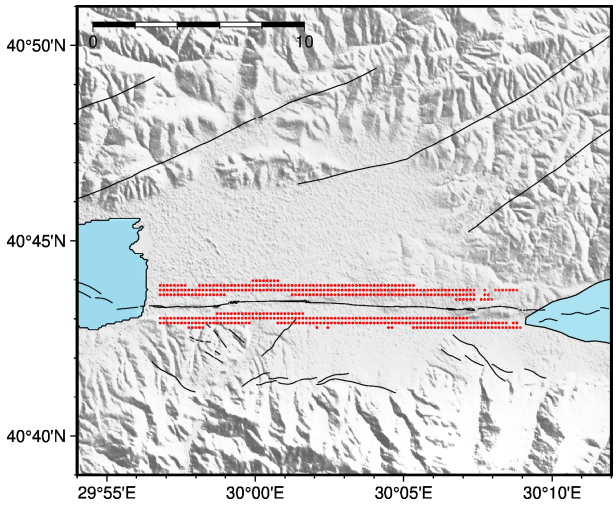

Figure C.11: Map centered on the Izmit basin with the location of the pixels used for the calculation of the relative displacement rates. The pixels are pointed out with red dots, on both side of the Izmit segment.

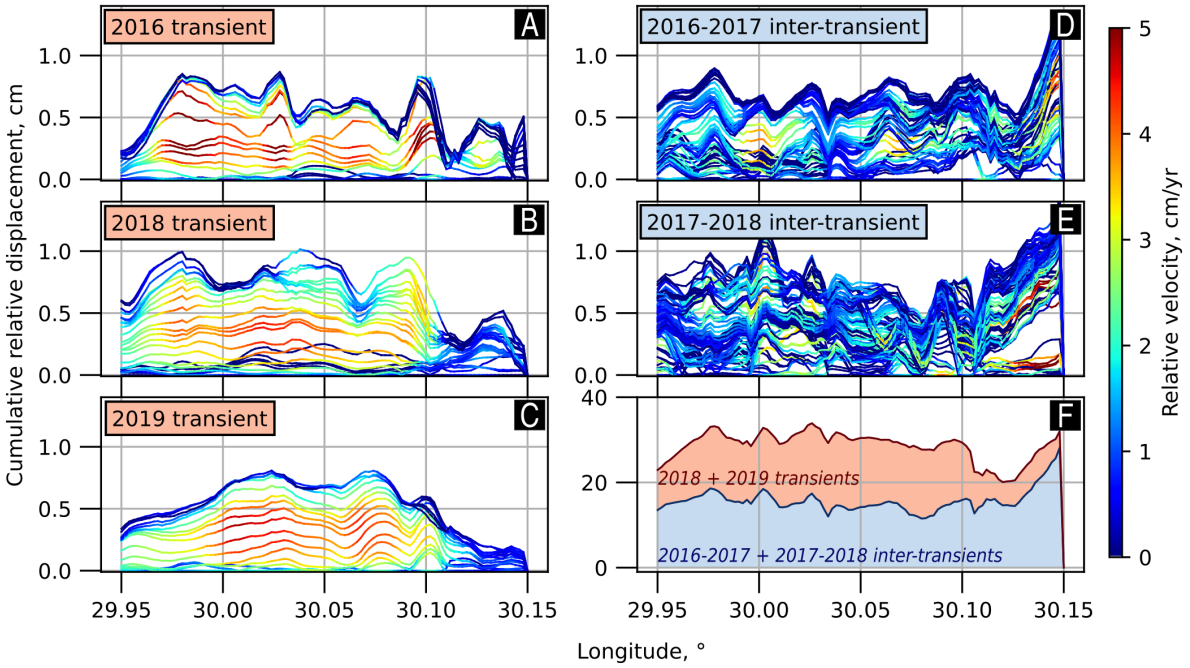

Figure C.12: Cumulative relative displacement using the data from the *TA160-D138* HV decomposition recorded during (A,B,C) and in between (D,E) three transient events: in December 2016, in March 2018 and in November 2019. The two inter-transient periods are between the 2016 (from the October 10, 2016 to the January 20, 2017) and 2018 (from the January 1st, 2018 to the May 20, 2018) events and 2018 and 2019 (from the October 10, 2019 to the January 10, 2020) events. (F) Sum of the relative cumulative displacement during the transient (red) and inter-transient (blue) periods.

C.1.5 Slip inference at depth

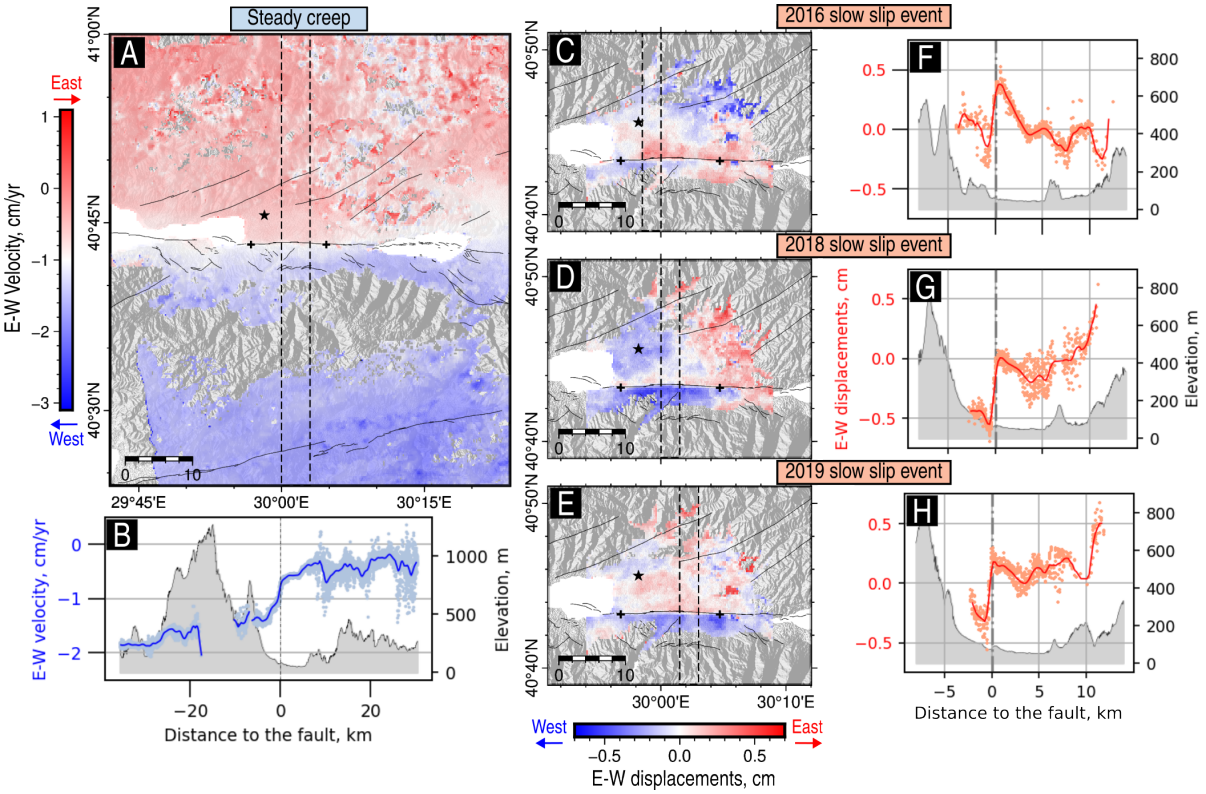

Figure C.13: East-West velocity field during the steady creep periods and East-West static offsets during the transient slow slip events from the *TA160-D138* HV decomposition. (A) Surface velocity computed during the steady creep periods. (B) Fault-perpendicular profile (location on A with the dashed lines) of the East-West velocity and of the mean elevation. (C-E) Static displacements offsets estimated during the three transient slow slip events in 2016 (C), 2018 (D) and 2019 (E). (F-H) Associated fault-perpendicular profiles from each map.

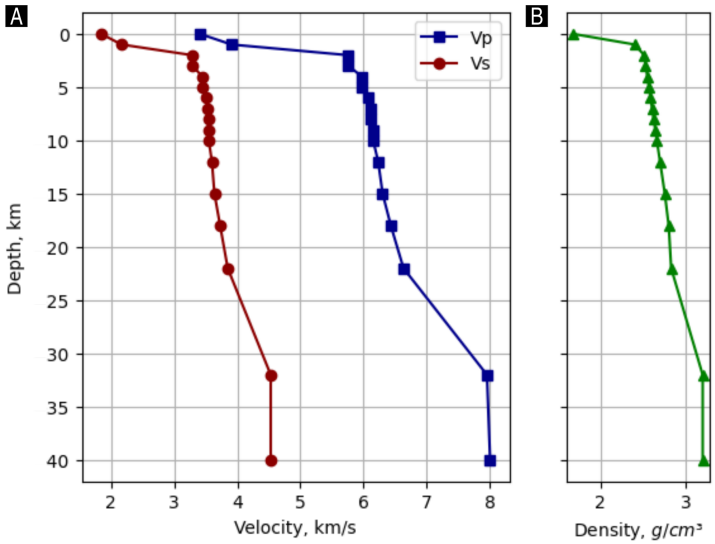

Figure C.14: (A) P-wave velocity V_p, S-wave velocity V_s and (B) density ρ values used for the Green's functions computation for a stratified medium. V_p and V_s values from the surface down to 40 *km*-depth come from Karabulut (2025), ρ values from the surface down to 1.5 *km*-depth come from Özalaybey et al. (2011), and the other values of ρ are chosen according to Crust 1.0 (Laske et al., 2013).

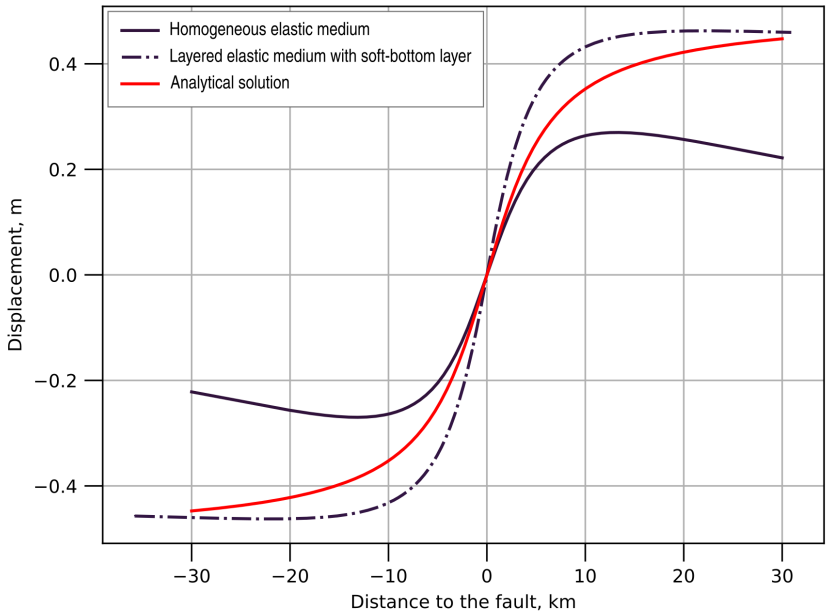

Figure C.15: Perpendicular to the fault profiles of displacements based on different Green's functions, for homogeneous slip with amplitude of 1 *cm* starting from 5 *km*-depth. Displacements using the Okada (1985) solution are shown with a solid blue line computed using a 4060 *km*-length and 35 *km*-deep fault. The dash-dotted line is the result for the same fault geometry but using the velocity model shown figure C.14 and a soft medium below 35 *km*-depth. The red line corresponds to the analytical solution of a dislocation in an infinite half space following the equation $d = \frac{s}{\pi}.atan(\frac{x}{D})$ (Savage and Burford, 1970).

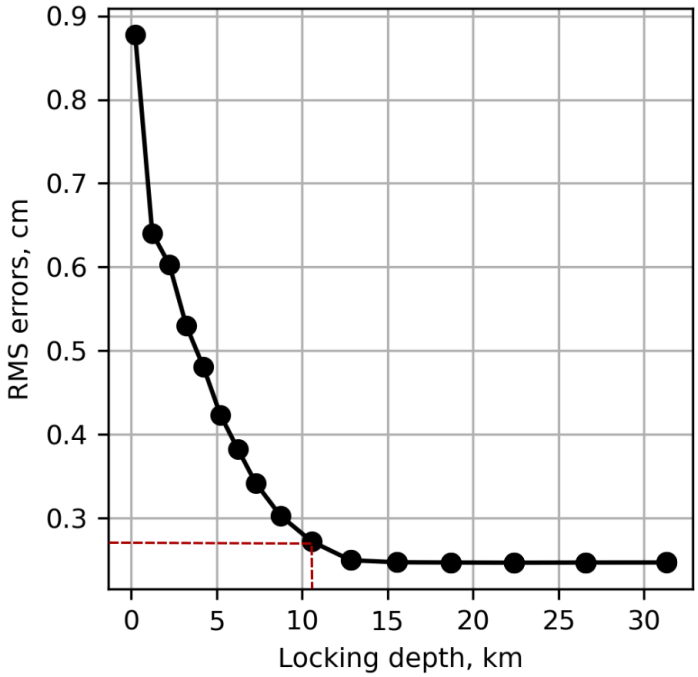

Figure C.16: RMS errors as a function of the *a priori* locking depth. The red dotted lines show the *a priori* locking depth for the preferred model.

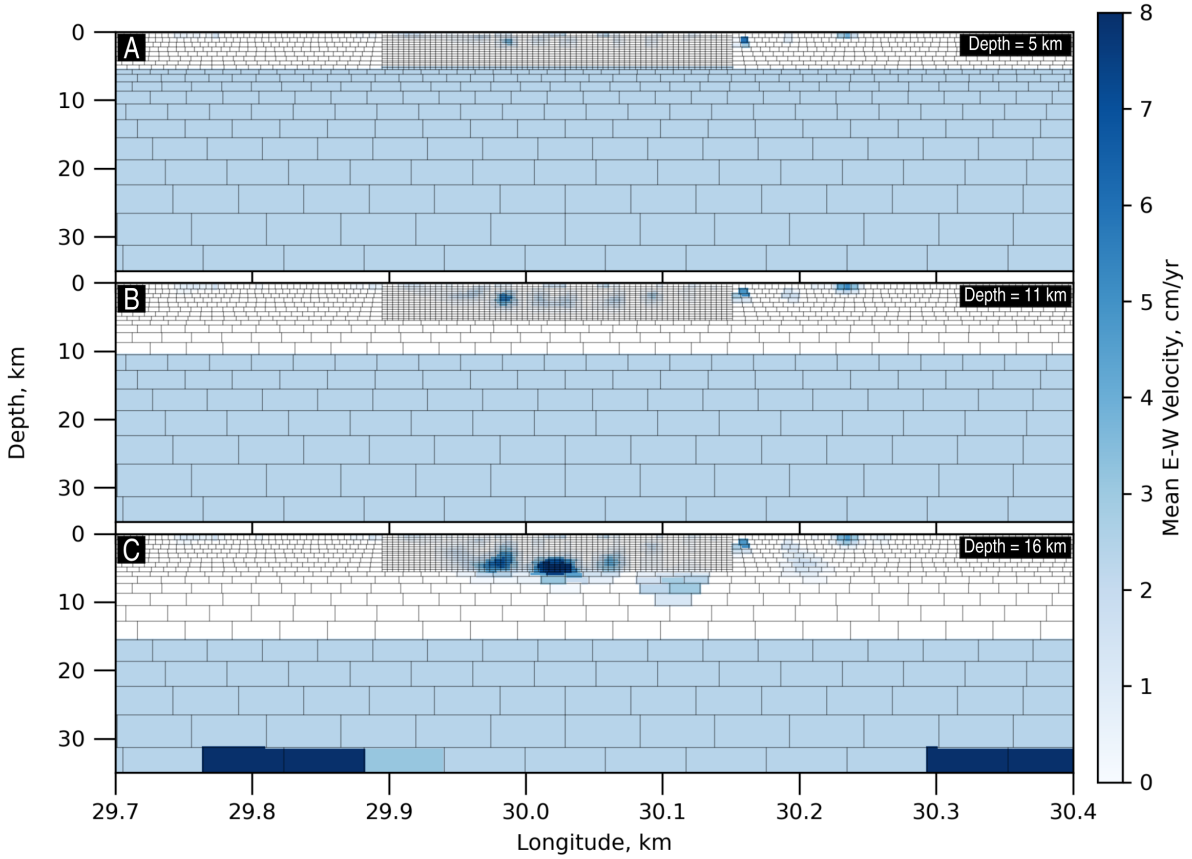

Figure C.17: Slip distributions obtained using several *a priori* models with locking depths of (A) 5 *km*, (B) 11 *km* and (C) 16 *km*.

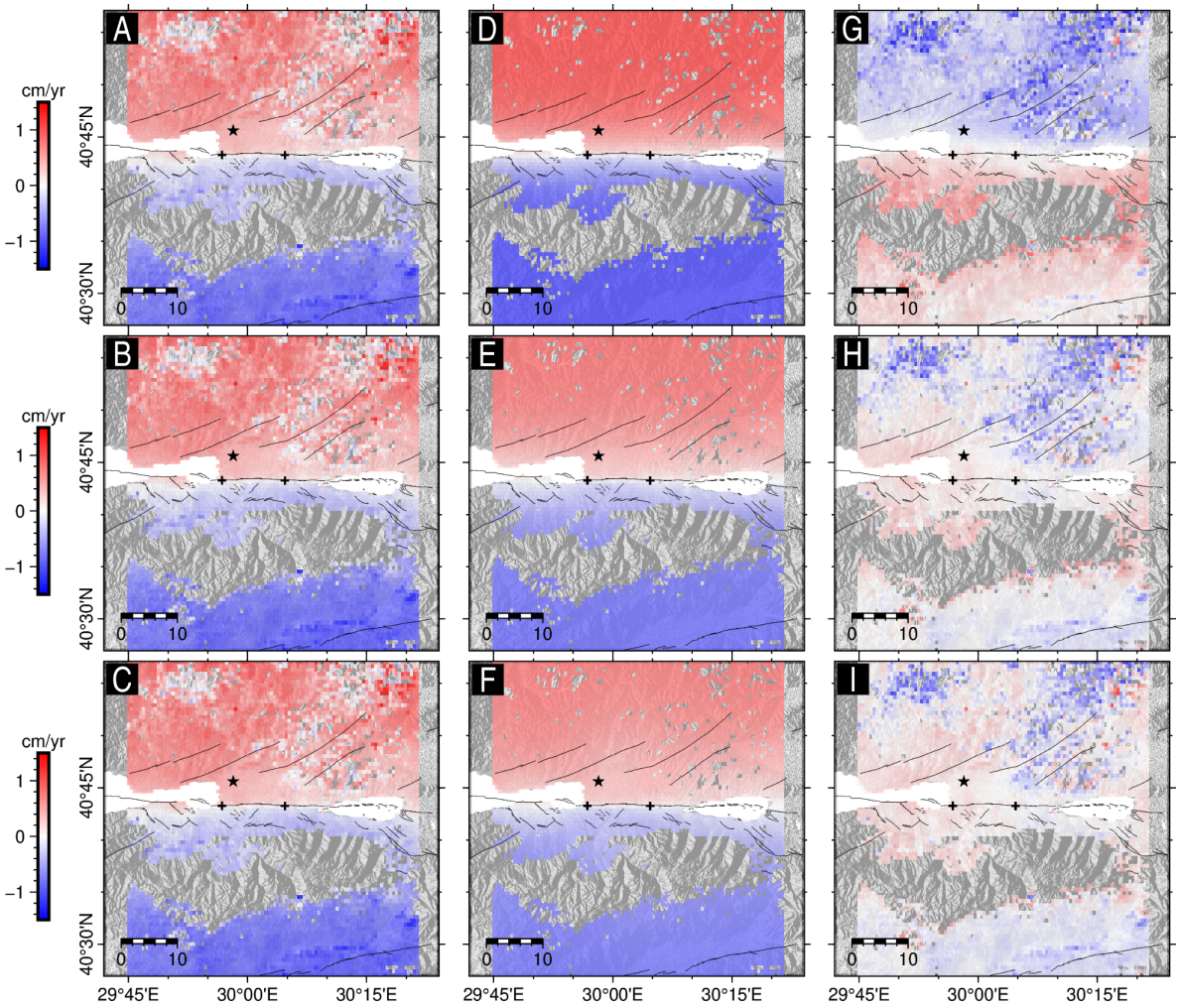

Figure C.18: Comparison between the East-West steady creep velocity field (A-C) and three model predictions obtained from the inversions based on *a priori* models with the locking depths of (D) 5 *km*, (E) 11 *km* and (F) 16 *km*. The maps from G to I correspond to the difference between the data and the model predictions for each *a priori* model.

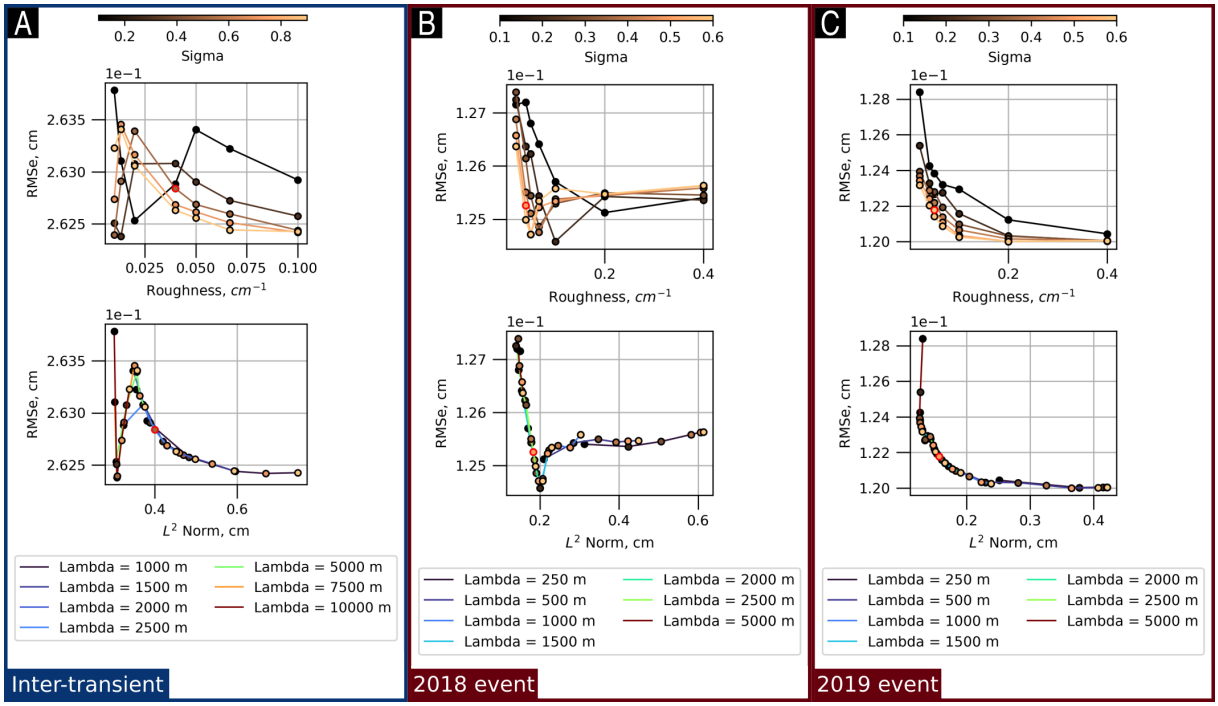

Figure C.19: L-curves obtained for (A) the steady creep, (B,C) the 2018 and 2019 slow slip events, respectively. The top panels correspond to the RMS errors as a function of slip roughness, and the bottom panels correspond to the RMS errors as a function of the L^2-norm. The red dots indicate the inversion parameters chosen for each inversion.

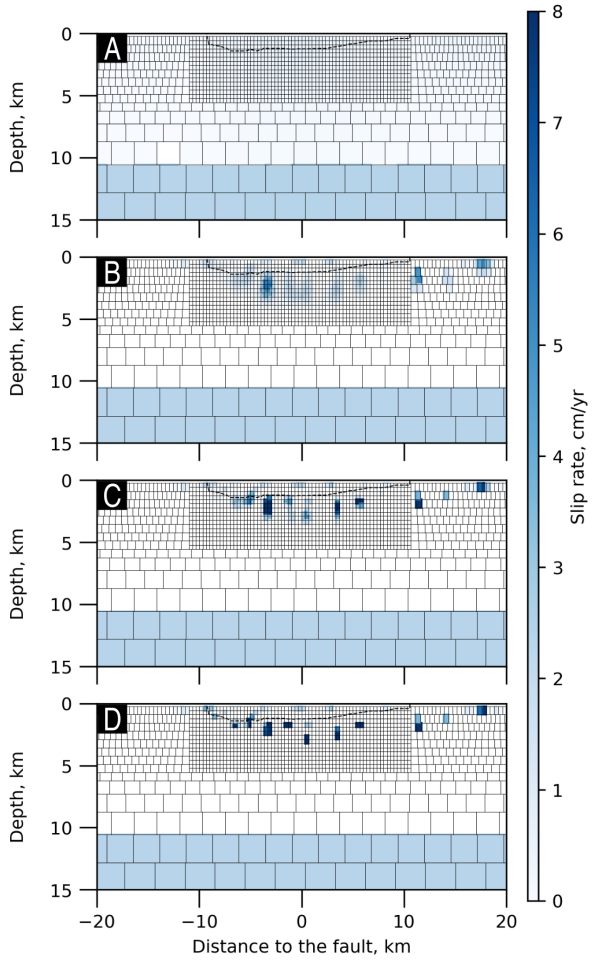

Figure C.20: Slip distributions obtained from the inversions of the mean inter-transient velocity, for several parameters. Slip distributions obtained using the following couples $(\lambda;\sigma_m)$: (A) $(\lambda = 10000\ m;\sigma_m = 0.1)$, (B) $(\lambda = 2000\ m;\sigma_m = 0.5)$, (C) $(\lambda = 1500\ m;\sigma_m = 0.7)$ and (D) $(\lambda = 1000\ m;\sigma_m = 0.9)$.

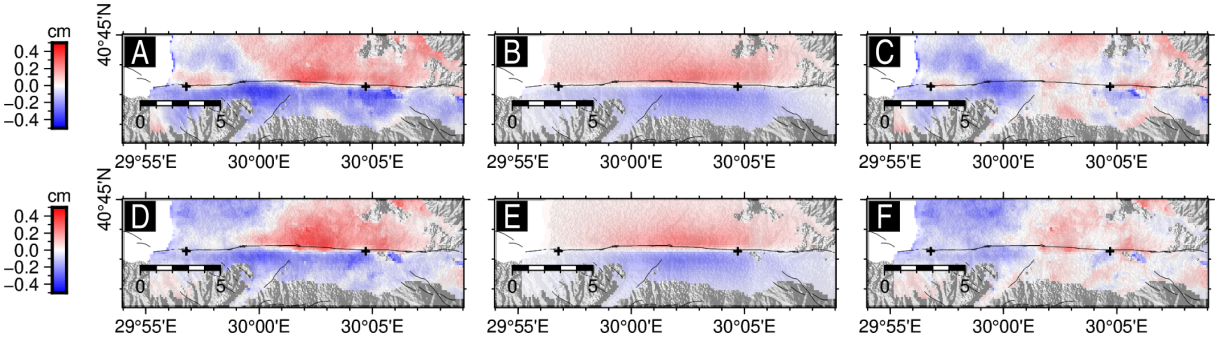

Figure C.21: Comparison between the InSAR East-West displacements recorded during the 2018 (A) and 2019 (D) transient events with the model predictions (B,E respectively). The residual displacements are shown on maps C and F respectively.

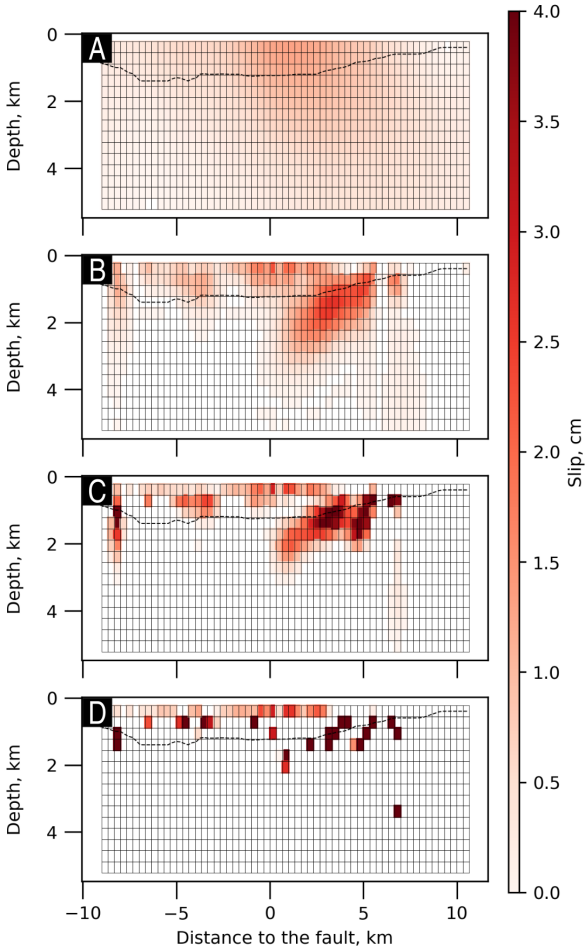

Figure C.22: Slip distributions obtained from the inversions of the 2018 transient event displacements, for several parameters. Slip distributions obtained using the following couples $(\lambda; \sigma_m)$: (A) $(\lambda = 5000\ m; \sigma_m = 0.1)$, (B) $(\lambda = 2000\ m; \sigma_m = 0.5)$, (C) $(\lambda = 1000\ m; \sigma_m = 0.4)$ and (D) $(\lambda = 250\ m; \sigma_m = 0.6)$.

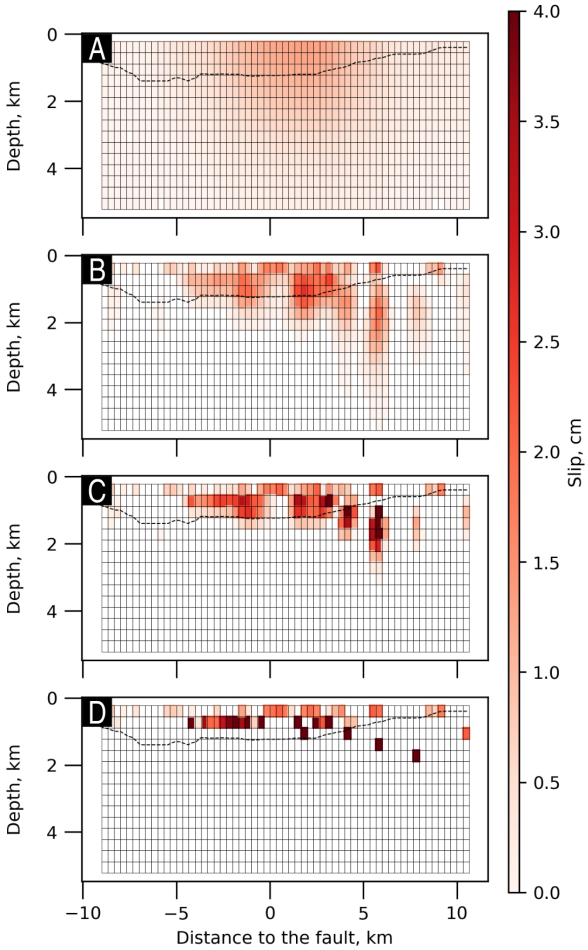

Figure C.23: Slip distributions obtained from the inversions of the 2019 transient event displacements, for several parameters. Slip distributions obtained using the following couples $(\lambda; \sigma_m)$: (A) $(\lambda = 5000\ m; \sigma_m = 0.1)$, (B) $(\lambda = 2000\ m; \sigma_m = 0.5)$, (C) $(\lambda = 1500\ m; \sigma_m = 0.7)$ and (D) $(\lambda = 1000\ m; \sigma_m = 0.9)$.

C.2 Discussion materials

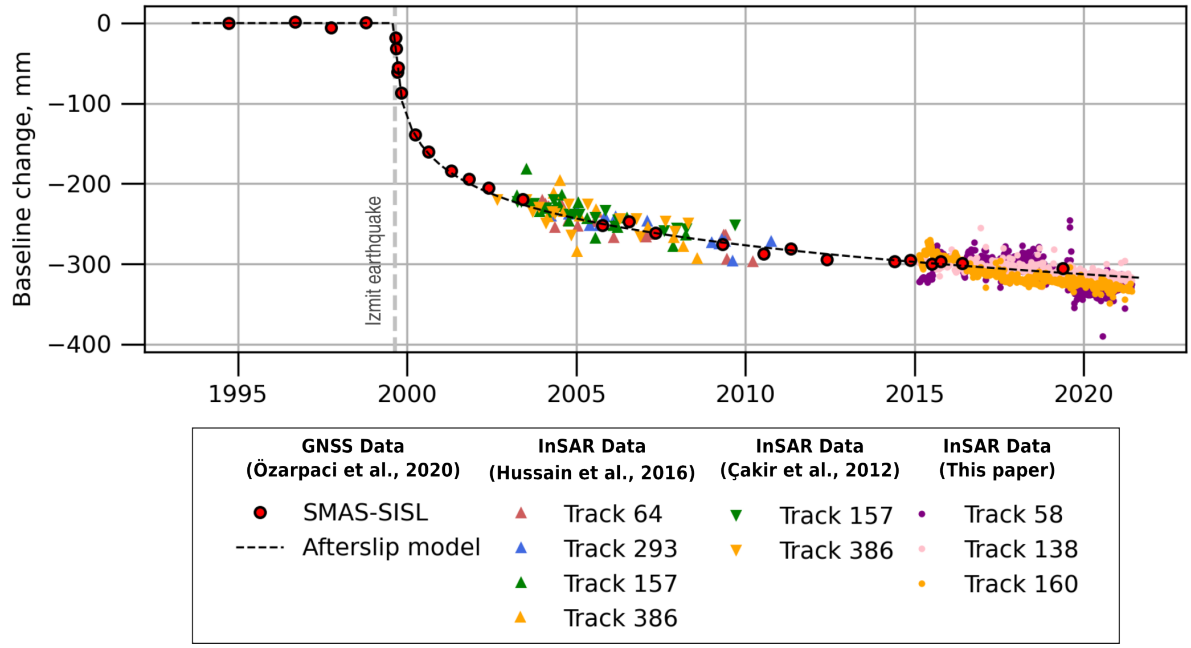

Figure C.24: Comparison between the GNSS SMAS-SISL baseline and the InSAR results. The red dots correspond to the East-West component of the GNSS baseline, after the removal of the interseismic behavior with an overlaying afterslip model in black dotted line determined by Özarpacı et al. (2020). The InSAR data come from Cakir et al. (2012), Hussain et al. (2016) and our study.

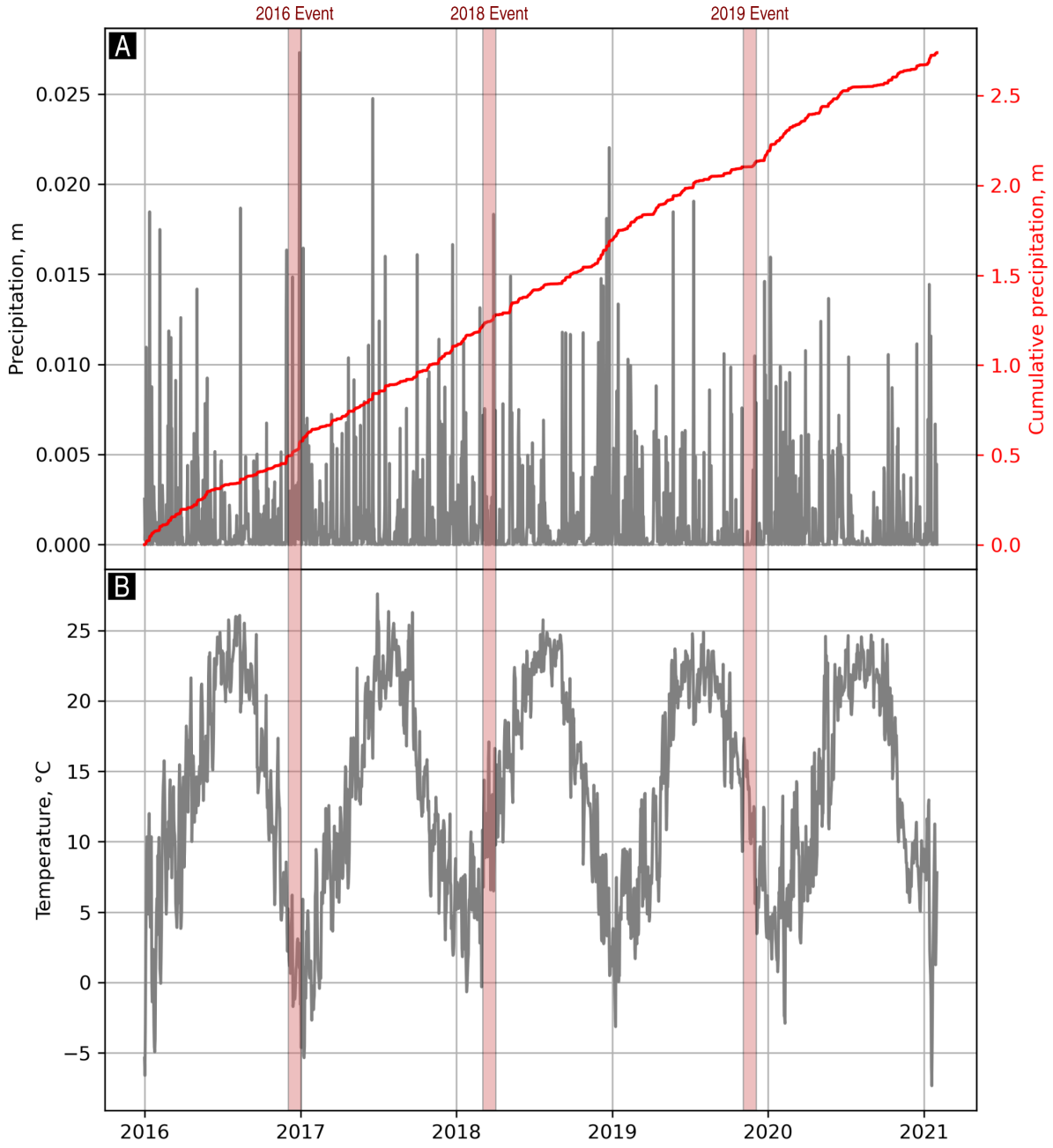

Figure C.25: Meteorological data over the period 2016 – 2021 within the Izmit basin. These data come from the ERA-5 models, averaged on the region between the longitudes $E029.8°$ and $E030.8°$ and the latitudes $N40.6°$ and $N40.9°$. (A) The daily precipitation is shown by the gray line, with the cumulative precipitation shown by the red line. (B) Time evolution of the daily temperature. The red periods correspond to the three slow slip events detected by InSAR.

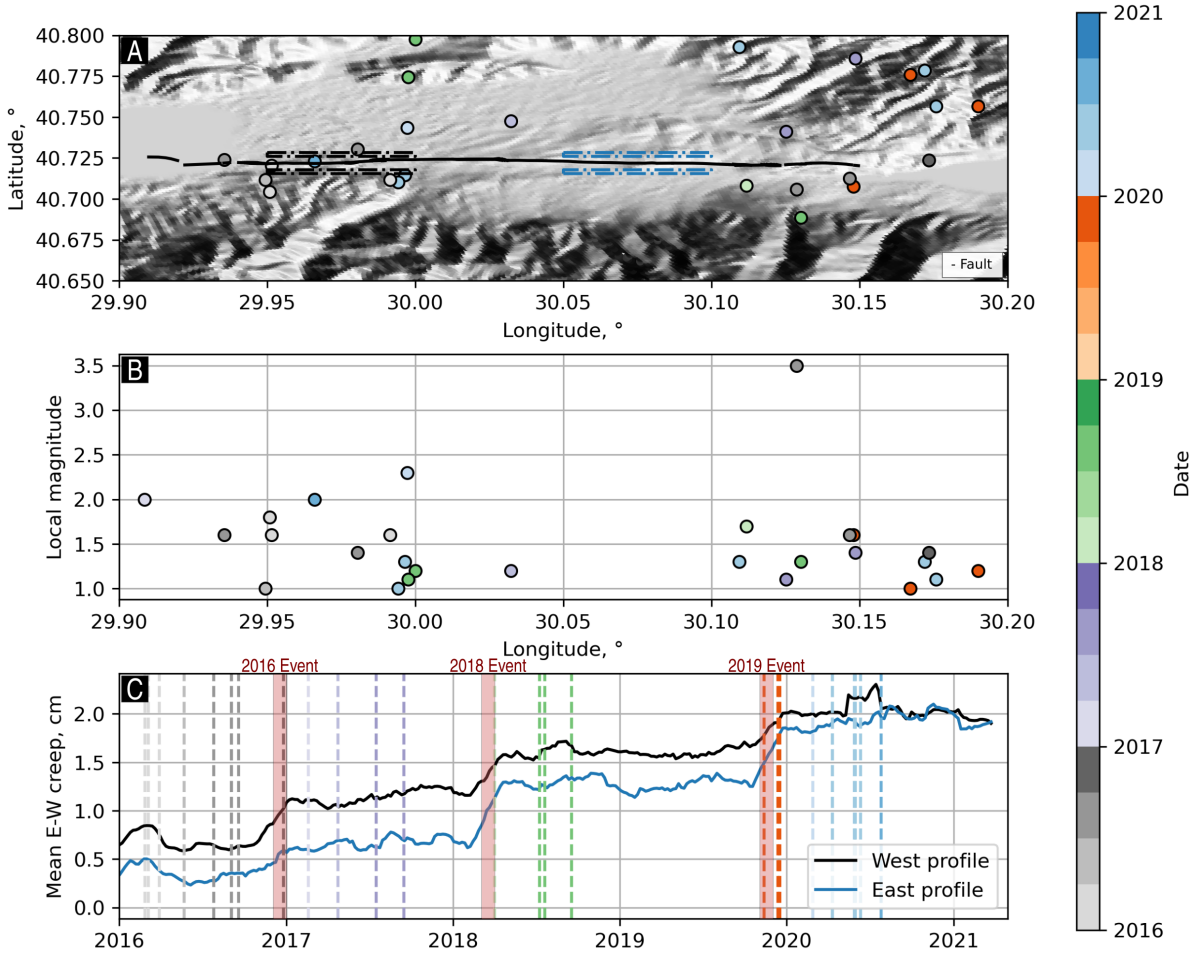

Figure C.26: Seismic events from the AFAD catalog, from the January 1st, 2016 to the March 1st, 2021. (A) Location of the events within the Izmit basin. The dotted-dashed boxes correspond to the pixels used for the mean East-West creep profiles presented in the graph (C). (B) Local magnitude M_L as a function of longitude. (C) Time evolution of the mean East-West relative displacement located west (black line) and on the central part (blue line) of the Izmit segment. The dates of each event are represented by the coloured vertical dotted line. The red periods correspond to the three slow slip events detected by InSAR.

Appendix D

Supplementary Materials: Postseismic and shallow slow slip events on the Izmit segment of the North Anatolian Fault controlled by depth-dependent frictional variations

Contents

D.1 Inputs of the simulation 238

D.1.1 Fixed parameters 238

D.1.2 Tests on the cohesion value at the surface 238

D.1 Inputs of the simulation

D.1.1 Fixed parameters

Parameters	Value
Along-dip fault width	32 km
Shear module μ	30 GPa
Grid size	25 m
Fault dip angle	90°
Shear wave speed c_s	3 km/s
Reference velocity V_0	1 mm/s
Steady state friction coefficient at V_0	0.6

Table D.1: Model simulation parameters.

D.1.2 Tests on the cohesion value at the surface

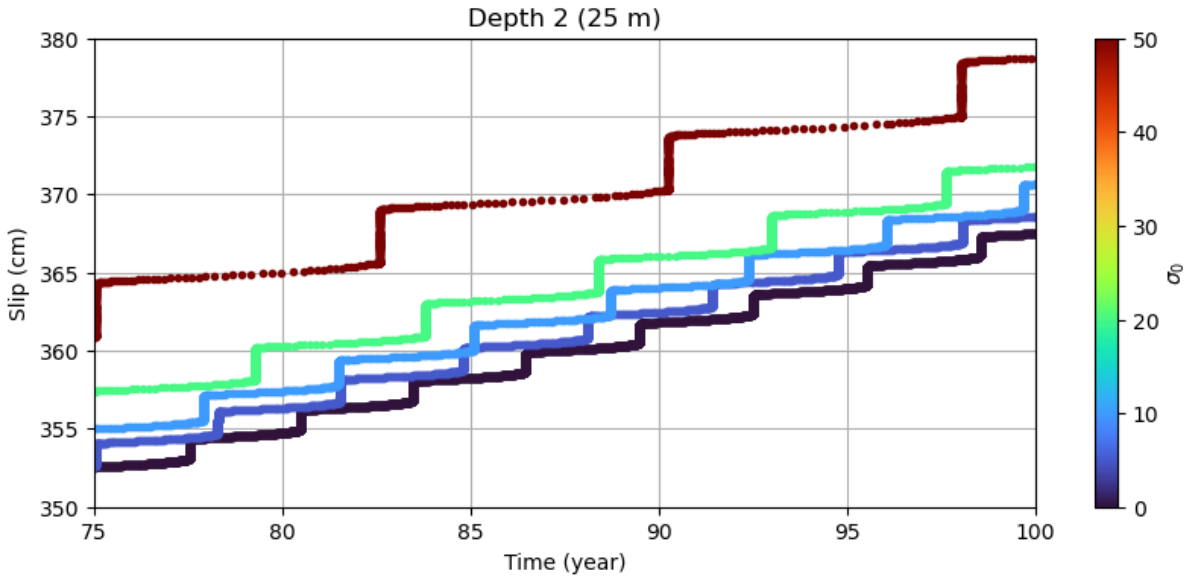

Figure D.1: Impact of the cohesion value σ_0 in MPa on the predictions of the cumulative displacement times series at the top cell. $\sigma_0 = 50\ MPa$ appears to be a limit value affecting the whole seismic cycle, whereas the lower values impact the amplitude and the return time of the slow slip events. Because of the lack of information along the Izmit segment, we assume a negligible cohesion value at the surface.

Bibliography

Akaike, H., 1974. A new look at the statistical model identification. IEEE Transactions on Automatic Control 19, 716–723. doi:10.1109/TAC.1974.1100705.

Akbayram, K., Okay, A.I., Satır, M., 2013. Early Cretaceous closure of the Intra-Pontide Ocean in western Pontides (northwestern Turkey). Journal of Geodynamics 65, 38–55. URL: https://www.sciencedirect.com/science/article/pii/S0264370712000877, doi:10.1016/j.jog.2012.05.003.

Akdoğan, R., Hu, X., Okay, A.I., Topuz, G., Xue, W., 2021. Provenance of the paleozoic to mesozoic siliciclastic rocks of the istanbul zone constrains the timing of the rheic ocean closure in the eastern mediterranean region. Tectonics 40, e2021TC006824.

Akyuz, H., Hartleb, R., Barka, A., Altunel, E., Sunal, G., Meyer, B., Armijo, v.R., 2002. Surface rupture and slip distribution of the 12 november 1999 duzce earthquake (m 7.1), north anatolian fault, bolu, turkey. Bulletin of the Seismological Society of America 92, 61–66.

Altay, C., 1991. Continuous creep measurement along the north anatolian fault zone. Bull. Geolog. Congr. Turkey 6, 77–84.

Ambraseys, N., 2000. The seismicity of the marmara sea area 1800–1899. Journal of Earthquake Engineering 4, 377–401.

Ambraseys, N., 2002. The seismic activity of the marmara sea region over the last 2000 years. Bulletin of the Seismological Society of America 92, 1–18.

Ambraseys, N., Zatopek, A., 1969. The mudurnu valley, west anatolia, turkey, earthquake of 22 july 1967. Bulletin of the Seismological Society of America 59, 521–589.

Ambraseys, N.N., 1970. Some characteristic features of the anatolian fault zone. Tectonophysics 9, 143–165.

Ambraseys, N.N., Finkel, C., 1995. The seismicity of turkey and adjacent areas: a historical review, 1500-1800. (No Title) .

An, M., Zhang, F., Zhang, L., Fang, Y., 2018. Effects of normal stress and clay content on the frictional properties of reservoir rocks under fully saturated conditions, in: GeoShanghai International Conference, Springer. pp. 220–231.

Ansari, H., De Zan, F., Parizzi, A., 2021. Fading signal: An overlooked error source for distributed scatterer interferometry, in: 2021 IEEE International Geoscience and Remote Sensing Symposium IGARSS, IEEE. pp. 3181–3184.

Armijo, R., Meyer, B., Barka, A., de Chabalier, J.B., Hubert, A., Cakir, Z., 2000. The fault breaks of the 1999 earthquakes in turkey and the tectonic evolution of the sea of marmara; a summary .

Arpat, E., Saroglu, F., 1972. The east anatolian fault system: thoughts on its development. Bull. Miner. Res. Explor. Inst. Turk 78, 33–39.

Aslan, G., Cakir, Z., Lasserre, C., Renard, F., 2019a. Investigating subsidence in the bursa plain, turkey, using ascending and descending sentinel-1 satellite data. Remote Sensing 11, 85.

Aslan, G., Lasserre, C., Cakir, Z., Ergintav, S., Özarpaci, S., Dogan, U., Bilham, R., Renard, F., 2019b. Shallow Creep Along the 1999 Izmit Earthquake Rupture (Turkey) From GPS and High Temporal Resolution Interferometric Synthetic Aperture Radar Data (2011–2017). Journal of Geophysical Research: Solid Earth 124, 2218–2236. URL: https://onlinelibrary.wiley.com/doi/abs/10.1029/2018JB017022, doi:10.1029/2018JB017022.

Avouac, J.P., 2015. From Geodetic Imaging of Seismic and Aseismic Fault Slip to Dynamic Modeling of the Seismic Cycle. Annual Review of Earth and Planetary Sciences 43, 233–271. URL: https://doi.org/10.1146/annurev-earth-060614-105302, doi:10.1146/annurev-earth-060614-105302. _eprint: https://doi.org/10.1146/annurev-earth-060614-105302.

Ayhan, M., Bürgmann, R., McClusky, S., Lenk, O., Aktug, B., Herece, E., Reilinger, R., 2001. Kinematics of the mw= 7.2, 12 november 1999, düzce, turkey earthquake. Geophysical Research Letters 28, 367–370.

Aysal, N., Şahin, S.Y., Güngör, Y., Peytcheva, I., Öngen, S., 2018. Middle permian–early triassic magmatism in the western pontides, nw turkey: Geodynamic significance for the evolution of the paleo-tethys. Journal of Asian Earth Sciences 164, 83–103.

Barbot, S., Fialko, Y., Bock, Y., 2009. Postseismic deformation due to the mw 6.0 2004 parkfield earthquake: Stress-driven creep on a fault with spatially variable rate-and-state friction parameters. Journal of Geophysical Research: Solid Earth 114.

Barbot, S., Lapusta, N., Avouac, J.P., 2012. Under the hood of the earthquake machine: Toward predictive modeling of the seismic cycle. Science 336, 707–710.

Barka, A., 1996. Slip distribution along the north anatolian fault associated with the large earthquakes of the period 1939 to 1967. Bulletin of the Seismological Society of America 86, 1238–1254.

Barka, A., 1999. The 17 august 1999 izmit earthquake. Science 285, 1858–1859.

Barka, A., 2002. The Surface Rupture and Slip Distribution of the 17 August 1999 Izmit Earthquake (M 7.4), North Anatolian Fault. Bulletin of the Seismological Society of America 92, 43–60. URL: https://pubs.geoscienceworld.org/bssa/article/92/1/43-60/102910, doi:10.1785/0120000841.

Barka, A., Akyuz, H., Altunel, E., Sunal, G., Cakir, Z., Dikbas, A., Yerli, B., Armijo, R., Meyer, B., De Chabalier, J., et al., 2002. The surface rupture and slip distribution of the 17 august 1999 izmit earthquake (m 7.4), north anatolian fault. Bulletin of the Seismological Society of America 92, 43–60.

Barka, A., Akyüz, H.S., Cohen, H.A., Watchorn, F., 2000. Tectonic evolution of the niksar and tasova–erbaa pull-apart basins, north anatolian fault zone: their significance for the motion of the anatolian block. Tectonophysics 322, 243–264.

Barka, A., Kadinsky-Cade, K., 1988. Strike-slip fault geometry in turkey and its influence on earthquake activity. Tectonics 7, 663–684.

Bartlow, N.M., Miyazaki, S., Bradley, A.M., Segall, P., 2011. Space-time correlation of slip and tremor during the 2009 Cascadia slow slip event. Geophysical Research Letters 38. URL: https://onlinelibrary.wiley.com/doi/abs/10.1029/2011GL048714, doi:10.1029/2011GL048714. _eprint: https://onlinelibrary.wiley.com/doi/pdf/10.1029/2011GL048714.

Bayrak, Y., Öztürk, S., 2004. Spatial and temporal variations of the aftershock sequences of the 1999 izmit and düzce earthquakes. Earth, planets and space 56, 933–944.

Bayramov, Z., Viltres, R., Doubre, C., Maggi, A., Jolivet, R., Rivera, L., 2025. Very-long-range dynamic triggering of mud volcano unrest and silent magnitude-6 fault slip. Science 389, 996–1002.

Becker, D., Martínez-Garzón, P., Wollin, C., Kılıç, T., Bohnhoff, M., 2023. Variation of fault creep along the overdue istanbul-marmara seismic gap in nw türkiye. Geophysical Research Letters 50, e2022GL101471.

Bekaert, D., Segall, P., Wright, T.J., Hooper, A.J., 2016. A network inversion filter combining gnss and insar for tectonic slip modeling. Journal of Geophysical Research: Solid Earth 121, 2069–2086.

Belcher, D., 2008. Theoretical limits on sar imposed by the ionosphere. IET Radar, Sonar & Navigation 2, 435–448.

Berardino, P., Fornaro, G., Lanari, R., Sansosti, E., 2003. A new algorithm for surface deformation monitoring based on small baseline differential sar interferograms. IEEE Transactions on geoscience and remote sensing 40, 2375–2383.

Bhattacharya, P., Rubin, A.M., Bayart, E., Savage, H.M., Marone, C., 2015. Critical evaluation of state evolution laws in rate and state friction: Fitting large velocity steps in simulated fault gouge with time-, slip-, and stress-dependent constitutive laws. Journal of Geophysical Research: Solid Earth 120, 6365–6385.

Bilham, R., Kakar, N.U., Kakar, D.M., Wang, K., Bürgmann, R., Barnhart, W.D., 2019. The 1892 chaman, pakistan, earthquake. Seismological Research Letters 90, 2293–2303.

Bilham, R., Ozener, H., Mencin, D., Dogru, A., Ergintav, S., Cakir, Z., Aytun, A., Aktug, B., Yilmaz, O., Johnson, W., Mattioli, G., 2016. Surface creep on the North Anatolian Fault at Ismetpasa, Turkey, 1944-2016: NORTH ANATOLIAN FAULT CREEP. Journal of Geophysical Research: Solid Earth 121, 7409–7431. URL: http://doi.wiley.com/10.1002/2016JB013394, doi:10.1002/2016JB013394.

Bilham, R., Suszek, N., Pinkney, S., 2004. California creepmeters. Seismological Research Letters 75, 481–492.

Blanpied, M., Marone, C., Lockner, D., Byerlee, J., King, D., 1998. Quantitative measure of the variation in fault rheology due to fluid-rock interactions. Journal of Geophysical Research: Solid Earth 103, 9691–9712.

Blanpied, M.L., Lockner, D.A., Byerlee, J.D., 1995. Frictional slip of granite at hydrothermal conditions. Journal of Geophysical Research: Solid Earth 100, 13045–13064.

Bletery, Q., Cavalié, O., Nocquet, J.M., Ragon, T., 2020. Distribution of interseismic coupling along the north and east anatolian faults inferred from insar and gps data. Geophysical Research Letters 47, e2020GL087775.

Bohnhoff, M., Grosser, H., Dresen, G., 2006. Strain partitioning and stress rotation at the north anatolian fault zone from aftershock focal mechanisms of the 1999 izmit m w= 7.4 earthquake. Geophysical Journal International 166, 373–385.

Bohnhoff, M., Ickrath, M., Dresen, G., 2016. Seismicity distribution in conjunction with spatiotemporal variations of coseismic slip and postseismic creep along the combined 1999 izmit-düzce rupture. Tectonophysics 686, 132–145.

Bouchon, M., Bouin, M.P., Karabulut, H., Toksöz, M.N., Dietrich, M., Rosakis, A.J., 2001. How fast is rupture during an earthquake? New insights from the 1999 Turkey Earthquakes. Geophysical Research Letters 28, 2723–2726. URL: https://onlinelibrary.wiley.com/doi/abs/10.1029/2001GL013112, doi:10.1029/2001GL013112. _eprint: https://onlinelibrary.wiley.com/doi/pdf/10.1029/2001GL013112.

Bouchon, M., Karabulut, H., 2008. The aftershock signature of supershear earthquakes. science 320, 1323–1325.

Bouchon, M., Karabulut, H., Aktar, M., Özalaybey, S., Schmittbuhl, J., Bouin, M.P., 2011. Extended nucleation of the 1999 m w 7.6 izmit earthquake. science 331, 877–880.

Bouchon, M., Toksoz, M.N., Karabulut, H., Bouin, M.P., Dietrich, M., Aktar, M., Edie, M., 2002. Space and time evolution of rupture and faulting during the 1999 izmit (turkey) earthquake. Bulletin of the Seismological Society of America 92, 256–266.

Bozkurt, E., 2003. Origin of ne-trending basins in western turkey. Geodinamica acta 16, 61–81.

Bozkurt, E., Mittwede, S.K., 2001. Introduction to the geology of turkey—a synthesis. International Geology Review 43, 578–594.

Brace, W., Byerlee, J., 1966. Stick-slip as a mechanism for earthquakes. Science 153, 990–992.

Bulut, F., Bohnhoff, M., Aktar, M., Dresen, G., 2007. Characterization of aftershock-fault plane orientations of the 1999 izmit (turkey) earthquake using high-resolution aftershock locations. Geophysical Research Letters 34.

Burgmann, R., 2002. Time-Dependent Distributed Afterslip on and Deep below the Izmit Earthquake Rupture. Bulletin of the Seismological Society of America 92, 126–137. URL: https://pubs.geoscienceworld.org/bssa/article/92/1/126-137/102924, doi:10.1785/0120000833.

Bürgmann, R., 2018. The geophysics, geology and mechanics of slow fault slip. Earth and Planetary Science Letters 495, 112–134.

Bürgmann, R., Ergintav, S., Segall, P., Hearn, E.H., McClusky, S., Reilinger, R.E., Woith, H., Zschau, J., 2002. Time-dependent distributed afterslip on and deep below the izmit earthquake rupture. Bulletin of the Seismological Society of America 92, 126–137.

Bürgmann, R., Rosen, P.A., Fielding, E.J., 2000. Synthetic aperture radar interferometry to measure earth's surface topography and its deformation. Annual review of earth and planetary sciences 28, 169–209.

Bürgmann, R., 2018. The geophysics, geology and mechanics of slow fault slip. Earth and Planetary Science Letters 495, 112–134. URL: https://linkinghub.elsevier.com/retrieve/pii/S0012821X18302760, doi:10.1016/j.epsl.2018.04.062.

Cakir, Z., Akoglu, A.M., Belabbes, S., Ergintav, S., Meghraoui, M., 2005. Creeping along the ismetpasa section of the north anatolian fault (western turkey): Rate and extent from insar. Earth and Planetary Science Letters 238, 225–234.

Çakir, Z., Chabalier, J.B.d., Armijo, R., Meyer, B., Barka, A., Peltzer, G., 2003. Coseismic and early post-seismic slip associated with the 1999 izmit earthquake (turkey), from sar interferometry and tectonic field observations. Geophysical Journal International 155, 93–110.

Cakir, Z., Ergintav, S., Ozener, H., Dogan, U., Akoglu, A.M., Meghraoui, M., Reilinger, R., 2012. Onset of aseismic creep on major strike-slip faults. Geology 40, 1115–1118. URL: https://pubs.geoscienceworld.org/geology/article/40/12/1115-1118/130811, doi:10.1130/G33522.1.

Çakir, Z., Ergintav, S., Özener, H., Dogan, U., Akoglu, A.M., Meghraoui, M., Reilinger, R., 2012. Onset of aseismic creep on major strike-slip faults. Geology 40, 1115–1118.

Candan, O., Akal, C., Koralay, O., Okay, A., Oberhänsli, R., Prelević, D., Mertz-Kraus, R., 2016. Carboniferous granites on the northern margin of gondwana, anatolide-tauride block, turkey–evidence for southward subduction of paleotethys. Tectonophysics 683, 349–366.

Castro-Perdomo, N., Jónsson, S., Klinger, Y., Masson, F., Becker, T.W., Johnson, K., 2025. Strain rates along the alpine-himalayan belt from a comprehensive gnss velocity field. Journal of Geophysical Research: Solid Earth 130, e2025JB031738.

Cavalié, O., 2007. Mesures InSAR et modélisation de faibles déformations d'origine anthropique (lac Mead, USA) ou tectonique (faille de Haiyuan, Chine). Ph.D. thesis. Université Paris Sud-Paris XI.

Cavalié, O., Doin, M.P., Lasserre, C., Briole, P., 2007. Ground motion measurement in the lake mead area, nevada, by differential synthetic aperture radar interferometry time series analysis: Probing the lithosphere rheological structure. Journal of Geophysical Research: Solid Earth 112.

Cavalié, O., Jónsson, S., 2014. Block-like plate movements in eastern anatolia observed by insar. Geophysical Research Letters 41, 26–31.

Cavalié, O., Lasserre, C., Doin, M.P., Peltzer, G., Sun, J., Xu, X., Shen, Z.K., 2008. Measurement of interseismic strain across the haiyuan fault (gansu, china), by insar. Earth and Planetary Science Letters 275, 246–257.

Cavazza, W., Cattò, S., Zattin, M., Okay, A.I., Reiners, P., 2018. Thermochronology of the miocene arabia-eurasia collision zone of southeastern turkey. Geosphere 14, 2277–2293.

Cengiz, M., 2023. Palaeomagnetic evidence of the deformation of the pontides during the closure of the intra-pontide ocean in the early cretaceous. Geophysical Journal International 234, 1835–1854.

Cetin, E., Cakir, Z., Meghraoui, M., Ergintav, S., Akoglu, A.M., 2014. Extent and distribution of aseismic slip on the ismetpaşa segment of the north anatolian fault (turkey) from persistent scatterer insar. Geochemistry, Geophysics, Geosystems 15, 2883–2894.

Chen, C.W., Zebker, H.A., 2001. Two-dimensional phase unwrapping with use of statistical models for cost functions in nonlinear optimization. Journal of the Optical Society of America A 18, 338–351.

Cinku, M.C., Hisarli, Z.M., Yılmaz, Y., Ülker, B., Kaya, N., Öksüm, E., Orbay, N., Özbey, Z.Ü., 2016. The tectonic history of the niğde-kırşehir massif and the taurides since the late mesozoic: Paleomagnetic evidence for two-phase orogenic curvature in central anatolia. Tectonics 35, 772–811.

Costantino, G., Giffard-Roisin, S., Dalla Mura, M., Socquet, A., 2024. Denoising of geodetic time series using spatiotemporal graph neural networks: application to slow slip event extraction. IEEE Journal of Selected Topics in Applied Earth Observations and Remote Sensing .

Costantino, G., Radiguet, M., El Yousfi, Z., Socquet, A., 2026. A continuum of slow slip events in the cascadia subduction zone illuminated by high-resolution deep-learning denoising. Geophysical Research Letters 53, e2025GL117446.

Crosetto, M., Monserrat, O., Cuevas-González, M., Devanthéry, N., Crippa, B., 2016. Persistent scatterer interferometry: A review. ISPRS Journal of Photogrammetry and Remote Sensing 115, 78–89.

Dalaison, M., 2021. Mesurer le glissement le long des failles par interférométrie radar: étude de la frontière de plaques de Chaman. Ph.D. thesis. Université Paris sciences et lettres.

Daout, S., 2016. Mesures géodésiques et modélisation de la convergence oblique au travers de failles transformantes. Application au bord Nord du Plateau Tibétain et à la Californie du Sud. Theses. Université Grenoble Alpes. URL: https://theses.hal.science/tel-01560620.

Delouis, B., 2002. Joint Inversion of InSAR, GPS, Teleseismic, and Strong-Motion Data for the Spatial and Temporal Distribution of Earthquake Slip: Application to the 1999 Izmit Mainshock. Bulletin of the Seismological Society of America 92, 278–299. URL: https://pubs.geoscienceworld.org/bssa/article/92/1/278-299/102952, doi:10.1785/0120000806.

Delouis, B., Giardini, D., Lundgren, P., Salichon, J., 2002. Joint inversion of insar, gps, teleseismic, and strong-motion data for the spatial and temporal distribution of earthquake slip: Application to the 1999 izmit mainshock. Bulletin of the Seismological Society of America 92, 278–299.

DeVries, P.M., Krastev, P.G., Meade, B.J., 2016. Geodetically constrained models of viscoelastic stress transfer and earthquake triggering along the north anatolian fault. Geochemistry, Geophysics, Geosystems 17, 2700–2716.

Dewey, J.W., 1976. Seismicity of northern anatolia. Bulletin of the Seismological Society of America 66, 843–868.

Dieterich, J.H., 1972. Time-dependent friction in rocks. Journal of Geophysical Research 77, 3690–3697.

Dieterich, J.H., 1981. Constitutive properties of faults with simulated gouge. Mechanical behavior of crustal rocks: the Handin volume 24, 103–120.

Doğan, B., Aşci, M., Karakaş, A., Pekşen, E., Erener, A., Çepni, M.S., Yavuzyilmaz, S., Alahmad, M., Sertçelik, F., Sertçelik, İ., et al., 2021. Basin progress: active deformation analysis by tectonostratigraphic elements and geophysical methods on north anatolian fault system (eastern marmara region, turkey). Natural Hazards 109, 1675–1716.

Doin, M.P., Lasserre, C., Peltzer, G., Cavalié, O., Doubre, C., 2009. Corrections of stratified tropospheric delays in sar interferometry: Validation with global atmospheric models. Journal of Applied Geophysics 69, 35–50.

Doin, M.P., Lodge, F., Guillaso, S., Jolivet, R., Lasserre, C., Ducret, G., Grandin, R., Pathier, E., Pinel, V., 2011. Presentation of the small baseline NSBAS processing chain on a case example: the Etna deformation monitoring from 2003 to 2010 using ENVISAT data , 8.

Doin, M.P., Twardzik, C., Ducret, G., Lasserre, C., Guillaso, S., Jianbao, S., 2015. Insar measurement of the deformation around siling co lake: Inferences on the lower crust viscosity in central tibet. Journal of Geophysical Research: Solid Earth 120, 5290–5310.

Doubre, C., Peltzer, G., 2007. Fluid-controlled faulting process in the asal rift, djibouti, from 8 yr of radar interferometry observations. Geology 35, 69–72.

Dragert, H., Wang, K., 2011. Temporal evolution of an episodic tremor and slip event along the northern cascadia margin. Journal of Geophysical Research: Solid Earth 116.

Dragert, H., Wang, K., James, T.S., 2001. A Silent Slip Event on the Deeper Cascadia Subduction Interface. Science 292, 1525–1528. URL: https://www.science.org/doi/10.1126/science.1060152, doi:10.1126/science.1060152.

Dragert, H., Wang, K., Rogers, G., 2004. Geodetic and seismic signatures of episodic tremor and slip in the northern cascadia subduction zone. Earth, planets and space 56, 1143–1150.

Duputel, Z., Agram, P.S., Simons, M., Minson, S.E., Beck, J.L., 2014. Accounting for prediction uncertainty when inferring subsurface fault slip. Geophysical journal international 197, 464–482.

Ellsworth, W.L., Bulut, F., 2018. Nucleation of the 1999 izmit earthquake by a triggered cascade of foreshocks. Nature Geoscience 11, 531–535.

Emre, Ö., Awata, Y., Duman, T., 2003. Surface rupture associated with the 17 august 1999 izmit earthquake. General Directorate of Mineral Research and Exploration, Ankara, Turkey , 29–271.

Emre, Ö., Duman, T.Y., Özalp, S., Şaroğlu, F., Olgun, , Elmacı, H., Çan, T., 2018. Active fault database of Turkey. Bulletin of Earthquake Engineering 16, 3229–3275. URL: https://doi.org/10.1007/s10518-016-0041-2, doi:10.1007/s10518-016-0041-2.

England, P., Houseman, G., Nocquet, J.M., 2016. Constraints from GPS measurements on the dynamics of deformation in Anatolia and the Aegean. Journal of Geophysical Research: Solid Earth 121, 8888–8916. URL: https://onlinelibrary.wiley.com/doi/abs/10.1002/2016JB013382, doi:10.1002/2016JB013382. _eprint: https://onlinelibrary.wiley.com/doi/pdf/10.1002/2016JB013382.

England, P., Jackson, J., 2011. Uncharted seismic risk. Nature Geoscience 4, 348–349.

Ergintav, S., Bürgmann, R., McClusky, S., Çakmak, R., Reilinger, R.E., Lenk, O., Barka, A., Özener, H., 2002. Postseismic Deformation near the İzmit Earthquake (17 August 1999, M 7.5) Rupture Zone. Bulletin of the Seismological Society of America 92, 194–207. URL: https://doi.org/10.1785/0120000836, doi:10.1785/0120000836.

Ergintav, S., McClusky, S., Hearn, E., Reilinger, R., Cakmak, R., Herring, T., Ozener, H., Lenk, O., Tari, E., 2009. Seven years of postseismic deformation following the 1999, M = 7.4 and M = 7.2, Izmit-Düzce, Turkey earthquake sequence. Journal of Geophysical Research: Solid Earth 114. URL: https://onlinelibrary.wiley.com/doi/abs/10.1029/2008JB006021, doi:10.1029/2008JB006021. _eprint: https://onlinelibrary.wiley.com/doi/pdf/10.1029/2008JB006021.

Ergintav, S., Reilinger, R.E., Çakmak, R., Floyd, M., Cakir, Z., Doğan, U., King, R.W., McClusky, S., Özener, H., 2014. Istanbul's earthquake hot spots: Geodetic constraints on strain accumulation along faults in the Marmara seismic gap. Geophysical Research Letters 41, 5783–5788. URL: https://onlinelibrary.wiley.com/doi/abs/10.1002/2014GL060985, doi:10.1002/2014GL060985. _eprint: https://onlinelibrary.wiley.com/doi/pdf/10.1002/2014GL060985.

Ertuncay, D., Buyukakpinar, P., Fornasari, S.F., Tan, O., 2025. 23 april 2025 marmara sea (mw 6.3), türkiye earthquake: mainshock, aftershock, and ground observations. Seismica 4.

Faccenna, C., Bellier, O., Martinod, J., Piromallo, C., Regard, V., 2006. Slab detachment beneath eastern anatolia: A possible cause for the formation of the north anatolian fault. Earth and Planetary Science Letters 242, 85–97.

Fagereng, Å., Toy, V.G., 2011. Geology of the earthquake source: an introduction .

Farr, T.G., Rosen, P.A., Caro, E., Crippen, R., Duren, R., Hensley, S., Kobrick, M., Paller, M., Rodriguez, E., Roth, L., et al., 2007. The shuttle radar topography mission. Reviews of geophysics 45.

Feigl, K.L., Sarti, F., Vadon, H., McClusky, S., Ergintav, S., Durand, P., Burgmann, R., Rigo, A., Massonnet, D., Reilinger, R., 2002. Estimating slip distribution for the izmit mainshock from coseismic gps, ers-1, radarsat, and spot measurements. Bulletin of the Seismological Society of America 92, 138–160.

Ferretti, A., Fumagalli, A., Novali, F., Prati, C., Rocca, F., Rucci, A., 2011. A new algorithm for processing interferometric data-stacks: Squeesar. IEEE transactions on geoscience and remote sensing 49, 3460–3470.

Ferretti, A., Prati, C., Rocca, F., 2000. Nonlinear subsidence rate estimation using permanent scatterers in differential sar interferometry. IEEE Transactions on geoscience and remote sensing 38, 2202–2212.

Ferretti, A., Prati, C., Rocca, F., 2001. Permanent scatterers in sar interferometry. IEEE Transactions on geoscience and remote sensing 39, 8–20.

Ferro-Famil, L., Pottier, E., 2016. Synthetic aperture radar imaging, in: Microwave remote sensing of land surface. Elsevier, pp. 1–65.

Fialko, Y., Sandwell, D., Agnew, D., Simons, M., Shearer, P., Minster, B., 2002. Deformation on Nearby Faults Induced by the 1999 Hector Mine Earthquake. Science 297, 1858–1862. URL: https://www.science.org/doi/10.1126/science.1074671, doi:10.1126/science.1074671.

Frank, W.B., Brodsky, E.E., 2019. Daily measurement of slow slip from low-frequency earthquakes is consistent with ordinary earthquake scaling. Science advances 5, eaaw9386.

Frank, W.B., Rousset, B., Lasserre, C., Campillo, M., 2018. Revealing the cluster of slow transients behind a large slow slip event. Science advances 4, eaat0661.

Ganas, A., Kourkouli, P., Briole, P., Moshou, A., Elias, P., Parcharidis, I., 2018. Coseismic displacements from moderate-size earthquakes mapped by sentinel-1 differential interferometry: The case of february 2017 gulpinar earthquake sequence (biga peninsula, turkey). Remote Sensing 10, 1089.

Gittins, D.B., Hawthorne, J.C., 2022. Are Creep Events Big? Estimations of Along-Strike Rupture Lengths. Journal of Geophysical Research: Solid Earth 127, e2021JB023001. URL: https://onlinelibrary.wiley.com/doi/abs/10.1029/2021JB023001, doi:10.1029/2021JB023001. _eprint: https://onlinelibrary.wiley.com/doi/pdf/10.1029/2021JB023001.

Goldberg, D.E., Taymaz, T., Reitman, N.G., Hatem, A.E., Yolsal-Çevikbilen, S., Barnhart, W.D., Irmak, T.S., Wald, D.J., Öcalan, T., Yeck, W.L., et al., 2023. Rapid characterization of the february 2023 kahramanmaraş, türkiye, earthquake sequence. The Seismic Record 3, 156–167.

Goldstein, R.M., Zebker, H.A., Werner, C.L., 1988. Satellite radar interferometry: Two-dimensional phase unwrapping. Radio science 23, 713–720.

Gomberg, J., Wech, A., Creager, K., Obara, K., Agnew, D., 2016. Reconsidering earthquake scaling. Geophysical Research Letters 43, 6243–6251.

Göncüoğlu, M., Turhan, N., Tekin, U.K., 2003. Evidence for the triassic rifting and opening of the neotethyan izmir-ankara ocean and discussion on the presence of cimmerian events at the northern edge of the tauride-anatolide platform, turkey. Bull. Soc. Geol. Spec 2, 203–212.

Goulty, N.R., Gilman, R., 1978. Repeated creep events on the san andreas fault near parkfield, california, recorded by a strainmeter array. Journal of Geophysical Research: Solid Earth 83, 5415–5419.

Govers, R., Fichtner, A., 2016. Signature of slab fragmentation beneath anatolia from full-waveform tomography. Earth and Planetary Science Letters 450, 10–19.

Grall, C., Henry, P., Tezcan, D., Mercier de Lepinay, B., Bécel, A., Géli, L., Rudkiewicz, J.L., Zitter, T., Harmegnies, F., 2012. Heat flow in the sea of marmara central basin: Possible implications for the tectonic evolution of the north anatolian fault. Geology 40, 3–6.

Grandin, R., 2015. Interferometric Processing of SLC Sentinel-1 TOPS Data, in: FRINGE'15: Advances in the Science and Applications of SAR Interferometry and Sentinel-1 InSAR Workshop, Frascati, Italy, 23-27 March 2015, Frascati, Italy. URL: https://hal.science/hal-01621519, doi:10.5270/Fringe2015.pp116.

Grandin, R., Doin, M.P., Bollinger, L., Pinel-Puysségur, B., Ducret, G., Jolivet, R., Sapkota, S.N., 2012. Long-term growth of the himalaya inferred from interseismic insar measurement. Geology 40, 1059–1062.

Grosser, H., Baumbach, M., Berckhemer, H., Baier, B., Karahan, A., Schelle, H., Krüger, F., Paulat, A., Michel, G., Demirtas, R., et al., 1998. The erzincan (turkey) earthquake (ms 6.8) of march 13, 1992 and its aftershock sequence. pure and applied geophysics 152, 465–505.

Gualandi, A., Liu, Z., 2021. Variational bayesian independent component analysis for insar displacement time-series with application to central california, usa. Journal of Geophysical Research: Solid Earth 126, e2020JB020845.

Gualandi, A., Nichele, C., Serpelloni, E., Chiaraluce, L., Anderlini, L., Latorre, D., Belardinelli, M.E., Avouac, J.P., 2017. Aseismic deformation associated with an earthquake swarm in the northern apennines (italy). Geophysical Research Letters 44, 7706–7714.

Gualandi, A., Serpelloni, E., Belardinelli, M.E., 2016. Blind source separation problem in gps time series. Journal of Geodesy 90, 323–341. doi:10.1007/s00190-015-0875-4.

Guglielmi, Y., Cappa, F., Avouac, J.P., Henry, P., Elsworth, D., 2015. Seismicity triggered by fluid injection–induced aseismic slip. Science 348, 1224–1226. URL: https://www.science.org/doi/full/10.1126/science.aab0476, doi:10.1126/science.aab0476. publisher: American Association for the Advancement of Science.

Guillaso, S., Lasserre, C., Doin, M.P., Cavalié, O., Sun, J., Peltzer, G., 2008. Insar measurement of interseismic strain in areas of low coherence: example across the haiyuan fault (gansu, china) using a local insar adaptive range filter, in: General Assembly European Geosciences Union.

Gülyüz, E., Durak, H., Özkaptan, M., Krijgsman, W., 2020. Paleomagnetic constraints on the early miocene closure of the southern neo-tethys (van region; east anatolia): Inferences for the timing of eurasia-arabia collision. Global and Planetary Change 185, 103089.

Guvercin, S.E., Barbot, S., 2025. Persistent rupture segmentation of the main marmara fault. Communications Earth & Environment .

Hanks, T.C., Kanamori, H., 1979. A moment magnitude scale. Journal of Geophysical Research: Solid Earth 84, 2348–2350. URL: https://agupubs.onlinelibrary.wiley.com/doi/10.1029/JB084iB05p02348, doi:10.1029/JB084iB05p02348. publisher: John Wiley & Sons, Ltd.

Hansen, P.C., 1992. Analysis of Discrete Ill-Posed Problems by Means of the L-Curve. SIAM Review 34, 561–580. URL: https://epubs.siam.org/doi/abs/10.1137/1034115, doi:10.1137/1034115. publisher: Society for Industrial and Applied Mathematics.

Hanssen, R.F., 2001. Stochastic model for radar interferometry. Radar Interferometry: Data Interpretation and Error Analysis , 81–159.

Hawthorne, J.C., Bostock, M.G., Royer, A.A., Thomas, A.M., 2016. Variations in slow slip moment rate associated with rapid tremor reversals in c ascadia. Geochemistry, Geophysics, Geosystems 17, 4899–4919.

Hawthorne, J.C., Rubin, A.M., 2013. Short-time scale correlation between slow slip and tremor in cascadia. Journal of Geophysical Research: Solid Earth 118, 1316–1329.

Hearn, E.H., Bürgmann, R., Reilinger, R.E., 2002. Dynamics of İzmit Earthquake Postseismic Deformation and Loading of the Düzce Earthquake Hypocenter. Bulletin of the Seismological Society of America 92, 172–193. URL: https://doi.org/10.1785/0120000832, doi:10.1785/0120000832.

Hearn, E.H., McClusky, S., Ergintav, S., Reilinger, R.E., 2009. Izmit earthquake postseismic deformation and dynamics of the North Anatolian Fault Zone. Journal of Geophysical Research: Solid Earth 114. URL: https://onlinelibrary.wiley.com/doi/abs/10.1029/2008JB006026, doi:10.1029/2008JB006026. _eprint: https://onlinelibrary.wiley.com/doi/pdf/10.1029/2008JB006026.

Heimisson, E.R., Dunham, E.M., Almquist, M., 2019. Poroelastic effects destabilize mildly rate-strengthening friction to generate stable slow slip pulses. Journal of the Mechanics and Physics of Solids 130, 262–279.

Hirose, H., Obara, K., 2005. Repeating short-and long-term slow slip events with deep tremor activity around the bungo channel region, southwest japan. Earth, planets and space 57, 961–972.

Hoechner, A., Ge, M., Babeyko, A., Sobolev, S.V., 2013. Instant tsunami early warning based on real-time gps–tohoku 2011 case study. Natural Hazards and Earth System Sciences 13, 1285–1292.

Hooper, A., Bekaert, D., Spaans, K., Arıkan, M., 2012. Recent advances in sar interferometry time series analysis for measuring crustal deformation. Tectonophysics 514, 1–13.

Hooper, A., Zebker, H., Segall, P., Kampes, B., 2004. A new method for measuring deformation on volcanoes and other natural terrains using insar persistent scatterers. Geophysical research letters 31.

Hussain, E., Wright, T.J., Walters, R.J., Bekaert, D., Hooper, A., Houseman, G.A., 2016. Geodetic observations of postseismic creep in the decade after the 1999 Izmit earthquake, Turkey: Implications for a shallow slip deficit: IZMIT CREEP. Journal of Geophysical Research: Solid Earth 121, 2980–3001. URL: http://doi.wiley.com/10.1002/2015JB012737, doi:10.1002/2015JB012737.

Hussain, E., Wright, T.J., Walters, R.J., Bekaert, D.P., Lloyd, R., Hooper, A., 2018. Constant strain accumulation rate between major earthquakes on the north anatolian fault. Nature communications 9, 1392.

Hyvärinen, A., Oja, E., 2000. Independent component analysis: algorithms and applications. Neural networks 13, 411–430.

Ickrath, M., Bohnhoff, M., Dresen, G., Martínez-Garzón, P., Bulut, F., Kwiatek, G., Germer, O., 2015. Detailed analysis of spatiotemporal variations of the stress field orientation along the izmit-düzce rupture in nw turkey from inversion of first-motion polarity data. Geophysical Journal International 202, 2120–2132.

Ida, Y., 1972. Cohesive force across the tip of a longitudinal-shear crack and griffith's specific surface energy. Journal of Geophysical Research 77, 3796–3805.

Ide, S., Beroza, G.C., 2023. Slow earthquake scaling reconsidered as a boundary between distinct modes of rupture propagation. Proceedings of the National Academy of Sciences 120, e2222102120. URL: https://www.pnas.org/doi/abs/10.1073/pnas.2222102120, doi:10.1073/pnas.2222102120. publisher: Proceedings of the National Academy of Sciences.

Ide, S., Beroza, G.C., Shelly, D.R., Uchide, T., 2007. A scaling law for slow earthquakes. Nature 447, 76–79.

Ide, S., Imanishi, K., Yoshida, Y., Beroza, G.C., Shelly, D.R., 2008. Bridging the gap between seismically and geodetically detected slow earthquakes. Geophysical Research Letters 35.

Im, K., Saffer, D., Marone, C., Avouac, J.P., 2020. Slip-rate-dependent friction as a universal mechanism for slow slip events. Nature Geoscience 13, 705–710.

Inbal, A., Ampuero, J.P., Avouac, J.P., 2017. Locally and remotely triggered aseismic slip on the central San Jacinto Fault near Anza, CA, from joint inversion of seismicity and strainmeter data. Journal of Geophysical Research: Solid Earth 122, 3033–3061. URL: https://onlinelibrary.wiley.com/doi/abs/10.1002/2016JB013499, doi:10.1002/2016JB013499. _eprint: https://onlinelibrary.wiley.com/doi/pdf/10.1002/2016JB013499.

Ito, A., Uçer, B., Baris, S., Nakamura, A., Honkura, Y., Kono, T., Hori, S., Hasegawa, A., Pektas, R., Isikara, A.M., 2002. Aftershock activity of the 1999 izmit, turkey, earthquake revealed from microearthquake observations. Bulletin of the Seismological Society of America 92, 418–427.

Jara, J., Jolivet, R., Socquet, A., Comte, D., Norabuena, E., 2024. Detection of slow slip events along the southern peru-northern chile subduction zone. Seismica 3, 17567–17579.

Jasir, M., Sreejith, K., Agrawal, R., Begum, S., 2024. Application of singular spectrum analysis to insar time-series for constraining the post-seismic deformation due to moderate magnitude earthquakes: the case of 2019 m w 6 mirpur earthquake, nw himalaya. Geophysical Journal International 239, 637–645.

Jiang, Y., Wdowinski, S., Dixon, T.H., Hackl, M., Protti, M., Gonzalez, V., 2012. Slow slip events in Costa Rica detected by continuous GPS observations, 2002–2011. Geochemistry, Geophysics, Geosystems 13. URL: https://onlinelibrary.wiley.com/doi/abs/10.1029/2012GC004058, doi:10.1029/2012GC004058. _eprint: https://onlinelibrary.wiley.com/doi/pdf/10.1029/2012GC004058.

Johnson, K., Villani, M., Bayliss, K., Brooks, C., Chandrasekhar, S., Chartier, T., Chen, Y., Garcia-Pelaez, J., Gee, R., Styron, R., et al., 2023. Global earthquake model (gem) seismic hazard map (version 2023.1-june 2023). Global Earthquake Model (GEM) 2023.

Johnston, G., Riddell, A., Hausler, G., 2017. The international gnss service, in: Springer handbook of global navigation satellite systems. Springer, pp. 967–982.

Jolivet, L., Faccenna, C., Huet, B., Labrousse, L., Le Pourhiet, L., Lacombe, O., Lecomte, E., Burov, E., Denèle, Y., Brun, J.P., et al., 2013. Aegean tectonics: Strain localisation, slab tearing and trench retreat. Tectonophysics 597, 1–33.

Jolivet, R., 2011. Déformation intersismique le long de la faille de Haiyuan, Chine: variations spatio-temporelles contraintes par interférométrie SAR. PhD Thesis. Université de Grenoble.

Jolivet, R., Frank, W., 2020. The transient and intermittent nature of slow slip. AGU Advances 1, e2019AV000126.

Jolivet, R., Grandin, R., Lasserre, C., Doin, M.P., Peltzer, G., 2011. Systematic insar tropospheric phase delay corrections from global meteorological reanalysis data. Geophysical Research Letters 38.

Jolivet, R., Jara, J., Dalaison, M., Rouet-Leduc, B., Özdemir, A., Dogan, U., Çakir, Z., Ergintav, S., Dubernet, P., 2023. Daily to Centennial Behavior of Aseismic Slip Along the Central Section of the North Anatolian Fault. Journal of Geophysical Research: Solid Earth 128, e2022JB026018. URL: https://onlinelibrary.wiley.com/doi/abs/10.1029/2022JB026018, doi:10.1029/2022JB026018. _eprint: https://onlinelibrary.wiley.com/doi/pdf/10.1029/2022JB026018.

Jolivet, R., Lasserre, C., Doin, M.P., Guillaso, S., Peltzer, G., Dailu, R., Sun, J., Shen, Z.K., Xu, X., 2012. Shallow creep on the haiyuan fault (gansu, china) revealed by sar interferometry. Journal of Geophysical Research: Solid Earth 117.

Kaduri, M., Gratier, J.P., Renard, F., Çakir, Z., Lasserre, C., 2017. The implications of fault zone transformation on aseismic creep: Example of the North Anatolian Fault, Turkey. Journal of Geophysical Research: Solid Earth 122, 4208–4236. URL: https://onlinelibrary.wiley.com/doi/abs/10.1002/2016JB013803, doi:10.1002/2016JB013803. _eprint: https://onlinelibrary.wiley.com/doi/pdf/10.1002/2016JB013803.

Kaneko, Y., Avouac, J.P., Lapusta, N., 2010. Towards inferring earthquake patterns from geodetic observations of interseismic coupling. Nature Geoscience 3, 363–369.

Kaneko, Y., Fialko, Y., Sandwell, D.T., Tong, X., Furuya, M., 2013. Interseismic deformation and creep along the central section of the North Anatolian Fault (Turkey): InSAR observations and implications for rate-and-state friction properties. Journal of Geophysical Research: Solid Earth 118, 316–331. URL: https://onlinelibrary.wiley.com/doi/abs/10.1029/2012JB009661, doi:10.1029/2012JB009661. _eprint: https://onlinelibrary.wiley.com/doi/pdf/10.1029/2012JB009661.

Kano, M., Aso, N., Matsuzawa, T., Ide, S., Annoura, S., Arai, R., Baba, S., Bostock, M., Chao, K., Heki, K., et al., 2018. Development of a slow earthquake database. Seismological Research Letters 89, 1566–1575.

Karabacak, V., Altunel, E., Çakir, Z., 2011. Monitoring aseismic surface creep along the north anatolian fault (turkey) using ground-based lidar. Earth and Planetary Science Letters 304, 64–70.

Karabacak, V., Sançar, T., Yildirim, G., Uysal, I.T., 2022. When did the north anatolian fault reach southern marmara, turkey? Geology 50, 432–436.

Karabulut, H., 2025. High-resolution p-wave tomography of the 1999 izmit and düzce earthquake rupture zones. Geophysical Journal International 241, 986–1008.

Karabulut, H., Schmittbuhl, J., Özalaybey, S., Lengliné, O., Kömeç-Mutlu, A., Durand, V., Bouchon, M., Daniel, G., Bouin, M., 2011. Evolution of the seismicity in the eastern Marmara Sea a decade before and after the 17 August 1999 Izmit earthquake. Tectonophysics 510, 17–27. URL: https://linkinghub.elsevier.com/retrieve/pii/S0040195111002903, doi:10.1016/j.tecto.2011.07.009.

Karakas, A., Coruk, O., 2010. Liquefaction analysis of soils in the western izmit basin, turkey. Environmental & Engineering Geoscience 16, 411–430.

Karasözen, E., Özacar, A.A., Biryol, C.B., Beck, S.L., 2014. Seismicity, focal mechanisms and active stress field around the central segment of the north anatolian fault in turkey. Geophysical Journal International 196, 405–421.

Karsli, O., Şengün, F., Dokuz, A., Kandemir, R., Aydin, F., Andersen, T., 2020. Silurian to early devonian arc magmatism in the western sakarya zone (nw turkey), with inference to the closure of the rheic ocean. Lithos 370, 105641.

Kato, A., Obara, K., Igarashi, T., Tsuruoka, H., Nakagawa, S., Hirata, N., 2012. Propagation of slow slip leading up to the 2011 m w 9.0 tohoku-oki earthquake. Science 335, 705–708.

Kato, N., Tullis, T.E., 2001. A composite rate-and state-dependent law for rock friction. Geophysical research letters 28, 1103–1106.

Kearse, J., Kaneko, Y., 2026. Stopping phase reveals abrupt arrest of large strike-slip earthquakes. Science , eaef3733.

Ketin, I., 1948. Über die tektonisch-mechanischen folgerungen aus den grossen anatolischen erdbeben des letzten dezenniums. Geologische Rundschau 36, 77–83.

Klein, E., Duputel, Z., Masson, F., Yavasoglu, H., Agram, P., 2017. Aseismic slip and seismogenic coupling in the Marmara Sea: What can we learn from onland geodesy? Geophysical Research Letters 44, 3100–3108. URL: https://onlinelibrary.wiley.com/doi/abs/10.1002/2017GL072777, doi:10.1002/2017GL072777. _eprint: https://onlinelibrary.wiley.com/doi/pdf/10.1002/2017GL072777.

Klein, E., Duputel, Z., Zigone, D., Vigny, C., Boy, J.P., Doubre, C., Meneses, G., 2018. Deep transient slow slip detected by survey gps in the region of atacama, chile. Geophysical research letters 45, 12–263.

Klinger, Y., Sieh, K., Altunel, E., Akoglu, A., Barka, A., Dawson, T., Gonzalez, T., Meltzner, A., Rockwell, T., 2003. Paleoseismic evidence of characteristic slip on the western segment of the north anatolian fault, turkey. Bulletin of the Seismological Society of America 93, 2317–2332.

Kositsky, A., Avouac, J.P., 2010. Inverting geodetic time series with a principal component analysis-based inversion method. Journal of Geophysical Research: Solid Earth 115.

Kreemer, C., Blewitt, G., Klein, E.C., 2014. A geodetic plate motion and global strain rate model. Geochemistry, Geophysics, Geosystems 15, 3849–3889.

Kurt, A.I., Özbakir, A.D., Cingöz, A., Ergintav, S., Doğan, U., Özarpaci, S., 2023. Contemporary velocity field for turkey inferred from combination of a dense network of long term gnss observations. Turkish Journal of Earth Sciences 32, 275–293.

Kuş, L., Laçin, D., Aykut, T., Uysal, I.T., 2025. Constraining the timing of the closure of the intra-pontide ocean by u–pb dating of syntectonic calcite. Terra Nova 37, 26–34.

LaBonte, A.L., Brown, K.M., Fialko, Y., 2009. Hydrologic detection and finite element modeling of a slow slip event in the costa rica prism toe. Journal of Geophysical Research: Solid Earth 114.

Lange, D., Kopp, H., Royer, J.Y., Henry, P., Çakir, Z., Petersen, F., Sakic, P., Ballu, V., Bialas, J., Özeren, M.S., et al., 2019. Interseismic strain build-up on the submarine north anatolian fault offshore istanbul. Nature communications 10, 3006.

Langridge, R., Stenner, H.D., Fumal, T., Christofferson, S., Rockwell, T., Hartleb, R., Bachhuber, J., Barka, A., 2002. Geometry, slip distribution, and kinematics of surface rupture on the sakarya fault segment during the 17 august 1999 izmit, turkey, earthquake. Bulletin of the Seismological Society of America 92, 107–125.

Lapusta, N., Rice, J.R., Ben-Zion, Y., Zheng, G., 2000. Elastodynamic analysis for slow tectonic loading with spontaneous rupture episodes on faults with rate- and state-dependent friction. Journal of Geophysical Research: Solid Earth 105, 23765–23789. URL: https://onlinelibrary.wiley.com/doi/abs/10.1029/2000JB900250, doi:10.1029/2000JB900250. _eprint: https://onlinelibrary.wiley.com/doi/pdf/10.1029/2000JB900250.

Larson, K.M., Bodin, P., Gomberg, J., 2003. Using 1-hz gps data to measure deformations caused by the denali fault earthquake. Science 300, 1421–1424.

Laske, G., Masters, G., Ma, Z., Pasyanos, M., 2013. Update on CRUST1.0 - A 1-degree Global Model of Earth's Crust .

Lawson, C.L., Hanson, R.J., 1995. Solving Least Squares Problems. SIAM. Google-Books-ID: AEwDbHp50FgC.

Lazeckỳ, M., Spaans, K., González, P.J., Maghsoudi, Y., Morishita, Y., Albino, F., Elliott, J., Greenall, N., Hatton, E., Hooper, A., et al., 2020. Licsar: An automatic insar tool for measuring and monitoring tectonic and volcanic activity. Remote Sensing 12, 2430.

Le Pichon, X., 1968. Sea-floor spreading and continental drift. Journal of geophysical research 73, 3661–3697.

Le Pichon, X., Şengör, A., Demirbağ, E., Rangin, C., Imren, C., Armijo, R., Görür, N., Çağatay, N., De Lepinay, B.M., Meyer, B., et al., 2001. The active main marmara fault. Earth and Planetary Science Letters 192, 595–616.

Le Pichon, X., Şengör, A.C., İmren, C., 2019a. A new approach to the opening of the eastern mediterranean sea and the origin of the hellenic subduction zone. part 1: The eastern mediterranean sea. Canadian Journal of Earth Sciences 56, 1119–1143.

Le Pichon, X., Şengör, A.C., İmren, C., 2019b. A new approach to the opening of the eastern mediterranean sea and the origin of the hellenic subduction zone. part 2: The hellenic subduction zone. Canadian Journal of Earth Sciences 56, 1144–1162.

Le Pichon, X., Şengör, A.C., Kende, J., İmren, C., Henry, P., Grall, C., Karabulut, H., 2016. Propagation of a strike-slip plate boundary within an extensional environment: the westward propagation of the north anatolian fault. Canadian Journal of Earth Sciences 53, 1416–1439.

Lemrabet, L., Doin, M.p., Lasserre, C., Durand, P., 2023. Referencing of continental-scale insar-derived velocity fields: Case study of the eastern tibetan plateau. Journal of Geophysical Research: Solid Earth 128, e2022JB026251.

Lengliné, O., Maurer, V., Yorillo, A., 2025. Intermittent induced seismicity during the multiyear operation of a geothermal reservoir. Geophysical Journal International 242, ggaf160.

Li, S., Xu, W., Li, Z., 2022. Review of the sbas insar time-series algorithms, applications, and challenges. Geodesy and Geodynamics 13, 114–126.

Li, Y., Bürgmann, R., Taira, T., 2023. Spatiotemporal Variations of Surface Deformation, Shallow Creep Rate, and Slip Partitioning Between the San Andreas and Southern Calaveras Fault. Journal of Geophysical Research: Solid Earth 128, e2022JB025363. URL: https://onlinelibrary.wiley.com/doi/abs/10.1029/2022JB025363, doi:10.1029/2022JB025363. _eprint: https://onlinelibrary.wiley.com/doi/pdf/10.1029/2022JB025363.

Lienkaemper, J.J., Galehouse, J.S., Simpson, R.W., 2001. Long-term monitoring of creep rate along the hayward fault and evidence for a lasting creep response to 1989 loma prieta earthquake. Geophysical Research Letters 28, 2265–2268.

Linde, A.T., Gladwin, M.T., Johnston, M.J., Gwyther, R.L., Bilham, R.G., 1996. A slow earthquake sequence on the san andreas fault. Nature 383, 65–68.

Linker, M., Dieterich, J.H., 1992. Effects of variable normal stress on rock friction: Observations and constitutive equations. Journal of Geophysical Research: Solid Earth 97, 4923–4940.

Liu, Y., Rice, J.R., 2007. Spontaneous and triggered aseismic deformation transients in a subduction fault model. Journal of Geophysical Research 112, B09404. doi:10.1029/2007JB004930.

Liu, Z., Wang, T., 2023. High-resolution interseismic strain mapping from insar phase-gradient stacking: Application to the north anatolian fault with implications for the non-uniform strain distribution related to coseismic slip distribution. Geophysical Research Letters 50, e2023GL104168.

López-Quiroz, P., Doin, M.P., Tupin, F., Briole, P., Nicolas, J.M., 2009. Time series analysis of mexico city subsidence constrained by radar interferometry. Journal of Applied Geophysics 69, 1–15.

Lorenzo-Martín, F., Roth, F., Wang, R., 2006. Elastic and inelastic triggering of earthquakes in the north anatolian fault zone. Tectonophysics 424, 271–289.

Louderback, G.D., 1942. Faults and earthquakes. Bulletin of the Seismological Society of America 32, 305–330.

Luckie, T.W., Choens, R.C., 2025. Hayward fault creep from coda wave interferometry. Geophysical Research Letters 52, e2025GL117929. URL: https://agupubs.onlinelibrary.wiley.com/doi/abs/10.1029/2025GL117929, doi:https://doi.org/10.1029/2025GL117929, arXiv:https://agupubs.onlinelibrary.wiley.com/doi/pdf/10.1029/2025 e2025GL117929 2025GL117929.

Maffione, M., van Hinsbergen, D.J., de Gelder, G.I., van der Goes, F.C., Morris, A., 2017. Kinematics of late cretaceous subduction initiation in the neo-tethys ocean reconstructed from ophiolites of turkey, cyprus, and syria. Journal of Geophysical Research: Solid Earth 122, 3953–3976.

Marconato, L., 2024. Active tectonics of Ecuador through multi-sensor InSAR time-series analysis. Ph.D. thesis. Université Grenoble Alpes [2020-....].

Marill, L., Marsan, D., Rousset, B., Socquet, A., 2024. Geodetic matched filter slow slip event detection along the northern japan subduction zones. Journal of Geophysical Research: Solid Earth 129, e2024JB029342.

Marone, C., 1998. Laboratory-derived friction laws and their application to seismic faulting. Annual Review of Earth and Planetary Sciences 26, 643–696.

Marone, C., Scholz, C., 1988. The depth of seismic faulting and the upper transition from stable to unstable slip regimes. Geophysical Research Letters 15, 621–624.

Marroni, M., Göncüoğlu, M.C., Frassi, C., Sayit, K., Pandolfi, L., Ellero, A., Ottria, G., 2020. The intra-pontide ophiolites in northern turkey revisited: From birth to death of a neotethyan oceanic domain. Geoscience Frontiers 11, 129–149.

Martínez-Garzón, P., Chen, X., Becker, D., Núñez-Jara, S., Kartal, R.F., Türker, E., Dresen, G., Ben-Zion, Y., Jara, J., Cotton, F., et al., 2026. Progressive eastward rupture of the main marmara fault toward istanbul. Science 391, 379–383.

Massonnet, D., Rossi, M., Carmona, C., Adragna, F., Peltzer, G., Feigl, K., Rabaute, T., 1993. The displacement field of the landers earthquake mapped by radar interferometry. nature 364, 138–142.

Materna, K., Bürgmann, R., Lindsay, D., Bilham, R., Herring, T., Crowell, B., Szeliga, W., 2024. Shallow Slow Slip Events in the Imperial Valley With Along-Strike Propagation. Geophysical Research Letters 51, e2023GL108089. URL: https://onlinelibrary.wiley.com/doi/abs/10.1029/2023GL108089, doi:10.1029/2023GL108089. _eprint: https://onlinelibrary.wiley.com/doi/pdf/10.1029/2023GL108089.

Maubant, L., Pathier, E., Daout, S., Radiguet, M., Doin, M.P., Kazachkina, E., Kostoglodov, V., Cotte, N., Walpersdorf, A., 2020. Independent Component Analysis and Parametric Approach for Source Separation in InSAR Time Series at Regional Scale: Application to the 2017–2018 Slow Slip Event in Guerrero (Mexico). Journal of Geophysical Research: Solid Earth 125, e2019JB018187. URL: https://onlinelibrary.wiley.com/doi/abs/10.1029/2019JB018187, doi:10.1029/2019JB018187. _eprint: https://onlinelibrary.wiley.com/doi/pdf/10.1029/2019JB018187.

McCaffrey, R., Wallace, L.M., Beavan, J., 2008. Slow slip and frictional transition at low temperature at the hikurangi subduction zone. Nature Geoscience 1, 316–320.

McCausland, W., Roeloffs, E., Silver, P., 2008. New insights into cascadia slow slip events using plate boundary observatory borehole strainmeters, in: AGU Fall Meeting Abstracts, pp. G21B–0691.

McClusky, S., Balassanian, S., Barka, A., Demir, C., Ergintav, S., Georgiev, I., Gurkan, O., Hamburger, M., Hurst, K., Kahle, H., Kastens, K., Kekelidze, G., King, R., Kotzev, V., Lenk, O., Mahmoud, S., Mishin, A., Nadariya, M., Ouzounis, A., Paradissis, D., Peter, Y., Prilepin, M., Reilinger, R., Sanli, I., Seeger, H., Tealeb, A., Toksöz, M.N., Veis, G., 2000. Global Positioning System constraints on plate kinematics and dynamics in the eastern Mediterranean and Caucasus. Journal of Geophysical Research: Solid Earth 105, 5695–5719. URL: https://onlinelibrary.wiley.com/doi/abs/10.1029/1999JB900351, doi:10.1029/1999JB900351. _eprint: https://onlinelibrary.wiley.com/doi/pdf/10.1029/1999JB900351.

Memiş, C., Göğüş, O.H., Uluocak, E.Ş., Pysklywec, R., Keskin, M., Şengör, A.C., Topuz, G., 2020. Long wavelength progressive plateau uplift in eastern anatolia since 20 ma: implications for the role of slab peel-back and break-off. Geochemistry, Geophysics, Geosystems 21, e2019GC008726.

Métois, M., Lasserre, C., Méridi, A., Henriquet, M., Bodin, T., 2025. Bayesian estimation of surface strain rates in the peri-adriatic, balkans and aegean region from gnss velocities. Tektonika 3, 82–98.

Michel, R., Avouac, J.P., 2002. Deformation due to the 17 august 1999 izmit, turkey, earthquake measured from spot images. Journal of Geophysical Research: Solid Earth 107, ETG–2.

Michel, S., Gualandi, A., Avouac, J.P., 2019. Similar scaling laws for earthquakes and cascadia slow-slip events. Nature 574, 522–526.

Mignan, A., 2015. Modeling aftershocks as a stretched exponential relaxation. Geophysical Research Letters 42, 9726–9732.

Moore, D.E., Rymer, M.J., 2007. Talc-bearing serpentinite and the creeping section of the san andreas fault. Nature 448, 795–797.

Morishita, Y., Lazecky, M., Wright, T.J., Weiss, J.R., Elliott, J.R., Hooper, A., 2020. Licsbas: An open-source insar time series analysis package integrated with the licsar automated sentinel-1 insar processor. Remote Sensing 12, 424.

Mueller, M., Licht, A., Campbell, C., Ocakoğlu, F., Taylor, M.H., Burch, L., Ugrai, T., Kaya, M., Kurtoğlu, B., Coster, P., et al., 2019. Collision chronology along the izmir-ankara-erzincan suture zone: Insights from the sarıcakaya basin, western anatolia. Tectonics 38, 3652–3674.

Muller, J.R., Aydin, A., Maerten, F., 2003. Investigating the transition between the 1967 mudurnu valley and 1999 izmit earthquakes along the north anatolian fault with static stress changes. Geophysical Journal International 154, 471–482.

Murase, M., Matta, N., Lin, C.H., Chen, W.S., Koizumi, N., 2013. An episodic creep-slip event detected by precise levelling surveys in the central part of the longitudinal valley fault, eastern taiwan, in 2011–2012. Tectonophysics 608, 904–913.

Nalbant, S.S., Barka, A.A., Alptekin, Ö., 1996. Failure stress change caused by the 1992 erzincan earthquake (ms= 6.8). Geophysical research letters 23, 1561–1564.

NASA/JPL-Caltech, 2001. Interferogram of the Izmit, Turkey 1999 earthquake. https://jpl.nasa.gov/images/pia00557-izmit-turkey-1999-earthquake-interferogram/. Accessed: 2026-05-22.

Neyrinck, E., Rousset, B., Doubre, C., Rivera, L., Lasserre, C., Doin, M.P., Durand, P., Bilham, R., Çakir, Z., Group, F.W., et al., 2024. The slow slip event cycle along the izmit segment of the north anatolian fault. Earth and Planetary Science Letters 648, 119104.

Nishimura, T., 2014. Short-term slow slip events along the ryukyu trench, southwestern japan, observed by continuous gnss. Progress in Earth and Planetary Science 1, 1–13. URL: https://doi.org/10.1186/s40645-014-0022-5, doi:10.1186/s40645-014-0022-5.

Nocquet, J.M., 2012. Present-day kinematics of the Mediterranean: A comprehensive overview of GPS results. Tectonophysics 579, 220–242. URL: https://www.sciencedirect.com/science/article/pii/S0040195112001953, doi:10.1016/j.tecto.2012.03.037.

Nuriel, P., Craddock, J., Kylander-Clark, A.R., Uysal, I.T., Karabacak, V., Dirik, R.K., Hacker, B.R., Weinberger, R., 2019. Reactivation history of the north anatolian fault zone based on calcite age-strain analyses. Geology 47, 465–469.

Obara, K., Hirose, H., Yamamizu, F., Kasahara, K., 2004. Episodic slow slip events accompanied by non-volcanic tremors in southwest Japan subduction zone. Geophysical Research Letters 31. URL: https://onlinelibrary.wiley.com/doi/abs/10.1029/2004GL020848, doi:10.1029/2004GL020848. _eprint: https://onlinelibrary.wiley.com/doi/pdf/10.1029/2004GL020848.

Obara, K., Sekine, S., 2009. Characteristic activity and migration of episodic tremor and slow-slip events in central Japan. Earth, Planets and Space 61, 853–862. URL: https://doi.org/10.1186/BF03353196, doi:10.1186/BF03353196.

Okada, Y., 1985. Surface deformation due to shear and tensile faults in a half-space. Bulletin of the Seismological Society of America 75, 1135–1154. URL: https://doi.org/10.1785/BSSA0750041135, doi:10.1785/BSSA0750041135.

Okada, Y., Nishimura, T., 2023. Systematic detection of short-term slow slip events in south-central alaska. Geophysical Research Letters 50, e2023GL104901.

Okada, Y., Nishimura, T., Tabei, T., Matsushima, T., Hirose, H., 2022. Development of a detection method for short-term slow slip events using gnss data and its application to the nankai subduction zone. Earth, Planets and Space 74, 1–18.

Okay, A., Satir, M., Maluski, H., Siyako, M., Monié, P., Metzger, R., Akyüz, S., 1996. 19 paleo-and neo-tethyan events in northwestern turkey: Geologic and geochronologic constraints. The Tectonic Evolution of Asia , 420–441.

Okay, A., Satir, M., Zattin, M., Cavazza, W., Topuz, G., 2008a. An oligocene ductile strike-slip shear zone: The uludağ massif, northwest turkey—implications for the westward translation of anatolia. Geological Society of America Bulletin 120, 893–911.

Okay, A.I., Bozkurt, E., Satır, M., Yiğitbaş, E., Crowley, Q.G., Shang, C.K., 2008b. Defining the southern margin of avalonia in the pontides: geochronological data from the late proterozoic and ordovician granitoids from nw turkey. Tectonophysics 461, 252–264.

Okay, A.I., Noble, P.J., Tekin, U.K., 2011a. Devonian radiolarian ribbon cherts from the karakaya complex, northwest turkey: Implications for the paleo-tethyan evolution. Comptes Rendus Palevol 10, 1–10.

Okay, N., Zack, T., Okay, A.I., Barth, M., 2011b. Sinistral transport along the trans-european suture zone: detrital zircon–rutile geochronology and sandstone petrography from the carboniferous flysch of the pontides. Geological Magazine 148, 380–403.

Omori, F., 1894. On after-shocks. Seismological journal of Japan 19, 71–80.

Ong, S.Q.M., Barbot, S., Hubbard, J., 2019. Physics-based scenario of earthquake cycles on the ventura thrust system, california: the effect of variable friction and fault geometry. Pure and Applied Geophysics 176, 3993–4007.

Ozalaybey, S., Ergin, M., Aktar, M., Tapirdamaz, C., Biçmen, F., Yoruk, A., 2002. The 1999 izmit earthquake sequence in turkey: seismological and tectonic aspects. Bulletin of the Seismological Society of America 92, 376–386.

Özalaybey, S., Zor, E., Ergintav, S., Tapırdamaz, M.C., 2011. Investigation of 3-d basin structures in the izmit bay area (turkey) by single-station microtremor and gravimetric methods. Geophysical Journal International 186, 883–894.

Özarpacı, S., Doğan, U., Ergintav, S., Çakır, Z., Özdemir, A., Floyd, M., Reilinger, R., 2021. Present gps velocity field along 1999 izmit rupture zone: evidence for continuing afterslip 20 yr after the earthquake. Geophysical Journal International 224, 2016–2027.

Özdemir, A., Jara, J., Doğan, U., Jolivet, R., Çakir, Z., Nocquet, J.M., Ergintav, S., Bilham, R., 2025. Detecting millimetric slow slip events along the north anatolian fault with gnss. Geophysical Research Letters 52, e2024GL111428.

Özden, S., Över, S., Poyraz, S.A., Güneş, Y., Pınar, A., 2018. Tectonic implications of the 2017 ayvacık (çanakkale) earthquakes, biga peninsula, nw turkey. Journal of Asian Earth Sciences 154, 125–141.

Özkan, A., Yavaşoğlu, H.H., Tiryakioğlu, İ., Uslular, G., Karabulut, M.F., Ulrich, P., Masson, F., 2025. New gps-derived velocity field for marmara region: Implications for the kinematics along the north anatolian fault zone. Tectonophysics , 230828.

Passelègue, F., Brantut, N., Chauris, H., Dublanchet, P., 2025. Propagation of fluid-driven aseismic slip fronts along crustal faults .

Peltzer, G., Rosen, P., Rogez, F., Hudnut, K., 1998. Poroelastic rebound along the landers 1992 earthquake surface rupture. Journal of Geophysical Research: Solid Earth 103, 30131–30145.

Peng, Z., Gomberg, J., 2010. An integrated perspective of the continuum between earthquakes and slow-slip phenomena. Nature geoscience 3, 599–607.

Perfettini, H., Avouac, J.P., Ruegg, J.C., 2005. Geodetic displacements and aftershocks following the 2001 mw= 8.4 peru earthquake: Implications for the mechanics of the earthquake cycle along subduction zones. Journal of Geophysical Research: Solid Earth 110.

Perrin, G., Rice, J.R., Zheng, G., 1995. Self-healing slip pulse on a frictional surface. Journal of the Mechanics and Physics of Solids 43, 1461–1495.

Pinar, A., Honkura, Y., Kikuchi, M., 1994. Rupture process of the 1992 erzincan earthquake and its implication for seismotectonics in eastern turkey. Geophysical Research Letters 21, 1971–1974.

Pinar, N., 1953. Etude géologique et macrosismique du tremblement de terre de kursunlu (anatolie septentrionale) du 13 aout 1951. Rev. Fac. Sci. Univ. Istanbul, Series A 18, 131–141.

Pollitz, F.F., 1997. Gravitational viscoelastic postseismic relaxation on a layered spherical earth. Journal of Geophysical Research: Solid Earth 102, 17921–17941.

Pousse-Beltran, L., Nissen, E., Bergman, E.A., Cambaz, M.D., Gaudreau, É., Karasözen, E., Tan, F., 2020. The 2020 m w 6.8 elazığ (turkey) earthquake reveals rupture behavior of the east anatolian fault. Geophysical Research Letters 47, e2020GL088136.

Provost, F., Karabacak, V., Malet, J.P., Van der Woerd, J., Meghraoui, M., Masson, F., Ferry, M., Michéa, D., Pointal, E., 2024. High-resolution co-seismic fault offsets of the 2023 türkiye earthquake ruptures using satellite imagery. Scientific Reports 14, 6834.

Pucci, S., De Martini, P., Pantosti, D., 2008. Preliminary slip rate estimates for the düzce segment of the north anatolian fault zone from offset geomorphic markers. Geomorphology 97, 538–554.

Pucci, S., Pantosti, D., Barchi, M., Palyvos, N., Palyvos, N., 2006. Evolution and complexity of the seismogenic düzce fault zone (turkey) depicted by coseismic ruptures, plio-quaternary structural pattern and geomorphology, in: Geophys. Res. Abstr, p. 08339.

Qing, X., Guowang, J., Caiying, Z., Zhengde, W., Yu, H., Peizhang, Y., 2004. The filtering and phase unwrapping of interferogram. Proc. ISPRS XXXV Comm V1/WG4 .

Rabinowicz, E., 1958. The intrinsic variables affecting the stick-slip process. Proceedings of the Physical Society 71, 668–675.

Radiguet, M., Cotton, F., Vergnolle, M., Campillo, M., Valette, B., Kostoglodov, V., Cotte, N., 2011. Spatial and temporal evolution of a long term slow slip event: the 2006 Guerrero Slow Slip Event. Geophysical Journal International 184, 816–828. URL: https://doi.org/10.1111/j.1365-246X.2010.04866.x, doi:10.1111/j.1365-246X.2010.04866.x.

Radiguet, M., Perfettini, H., Cotte, N., Gualandi, A., Valette, B., Kostoglodov, V., Lhomme, T., Walpersdorf, A., Cabral Cano, E., Campillo, M., 2016. Triggering of the 2014 m w 7.3 papanoa earthquake by a slow slip event in guerrero, mexico. Nature Geoscience 9, 829–833.

Reid, H.F., 1910. The mechanism of the earthquake, the california earthquake of april 18, 1906. Report of the Research Senatorial Commission, Carnegie Institution, Washington, DC 2, 16–18.

Reilinger, R., Ergintav, S., Burgmann, R., Mcclusky, S., Lenk, O., Barka, A., Gurkan, O., Hearn, L., Feigl, K., Cakmak, R., et al., 2000. Coseismic and postseismic fault slip for the 17 august 1999, m= 7.5, izmit, turkey earthquake. Science 289, 1519–1524.

Reilinger, R., McClusky, S., Vernant, P., Lawrence, S., Ergintav, S., Cakmak, R., Ozener, H., Kadirov, F., Guliev, I., Stepanyan, R., Nadariya, M., Hahubia, G., Mahmoud, S., Sakr, K., ArRajehi, A., Paradissis, D., Al-Aydrus, A., Prilepin, M., Guseva, T., Evren, E., Dmitrotsa, A., Filikov, S.V., Gomez, F., Al-Ghazzi, R., Karam, G., 2006. GPS constraints on continental deformation in the Africa-Arabia-Eurasia continental collision zone and implications for the dynamics of plate interactions. Journal of Geophysical Research: Solid Earth 111. URL: https://onlinelibrary.wiley.com/doi/abs/10.1029/2005JB004051, doi:10.1029/2005JB004051. _eprint: https://onlinelibrary.wiley.com/doi/pdf/10.1029/2005JB004051.

Rice, J.R., 1993. Spatio-temporal complexity of slip on a fault. Journal of Geophysical Research: Solid Earth 98, 9885–9907.

Rice, J.R., Lapusta, N., Ranjith, K., 2001. Rate and state dependent friction and the stability of sliding between elastically deformable solids. Journal of the Mechanics and Physics of Solids 49, 1865–1898.

Riel, B., Simons, M., Agram, P., Zhan, Z., 2014. Detecting transient signals in geodetic time series using sparse estimation techniques. Journal of Geophysical Research: Solid Earth 119, 5140–5160.

Robertson, A.H., Ustaomer, T., Pickett, E.A., Collins, A.S., Andrew, T., Dixon, J.E., 2004. Testing models of late palaeozoic–early mesozoic orogeny in western turkey: support for an evolving open-tethys model. Journal of the Geological Society 161, 501–511.

Rockwell, T., Ragona, D., Seitz, G., Langridge, R., Aksoy, M.E., Ucarkus, G., Ferry, M., Meltzner, A.J., Klinger, Y., Meghraoui, M., Satir, D., Barka, A., Akbalik, B., 2009. Palaeoseismology of the North Anatolian Fault near the Marmara Sea: implications for fault segmentation and seismic hazard. Geological Society, London, Special Publications 316, 31–54. URL: https://www.lyellcollection.org/doi/10.1144/SP316.3, doi:10.1144/SP316.3.

Rockwell, T.K., Lindvall, S., Dawson, T., Langridge, R., Lettis, W., Klinger, Y., 2002. Lateral offsets on surveyed cultural features resulting from the 1999 izmit and duzce earthquakes, turkey. Bulletin of the Seismological Society of America 92, 79–94.

Roeloffs, E.A., 2001. Creep rate changes at Parkfield, California 1966–1999: Seasonal, precipitation induced, and tectonic. Journal of Geophysical Research: Solid Earth 106, 16525–16547. URL: https://onlinelibrary.wiley.com/doi/abs/10.1029/2001JB000352, doi:10.1029/2001JB000352. _eprint: https://onlinelibrary.wiley.com/doi/pdf/10.1029/2001JB000352.

Rogers, G., Dragert, H., 2003. Episodic tremor and slip on the cascadia subduction zone: The chatter of silent slip. Science 300, 1942–1943.

Rogers, T.H., Nason, R.D., 1971. Active displacement on the calaveras fault zone at hollister, california. Bulletin of the Seismological Society of America 61, 399–416.

Rolandone, F., Nocquet, J.M., Mothes, P.A., Jarrin, P., Vallée, M., Cubas, N., Hernandez, S., Plain, M., Vaca, S., Font, Y., 2018. Areas prone to slow slip events impede earthquake rupture propagation and promote afterslip. Science advances 4, eaao6596.

Romanet, P., Bhat, H.S., Jolivet, R., Madariaga, R., 2018. Fast and slow slip events emerge due to fault geometrical complexity. Geophysical Research Letters 45, 4809–4819.

Rosen, P.A., Hensley, S., Peltzer, G., Simons, M., 2004. Updated repeat orbit interferometry package released. Eos, Transactions American Geophysical Union 85, 47–47.

Rouet-Leduc, B., Jolivet, R., Dalaison, M., Johnson, P.A., Hulbert, C., 2021. Autonomous extraction of millimeter-scale deformation in insar time series using deep learning. Nature communications 12, 6480.

Rousset, B., Bürgmann, R., Campillo, M., 2019a. Slow slip events in the roots of the san andreas fault. Science advances 5, eaav3274.

Rousset, B., Campillo, M., Lasserre, C., Frank, W.B., Cotte, N., Walpersdorf, A., Socquet, A., Kostoglodov, V., 2017. A geodetic matched filter search for slow slip with application to the mexico subduction zone. Journal of Geophysical Research: Solid Earth 122, 10–498.

Rousset, B., Fu, Y., Bartlow, N., Bürgmann, R., 2019b. Weeks-Long and Years-Long Slow Slip and Tectonic Tremor Episodes on the South Central Alaska Megathrust. Journal of Geophysical Research: Solid Earth 124, 13392–13403. URL: https://onlinelibrary.wiley.com/doi/abs/10.1029/2019JB018724, doi:10.1029/2019JB018724. _eprint: https://onlinelibrary.wiley.com/doi/pdf/10.1029/2019JB018724.

Rousset, B., Jolivet, R., Simons, M., Lasserre, C., Riel, B., Milillo, P., Çakir, Z., Renard, F., 2016. An aseismic slip transient on the North Anatolian Fault. Geophysical Research Letters 43, 3254–3262. URL: https://onlinelibrary.wiley.com/doi/10.1002/2016GL068250, doi:10.1002/2016GL068250.

Rubin, A.M., Ampuero, J.P., 2005. Earthquake nucleation on (aging) rate and state faults. Journal of Geophysical Research: Solid Earth 110.

Ruina, A., 1983. Slip instability and state variable friction laws. Journal of Geophysical Research: Solid Earth 88, 10359–10370.

Ruiz, S., Klein, E., Del Campo, F., Rivera, E., Poli, P., Metois, M., Christophe, V., Baez, J.C., Vargas, G., Leyton, F., et al., 2016. The seismic sequence of the 16 september 2015 m w 8.3 illapel, chile, earthquake. Seismological Research Letters 87, 789–799.

Sakic, P., Piété, H., Ballu, V., Royer, J.Y., Kopp, H., Lange, D., Petersen, F., Özeren, M.S., Ergintav, S., Geli, L., et al., 2016. No significant steady state surface creep along the north anatolian fault offshore istanbul: Results of 6 months of seafloor acoustic ranging. Geophysical Research Letters 43, 6817–6825.

Sarıfakıoğlu, E., Dilek, Y., Sevin, M., 2017. New synthesis of the izmir-ankara-erzincan suture zone and the ankara mélange in northern anatolia based on new geochemical and geochronological constraints .

Şaroğlu, F., Emre, Ö., Kuşçu, İ., 1992. Active fault map of turkey. General Directorate of Mineral Research and Exploration, Ankara, Turkey 2.

Savage, J., Burford, R., 1973. Geodetic determination of relative plate motion in central california. Journal of Geophysical Research 78, 832–845.

Savage, J.C., Burford, R.O., 1970. Accumulation of tectonic strain in California. Bulletin of the Seismological Society of America 60, 1877–1896. URL: https://pubs.geoscienceworld.org/bssa/article/60/6/1877/116823/Accumulation-of-tectonic-strain-in-California, doi:10.1785/BSSA0600061877.

Schmittbuhl, J., Karabulut, H., Lengliné, O., Bouchon, M., 2016a. Long-lasting seismic repeaters in the central basin of the main marmara fault. Geophysical Research Letters 43, 9527–9534.

Schmittbuhl, J., Karabulut, H., Lengliné, O., Bouchon, M., 2016b. Seismicity distribution and locking depth along the main marmara fault, turkey. Geochemistry, Geophysics, Geosystems 17, 954–965.

Scholz, C.H., 1998. Earthquakes and friction laws. Nature 391, 37–42. URL: https://www.nature.com/articles/34097, doi:10.1038/34097. publisher: Nature Publishing Group.

Schurr, B., Asch, G., Hainzl, S., Bedford, J., Hoechner, A., Palo, M., Wang, R., Moreno, M., Bartsch, M., Zhang, Y., et al., 2014. Gradual unlocking of plate boundary controlled initiation of the 2014 iquique earthquake. Nature 512, 299–302.

Segall, P., Matthews, M., 1997. Time dependent inversion of geodetic data. Journal of Geophysical Research 102, 22,391–22,409. doi:10.1029/97JB01795.

Segall, P., Rice, J.R., 1995. Dilational fault slip and earthquake sequence modeling. Journal of Geophysical Research 100, 22155–22163. doi:10.1029/95JB02403.

Segall, P., Rubin, A.M., Bradley, A.M., Rice, J.R., 2010. Dilatant strengthening as a mechanism for slow slip events. Journal of Geophysical Research: Solid Earth 115.

Sekiguchi, H., Iwata, T., 2002. Rupture process of the 1999 kocaeli, turkey, earthquake estimated from strong-motion waveforms. Bulletin of the Seismological Society of America 92, 300–311.

Sengor, A., NATAL'IN, B.A., 1996. 21 paleotectonics of asia: fragments of a synthesis .

Şengör, A., Tüysüz, O., Imren, C., Sakınç, M., Eyidoğan, H., Görür, N., Le Pichon, X., Rangin, C., 2005. The north anatolian fault: A new look. Annu. Rev. Earth Planet. Sci. 33, 37–112.

Şengör, A., Yılmaz, Y., Sungurlu, O., 1984. Tectonics of the mediterranean cimmerides: nature and evolution of the western termination of palaeo-tethys. Geological Society, London, Special Publications 17, 77–112.

Şengör, A.C., Yilmaz, Y., 1981. Tethyan evolution of turkey: a plate tectonic approach. Tectonophysics 75, 181–241.

Shelly, D.R., Beroza, G.C., Ide, S., Nakamula, S., 2006. Low-frequency earthquakes in Shikoku, Japan, and their relationship to episodic tremor and slip. Nature 442, 188–191. URL: https://www.nature.com/articles/nature04931, doi:10.1038/nature04931. publisher: Nature Publishing Group.

Sibson, R., 1992. Implications of fault-valve behaviour for rupture nucleation and recurrence. Tectonophysics 211, 283–293. doi:https://doi.org/10.1016/0040-1951(92)90065-E.

Skarbek, R.M., Rempel, A.W., Schmidt, D.A., 2012. Geologic heterogeneity can produce aseismic slip transients. Geophysical Research Letters 39.

Stein, R.S., Barka, A.A., Dieterich, J.H., 1997. Progressive failure on the North Anatolian fault since 1939 by earthquake stress triggering. Geophysical Journal International 128, 594–604. URL: https://academic.oup.com/gji/article-lookup/doi/10.1111/j.1365-246X.1997.tb05321.x, doi:10.1111/j.1365-246X.1997.tb05321.x.

Steinbrugge, K.V., Zacher, E.G., Tocher, D., Whitten, C.A., Claire, C.N., 1960. Creep on the San Andreas fault. Bulletin of the Seismological Society of America 50, 389–415. URL: https://doi.org/10.1785/BSSA0500030389, doi:10.1785/BSSA0500030389.

Stephenson, R., Schellart, W.P., 2010. The black sea back-arc basin: insights to its origin from geodynamic models of modern analogues .

Sudhaus, H., Jónsson, S., 2009. Improved source modelling through combined use of InSAR and GPS under consideration of correlated data errors: application to the June 2000 Kleifarvatn earthquake, Iceland. Geophysical Journal International 176, 389–404. URL: https://academic.oup.com/gji/article-lookup/doi/10.1111/j.1365-246X.2008.03989.x, doi:10.1111/j.1365-246X.2008.03989.x.

Sun, Y., Cattania, C., 2025. Propagation of slow slip events on rough faults: Clustering, back propagation, and re-rupturing. Journal of Geophysical Research: Solid Earth 130, e2024JB029384.

Tamburini, A., Del Conte, S., Ferretti, A., Cespa, S., 2014. Advanced satellite insar technology for fault analysis and tectonic setting assessment. application to reservoir management and monitoring, in: IPTC 2014: International Petroleum Technology Conference, European Association of Geoscientists & Engineers. pp. cp–395.

Tarantola, A., Valette, B., 1982. Generalized nonlinear inverse problems solved using the least squares criterion. Reviews of Geophysics 20, 219. URL: http://doi.wiley.com/10.1029/RG020i002p00219, doi:10.1029/RG020i002p00219.

Taylor, G., Rost, S., Houseman, G.A., Hillers, G., 2019. Near-surface structure of the North Anatolian Fault zone from Rayleigh and Love wave tomography using ambient seismic noise. Solid Earth 10, 363–378. URL: https://se.copernicus.org/articles/10/363/2019/, doi:10.5194/se-10-363-2019. publisher: Copernicus GmbH.

Tchalenko, J., 1970. Similarities between shear zones of different magnitudes. Geological Society of America Bulletin 81, 1625–1640.

Thatcher, W., Rundle, J.B., 1979. A model for the earthquake cycle in underthrust zones. Journal of Geophysical Research: Solid Earth 84, 5540–5556.

Thollard, F., Clesse, D., Doin, M.P., Donadieu, J., Durand, P., Grandin, R., Lasserre, C., Laurent, C., Deschamps-Ostanciaux, E., Pathier, E., Pointal, E., Proy, C., Specht, B., 2021. FLATSIM: The ForM@Ter LArge-Scale Multi-Temporal Sentinel-1 InterferoMetry Service. Remote Sensing 13, 3734. URL: https://www.mdpi.com/2072-4292/13/18/3734, doi:10.3390/rs13183734.

Thomas, M.Y., Avouac, J.P., Gratier, J.P., Lee, J.C., 2014a. Lithological control on the deformation mechanism and the mode of fault slip on the longitudinal valley fault, taiwan. Tectonophysics 632, 48–63.

Thomas, M.Y., Lapusta, N., Noda, H., Avouac, J.P., 2014b. Quasi-dynamic versus fully dynamic simulations of earthquakes and aseismic slip with and without enhanced coseismic weakening. Journal of Geophysical Research: Solid Earth 119, 1986–2004.

Tibi, R., Bock, G., Xia, Y., Baumbach, M., Grosser, H., Milkereit, C., Karakisa, S., Zünbül, S., Kind, R., Zschau, J., 2001. Rupture processes of the 1999 august 17 izmit and november 12 düzce (turkey) earthquakes. Geophysical Journal International 144, F1–F7.

Titus, S.J., DeMets, C., Tikoff, B., 2006. Thirty-five-year creep rates for the creeping segment of the san andreas fault and the effects of the 2004 parkfield earthquake: Constraints from alignment arrays, continuous global positioning system, and creepmeters. Bulletin of the Seismological Society of America 96, S250–S268.

Tocher, D., 1960. Creep rate and related measurements at vineyard, california. Bull. Seism. Soc. Am. 50, 396–404.

Toksöz, M., Reilinger, R., Doll, C., Barka, A., Yalcin, N., 1999. Izmit (turkey) earthquake of 17 august 1999: first report. Seismological Research Letters 70, 669–679.

Tong, X., Sandwell, D., Smith-Konter, B., 2013. High-resolution interseismic velocity data along the san andreas fault from gps and insar. Journal of Geophysical Research: Solid Earth 118, 369–389.

Topuz, G., Candan, O., Okay, A.I., Von Quadt, A., Othman, M., Zack, T., Wang, J., 2020. Silurian anorogenic basic and acidic magmatism in northwest turkey: Implications for the opening of the paleo-tethys. Lithos 356, 105302.

Tüysüz, O., Tekin, U.K., 2007. Timing of imbrication of an active continental margin facing the northern branch of neotethys, kargı massif, northern turkey. Cretaceous Research 28, 754–764.

Twardzik, C., Vergnolle, M., Sladen, A., Avallone, A., 2019. Unravelling the contribution of early postseismic deformation using sub-daily GNSS positioning. Scientific Reports 9, 1775. URL: https://www.nature.com/articles/s41598-019-39038-z, doi:10.1038/s41598-019-39038-z. publisher: Nature Publishing Group.

Tymofyeyeva, E., Fialko, Y., Jiang, J., Xu, X., Sandwell, D., Bilham, R., Rockwell, T.K., Blanton, C., Burkett, F., Gontz, A., Moafipoor, S., 2019. Slow Slip Event On the Southern San Andreas Fault Triggered by the 2017 M8.2 Chiapas (Mexico) Earthquake. Journal of Geophysical Research: Solid Earth 124, 9956–9975. URL: https://onlinelibrary.wiley.com/doi/abs/10.1029/2018JB016765, doi:10.1029/2018JB016765. _eprint: https://onlinelibrary.wiley.com/doi/pdf/10.1029/2018JB016765.

Umutlu, N., Koketsu, K., Milkereit, C., 2004. The rupture process during the 1999 düzce, turkey, earthquake from joint inversion of teleseismic and strong-motion data. Tectonophysics 391, 315–324.

Usai, S., 2003. A least squares database approach for sar interferometric data. IEEE Transactions on Geoscience and Remote Sensing 41, 753–760.

Ustaömer, P.A., Ustaömer, T., Robertson, A., 2012. Ion probe u-pb dating of the central sakarya basement: a peri-gondwana terrane intruded by late lower carboniferous subduction/collision-related granitic rocks. Turkish Journal of Earth Sciences 21, 905–932.

Utkucu, M., Nalbant, S.S., McCloskey, J., Steacy, S., Alptekin, Ö., 2003. Slip distribution and stress changes associated with the 1999 november 12, düzce (turkey) earthquake (mw= 7.1). Geophysical Journal International 153, 229–241.

Utsu, T., Ogata, Y., et al., 1995. The centenary of the omori formula for a decay law of aftershock activity. Journal of Physics of the Earth 43, 1–33.

Uysal, I.T., Karabacak, V., Aykut, T., Ring, U., Liu, E., Sancar, T., Leonard, N., Tong, K., Todd, A.J., Temel, A., 2025. Was the formation of the north anatolian fault influenced by the aegean extension? Terra Nova .

Vaca, S., Vallée, M., Nocquet, J.M., Battaglia, J., Régnier, M., 2018. Recurrent slow slip events as a barrier to the northward rupture propagation of the 2016 Pedernales earthquake (Central Ecuador). Tectonophysics 724-725, 80–92. URL: https://www.sciencedirect.com/science/article/pii/S0040195117305152, doi:10.1016/j.tecto.2017.12.012.

Vallée, M., Douet, V., 2016. A new database of source time functions (stfs) extracted from the scardec method. Physics of the Earth and Planetary Interiors 257, 149–157.

Vavra, E.J., Fialko, Y., Rockwell, T., Bilham, R., Štěpančíková, P., Stemberk, J., Táborík, P., Stemberk, J., 2024. Characteristic slow-slip events on the superstition hills fault, southern california. Geophysical Research Letters 51, e2023GL107244.

Wallace, L.M., Beavan, J., Bannister, S., Williams, C., 2012. Simultaneous long-term and short-term slow slip events at the hikurangi subduction margin, new zealand: Implications for processes that control slow slip event occurrence, duration, and migration. Journal of Geophysical Research: Solid Earth 117.

Wallace, L.M., Webb, S.C., Ito, Y., Mochizuki, K., Hino, R., Henrys, S., Schwartz, S.Y., Sheehan, A.F., 2016. Slow slip near the trench at the Hikurangi subduction zone, New Zealand. Science 352, 701–704. URL: https://www.science.org/doi/full/10.1126/science.aaf2349, doi:10.1126/science.aaf2349. publisher: American Association for the Advancement of Science.

Walwer, D., Gonzalez-Santana, J., Wauthier, C., Calais, E., Ghil, M., 2025. Multichannel singular spectrum analysis (m-ssa) of insar datasets: data-adaptive interpolation and decomposition of sentinel-1 time series at pacaya volcano, guatemala. Geophysical Journal International , ggaf257.

Wang, K., Bürgmann, R., 2020. Probing fault frictional properties during afterslip updip and downdip of the 2017 mw 7.3 sarpol-e zahab earthquake with space geodesy. Journal of Geophysical Research: Solid Earth 125, e2020JB020319.

Wang, L., Wang, R., Roth, F., Enescu, B., Hainzl, S., Ergintav, S., 2009. Afterslip and viscoelastic relaxation following the 1999 M 7.4 İzmit earthquake from GPS measurements. Geophysical Journal International 178, 1220–1237. URL: https://doi.org/10.1111/j.1365-246X.2009.04228.x, doi:10.1111/j.1365-246X.2009.04228.x.

Weertman, J., Weertman, J.R., 1964. Elementary dislocation theory. (No Title) .

Wei, M., Kaneko, Y., Liu, Y., McGuire, J., 2013. Episodic fault creep events in California controlled by shallow frictional heterogeneity. Nature Geoscience 6, 566–570. doi:10.1038/ngeo1835.

Wei, M., Sandwell, D., Fialko, Y., 2009. A silent M 4.7 slip event of October 2006 on the Superstition Hills fault, southern California. Journal of Geophysical Research: Solid Earth 114. URL: https://onlinelibrary.wiley.com/doi/abs/10.1029/2008JB006135, doi:10.1029/2008JB006135. _eprint: https://onlinelibrary.wiley.com/doi/pdf/10.1029/2008JB006135.

Wei, M., Sandwell, D., Fialko, Y., Bilham, R., 2011. Slip on faults in the Imperial Valley triggered by the 4 April 2010 Mw 7.2 El Mayor-Cucapah earthquake revealed by InSAR. Geophysical Research Letters 38. URL: https://onlinelibrary.wiley.com/doi/abs/10.1029/2010GL045235, doi:10.1029/2010GL045235. _eprint: https://onlinelibrary.wiley.com/doi/pdf/10.1029/2010GL045235.

Weiss, J.R., Walters, R.J., Morishita, Y., Wright, T.J., Lazecky, M., Wang, H., Hussain, E., Hooper, A.J., Elliott, J.R., Rollins, C., et al., 2020. High-resolution surface velocities and strain for anatolia from sentinel-1 insar and gnss data. Geophysical Research Letters 47, e2020GL087376.

Wright, T., Fielding, E., Parsons, B., 2001a. Triggered slip: observations of the 17 august 1999 izmit (turkey) earthquake using radar interferometry. Geophysical Research Letters 28, 1079–1082.

Wright, T., Parsons, B., Fielding, E., 2001b. Measurement of interseismic strain accumulation across the north anatolian fault by satellite radar interferometry. Geophysical Research Letters 28, 2117–2120.

Yabe, S., Ochi, T., Matsumoto, N., Itaba, S., Kitagawa, Y., Matsuzawa, T., 2023. Eight-year catalog of deep short-term slow slip events at the nankai trough based on objective detection algorithm using strain and tilt records. Earth, Planets and Space 75, 1–21.

Yagi, Y., Kikuchi, M., 2000. Source rupture process of the kocaeli, turkey, earthquake of august 17, 1999, obtained by joint inversion of near-field data and teleseismic data. Geophysical Research Letters 27, 1969–1972.

Yamamoto, R., Kido, M., Ohta, Y., Takahashi, N., Yamamoto, Y., Pinar, A., Kalafat, D., Özener, H., Kaneda, Y., 2019. Seafloor geodesy revealed partial creep of the north anatolian fault submerged in the sea of marmara. Geophysical Research Letters 46, 1268–1275.

Yavaşoğlu, H., Tarı, E., Tüysüz, O., Çakır, Z., Ergintav, S., 2011. Determining and modeling tectonic movements along the central part of the north anatolian fault (turkey) using geodetic measurements. Journal of Geodynamics 51, 339–343.

Yıldırım, C., 2014. Relative tectonic activity assessment of the tuz gölü fault zone; central anatolia, turkey. Tectonophysics 630, 183–192.

Yousfi, Z.E., Rousset, B., Radiguet, M., Frank, W.B., 2026. Temperature controls the episodic dynamics of deep slow slip. Proceedings of the National Academy of Sciences 123, e2524741123.

Zali, Z., Martínez-Garzón, P., Mencin, D., Beroza, G., 2025. Slow slip modulates low-frequency seismicity on the san andreas fault .

Zhu, L., Rivera, L.A., 2002. A note on the dynamic and static displacements from a point source in multilayered media. Geophysical Journal International 148, 619–627. URL: https://doi.org/10.1046/j.1365-246X.2002.01610.x, doi:10.1046/j.1365-246X.2002.01610.x.

Çakir, Z., Chabalier, J.B.d., Armijo, R., Meyer, B., Barka, A., Peltzer, G., 2003. Coseismic and early post-seismic slip associated with the 1999 Izmit earthquake (Turkey), from SAR interferometry and tectonic field observations. Geophysical Journal International 155, 93–110. URL: https://academic.oup.com/gji/article-lookup/doi/10.1046/j.1365-246X.2003.02001.x, doi:10.1046/j.1365-246X.2003.02001.x.

Özalaybey, S., Zor, E., Ergintav, S., Tapırdamaz, M.C., 2011. Investigation of 3-D basin structures in the İzmit Bay area (Turkey) by single-station microtremor and gravimetric methods. Geophysical Journal International 186, 883–894. URL: https://doi.org/10.1111/j.1365-246X.2011.05085.x, doi:10.1111/j.1365-246X.2011.05085.x.

Özarpacı, S., Doğan, U., Ergintav, S., Çakır, Z., Özdemir, A., Floyd, M., Reilinger, R., 2020. Present GPS velocity field along 1999 Izmit rupture zone: evidence for continuing afterslip 20 yr after the earthquake. Geophysical Journal International 224, 2016–2027. URL: https://academic.oup.com/gji/article/224/3/2016/5992340, doi:10.1093/gji/ggaa560.

Estelle NEYRINCK

Dynamics of transient aseismic slip along the North Anatolian Fault from InSAR observations

Résumé

La déformation associée au mouvement des plaques tectoniques peut être libérée de manière asismique sous forme de glissements lents transitoires (SSEs), dont les mécanismes restent encore aujourd'hui mal compris. À partir de séries temporelles InSAR dérivées d'images Sentinel-1 traitées dans le cadre du projet FLATSIM, cette thèse détecte, caractérise et modélise des SSEs le long de la faille nord-anatolienne (NAF), en Turquie. Un champ de déformation à grande échelle confirme le glissement asismique superficiel le long des segments d'Izmit et d'Ismetpasa. Une méthode de détection automatique, calibrée par tests synthétiques, identifie cinq événements transitoires sur données réelles, de magnitude 4,0 à 4,5. L'analyse détaillée du segment d'Izmit révèle des SSEs superficiels récurrents tous les ~1,3 ans, localisés dans le bassin sédimentaire. Des modèles de friction *rate-and-state* reproduisent le cycle sismique complet, soulignant le rôle des hétérogénéités frictionnelles superficielles dans la génération des SSEs.

Mots clés : Glissements lents; Faille nord-anatolienne; Glissement asismique; Cycle sismique; Faille décrochante; Aléa sismique

Abstract

Slow slip events (SSEs) represent a key component of the seismic cycle, yet their driving mechanisms remain poorly understood. Using InSAR time series derived from Sentinel-1 images processed within the FLATSIM project, this thesis detects, characterizes, and models transient slow slips along the North Anatolian Fault (NAF), Türkiye. A large-scale deformation field confirms shallow aseismic creep along the Izmit and Ismetpasa segments. An automatic SSE detection method, calibrated with synthetic tests, successfully identifies five transient events on real data, with magnitudes ranging from 4.0 to 4.5. Detailed analysis of the Izmit segment reveals shallow SSEs recurring every ~1.3 years, localized within the sedimentary basin. Rate-and-state friction models reproduce the full seismic cycle, highlighting the role of frictional heterogeneities in driving recurrent SSEs. These results suggest that shallow SSEs along strike-slip faults might share common hydromechanical mechanisms with those observed in subduction zones.

Keywords : InSAR; Slow Slip Events; North Anatolian Fault; Aseismic creep; Seismic cycle; Strike-slip fault; Seismic hazard